SANDIA REPORT

SAND96-8259 • UC–411
Unlimited Release
Printed September 1996

M9705238 6

Mercuric Iodide Sensor Technology

R.B. James, T.E. Schlesinger, R.J. Anderson, A. Antolak, X.J. Bao, G.S. Bench, D. Boehme, B.A. Brunett, G. Buffleben, A. Burger, Y.C. Chang, A.Y. Cheng, K.T. Chen, E. Cross, D.C. David, M. DeVries, V.M. Gerrish, T.S. Gilbert, M. Goorsky, D.W. Heikkinen, H. Hermon, C.-Y. Hung, J.S. Iwanczyk, M. Khudatyan, L.A. Lim, D. S. McGregor, D.L. Medlin, D.H. Morse, M. Natarajan, C. Ortale, B.E. Patt, C. Perrino, A.E. Pontau, M. Roth, L. Salary, M. Schieber, H.K. Sim, E. Soria, R.H. Stulen, L. van den Berg, J.M. Van Scyoc, H. Yao

Prepared by
Sandia National Laboratories
Albuquerque, New Mexico 87185 and Livermore, California 94551
for the United States Department of Energy
under Contract DE-AC04-94AL85000

SAND96-8259
Unlimited Release
Printed September 1996

Distribution
Category UC-411

Mercuric Iodide Sensor Technology

R.B. James[1], T.E. Schlesinger[2], R.J. Anderson[1], A. Antolak[1], X.J. Bao[2,5], G.S. Bench[8], D. Boehme[1], B.A. Brunett[2], G. Buffleben[1], A. Burger[4], Y.-C. Chang[9], A.Y. Cheng[3], K.-T. Chen[4], E. Cross[1], D.C. David[2], M. DeVries[6], V.M. Gerrish[3], T.S. Gilbert[2], M. Goorsky[10], D.W. Heikkinen[8], H. Hermon[1], C.-Y. Hung[2], J.S. Iwanczyk[11], M. Khudatyan[1], L.A. Lim[6], D. S. McGregor[1], D.L. Medlin[1], D.H. Morse[1], M. Natarajan[5], C. Ortale[3], B.E. Patt[11], C. Perrino[1], A.E. Pontau[1], M. Roth[7], L. Salary[4], M. Schieber[1], H.-K. Sim[9], E. Soria[1], R.H. Stulen[1], L. van den Berg[3], J.M. Van Scyoc[1], H. Yao[6]

[1]Sandia National Laboratories, Livermore, CA 94551
[2]Carnegie Mellon University, Pittsburgh, PA 15213
[3]EG&G Energy Measurements, Inc., Goleta, CA 93116
[4]Fisk University, Nashville, TN 37208
[5]TN Technologies, Inc., Round Rock TX 78680
[6]University of Nebraska, Lincoln, NB 68588
[7]The Hebrew University of Jerusalem, Jerusalem, Israel 91440
[8]Lawrence Livermore National Laboratory, Livermore, CA 94550
[9]University of Illinois at Urbana-Champaign, Urbana, IL 61801
[10] University of California at Los Angeles, Los Angeles, CA 90024
[11]Xsirius, Inc. Camarillo, CA 93012

Abstract

This report describes the improvement in the performance and the manufacturing yield of mercuric iodide detectors achieved by identifying the dominant impurities, carrier traps, and processing steps limiting device performance. Theoretical studies of electron and hole transport in this material set fundamental limits on detector performance and provided a standard against which to compare experimental results. Spectroscopic techniques including low temperature photoluminescence and thermally stimulated current spectroscopy were applied to characterize the deep level traps in this material. Traps and defects that can be introduced into the detector during growth, from the contact, and during the various steps in detector fabrication were identified. Trap energy levels and their relative abundances were determined. Variations in material quality and detector performance at the micron scale were investigated to understand the distribution in electric field in large volume detectors suitable for gamma-ray spectroscopy. Surface aging and contact degradation was studied extensively by techniques including atomic force microscopy, transmission electron microscopy, and variable angle spectroscopic ellipsometry. Preferred handling and processing procedures for maximizing detector performance and yield were established. The manufacturing yield of high resolution gamma-ray detectors was improved from a few percent to more than 30%.

Acknowledgment

We gratefully acknowledge the support of the U.S. Department of Energy under contract number DE-AC04-76DP00789. In addition we would like to acknowledge the efforts of the various graduate students and researchers who have contributed to this effort and have helped to make this project a success.

Contents

Preface

The ability to detect and perform energy-dispersive spectroscopy on incident X-rays and gamma-rays is of great importance, since it makes possible a wide variety of analysis and imaging techniques that may have value both commercially as well as to DOE/DP applications. However, the use of this technology has generally been limited to the laboratory since, in the past, the detectors and spectrometers that offered high resolution spectroscopic capabilities were limited to operation at cryogenic temperatures (77 K). These devices included lithium-drifted silicon and high purity germanium. Thus, the widespread application of these and other spectroscopic tools has been limited by the need for a cumbersome cooling apparatus and the constant attention these systems require. Size alone often impedes the use of these systems in some applications.

In recent years the technology of x-ray and gamma-ray detectors that operate at room temperature has greatly improved. The reason for this is that the ability to grow a number of semiconductor materials with the appropriate properties required for high performance spectrometers has been developed. Mercuric iodide (HgI_2) is a leading candidate because its high atomic number and large band gap make it particularly well suited for fabrication of compact spectrometers operating at room temperature. A great deal of effort has been dedicated to the growth of single crystal large volume mercuric iodide which is high resistivity, highly uniform, stoichiometric, and has a minimum of structural and chemical defects. The material and electronic advances that have been made have permitted the production of systems operating at room temperature whose performance rivals that of cryogenically cooled systems in terms of energy resolution, signal-to-noise ratio, collection efficiency, and sensitivity. With the need for expensive and cumbersome cooling apparatus eliminated, these systems can be lightweight, even hand-held, and operate for long periods of time unattended. Some general purpose commercial systems capable of performing x-ray fluorescence spectroscopy over a wide range of elements are now available, as are less expensive systems used for the identification of particular elements such as lead. Practical imaging systems operating at X-ray or gamma-ray energies are only a few years away from realization, and prototype systems have already been demonstrated. The importance of this technology for fields as diverse as national security, treaty verification, medicine, environmental remediation, personal safety, as well as basic science instrumentation should not be underestimated.

However, one of the major obstacles to the widespread use of these mercuric iodide based systems has been the very low manufacturing yield, of only a few percent, of high resolution detectors. This has resulted in very high system costs. This low manufacturing yield has been a result of the presence of impurities and defects that have limited detector performance. These defects are introduced into the material during growth, contact deposition, or at various stages during detector fabrication. The object of this program was to identify the dominant traps and defects limiting detector performance, identify their origin, and by eliminating them, improve the manufacturing yield of high resolution devices. The work that was performed to do this is described in this report and, we note, manufacturing yield of high quality gamma-ray detectors now exceeds 30%.

Summary

The objective of this project was to improve the performance and the manufacturing yield of commercial mercuric iodide detectors by identifying and eliminating the dominant carrier traps limiting device performance. The role of the laboratory personnel and facilities was to coordinate and couple material, and electrical engineering studies with device information obtained through the use of a wide variety of experimental analysis techniques. This work paralleled related efforts at Sandia supporting the development of improved mercuric iodide gamma-ray detectors for military applications. Theoretical studies of the electron and hole transport properties in this material allowed us to set fundamental limits on detector performance and thus provided a standard, based on sound physical principles, against which we were able to compare our experimental results. In particular, limits on the mobility of electrons and holes in this material were established. A variety of spectroscopic techniques including low temperature photoluminescence and thermally stimulated current spectroscopy were applied to characterize the deep level traps in this material. Traps and defects that can be introduced into the detector during growth, from the contact, and during the various steps in detector fabrication were identified. Trap energy levels and their relative abundance after specific growth, processing, or contacting procedures were determined. Some of these traps, especially those related to extrinsic impurities such as copper and silver were shown to be particularly harmful in terms of detector performance while, at the same time, easily incorporated during processing if care is not taken to prevent their introduction. However, it soon became apparent during measurements of the diffusion of these defects into mercuric iodide that the application of an electric field could be used to force these and other extrinsic impurities to drift across large volumes of mercuric iodide. This observation resulted in a patent application related to the electrodrift purification of mercuric iodide source material for improved x-ray and gamma-ray detector performances. Variations in material quality and detector performance at the micron scale were investigated and this has lead to a better understanding of the distribution in the electric field in large volume detectors suitable for gamma-ray spectroscopy. Surface aging and contact degradation was studied extensively by a variety of techniques including atomic force microscopy and variable angle spectroscopic ellipsometry. Thus the work that was performed within the framework of this project led to the establishment of preferred handling and processing procedures for maximizing detector performance. We can unequivocally state that all the milestones established for this program were met or exceeded.

Nomenclature

AES	Auger electron spectroscopy
AFM	atomic force microscopy
DSC	differential scanning calorimetery
HgI_2	Mercuric iodide
ICP-AES	inductively coupled plasma atomic emission spectroscopy
NEST	Nuclear Emergency Search Team
PL	photoluminescence
TAD	triple axis x-ray diffraction
TCT	transient charge technique
TEM	transmission electron microscopy
TSC	thermally stimulated current
VASE	variable angle spectroscopic ellipsometry
Z	atomic mass

Mercuric Iodide Sensor Technology

Introduction

Mercuric iodide (HgI_2) in its red tetragonal form has many properties that make it well suited for use as a gamma- and x-ray spectrometer that can be operated at room temperature.[1-3] These properties include the large atomic masses of its constituent atoms (Z = 80 and 53 for Hg and I, respectively) which allows for a high stopping power to energetic photons, a high bulk resistivity ($\approx 10^{13}$ Ωcm) [4] which ensures a low dark current during detector operation, and a high photosensitivity so that the number of photogenerated electron-hole pairs is proportional to the energy of the incident photon. Although the potential of HgI_2 for fabricating high-resolution x-ray and gamma-ray spectrometers has been well demonstrated,[5] there continues to be significant problems associated with carrier trapping, in which case the amount of charge collected is not a unique function of the gamma- or x-ray energy. These transport problems have motivated considerable research into the electrical and optical properties that might be related to detector performance.[6-8]

Background

Mercuric iodide is a unique material from which nuclear radiation detectors can be fabricated that operate at room temperature and directly measure the number (detection) and energy (spectroscopy) of x-ray and gamma-ray photons that impinge on the detector. This capability in a room temperature detector allows for the production of portable hand-held detector and spectrometer systems that may even be operated for long periods of time in an unattended mode. DOE/Defense Programs have employed semiconductor x-ray and gamma-ray detectors fabricated in silicon or germanium for many years. These devices, while operating well in certain applications, require cryogenic cooling and are thus excluded from operation in a number of arenas vital to DOE/DP where portable compact spectrometers operating at room temperature are required. One of the leading candidate materials for operation at room temperature and with the required cross section for interaction with photons in the 10 keV to 1 MeV range is mercuric iodide. This capability allows for both the detection of the incident photon as well as the identification of the atoms emitting the photons. Specific applications for the use of mercuric iodide instruments include high sensitivity gamma-ray spectrometers that are used to locate nuclear materials by the Nuclear Emergency Search Team (NEST), the verification of nuclear materials in international safeguards, and the satellite detection of nuclear detonations or other radioactive releases. Gamma ray cameras that image nuclear material at gamma-ray energies and allow for the inspection of suspected enclosures without the need to gain access to the enclosure are also critical in arms control and treaty verification applications. Radiation monitors that are compact and hand held can be used for the monitoring of the movement of weapons-grade materials and to facilitate covert search operations. Sandia National Laboratories has projects to develop instruments suitable for all these applications as well as for medical imaging, environmental remediation, nuclear safety, and basic science. The major obstacle to the widespread use of these devices has been the low manufacturing yield of a few percent of ultra-high resolution x- and gamma-ray detectors and the resulting high cost of instruments based on these detectors.

Theoretical Studies

Empirical nonlocal pseudopotential calculations of the electronic band structure of undoped mercuric iodide in its red tetragonal form were performed including the spin-orbit interaction. Both the conduction band minimum and the valence band maximum were found to be at the zone center. Thus mercuric iodide was determined to be a direct gap material. The conduction band was found to be nearly isotropic whereas the valence band was shown to be much more anisotropic. The curvature of the bands near the zone center were used to calculate the electron and hole effective mass and these are presented in table I. Calculated values for the absorption coefficient and real and imaginary parts of the dielectric function were also calculated. The dielectric-function spectra for photon energies between 2 and 10 eV was in fair agreement with the available data. Excitonic effects on the absorption coefficients near the fundamental band gap were included within the effective mass approximation. The absorption spectra and the polarization dependence are in good agreement with experiment and these results are presented in detail in Appendix A.

	$m_{e,\perp}$	$m_{e,\parallel}$	$m^e_\perp$	$m^e_\parallel$	$m_{h,\perp}$	$m_{h,\parallel}$	$m^h_\perp$	$m^h_\parallel$	$\mu_\perp$	$\mu_\parallel$
Theory	0.22	0.30	0.29	0.37	0.59	1.02	0.89	1.43	0.22	0.29
Experiment	0.29[a]	0.25[a]	0.37[a]	0.31[a]	0.56[a]	1.72[a]	1.03[a]	2.06[a]	0.24[b]	0.31[b]

a Reference 9
b Reference 10

Table 1: Effective masses for motion perpendicular to ($\perp$) and parallel to ($\parallel$) the c-axis. The subscripts and superscripts e and h denote the electron and hole, respectively. The subscripts apply to the bare effective masses and the superscripts apply to the polaron effective masses.

Theoretical studies of the phonon modes of undoped mercuric iodide were also conducted. A rigid-ion model including the Coulomb interaction was used which gave the best fit to the neutron scattering, infrared reflectivity, and Raman scattering data. The angular dispersion of the modes was investigated. The calculated sound velocities were also in agreement with the experimental data. It was found that as a result of crystal symmetry TA and TO modes do not coincide at the zone center, whereas LA and LO modes do.

With the electronic states and phonon modes established it was then possible to study the electron-phonon coupling and carrier mobility in mercuric iodide. The effects of deformation potential and polar optical scattering were studied, and the carrier mobilities along both the c- and a-axes as a function of temperature were calculated. The polar-optical phonon scattering dominates the transport properties for low energy carriers which are of interest in the operation of nuclear detectors. For electrons the mobility along the c-axis is slightly higher than perpendicular to the c-axis (see Table I), while the opposite is true for holes. The experimental and theoretical values of mobility for electrons and holes were found to be in good agreement (within a factor of two) when the sample is sufficiently pure and where intrinsic scattering dominates.

Purification of Mercuric Iodide

Inductively Coupled Plasma-Atomic Emission Spectroscopy (ICP-AES) was used to investigate the efficacy of zone refining in the purification of mercuric iodide starting material. The ICP-AES was employed to determine the distribution of impurity concentrations along the ampoule after zone refining, and the results show that for Ag, Cu, Fe, Mg, Ca, Zn, Cr, and Al the zone refining process does sweep the impurities to the last to freeze zone due to an effective distribution coefficient $k_{eff} < 1$. Concentrations of about 75 ppm were observed for these elements. For the rest of the ingot total concentrations of these impurities ranged from a few to no more than 15 ppm. For Na, Ni, Cd, Mn, and Pb the concentration is fairly independent of the position along the ingot and their concentrations range from sub to a few ppm. Differential Scanning Calorimetery (DSC) was also employed to investigate any deviations from stoichiometry that resulted from the zone refining process. It was found that the first to freeze section of the ingot is Hg-rich, the central section of the ingot tends to be slightly Hg-rich, while the last to freeze section becomes I-rich.

Zone refining alone is not sufficient to produce material that is completely free of extrinsic impurities. Indeed, zone refining along with sublimation and solvent extraction, while excellent and commonly used procedures to purify mercuric iodide starting materials, are not ideal given the non-stoichiometry that can develop in material so processed. Non-stoichiometry has been shown to degrade the electronic properties of mercuric iodide particularly in the case of excess mercury[11,12]. We have developed an electrodrift method to further purify starting material for mercuric iodide growth. In this electrodrift process a sample of bulk mercuric iodide is secured in position and contacted at either end by stable high-purity contacts such as thin films of palladium or platinum. A high voltage power supply of sufficient current-sourcing capacity is used to apply a fixed bias across the sample. A current meter is used to monitor the leakage current throughout the process. As extrinsic metallic impurities drift through the sample, a relatively high current is observed initially which eventually decreases to background levels. Inductively coupled plasma mass spectroscopy was used to quantify the level of impurities in the sections taken from either end and from the middle of the sample. Higher concentrations of Ga, Zn, Mg, Pb, As, Na, Al, Rb, and Sr all were seen to develop at either end of the sample while the middle section had the lowest impurity levels. The lower level of impurities results in fewer charge trapping centers, and therefore improved detector performance and stability. A patent application has been submitted for this purification method titled "Electro-drift Purification of Materials for Room Temperature Radiation Detectors". Appendix B details the results of these efforts.

Structure and Surface

The crystalline perfection of mercuric iodide was investigated using triple axis x-ray diffraction (TAD). This technique permits one to analyze the origin of diffraction peak broadening. The effects of strain (due to deviations in alloy composition or stoichiometry) and lattice tilts (mosaic structure) can also be separated. The crystalline perfection of HgI_2 detectors with different spectral response to gamma-radiation was determined. Increased mosaicity was found to be related to decreasing detector performance. In addition deviations from stoichiometry were also found to be related to decreased detector performance. On the other hand mercuric iodide detectors which possessed a well resolved spectral response to gamma-radiation but which also show significant polarization effects (time varying response) were found to be of comparable crystalline quality as high resolution detectors which did not display

any polarization effects. This latter observation suggests that while crystal perfection is required for high resolution spectrometers, polarization is a consequence of native point defects or extrinsic chemical impurities. Overall improved detector performance was always correlated with improved crystallinity.

Variable angle spectroscopic ellipsometry (VASE) and atomic force microscopy (AFM) were also employed to investigate the surface structure of the mercuric iodide. As-grown surfaces, cleaved surfaces, chemically etched (10% KI solution), and parylene coated surfaces were all considered. A model was employed to analyze the data which included a top surface roughness and a subsurface defect layer. Surface aging was characterized as a function of time. The VASE measurements indicated that high surface aging rates were related to high initial densities of two dimensional surface defects. The AFM profiles revealed increasing physical surface roughening as aging proceeded. The cleaved surface presented a smooth surface and the lowest aging rate. Parylene coating decreases the surface aging rate markedly. The mechanism of surface aging has been related to the loss of I from the surface due to its higher vapor pressure. Details of the model used to analyze this data are presented in Appendix C.

TEM studies of the reaction between Pd and mercuric iodide showed that even this most commonly used contact material was not immune from reaction with the mercuric iodide. This work pointed out the need to develop alternative contact technology. Appendix C details the observed reaction products.

Deep Traps and Processing

Low temperature PL, TSC, and transient charge technique (TCT) were all employed to identify features associated with deep level traps and particular metal overlayers or processing steps used in the fabrication of mercuric iodide nuclear detectors. Processing steps considered included chemical etching, vacuum exposure, heating, and a variety of metal depositions. It was shown, for example, that etching with a 10% KI solution removes a surface layer in which there is a significant iodine deficiency. This surface layer could also be removed congruently by vacuum exposure. Thus, placing a sample of mercuric iodide in a vacuum system for contact deposition is an excellent method of ensuring a stoichiometric surface during processing. The signature of an iodide deficient surface was seen to be the ratio of two emission lines in the low temperature PL spectrum of this material. The P2/P3 ratio (as these two lines are labeled) increases as iodine deficiency increases. A variety of contact materials were investigated in terms of their stability on mercuric iodide and also to determine whether particular metals are correlated with particular deep traps in the material. Some of the metals investigated and the trap characteristics observed are summarized in table 2 below. Low temperature PL measurements also showed emission features that could be associated with Cu, Ag, Cr, and C. Excess Hg and I_2 as well as naphthalene, butane, heavy paraffins, polyethylene, and polyethylene glycol were also studied as dopants in HgI_2 and the deep traps related to these identified. These latter dopants and inert hydrocarbons were seen to affect the crystalline perfection and thereby the nuclear spectrometer response of the detectors.

Contact	T_1	T_2	T_3	T_5	T_6	T_8	T_{10}

Cu	T_m (K)			116		161		
	β (K/s)			0.51		0.34		
	comments			h		h		
Ag	T_m (K)	90	96				212	
	β (K/s)	0.27	0.39				0.14	
	comments							
Al	T_m (K)	83		119	146	170		
	β (K/s)	0.24		0.48	0.38	0.30		
	comments							
Mg	T_m (K)				147	162	206	273
	β (K/s)				0.39	0.35	0.25	0.16
	comments					e		e
Au	T_m (K)						193	
	β (K/s)						0.28	
	comments						h	
Ni	T_m (K)	89			147	166	202	
	β (K/s)	0.21			0.39	0.33	0.24	
	comments				e	e	h	
In	T_m (K)	87		119	150	168		
	β (K/s)	0.24		0.56	0.39	0.33		
	comments							
Sn	T_m (K)				149	163		
	β (K/s)				0.44	0.40		
	comments							
Pd	T_m (K)				149	163		
	β (K/s)				0.44	0.40		
	comments					e		
Cr	T_m (K)				144	157	211	
	β (K/s)				0.10	0.086	0.048	
	comments							
ITO	T_m (K)		95	113	144	165	213	
	β (K/s)		0.59	0.61	0.35	0.35	0.29	
	comments			h		e		

Table 2: Summary of traps observed by TSC in this work. The labels "e" and "h" indicate whether the center is believed to be an electron or hole trap.

When polarization effects were not present in the sample, that is, the material was relatively free of extrinsic impurities, it was possible to measure the Schottky barrier height associated with the metal contact using internal photoemission measurements. Thus, in the case of Pd, we observed a hole barrier of approximately 1.05 eV at the Pd/HgI_2 interface.

These measurements showed that particular traps are related to individual metals or particular processing steps. In addition these traps can be detrimental to detector performance, and care must be taken during processing to prevent the in-diffusion of these materials or the generation of defects related to the fabrication process.

Devices

Mercuric iodide detectors and spectrometers were fabricated and their degradation was studied as a consequence of the introduction of the types of impurities and defects investigated above. In particular both Cu and Ag were shown to be fast diffusers in mercuric iodide, commonly present in the material, easily incorporated during processing, and extremely detrimental to device operation. Copper diffusion was studied by low temperature PL and Auger electron spectroscopy (AES). A broad radiative emission at a wavelength of about 6720 Å in the PL spectra was found to be characteristic of the presence of Cu. Cu was shown to be present in the mercuric iodide if Cu electrodes were used in device fabrication or if Cu was present at doping levels in any etching solution or other materials brought in contact with the detector. AES was performed as a function of depth from the crystal surface, and the test results confirmed that Cu is a fast diffuser in this material. Mercuric iodide detectors with Cu electrodes were fabricated and tested with an ^{241}Am source. The photopeak expected in the spectrum of this source was not observed and the leakage current was observed to be quite high in the device. This was a dramatic demonstration of the degree to which high concentrations of a particular impurity can completely destroy spectrometer operation.

In a related set of studies, Ag was introduced into mercuric iodide spectrometers that employed Pd electrodes in the device structure. As the spectrometer was biased a large leakage current was initially observed, which then decreased over time. If the bias was reversed, the observed leakage current would increase again, initially, and then decrease over time. In addition, the measured pulse height spectrum of an ^{241}Am source was found to vary with the observed changes in the leakage current. The pulse height spectrum would improve over time as the sample was maintained under bias. If the bias was reversed, the sample would again display a very poorly resolved pulse height spectrum which would improve over time. It was concluded that these observations, which are discussed in greater detail in appendix E, are the consequence of mobile Ag atoms drifting across the detector under the influence of the externally applied bias.

Finally, large volume detectors (1x1x1 cm^3) were mapped in terms of their photocurrent response using optical excitation in a cross-sectional geometry. The photocurrent was measured as a function of position on a micron scale, and the observed variations in the photocurrent as a function of position between the contacts was described using a model which accounts for the charge transport in the material. While order of magnitude agreement was obtained between the calculated and observed photocurrent as a function of applied bias it was clear that the large volume detectors suffered from a nonuniform electric field internally and that this is an issue that must be investigated in more detail. Origins of nonuniform fields can include poor contact uniformity, material nonstoichiometry, and the presence and nonuniform distribution of charged defects. The method that was developed to map photocurrent can be applied to other materials and with other excitation sources and is already proving to be useful in understanding the operation of x-ray and gamma-ray spectrometers in these systems as well.

Conclusions

The state of the art in spectrometers and detectors employing mercuric iodide has been advanced markedly. Fabrication yield of high quality gamma-ray detectors now typically exceeds 30%. In addition, the understanding of the approaches that will be fruitful in overcoming barriers to further improvement of this material and these detectors has been made clear. A patent application has been submitted titled; "Electro-drift Purification of Materials for Room Temperature Radiation Detectors". Sandia National Laboratories now maintains active research collaborations with a number of industrial and academic institutions which have grown out of this as well as other efforts related to this technology. A recent workshop on this topic hosted by Sandia (California) included over seventy participants representing most of the country's organizations who are currently working in this technology area. These interactions have allowed Sandia National Laboratories to effectively leverage the efforts it maintains in this field.

References

[1] W.R. Willig, *Nucl. Instrum. Methods* **96**, 615(1971).

[2] J.P. Ponpon, R. Stuck, P. Siffert, B. Meyer, and C. Schwab, *IEEE Trans. Nucl. Sci.* **NS-22**, 182(1975).

[3] A.J. Dabrowski, W.M. Szymczyk, J.S. Iwanczyk, J.H. Kusmiss, W. Drummond, and L. Ames, *Nucl. Instrum. Methods* **213**, 89(1983).

[4] H. L. Malm, T.W. Raudoff, M. Martina, and K.R. Zanio, *IEEE Trans. Nucl. Sci.* **NS-20**, 500(1973).

[5] See, for example, the review by R.C. Whited and M. Schieber, *Nucl. Instrum. Methods* **162**, 119(1979).

[6] B.V. Novikov and M.M. Pimonenko, *Fiz. Tekh. Poluprovodn.* **4**, 2077(1970) [*Sov. Phys. Semicond.* **4**, 1785(1970)]

[7] J.C. Muller, A. Friant, and P. Siffert, *Nucl. Instrum. Methods* **150**, 97(1978).

[8] R.B. James, X.J. Bao, T.E. Schlesinger, J.M. Markakis, A.Y. Cheng, C. Ortale *J. Appl. Phys.* **66**, 2578(1989).

[9] I.Ch. Schluter and M. Schluter, *Phys. Rev. B.* **9**, 1652(1974).

[10] T. Goto and A. Kasuya, *J. Soc. Jpn.* **50**, 520(1981).

[11] R.C. Whited and L. van den Berg, *IEEE Trans. Nucl. Sci.* **NS-24**, 165(1977).

[12] M. Schieber, H. Hermon, and M. Roth, in *Semiconductors for Room-Temperature Radiation Detector Applications,* Materials Research Society Symposium Proceedings **302**, 347(1993).

APPENDIX A

Theoretical Studies

Left Intentionally Blank

PHYSICAL REVIEW B VOLUME 46, NUMBER 23 15 DECEMBER 1992-I

Electronic and optical properties of HgI_2

Yia-Chung Chang
Department of Physics, University of Illinois at Urbana-Champaign, 1110 West Green Street, Urbana, Illinois 61801 and Materials Research Laboratory, University of Illinois at Urbana-Champaign, 1110 West Green Street, Urbana, Illinois 61801

R. B. James
Advanced Material Research Division, Sandia National Laboratories, Livermore, California 94550
(Received 28 February 1992)

Empirical nonlocal pseudopotential calculations of the electronic band structure of undoped mercuric iodide in its red tetragonal form are presented. Values for the electron and hole effective masses, optical matrix elements for interband transitions, and complex dielectric function are reported. Excitonic effects on the absorption coefficient near the fundamental band gap are included within the effective-mass approximation. The resulting absorption spectra and the polarization dependence are in good agreement with experiment. The dielectric-function spectra for photon energies between 2 and 10 eV are also calculated and they are in fair agreement with available data.

I. INTRODUCTION

Mercuric iodide (HgI_2) in its red tetragonal form has many properties that make it well suited for use as a γ- and x-ray spectrometer that can be operated at room temperature.[1–5] These properties include relatively large atomic masses (i.e., $Z = 80$ and 53 for Hg and I, respectively) which allows for a high stopping power to energetic photons, a high bulk resistivity ($\approx 1013\ \Omega\,\mathrm{cm}$) (Ref. 6) which ensures a low dark current during detector operation, and a high photosensitivity so that the number of photogenerated electron-hole pairs is proportional to the energy of the incident photon. Although the potential of HgI_2 for fabricating high-resolution x-ray and γ-ray spectrometers has been well demonstrated,[7] there continues to be significant problems associated with carrier trapping, in which case the amount of charge collected is not a unique function of the γ- or x-ray energy. These transport problems have motivated considerable research in the optical and electrical properties of HgI_2, particularly those properties that might be related to detector performances.[8–24]

There have been numerous experimental reports on the optical properties of HgI_2.[8–11,16,17] However, theoretical investigations on this subject are still lacking. One difficulty frequently encountered in interpreting the optical and electrical measurements is the lack of knowledge of the electronic band structure of the material. Yee, Sherohman, and Armantrout reported the first empirical pseudopotential calculation on HgI_2.[25] Unfortunately, the crystal structure used in their calculations is incorrect; thus, their results bear little relation with reality. Turner and Harmon[26] reported the first self-consistent calculation within the local-density approximation. They also included the relativistic effect and the spin-orbit interaction. The overall band structures obtained by this method are quite reliable, except that the fundamental band gap is too small due to the local-density approximation. As a result, the effective masses predicted by this calculation are also too small. In this paper, we report an empirical nonlocal pseudopotential calculation of the electronic and optical properties of HgI_2, including the effects of the spin-orbit interaction. Values for the effective masses and real and imaginary part of the complex dielectic function are also presented.

II. METHOD

The method used here is basically the same as that described in Ref. 27. The local pseudopotentials of the mercury and iodine are taken to have the form introduced in Ref. 28. Namely,

$$V_L(\mathrm{q}) = a_1(q^2 - a_2)/(e^{a_3(q^2-a_4)} + 1). \quad (1)$$

The parameters a_2, a_3, and a_4 for I are taken to be the same as given in Ref. 28, and those for Hg are determined by fitting the screened atomic pseudopotential given in Ref. 29. These parameters for both Hg and I are tabulated in Table I. The parameter a_1 which determines the strength of the pseudopotential is treated as an empirical parameter. The nonlocal pseudopotentials are taken to have the form given in Ref. 27,

TABLE I. Empirical parameters for Hg and I local pseudopotentials defined in Eq. (1). The units of distances are in Bohrs and the energy units are in Rydbergs.

	a_1	a_2	a_3	a_4
Hg	0.35	1.4	0.55	−2.5
I	5.294	1.7	0.46	−6.5

$$V_{\rm NL}(\mathbf{k},\mathbf{G}-\mathbf{G}')$$

$$= 4\pi \sum_l (2l+1) P_l(\cos\theta) \times \int dr\, r^2 V_l(r) j_l(Kr) j_l(K'r)/\Omega_a, \qquad (2)$$

where $\mathbf{K} = \mathbf{k}+\mathbf{G}$, $\cos\theta = \mathbf{K}\cdot\mathbf{K}'/KK'$, Ω_a is the atomic volume, P_l is a Legendre polynomial, j_l is a spherical Bessel function, and $V_l(r) = A_l e^{-(r/R)^2}$. We use $R = 2.3a_B$, where a_B is the Bohr radius. A_l is an adjustable parameter for each value of l. Since the states of interest are either s-like or p-like, we only keep $l = 0$ and 1. In order to fit the energy spacing between the heavy-hole and light-hole states due to the tetragonal crystal field, we introduce an anisotropy factor μ, which modifies the spherical local pseudopotential to describe a tetragonal one, i.e.,

$$V_L(q_x, q_y, q_z) \rightarrow V_L(q_x, q_y, \mu q_z).$$

Thus we have seven empirical parameters: a_1, A_0, A_1 for both Hg and I plus the anisotropy factor μ. These parameters are adjusted to fit the band gap to the experimental value (2.37 eV) (Ref. 8) and the overall band structure to the results obtained by a first-principles calculation.[26] The optimized parameters are listed in Tables I and II. In our calculations, approximately 620 plane waves with energies less than E_1 (=8 Ry) are included in the diagonalization procedure. Here Ry denotes a rydberg.

The unit cell consists of two Hg atoms and four I atoms (see Ref. 26). The solid has inversion symmetry about the midpoint between the two Hg atoms in a unit cell. If we choose the point as the origin of the coordinate system, the atomic positions of the two Hg atoms are $(-a/4, -a/4, -c/4)$ and $(a/4, a/4, c/4)$, and those of the four I atoms are $(-a/4, a/4, -0.111c)$, $(a/4, -a/4, 0.111c)$, $(-a/4, a/4, 0.389c)$, and $(a/4, -a/4, -0.389c)$. Here, $a = b = 4.37$ Å and $c = 12.44$ Å. With the inversion symmetry, the Hamiltonian matrix elements between any two plane waves are real, and the eigenvalue problem can be solved efficiently.

When the spin-orbit interaction is included, the Hamiltonian matrix becomes complex and its dimension is doubled. This makes the direct diagonalization very time consuming. We thus elect to include the spin-orbit-interaction effects by first-order degenerate perturbation theory. We first evaluate the matrix elements of the spin-orbit term using the zero-order eigenstates of the lowest-lying 30 bands (or 60 bands including the spin degeneracy). We then diagonalize the 60×60 complex matrix to obtain the energy eigenvalues which include the effect of spin-orbit interaction. The matrix elements of the spin-orbit term for p-like states are given by[28,30]

$$\langle \mathbf{K}, s | H_{\rm so} | \mathbf{K}', s' \rangle = -i \sum_j \lambda_j S_j(\mathbf{K}-\mathbf{K}') \sigma_{ss'} \cdot (\mathbf{K}\times\mathbf{K}'),$$

where the subscript j denotes the atomic species (Hg or I), S_j is the structure factor, $\sigma_{ss'}$ are elements of the Pauli matrices between two spin states s and s', and λ_j is the atomic spin-orbit coupling parameter, which is adjusted to give the correct spin-orbit splitting at the zone center. We found that the most appropriate value for λ is 0.023 (in units of $\mathrm{Ry}a_B^2$).

The imaginary part of the dielectric function (ϵ_2) is given by[31]

$$\epsilon_2(\omega) = \frac{4\pi^2 e^2}{m^2 V \omega^2} \sum_{\mathbf{k},ij} |\langle \mathbf{k}, i | \hat{e}\cdot\mathbf{p} | \mathbf{k}, j\rangle|^2 \times \delta[E_j(\mathbf{k}) - E_i(\mathbf{k}) - \hbar\omega], \qquad (3)$$

where $|\mathbf{k}, i\rangle$ denotes the ith electronic state of the solid associated with wave vector $\mathbf{k}$, $\hat{e}$ is the polarization vector, $\mathbf{p}$ is the momentum operator, and V is the volume of the solid. To perform the sum in Eq. (3), we used 75 special points in the irreducible $\frac{1}{16}$ section of the first Brillouin zone, and the δ function was replaced by a Lorentzian function with half-width of 0.1 eV to account for lifetime broadening of the electrons and holes.

III. RESULTS

Figure 1 shows the calculated band structure of HgI_2 without including the spin-orbit interaction. The band structure has been rigidly shifted by a constant so that the energy of the valence-band maximum is zero after inclusion of the spin-orbit interaction effects. Since the space group of the crystal is D_{4h}, the states with x- and y-like symmetry are degenerate at the zone center, whereas states with s-like and z-like symmetry are nondegenerate. Throughout the paper, we have chosen the z direction to be parallel to the c axis of the crystal. In Fig. 1 we see

TABLE II. Empirical parameters for Hg and I nonlocal pseudopotentials defined in Eq. (2) and the anisotropy factor squared, μ^2. All energy parameters are in units of Rydbergs.

	A_0	A_1	μ^2
Hg	−0.575	0.0	1.06
I	−0.9	−0.4	1.06

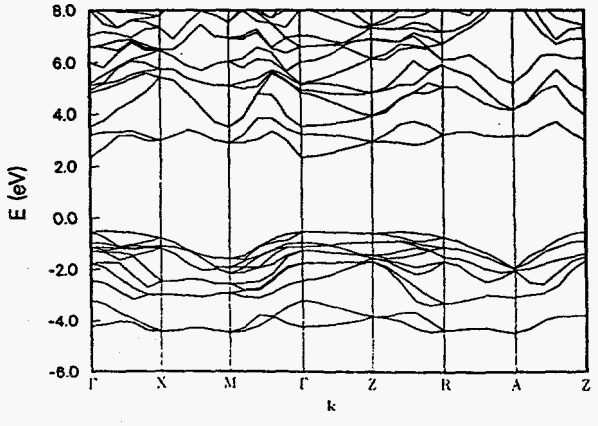

FIG. 1. Band structures of HgI_2 without spin-orbit interaction.

four pairs of doubly degenerate levels at the zone center with energies between −2 and 0 eV. They correspond to the I $5p_x$ and $5p_y$ nonbonding states (see Ref. 26). The two nondegenerate levels near −1.5 and −2.5 eV correspond to the I $5p_z$ nonbonding states. The two remaining I $5p_z$ orbitals interact with the two Hg $6s$ orbitals to form two bonding states with energies between −4.5 and −3 eV and two antibonding states with energies between 2.3 and 3.5 eV. The I $5s$ levels are near −11 eV (not shown). The Hg $6p$ and I $5d$ levels are distributed from 3.5 to 10 eV, among which the doubly degenerate ones can be identified as the Hg p_x and p_y states. Note that the Hg $5d$ levels, which are between the I $5s$ and Hg $6s$–I $5p_z$ bonding states, are considered as core levels in the present pseudopotential model. Hence, they will not show up in the band structure.

Figure 2 shows the calculated band structure of HgI_2 with the spin-orbit interaction. All bands are rigidly shifted by a constant so that the valence-band maximum is at zero. The main difference between this figure and Fig. 1 is that the doubly degenerate levels at zone center in Fig. 1 are now split by the spin-orbit interaction with a splitting of ≈ 0.7 eV. With the adjusted parameters listed in Tables I and II, the fundamental band gap becomes 2.37 eV and the splitting between the first two valence bands (i.e., heavy-hole and light-hole bands) is 0.2 eV, which both agree with the measured values at 4.2 K.[8,9] The overall band structures are also in qualitative agreement with those obtained by Turner and Harmon.[26]

Figure 3 shows the closeup view of the band structures of HgI_2 near the zone center. In the left part the wave vector k is along the [110] direction, and in the right part it is along the [001] direction. The unit of k is in $2\pi/a$. We have found that the conduction band is nearly isotropic, whereas the valence band is more anisotropic. The effective masses deduced from this plot are shown in Table III, together with the experimental values. The agreement between theory and experiment is fairly good. The polaron masses (m^e and m^h) are obtained by an intermediate-coupling polaron theory with the use of LO-phonon energies and high-freqency and low-frequency anisotropic dielectric constants as provided in Ref. 11. The theory predicts that $m_{e,\parallel} > m_{e,\perp}$, while the cyclotron-resonance measurements found the opposite. On the other hand, the values deduced from optical measurements[17] seem to support our prediction.

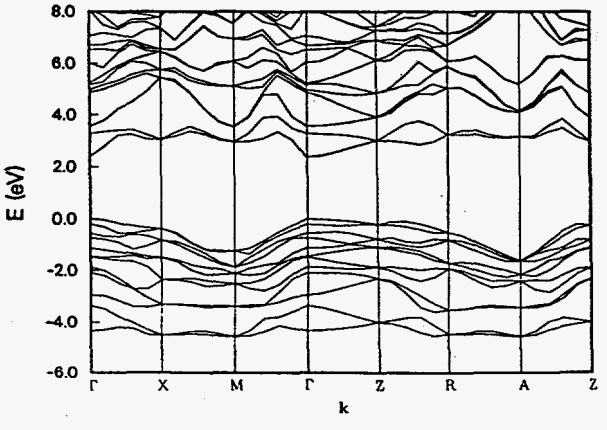

FIG. 2. Band structures of HgI_2 with spin-orbit interaction.

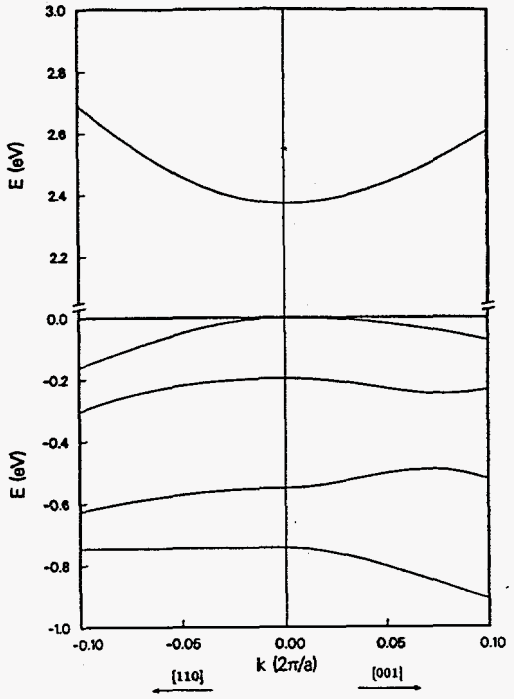

FIG. 3. Band structures of HgI_2 near the zone center.

Figure 4 shows the squared optical matrix elements P^2 for interband transitions involving the topmost five valence bands and the lowest conduction band near the zone center. Here P^2 is defined as

$$P_{ij}^2 = \frac{2}{m}|\langle \mathbf{k}, i|\hat{e}\cdot\mathbf{p}|\mathbf{k}, j\rangle|^2. \tag{4}$$

The solid curves are for the in-plane polarization ($\hat{e}\perp\hat{z}$) and the dashed curves are for polarization along the c axis ($\hat{e}\|\hat{z}$). The labels $v1,...,v5$ denote the first to fifth valence band. We see that for the $v1$ curve, the z-polarization component is very weak for all values of k and vanishes at the zone center. This is consistent with the heavy-hole character, since the heavy-hole state transforms like $(x+iy)\uparrow$. Here $\uparrow$ denotes an up spin. For the $v2$ curve, the z component is strong and the x (or y) component is about $\frac{1}{6}$ of that for the $v1$ curve. This is consistent with the nature of the light-hole state, since the light-hole state is the linear combination of states transforming like $(x+iy)\downarrow$ and $z\uparrow$ with a majority component in $z\uparrow$. It should be noted that the optical matrix elements calculated by using the pseudo-wave-functions are not precise, because the corrections due to orthogonalization to the core electronic states are not included. The size of the correction is difficult to estimate. However, based on a comparison between the experimental value and the calculated value within the pseudopotential method for

TABLE III. Effective masses for motion perpendicular to ($m_\perp$) and parallel to the c axis ($m_\parallel$). The subscripts and superscripts e and h denote electron and hole, respectively. The subscripts apply to the bare effective masses and the superscript apply to the polaron effective masses.

	$m_{e,\perp}$	$m_{e,\parallel}$	$m^e_\perp$	$m^e_\parallel$	$m_{h,\perp}$	$m_{h,\parallel}$	$m^h_\perp$	$m^h_\parallel$	$\mu_\perp$	$\mu_\parallel$
Theory	0.22	0.30	0.29	0.37	0.59	1.02	0.89	1.43	0.22	0.29
Experiment	0.29[a]	0.25[a]	0.37[a]	0.31[a]	0.56[a]	1.72[a]	1.03[a]	2.06[a]	0.24[b]	0.31[b]

[a]Reference 28.
[b]Reference 17.

typical semiconductors (see Ref. 31), the error in optical responses is about 10–20 %.

Knowing the optical matrix elements and effective masses near the zone center, we can model the absorption coefficient near the fundamental band gap, including the excitonic effect. This is done within the effective-mass approximation. The effective-mass Hamiltonian for the exciton in an anisotropic medium is

$$H_{ex} = -\frac{1}{2\mu_\perp}(\partial_x^2 + \partial_y^2) - \frac{1}{2\mu_\parallel}\partial_z^2 - \frac{e^2}{\epsilon_a r}, \tag{5}$$

where $\mathbf{r}$ is the electron-hole relative coordinate, ϵ_a is some average dielectric constant, which will be determined later, and $\mu_\perp$ and $\mu_\parallel$ are the in-plane and c-axis reduced effective masses, respectively. They are related to the corresponding electron and hole polaron masses via

$$\frac{1}{\mu_{\perp,\parallel}} = \frac{1}{m^e_{\perp,\parallel}} + \frac{1}{m^h_{\perp,\parallel}}.$$

The predicted reduced polaron masses are also shown in Table III.

The eigenstates for an anisotropic Hamiltonian can be solved by numerical methods.[32] However, for our purposes here, it suffices to use a spherical approximation in which the anisotropic reduced mass is replaced by a spherically averaged reduced mass given by[33]

$$\frac{1}{\mu_a} = \left(\frac{2}{\mu_\perp} + \frac{1}{\mu_\parallel}\right)\Big/ 3.$$

In this approximation, the exciton binding energy is given by $E_X = (\mu_a/m_0\epsilon_a^2)13.6$ eV. We choose a value for ϵ_a such that E_X is equal to the experimental value of 0.032 eV.[17] We found that $\epsilon_a \approx 10.1$, which is between the average low-frequency and high-frequency dielectric constants.[11] In the spherical effective-mass theory, the absorption coefficient for each pair of conduction and valence bands is given by[31]

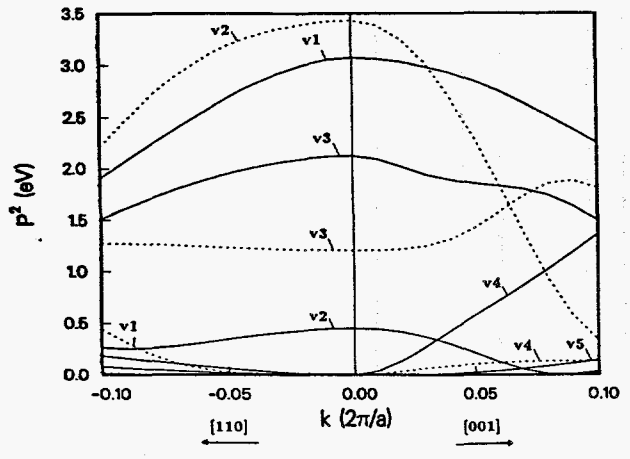

FIG. 4. Optical matrix elements near the zone center for interband transitions.

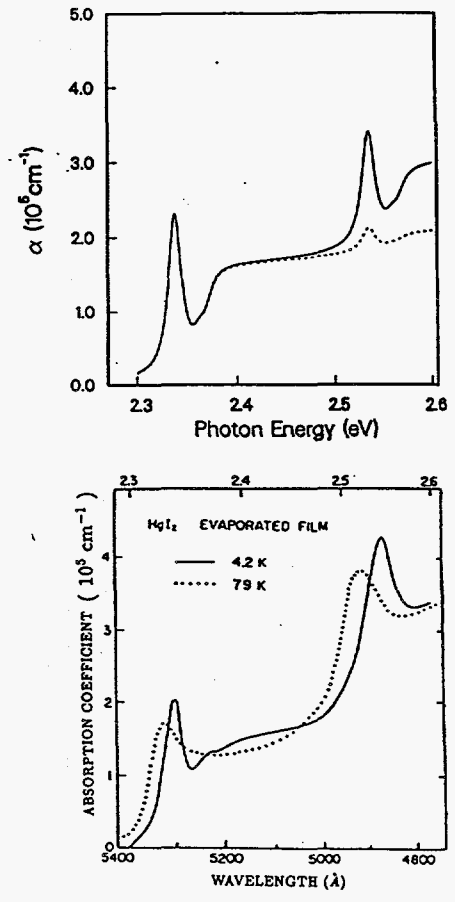

FIG. 5. Absorption spectra of HgI_2 near the fundamental absorption edge. Top: theoretical prediction; the solid curve is for unpolarized light and the dashed curve is for light polarized perpendicular to the c axis. Bottom: data from Ref. 26; both curves are for unpolarized light.

$$\alpha(\omega) = \frac{4\pi^2 e^2}{mcnV\omega} \times P^2 \left[(2m/\hbar^2)^{3/2} \pi E_X e^u / \sinh u + \sum_n |\phi_n(0)|^2 \delta(\hbar\omega - E_g + E_X/n^2) \right], \quad (6)$$

where P^2 is the squared optical matrix element defined in Eq. (4) and evaluated at the zone center, $u = \pi[E_X/(\hbar\omega - E_g)]^{1/2}$, E_g denotes the band gap, n denotes the principal quantum number for the exciton bound states, and $\phi_n(0)$ is the exciton envelope function evaluated at the origin for the nth bound state. Using Eq. (6) and including the $n = 1$ and 2 exciton bound states, we obtain an absorption spectrum for HgI_2 near the fundamental gap as shown in Fig. 5. Both the transitions from the heavy-hole and light-hole bands to the lowest conduction band are included. The binding energies of the heavy-hole and light-hole excitons are both taken to be 0.032 eV.[6] The solid curve shows the absorption spectrum for an unpolarized light, and the dashed curve shows the contribution due to the in-plane polarization alone (i.e., $\frac{2}{3}\alpha_\perp$, where $\alpha_\perp$ is the absorption coefficient for a linearly polarized light with $\hat{e} \perp \hat{z}$). Note that here

$$\alpha = (2\alpha_\perp + \alpha_\parallel)/3,$$

where $\alpha_\parallel$ is the absorption coefficient for a linearly polarized light with $\hat{e} \parallel \hat{z}$. The broadening parameter used is 0.008 eV. In Fig. 5 we have also included for comparison the experimental absorption coefficient for unpolarized light from Ref. 9. The calculated spectrum for the heavy-hole exciton agrees very well with experiment, while for the light-hole exciton, the calculated spectrum is about a factor of 2 too low compared to the experiment. We notice that the heavy-hole exciton absorption is nonzero only for light polarized perpendicular to the c axis, while the light-hole exciton absorption is nonzero for both polarizations with $\alpha_\parallel$ much stronger than $\alpha_\perp$. This is in qualitative agreement with the reflectivity measurement.[9]

Figure 6 shows the calculated dielectric-function spectra of HgI_2. The solid (dashed) curve is for polarization perpendicular (parallel) to the c axis. The ϵ_2 spectrum shows two major structures, centered around 4 and 7 eV, respectively. This is in qualitative agreement with the experimental results.[10] However, the height of the first structure is about a factor of 2 too small compared to data, whereas the integrated strength of the second strucure is too high. The calculated results shown here did not include the excitonic and local-field effects, which tend to enhance the lower-energy structure and reduce the higher-energy structure. These effects can be included approximately and empirically by using a "contact" excitonic potential with adjustable strength.[34] The corrected dielectric function ($\tilde{\epsilon}$) (i.e., including the exciton and local-field effects) is related to the "bare" dielectric function by[34,35]

$$\tilde{\epsilon}(\omega) - 1 = \frac{\epsilon(\omega) - 1}{1 - g_0\hbar^2\omega^2[\epsilon(\omega) - 1]}.$$

Here g_0 is an empirical parameter.

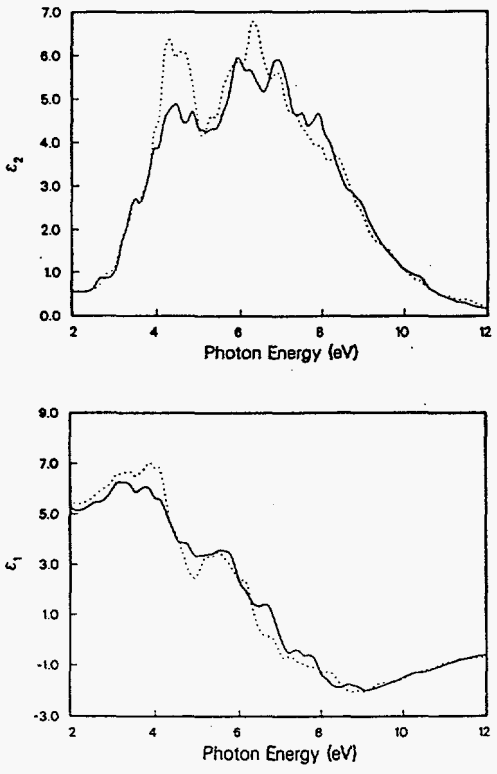

FIG. 6. Dielectric functions of HgI_2. Solid: $\hat{e} \perp \hat{z}$. Dotted: $\hat{e} \parallel \hat{z}$. Top: imaginary part. Bottom: real part.

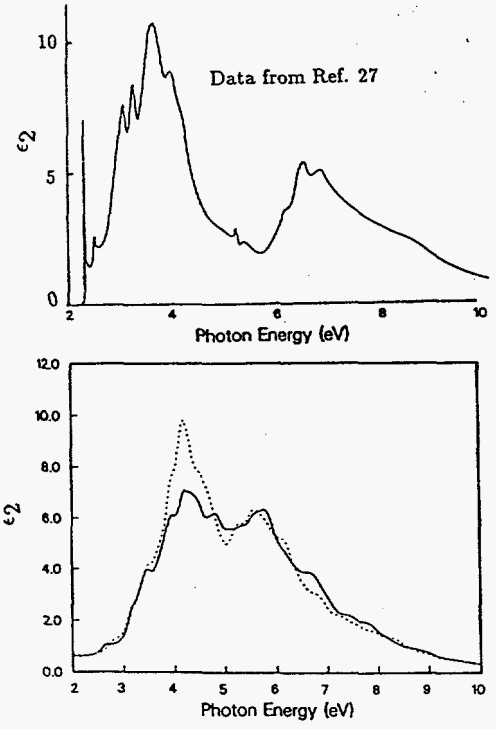

FIG. 7. Comparison of the imaginary part of the dielectric functions of HgI_2 between theory (bottom) and experiment (top). Data are taken from Ref. 27. For the bottom two curves, solid is for $\hat{e} \perp \hat{z}$ and dotted is for $\hat{e} \parallel \hat{z}$.

We found that with $g_0 \approx 0.003$ eV^{-2}, the corrected dielectric function is in better agreement with the experiment. This is shown in Fig. 7, in which we also include the experimental results obtained by Anedda *et al.* (Ref. 10). However, after including the exciton effects, the second structure becomes peaked at 6 eV, which is about 1 eV lower than the experimental value. The first structure is still too low compared to data, but the integrated strength is roughly correct. The real part of the dielectric constant is also slightly enhanced near the fundamental band gap. We get $\epsilon_\perp \approx 5.4$ and $\epsilon_\parallel \approx 5.8$ near the band gap, wheras the experimental values are $\epsilon_\perp \approx 5.15$ and $\epsilon_\parallel \approx 6.8$.[11]

IV. SUMMARY AND CONCLUSIONS

We have performed empirical nonlocal pseudopotential calculations on the electronic and optical properties of HgI_2, including the spin-orbit interaction. Both the conduction-band minimum and valence-band maximum are found to occur at the zone center. The conduction band is nearly isotropic, whereas the valence band is much more anisotropic. The curvatures of the bands near the zone center are used to calculate electron and hole effective masses, and comparisons with experiment are noted. Calculated values for the absorption coefficient and real and imaginary parts of the dielectric function are also presented.

ACKNOWLEDGMENTS

We acknowlege fruitful discussions with C. Y. Fong. We also thank D. N. Harmon for sending us some unpublished results, which have helped us greatly.

[1]W. R. Willig, Nucl. Instrum. Methods **96**, 615 (1971).
[2]J. P. Ponpon, R. Stuck, P. Siffert, B. Meyer, and C. Schwab, IEEE Trans. Nucl. Sci. **NS-22**, 182 (1975).
[3]A. J. Dabrowski, W. M. Szymczyk, J. S. Iwanczyk, J. H. Kusmiss, W. Drummond, and L. Ames, Nucl. Instrum. Methods **213**, 89 (1983).
[4]S. P. Swierkowski, G. A. Armantrout, and R. Wichne, IEEE Trans. Nucl. Sci. **NS-21**, 302 (1974).
[5]J. H. Howes and J. Watling, in *Nuclear Radiation Detector Materials*, edited by E. E. Haller, H. W. Kramer, and W. A. Higinbotham, MRS Symposia Proceedings No. 16 (Materials Research Society, Pittsburgh, 1983), p. 207.
[6]H. L. Malm, T. W. Raudoff, M. Martina, and K. R. Zanio, IEEE Trans. Nucl. Sci. **NS-20**, 500 (1973).
[7]See, for example, the review by R. C. Whited and M. Schieber, Nucl. Instrum. Methods **162**, 119 (1979).
[8]B. V. Novikov and M. M. Pimonenko, Fiz. Tekh. Poluprovodn. **4**, 2077 (1970) [Sov. Phys. Semicond. **4**, 1785 (1970)].
[9]K. Kanzaki and I. Imai, J. Soc. Jpn. **32**, 1003 (1972).
[10]A. Anedda, F. Raga, E. Grilli, and M. Guzzi, Nuovo Cimento **38**, 439 (1977).
[11]P. D. Bloch, J. W. Hodby, C. Schwab, and D. W. Stacey, J. Phys. C **11**, 2579 (1978).
[12]C. Dlasi, S. Galassini, C. Manfredotti, G. Micocci, L. Ruggiero, and A. Tepore, Nucl. Instrum. Methods **150**, 103 (1978).
[13]U. Gelbert, Y. Yacoby, I. beinglass, and A. Holzer, IEEE Trans. Nucl. Sci. **NS-24**, 135 (1977).
[14]J. C. Muller, A. Friant, and P. Siffert, Nucl. Instrum. Methods **150**, 97, (1978).
[15]M. Schieber, I. Beinglass, G. Dishon, A. Holzer, and G. Yaron, Nucl. Instrum. Methods **150**, 71 (1978).
[16]A. Anedda, E. Grilli, M. Guzzi, F. Raga, and A. Serpi, Solid State Commun. **39**, 1121 (1981).
[17]T. Goto and A. Kasuya, J. Soc. Jpn. **50**, 520 (1981).
[18]S. R. Kurtz, R. C. Hughes, C. Ortale, and W. F. Schnepple, J. Appl. Phys. **62**, 4308 (1987).
[19]D. Wong, X. J. Bao, T. E. Schlesinger, R. B. James, A. Cheng, C. Ortale, and L. van den Berg, Appl. Phys. Lett. **53**, 1536 (1988).
[20]R. B. James, X. J. Bao, T. E. Schlesinger, J. M. Markakis, A. Y. Cheng, and C. Ortale, J. Appl. Phys. **66**, 2578 (1989).
[21]R. B. James, X. J. Bao, T. E. Schlesinger, C. Ortale, and L. van den Berg, J. Appl. Phys. **67**, 2571 (1990).
[22]X. J. Bao, T. E. Schlesinger, R. B. James, R. H. Stulen, C. Ortale, and L. van den Berg, J. Appl. Phys. **68**, 86 (1990).
[23]L. R. Williams, R. J. M. Anderson, and M. J. Banet, Chem. Phys. Lett. **182**, 422 (1991).
[24]X. J. Bao, T. E. Schlesinger, R. B. James, G. L. Gentry, A. Y. Cheng, and C. Ortale, J. Appl. Phys. **69**, 4247 (1991).
[25]J. H. Yee, J. W. Sherohman, and G. A. Armantrout, IEEE Trans. Nucl. Sci. **NS-23**, 117 (1976).
[26]D.E. Turner and B. N. Harmon, Phys. Rev. B **40**, 10 516 (1989).
[27]J. R. Chelikowsky and M. L. Cohen, Phys. Rev. B **14**, 556 (1976).
[28]I. Ch. Schluter and M. Schluter, Phys. Rev. B **9**, 1652 (1974).
[29]G. B. Brandt and J. A. Rayne, Phys. Rev. **148**, 644 (1966).
[30]G. Weisz, Phys. Rev. **149**, 504 (1966).
[31]F. Bassani and C. P. Parrasvacini, *Electronic States and Optical Properties in Solids* (Pergamon, New York, 1975).
[32]R. A. Faukner, Phys. Rev. **184**, 713 (1965).
[33]W. Kohn, in *Solid State Physics*, edited by F. Seitz and D. Turbull (Academic, New York, 1964), Vol. 5, p. 257.
[34]J. E. Rowe and D. E. Aspnes, Phys. Rev. Lett. **25**, 162 (1970).
[35]R. M. Martin, J. A. Van Vechten, J. E. Rowe, and D. E. Aspnes, Phys. Rev. B **6**, 2500 (1972).

MATERIALS RESEARCH SOCIETY SYMPOSIUM PROCEEDINGS VOLUME 302

Semiconductors For Room-Temperature Radiation Detector Applications

Symposium held April 12-16, 1993, San Francisco, California, U.S.A.

EDITORS:

R.B. James
Sandia National Laboratories
Livermore, California, U.S.A.

T.E. Schlesinger
Carnegie Mellon University
Pittsburgh, Pennsylvania, U.S.A.

Paul Siffert
Laboratorie PHASE/CRN
Strasbourg, France

Larry Franks
EG&G Energy Measurements
Goleta, California, U.S.A.

MRS
MATERIALS RESEARCH SOCIETY
Pittsburgh, Pennsylvania

ELECTRONIC AND OPTICAL PROPERTIES OF HgI_2

YIA-CHUNG CHANG*, HOCK-KEE SIM*,†, and R. B. JAMES**
*Department of Physics and Materials Research Laboratory, University of Illinois at Urbana-Champaign, 1110 West Green Street, Urbana, Illinois 61801
† Department of Physics, National University of Singapore, Singapore 0511
**Advanced Material Research Division, Sandia National Laboratories, Livermore, CA 94550

ABSTRACT

We present theoretical studies of electronic structures, optical responses, and phonon modes of undoped HgI_2 in its red tetragonal form. The electronic band structure is studied via an empirical nonlocal pseudopotential model, including the spin-orbit interaction. The electron and hole effective masses, optical matrix elements for interband transitions, and complex dielectric function are computed. Excitonic effects on the absorption coefficient near the fundamental band gap are included within the effective-mass approximation. The resulting absorption spectra and their polarization dependence are compared with experiment with favorable agreement. The phonon modes of HgI_2 are studied with a microscopic model and a good fit to the neutron scattering data is obtained.

Electronic structures

We first present an empirical nonlocal pseudopotential calculation of the electronic and optical properties of HgI_2, including the effects of the spin-orbit interaction. Details of the calculations have been presented elsewhere.[1] In this paper, we only summarize the important results.

The unit cell of HgI_2 consists of two Hg atoms and four I atoms (see Figure 1). The solid has inversion symmetry about the mid point between the two Hg atoms in a unit cell. With the inversion symmetry, the Hamiltonian matrix elements between any two plane waves are real, and the eigenvalue problem can be solved efficiently. The parameters for describing the local and nonlocal pseudopotentials are adjusted to fit the experimental band gap, the heavy-hole light-hole splitting, and the over-all band structures calculated by a first-principle method.[2]

Figure 2 shows the calculated band structure of HgI_2 including the spin-orbit interaction. All bands are rigidly shifted by a constant so that the valence band maximum is at zero. Throughout the paper, we have chosen the z direction to be parallel to the c axis of the crystal. In Figure 2, we see four pairs of doubly degenerate levels at the zone center with energies between -2 and $0eV$. They correspond to the I $5p_x$ and $5p_y$ non-bonding states (see Ref. 2). The two non-degenerate levels near $-1.5eV$ and $-2.5eV$ correspond to the I $5p_z$ non-bonding states. The two remaining I $5p_z$ orbitals interact with the two Hg $6s$ orbitals to form two bonding states with energies between $-4.5eV$ and $-3eV$ and two antibonding states with energies between $2.3eV$ and $3.5eV$. The I $5s$ levels are near $-11eV$ (not shown). The Hg $6p$ and I $5d$ levels are distributed from $3.5eV$ to $10eV$, among which the doubly degenerate ones can be identified as the Hg p_x and p_y states. Note that the Hg $5d$ levels, which are between the I $5s$ and Hg$6s$-I$5p_z$ bonding states, are considered as core levels in the present pseudopotential model. Hence, they will not show up in the band structure. The spin-orbit splittin

for valence-band states at the zone center is around $0.7eV$. The fundamental band gap is $2.37eV$ and the splitting between the first two valence bands (i.e. heavy-hole and light-hole bands) is $0.2eV$, which both agree with the measured values at $4.2K$.[3] The over-all band structures are also in qualitative agreement with those obtained by Turner and Harmon[2].

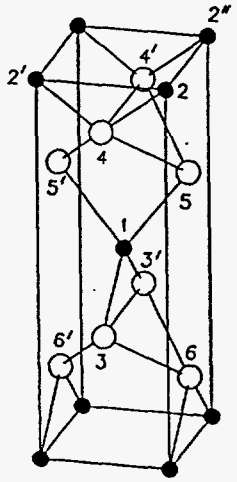

Fig. 1. Crystal structure of HgI_2.

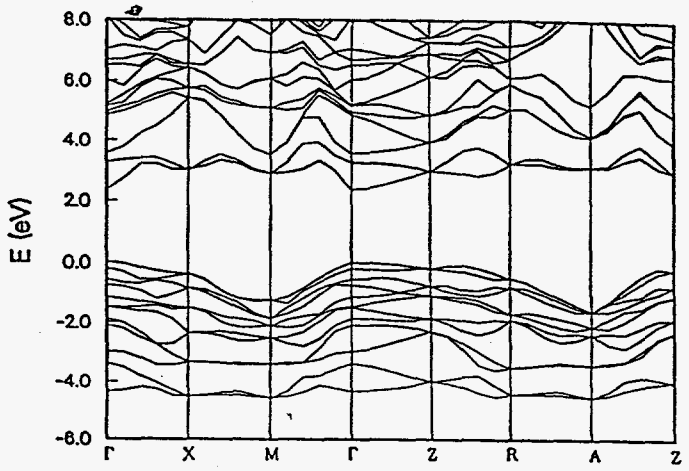

Fig. 2. Band structures of HgI_2.

Figure 3 shows the close-up view of the band structures of HgI_2 near the zone center. In the left part the wave vector $\vec{k}$ is along the [110] direction, and in the right part it is along the [001] direction. The unit of k is in $2\pi/a$. We have found that the conduction band is nearly isotropic, whereas the valence band is more anisotropic. The effective masses deduced from this plot are shown in Table I, together with the experimental values. The agreement between theory and experiment is fairly good. The polaron masses (m^e and m^h) are obtained by an intermediate-coupling polaron theory with the use of LO phonon energies and high-frequency and low-frequency anisotropic dielectric constants as provided in Ref. 4. The theory predicts that $m_{e,\|} > m_{e,\perp}$, while the cyclotron-resonance measurements found the opposite. On the other hand, the values deduced from optical measurements[5] seem to support our prediction.

Table I. Effective masses for motion perpendicular to ($m_\perp$) and parallel to the c axis ($m_\|$). The subscripts and superscripts e and h denote electron and hole, respectively. The subscripts apply to the bare effective masses and the superscript apply to the polaron effective masses.

	$m_{e,\perp}$	$m_{e,\|}$	$m^e_\perp$	$m^e_\|$	$m_{h,\perp}$	$m_{h,\|}$	$m^h_\perp$	$m^h_\|$	$\mu_\perp$	$\mu_\|$
Theory	0.22	0.30	0.29	0.37	0.59	1.02	0.89	1.43	0.22	0.29
Experiment	0.29[a]	0.25[a]	0.37[a]	0.31[a]	0.56[a]	1.72[a]	1.03[a]	2.06[a]	0.24[b]	0.31[b]

a. Ref. 4, *b*. Ref. 5.

Optical properties

The absorption coefficient near the fundamental band gap including the excitonic effect is calculated within a spherical effective-mass approximation.[6] In this approx-

imation, the exciton binding energy is given by $E_X = (\mu_a/m_0\epsilon_a^2)13.6eV$, where μ_a is the spherically averaged reduced mass given by $\frac{1}{\mu_a} = (\frac{2}{\mu_\perp} + \frac{1}{\mu_\parallel})/3$. $\mu_\perp$ and $\mu_\parallel$ are the reduced masses perpendicular and parallel to the c-axis. We choose a value for ϵ_a such that E_X is equal to the experimental value of $0.032eV$.[3] We found that $\epsilon_a \approx 10.1$, which is between the average low-frequency and high-frequency dielectric constants.[4] In the spherical effective-mass theory, the absorption coefficient for each pair of conduction and valence bands is given by[7]

$$\alpha_{ij}(\omega) = \frac{4\pi^2 e^2}{mcnV\omega} P_{ij}^2[(2m/\hbar^2)^{3/2}\pi E_X e^u/\sinh u + \sum_n |\phi_n(\vec{0})|^2 \delta(\hbar\omega - E_g + E_X/n^2)], \quad (1)$$

where P_{ij}^2 is the squared optical matrix element defined by $P_{ij}^2 = \frac{2}{m}| < \vec{k}, i|\hat{e}\cdot\vec{p}|\vec{k}, j > |^2$ and evaluated at the zone center, $u = \pi[E_X/(\hbar\omega - E_g)]^{1/2}$, E_g denotes the band gap, n denotes the principal quantum number for the exciton bound states, and $\phi_n(\vec{0})$ is the exciton envelope function evaluated at the origin for the nth bound state. Using Eq. (1) and including the $n = 1$ and $n = 2$ exciton bound states, we obtain an absorption spectrum for HgI_2 near the fundamental gap as shown in Figure 4. Both the transitions from the heavy-hole and light-hole bands to the lowest conduction band are included. The binding energies of the heavy-hole and light-hole excitons are both taken to be $0.032eV$.[6] The solid curve shows the absorption spectrum for an unpolarized light, and the dashed curve shows the contribution due to the in-plane polarization alone (i.e. $\frac{2}{3}\alpha_\perp$, where $\alpha_\perp$ is the absorption coefficient for a linearly polarized light with $\hat{e} \perp \hat{z}$). Note that here $\alpha = (2\alpha_\perp + \alpha_\parallel)/3$, where $\alpha_\parallel$ is the absorption coefficient for a linearly polarized light with $\hat{e}\parallel\hat{z}$. The broadening parameter used is $0.008eV$. The calculated spectrum for the heavy-hole exciton agrees very well with data reported in Ref. 3, while for the light-hole exciton, the calculated spectrum is about a factor two too low compared to the experiment. We notice that the heavy-hole exciton absorption is nonzero only for light polarized perpendicular to the c axis, while the light-hole exciton absorption are nonzero for both polarizations with $\alpha_\parallel$ much stronger than $\alpha_\perp$. This is in qualitative agreement with the reflectivity measurement.[3]

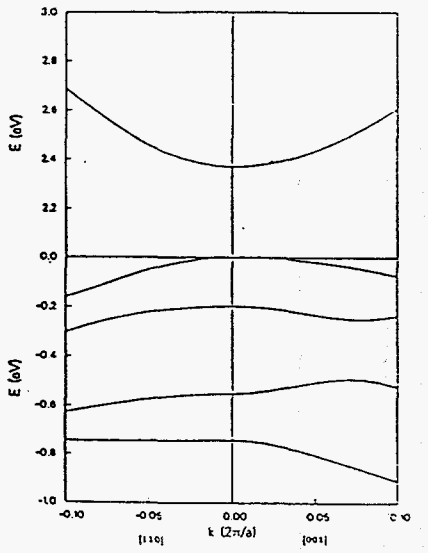

Fig. 3. Band structures of HgI_2 near the zone center.

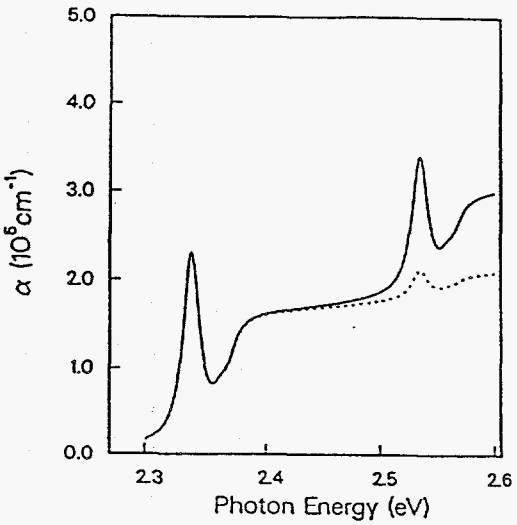

Fig. 4. Absorption spectra of HgI_2 near the fundamental absorption edge.

The imaginary part of the dielectric function (ϵ_2) is given by[7]

$$\epsilon_2(\omega) = \frac{4\pi^2 e^2}{m^2 V \omega^2} \sum_{\vec{k},ij} | < \vec{k},i|\hat{e}\cdot\vec{p}|\vec{k},j > |^2 \delta(E_j(\vec{k}) - E_i(\vec{k}) - \hbar\omega), \quad (2)$$

where $|\vec{k},i>$ denotes the i-th electronic state of the solid associated with wave vector $\vec{k}$, $\hat{e}$ is the polarization vector, $\vec{p}$ is the momentum operator, and V is the volume of the solid. Seventy-five special points in the irreducible $\frac{1}{16}$th section of the first Brillouin zone are used in performing the sum over $\vec{k}$, and the delta function was replaced by a Lorentzian function with halfwidth of 0.1 eV to account for lifetime broadening of the electrons and holes.

The exciton and local-field effects are included empirically by using a "contact" excitonic potential with adjustable strength.[8] The corrected dielectric function ($\tilde{\epsilon}$) is related to the "bare" dielectric function by[8,9]

$$\tilde{\epsilon}(\omega) - 1 = \frac{\epsilon(\omega) - 1}{1 - g_0\hbar^2\omega^2[\epsilon(\omega) - 1]}.$$

Here g_0 is an empirical parameter. We found that with $g_0 \approx 0.003 eV^{-2}$, the corrected dielectric function is in resonable agreement with the experiment. This is shown in Figure 5, in which we also include the experimental results obtained by Anedda et al (Ref. 10). There are two major peak structures in the spectrum. The first structure obtained theoretically is too low compared to data, but the integrated strength is roughly correct. The second structure predicted theoretically has approximately the right strength, but the peak position is about 1 eV lower than the measured peak. The perpendicular and parallel components of the real part of the dielectric constant near the fundamental band gap are predicted to be $\epsilon_\perp \approx 5.4$ and $\epsilon_\parallel \approx 5.8$, whereas the experimental values are $\epsilon_\perp \approx 5.15$ and $\epsilon_\parallel \approx 6.8$.[4]

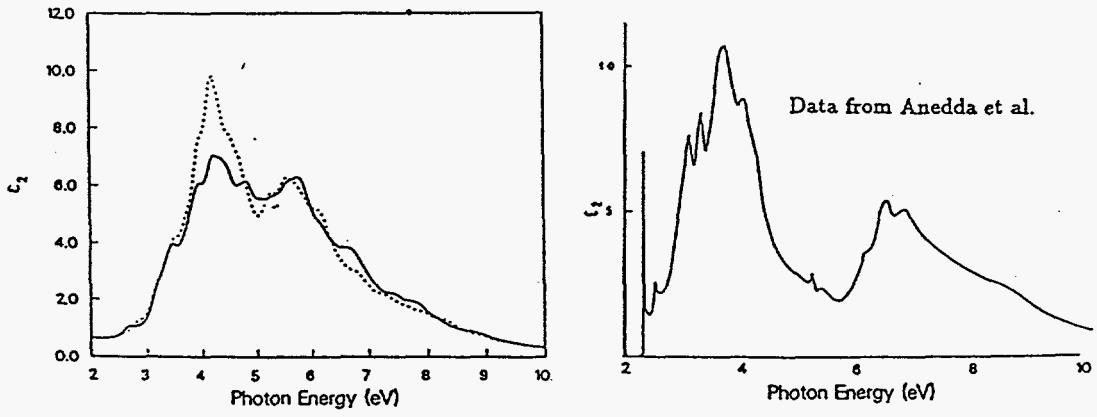

Fig. 5. Comparison of the imaginary part of the dielectric functions of HgI_2 between theory (left) and experiment (right). Data are taken from Ref. 10. For the bottom two curves, solid is for $\hat{e} \perp \hat{z}$ and dotted is for $\hat{e} \| \hat{z}$.

Phonon modes

The phonon frequencies of HgI_2 are calculated by a rigid-ion model similar to that described in Ref. 11. The point group of the system is $\{E, \sigma_1, \sigma_2, S_1, S_2, S_3, \sigma_2 S_1, S_1\sigma_2\}$, where E is the identity, σ_1 (σ_2) is a reflection about the y-z (x-z) plane, S_1 is a 90^0 rotation about the z axis followed by a reflection about the x-y plane, $S_2 = S_1^2$,and $S_3 = S_1^3$. In addition, the system has inversion symmetry about the mid point connecting two Hg atoms. The group theory analysis for HgI_2 structure has been reported in Ref. 12. With the use of symmetry, the dynamic matrices are given by (The indices for ions are shown in Figure 1)
for nearest-neighbor Hg-I interactions:

$$\Phi(1,5) = \begin{pmatrix} A_1 & 0 & 0 \\ 0 & B_1 & D_1 \\ 0 & E_1 & C_1 \end{pmatrix} = \sigma_2\Phi(1,5')\sigma_2^{-1} = \sigma_1\Phi(1,3)\sigma_1^{-1} = S_1\Phi(1,3')S_1^{-1}, \tag{3}$$

for nearest-neighbor I-I interactions:

$$\Phi(3,6) = \begin{pmatrix} A_2 & D_2 & E_2 \\ D_2 & B_2 & F_2 \\ E_2 & F_2 & C_2 \end{pmatrix} = \sigma_2\Phi(3,6')\sigma_2^{-1} = \sigma_1\Phi(3',6)\sigma_1^{-1} = S_1\Phi(5,4')S_1^{-1} \tag{4}$$

for nearest-neighbor Hg-Hg interactions:

$$\Phi(2,2') = \begin{pmatrix} A_3 & 0 & 0 \\ 0 & B_3 & D_3 \\ 0 & -D_3 & C_3 \end{pmatrix} = \sigma_1 S_1\Phi(2,2'')S_1^{-1}\sigma_1^{-1} = \Phi(1,1') \tag{5}$$

and for second nearest-neighbor I-I interactions:

$$\Phi(3,3') = \begin{pmatrix} A_4 & 0 & -D_4 \\ 0 & B_4 & 0 \\ D_4 & 0 & C_4 \end{pmatrix} = S_1\Phi(5,5')S_1^{-1}. \tag{6}$$

$$\Phi(4,4') = \begin{pmatrix} A_5 & 0 & -D_5 \\ 0 & B_5 & 0 \\ D_5 & 0 & C_5 \end{pmatrix} = S_1\Phi(6,6')S_1^{-1}. \tag{7}$$

The other dynamic matrices not listed here can be obtained by symmetry operations similar to ones described above. Two constraints are imposed due to the translational invariance:

$$2(A_1 + B_1 + A_2 + B_2) + A_3 + B_3 + A_4 + B_4 + A_5 + B_5 = 0,$$

$$2(C_1 + C_2) + C_3 + C_4 + C_5 = 0.$$

Thus, we have 21 independent adjustable parameters for the short-range interactions. The long-range Coulomb interaction is calculated by the Ewald method with $2e^*$ on Hg ions and $-e^*$ on I ions, where e^* is the effective charge transfer. We treat e^{*2}/ϵ as another adjustable parameter, where ϵ is the dielectric constant. The lowest six phonon branches fitted to the neutron scattering data[13] are shown in Figure 6. The branches are labeled by LA(x,y,z), TA(x,y,z), LO(x,y,z), TO(x,y,z), where LA, TA, LO, and TO denote the longitudinal-acoustic, transverse-acoustic, longitudinal-optic, and

transverse-optic respectively. It is convenient to consider symmetric and antisymmetric sums of displacements for atoms connected by the inversion center, namely those labeled by 1 and 2, 3 and 6, or 4 and 5 (see Fig. 1). For acoustic modes only symmetric sums appear whereas for optic modes only antisymmetric sums are present. x, y, z inside parentheses denote the primary direction for lattice vibrations. Along the Λ direction ([001]) the fit is excellent. The TA branch is not available in Ref. 13; thus, no constraints are imposed on the TA modes in our fitting procedure. It is interesting to note that although the TA and TO frequencies appear to coincide with each other at Z, they really do not. This is a consequence of the symmetry of the crystal, since all irreducible representations are two-dimensional for the space group at Z (see Ref. 12). On the other hand, the LA and LO frequencies do coincide at Z. Along the Δ direction ([100]), the over-all fit is good except that the theory predicts too big a gap between the fourth and fifth branches near $k_x = 0.15\frac{2\pi}{a}$. The irreducible representations for the space group along Δ are denoted Δ_1, Δ_2, Δ_3, Δ_4 (all one dimensional). TA(y) and TO(y) modes have Δ_2 and Δ_3, respectively. Both LA(x) and TO(z) modes have Δ_1 symmetry, thus they are coupled strongly when their frequencies are close, leading to an "anti-crossing" pattern in dispersion curve at $k_x = 0.15\frac{2\pi}{a}$ (see Fig. 6). The coupling strength between these two modes appear to be too strong in the theoretical calculation. All modes are doubly degenerate at X, since the irreducible representations for the space group at X are all two dimensional. The seventh and eighth branches cross the fifth and sixth branches at $k_x > 0.5\frac{2\pi}{a}$. These two branches are ignored when compared with neutron scattering data. It is unclear whether these two branches should have been observed by neutron scattering.

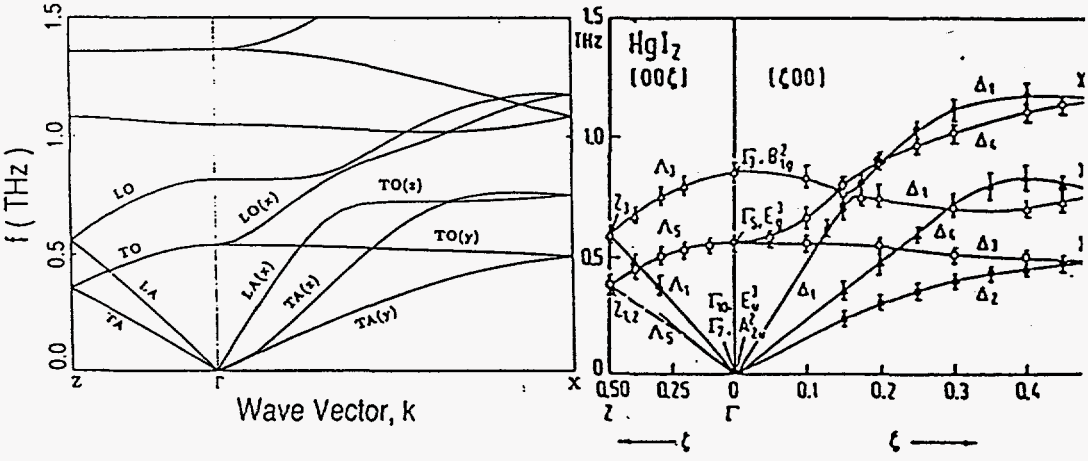

Fig. 6. Phonon dispersion curves for the lowest six branches deduced from the rigid-ic model (left) and from the neutron scattering data of Ref. 13 (right).

Summary

We have performed empirical nonlocal pseudopotential calculations on the electronic and optical properties of HgI_2, including the spin-orbit interaction. Both the conduction band minimum and valence band maximum are found to occur at the zone center. The conduction band is nearly isotropic, whereas the valence band is much more anisotropic. Calculated values for the effective masses, exciton oscillator strengths and dielectric functions are all in fairly good agreement with available data. The phonon dispersion curves for the lowest six branches are calculated via the rigid-ion model. With 22 adjustable parameters, the fit to the neutron scattering data is satisfactory.

Acknowledgments

We acknowledge fruitful discussions with C. Y. Fong. We also thank D. N. Harmon for sending us some unpublished results, which have helped us greatly.

References

[1] Y. C. Chang and J. B. James, Phys. Rev. B 46, 15040 (1992).
[2] D.E. Turner and B. N. Harmon, Phys. Rev. B 40, 10516 (1989).
[3] K. Kanzaki and I. Imai, J. Soc. Japan, 32, 1003 (1972).
[4] P. D. Bloch, J. W. Hodby, C. Schwab, and D. W. Stacey, J. Phys. C: Solid State Phys. 11, 2579 (1978).
[5] T. Goto and A. Kasuya, J. Soc. Japan 50, 520 (1981).
[6] W. Kohn, *Solid State Physics*, edited by F. Seitz and D. Turbull (Academic, New York, 1964), Vol. 5, p. 257.
[7] F. Bassani and C. P. Parrasvacini, *Electronic States and Optical Properties in Solids* (Pergammon, New York, 1975).
[8] J. E. Rowe and D. E. Aspnes, Phys. Rev. Lett. 25, 162 (1970).
[9] R. M. Martin, J. A. Van Vechten, J. E. Rowe, and D. E. Aspnes, Phys. Rev. B6, 2500 (1972).
[10] A. Anedda, F. Raga, E. Grilli, and M. Guzzi, Il Nuovo Cimento 38, 439 (1977).
[11] K. Kunc, Ann. Phys. (paris) 8, 319 (1973).
[12] M. Sieskind, J. Phys. Chem. Solids, 39, 1251 (1978).
[13] B. Prevot, C. Schwab, and B. Dorner, Phys. Stat. Sol. (b) 88, 327 (1978).

APPENDIX B

Purification of Mercuric Iodide

Left Intentionally Blank

Phonon dispersion in red mercuric iodide

Hock-Kee Sim* and Yia-Chung Chang
Department of Physics and Materials Research Laboratory, University of Illinois at Urbana-Champaign, Urbana, Illinois 61801

R. B. James
Physical Sciences Department, Sandia National Laboratories, P. O. Box 969, Livermore, California 94550
(Received 28 June 1993)

We present theoretical studies of phonon modes of undoped HgI_2 in its red tetragonal form. A rigid-ion model including the Coulomb interaction is used which gives the best fit to the neutron scattering, infrared reflectivity, and Raman scattering data. The calculated sound velocities are also in accord with experiment.

I. INTRODUCTION

Red mercuric iodide (HgI_2) is a semiconductor which shows great potential for γ- and x-ray-spectrometry applications.[1–24] The electronic structures of the system have recently been studied by a relativistic linearized augmented-plane-wave method[25] and by an empirical pseudopotential method.[26] However, no theoretical studies on the phonon modes have been reported so far to our knowledge. Among the known experimental results on HgI_2 phonon spectra, only six low-lying branches have been measured by inelastic neutron scattering.[27] The measurements were along the two high-symmetry directions, i.e., Δ and Λ, in the reciprocal lattice space. Thus far, infrared[28] and Raman measurements[29,30] have only dealt with the higher-frequency modes at small wave vectors. In this paper, we present a theoretical study of the phonon dispersion curves by using a rigid-ion model similar to the one described in Ref. 31. We show that the model gives a good fit to the neutron scattering, infrared reflectivity, and Raman scattering data when the long-range Coulomb interaction and short-range force constants up to second-nearest-neighbor distances are included.

II. THEORETICAL MODEL

HgI_2 is a tetragonal crystal whose unit cell consists of two Hg and four I atoms as illustrated in Fig. 1, with lattice constants $a = b = 4.37$ Å, and $c = 12.44$ Å. The lattice has inversion symmetry about the midpoint between two neighboring Hg atoms. It is convenient to choose a tetragonal unit cell in which the four corners are occupied by Hg atoms. The x, y, and z axes are chosen to be parallel to the lattice vectors a, b, and c. If the origin is chosen at the center of the tetragon, the atomic positions of the two Hg atoms are (0,0,0) and $(\frac{a}{2},\frac{a}{2},\frac{c}{2})$ and those of the four I atoms are $(\frac{a}{2},0,-0.139c)$, $(\frac{a}{2},0,0.361c)$, $(0,\frac{a}{2},0.139c)$, and $(0,\frac{a}{2},-0.361c)$. The nearest-neighbor Hg-I, I-I, and Hg-Hg separations are 2.79 Å, 4.14 Å, and 4.37 Å, respectively. The next nearest-neighbor I-I and Hg-I separations are 4.37 Åand 4.99 Å, respectively. The third-nearest-neighbor I-I distance (4.64 Å) is less than the second-nearest-neighbor Hg-I distance. The third-neighbor force constants have not been included in the present calculation, since we find that the I-I interactions play a less significant role than the Hg-I interaction. There are two layers of I atoms between two closest Hg planes. As there are six atoms per unit cell, the total number of phonon branches is 18. The point group of the system is $\{E,\sigma_1,\sigma_2,S_1,S_2,S_3,\sigma_2S_1,S_1\sigma_2\}$, where E is the identity, σ_1 (σ_2) is a reflection about the y-z (x-z) plane, S_1 is a 90° rotation about the z axis followed by a reflection about the x-y plane, $S_2 = S_1^2$, and $S_3 = S_1^3$. The representation of the point group is given in Table I. In addition, the system has inversion symmetry as mentioned earlier. The complete group-theory analysis for the HgI_2 structure has been reported in Ref. 32.

With the use of symmetry, the dynamic matrices are readily obtained. The indices for atoms enclosed in the tetragonal unit cell are shown in Fig. 1. For equivalent atoms displaced by one lattice vector in the x-y plane

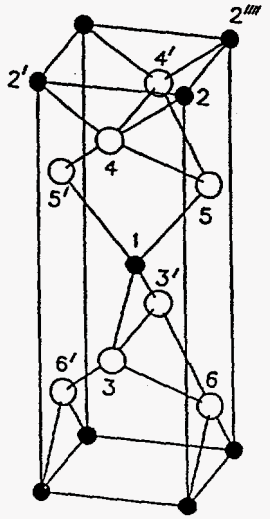

FIG. 1. Crystal structure of HgI_2.

TABLE I. The representation of the point group for HgI_2.

$$\sigma_1=\begin{pmatrix}-1&0&0\\0&1&0\\0&0&1\end{pmatrix},\qquad \sigma_2=\begin{pmatrix}1&0&0\\0&-1&0\\0&0&1\end{pmatrix},$$

$$S_1=\begin{pmatrix}0&-1&0\\1&0&0\\0&0&-1\end{pmatrix},\qquad S_2=\begin{pmatrix}-1&0&0\\0&-1&0\\0&0&1\end{pmatrix},$$

$$S_3=\begin{pmatrix}0&1&0\\-1&0&0\\0&0&-1\end{pmatrix},\qquad \sigma_2S_1=\begin{pmatrix}0&-1&0\\-1&0&0\\0&0&-1\end{pmatrix},$$

$$S_1\sigma_2=\begin{pmatrix}0&1&0\\1&0&0\\0&0&-1\end{pmatrix},\qquad E=\begin{pmatrix}1&0&0\\0&1&0\\0&0&1\end{pmatrix}.$$

(±a or ±b), we denote them by the same index number with superscript ′, ″, ‴, and ⁗ in a counterclockwise order when viewed from the top. For an equivalent atom displaced by a lattice vector c, we denote it by the same index number with a bar on top.

For nearest-neighbor Hg-I interactions, we have

$$\Phi(3,6)=\begin{pmatrix}A_2&D_2&E_2\\D_2&B_2&F_2\\E_2&F_2&C_2\end{pmatrix}$$
$$=\sigma_2\Phi(3,6')\sigma_2^{-1}=\sigma_1\Phi(3',6)\sigma_1^{-1}=\sigma_1\sigma_2\Phi(3',6')\sigma_2^{-1}\sigma_1^{-1}=S_1\Phi(5,4')S_1^{-1}$$
$$=\sigma_1S_1\Phi(5,4)S_1^{-1}\sigma_1^{-1}=S_3\Phi(5',4)S_3^{-1}=\sigma_1S_3\Phi(5',4')S_3^{-1}\sigma_1^{-1}.$$

For nearest-neighbor Hg-Hg interactions:

$$\Phi(1,1')=\begin{pmatrix}A_3&0&0\\0&B_3&D_3\\0&-D_3&C_3\end{pmatrix}$$
$$=S_1\Phi(1,1'')S_1^{-1}=\sigma_2\Phi(1,1''')\sigma_2^{-1}$$
$$=S_1^{-1}\Phi(1,1'''')S_1,$$

where we have again used the fact that $\Phi(1,1')$ is invariant under σ_1. With use of inversion, we further obtain

$$\Phi(2,2')=\Phi(1,1'),\quad \Phi(2,2'')=\Phi(1,1''),$$

$$\Phi(2,2''')=\Phi(1,1'''),\quad \Phi(2,2'''')=\Phi(1,1'''').$$

For second-neighbor I-I interactions, we have

$$\Phi(3,3')=\begin{pmatrix}A_4&0&D_4\\0&B_4&0\\-D_4&0&C_4\end{pmatrix}$$
$$=S_1\Phi(5,5')S_1^{-1}$$
$$=\sigma_1\Phi(3,3''')\sigma_1^{-1}$$
$$=S_1\sigma_2\Phi(5,5''')\sigma_2^{-1}S_1^{-1},$$

$$\Phi(4,4')=\begin{pmatrix}A_5&0&D_5\\0&B_5&0\\-D_5&0&C_5\end{pmatrix}$$
$$=S_1\Phi(6,6')S_1^{-1}$$
$$=\sigma_1\Phi(4,4''')\sigma_1^{-1}$$
$$=S_1\sigma_2\Phi(6,6''')\sigma_2^{-1}S_1^{-1},$$

$$\Phi(1,5)=\begin{pmatrix}A_1&0&0\\0&B_1&D_1\\0&E_1&C_1\end{pmatrix}=\sigma_2\Phi(1,5')\sigma_2^{-1}$$
$$=S_1\sigma_1\Phi(1,3)\sigma_1^{-1}S_1^{-1}$$
$$=S_1\Phi(1,3')S_1^{-1},$$

where we have used the fact that $\Phi(1,5)$ is invariant under σ_1 (see Fig. 1), which leads to vanishing xy, xz, yz and zx components. With use of inversion, we further obtain

$$\Phi(2,4)=\Phi(1,5),\quad \Phi(2,4')=\Phi(1,5'),$$

$$\Phi(2,\bar6)=\Phi(1,3),\quad \Phi(2,\bar6'')=\Phi(1,3'),$$

where $\bar6$ denotes an atom equivalent to atom 6, but displaced by a lattice vector c.

For nearest-neighbor I-I interactions, the use of inversion symmetry will lead to symmetric matrices, and we have

where we have used the fact that $\Phi(3,3')$ and $\Phi(4,4')$ are invariant under σ_2. With use of inversion, we further obtain

$$\Phi(4,4'''')=\Phi(5,5'),\quad \Phi(4,4'')=\Phi(5,5'''),$$

$$\Phi(6,6'')=\Phi(3,3'),\quad \Phi(6,6'''')=\Phi(3,3''').$$

$$\Phi(5,5'')=\Phi(4,4'),\quad \Phi(5,5'''')=\Phi(4,4'''),$$

$$\Phi(3,3'''')=\Phi(6,6'),\quad \Phi(3,3'')=\Phi(6,6''').$$

For second-neighbor Hg-I interactions, we have

$$\Phi(1,6)=\begin{pmatrix}A_6&0&0\\0&B_6&D_6\\0&E_6&C_6\end{pmatrix}$$
$$=\sigma_2\Phi(1,6')\sigma_2^{-1}=(S_1\sigma_1)\Phi(1,4)(S_1\sigma_1)^{-1}$$
$$=S_1\Phi(1,4')S_1^{-1},$$

and with use of inversion

$$\Phi(2,\bar3)=\Phi(1,6),\quad \Phi(2,\bar3'''')=\Phi(1,6'),$$

$$\Phi(2,5)=\Phi(1,4),\quad \Phi(2,5'')=\Phi(1,4').$$

The other interaction matrices not listed here can be obtained by using the Hermitian property of the dynamic matrix. Two constraints are imposed due to the translational invariance:

$$2(A_1 + B_1 + A_2 + B_2 + A_6 + B_6)$$

$$+A_3 + B_3 + A_4 + B_4 + A_5 + B_5 = 0,$$

$$2(C_1 + C_2 + C_6) + C_3 + C_4 + C_5 = 0.$$

In all, we have 26 independent adjustable parameters for describing the short-range interaction.

The long-range Coulomb interaction is calculated by the Ewald method, with $2e^*$ on Hg ions and $-e^*$ on I ions, where e^* is the effective charge transfer. We treat e^{*2}/ϵ as another adjustable parameter, where ϵ is the dielectric constant.

III. RESULTS AND DISCUSSION

The dispersion curves for the lowest ten phonon branches with six fitted to the neutron scattering data are shown in Fig. 2(a). The values of the parameters that provide the fitting are given in Table II. The branches are labeled by their symmetry representations according to the notation of Ref. 32 (i.e., $\Lambda_1, \Lambda_3, \Lambda_5$ along Γ-Z and $\Delta_1, \Delta_2, \Delta_3, \Delta_4$ along Γ-X). The Λ_5 is twofold, indicating transverse modes (with vibrations along x and y), where Λ_1 and Λ_3 are nondegenerate, indicating longitudinal modes (with vibrations along z). It is interesting to note that the two transverse modes do not coincide with each other at Z, while the two longitudinal modes do. This is a consequence of the symmetry of the crystal, since all irreducible representations are two dimensional for the space group at Z (see Ref. 32). The irreducible representations for the space group along the x axis are denoted Δ_1, Δ_2, Δ_3, and Δ_4 (all one dimensional). The Δ_2 and Δ_3 modes have symmetric and antisymmetric sums of y displacements, respectively. The Δ_1 mode contains an admixture of symmetric sums of x displacements (denoted the $x+$ component) and antisymmetric sums of z displacements (denoted the $z-$ component). Similarly, the Δ_4 mode contains an admixture of $x-$ and $z+$ components. An anticrossing behavior is found near $k_x = 0.15(2\pi/a)$ between an optical branch (with mostly the $z-$ component) and an acoustical branch (with mostly the $x+$ component), because they both have Δ_1 symmetry. All modes are doubly degenerate at X, since the irreducible representations for the space group at X are all two dimensional.

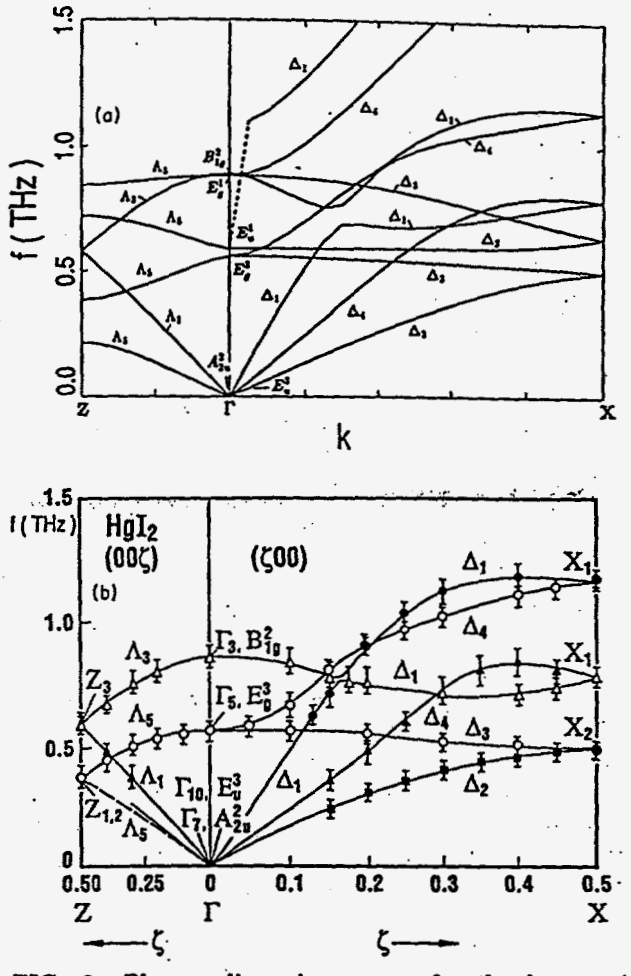

FIG. 2. Phonon dispersion curves for the lowest six branches (a) deduced from the present rigid-ion model and (b) taken from neutron scattering data of Ref. 27.

The symmetries of zone-center modes are labeled according to the notation used in Ref. 28. The E (E_g or E_u) modes are twofold degenerate when the wave vector approaches zero from the c axis, which corresponds to vibrations along the x and y directions. The A (A_{1g} or A_{2u}) and B (B_{1g} or B_{2u}) modes are nondegenerate, which corresponds to vibrations along the z axis. The subscribes g (gerade) and u (ungerade) denote even- and odd-parity modes with respect to the inversion center. Note that if we take symmetric and antisymmetric sums of displacements for atoms connected by the inversion

TABLE II. Parameters used in the rigid-ion model (measured in units of e^2/v_c, where v_c is the unit-cell volume).

A_1	B_1	C_1	D_1	E_1	
1.79347	-38.03613	-29.98524	17.45110	7.94596	
A_2	B_2	C_2	D_2	E_2	F_2
-8.86256	-0.23979	-4.91794	-77.76311	-6.85426	2.54791
A_3	D_3	A_4	B_4	C_4	D_4
7.01133	2.59967	-4.78037	-3.98045	-59.02348	-4.47929
A_5	B_5	C_5	D_5		
-27.74231	8.52126	19.87320	10.60398		
A_6	B_6	C_6	D_6	E_6	e^{*2}/ϵ
6.18102	-0.00736	2.48234	-18.88040	2.96253	0.26591

center, namely, those labeled by 1 and 2, 3 and 6, or 4 and 5 (see Fig. 1), the symmetric sums have odd parity (u modes) whereas the antisymmetric sums have even parity (g modes). A schematic diagram for atomic displacements in modes of various symmetries can be found in Fig. 1 of Ref. 28.

For comparison, the neutron scattering data[27,33] for six low-lying phonon branches are reproduced in Fig. 2(b). The six branches include three acoustical branches and three optical branches that are derived from the E_g^3 (the rigid-layer mode) and the B_{1g}^2 mode. The fit between theory and experiment for these modes is quite good. There are a few other branches derived from the E_u^1 mode and the E_g^1 mode, which lie among the above six branches. These modes have been obsevered by infrared or Raman measurements, but they are not observed by neutron scattering. We note that all these modes correspond to transverse vibrations (they have Λ_5 symmetry along z and Δ_2 or Δ_3 symmetries along x) when their frequencies fall within the range of observation reported in Ref. 27. It is conceivable that these transverse branches have too weak neutron scattering cross sections to be observed, since the one-phonon neutron scattering cross section is proportional to $|\mathbf{k}\cdot\epsilon_s(\mathbf{k})|^2$, where $\epsilon_s(\mathbf{k})$ is the phonon polarization vector.[34] The only branch (with Δ_1 symmetry) derived from the E_u^1 mode which has a longitudinal component lies far above the range of observation. Note that there is a distinct jump in frequency at the zone center for this branch which is indicated by a dashed line. This is due to the anisotropy effect to be discussed below. The sound velocities obtained here are listed in Table III and they are in good agreement with data.

The dispersion curves for all 18 branches are shown in Fig. 3. It is noted that the phonon frequencies for three particular branches are different when the wave vector approaches zero from different directions. Thus there are discontinuities in the dispersion curves at the Γ point. The dashed lines indicate where the discontinuities occur and how the branches are connected. This anisotropic behavior is typical for polar crystals with tetragonal symmetry[35] and for polar semiconductor superlattices.[36,37] The physical origin for this is explained in Refs. 36 and 37 in the context of the rigid-ion model. The anisotropy is caused by the long-range Coulomb interaction, which in the long-wavelength limit ($k \to 0$) takes the form[36]

$$C_{i,j}(\mathbf{k},l,l') = \frac{4\pi Q_l Q_{l'}}{v}\left(\frac{k_i k_j}{k^2} - \delta_{iz}\delta_{jz}\right) + D_{i,j}(l,l'),$$

where Q_l is the amount of charge transfer for ion l, v is the volume of the unit cell, and D is the Coulomb

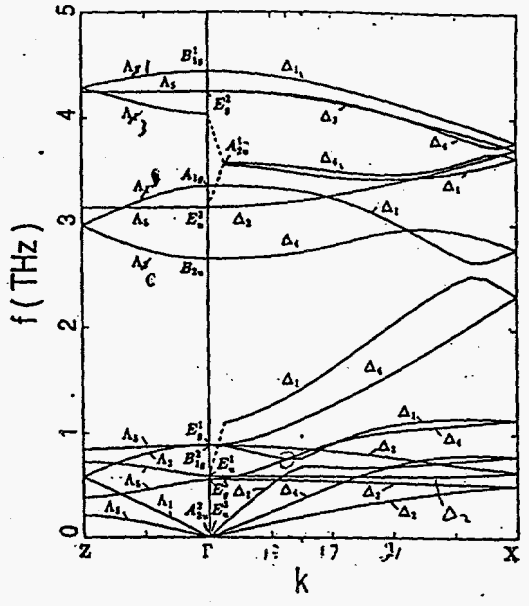

FIG. 3. Phonon dispersion curves for all 18 branches deduced from the present rigid-ion model.

part of the dynamic matrix of the crystal at $k = 0$ when approached from the (0,0,1) direction (c axis). The term $k_i k_j/k^2 \equiv S_{ij}$ takes the matrix form

$$\mathbf{S} = \begin{pmatrix} \sin^2\theta & 0 & \sin\theta\cos\theta \\ 0 & 0 & 0 \\ \sin\theta\cos\theta & 0 & \cos^2\theta - 1 \end{pmatrix}$$

for k in the x-z plane, where θ is the polar angle with respect to the z axis. This term gives rise to angular-dependent phonon frequencies at the zone center if the short-range part is not invariant under rotation. The angular dependence of phonon frequencies of HgI_2 is shown in Fig. 4. The three zero-frequency acoustic modes have no angular dependence, since in these modes all six ions vibrate in the same direction, which leads to zero polarization, defined as

$$\mathbf{P} = \sum_l \mathbf{u}_l Q_l,$$

where $\mathbf{u}_l$ is the displacement vector. Note that the angular-dependent part of the phonon frequency in a given mode is described by

$$\omega^2(\theta) = \text{const} \times \sum_{i,j} P_i^* S_{i,j}(\theta) P_j,$$

where P_i is the ith component of the polarization vector in the mode. The three branches (labeled E_u^1, E_u^2, and A_{2u}^1) that display significant angular disper-

TABLE III. Sound velocities (in 10^5 cm s^{-1}) of acoustic branches for HgI_2 obtained in the present rigid-ion model and from Ref. 27.

	$v_{t,\parallel}(001)$ (LA)	$v_{t,\perp}(001)$ (TA)	$v_{l,\perp}(100)$ [LA(x)]	$v_{t,\parallel}(001)$ [TA(z)]	$v_{t,\perp}(001)$ [TA(y)]
Expt.	1.55		2.23	1.07	0.74
Theory	1.51	0.67	2.34	1.01	0.58

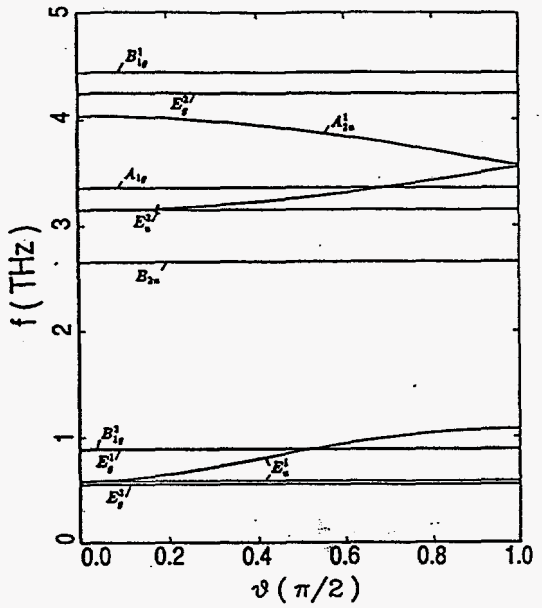

FIG. 4. Angular dispersion of phonon frequencies for HgI_2 deduced from the present rigid-ion model.

sion are modes with large strengths of polarization. In these modes, ions of opposite charges vibrate against each other. Thus they are also infrared active. The phonon frequencies of these infrared-active modes were observed[28] to be at 0.52, 3.14, and 3.76 THz. Our calculated frequencies for these three modes are 0.587, 3.145, and 3.57 THz, respectively, in fair agreement with experiment. Note that the A_{2u}^1 mode has a polarization vector parallel to the z axis. Thus the infrared measurement must be performed with incident radiation propagating perpendicular to the c axis, and we have used the calculated A_{2u}^1 frequency at $\theta = \pi/2$ to compare with experiment. To compare with experimental data for infrared- and Raman-active modes, we list the calculated phonon frequencies at the zone center in Table IV, in conjunction with experimental values. The agreement between theory and experiment is fairly good.

TABLE IV. Zone-center phonon frequencies (in THz) for HgI_2 obtained in the present rigid-ion model and from various experimental measurements. All but the A_{2u}^1 mode are calculated at $\theta = 0$. The A_{2u}^1 mode is calculated at $\theta = \pi/2$.

	E_u^1	E_g^3	B_{1g}^2	E_g^1	B_{2u}
Theory	0.587	0.556	0.889	0.881	2.653
Expt.	0.52[a]	0.56[b]	0.85[b]	0.87[c]	
	E_u^2	A_{1g}	A_{2u}^1	E_g^2	B_{1g}^1
Theory	3.145	3.352	3.570	4.245	4.437
Expt.	3.14[a]	3.42[c]	3.69[a]		4.38[d]

[a]Infrared reflectivity (Ref. 28).
[b]Neutron scattering (Ref. 27).
[c]Raman scattering (Ref. 29).
[d]Raman scattering (Ref. 27).

IV. CONCLUSIONS

We have calculated the phonon dispersion curves for HgI_2 by using a rigid-ion model, including the long-range Coulomb interaction. With 27 adjustable parameters, the fit of six low-lying branches to the neutron scattering data is very good. We found that as a result of crystal symmetry TA and TO modes do not coincide at Z whereas the LA and LO modes do. The angular dispersion of the phonon modes is studied, and three infrared-active modes are found which display large angular dispersion. The frequencies of these modes and all Raman-active modes are also in good agreement with experiment.

ACKNOWLEDGMENTS

This work was supported in part by the Department of Energy. The use of computing facilities of the University of Illinois Material Research Laboratory is acknowledged.

*Permanent address: Department of Physics, National University of Singapore, Singapore 0511.
[1]W. R. Willing, Nucl. Instrum. Methods 96, 615 (1971).
[2]J. P. Ponpon, R. Stuck, P. Siffert, B. Meyer, and C. Schwab, IEEE Trans. Nucl. Sci. NS-22, 182 (1975).
[3]A. J. Dabrowski, W. M. Szymczyk, J. S. Iwanczyk, J. H. Kusmiss, W. Drummond, and L. Ames, Nucl. Instrum. Methods 213, 89 (1983).
[4]S. P. Swierkowski, G. A. Armantrout, and R. Wichne, IEEE Trans. Nucl. Sci. NS-21, 302 (1974).
[5]J. H. Howes and J. Watling, in *Nuclear Radiation Detector Materials*, edited by E. E. Haller, H. W. Kraner, and W. A. Higinbotham, MRS Symposia Proceedings No. 16 (Materials Research Society, Pittsburgh, 1983), p. 207.
[6]H. L. Malm, T. W. Raudoff, M. Martina, and K. R. Zanio, IEEE Trans. Nucl. Sci. NS-20, 500 (1973).
[7]R. C. Whited and M. Schieber, Nucl. Instrum. Methods 162, 119 (1979).
[8]B. V. Novikov and M. M. Pimonenko, Fiz. Tekh. Poluprovodn. 4, 2077 (1970) [Sov. Phys. Semicond. 4, 1785 (1971)].
[9]K. Kanzaki and I. Imai, J. Phys. Soc. Jpn. 32, 1003 (1972).
[10]A. Anedda, F. Raga, E. Grilli, and M. Guzzi, Nuovo Cimento 38, 439 (1977).
[11]P. D. Bloch, J. W. Hodby, C. Schwab, and D. W. Stacey, J. Phys. C 11, 2579 (1978).
[12]C. Dlasi, S. Galassini, C. Manfredotti, G. Micocci, L. Ruggiero, and A. Tepore, Nucl. Instrum. Methods 150, 103 (1978).
[13]U. Gelbert, Y. Yacoby, I. Beinglass, and A. Holzer, IEEE Trans. Nucl. Sci. NS-24, 135 (1977).
[14]J. C. Muller, A. Friant, and P. Siffert, Nucl. Instrum. Methods 150, 97 (1978).
[15]M. Schieber, I. Beinglass, G. Dishon, A. Holzer, and G.

Yaron, Nucl. Instrum. Methods **150**, 71 (1978).
[16]A. Anedda, E. Grilli, M. Guzzi, F. Raga, and A. Serpi, Solid State Commun. **39**, 1121 (1981).
[17]T. Goto and A. Kasuya, J. Phys. Soc. Jpn. **50**, 520 (1981).
[18]S. R. Kurtz, R. C. Huges, C. Ortale, and W. F. Schnepple, J. Appl. Phys. **62**, 4308 (1987).
[19]D. Wong, X. J. Bao, T. E. Schlesinger, R. B. James, A. Cheng, C. Ortale, and L. van den Berg, Appl. Phys. Lett. **53**, 1536 (1988).
[20]R. B. James, X. J. Bao, T. E. Schlesinger, J. M. Markakis, A. Y. Cheng, and C. Ortale, J. Appl. Phys. **66**, 2578 (1989).
[21]R. B. James, X. J. Bao, T. E. Schlesinger, C. Ortale, and L. van den Berg, J. Appl. Phys. **67**, 2571 (1990).
[22]X. J. Bao, T. E. Schlesinger, R. B. James, R. H. Stulen, C. Ortale, and L. van den Berg, J. Appl. Phys. **68**, 86 (1990).
[23]L. R. Williams, R. J. M. Anderson, and M. J. Banet, Chem. Phys. Lett. **182**, 422 (1991).
[24]X. J. Bao, T. E. Schlesinger, R. B. James, G. L. Gentry, A. Y. Cheng, and C. Ortale, J. Appl. Phys. **69**, 4247 (1991).
[25]D. E. Turner and B. N. Harmon, Phys. Rev. B **40**, 10516 (1989).
[26]Y. C. Chang and R. B. James, Phys. Rev. B **46**, 15040 (1992).
[27]B. Prevot, C. Schwab, and B. Dorner, Phys. Status S B **88**, 327 (1978).
[28]J. Biellmann and B. Prevot, Infrared Phys. **20**, 99 (1979
[29]S. Nakashima and M. Balkanski, Phys. Rev. B **34**, 58 (1986).
[30]N. Kuroda, T. Iwabuchi, and Y. Nishina, J. Phys. Soc. Jp **52**, 2419 (1983).
[31]K. Kunc, Ann. Phys. (Paris) **8**, 319 (1973).
[32]M. Sieskind, J. Phys. Chem. Solids **39**, 1251 (1978).
[33]*Landolt-Börnstein Numerical Data and Functional R lationships in Science and Technology*, edited by O Madelung, Vol. 17 (Springer-Verlag, New York, 1984), p 530.
[34]See, for example, N. W. Ashcroft and N. D. Mermin, *Soli State Physics* (Saunders, Philadelphia, 1976), p. 794.
[35]C. A. Arguelloo, D. L. Rousseau, and S. P. Porto, Phys Rev. **181**, 1351 (1969).
[36]S. F. Ren, H. Chu, and Y. C. Chang, Phys. Rev. B **37**, 889 (1988).
[37]H. Chu, S. F. Ren, and Y. C. Chang, Phys. Rev. B **37** 10746 (1988).

Theoretical studies of carrier transport in HgI_2

Yia-Chung Chang
Department of Physics, University of Illinois at Urbana-Champaign, 1110 West Green Street, Urbana, Illinois 61801

R. B. James
Department of Advanced Materials Research, Sandia National Laboratory, Livermore, California 94550
(Received 28 August 1995; revised manuscript received 14 February 1996)

Theoretical studies of the electron-phonon coupling and carrier mobility for red mercuric iodide are presented. The electronic states are calculated by an empirical pseudopotential method, while the lattice vibrations are described via a rigid-ion model. Effects due to the deformation potential and polar-optical scattering are discussed. Carrier mobilities along both c and a axes as functions of temperature are calculated and they are in good agreement with the experimental data. [S0163-1829(96)03821-0]

I. INTRODUCTION

Red mercuric iodide (HgI_2) is an important material for γ- and x-ray detectors. The electronic and phonon properties of HgI_2 are known fairly well due to recent theoretical studies.[1–4] A reliable description of the detailed electronic structures of the system was given by Turner and Harmon[1] via a relativistic linearized augmented plane-wave (RLAPW) calculation. We have recently reported an empirical nonlocal pseudopotential calculation of the electronic and optical properties of HgI_2 including the effects of the spin-orbit interaction.[2] The near-band-gap optical properties and effective masses obtained in this calculation are in good agreement with experimental data.[5–8]

The lattice vibrations of HgI_2 were studied by a rigid-ion model.[3,4] The model includes the long-range Coulomb interaction and short-range force constants up to second-nearest neighbors. An excellent fit to the available inelastic neutron scattering data[9] for six low-lying phonon branches as well as Raman scattering[10,11] and far-infrared[12] measurements for zone-center phonon modes was obtained.

There have been a great deal of experimental studies of transport properties of HgI_2.[13–17] However, a theoretical understanding of them is still lacking. A thorough review of carrier transport in HgI_2 can be found in Ref. 13. In this paper, we present theoretical studies of carrier transport in HgI_2. We have considered the scattering of electrons and holes from all possible phonon modes. The electron-phonon coupling is calculated based on the empirical pseudopotential model[2] for the electronic states and the rigid-ion model for the phonon modes.[4] It is found that polar-optical scattering is by far the strongest for low-energy carriers, and it is responsible for the low mobility observed experimentally. Our theoretical prediction for the intrinsic mobility as a function of temperature is in fairly good agreement with the experimental data.[14]

In Sec. II, we present the theory for the electron-phonon coupling of HgI_2. In Sec. III, we describe the theoretical predictions for the deformation potentials associated with various phonon modes of HgI_2. In Sec. IV, we describe the polar-optical scattering for noncubic crystals and examine the angular dependence of the electron-phonon coupling constant for HgI_2. In Sec. V, we discuss our calculated results for momentum relaxation rate and the carrier mobility. A summary of the paper is given in Sec. VI.

II. ELECTRON-PHONON COUPLING

In the rigid-ion model, the electron-phonon interaction is given by[18]

$$H_{\text{el-ph}}=-\sum_{\alpha\mathbf{R}}\frac{1}{\sqrt{NM_\alpha}}\sum_{\mathbf{q}j}Q_{\mathbf{q}j}e^{i\mathbf{q}\cdot\mathbf{R}}\hat{\epsilon}_\alpha^{(j)}\cdot\nabla V_\alpha(\mathbf{r}-\mathbf{R}-\tau_\alpha), \tag{1}$$

where N is the number of unit cells in the sample, α labels the different ions in a unit cell (two Hg's and four I's in the present case), M_α and τ_α denote the mass and position within a unit cell of ion α, $\mathbf{q}$ and $\hat{\epsilon}_\alpha^{(j)}$ denote the wave vector and polarization vector at position τ_α of phonon mode j, and V_α describes the pseudopotential for an electron interacting with ion α. $Q_{\mathbf{q}_j}$ is the normal mode coordinate of mode j which takes the second quantization form

$$Q_{\mathbf{q}_j}=\sqrt{\frac{\hbar}{2\omega_{\mathbf{q}_j}}}(a_{\mathbf{q}_j}^\dagger+a_{\mathbf{q}_j}),$$

where $\omega_{\mathbf{q}_j}$ denotes the frequency of mode j.

A schematic diagram of the unit cell of HgI_2 can be found in Ref. 3. Note that the solid has inversion symmetry about the midpoint between the two Hg atoms in a unit cell. If we choose the point as the origin of the coordinate system, the atomic positions of the two Hg atoms are $(-a/4,-a/4,-c/4)$ and $(a/4,a/4,c/4)$, and those of the four I atoms are $(-a/4,a/4,-0.111c)$, $(a/4,-a/4,0.111c)$, $(-a/4,a/4,0.389c)$, and $(a/4,-a/4,-0.389c)$. Here, $a=4.37$ Å and $c=12.44$ Å. We adopt a coordinate system in which the z axis is parallel to the c axis.

The local pseudopotentials of the mercury and iodine have the form

$$V_L(\mathbf{q})=a_1(q^2-a_2)/(e^{a_3(q^2-a_4)}+1), \tag{2}$$

and the nonlocal pseudopotentials have the form

$$V_{NL}(\mathbf{K},\mathbf{K}')=4\pi\sum_l (2l+1)P_l(\cos\theta) \times\int dr r^2 V_l(r) j_l(Kr) j_l(K'r)/\Omega_a , \quad (3)$$

where $\cos\theta=\mathbf{K}\cdot\mathbf{K}'/KK'$, Ω_a is the atomic volume, P_l is a Legendre polynomial, j_l is a spherical Bessel function, and $V_l(r)=A_l e^{-(r/R)^2}$. We use $R=2.3a_B$, where a_B is the Bohr radius. $a_i (i=1,2,3,4)$ and $A_l (l=0,1)$ are adjustable parameters which are tabulated in Ref. 2.

The matrix element of $H_{\text{el-ph}}$ between two electronic states with wave vectors $\mathbf{k}$ and $\mathbf{k}'$ is given by

$$\langle \mathbf{k}'|H_{\text{el-ph}}|\mathbf{k}\rangle=-i\sum_\alpha \sqrt{\frac{\hbar}{2\omega_{\mathbf{q}j}NM_\alpha}}\sum_{\mathbf{q}j,\mathbf{G},\mathbf{G}'} \Delta(\mathbf{k}'-\mathbf{k}\mp\mathbf{q})\hat{\epsilon}_\alpha^{(j)}\cdot(\mathbf{K}'-\mathbf{K})C^*_{\mathbf{k}'}(\mathbf{G}')C_{\mathbf{k}}(\mathbf{G}) \times[V_L^{(\alpha)}(\mathbf{K}'-\mathbf{K})+V_{\text{NL}}^{(\alpha)}(\mathbf{K},\mathbf{K}')]e^{-i(\mathbf{K}'-\mathbf{K})\cdot\tau_\alpha}/N_a , \quad (4)$$

where $\mathbf{K}=\mathbf{k}+\mathbf{G}$ and $\mathbf{G}$ denotes a reciprocal lattice vector. $C_{\mathbf{k}}(G)$ is the expansion coefficient for the electronic eigenstate of the pseudopotential Hamiltonian in terms of plane waves. N_a is the number of atoms per unit cell,

$$\Delta(\mathbf{k}'-\mathbf{k}\mp\mathbf{q})=\delta_{\mathbf{k}',\mathbf{k}\pm\mathbf{q}+\mathbf{G}},$$

which means that the momentum is conserved with or without the help of a reciprocal lattice vector $\mathbf{G}$. Since we are only concerned with transport properties of Γ-valley electrons (or holes), the umklapp process ($\mathbf{G}\neq 0$) can be ignored. The $+(-)$ sign in the above equation denotes a phonon absorption (emission) process.

In a deformation potential model appropriate for acoustic phonons, the electron-phonon interaction is described by

$$H_{\text{el-ph}}=\frac{1}{\sqrt{NM_{\text{cell}}}}\sum_{\mathbf{q}j} Q_{\mathbf{q}j}e^{i\mathbf{q}\cdot\mathbf{r}}\hat{\epsilon}\cdot\mathbf{q}\Xi_d , \quad (5)$$

where Ξ_d is the deformation potential associated with pure dilation and M_{cell} denotes the total mass per unit cell. One can generalize the above form to an optical phonon labeled with j by defining a coupling coefficient $D_0^{(j)}$ such that

$$H_{\text{el-ph}}=\sum_\alpha \frac{1}{\sqrt{NM_{\text{cell}}}}\sum_{\mathbf{q}j} Q_{\mathbf{q}}e^{i\mathbf{q}\cdot\mathbf{r}}D_0^{(j)}(\mathbf{q}). \quad (6)$$

For longitudinal optical-phonons $D(\mathbf{q})$ is approximately independent of q for small q, while for acoustical phonons, we have the simple relation

$$D_0(\mathbf{q})=\hat{\epsilon}\cdot\mathbf{q}\Xi_d .$$

The matrix element between two electronic states in this model can be written as

$$\langle \mathbf{k}'|H_{\text{el-ph}}|\mathbf{k}\rangle=-i\sqrt{\frac{\hbar}{2\omega_{qj}NM_{\text{cell}}}}\sum_{\mathbf{q}}\delta_{\mathbf{k}',\mathbf{k}\pm\mathbf{q}}D_0^{(j)}(\mathbf{q})I(\mathbf{k}',\mathbf{k}), \quad (7)$$

where

$$I(\mathbf{k}',\mathbf{k})\equiv\sum_G C^*_{\mathbf{k}'}(G')C_{\mathbf{k}}(G)$$

denotes an overlap integral.

Comparing Eq. (7) with Eq. (4), we can define the effective coupling coefficient as

$$D(\mathbf{q})\equiv D_0^{(j)}(q)I(\mathbf{k}',\mathbf{k}) =\left|\sum_\alpha\sqrt{\frac{M_{\text{cell}}}{M_\alpha}}\sum_{j,\mathbf{G},\mathbf{G}'}\hat{\epsilon}_\alpha^{(j)}\cdot(\mathbf{K}'-\mathbf{K})C^*_{\mathbf{k}'}(\mathbf{G}') \times C_{\mathbf{k}}(\mathbf{G})[V_L^{(\alpha)}(\mathbf{K}'-\mathbf{K}) +V_{\text{NL}}^{(\alpha)}(\mathbf{K},\mathbf{K}')]e^{-i(\mathbf{K}'-\mathbf{K})\cdot\tau_\alpha}/N_a\right| , \quad (8)$$

where $\mathbf{K}=\mathbf{k}+\mathbf{G}$ and $\mathbf{q}=\pm(\mathbf{k}'-\mathbf{k})$.

In a scattering event, both energy and momentum should be conserved, i.e.,

$$\mathbf{k}'=\mathbf{k}\pm\mathbf{q}$$

and

$$E_{\mathbf{k}'}=E_{\mathbf{k}}\pm\hbar\omega_q ,$$

where $E_{\mathbf{k}}$ is the energy of electron at wave vector $\mathbf{k}$, and $\mathbf{q}$ is the wave vector of a phonon absorbed or emitted. For acoustical phonons whose deformation potentials are of primary interest, the typical frequencies are less than 0.1 THz which correspond to energies less than 0.4 meV. Thus, the following relation approximately holds:

$$\mathbf{k}'=-\mathbf{k}=\pm\mathbf{q}/2, \quad (9)$$

since $E_{-\mathbf{k}}=E_{\mathbf{k}}$ as a consequence of time reversal. For optical phonons, the frequencies are between 0.5 and 4.5 THz (with energies from 2 to 18 meV) for HgI_2, and the above relation is not quite valid. However, since the electron-phonon cou-

pling for high-frequency optical-phonons is insensitive to $\mathbf{k}$ and $\mathbf{q}$ near the zone center, the result obtained this way is still adequate.

To understand the behavior of these coupling constants, we must first examine the symmetry properties of phonons in HgI_2. The point group of the system is D_{4h} which contains elements E, σ_1, σ_2, S_1, S_2, S_3, $\sigma_2 S_1$, and $S_1\sigma_2$, where E is the identity, $\sigma_1(\sigma_2)$ is a reflection about the y-z (x-z) plane, S_1 is a 90° rotation about the z axis followed by a reflection about the x-y plane, $S_2=S_1^2$, and $S_3=S_1^3$. The group theory analysis for HgI_2 structure has been reported in Ref. 19. The phonon dispersion curves of all 18 branches were shown in Fig. 3 of Ref. 4. The phonon branches are labeled by their space group representations according to the notation of Ref. 19. There are three irreducible representations $\Lambda_1,\Lambda_3,\Lambda_5$ for $\mathbf{q}$ along the [001] direction (Γ to Z). The Λ_5 representation is two dimensional, indicating transverse modes, whereas the Λ_1 and Λ_3 representations are one dimensional, indicating longitudinal modes. For $\mathbf{q}$ along [100] (Γ to X), there are four irreducible representations $\Delta_1,\Delta_2,\Delta_3,\Delta_4$ (all one dimensional). The Δ_2 and Δ_3 modes contain symmetric and antisymmetric sums of y displacements associated with atoms related by inversion, namely, those labeled by 1 and 2, 3 and 6, or 4 and 5 (see Fig. 1 of Ref. 3); hence, they are transverse modes. The Δ_4 modes contain admixture of $x-$ and $z+$ components, while the Δ_1 modes contain admixture of symmetric sum of x displacements (denoted $x+$ component).

The symmetries of zone-center modes are labeled according to the point group representations (Ref. 12). The E (E_g or E_u) modes are twofold degenerate when the wave vector approaches zero from the c axis. They correspond to vibrations along the x and y directions. The A (A_{1g} or A_{2u}) and B (B_{1g} or B_{2u}) modes are singlefold, corresponding to vibrations along the z axis. The subscripts g (gerade) and u (ungerade) denote even and odd parity modes with respect to the inversion center. A schematic diagram for atomic displacement in modes of various symmetries can be found in Fig. 1 of Ref. 12.

In our calculation, the spin-orbit interaction is included for the electron band structures. Thus, each band is doubly degenerate due to Kramers degeneracy. In our calculation, we sum over the final spin index and average over the initial spin index. Namely, we replace the intraband coupling matrix element in Eqs. (4) and (7) by

$$\langle \mathbf{k}'|H_{\text{el-ph}}|\mathbf{k}\rangle=\left(\frac{1}{2}\sum_{s,s'}|\langle \mathbf{k}',s'|H_{\text{el-ph}}|\mathbf{k},s\rangle|^2\right)^{1/2},$$

where s,s' sum over the two Kramers degenerate states.

Using Eqs. (8) and (9), we have calculated the effective coupling coefficient $D(\mathbf{q})$ as a function of q. The deformation-potential coupling is nonzero only for longitudinal phonon modes (i.e., with Λ_1 or Λ_3 symmetry for $\mathbf{q}$ along [001] and Δ_1 or Δ_4 symmetry for $\mathbf{q}$ along [100]). At the zone center ($\mathbf{q}=0$), only the A_{1g} mode (totally symmetric with respect to all point operations) has nonzero coupling coefficient. This is because we have only considered intraband scattering here, in which case the initial and final states are the same and the electron can only scatter with a totally symmetric mode. The results for (a) the lowest conduction band (C1), (b) the heavy-hole band (HH), and (c) the light-hole band (LH) are shown in Fig. 1. The three solid (dotted) curves labeled 1–3 in the left panels are associated with the three Λ_1 (Λ_3) modes ordered according to their frequencies. Similarly, the six solid (dotted) curves labeled 1–6 in the

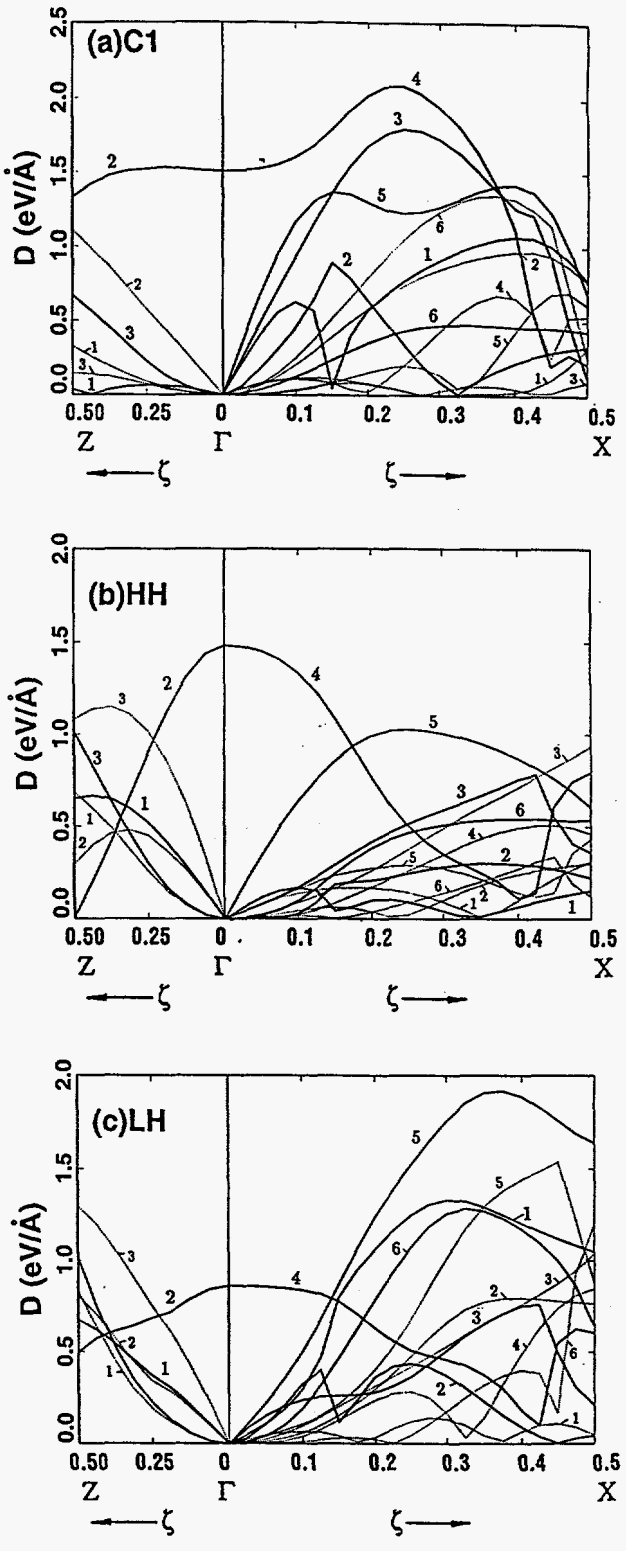

FIG. 1. Electron-phonon coupling coefficients as a function of phonon wave vector for (a) the lowest conduction band (C1), (b) the heavy-hole band (HH), and (c) the light-hole band (LH).

right panels are associated with the six Δ_1 (Δ_4) modes ordered according to their frequencies. The first Λ_1 and $\Delta_1(\Delta_4)$ modes correspond to the longitudinal acoustical branch along the c and a axes, respectively.

The second Λ_1 mode and the fourth Δ_1 mode merge into the A_{1g} mode at the zone center. The A_{1g} mode (a breathing mode) creates a lattice vibration that preserves the point symmetry of the crystal; thus, the electronic energy will suffer a change even when $q=0$. As shown in Fig. 1, $D(\mathbf{q})$ is finite at the zone center only for this mode.

III. DEFORMATION POTENTIALS

Since HgI_2 has six atoms per unit cell, there exist 15 optical branches in addition to the three acoustical branches. For acoustic branches and for some optical branches, the effective electron-phonon coupling constant $D(\mathbf{q})$ is linear in q for small q. We then define effective deformation potentials as

$$\Xi^*(\theta_q)=D(\mathbf{q})/q,$$

where θ_q is the polar angle of q with respect to the z axis (c axis). Due to the fact that the crystal is noncubic, there is in general a θ_q dependence in the deformation potential. We examine the angular dependence of the deformation potential by calculating $\Xi^*(\theta_q)=D(\mathbf{q})/q$ at $q=0.02$ Å^{-1} with θ_q varying from zero to $\pi/2$. The angular dependence is quite complicated due to the mixing of several modes with similar frequencies. However, for modes with similar frequencies, we can simply add up their corresponding coupling coefficients squared and use the square root of the sum to represent the net effect of all these nearly degenerate modes.

Following the elastic theory of Herring and Vogt,[20] the θ_q dependences of the acoustical-phonon deformation potentials for anisotropic systems are fitted by polynomials of $\cos^2\theta_q$,

$$\Xi_L^*(\theta_q)=\Xi_d^*+\Xi_r^*\cos^2\theta_q+\Xi_s^*\cos^4\theta_q \qquad (10)$$

for longitudinal modes and by

$$\Xi_T^*(\theta_q)=\Xi_u^*\sin\theta_q\cos\theta_q \qquad (11)$$

for transverse modes. These expressions would allow the scattering rates to be calculated analytically.

Figure 2 shows the angular dependence of the deformation potential $\Xi^*(\theta_q)$ for the longitudinal acoustical (LA) and transverse acoustical (TA) modes. The solid curves are calculated results and the dotted curves are fitted results obtained by using Eq. (10) for the LA mode and Eq. (11) for the TA modes. The parameters Ξ_d^*, Ξ_r^*, Ξ_s^*, and Ξ_u^* used for the fit are listed in Table I.

From Fig. 2, we find that the angular dependence of the effective deformation potentials for the LA mode are indeed well described by the simple analytic expressions given in Eq. (10). For the TA mode, the fit to Eq. (11) is rather poor. Here, we choose the maximum values of fitted $\Xi^*(\theta_q)$ to be the same as the actually calculated ones, with a displaced peak positions in θ_q. Thus, when we integrate over θ_q to obtain the total scattering rate, the deviation becomes insignificant. Furthermore, since average value of $\Xi^*(\theta_q)$ for the TA mode is much smaller than that for the LA mode, such a poor fit will not alter the final acoustical-phonon scattering rate in which the LA mode dominates.

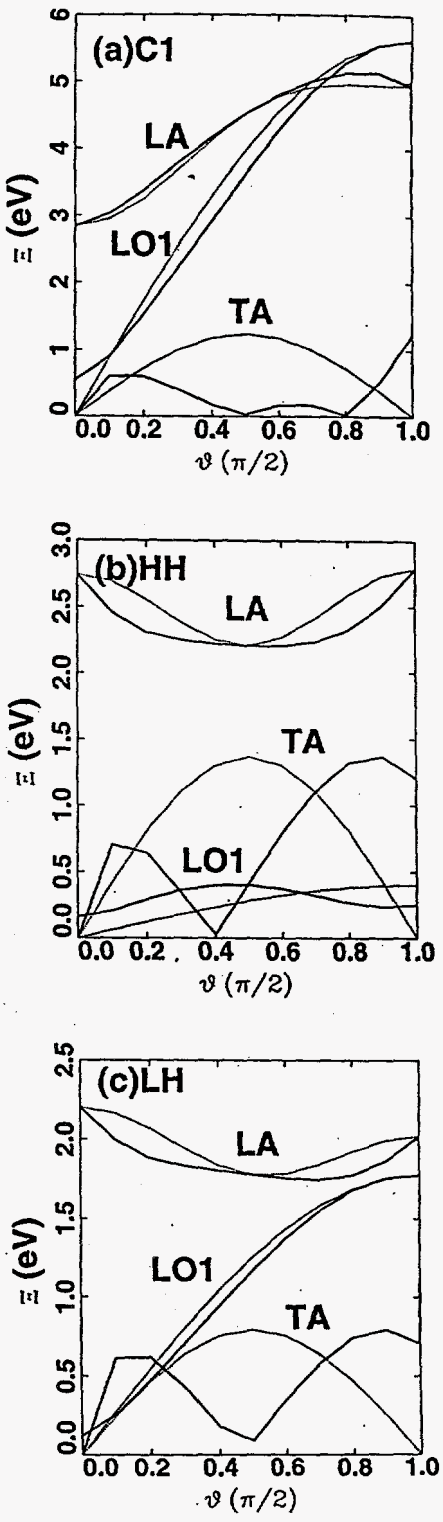

FIG. 2. Angular dependence of the effective deformation potential for (a) the lowest conduction band (C1), (b) the heavy-hole band (HH), and (c) the light-hole band (LH). Solid curves: calculated based on Eq. (8). Dotted curves: calculated based on Eqs. (9), (10), and (14).

As we mentioned in the previous section there is only one

TABLE I. Effective deformation potentials Ξ_d^*, Ξ_u^*, and Ξ_l^* and the coupling coefficient D_0 for the optical-phonon for the conduction (C1), heavy-hole (HH), and light-hole (LH) bands. All deformation potentials are in units of eV and D_0 is in units of eV/Å.

Band	Ξ_d^*	Ξ_r^*	Ξ_s^*	Ξ_u^*	Ξ_l^*	D_0
C1	4.95	0.376	-2.49	2.45	5.62	1.50
HH	2.79	-2.29	2.25	2.74	0.404	1.49
LH	2.02	-1.16	1.33	1.59	1.77	0.87

optical mode with A_{1g} symmetry whose coupling coefficient $D(\mathbf{q})$ is finite at $q=0$. Thus it contributes to the zeroth-order optical-phonon scattering. If we approximate both $D(\mathbf{q})$ and $\omega(q)$ for the A_{1g} mode by constant values D_0 and ω_0 corresponding to their respective values at $q=0$, we obtain the scattering rate as[21]

$$W(E_{\mathbf{k}})=(\pi D_0^2/\rho\omega_0)\{n(\omega_0)N(E_{\mathbf{k}}+\hbar\omega_0)+[n(\omega_0)+1]N(E_{\mathbf{k}}-\hbar\omega_0)\}, \tag{12}$$

where ρ is the mass density,

$$E_{\mathbf{k}}=\frac{\hbar^2(k_x^2+k_y^2)}{2m_t^*}+\frac{\hbar^2k_z^2}{2m_l^*}$$

is the carrier energy, $N(E)=(2m_l^*m_t^{*2}E)^{1/2}/4\pi^2\hbar^3$ is the carrier density of states for a given spin, and $n(\omega_0)$ is the phonon population given by

$$n(\omega_0)=(e^{\hbar\omega_0/k_BT}-1)^{-1}.$$

For all other 14 optical branches, the deformation potential constant vanishes at $q=0$. However, several modes have appreciable deformation potential at finite q. We shall add the contributions to $[D(\mathbf{q})]^2$ for all modes with frequencies higher than 2 THz (which include the Λ_1 and Λ_3 modes labeled by 2 and 3 and the Δ_1 and Δ_4 modes labeled by 4–6) and define the net contribution as $D_0(q)$. The net contribution becomes even less q dependent near the zone center. Therefore, Eq. (12) becomes a better approximation for describing optical-phonon scattering when we consider the net effect of all optical branches with high frequencies. We shall use Eq. (12) to calculate the net contribution of these higher-lying optical modes to the scattering rate with the coupling coefficient D_0 given in Table I and $\omega_0/2\pi=3.352$ THz.

For those optical branches (i.e., the seven lower-lying optical modes) with frequencies substantially lower than ω_0, they also have appreciable contribution to the scattering rate. The frequencies of these modes are ranging from 0.6 THz to 1.1 THz near the zone center (see Fig. 4 of Ref. 4). We shall show below that the angular dependence of the deformation potential can be approximately written as

$$\Xi_l^*(\theta_q)=\Xi_l^*\sin\theta_q. \tag{13}$$

The angular dependence of the effective deformation potential representing the net effect of these modes (denoted LO1) is plotted in Fig. 2 for (a) the lowest conduction band (C1), (b) the heavy-hole band (HH), and (c) the light-hole band (LH). The solid curves are calculated results and the dotted curves are fitted results obtained by using Eq. (13). The parameter Ξ_l^* used for the fit is listed in Table I. We find that the angular dependence of the effective deformation potentials for the LO1 modes is indeed well described by the simple analytic expression given in Eqs. (13). With this simple expression, the scattering rate is given by

$$W_1(\mathbf{k})=\frac{\Xi_l^{*2}}{8\pi^2\rho\omega_1}\int q^2\sin^2\theta_q\{n(\omega_1)\delta_{\mathbf{k}',\mathbf{k}+\mathbf{q}}\times\delta(E_{\mathbf{k}'}-E_{\mathbf{k}}-\hbar\omega_1)+[n(\omega_1)+1]\delta_{\mathbf{k}',\mathbf{k}-\mathbf{q}}\times\delta(E_{\mathbf{k}'}-E_{\mathbf{k}}+\hbar\omega_1)\}d\mathbf{k}'d\mathbf{q}. \tag{14}$$

Carrying out the integral we obtain

$$W_1(\mathbf{k})=\frac{\Xi_l^{*2}m_t^{*2}\sqrt{2m_l^*}}{\pi\rho\omega_1\hbar^5}\{n(\omega_1)\sqrt{E_{\mathbf{k}}+\hbar\omega_1}\times[\tfrac{2}{3}(E_{\mathbf{k}}+\hbar\omega_1)+u_k]+[n(\omega_1)+1]\sqrt{E_{\mathbf{k}}-\hbar\omega_1}\times[\tfrac{2}{3}(E_{\mathbf{k}}-\hbar\omega_1)+u_k]\}, \tag{15}$$

where m_l^* and m_t^* are the longitudinal and transverse effective masses as listed in Table II, $u_k\equiv\hbar^2(k_x^2+k_y^2)/2m_t^*$, and $\omega_1/2\pi=0.868$ THz is the average frequency of the optical-phonons of interest.

TABLE II. Effective masses (in units of free electron mass) and their ratios for the conduction (C1), heavy-hole (HH), and light-hole (LH) bands.

	C1	HH	LH
m_l^*	0.37[a]	2.06[b]	0.60[a]
m_t^*	0.29[a]	1.03[b]	0.60[a]

[a]Obtained by the empirical pseudopotential method (EPM) as described in Ref. 2.
[b]Bloch *et al.* (Ref. 6).

IV. POLAR-OPTICAL SCATTERING

In addition to deformation potentials, the ions with opposite charges vibrating against each other give rise to a long-range macroscopic electric field. The interaction of a carrier with such field is known as the polar-optical scattering (or Frölich scattering).[22] In HgI_2, there exist three optical modes (labeled by E_u^1, E_u^2, and A_{2u}^1) which lead to a nonzero dipole moment. As a result, these modes are infrared active and possess angular dispersion at $\mathbf{q}$ near zero (see Fig. 4 of Ref. 4). The electron-phonon interaction due to polar-optical scattering associated with mode j is given by

$$H_{\text{el-ph}}=\frac{1}{\sqrt{NM_{\text{cell}}}}\sum_{\mathbf{q},\alpha}\sqrt{\frac{M_{\text{cell}}}{M_\alpha}}\frac{e}{v_c}\frac{e_\alpha^*\hat{\epsilon}_\alpha^{(j)}\cdot\hat{q}}{\epsilon(\infty)}\left(\frac{4\pi q}{q^2+q_0^2}\right)Q_{\mathbf{q}j}e^{i\mathbf{q}\cdot\mathbf{r}}, \tag{16}$$

where e is the free electron charge, e_α^* is the effective dynamic charge of ion α, $\epsilon(\infty)$ is the high-frequency dielectric constant, $\hat{\epsilon}_\alpha^{(j)}$ is the polarization vector, v_c is volume of the unit cell, and q_0 is the reciprocal Debye screening length

(which depends on the free carrier concentration). The effective dynamic charge e_α^* is defined as $|\partial M/\partial u|$, where u is the relative displacement and M is the corresponding electric moment. For noncubic crystals, e_α^* should be different for different directions of the applied electric field. The parallel and perpendicular components of e_α^* can be related to the longitudinal and transverse phonon frequencies defined as zeros and poles of $\epsilon(\omega)$ of the three infrared active modes by[28]

$$4\pi(N/V)\sum_\alpha \frac{e_\alpha^{*2}}{M_\alpha}=\epsilon(\infty)\sum_j(\omega_{jL}^2-\omega_{jT}^2).$$

Their values, determined by reflectivity measurements, are $e_l^*=2.27e$ and $e_t^*=3.06e$ for the Hg ion.[12] Here the subscript $l(t)$ indicates parallel (perpendicular) to the c axis. For the I ion, the charge neutrality gives $e_I^*=-\frac{1}{2}e_{Hg}^*$. In the rigid-ion model,[3] the anisotropy for both the dynamic charge and dielectric constant is ignored, and it is found that[4] $e^{*2}/\epsilon(\infty)=0.266$ for the I ion. Using $\epsilon_l(\infty)=5.2$ and $\epsilon_t(\infty)=5.45$ and the experimental values for e_l^* and e_t^* (see Ref. 12), we obtain $e_l^{*2}/\epsilon_l(\infty)=0.248$ and $e_t^{*2}/\epsilon_t(\infty)=0.429$ for the I ion. The rigid-ion model prediction turns out to be quite close to the experimental result for the electric field along the c axis. It should be pointed out here that the effective dynamic charge appears to be too large compared with that inferred from the first-principles calculation.[1] If we write the total longitudinal polarization (including contribution from ions and valence electrons) as[23]

$$\mathbf{P}_l=\sum_\alpha e_{l\alpha}^*\mathbf{u}_\alpha,$$

where $\mathbf{u}_\alpha$ denotes the displacement vector for atom α, then $e_{l\alpha}^*=e_\alpha^*/\epsilon(\infty)$ corresponds to the effective charge introduced by Callen[24] in the diatomic case. This effective charge is a measure of the ionicity and its value for I in HgI_2 is around $-0.25e$, indicating that the material is more covalent than ionic, consistent with the prediction given in Ref. 1. Comparing Eq. (17) with Eq. (6), the effect of polar-optical scattering can be described by a q-dependent coupling coefficient with

$$D_j^*(\mathbf{q})=\left|\sum_\alpha\sqrt{\frac{M_{cell}}{M_\alpha}}\frac{e}{v_c}\frac{e_\alpha^*\hat{\epsilon}_\alpha^{(j)}\cdot\hat{q}}{\epsilon(\infty)}\right|\left(\frac{4\pi q}{q^2+q_0^2}\right)$$

$$\equiv C_j(\theta_q)\left(\frac{q}{q^2+q_0^2}\right). \tag{17}$$

Using the displacement vectors obtained by the rigid-ion model,[4] we can obtain the angular-dependent coefficients $C_j(\theta_q)$ for the E_u^1, E_u^2, and A_{2u}^1 modes. To include the anisotropy effect, we simply replace $e_\alpha^*\hat{\epsilon}_\alpha^{(j)}\cdot\hat{q}/\epsilon(\infty)$ in Eqs. (16) and (17) by

$$\left[\frac{e_{\alpha,l}^*\hat{\epsilon}_{\alpha,l}^{(j)}}{\epsilon_l(\infty)}+\frac{e_{\alpha,t}^*\hat{\epsilon}_{\alpha,t}^{(j)}}{\epsilon_t(\infty)}\right]\cdot\hat{q}. \tag{18}$$

In Fig. 3, we plot the angular dependent coupling coefficient C_j for the three infrared active optical branches (E_u^1, E_u^2, and A_{2u}^1). The solid curves are results obtained by using Eq. (17) and the isotropic effective dynamic charge predicted by the rigid-ion model[4] and a spherical dielectric constant $\epsilon(\infty)=5.2$. The dotted curves are results obtained by using the anisotropic expression (18) and the low-temperature experimental values[12] for $e_{l,t}^*$ and $\epsilon(\infty)$.

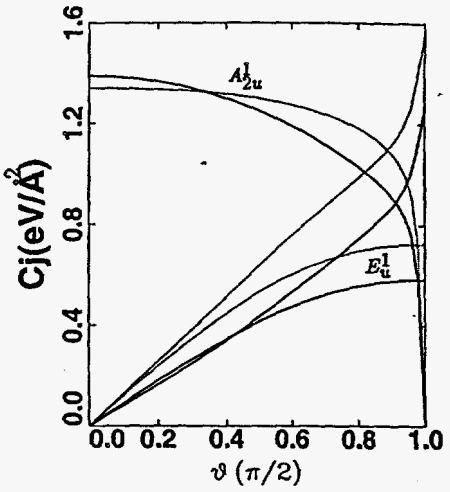

FIG. 3. Angular dependence of the coupling coeficient for polar-optical-phonon scattering for the three infrared-active modes. Solid curves: with isotropic dynamic charge as given in Ref. 4. Dotted curves: with anisotropic dynamic charges as given in Ref. 12.

The scattering rate due to polar-optical-scattering associated with mode j is given by

$$W_j(\mathbf{k})=\frac{1}{8\pi^2\rho}\int\frac{C_j^2(\theta_q)q^2}{\omega_j(\theta_q)(q^2+q_0^2)^2}\{n(\omega_j(\theta_q))\delta_{\mathbf{k}',\mathbf{k}+\mathbf{q}}\times\delta(E_{\mathbf{k}'}-E_{\mathbf{k}}-\hbar\omega_j(\theta_q))+[n(\omega_j)+1]\delta_{\mathbf{k}',\mathbf{k}-\mathbf{q}}\times\delta(E_{\mathbf{k}'}-E_{\mathbf{k}}+\hbar\omega_j)\}d\mathbf{k}'d\mathbf{q}. \tag{19}$$

In this paper, we are only interested in low carrier concentrations so that q_0 in Eq. (14) can be neglected. For $\mathbf{k}$ along a general direction, including the anisotropy of band structure and phonon dispersion is complicated. We therefore adopt a spherical approximation in which we ignore the angular dependence of the phonon dispersion $\omega_j(\theta_q)$, and we define new variables

$$q_i^*=\sqrt{\sigma}q_i \quad \text{for } i=x,y$$

and $q_z^*=q_z$, where $\sigma\equiv m_t^*/m_l^*$, and similarly for $\mathbf{k}^*(\mathbf{k}'^*)$, so that $E_{\mathbf{k}}(E_{\mathbf{k}'})$ becomes a spherical function of $\mathbf{k}^*(\mathbf{k}'^*)$. Equation (19) becomes

TABLE III. Spherical averages of the coupling coefficients C_j for polar-optical scatterings associated with the E_u^1, E_u^2, and A_{2u}^1 modes calculated by the rigid-ion model and by using experimental values for effective dynamic charges (in parentheses). All coefficients are in units of eV/Å^2. The optimum frequencies $\bar{\omega}_j$ used in Eq. (29) in units of THz are included in parentheses following the band symmetry label.

Band	$E_u^1(1.078)$	$E_u^2(3.549)$	$A_{2u}^1(4.035)$
C1	0.460(0.580)	0.626(0.832)	1.115(1.190)
HH	0.427(0.539)	0.573(0.766)	1.089(1.153)
LH	0.478(0.601)	0.655(0.869)	1.126(1.208)

$$W_j(\mathbf{k})=\frac{1}{8\pi^2\rho}\int\frac{C_j^2(\theta_q)}{\omega_j q^{*2}(\sin^2\theta_q^*/\sigma+\cos^2\theta_q^*)}\times\{n(\omega_j)\delta_{\mathbf{k}^{*\prime},\mathbf{k}^*+\mathbf{q}^*}\delta(E_{\mathbf{k}'}-E_{\mathbf{k}}-\hbar\omega_j)+[n(\omega_j)+1]\delta_{\mathbf{k}^{*\prime},\mathbf{k}^*-\mathbf{q}^*}\times\delta(E_{\mathbf{k}'}-E_{\mathbf{k}}+\hbar\omega_j)\}d\mathbf{q}^*d\mathbf{k}^{*\prime}/\sigma, \quad (20)$$

where $\cos\theta_q^*\equiv q_z^*/q^*$. Furthermore, we replace $C_j^2(\theta_q)/(\sin^2\theta_q^*+\sigma\cos^2\theta_q^*)$ by a spherically averaged coupling constant $\bar{C}_j^2$ defined by

$$\bar{C}_j^2=\int_{-1}^{1}\frac{C_j^2(\theta_q)}{\sin^2\theta_q^*+\sigma\cos^2\theta_q^*}d\cos\theta_q^*/2. \quad (21)$$

Carrying out the integral in Eq. (19) we obtain[21]

$$W_j(\mathbf{k})=\frac{\bar{C}_j^2}{2\pi\rho\hbar\omega_j v_k}\left\{n(\omega_j)\sinh^{-1}\sqrt{\frac{E_{\mathbf{k}}}{\hbar\omega_j}}+[n(\omega_j)+1]\sinh^{-1}\sqrt{\frac{E_{\mathbf{k}}}{\hbar\omega_j}-1}\right\}, \quad (22)$$

where $v_k=\hbar k^*/m_l^*=\sqrt{2E_{\mathbf{k}}/m_l^*}$. The spherically averaged coupling constants as defined in Eq. (21) are listed in Table III.

TABLE IV. Coefficients for transport parameters for acoustical phonons as given in Eqs. (21) and (22). The abbreviations $c^*=c_{11}-c_{12}-2c_{44}$, $c_l=c_{12}+2c_{44}+\frac{3}{5}c^*$, and $\bar{c}=(c_{44}+\frac{1}{2}c^*)(c_{44}+\frac{1}{3}c^*)$ have been used. The integrals I_n and J_n are the same as defined in Ref. 20.

ξ_l	$I_0+(c^*/c_l)(-0.15I_0+1.5I_2-1.75I_2)$
η_l	$2I_1+(c^*/c_l)(-0.3I_1+3I_2-3.5I_3$
ζ_l	$I_2+(c^*/c_l)(-0.15I_2+1.5I_3-1.75I_4)$
ξ_l'	$\frac{c_l(c_{44}+5c^*/6)}{\bar{c}}(I_1-I_2)-\frac{c^*c_l}{\bar{c}}(I_2-I_3)$
η_l'	$2I_3+(c^*/c_l)(-0.3I_3+3I_4-3.5I_5)$
ζ_l'	$2I_4+(c^*/c_l)(-0.3I_4+3I_5-3.5I_6)$
$\xi_t,\eta_t,\zeta_t,$ ξ_t',η_t',ζ_t'	same as parallel cases above but with $\frac{1}{2}J_n$ replacing each I_n

V. MOMENTUM RELAXATION RATES AND MOBILITY

To calculate the carrier mobility, we also need the momentum relaxation time τ_i (the subscript i denotes the direction of transport) which is related to the scattering rate via the expression[20,25]

$$\frac{1}{\tau_i(E)}=\int k_i(k_i-k_i')W(\mathbf{k}',\mathbf{k})d\mathbf{k}'\,\delta(E-E_{\mathbf{k}})d\mathbf{k}\Big/\int k_i^2\delta(E-E_{\mathbf{k}})d\mathbf{k}, \quad (23)$$

where $W(\mathbf{k}',\mathbf{k})$ denotes the scattering rate from state $\mathbf{k}$ to $\mathbf{k}'$.

The momentum relaxation rates for acoustical phonons with deformation potentials described by Eqs. (10) and (11) can be worked out analytically similar to the theory of Herring and Vogt[20] and we obtain

$$\frac{1}{\tau_l(E)}=(2\pi/\hbar c_L)\frac{3}{4}[\xi_l\Xi_d^{*2}+\eta_l\Xi_d^*\Xi_r^*+\zeta_l(\Xi_r^{*2}+2\Xi_d^*\Xi_s^*)+\xi_l'\Xi_u^{*2}+\eta_l'\Xi_r^*\Xi_s^*+\zeta_l'\Xi_s^{*2}]k_BTN(E) \quad (24)$$

for transport parallel to the c axis and

$$\frac{1}{\tau_t(E)}=(2\pi/\hbar c_L)\frac{3}{4}[\xi_t\Xi_d^{*2}+\eta_t\Xi_d^*\Xi_r^*+\zeta_t(\Xi_r^{*2}+2\Xi_d^*\Xi_s^*)+\xi_t'\Xi_u^{*2}+\eta_t'\Xi_r^*\Xi_s^*+\zeta_t'\Xi_s^{*2}]k_BTN(E) \quad (25)$$

for transport perpendicular to the c axis. Here E is the energy of the carrier, $c_L=c_{12}+2c_{44}+\frac{3}{5}(c_{11}-c_{12}-2c_{44})$ is the average elastic constant, k_B is the Boltzmann constant, and T is the temperature. $\xi_{l,t}$, $\eta_{l,t}$, $\zeta_{l,t}$, $\xi_{l,t}'$, $\eta_{l,t}'$, and $\zeta_{l,t}'$ are constants depending on the effective mass ratio $\sigma\equiv m_t^*/m_l^*$ and the elastic constants c_{11}, c_{12}, and c_{44}. Explicit expressions for these constants are given in Table IV and their values for HgI_2 are listed in Table V. The elastic constants used are (in units of 10^{11} dyn cm^{-2}) $c_{11}=3.16$ (Ref. 9), $c_{12}=0.559$ (Ref.

TABLE V. Transport parameters for acoustical phonons of HgI_2.

Band	ξ_l	η_l	ζ_l	ξ_l'	η_l'	ζ_l'	ξ_t	η_t	ζ_t	ξ_t'	η_t'	ζ_t'
C1	1.322	1.647	0.603	0.435	1.501	0.399	1.338	0.628	0.145	0.393	0.224	0.051
HH	1.297	1.797	0.724	0.376	1.829	0.478	1.343	0.783	0.203	0.420	0.353	0.083
LH	1.333	1.566	0.548	0.447	1.096	0.340	1.333	0.551	0.118	0.371	0.170	0.038

27), and $c_{44}=0.727$ (Ref. 9). Note that in the above equations we have used the equipartition approximation, i.e.,

$$n(\omega_q)=(e^{\hbar\omega_q/k_BT}-1)^{-1}\approx\frac{k_BT}{\hbar\omega_q}.$$

This is a good approximation, since at room temperature, we have $\hbar\omega_q/k_BT\ll 1$.

For zeroth-order optical-phonon scattering, one can show that $1/\tau=W(k)$ as given in Eq. (12) because the coupling coefficient is independent of $\mathbf{q}$ and the angular average of the term proportional to k_ik_i' in Eq. (19) vanishes.[21] For the first-order optical-phonon scattering, we obtain

$$\frac{1}{2\tau_t(E)}=\frac{1}{\tau_l(E)}=\frac{\Xi_l^{*2}m_t^{*2}\sqrt{2m_l^*}}{\pi\rho\omega_1\hbar^5}\times n(\omega_1)\sqrt{E+\hbar\omega_1}\left[\tfrac{2}{3}(E+\hbar\omega_1)+\tfrac{2}{5}E\right]+[n(\omega_1)+1]\sqrt{E-\hbar\omega_1}\left[\tfrac{2}{3}(E-\hbar\omega_1)+\tfrac{2}{5}E\right]. \tag{26}$$

Note that τ_t^{-1} is twice as large as τ_l^{-1}. This is due to the fact that $\Xi_l^*(q)=\Xi_l^*\sin\theta_q$ which suppressed the scattering along the c axis.

To calculate the momentum relaxation rate for polar-optical scattering, we set $q_0=0$. This is valid for the low carrier concentration ($<10^{14}\ \mathrm{cm}^{-3}$) considered here. Substituting Eq. (17) into Eq. (20) we obtain

$$\frac{1}{\tau_l(E)}=\frac{3\hbar^3}{16\pi^2\rho(2m_l^*E)^{3/2}}\sum_j\int_{-k_m}^{k_m}dk_zk_z\int d\phi_q^*\int_0^{\pi}d\theta_q^*\frac{C_j^2(\theta_q)\cos\theta_q^*\sin\theta_q^*}{\omega_j(\sin^2\theta_q^*+\sigma\cos^2\theta_q^*)}\times\{-n(\omega_j)[q_+^{(1)}/R_+(q_+^{(1)})+q_+^{(2)}/R_+(q_+^{(2)})]+[n(\omega_j)+1][q_-^{(1)}/R_-(q_-^{(1)})+q_-^{(2)}/R_-(q_-^{(2)})]\}, \tag{27}$$

$$\frac{1}{\tau_t(E)}=\frac{3\hbar^3}{32\pi^2\rho(2m_l^*E)^{3/2}}\sum_j\int_{-k_m}^{k_m}(k_m^2-k_z^2)^{1/2}dk_z\int d\phi_q^*\int_0^{\pi}d\theta_q^*\frac{C_j^2(\theta_q)\sin^2\theta_q^*\cos\phi_q^*}{\omega_j(\sin^2\theta_q^*+\sigma\cos^2\theta_q^*)}\times\{-n(\omega_j)[q_+^{(1)}/R_+(q_+^{(1)})+q_+^{(2)}/R_+(q_+^{(2)})]+[n(\omega_j)+1][q_-^{(1)}/R_-(q_-^{(1)})+q_-^{(2)}/R_-(q_-^{(2)})]\}, \tag{28}$$

where $k_m=\sqrt{2m_l^*E}/\hbar$, $R_\pm(q)=(\hbar^2/m_l^*)|q\pm(k_z\cos\theta_q^*+(k_m^2-k_z^2)^{1/2}\sin\theta_q^*\cos\phi_q^*)|$. $q_\pm^{(1)}$ and $q_\pm^{(2)}$ are two positive real roots of the equation

$$\frac{\hbar^2}{2m_l^*}[q^2\pm 2q(k_z\cos\theta_q^*+(k_m^2-k_z^2)^{1/2}\sin\theta_q^*\cos\phi_q^*)]=\pm\hbar\omega_j.$$

Here θ_q^* is the polar angle of $\mathbf{q}^*$ with respect to the c axis and ϕ_q^* is the azimuthal angle between $\mathbf{q}^*$ and $\mathbf{k}$.

If we replace $C_j^2(\theta_q)/(\sin^2\theta_q^*+\sigma\cos^2\theta_q^*)$ by its spherically averaged value and $\omega_j(\theta_q)$ by its value at the angle where $C_j(\theta_q)$ is peaked, the above results reduce to[21]

$$\frac{1}{\tau(E)}=\frac{\bar{C}_j^2}{4\pi\rho\hbar\bar{\omega}_jv_E}\left\{n(\bar{\omega}_j)\left[\sqrt{1+\frac{\hbar\bar{\omega}_j}{E}}-\frac{\hbar\bar{\omega}_j}{E}\sinh^{-1}\sqrt{\frac{E}{\hbar\bar{\omega}_j}}\right]\right\}+\left\{[n(\bar{\omega}_j)+1]\left[\sqrt{1-\frac{\hbar\bar{\omega}_j}{E}}+\frac{\hbar\bar{\omega}_j}{E}\sinh^{-1}\sqrt{\frac{E}{\hbar\bar{\omega}_j}-1}\right]\right\}, \tag{29}$$

where $v_E=\sqrt{2E/m_l^*}$. The values of $\bar{\omega}_j$ [$=\omega_j(\pi/2)$ for the E_u^1 and E_u^2 modes and $\omega_j(0)$ for the A_{1u} mode] are listed in Table III.

Using Eqs. (24)–(29) and Tables I–V, we can calculate the momentum relaxation rates due to both deformation-potential and polar-optical scatterings. Figure 4 (Fig. 5) shows the results for the electron (hole) at (a) 300 K and (b) 77 K. For simplicity, the polar-optical scattering rates were calculated in the spherical model [Eq. (29)]. In Fig. 4, the three peak structures for the polar-optical scattering are due to the onset of the optical-phonon emission at the phonon energies for modes E_u^1, E_u^2, and A_{2u}^1, with the E_u^1 mode being the strongest, since it has much lower phonon energy compared with the other two modes and $1/\tau$ is inversely proportional to ω_j [see Eq. (29)]. In Fig. 5, both the heavy-hole and light-hole contributions are included. The light-hole contribution starts at hole energy of 0.2 eV which corresponds to the heavy-hole and light-hole splitting at the zone center (see, Ref. 2). We note that the polar-optical scattering dominates the other scatterings for carrier energies less than 0.1 eV, and it becomes comparable to the sum of all other scattering rates at carrier energies around 0.5 eV. For carriers with energies higher than 0.5 eV, the deformation-potential scattering becomes more important. However, for high-

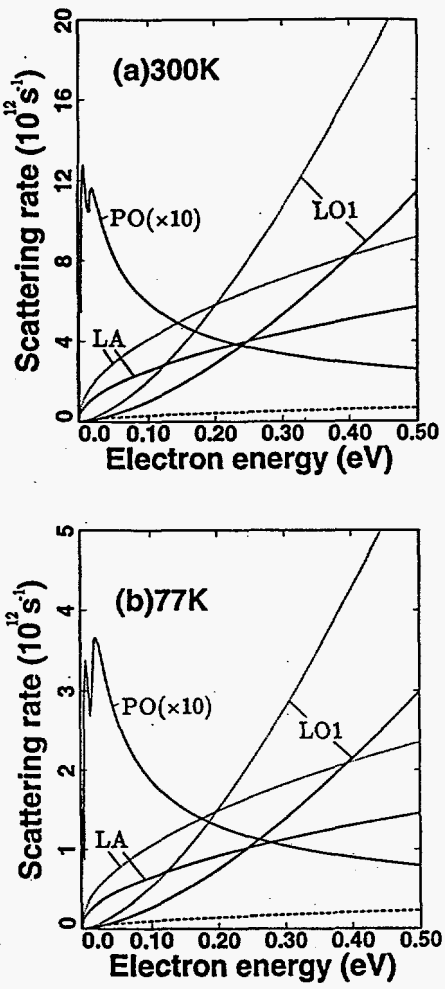

FIG. 4. Momentum relaxation rates associated with various phonon branches at (a) 300 K and (b) 77 K as functions of the electron energy for the lowest conduction band. The polar-optical-phonon rates have been scaled down by a factor 10. Solid curves: parallel to the c axis. Dotted curves: perpendicular to the c axis. Dashed curve: LO deformation potential scattering (isotropic).

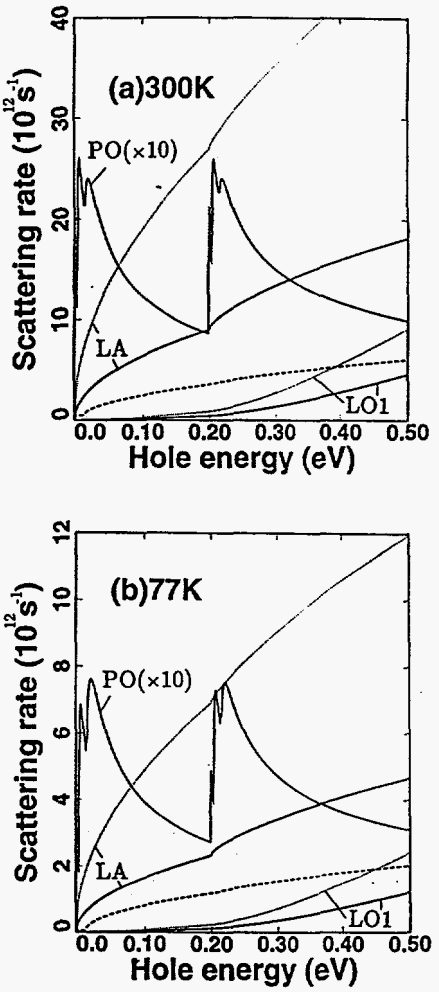

FIG. 5. Momentum relaxation rates associated with various phonon branches at (a) 300 K and (b) 77 K as functions of the hole energy for the heavy-hole band. The polar-optical-phonon rates have been scaled down by a factor 10. Solid curves: parallel to the c axis. Dotted curves: perpendicular to the c axis. Dashed curve: LO deformation potential scattering (isotropic).

energy carriers, the scattering with large-momentum phonons becomes important, and the deformation potential approximation adopted here which assumes that $D(q)$ is proportional to q will be invalidated. In addition, the deformation potentials for interband scattering as well as intervalley scattering also need to be considered.

The anisotropy in the momentum relaxation rate due to polar-optical scattering is also examined based on Eqs. (27) and (28). The results for the electron (hole) are shown in Fig. 6 (Fig. 7) for (a) $T=300$ K and (b) $T=77$ K. The solid (dotted) curves are for $\tau_l^{-1}(\tau_t^{-1})$. Also shown in these figures are the results (dash-dotted curves) obtained by using the spherical-model expression [Eq. (29)]. For both the electron and hole, the anisotropy is quite large with τ_t^{-1} larger than τ_l^{-1} by about a factor between 1.5 and 2. We can understand this behavior by examining Fig. 3 in which we find that C_j is zero at $\theta=0$ (parallel to c axis) and large at $\theta=\pi/2$ (perpendicular to c axis) for the E_u^1 and E_u^2 modes. This enhances the scattering rates perpendicular to the c axis.

Finally the mobilities are related to the momentum relaxation times via[20]

$$\mu_l=\frac{e}{m_l^*}\frac{\langle E\tau_l(E)\rangle}{\langle E\rangle},$$

$$\mu_t=\frac{e}{m_t^*}\frac{\langle E\tau_t(E)\rangle}{\langle E\rangle},$$

where $\langle\ \rangle$ denotes a thermal average with a Boltzmann distribution in the nondegenerate limit. To calculate the mobility, we use the momentum relaxation rates for deformation potential as obtained above. To simplify the calculation, we use the spherical-model expression [Eq. (29)] for the polar-optical scattering, but scale it by appropriate factors to take into account the anisotropy for the electron. As shown in Fig. 6, τ_l^{-1} and τ_t^{-1} differ from the spherical results $(1/\tau)$ approximately by an energy-independent factor. We find $\tau_l^{-1}\approx 0.821\tau^{-1}$ and $\tau_t^{-1}\approx 1.281\tau^{-1}$ for the electron. For the hole, we find $\tau_l^{-1}\approx 0.734\tau^{-1}$ and $\tau_t^{-1}\approx 1.335\tau^{-1}$. Figures 8 and 9 show the mobility as a function of temperature for the electron and hole, respectively. The results are in fairly good

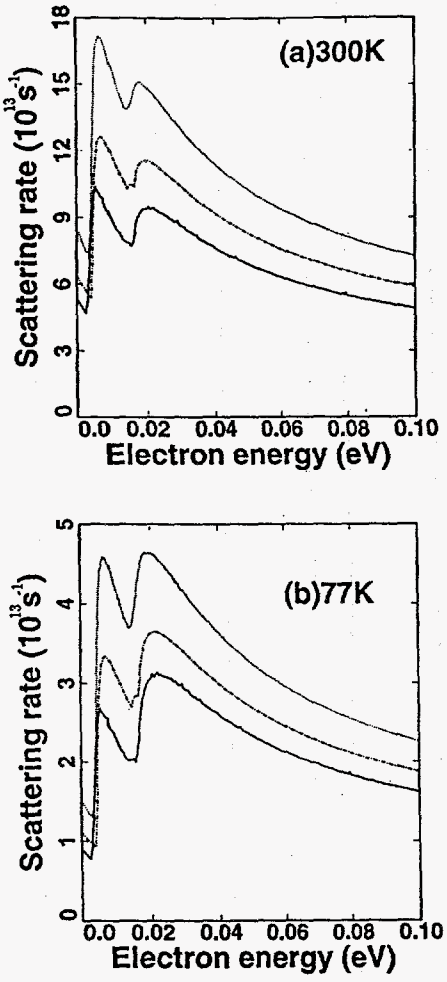

FIG. 6. Momentum relaxation rates associated with polar-optical scattering at (a) 300 K and (b) 77 K as functions of the electron energy for the lowest conduction band. Solid curves: τ_t^{-1}. Dotted curves: τ_l^{-1}. Dot-dashed curve: τ^{-1} (spherical model).

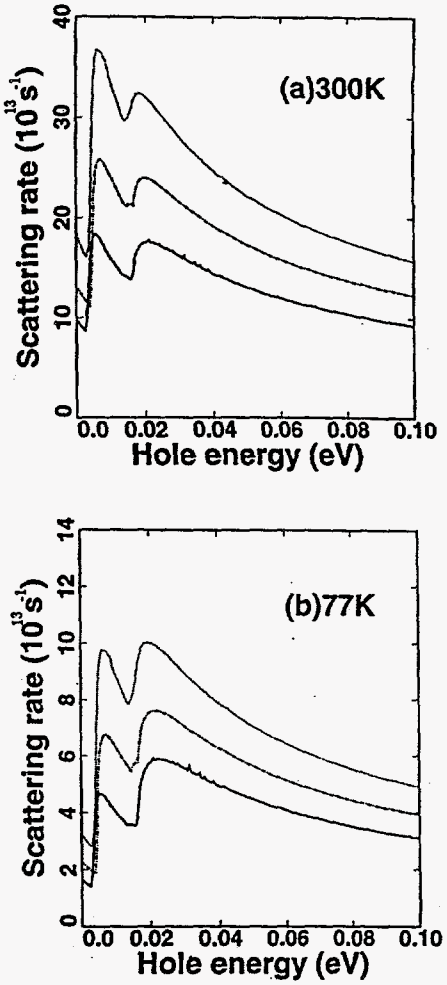

FIG. 7. Momentum relaxation rates associated with polar-optical scattering at (a) 300 K and (b) 77 K as functions of the hole energy for the heavy-hole band. Solid curves: τ_t^{-1}. Dotted curves: τ_l^{-1}. Dot-dashed curve: τ^{-1} (spherical model).

agreement with the experimental data taken by Minder *et al.*,[14,15] indicating that the intrinsic scattering mechanism plays a major role in the observed mobility. Table VI shows a comparison between our theoretical predictions and experimental data for the mobilities at 200 and 300 K. The calculated mobilities are in general within a factor of 2 of the experimental values. The discrepency may be attributed to the uncertainty in the effective masses and dynamic charges used. We predict that the electron mobility is higher for transport parallel to the c axis than that perpendicular to the c axis for all temperatures, while the opposite is true for the hole mobility. This qualitative difference is consistent with experimental data and it can be explained with our theoretical analysis. For the electron transport, the polar-optical scattering rate perpendicular the c axis is about 1.6 times that parallel to the c axis (see Fig. 7) and the longitudinal to transverse effective mass ratio is 1.276; thus the combined effect favors the mobility parallel to the c axis. For the hole transport, the polar-optical scattering rate perpendicular the c axis is about 1.8 times that parallel to the c axis (see Fig. 7) and the logitudinal to transverse effective mass ratio is 2.0, which causes the mobility parallel to the c axis to be slightly

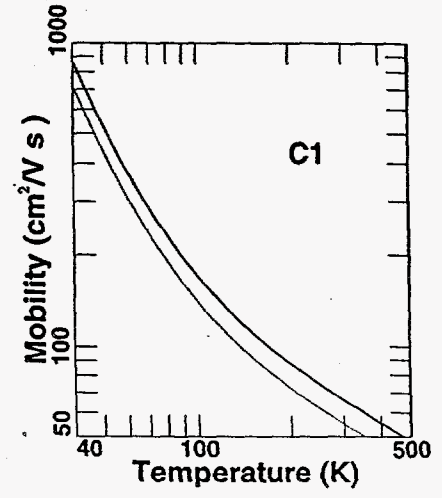

FIG. 8. Electron mobilities as functions of temperature. Solid (dotted) curve is for transport parallel (perpendicular) to the c axis.

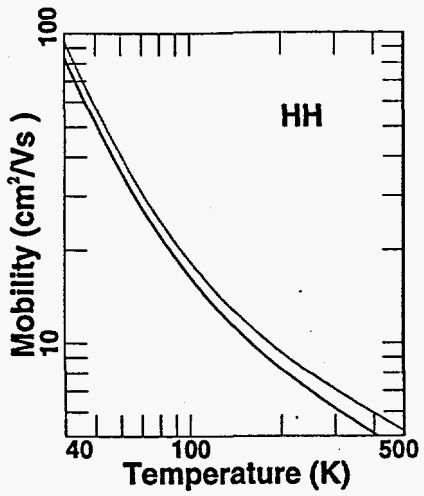

FIG. 9. Hole mobilities as functions of temperature. Solid (dotted) curve is for transport parallel (perpendicular) to the c axis.

smaller than that perpendicular to the c axis. Experimentally, the ratio of longitudinal to transverse mobility (μ_l/μ_t) is about 1.4 for the electron and 0.5 for the hole for temperatures below 200 K.[13] The corresponding values obtained here is 1.2 and 0.85, respectively. The discrepency is most likely caused by the uncertainty in the values of effective masses used here. Had we used different hole effective masses such that the ratio m_l^*/m_t^* is 4.2 as suggested by the first-principles calculation,[1] then the calculated mobility ratio (μ_l/μ_t) would have been about 0.5, in good agreement with data. It should be noted that HgI_2 undergoes a structural phase transition (from α to β phase) at a temperature around 427 K.[26] Thus, our theoretical predictions for the mobilities at temperatures beyond 427 K should not be taken seriously.

VI. CONCLUSION

We have presented detailed theoretical studies of the carrier-phonon scattering due to all possible phonon modes. It is found that the polar-optical phonon scattering dominates the transport properties for low-energy carriers which are of common interest. For the electron, the mobility along the c axis is slightly higher than that perpendicular to the c axis, while for the hole the reverse is true. This qualitative difference is explained by the anisotropy in the momentum relaxation rate and the large anisotropy in the hole effective mass. The calculated results for both electron and hole mobilities are in good agreement with the experiment (within a factor of 2) when the sample is sufficiently pure where the intrinsic scattering dominates. The discrepency between theory and transport data is most likely caused by the uncertainty in the input values of effective masses and dynamic charges used in the calculation. The uncertainty in the phonon polarization vectors calculated by the rigid-ion model can be another source of error, since the empirical phonon model contains a large number of adjustable parameters. On the other hand, since the polar-optical phonons dominate transport and their polarization vectors are largely determined by the dynamic charges and symmetry, the error introduced by the nonuniqueness of short-range parameters should be small. Namely, the angular dependence of the electron-phonon coupling and hence the anisotropy in scattering rates obtained this way should be fairly reliable. By comparing the anisotropy in calculated and measured mobilities, we conclude that the longitudinal to transverse effective mass ratio for the hole should be around 4, in agreement with the first-principles calculation of Ref. 1. Although the deformation-potential scattering is found to be relatively unimportant in determining the mobility for HgI_2, it will play an important role in the analysis of Raman and photoluminescence spectra of HgI_2.

TABLE VI. Comparison between theory and experiment on the carrier mobilities of HgI_2 (in units of cm^2/V sec).

Temperature		μ_l^e	μ_t^e	μ_l^h	μ_t^h
200 K	Theory	88	72	8.2	9.3
	Experiment	145[a]	90[b]	10[a]	
300 K	Theory	67	55	6.2	7.1
	Experiment	100[a]	65[b]	4[a]	23[c]

[a]Minder *et al.* (Ref. 14).
[b]Minder *et al.*. (Ref. 15).
[c]Manfredotti *et al.* (Ref. 16).

ACKNOWLEDGMENT

This work is supported in part by the U.S. Department of Energy.

[1] D. E. Turner and B. N. Harmon, Phys. Rev. B **40**, 10 516 (1989).
[2] Y. C. Chang and R. B. James, Phys. Rev. B **46**, 15 040 (1992).
[3] Y. C. Chang, H. K. Sim, and R. B. James, in *Semiconductors for Room Temperature Radiation Detector Application*, edited by R. B. James, T. E. Schlesinger, P. Siffert, and L. Franks, MRS Symposia Proceedings No. 302 (Materials Research Society, Pittsburgh, 1993), p. 121.
[4] H. K. Sim, Y. C. Chang, and R. B. James, Phys. Rev. B **49**, 4559 (1994).
[5] K. Kanzaki and I. Imai, J. Phys. Soc. Jpn. **32**, 1003 (1972).
[6] P. D. Bloch, J. W. Hodby, C. Schwab, and D. W. Stacey, J. Phys. C **11**, 2579 (1978).
[7] T. Goto and A. Kasuya, J. Phys. Soc. Jpn. **50**, 520 (1981).
[8] A. Anedda, F. Raga, E. Grilli, and M. Guzzi, Nuovo Cimento **38**, 439 (1977).
[9] B. Prevot, C. Schwab, and B. Dorner, Phys. Status Solidi B **88**, 327 (1978).
[10] S. Nakashima and Z. M. Balkanski, Phys. Rev. B **34**, 5801 (1986).
[11] N. Kuroda, T. Iwabuchi, and Y. Nishina, J. Phys. Soc. Jpn. **52**, 2419 (1983).
[12] J. Biellmann and B. Prevot, Infrared Physics, **20**, 99 (1979).
[13] X. J. Bao, T. E. Schlesinger, and R. B. James, in *Semicoductors and Semimetals*, edited by T. E. Schlesinger and R. B. James (Academic Press, San Diego, 1995), Vol. 43, Chap. 4.
[14] R. Minder, G. Majni, C. Canali, G. Ottaviani, R. Stuck, J. P.

Ponpon, C. Schwab, and P. Siffert, J. Appl. Phys. **45**, 5074 (1974).
[15]R. Minder, G. Ottaviani, and C. Canali, J. Phys. Chem. Solids **37**, 417 (1976).
[16]C. Manfredotti, R. Murri, and L. Vasanelli, Solid State Commun. **21**, 53 (1977).
[17]P. D. Bloch, J. W. Hodby, T. E. Jenkins, D. W. Stacey, and C. Schwab, Nuovo Cimento B **38**, 337 (1977).
[18]O. Madelung, *Introduction to Solid State Theory* (Springer-Verlag, New York, 1978), Chap. 4.
[19]M. Sieskind, J. Phys. Chem. Solids **39**, 1251 (1978).
[20]C. Herring and E. Vogt, Phys. Rev. **101**, 944 (1956).
[21]B. K. Ridley, *Quantum Process in Semiconductors* (Oxford University Press, New York, 1982).
[22]H. Frölich, Proc. R. Soc. London A **160**, 230 (1937).
[23]T. Kurosawa, J. Phys. Soc. Jpn. **16**, 1298 (1961).
[24]H. Callen, Phys. Rev. **76**, 1394 (1949).
[25]This expression is valid for elastic scattering for anisotropic band and for both elastic and inelastic scaterings for isotropic band. For inelastic scattering and anisotropic band, the expression is not quite valid. In our case, however, since the dominant optical-phonon (E_u^1) mode has an energy (~3 meV) much smaller than the average electron (hole) energy at room temperature (~26 meV), the scattering is almost elastic. So we expect that the use of this expression will not lead to significant error.
[26]J. B. Newkirk, Acta Metall. **4**, 316 (1956).

APPENDIX C

Structure and Surface

Left Intentionally Blank

Electrodrift Purification of Mercuric Iodide for Improved Gamma-Ray Detector Performance

J. M. Van Scyoc[1], R. B. James[1], A. Burger[2], E. Soria[1], C. Perrino[1], E. Cross[1], M. Schieber[1], and M. Natarajan[3]

[1]Advanced Materials Research Department, Sandia National Laboratories, Livermore, CA 94550
[2]Center for Photonic Materials and Devices, Department of Physics, Fisk University, Nashville, TN 37208
[3]TN Technologies, Inc., Round Rock, TX 78680

Abstract

The primary problems with mercuric iodide for use in room-temperature radiation detectors are the low yield of high quality devices and the problems with detector stability. It is believed that one of the prime causes of these failures is the presence of certain detrimental impurities. Previous experiments have demonstrated that these impurities can be introduced during processing and that they can strongly affect detector performance. Significant effort has been expended to develop and utilize various mercuric iodide purification schemes. While these techniques are effective to some degree, the level of impurities in detector materials is still higher than that found in more established semiconductors. In this work we developed and investigated a new purification scheme that is based on the mobility of many of the impurities in mercuric iodide under an applied electric field. In this "electrodrift" process undesirable metallic impurities are removed from a portion of a bulk mercuric iodide charge to produce higher purity material for detector crystal growth. The lower level of impurities results in fewer charge-trapping centers, and therefore improved detector performance and stability. This paper reports on some preliminary results of the effectiveness of this method.

Introduction

Although mercuric iodide (HgI_2) has been studied for over two decades as a material for room-temperature radiation detectors, it has not yet found widespread usage in the rapidly expanding number of applications being developed for such devices. It has only been in recent years that it

has found a commercial market, primarily in portable x-ray fluorescence analyzers. The two main problems with mercuric iodide detectors are the low yield of high quality devices and the short-term and long-term instability of detector performance. Given that the fabrication technology of mercuric iodide devices has not yet had sufficient development time to approach the level of sophistication of that used for traditional semiconductors, it is quite likely that the processing is not yet optimized. Therefore, it should be possible to eventually achieve satisfactory device yields and performance.

Although the specific underlying causes of these detector failures are not yet completely understood, it is believed that impurities are still one of the primary limiting factors in mercuric iodide detectors. For example, many metallic impurities are found in the range of hundreds of ppb to several ppm in the mercuric iodide used for crystal growth. There has been considerable work done in developing and implementing various purification techniques, and a great deal of the time and resources involved in detector crystal production go into the initial purification of materials prior to the crystal growth.

Several techniques have been pursued for mercuric iodide purification, including zone-refining, sublimation, and solvent extraction.[1] Of these methods, sublimation has been found to be the most effective, and specific multi-step sublimation sequences have been developed for the purification process. One common procedure starts with the synthesis of HgI_2 from $HgCl_2$ and KI purified themselves in a similar process [2] and progresses through multiple vacuum sublimations, a melt and resolidification, and a closed tube sublimation.[3,4] Zone-refining was initially studied and rejected, as the results were not promising at that time [1]; however, there have been somewhat successful recent efforts with zone-refining [5], and it may yet become useful as a replacement for the melt and resolidification step in the above sequence. With all of these methods there is a concern with the final stoichiometry of the material, as non-stoichiometry has been shown to degrade the electronic properties of the material, particularly in the case of excess mercury. [6,7]

In this work we have developed a new method for mercuric iodide purification that could be used either in addition to or to replace portions of the current process to achieve higher purity

materials. The present methods rely on the selective movement of impurities based on their preferential segregation in different phases of matter. In the sublimation methods the mercuric iodide is preferentially transported in the vapor to another location, leaving behind the impurities. In zone-refining the impurities are selectively concentrated in a moving melted zone, with purer mercuric iodide left behind. In both of these techniques there may be some impurities -- not necessarily the same ones -- that are not effectively removed because of a low selectivity.

The method discussed here relies on the fact that many of the impurities in mercuric iodide are mobile and strongly affected by applied electric fields. By applying an electric field to the mercuric iodide it is possible to "sweep out" the impurities from a section of material that can then be used for crystal growth. It is expected that some types of impurities would pile up at the negative end, while others would pile up at the positive end of the bulk mercuric iodide, leaving the center portion as the purest material. This technique would only be effective on impurities that are mobile in electric fields, i.e. those that exhibit a charge when in the mercuric iodide. Given that the electrodrift, sublimation, and zone-refining may be more effective for different particular impurities, they are complementary and would be integrated into a complete purification process.

Experiments

In the electrodrift process developed in this work a sample of bulk mercuric iodide is secured in position and contacted at either end by stable high-purity contacts, such as thin films of palladium or platinum. A high voltage power supply of sufficient current-sourcing capacity is used to apply a fixed bias across the sample. A current meter is used in the circuit to measure the leakage current throughout the process.

The room-temperature resistivity of mercuric iodide is very high, on the order of 10^{13} Ω*cm for high purity material, meaning that the expected current level is very low. In the initial stages of the process, however, the material will have a much lower resistivity because of the higher level of impurities. However, in the samples studied thus far, the current density has still peaked at only a few microamps per square centimeter at fields on the order of 0.1 to 1.0 V/μm.

The current is closely monitored versus time to give an indication of the progress of the process. As the material approaches a higher purity, it is expected that the resistivity should increase and the current decrease. Figure 1 gives a schematic diagram of the general electrodrift setup, along with the expected general shapes of the current versus time and impurity distributions.

In the present work two polycrystalline mercuric iodide samples were prepared in 7 mm inner diameter Pyrex tubes. Unpurified HgI_2 powder was packed into the tube, then melted and resolidified. The final HgI_2 slugs were 26 mm long for sample ED1, and 39 mm long for ED2. Sample ED1 was shorter than ED2 because a portion of ED1 was removed from one end prior to the electrodrift biasing to provide a control for estimating initial impurity concentrations. For these two samples simple painted aquadag contacts were applied to either end and the sample sealed. Unfortunately, aquadag is rather "unclean" and is believed to have introduced impurities into the HgI_2 as discussed later.

The samples were electrically connected to the biasing and measuring system, and placed in a dark temperature-controlled chamber. The current versus time data were recorded the entire time the samples were under bias. Sample ED1 had a bias of 1100 V and sample ED2 had a bias of 975 V applied. Assuming a uniform field distribution in the bulk mercuric iodide -- a rather poor assumption for polycrystalline material -- this gives fields of 0.042 V/μm and 0.025 V/μm, respectively. Sample ED1 was subjected to elevated temperatures up to 50 °C and only biased over a period of a few days, while ED2 was kept at room temperature and biased over a period of over a month.

Immediately following removal of the bias, the samples were sectioned (ED1 into three pieces and ED2 into five pieces) and the impurities quantified via Inductively Coupled Plasma Mass Spectroscopy (ICP-MS) and Inductively Coupled Plasma Optical Emission Spectroscopy (ICP-OES)[8]. ICP-MS is routinely used in the impurity analysis of mercuric iodide and can quantify many impurities into the low ppb range. ICP-OES, while in general not as sensitive as ICP-MS, is more reliable, and was used here to confirm the ICP-MS measurements. Further details on the chemical analyses done in this work can be found in reference 8.

Results and Discussion

A previous set of experiments conducted on single-crystal detector-scale mercuric iodide slabs with intentional doping revealed the movement of impurities under an applied electric field. It is known that many impurities have high diffusivities in mercuric iodide, particularly copper and silver. Four-point-probe measurements on unbiased metal layers of copper showed a sharp rise in the measured sheet resistance, indicating a loss of the conductive thin film as copper diffused into the bulk HgI_2.[9] The entire 2000 Å Cu film apparently disappeared within a few days. Subsequent leakage current experiments on biased detector slabs revealed that copper [10] and silver [11] are mobile in electric fields and exhibit a positive charge. Both of these impurities were forced from the positive contact to the negative contact, with a few hundred Å film swept across the detector in a few hours. Qualitatively, this means that the electrodrift process was about an order of magnitude faster than diffusion. As these are the two primary competing processes in the electrodrift process, it is the ratio of the diffusivity to the "electrodrift mobility" that determines the effectiveness of the purification for a particular element.

The initial resistivity of the mercuric iodide, as determined by I-V measurements, was about 2 x 10^8 Ω*cm for ED1 and 7 x 10^7 Ω*cm for ED2. The factor of three difference can be readily explained by differences in the detailed structure of the polycrystalline masses, as the conductivity is dependent on the grain boundary structure, for example. Also, it is possible that there were gross voids in the HgI_2 that effected the conduction pathways, as well as the electric field structure.

Sample ED1 was subjected to electrodrift at temperatures of 34 °C and 50 °C, since increases in temperature are expected to increase the rate of impurity movement. Both the diffusivity and the electrodrift mobility would increase with increasing temperature, though not necessarily at the same rate. Part of the optimization of the process would be finding a temperature where the ratio is most favorable. Figure 2 shows the leakage current as a function of time for this sample. ED2 was biased at room temperature, but for a much longer period, and its current plot is shown in Figure 3. Between 500 and 600 hours a failure in the biasing system resulted in the sample being

unbiased for two days. As can be seen by the rise in the current upon rebiasing, diffusion dominated during the outage, and some of the impurities had to be reswept. At the time of the biasing failure there was arcing in the system for an estimated period of 10 minutes. After rebiasing, the background level had increased by a factor of five, possibly indicating some undetermined damage to the sample.

As can be seen in Figures 2 and 3, the current in both samples rose to a peak value on the order of tenths of a microamp and very slowly decayed to a lower level. The peak current is caused by the movement of impurities across the bulk mercuric iodide, as those with negative charge are accelerated toward the positive contact, and those with positive charge move toward the negative contact. The total integrated charge moved in the process was on the order of 10^{16} charges for ED1 and 5 x 10^{15} charges for ED2. Once the mobile impurities have been swept out, the low current level that results is the background electronic conduction. The detailed shape of the current curves are dependent on the details of the underlying processes, which are not yet fully understood. One prime characteristic that needs to be determined is the conduction pathway for the impurities. It is not known if these impurities move along grain boundaries, or as interstitials, or by some other mechanism. From the model of the mechanism the electrodrift mobility could be defined. This would then allow for predicting the optimal conditions for electrodrift to dominate over diffusion.

After the leakage current has decreased to the background level, it is expected that the impurities will be piled up at the ends, with the center portion of the sample at the lowest level in all impurities. ED1 was sectioned into three pieces after electrodrift, labeled ED1-N for the portion adjacent to the negative contact, ED1-C for the center portion, and ED1-P for the portion adjacent to the positive contact. In addition, a sample of the original starting material was studied and was labeled ED1-S. Finally, given the concern of contamination from the aquadag, a sample of the dag was analyzed. Figure 4 shows a few of the chemical analyses results for sample ED1. In particular, Cu and Ag, which were previously shown to be positively charged, have piled up at the negative electrode. The overall level of the impurity is about an order of magnitude lower for the

silver than for the copper. Cd, on the other hand, appears to be negatively charged and collects at the positive contact. As can be seen from the data, the aquadag does contain non-negligible amounts of impurities. These impurities complicate the situation, as they form a large source at both ends of the sample and will be swept into the HgI_2. This is why the use of a high purity material for the contacts is desirable.

Figure 5 shows some results for ED2. This sample was sectioned into more pieces, to give a better measure of the impurity distribution. Ag again piles up at the negative electrode, and Cd piles up at the positive electrode.

In both samples there were other elements that appear to have possibly moved, but the results were not as clear as for those shown above. In particular, Ga, Zn, Mg, Pb, As, Na, Al, Rb, and Sr all appear to develop monotonic concentration gradients, while Cr, Fe, Co, Ni, Se, and Cs do not preferentially pile up at either end. Although the results are not yet fully understood, it is the case that the center portion (ED1-C or ED2-C) always has the lowest concentration of total impurities. Therefore, the electrodrift process does indeed produce an amount of purified mercuric iodide. Further work is required to understand the process, however.

Summary and Conclusions

This work has shown that by utilizing the mobility of impurities in biased mercuric iodide it is possible to purify the material. This electrodrift purification can be used to produce material of higher purity for detector crystal growth, which should lead to improvements in the resultant devices. Work continues, in order to develop an understanding of the process of electrodrift in detail. In particular, in addition to a larger database of samples, several other experiments are suggested by the results thus far. Given the randomness in the polycrystalline material, the electric field structure in the sample is not uniform, and it is difficult to study the motion of the impurities. Work is underway on single crystal samples which should have a more uniform field distribution, as well as being easier to cleanly cleave into multiple small sections for chemical analyses. Finally, the ultimate goal is to produce better detectors, so growth of crystals from the central swept portion is planned. It is believed that given the effects of impurities on detector performance and the

effectiveness of the electrodrift process for certain impurities, detectors grown from electrodrifted material should show improved performance.

References

[1] M. Schieber, W. F. Schnepple, and L. van den Berg, *J. Crystal Growth* **33**, (1976) 125.

[2] N. L. Skinner, C. Ortale, M. M. Schieber, and L. van den Berg, *J. Crystal Growth* **89**, (1988) 86.

[3] V. Gerrish, in *Semiconductors for Room-Temperature Radiation Detector Applications*, Materials Research Society Symposium Proceedings **302**, (1993) 129.

[4] A. Burger, D. Nason, L. van den Berg, and M. Schieber, in *Semiconductors for Room Temperature Nuclear Detector Applications*, edited by T. E. Schlesinger and R. B. James, Academic Press (1995) Chapter 3: Growth of Mercuric Iodide.

[5] A. Burger, S. H. Morgan, C. He, E. Silberman, L. van den Berg, C. Ortale, L. Franks, and M. Schieber, *J. Crystal Growth* **99**, (1990) 988.

[6] R. C. Whited and L. van den Berg, *IEEE Trans. Nucl. Sci.* **NS-24**, (1977) 165.

[7] M. Schieber, H. Hermon, and M. Roth, in *Semiconductors for Room-Temperature Radiation Detector Applications*, Materials Research Society Symposium Proceedings **302**, (1993) 347.

[8] E. Cross et al., Grenoble paper.

[9] J. M. Van Scyoc, T. E. Schlesinger, R. B. James, A. Y. Cheng, C. Ortale, and L. van den Berg, in *Semiconductors for Room-Temperature Radiation Detector Applications*, Materials Research Society Symposium Proceedings **302**, (1993) 115.

[10] J. M. Van Scyoc, R. B. James, T. E. Schlesinger, and T. S. Gilbert, in *Defect- and Impurity-Engineered Semiconductors and Devices*, Materials Research Society Symposium Proceedings **378** (in press).

[11] J. M. Van Scyoc, R. B. James, T. E. Schlesinger, T. S. Gilbert, and M. Schieber, *J. Crystal Growth* (in press).

Figure Captions

Figure 1. Basic schematic of the setup used for the electrodrift purification process. Also shown are the general shapes expected for the leakage current versus time and the impurity distributions. As seen in the impurity distribution plot, the center portion of the mercuric iodide bulk, where the total impurity level is the lowest, is the material used for detector crystal growth.

Figure 2. Leakage current versus time for sample ED1 as discussed in the text for two sample temperatures.

Figure 3. Leakage current versus time for sample ED2 as discussed in the text. The break between 500 and 600 hours is the result of a loss of bias.

Figure 4. Quantitative chemical analyses results for sample ED1. The Cu, Ag, and Cd results are shown for the three sections of the sample after electrodrift, the initial material before electrodrift, and the aquadag used for the contacts.

Figure 5. Quantitative chemical analyses results for sample ED2. The Ag and Cd results are shown for the five sections of the sample after electrodrift processing.

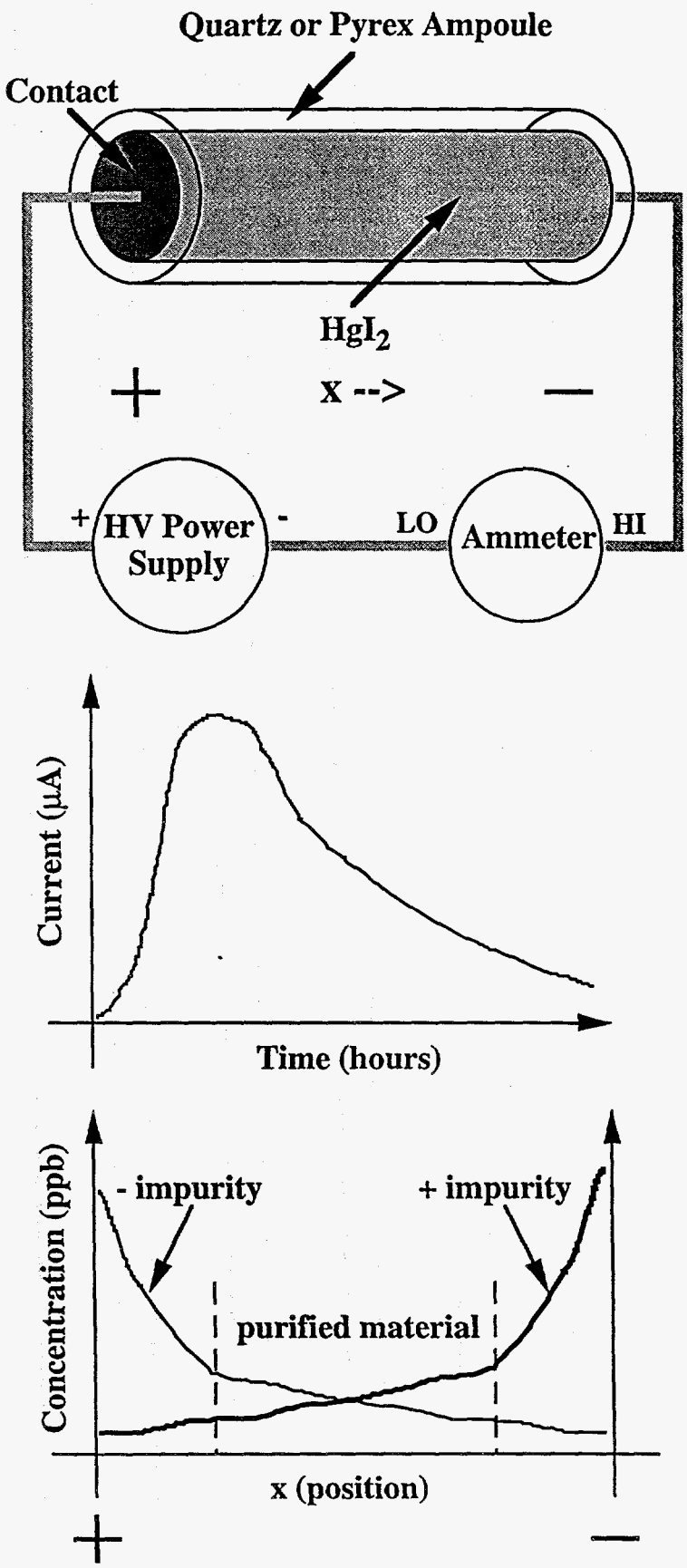
Quartz or Pyrex Ampoule
Contact
HgI_2
x -->
+
—
+
HV Power Supply
-
LO
Ammeter
HI
Current (μA)
Time (hours)
Concentration (ppb)
- impurity
+ impurity
purified material
x (position)
+
—

Figure 1

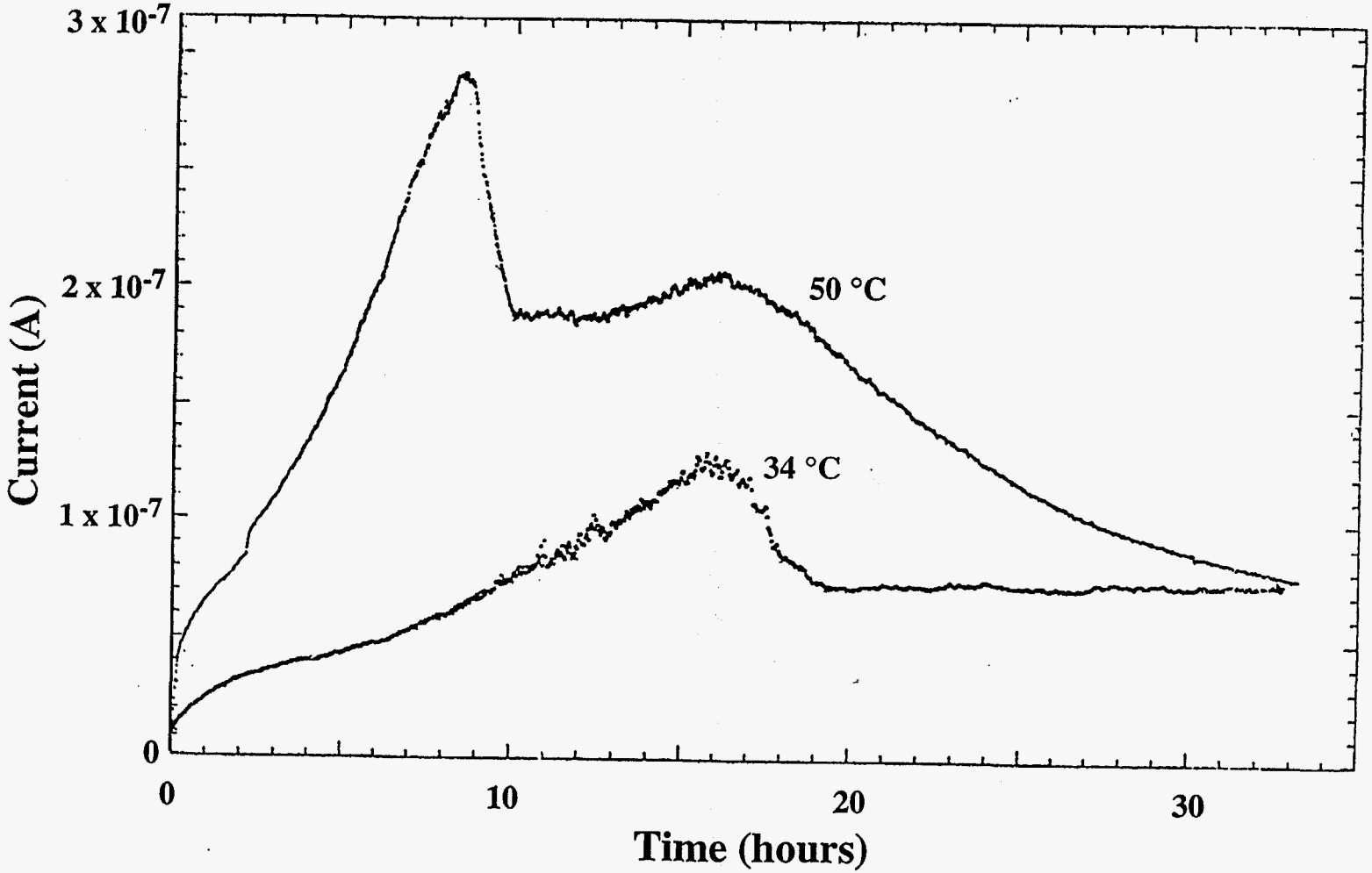

Figure 2

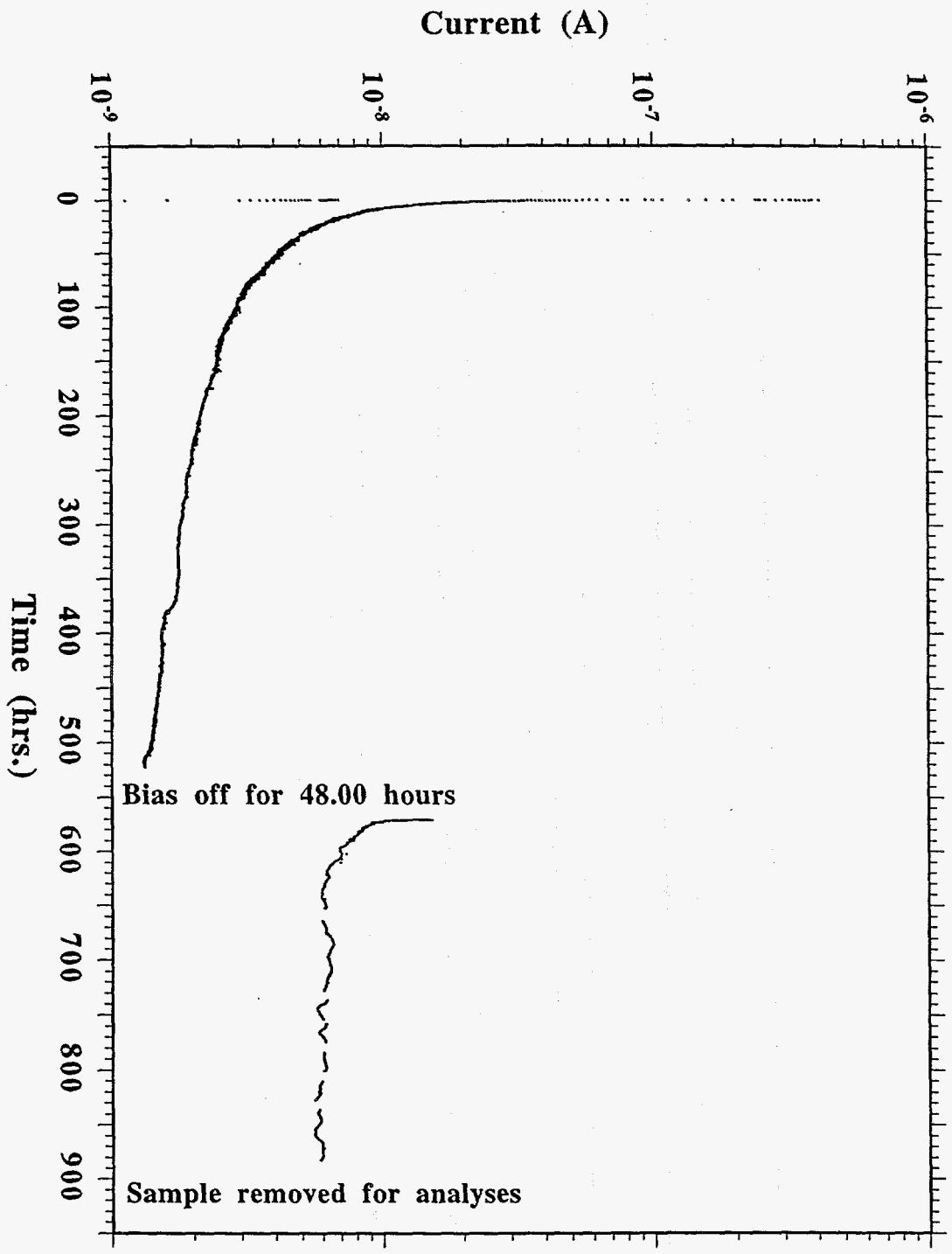
Current (A)
10-9
10-8
10-7
10-6
Time (hrs.)
0
100
200
300
400
500
600
700
800
900
Bias off for 48.00 hours
Sample removed for analyses

Figure 3

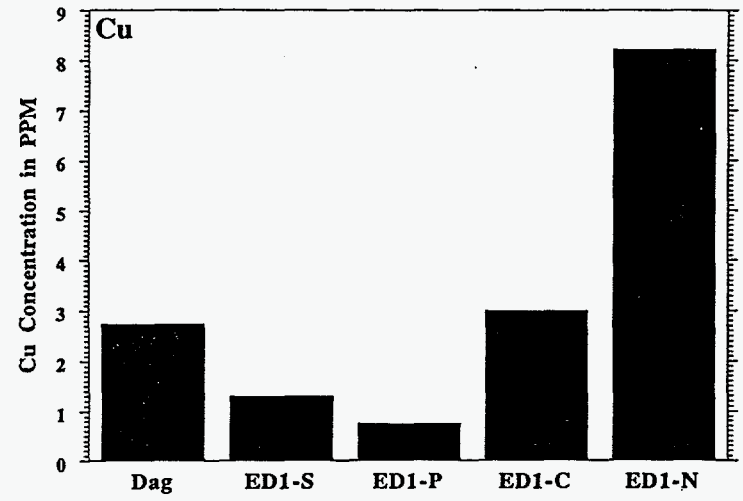
Cu
Cu Concentration in PPM
0
1
2
3
4
5
6
7
8
9
Dag
ED1-S
ED1-P
ED1-C
ED1-N

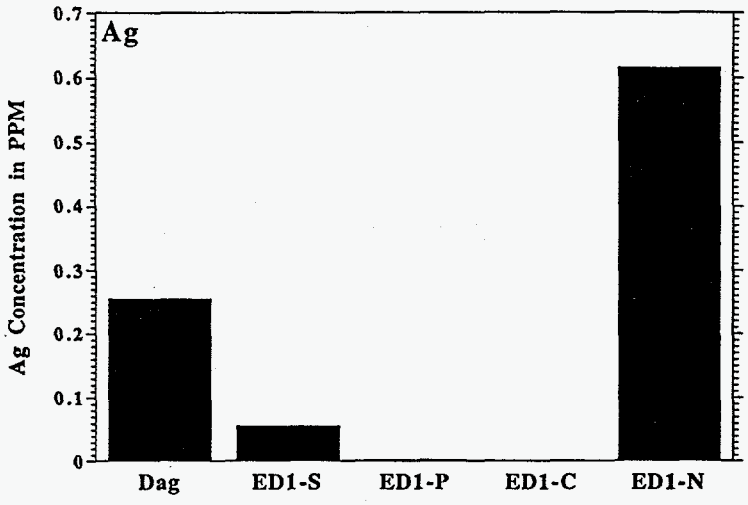
Ag
Ag Concentration in PPM
0
0.1
0.2
0.3
0.4
0.5
0.6
0.7
Dag
ED1-S
ED1-P
ED1-C
ED1-N

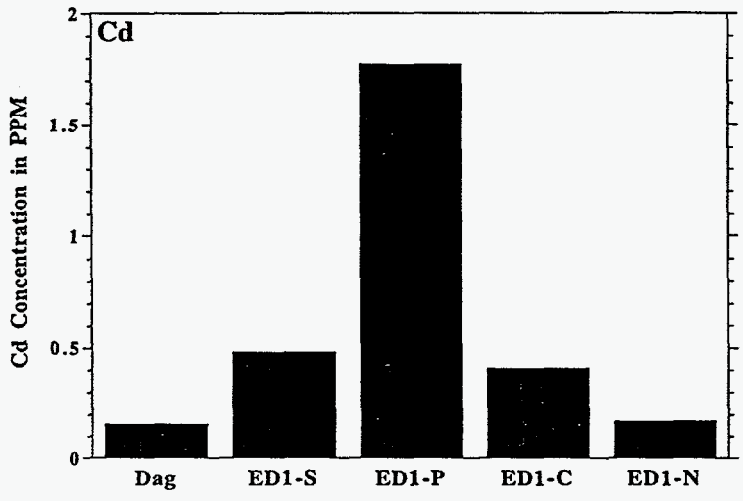
Cd
Cd Concentration in PPM
0
0.5
1
1.5
2
Dag
ED1-S
ED1-P
ED1-C
ED1-N

Figure 4

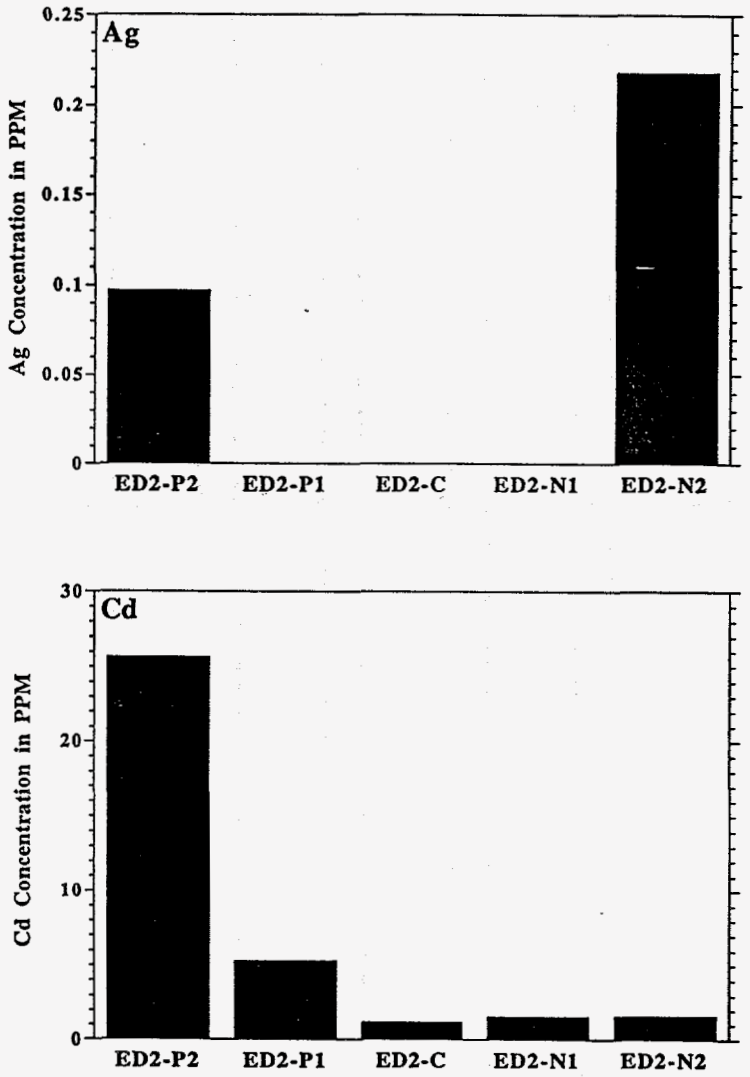
Ag
Ag Concentration in PPM
0.25
0.2
0.15
0.1
0.05
0
ED2-P2
ED2-P1
ED2-C
ED2-N1
ED2-N2
Cd
Cd Concentration in PPM
30
20
10
0
ED2-P2
ED2-P1
ED2-C
ED2-N1
ED2-N2

Figure 5

Nuclear Instruments and Methods in Physics Research A 000 (1996) 000–000 8339

NUCLEAR INSTRUMENTS & METHODS IN PHYSICS RESEARCH Section A

ELSEVIER

Chemical analysis of metal impurity distribution of zone-refined mercuric iodide by ICP-AES and DSC

K.-T. Chen[a,*], L. Salary[a], A. Burger[a], E. Soria[b], A. Antolak[b], R.B. James[b]

[a]*Center for Photonic Materials and Devices, Department of Physics, Fisk University, Nashville, TN 37208, USA*
[b]*Advanced Materials Research Division, Sandia National Laboratories, Livermore, CA 94550, USA*

Abstract

A mercuric iodide single crystal is being developed for X-ray and gamma-ray detector applications where high-purity starting material is required. Zone-refining processing has been proven to be an effective step in the purification of large amounts of mercuric iodide for crystal growth. In this study we used the Inductively Coupled Plasma-Atomic Emission Spectroscopy (ICP-AES) to identify and determine the distribution of impurity concentrations along the ampoule after zone-refining mercuric iodide. The results show that for Ag, Cu, Fe, Mg, Ca, Zn, Cr and Al, the zone-refining process does sweep the impurities to the last-to-freeze zone, due to an effective distribution coefficient, $k_{eff} < 1$. For Na, Ni, Cd, Mn and Pb the concentration gradient seems to be fairly independent of the position along the ingot. Differential Scanning Calorimetry was also employed to investigate the deviation from stoichiometry caused by the zone-refining process, and the results indicated that the first-to-freeze section is Hg-rich, and the middle section tends to become slightly Hg-rich, while the last-to-freeze section becomes I-rich.

1. Introduction

The zone-refining process has been developed for materials purification since 1952 [1]. This technique has become one of the important techniques used to produce a significant amount of high-purity materials, especially for elemental and compound materials. Pb [2], Ge [3], $PbBr_2$ [4] and β-BaB_2O_4 [5] starting materials are just a few examples of recent reports on purification using the zone-refining process. Chemical analysis using Inductively Coupled Plasma [5] and Spark Source Spectroscopy [4] revealed that the zone-refined sections of these materials have higher purities than the original starting materials. However, the possible alteration of the stoichiometry composition due to the zone-refining process needs to be taken into account. It has been shown that for the Sb_2S_3 [6] system zone-refining caused a redistribution of S.

α-phase mercuric iodide (α-HgI_2) has been developed as room-temperature X-ray and gamma-ray detectors due to its high atomic number, large bandgap (2.2 eV) and the low energy needed to generate an electron-hole pair. However, the performance of these detectors has been limited by trapping centers which decrease the lifetime of the charge carriers. The presence of such trapping centers can be induced by defects caused by impurities and deviation from the stoichiometry originating from the starting materials or produced during the crystal growth process. Past correlations of the impurity content in starting materials with detector performance suggests that impurities greatly affect the electronic properties of α-HgI_2 [7,8]. Therefore, in order to optimize the detector performance, high-purity α-HgI_2 starting materials are vital. Several purification methods have been developed to reduce the impurity concentrations of starting materials before crystal growth, such as zone refining, solvent extraction and repeated sublimation. Among them, the zone-refining method has been proved to be an effective way of purifying a significant amount of α-HgI_2 starting materials [9]. The effectiveness of the zone-refining process for α-HgI_2 was also evaluated indirectly by differential scanning calorimetry (DSC) measurements [9]. DSC results showed that the impurities accumulated at the last-to-freeze zone of the ingot, but they were unable to identify and determine impurities. The crystal growth by physical vapor transport using the purest part of the zone-refined materials showed easier nucleation and a reduced ampoule residue after growth. Spark source mass spectrographic [10–14] and low-temperature thermal conductivity [13] measurements have been employed to investigate the concentrations of both organic and inorganic impurities in α-HgI_2 single crystals grown from different purified starting materials and methods. It was found that the highest level of impurity is carbon in hydrocarbons up to 50,000 ppm. Other impurities have also been identified and their concentrations ranged from tens to hundreds of ppm. In this study Inductively Coupled Plasma-Atomic

*Corresponding author.

0168-9002/96/$15.00
PII S0168-9002(96)00327-0

Emission Spectroscopy (ICP-AES) was employed to identify impurities and determine their concentration distributions along the zone-refined α-HgI_2 ingot. The ICP-AES technique was used to quantify impurities in PbI_2 crystals [15], a material similar to α-HgI_2 used for gamma-ray detectors. The ICP-AES results revealed the presence of various impurities and trace concentrations to sub-ppm level. Improvements have been done to increase the capability of this technique for impurity identification and detection limits. The results were evaluated to reveal the effectiveness and to optimize the parameters of the zone-refining process.

2. Experiment

The α-HgI_2 starting materials were vacuum sublimated 4 times before zone-refining in a zone refiner which produced a 1 in. melting zone [9]. Quartz silica tubing with 1.5 mm wall thickness, 10 mm internal diameter and 60 cm in length was used as the zone-refining ampoule. The ampoule was first cleaned with an acetic/nitric/hydrofluoric acid solution, rinsed with deionized water and outgassed under 10^{-3} Torr vacuum for 2 h. Then α-HgI_2 starting materials with a typical weight of about 100 g were loaded into ampoules. Standard zone-refining parameters, consisting of 100 vertical zone passes, a zone travel rate of 8.5 cm/h and 270 °C of melting temperature, were used. After the completion of the zone-refining process, the ampoules were opened to recover the refined materials. The refined ingots were divided into 13 sections starting from the last-to-freeze zone where the travelling of heaters ended. For each section, a few g of samples were extracted and homogenized by thorough grinding.

A Perkin Elmer P-1000 sequential (ICP-OES) Inductively Coupled Plasma Optical Emission Spectroscopy instrument with a Cetac U-5000AT Ultrasonic Nebulizer was employed to determine the concentrations of impurities in each sample. The power setting for the plasma was 1200 W for all elements except Na (840 W) and Mn (1140 W). The nebulizer flow was set at 0.89 l/min for all elements except for Na (1.43 ml/min), Mn (0.72 ml/min) and Fe (0.82 ml/min). Optimization of the operating parameters in the presence of 4% HgI_2 was performed prior to analysis for each element. Each sample was carefully weighed (~4 g) and then transferred to a Teflon microwave digestion vessel where 8 ml of neat aqua regia were added to each sample and allowed to set overnight. The use of aqua regia interferes with the determination of the Cl impurity which was reported [9]. The samples were then diluted with 18 MΩ deionized water to an approximate volume of 50 ml each. The samples were placed in a CEM 81-D microwave oven separately and open digested for 40 min. The samples were then capped and closed-vessel digestion was performed for another 40 min. The samples were then allowed to cool down, opened for filtration and transferred into a 100 ml flask (final volume was made up with 10% aqua regia solution). This 100 ml sample was split into 2 separate 50 ml samples. A 400 ppb standard spike addition was added to one 50 ml sample and to the other a similar volume of 10% aqua regia blank (2 ml) was added. This was done to later compare percent spike recoveries for each sample. The detection wavelengths and the instrumental detection limits of all elements are listed in Table 1. A DSC-10 equipped with the thermal analyst

Table 1
The detection limits and impurity concentration distributions along zone-refined α-HgI_2 ingot measured by ICP-AES (wavelength in nm; instrumental detection limit (IDL); sections 1–3: last-to-freeze; 4–10: middle; 11–13: first-to-freeze)

Detection Limits (ppb)													
Element	Ag	Cd	Cu	Cr	Fe	Mg	Mn	Na	Ni	Pb	Ca	Al	Zn
Wavelength	328	229	325	268	240	280	259	590	232	220	393	396	214
IDL	1.5	0.6	2.1	1.5	2.4	0.6	-	0.9	6.6	27	0.6	6	0.5
Impurity Concentration Distribution (ppm)													
Section	Ag	Cd	Cu	Cr	Fe	Mg	Mn	Na	Ni	Pb	Ca	Al	Zn
1	1.18	0	0.71	0.35	7.54	1.65	0.06	5.23	0.21	0.11	7.95	2.38	1.09
2	1.36	0	0.86	0.38	6.28	1.75	0.03	7.66	0.14	0.12	8.69	2.57	1.19
3	0.87	0	0.42	0.14	2.21	0.87	0.03	3.34	0.07	0.08	4.73	1.39	0.83
4	1.29	0.08	0.52	0.22	2.68	0.98	1.42	1.19	0	0	2.34	1.69	0.56
5	0.76	0.08	0.41	0.15	1.88	0.66	5.02	1.33	0	0.09	1.81	1.34	0.54
6	0.42	0.04	0.15	0.12	1.59	0.74	2.87	0.84	0	0	1.68	1.27	0.51
7	0.14	0	0.12	0.06	1.26	0.83	0	4.89	0	0.07	3.53	0.51	0.79
8	0.05	0	0.24	0.05	1.16	0.82	0.03	4.53	0	0.18	3.76	0.15	0.47
9	0.08	0	0.09	0.05	0.77	0.51	0	1.48	0.06	0.13	1.41	0.29	0.27
10	0.11	0	0.11	0.11	2.67	0.44	0	1.29	0.21	0.17	1.65	0.73	1.27
11	0.11	0	0.12	0.11	2.05	1.01	0.03	3.89	0.05	0	3.41	0.67	0.42
12	0.15	0	0.16	0.07	1.27	1.08	0.03	5.36	0.11	0	5.02	0.44	0.55
13	0.12	0	0.14	0.09	0.97	0.33	1.57	0.61	0	0	0.61	0.62	0.24

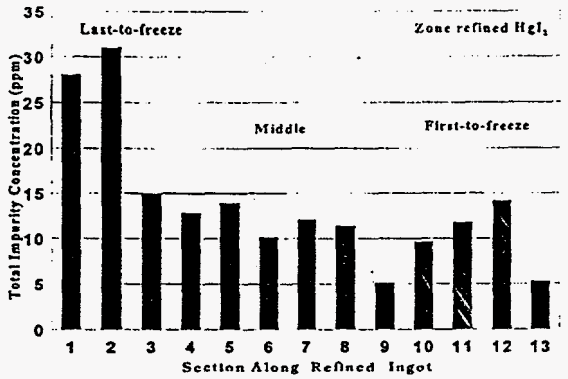

Fig. 1. The total impurity concentration distributions along the zone-refined HgI_2 ingot.

2000 (TA Instruments) was employed to investigate the alteration of the stoichiometry caused by the zone-refining process. Typical sample sizes of about 160 mg and sealed stainless-steel pans were used. Samples were extracted from first-to-freeze, middle and last-to-freeze sections along the zone-refined ingot. For each sample 3 heating rates, 2, 5 and 10 °C/min were used within the temperature range 50–300 °C.

3. Results and discussion

Visual observation indicated that the last-to-freeze zone (where the molten zone travel terminates) is the darkest region, gradually turning into bright reddish in the middle region and becoming slightly darker in the first-to-freeze region (where the molten zone travel begins). This observation is consistent with previous studies [9] using DSC measurement to show the depression of the transition and melting temperatures at the darkest last-to-freeze region due to accumulation of impurities. The ICP-AES results are also tabulated in Table 1 and the total impurity concentrations are shown in Fig. 1. The results revealed that the zone-refined α-HgI_2 contained impurities of Ag, Cd, Cu, Cr, Fe, Mg, Mn, Na, Ni, Pb, Ca, Zn and Al. There is a clear demonstration that Ag, Cu, Cr, Fe, Mg, Ca, Zn and Al impurities accumulated most at the last-to-freeze zone, having a distribution coefficient $k_{eff} < 1$. The total concentration of these impurities, Fig. 1, from sections 1 to 3, the last-to-freeze region, is about 75 ppm. For the rest of the sections, the total concentrations of these impurities range from a few to no more than 15 ppm. For Na, Ni, Cd, Mn and Pb the concentration gradient seems to be fairly independent of the position in the ampoule, and their concentrations range from sub-ppm to a few ppm. In previous studies, several synthesis and purification methods have been used to obtain high-purity HgI_2 starting materials. These starting materials and the as-grown crystals have been analyzed by different techniques [8–13]. For those impurities with $k_{eff} < 1$ in this study, they found that for the same impurity the concentrations range from a few ppm to tens of ppm levels. This comparison indicates that by combining multiple vacuum sublimation, the zone-refining process can purify large amounts and a higher purity of HgI_2 starting material. We found no evidence for impurities having $k_{eff} \lesssim 1$. One possible reason for this might be the fact that, in the vertical zone-refining process, sample 13 (first-to-freeze) is the only material having an equilibrium between liquid and gas phase and the possibility of sublimation of those impurities therefore exists.

DSC results are tabulated in Table 2, and 3 phase transitions were observed for all samples, namely $\alpha \rightarrow \beta$, second phase and melting. The final transition temperatures were calculated by extrapolating to a 0 °C/min heating rate from a linear least square fit of 3 transition temperatures obtained by 3 heating rates (2, 5 and 10 °C/min). For the first-to-freeze and middle section samples, the thermogram shows peaks around 130, 235 and 259 °C corresponding to the $\alpha \rightarrow \beta$ solid phase transition, the Hg-rich second phase or the eutectic temperature of the HgI_2–Hg_2I_2 solid solution, and the melting temperature of HgI_2 [16], respectively. The transition temperatures of Hg-rich second phase and melting from the first-to-freeze sample were depressed by about 5 °C, while all transition temperatures from the middle section are consistent with the literature data [16] within the experimental error. It has been observed that the depression of the melting temperature in zone-refined HgI_2 material is caused by accumulation of the impurity and not by the stoichiometry change [16]. Therefore, the first-to-freeze material became more Hg-rich in composition than the middle section material. The thermogram of the last-to-freeze sample shows a different $\alpha \rightarrow \beta$ transition temperature profile than the other 2 samples. First, the transition temperature at 156 °C is 26 °C higher than $\alpha \rightarrow \beta$ transition, and 2 melting peaks occurred at 214 °C and 250 °C. The major peak at 250 °C

Table 2
DSC peaks from the first-to-freeze, middle and last-to-freeze sections. The peaks with 0 °C/min heating rate were extrapolated from a linear least square fit of peaks with 2, 5 and 10 °C/min heating rates

Transition (°C)	$\alpha \rightarrow \beta$ Transition				Second Phase Melting				Melting			
Heating Rate (°C/min)	0	2	5	10	0	2	5	10	0	2	5	10
First-to-freeze	131	135	137	145	230	234	234	239	255	257	258	262
Middle	129	134	139	150	234	233	234	234	257	258	259	261
Last-to-freeze	156	158	162	167	214	215	220	226	250	249	250	250

indicates that the last-to-freeze material contained more impurities than the other sections. It has been reported that the $\alpha \rightarrow \beta$ transition temperature increases as a function of the excess iodine concentration with a rate of 0.6 °C/1000 ppm [16], and the transition temperature reached a value of 157 °C when the iodine content reached 59.88 wt.% [17]. The $\alpha \rightarrow \beta$ heat of the transition was found to have a similar value within the experimental error. Therefore, the shift of the $\alpha \rightarrow \beta$ transition to a higher temperature is probably caused by the excess iodine which was shown in Fig. 2. A secondary melting peak at 214 °C always occurs, even after multiple melting/solidification cycles. The intensity is about 4% of the main melting peak and its peak position indicates the presence of a second phase. Although insoluble impurities could be responsible, it is also possible that gaseous-phase free iodine condenses on the top of the samples creating a richer iodine surface phase.

In this study, the purity of the HgI_2 material is the main concern, but, at the same time, the issue of possible deviations from stoichiometry after the zone-refining process needs to be addressed. Fig. 3 shows part of the typical thermograms with a 5 °C/min heating rate from all 3 sections. It is clear that the first-to-freeze section becomes Hg-rich in composition, while the middle section is only slightly Hg-rich. This suggests that the materials in the middle section, while being the purest material after the zone refining, may need an additional open/closed sublimation to adjust its stoichiometry composition before the actual crystal growth process.

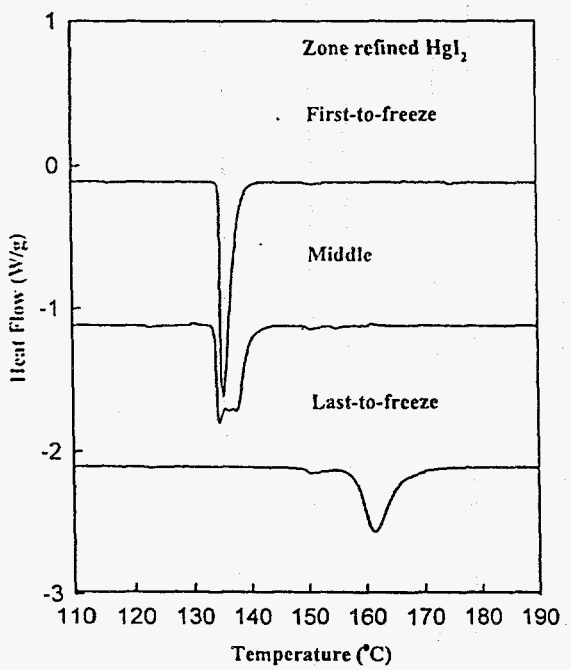

Fig. 2. Part of the typical thermograms from all 3 sections near the $\alpha \rightarrow \beta$ transition temperature, 130 °C. The heating rate was 2 °C/min.

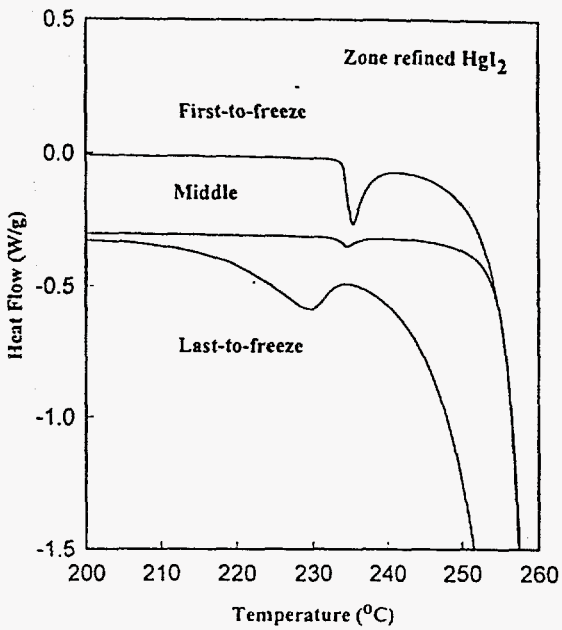

Fig. 3. Part of the typical thermograms from all 3 sections near the 235 °C regions. The heating rate was 5 °C/min.

4. Conclusions

The zone-refining process has been employed to further purify multiple sublimed HgI_2 starting materials. ICP-AES and DSC measurements have been performed to investigate the impurity concentration distribution and the deviation from stoichiometry along a zone-refined ingot. The results show that impurities with distribution coefficient $k_{eff} < 1$ have been swept and accumulated at the last-to-freeze section leaving the purest materials in the middle section. ICP-AES measurements also identified the impurities with $k_{eff} < 1$ are Ag, Cu, Cr, Fe, Mg, Ca, Zn and Al, and have typical concentrations no more than 15 ppm in the middle materials. For Na, Ni, Cd, Mn and Pb, their concentrations distributed randomly along the zone-refined ingot, and ranged from sub-ppm to a few ppm. DSC results revealed that the middle section is the purest material but it became slightly Hg-rich in composition while the first-to-freeze and the last-to-freeze materials became Hg-rich and I-rich in composition, respectively. The results suggest that the purest materials in the middle section may need further sublimation or sublimation under iodine vapor to adjust the stoichiometry composition before crystal growth.

Acknowledgments

The authors at Fisk acknowledge the support of Sandia National Labs and of NASA through the Center for Photonic Materials and Devices, Department of Energy,

under Grant DE-FG08-94NV11502, and The Office of Naval Research under Contract BMDO/ONR N00014-93.

References

[1] W.G. Pfann, Trans. AIME 194 (1952) 747.
[2] G.H. Rodway and J.D. Hunt, J. Cryst. Growth 112 (1992) 563.
[3] C.K. Jen, Ph. de Heering, P. Sutchiffe and J.F. Bussiere, Mater. Evaluation (June) (1991) 701.
[4] N.B. Singh, M. Gottlib, T. Henningsen, R.H. Hopkins, R. Mazelsky, M.E. Glicksman, S.R. Coriell, G.J. Santoro and W.M.B. Duval, J. Cryst. Growth 123 (1992) 221.
[5] T Katsumata, H. Ishijima, T. Sugano, M. Yamagishi and K. Takahashi, J. Cryst. Growth 123 (1992) 597.
[6] P. Bohac and P. Kaufmann, Mater. Res. Bull. 10 (1975) 613.
[7] A. Tadjine, D. Gosselin, J.M. Koebel and P. Siffert, Nucl. Instr. and Meth. 213 (1983) 77.
[8] N.L. Skinner, C. Ortale, M.M. Schieber and L. van den Berg, J. Cryst. Growth 89 (1988) 86.
[9] A. Burger, S.H. Morgan, D.O. Henderson, Y. Biao, K. Zhang, E. Silberman, D. Nason, L. van den Berg, C. Ortale-Baccash and E. Cross, J. Cryst. Growth 128 (1993) 1047.
[10] Y.F. Nicolau, Nucl. Instr. and Meth. 213 (1983) 13.
[11] J.T. Muheim, T. Kobayashi and E. Kaldis, Nucl. Instr. and Meth. 213 (1983) 39.
[12] T. Kobayshi, J.T. Muheim, P. Waegli and E. Kaldis, J. Electrochem. Soc. 130 (1983) 1183.
[13] Y.F. Nicolau and A.M. Andreani, J. Cryst. Growth 87 (1988) 117.
[14] A.M. de Goer, M. Locatelli and Y.F. Nicolau, J. Phys. Chem. Solids 43 (1982) 311.
[15] D.C. David, R.B. James, H. Feemster, R. Anderson, A.J. Antolak, D.H. Morse, A.E. Pontau, H. Jayatirtha, A. Burger, X.J. Bao, T.E. Schlesinger, G.S. Bench and D.W. Heikkinen, Mat. Res. Symp. Proc. 302 (1993) 335.
[16] A. Burger, S. Morgan, C. He, E. Silberman, L. van den Berg, C. Ortale, L. Franks and M. Schieber, J. Cryst. Growth 99 (1990) 988.
[17] Hua Jiang, Masters Thesis, Department of Physics, Fisk University, Nashville, TN, 1987.

Left Intentionally Blank

MATERIALS RESEARCH SOCIETY SYMPOSIUM PROCEEDINGS VOLUME 302

Semiconductors For Room-Temperature Radiation Detector Applications

Symposium held April 12-16, 1993, San Francisco, California, U.S.A.

EDITORS:

R.B. James
Sandia National Laboratories
Livermore, California, U.S.A.

T.E. Schlesinger
Carnegie Mellon University
Pittsburgh, Pennsylvania, U.S.A.

Paul Siffert
Laboratorie PHASE/CRN
Strasbourg, France

Larry Franks
EG&G Energy Measurements
Goleta, California, U.S.A.

MRS
MATERIALS RESEARCH SOCIETY
Pittsburgh, Pennsylvania

INVESTIGATION OF AN ALTERNATIVE CHEMICAL ETCHANT FOR MERCURIC IODIDE DETECTORS

DOMINIQUE C DAVID§, J. VAN SCYOC◊, MARDIK KHUDATYAN§, R. B. JAMES§, R. J. ANDERSON§, and T. E. SCHLESINGER◊
§Sandia National Laboratories, Livermore, CA 94550
◊Carnegie Mellon University, Pittsburgh, PA 15213

ABSTRACT

At present a 10% KI solution is commonly used as an etchant for HgI_2 crystals. Recent photoluminescence (PL) spectra from such etched samples show that impurities contained in the KI solution dope the HgI_2 during the etching process. Some of these dopants are known to cause carrier trapping in the detectors fabricated from the material. Thus, it is desirable to find an alternative etchant that does not create new defects in HgI_2. Etchants studied here include deionized water, 10% potassium iodide (KI), methanol, and acetone. The results of acetone as an etchant reveal only small changes in the PL spectra after etching. Methanol etching causes the incorporation of a deep radiative recombination center in HgI_2.

INTRODUCTION

Chemical etching is commonly used as a technique for preparing and cleaning the surfaces of room-temperature semiconductor materials, such as mercuric iodide. Chemical etching is very important as a surface treatment, because it removes a degraded surface layer which forms on HgI_2 crystals that have been exposed to air. In device fabrication, the possibility of contamination by the processing steps (e.g., cutting and polishing) and exposure to the environment requires improved process control and care during handling. Since low-temperature photoluminescence reveals information on defects in HgI_2, this technique was employed to investigate the physical changes in the near-surface region of HgI_2 after chemical etching.

Currently, 10% KI aqueous solution is typically used to chemically etch and polish HgI_2 surfaces. This chemical treatment improves the smoothness and cleanliness of the surfaces, which is probably critical to obtaining good detector performance. Unfortunately, the use of 10% KI is not ideal for use as a chemical treatment because KI also contaminates the HgI_2. Consequently, finding an alternative etchant or increasing the purity of the KI is important to improving the manufacturing yield and state-of-the-art for the detector technology.

Several previous investigators have used low-temperature PL to study the electronic behavior of impurities, dopants, and native defects in HgI_2 [1-11]. The leading motive for PL's acceptance in semiconductor materials

analysis is its unrivaled ability to yield information on copious amounts of defect states, as well as its relatively ease in implementation. However, the interpretation of the PL spectra of HgI_2 is not always straightforward, particularly if one wants to know the identification and nature of each recombination center. Ambiguities may arise from efforts to dope the material with specified impurities, e.g., the stoichiometry can also be modified due to the presence of contaminants. It is the aim of this paper to investigate the effects of chemical polishing with a few different etchants. Results and discussion of these investigations are presented in the next sections.

EXPERIMENTAL DETAILS

Deionized water, 10% KI, acetone, and methanol solutions were used as possible etchants. The deionized water (DI) used was between 16-18 MΩ resistance. The highest grade of purity of commercially available KI was used, and semiconductor grades of acetone and methanol were used. The KI was a 10% by weight solution of KI dissolved in deionized water. The acetone and methanol were undiluted. To conserve sample material, the same sample was sometimes used for multiple etchants, resulting in the transfer of some features from spectra to spectra. However, the changes induced by different etchants were easily distinguished.

The times intervals of the chemical etching for each etch-rate measurement were 30, 60, and 90 seconds for 10% KI and acetone, 300, 600, and 900 seconds for DI water, and 15, 30, 45 seconds for methanol. Five trial runs at each of the various time intervals were obtained to get a statistical average of each etch rate. A 3-min etching time was used for each etchant for the PL measurements. For each experiment, the samples were placed at the bottom corner of a 100-ml beaker in about 25 ml of etchant solution. The beaker was agitated gently, and the sample was flipped over half way through the time period to allow for more even etching of all surfaces. Etching was followed by a three minute DI rinse.

In this work an argon ion laser was used as the excitation source for the PL technique. The laser had a wavelength of 488 nm, power of approximately 20 mW, and a spot size of about 1-mm diameter. The laser excitation was chopped at 750 Hz. The low-temperature photoluminescence was generated in the first few microns of the sample. Therefore, the PL gave an excellent indication of the radiative recombination centers in the near-surface region. The sample was held in an optical cryostat above a pool of liquid He resulting in temperatures just below 5 K. The photoluminescence spectrum was collected by lenses and passed through a SPEX 1404 0.85-m double spectrometer, and it was detected by an S-20 photomultiplier tube. The signal was then amplified by a Keithley 427 current amplifier, measured using an EG&G 5207 lock-in amplifier, and recorded by an HP 9836 computer.

RESULTS AND DISCUSSION

Table I shows a summary of the approximate volume loss and the etch rate for each respective etchant. Knowing the dimensions of the crystal, the mass before the etch trial, and the measured mass loss, one can easily calculate the etch rate of HgI_2. The results from the DI etching measurements shows that the etch rates are a lot smaller compared to the other etchant solutions. 10% KI solution etches the surface well and visually gives the surface a shiny appearance. There is some speculation that the 10% KI can remove the degraded surface layer and restore a stoichiometric HgI_2 surface. It appears more likely that the KI etch may actually dope the surface with excess iodine. Most of the material loss for KI solutions occurs in the first 30 second of the etching, and for longer etch times the rate of material loss decreases significantly as the concentration of HgI_2 in the KI aqueous solution increases. Methanol shows promise in terms of material loss and the visual quality of the crystal surface after etching. Qualitatively, acetone did not visually show a polished smooth surface after etching, although it had about the same rate of material loss as methanol and KI.

Table I. Calculated etch rates of etchants used in study.

ETCHANT	TIME (sec)	Δ VOL (cm^3)	Etch Rate (cm^3/sec
DI	300	3.1×10^{-4}	1.0×10^{-6}
	600	9.4×10^{-4}	1.6×10^{-6}
	900	1.1×10^{-3}	1.2×10^{-6}
Acetone	30	8.3×10^{-3}	2.8×10^{-4}
	60	9.6×10^{-3}	1.6×10^{-4}
	90	13.8×10^{-3}	1.5×10^{-4}
Methanol	15	5.0×10^{-3}	3.3×10^{-4}
	30	7.7×10^{-3}	2.6×10^{-4}
	45	8.3×10^{-3}	1.8×10^{-4}

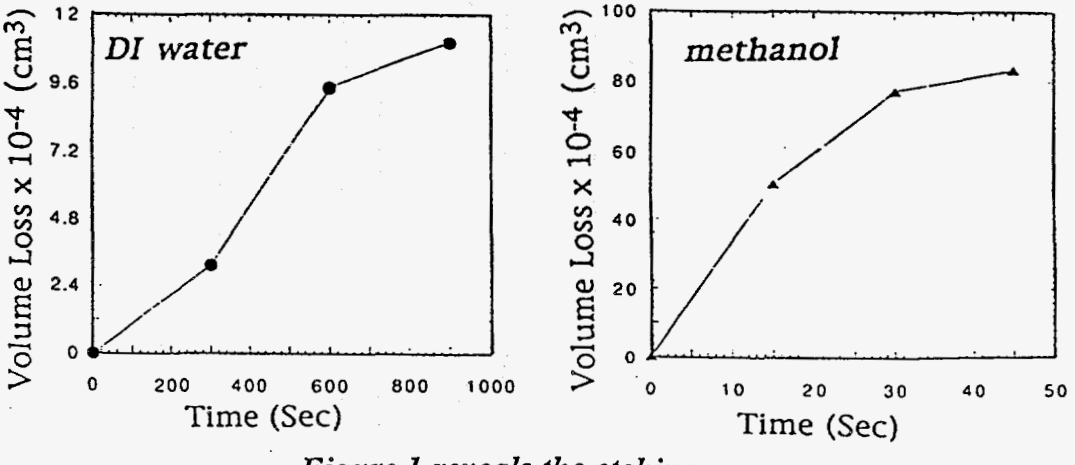

Figure 1 reveals the etching curves

The graphs of the etch-rate curves are shown for in figures 1 and 2 for DI, methanol, and acetone. The etch rate for 10-% KI has been previously reported to be about 0.4 micron/sec for 60-sec etch times [5]. All of the curves show a decrease in the etching rates at sufficiently long times. This information is indicative of when the etching solution is less effective in removing the surface layers of HgI_2.

Low temperature photoluminescence spectroscopy (PL) measurements were used to study the effects of different etchants on the defect states of HgI_2. PL has been previously demonstrated to be a useful method for characterizing processing-induced defects in the near-surface region of HgI_2. In particular, processing steps such as crystal growth, chemical etching, annealing, and contact formation can have a strong influence on PL spectra [1-3]. For some impurities, such as C, Ag, Cu, Sn and In, signature peaks have been found [4-6] and attributed to the concentration of these contaminants. The relation between the PL spectrum and subsequent detector quality has also been studied [7].

Several sharp exciton-related emission lines were found in the near-band-edge region of typical mercuric iodide PL spectra from 5290 Å to 5410 Å. This region is collectively called Band 1. The two most dominant peaks are P2 near 5318 Å and P3 near 5321 Å [8-11]. The long wavelength range of 5400 Å to 8050 Å contains several broad emissions, the most common of which are Band 2 around 5600 Å, Band 3 around 6200 Å, and Band 4 around 7550 Å [5].

Figure 3 shows the PL spectra from before and after the 10% KI etch. The largest difference noted were the decrease in the ratios of peaks between P2 and P3, and also between Band 2 and P3. Both of these are caused by the overall increase in P3. A wide variability in the PL is often observed after KI etching. This could relate to the variability of etching process, to large differences between aged HgI_2 surfaces, or to true differences in the bulk. The acetone results shown in figure 4 are for a freshly KI-etched specimen immediately before and after acetone etching Only small changes in the visible spectra are observed. The same decrease in P2/P3 and Band2/P3 ratios are noticeable, but to a much lesser extent These results suggest that the acetone etch does not introduce new defects in the near-surface region of HgI_2. Figure 5 shows the PL spectra before and after the methanol etch. The methanol etching process introduces a deep broad band centered at about 6780 Å, which is close to a Cu band peaked at 6720 Å. In general, the PL measurements have shown that deep recombination sites are detrimental to device performance and should be avoided during processing. This observation implies that methanol is not a strong candidate for replacing KI as a chemical etchant.

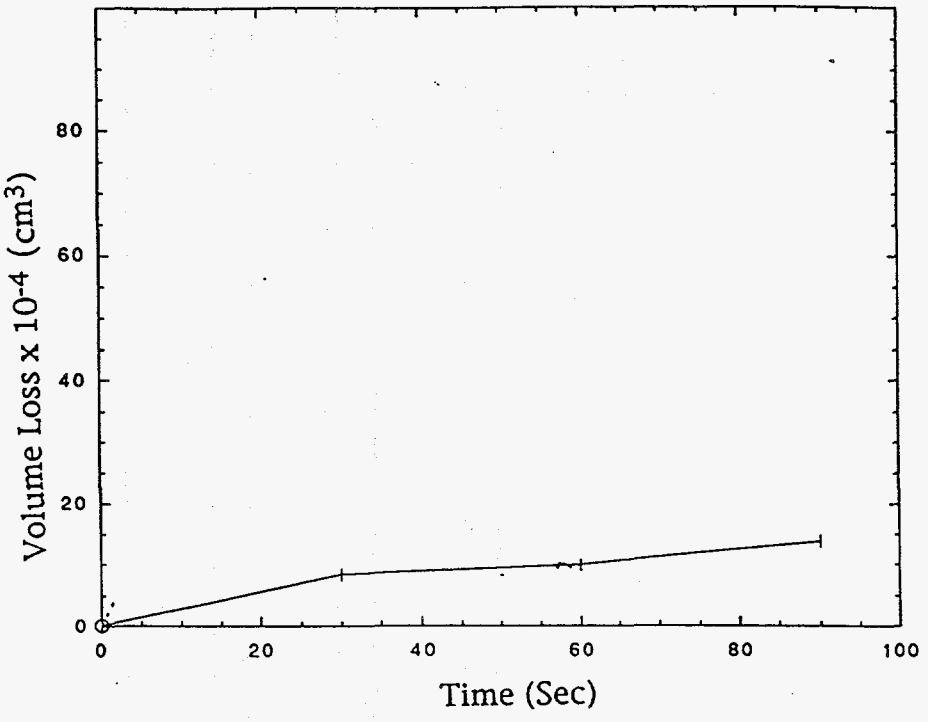

Figure 2 shows the curve for acetone (+) etchant solution.

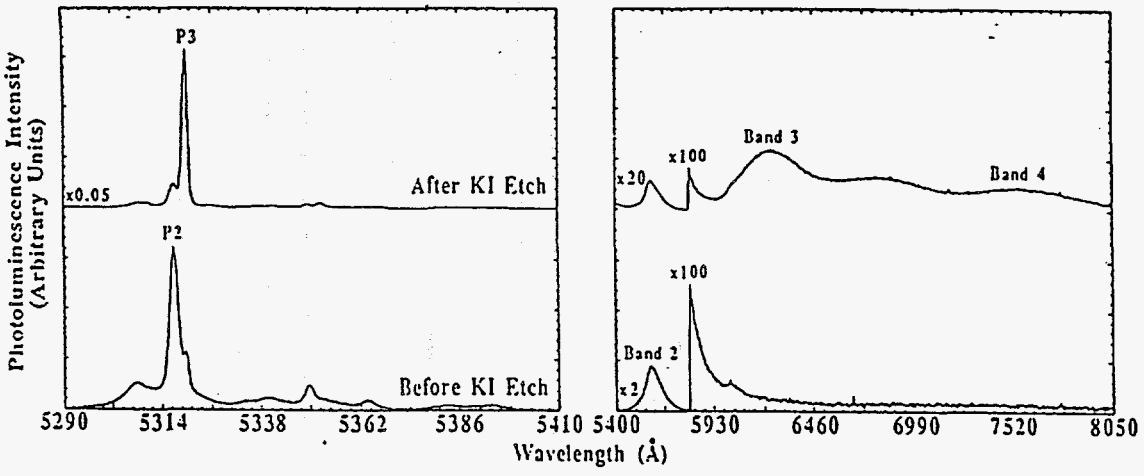

Figure 3. PL spectra from HgI2 before and after etching in 10% KI.

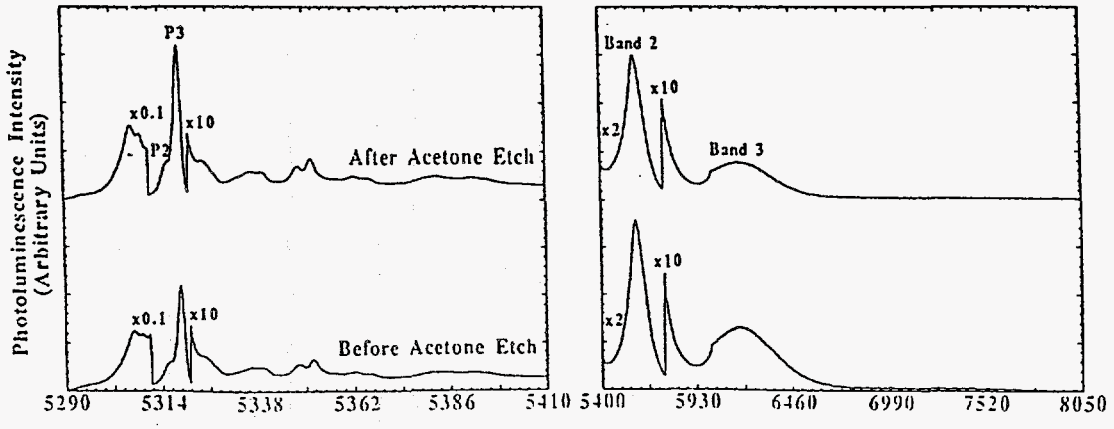

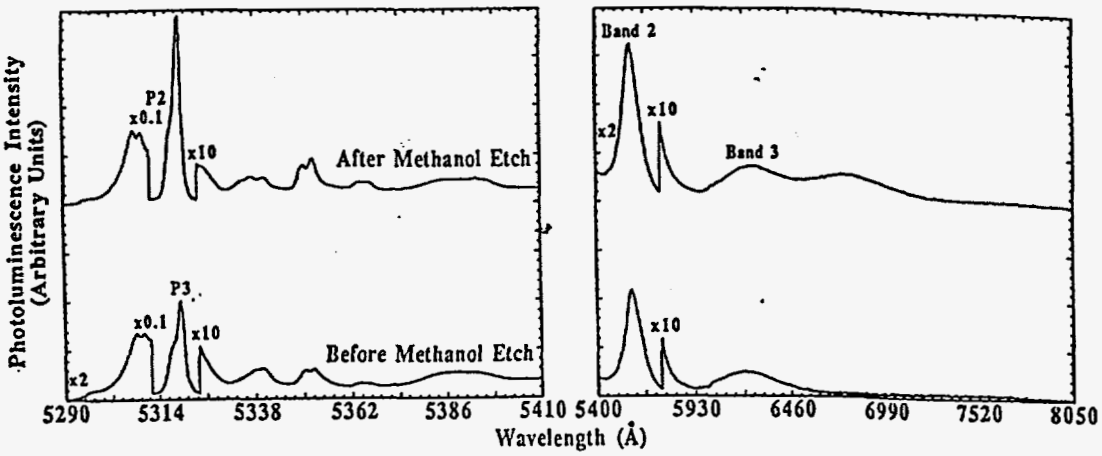

Figures 4 and 5. PL spectra from HgI_2 before and after etching in acetone and methanol, respectively.

CONCLUSIONS

This paper reports investigations of etch rates and the modifications of the photoluminescence of HgI_2 crystals after chemical etching. The etchants considered were deionized water, 10% aqueous potassium iodide, acetone, and methanol solutions. The etch rates were measured for each etchant. The PL results indicate that acetone etches without introducing new defect states, whereas both KI and methanol cause the incorporation of deep traps. Future work will study the effects of temperature of the etchant solutions as a means to control the etch rates and improve the quality of the surface finish.

ACKNOWLEDGMENT

The authors would like to thank A. J. Antolak for many useful discussions and the U. S. Department of Energy for financial support.

REFERENCES

1. X. J. Bao, T. E. Schlesinger, R. B. James, R. H. Stulen, C. Ortale, and A. Y. Cheng, *J. Appl. Phys.* 68, 86 (1990).
2. R. B. James, X. J. Bao, T. E. Schlesinger, J. M. Markakis, A. Y. Cheng, and C. Ortale, *J. Appl. Phys.* 66, 2578 (1989).
3. X. J. Bao, T. E. Schlesinger, R. B. James, G. L. Gentry, A. Y. Cheng, and C. Ortale, *J. Appl Phys.* 69, 4247 (1991).
4. X. J. Bao, T. E. Schlesinger, R. B. James, R. H. Stulen, C. Ortale and L. van den Berg, *J. Appl. Phys.* 67 ,7265 (1990).
5. X. J. Bao, Ph.D. Dissertation, Carnegie Mellon University, 1991.
6. R. B. James , X. J. Bao , T. E. Schlesinger, C. Ortale, and A. Y. Cheng, *J. Appl. Phys.* 67, 2571 (1990).
7. R. B. James, X. J. Bao, T. E. Schlesinger, S. J. Haney, A. Y. Cheng, V. Gerrish, and C. Ortale, *Nucl. Instrum. Meth.* A317, 194 (1992).
8. X. J. Bao, T. E. Schlesinger, R. B. James, C. Ortale, and L. van den Berg, *J. Appl. Phys.* 68, 2951 (1990).
9. B. V. Novikov and M. M. Pimonenko, *Sov. Phys. Semicond.* 4, 1785 (1971).

Left Intentionally Blank

ELSEVIER

Journal of Crystal Growth 146 (1995) 15–22

JOURNAL OF CRYSTAL GROWTH

Bulk and surface stoichiometry of vapor grown mercuric iodide crystals

M. Schieber [a,c,*], M. Roth [a], H. Yao [b], M. DeVries [b], R.B. James [c], M. Goorsky [d]

[a] *Graduate School of Applied Science, Hebrew University of Jerusalem, Jerusalem 91904, Israel*

[b] *University of Nebraska, Center for Microelectronic and Optical Materials Research and Department of Electrical Engineering, Lincoln, Nebraska 68588-0511, USA*

[c] *Sandia National Laboratory, Department 8347, MS 9162, Livermore, California 94550, USA*

[d] *Department of Materials Science and Engineering, University of California at Los Angeles, Los Angeles, California 90024, USA*

Abstract

The stoichiometry of HgI_2 is reviewed as a function of the various stages of preparation including synthesis, purification, crystal growth and ending with device fabrication. Original data are presented on surface roughness of free surfaces of HgI_2 determined by variable angle spectroscopic ellipsometry (VASE) and atomic force microscopy (AFM) and their relation to stoichiometry. The spread of the "c" lattice constant variation in bad HgI_2 nuclear detectors was determined by triaxial X-ray diffraction (TAXRD), and the results are discussed in relation with deviation from stoichiometry. It is suggested that crystals purified by open tube sublimation are stoichiometric. However, high temperature purification treatments, such as melting and even growth, may induce a certain dissociation of HgI_2 into Hg_2I_2 and free iodine. The latter diffuses, through a complex process, out of the crystal leaving a very rough outer surface and inhomogeneous stoichiometry in the bulk, which may be detrimental to device performance as a nuclear radiation detector.

1. Introduction

The deviation from stoichiometry of HgI_2 has been widely studied using many methods, such as classical chemical analysis [1,2], mass spectroscopy [3,4], Rutherford backscattering [5], Raman spectroscopy [6,7], differential scanning calorimetry [6], photoluminescence [8,9], X-ray diffraction [10,11], etc. The extent of departure from stoichiometry of undoped HgI_2 has been estimated to vary from 10^2 ppm [12] to 10^5 ppm [5] for both Hg and I, the results depending on the method used to determine the stoichiometry. Some earlier studies [1] claimed that HgI_2 can exist only in the Hg rich region. Important experiments were performed by Hermon and coworkers [11] to clarify the extent of non-stoichiometry of HgI_2 in samples doped with either Hg or I_2, homogenized, and heated to temperatures varying from 50 to 150°C. The samples were quenched to room temperature and then analysed [11,13]. A phase diagram near the stoichiometric composition was established [13] up to 120°C. The maximum amount of Hg dissolved in HgI_2 as Hg_2I_2 at 120°C is 720 ppm which decreases to below 150 ppm at 50°C. The free iodine solubility in orthorhombic HgI_2 is about 210 ppm at 130°C and in tetragonal HgI_2 it is ~ 130 ppm at 120°C.

* Corresponding author.

SSDI 0022-0248(94)00572-9

The present paper will analyse the stoichiometry problems as they are pertinent at the different stages of HgI_2 radiation detector preparation procedure, including synthesis, purification, crystal growth and device fabrication. It will also review results obtained with three novel methods of characterization which may relate to the stoichiometry of HgI_2 crystals used as radiation detectors, i.e. the variable angle spectroscopic ellipsometry (VASE) [14], atomic force microscopy (AFM) and triaxial X-ray diffraction (TAXRD) [15].

2. Stoichiometry problems of starting materials and crystal growth process

The starting materials of HgI_2 are mainly prepared by either (a) direct synthesis of purified elements or (b) the reaction between $HgCl_2$ and KI. In the first case it is easy to prepare non-stoichiometric compositions according to the phase diagram published in Ref. [13] and summarized in the introduction of this paper. It should be mentioned that iodine-rich HgI_2 directly synthesized from elements or doped with iodine and kept in a closed ampoule under a moderate vacuum of 10^{-2} Torr at room temperature shows a gradual release of free iodine which is visible by the intense pink color of free iodine. Reheating the closed ampoule to $\sim 150°C$ redissolves the free iodine as is evident from the disappearance of the pink color. In the case of the reaction between $HgCl_2$ and KI the sample is close to stoichiometry, but may contain some Hg_2I_2 on the order of ~ 50 ppm [12].

The purification of HgI_2 consists of several closed tube sublimation cycles and melting procedure, followed by open tube sublimation [16]. It is during this purification by sublimation that the excess of Hg_2I_2 to I_2 are eliminated due to the much higher vapor pressure of both species compared with that of HgI_2.

The melting stage during purification is where the excess I_2 is produced, as can be seen by the appearance of a pink color in the closed tube where the HgI_2 is molten. The visible free iodine is most probably being produced by the partial decomposition of HgI_2 into Hg_2I_2 and I_2. After cooling, the pink color disappears, but it is not known if the free iodine is reversibly reiodizing Hg_2I_2 to HgI_2, and if this reiodizing and redressing of stoichiometry is homogeneously distributed in the bulk of the crystal. The disappearance of the pink color can also be caused if part of the free I_2 recombines with the various hydrocarbons or metallic impurities causing other chemical defects in the HgI_2 crystal. All three enumerated possibilities may occur separately or at the same time to explain the occurrence or disappearance of the free-iodine in the closed ampoule. The pink color will be further discussed at the end of this section. Nevertheless, if open tube sublimation follows the melting stage, any Hg_2I_2 or free I_2 can be removed and the HgI_2 thus produced is again close to be stoichiometric.

In the most frequently used method of crystal growth of HgI_2 from the vapor phase, the so-called temperature oscillation method (TOM) [17], the starting material is sublimed on a certain cooler area of the hot walls of a vertical growth ampoule, whereas the crystal is grown on a cooler area of the bottom of the ampoule called the pedestal. The hotter areas of the walls of the ampoule and of the pedestal may reach some higher temperatures of $\sim 150°C$ or even higher as compared with the $\sim 110°C$, which is the growth temperature. It should be noted that the temperature difference between the source and pedestal is only about 2°C. The pink color of free iodine may appear during the crystal growth process in the closed and evacuated ampoule. The intensity of this I_2 color is defined by a qualitative eye-ball comparison of the free iodine color in the growth ampoule with that of series of empty ampoules filled with increasing quantities of free iodine at room temperature. The pink color intensity is indicated arbitrarily with numbers from 0 to 10 and sometimes the color is even much more intense and registered as 100. These numbers are called the I_2 color code. Even when the I_2 color code is very high during crystal growth, after the final cooling stage of the grown HgI_2 crystal, the pink color disappears in a similar way as described earlier in this section for the melting process during the purification stage of

the starting materials. A more quantitative study of the iodine vapor pressure above the growing HgI_2 is published elsewhere [18]. The pink color of iodine and color code numbers are correlated with the absorption of light at the wavelength of 514 nm quantitizing the free iodine in the concentration range 4–400 $\mu mol/\ell$. In the present paper we will use, however, the I_2 color code.

3. Stoichiometry and device fabrication

The operations of cutting, polishing and etching of the crystal needed to produce the detector do not relate directly to changes in stoichiometry. However, deposition of metal electrodes can change the stoichiometry. For example, the decomposition of Cu on HgI_2 leads immediately to the formation of CuI and, possibly, Hg_2I_2 rather than free Hg. Thermodynamic calculations performed by Cheng [19], analysing various possible reaction products between HgI_2 and electrode metals, predict that under worst case conditions only B, C, W, Ir and Pt may be stable. Indeed, this has been confirmed by James and coworkers [20,21]. The most common electrode, Pd, is also attacked chemically by I_2 diffusing out of HgI_2.

The fact that free iodine is formed even at room temperature and is capable to react with relatively inert metals, such as Pd, triggered the study of aging of HgI_2 surfaces, i.e. the study of changes which occur in these surfaces as a function of time. Surfaces were etched with a 10% aqueous solution of KI for 2 minutes, which removes ~ 60 μm from the surface. The samples were then exposed to air and subsequently measured by VASE and AFM as a function of exposure time [14]. The samples were obtained by the courtesy of EEG/EM Inc., Santa-Barbara. Characteristic AFM surface images of a HgI_2 "c" plane are shown in Fig. 1: (a) before, (b) after 12 minutes and (c) after 545 hours of exposure to air after KI etching. The sample shown in Figs. 1a–1c was grown in the presence of an excess of free iodine and by comparison with the intensity of the pink color was registered as an iodine color code of 3. A comparison of the VASE measurements performed on the samples shown in Fig. 1 and a similar sample having an iodine code of 0 is shown in Fig. 2a. The two-dimensional (2D) void densities have been obtained from the real time VASE measurements and the analysis is based on the assumed surface model shown in Fig. 2b. The HgI_2 surface was modeled as two graded layers containing voids, labeled as d_1 and d_2 in thick-

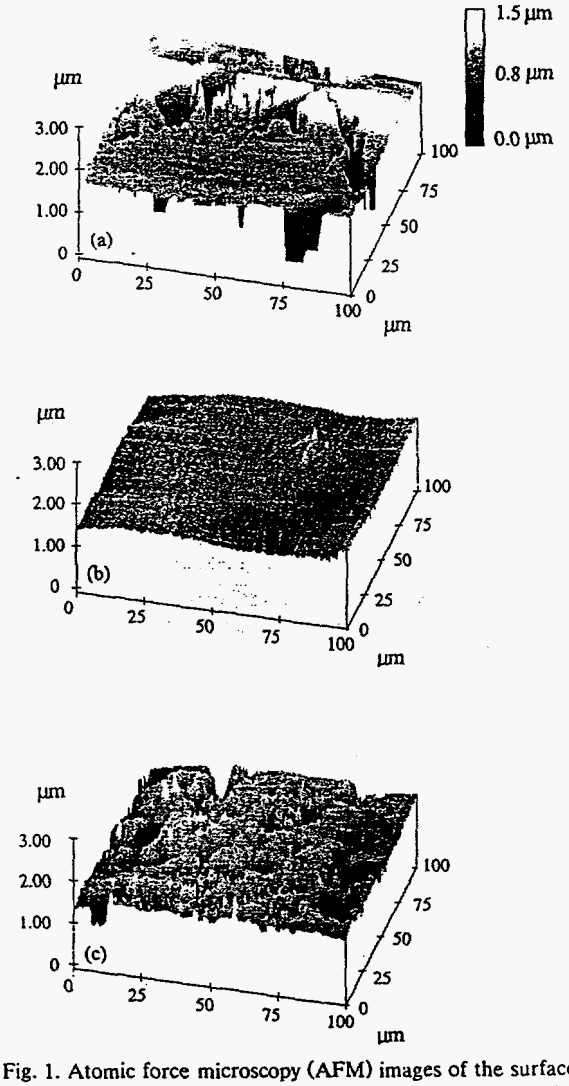

Fig. 1. Atomic force microscopy (AFM) images of the surface of a "c" plane of HgI_2 crystal plate with I_2 color code 3. (a) Before etching; (b) 12 minutes after etching; and (c) 545 hours after etching with 10% KI. The depth scale is shown on the right side of the figure.

nesses. In the top layer (d_1), the volume voids percentage was graded from 50% to x%, while on the sublayer (d_2) the voids percentage was graded from x% to 0%. The effective optical constants of the mixed graded layers used in the VASE analysis were calculated using the Bruggeman effective-medium approximation (EMA) [22,23]. The determination of the anisotropic dielectric function of HgI_2 crystals will be reported in a separate paper. In the VASE analysis, the voids volume percentage x and the surface-layer thicknesses d_1 and d_2 were allowed to vary, and a regression process was employed to minimize differences between the measured and calculated parameter values. The fitted value of volume voids percentage was then converted into an effective 2D voids density representing the surface layer d ($d = d_1 + d_2$), as shown in Fig. 2a.

The physical meaning of voids may be explained as following: (1) it can be used to describe the physical surface roughness of HgI_2 (i.e., on the very top of HgI_2 surface): (2) the voids, especially in the sub-surface layer, may represent defects near the surface, possibly caused by evaporation of iodine, which is supported by the fact that samples having larger iodine color codes have higher 2D voids values. This correlation indicates that different surface aging rates and conditions of HgI_2 may be related with HgI_2 dissociation and dissociation of iodine during crystal growth. However, the picture seems to be

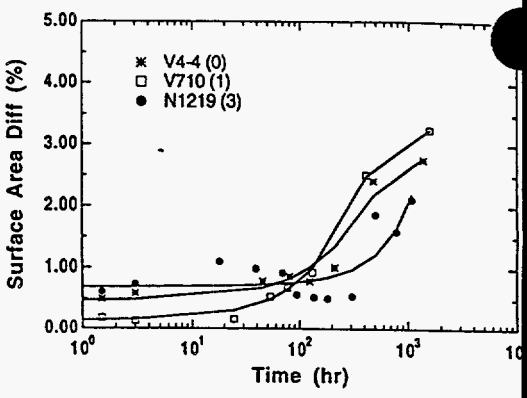

Fig. 3. Surface area differential (SAD) in % representing two-dimensional roughness as a function of time of aging a etching of three HgI_2 crystals of: V4-4 (I_2 color code V7-10 (I_2 color code 1) and N12-19 (I_2 color code 3). E solid line represents the best fit of the data.

more complicated. Atomic force microsc (AFM) images of three crystal plates with iod color codes 0, 1 and 3 show a different surf roughness behavior as a function of time t that shown above in Fig. 2, as detected by VA measurements. Expressing the AFM surf roughness via a surface area differentiation (SA in % as a function of time we have found that crystal with iodine code 1 has the roughes surface followed by iodine code 0 and io code 3 as shown in Fig. 3. Fig. 4 shows the act AFM 3D and 2D surface pictures of two cryst one with iodine code 3 (N12-19) and one w

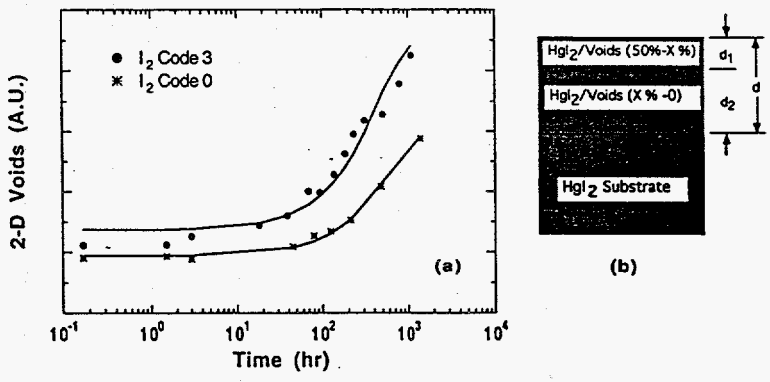

Fig. 2. (a) A comparison of VASE determined two-dimensional void densities in arbitrary units as a function of aging time etc of two HgI_2 crystal surfaces with I_2 color code 0 (lower curve) and with I_2 color code 3 (upper curve). (b) The model of V analysis taking HgI_2 as a substrate followed by subsurface structure (d_2) and upper surface roughness (d_1).

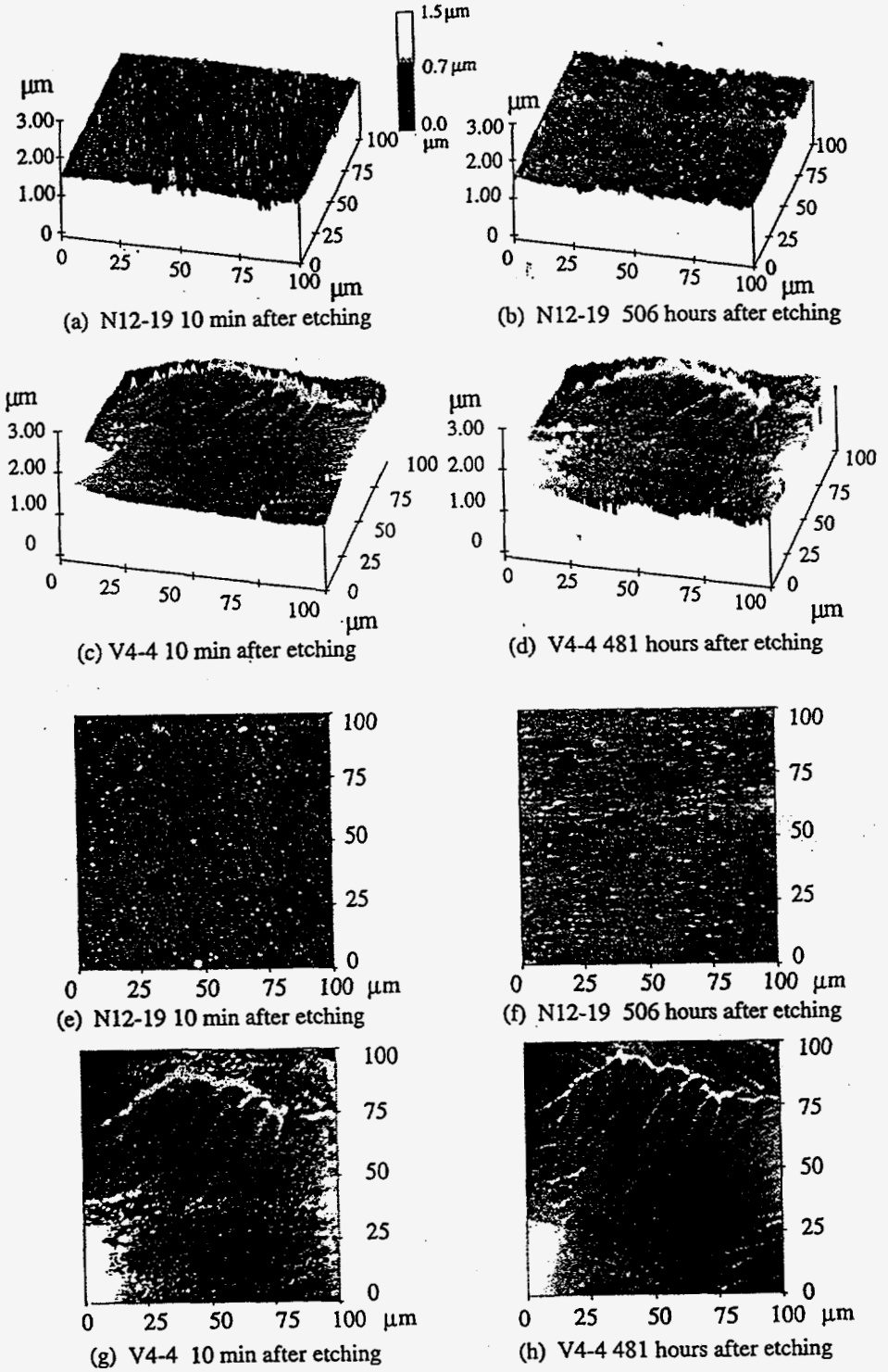

Fig. 4. Atomic force microscopy (AFM) images: three-dimensional (a)–(d) and two-dimensional (e)–(h) on aged HgI_2 crystal surfaces, N12-19 (iodine color code 3) and V4-4 (iodine color code 0) as a function of exposure in air after etching with 10% KI.

iodine code 0 (V4-4) as a function of time after the 10% KI etching. The difference between the AFM and VASE measurements is that AFM shows only the outer surface whereas VASE shows also the subsurface structure. It is interesting to note that there is an incubation time where the SAD hardly changes (Fig. 3) and, after aging around 400 hours, the surface roughness increases by at least a factor of two. These results will be further discussed below.

4. Stoichiometry, crystalline perfection and detector evaluation

Crystalline perfection, as determined by two-axial double crystal X-ray diffraction rocking curves (DCD-RC), has long been proven to affect strongly the nuclear detector response of the HgI_2 single crystal plates [24]. Narrow rocking curves, which are indicative of better crystallinity, were correlated with better nuclear detection response. Since as-grown single crystals of HgI_2 show only small deviations from stoichiometry, it was thought that these deviations cannot affect the radiation detector performance. However, using the TAXRD [15] one can determine not only the spread of small angle grain boundaries and mosaicity, as in the two-axial case, but one can also find small deviations in the XRD lattice parameters. Comparing the TAXRD results taken from excellent and bad HgI_2 detectors one can see that the bad detector shows a spread in mosaicity and a spread in the unit cell dimensions.

Fig. 5a shows the TAXRD of an excellent HgI_2 radiation detector. The narrow 3D strong peak represents both a very small mosaicity in the ω-plane and a very small spread in the lattice parameter in the ω–2θ plane. In Fig. 5b, for the same ω–2θ planes one can also see the TAXRD of a bad radiation detector with a very low number of counts. The reason for the TAXRD peaks of the bad detector being weak in comparison with the strong peaks of the good detector is the misalignment by $\sim 5°$ from the "c" plane for the bad detector relative to the much better alignment of the good detector. The unit cell dimension along the tetragonal "c" axis calculated from the (008) reflection of the bad detector is about 12.428 Å and the lattice parameter spread is about 0.004 Å. This is rather a small change in the lattice constant in order to reach conclusions, but the small spread in the lattice constant is real,

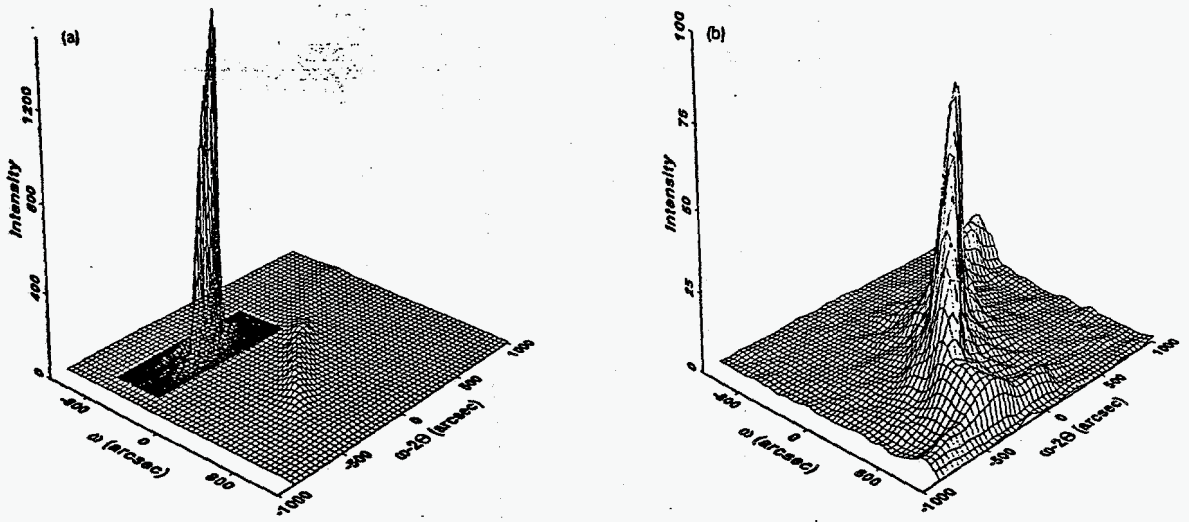

Fig. 5. Triple axis X-ray diffraction (TAXRD) of two detector crystals of HgI_2, one (a) with excellent spectral resolution (narrow and strong three-dimensional peak) and (b) a bad detector with very weak intensity wide spread mosaicity in the ω-plane and lattice parameter in the ω–2θ plane.

as can be seen in the TAXRD of the bad detector shown in Fig. 5b. The small spread could be caused by non-uniform distribution of Hg_2I_2 or iodine impurities diffusing out the detector plate. The variation of the lattice parameter "*c*" with that of HgI_2 doped with hydrocarbon impurities or with excess of Hg or I_2 is reported in Ref. [11]. Doping fresh HgI_2 samples with I_2 increases significantly the "*c*" lattice constant. However, the excess of I_2 may not be uniformly distributed in the crystal, and the amount of free I_2 may vary in decreasing amounts from the center to the outer boundaries of a grown crystal [11]. Variations from ~33 to ~20 ppm are expected when HgI_2 is grown in an I_2 atmosphere having a color code of 10. It should be noted that Hg doping increases onle slightly the "*c*" lattice constant of HgI_2 [11].

5. Discussion and conclusions

Both literature data cited and original results on stoichiometry are presented in this paper. The data suggest the following conclusions:

(1) Any HgI_2 produced from liquid solutions, such as $HgCl_2$ and KI, seems to be close to stoichiometry or, sometimes, slightly Hg-rich. Purification by sublimation helps to restore the stoichiometry and the deviations (in rare cases) seem to be close to about 10 ppm excess of Hg [11,12]. High-temperature processes used during purification, such as melting at ~245°C or higher, and even the hot spots in the crystal growth ampoule, which can reach ~150°C, may cause dissociation of HgI_2 into Hg_2I_2 and free I_2. This dissociation is manifested in the appearance of a pink color and graded by the I_2 color codes. Hydrocarbons may play an important role in the deviation from stoichiometry at all stages of preparation, but this dependence is not yet well established.

(2) A phase diagram study [13] of the stoichiometry range of HgI_2 shows that large deviations of both excess of Hg and excess of I_2 are possible at the growth temperature of ~110°C. However, at room temperature the solubility of both Hg_2I_2 and I_2 is much smaller than at ~110°C and, therefore, precipitation of excess Hg_2I_2 and I_2 at room temperature is possible. The higher vapor pressure of I_2 causes this free I_2 to diffuse to the outer surface and evaporate.

(3) Aging studies of a free HgI_2 surface in air at room temperature show that it becomes rough with time. VASE spectroscopy analysis shows that the rate of surface aging depends on the original growth conditions in the presence or absence of free I_2 during growth, i.e., the I_2 code color. It was found that higher I_2 color code means a higher rate of surface aging and roughness. AFM surface roughness is not proportional to the I_2 color code. However, one should notice that AFM measures only the outer surface roughness whereas VASE measures also the subsurface roughness.

There are perhaps several models to explain the surface roughness and its dependence on stoichiometry:

(a) The crystal grown with non-zero iodine color code has an excess of iodine which is dissolved in the lattice at 110°C. This excess is precipitated at room temperature and diffuses to the outer surface and evaporates slowly, leaving voids which form the measured surface roughness.

(b) The origin of I_2 which diffused out as described in model (a) stems from the thermal dissociation of HgI_2 to Hg_2I_2 and I_2, which is faster at higher temperatures (110°C) than at room temperature. This dissociation may be assisted by light, which can cause a photodissociation, particularly at room temperature when the thermal energy alone is not sufficient.

(c) Stoichiometric HgI_2 is evaporated at room temperature from irregularly distributed warmer spots to lightly cooler spots of the outer surface where it deposits back non-uniformly as small polycrystalline HgI_2 particles. This deposition on cooler spots of the outer surface causes surface roughness.

Competition between the three mechanisms suggested above provides the reason for the difference between AFM and VASE results where roughness does not or does depend on I_2 color code. Model (c) can be, however, verified by optical microscopy where one can see the appearance of unattached tiny particles on the outer

surface of HgI_2. The small particles are distinctly different from the shiny appearance of the single crystalline surface. If the particles are red in color they are HgI_2, and if yellow-greenish they are Hg_2I_2 as described in model (2). The tiny particles can also be identified by reflectance electron diffraction. Such measurements have not been made. In any case, etching removes the roughness of the outer surface, and it is mandatory to produce high quality detectors.

(4) Since most of the crystals are stoichiometric, it is improbable that very small deviations are critical to the nuclear spectroscopic response of HgI_2 detectors. However, it is proven that bad detectors have a spread not only in mosaicity, which was known before, but also in the spread of the relative size of the lattice parameter "c" as proven by TAXRD measurements. Despite the small deviations of only 10^{-3} Å in the value of the "c" parameter, which most probably stem from a small variation in stoichiometry, they are known to deteriorate the lifetimes of both electrons and holes [11]. The aging of the surface in air and the roughness associated with it, which can be due to out-diffusion of free iodine from the surface, may contribute to the non-uniformity of the stoichiometry of individual regions in the bulk of the crystal and may also lead to the formation of an increased number of small angle grain boundaries and mosaicity, which is known to be common in bad detectors [7,11].

References

[1] M.C. DeLong and F. Rosenberger, Mater. Res. Bull. 16 (1981) 1445.

[2] G. Dishon, M. Schieber, L. Ben-Dor and L. Halitz, Mater. Res. Bull. 16 (1981) 759.

[3] M. Piechotka and E. Kaldis, J. Electrochem. Soc. 133 (1986) 200.

[4] M. Piechotka and E. Kaldis, J. Crystal Growth 79 (1986) 469.

[5] C. Charager, A. Tadjine, N.T. Toulemonde, J.T. Grob and P. Siffert, in: Proc. Nuclear Physics 7th Divisional Conf., Nuclear Physics Methods in Material Research, Darmstadt, September, 1980.

[6] A. Burger, S. Morgan, C. He, E. Silberman, L. Van den Berg, L. Franks and M. Schieber, J. Crystal Growth 99 (1990) 988.

[7] A. Burger, S. Morgan, H. Jiang, E. Silberman, M. Schieber, L. Van den Berg, M. Keller and C.N.J. Wagner, Nucl. Instrum. Methods. A 283 (1989) 130.

[8] J.L. Merz, Z.L. Wu, L. Van der Berg and W.F. Schnepple. Nucl. Instrum. Methods 213 (1983) 51.

[9] J. Bao, R.B. James, C.Y. Hung, T.E. Schlesinger, A.Y. Cheng, C. Ortale and L. Van den Berg, in: X-ray Detectors, Physics and Applications, Ed. R.B. Hoover, SPIE 1736 (1992) 60.

[10] F.Y. Nicolau and G. Rolland, Mater. Res. Bull. 16 (1981) 759.

[11] M. Schieber, H. Hermon and M. Roth, in: Semiconductors for Room Temperature Radiation Detector Applications, Eds. R.B. James, T.E. Schlesinger, P. Siffert and L. Franks, Mater. Res. Soc. Symp. Proc. 302 (1993) 347.

[12] H. Hermon, M. Roth, J. Nissenbaum, M. Schieber and J. Shamir, J. Crystal Growth 109 (1991) 376.

[13] H. Hermon, M. Roth, M. Schieber and J. Shamir, Mater. Res. Bull. 28 (1993) 229.

[14] H. Yao and B. Jhos, in: Semiconductors for Room Temperature Radiation Detector Applications, Eds. R.B. James, T.E. Schlesinger, P. Siffert and L. Franks, Mater. Res. Soc. Symp. Proc. 302 (1993) 341.

[15] M. Goorsky, M. Schieber and R. James, to be published.

[16] M. Schieber, M. Roth and W.F. Schnepple, J. Crystal Growth 65 (1983) 353.

[17] M. Schieber, W.F. Schnepple and L. Van den Berg, J. Crystal Growth 33 (1976) 125.

[18] D. Nason, Y. Biao and A. Burger, J. Crystal Growth 146 (1995) 23.

[19] A.Y. Cheng, in: Semiconductors for Room Temperature Radiation Detector Applications, Eds. R.B. James, T.E. Schlesinger, P. Siffert and L. Franks, Mater. Res. Soc. Symp. Proc. 302 (1993) 141.

[20] R.B. James, X.J. Bao, T.E. Schlesinger, C. Ortale, A.Y. Cheng, J. Appl. Phys. 67 (1990) 251.

[21] X.J. Bao, T.E. Schlesinger, R.B. James, R.H. Stulen, C. Ortale and L. Van der Berg, J. Appl. Phys. 67 (1990) 7265.

[22] D.E. Aspens and T.B. Theeten, Phys. Rev. B 20 (1979) 3292.

[23] H. Yao and P.G. Snyder, Thin Solid Films 206 (1991) 283.

[24] M. Schieber, C. Ortale, L. Van den Berg, W. Schnepple, L. Keller, C.N.J. Wagner, W. Yelon, F. Ross, G. Georgeson and F. Milstein, Nucl. Instrum. Methods A 283 (1989) 172.

Nucl. Instrum. Methods (to be published 1996)

Surface Aging of HgI_2 Crystals Studied by VASE and AFM

H. Yao, and L.A. Lim
University of Nebraska, Lincoln, Nebraska USA;

R. B. James, and M. Schieber
Sandia National Laboratories, Livermore, California USA;

M. Natarajan
TN Technologies, Round Rock, Texas USA

ABSTRACT

Variable angle spectroscopic ellipsometry (VASE) and atomic force microscopy (AFM) measurements have been employed to characterize the surface aging of HgI_2 crystals -- a material for room-temperature radiation detectors. Four different initial HgI_2 surface conditions were selected, i.e., an as-grown surface, a cleaved surface, a surface chemically etched by 10% KI solution, and a parylene coated surface. A model including top surface roughness and subsurface defects of HgI_2 crystal, related to surface aging, was established and characterized, as a function of real time, by the VASE analysis. The VASE measurements indicated that high surface aging rates were related to high initial effective two-dimensional (2D) surface-defect densities. The AFM profiles revealed increasing physical surface roughness as surface aging took place. The cleaved HgI_2 crystal surface presented a smooth surface and the lowest surface aging rate, while the as-grown HgI_2 surface also presented a very low surface aging. The parylene coating on HgI_2 surface can greatly slow down the surface aging.

1. INTRODUCTION

Crystal mercuric iodide (HgI_2) is an important technological material for room-temperature radiation (i.e., gamma- and x-ray) detectors [1-5]. It is a well-known fact that the bare surface of a HgI_2 crystal will be aging in air. The origin of surface aging is still under study [6,7]. It has been suggested that the surface aging is related with the deviation from stoichiometry of HgI_2 by losing I_2 from the crystal surface, due to its higher vapor pressure [7]. In this paper, we report, results of surface aging studies of different HgI_2 surface conditions characterized by variable angle spectroscopic ellipsometry (VASE) and atomic force microscopy (AFM) measurements.

2. EXPERIMENTAL BACKGROUND AND SAMPLE PREPARATION

A. VASE and AFM Measurements

The spectroscopic ellipsometry (SE) is a surface-sensitive, nondestructive optical technique used to characterize surface changes, overlayer thicknesses, multilayer structures, optical constants of bulk materials, and surface or interface roughness [8,9]. Ellipsometry determines the complex reflectance ratio r_p to r_s, defined as

$$\rho = r_p / r_s = \tan(\psi) e^{i\Delta}, \tag{1}$$

where r_p and r_s are the reflectance coefficients of light polarized parallel to (p) or perpendicular to (s) the plane of incidence, and the values of $\tan(\psi)$ and Δ, which are the amplitude and projected phase of the complex reflectance ratio.

AFM measurements provide surface probes with atomic layer scale. In this application it is utilized to monitor the top surface roughness changes, as a function of real time, in the surface aging process of HgI_2.

B. Sample Preparations

Three HgI_2 surfaces were cut from a same crystal grown at EG&G/EM Inc. Santa-Barbara, with different initial surface conditions, i.e., (1) as-grown surface; (2) cleaved surface; (3) mechanically and chemically polished surface. All three samples are c-plane surfaces, to which the c-axis of the crystal is perpendicular.

The as-grown and cleaved surfaces were characterized by VASE and AFM about 48 hours after the sample being exposed to air. The mechanically and chemically polished sample was subjected to a 10% KI etching to ensure clean and fresh surface before the characterization [6,10]. In the etching process, the sample was immersed in a 10% KI (by weight) solution for about 2 min. After the KI etching, the sample was rinsed immediately with deionized water for ~ 2-3 min. The VASE and AFM measurements were made on all three samples in air at room temperature over a period of several months after the samples being exposed to air.

3. MEASUREMENTS AND ANALYSIS

Fig. 1 includes a group of AFM images showing a typical surface aging process of a c-plane HgI_2 crystal surface: (a) before etching; (b) 12 min. and (c) 545 hours after etching and being exposed to air. The AFM measurements were made in a fixed position of a 100 μm window on the sample surface. It is clearly shown, in (a) and (b), that the 10% KI etching removed the old aged materials, and provided a clean and ruby red fresh HgI_2 surface. After 545 hours of exposure to air after the KI etching, the surface became rough and aged, as shown in (c). The visible color change of the top surface layer, from ruby red into whitish, indicated a possible stoichiometry change.

VASE measurements were made, side by side with AFM probes, in a spectral range of 1.24 to 5.1 eV, with an increment of 0.05 eV and angles of incidence of 67.5°, 70°, 72.5° and 75°. A surface model was established, for the VASE analysis, to describe the top surface roughnesses and possible subsurface defects, as shown in Fig.

2 (b). The HgI_2 surface was modeled as two graded layers containing voids, labeled as d_1 and d_2 in thickness. The top layer (d_1) is mainly used to describe the physical roughness of the sample surface, while the sublayer (d_2) is designed to reflect the possible subsurface defects. In the top layer (d_1), the volume voids percentage was graded from 50% to x%, while in the sublayer (d_2) the voids percentage was graded from x% to 0%. The effective optical constants of the mixed graded layers used in the VASE analysis were calculated using the Bruggeman effective-medium approximation (EMA) [11,12]. The determination of the anisotropic dielectric function of HgI_2 crystals is reported in a separated paper [13]. During the VASE analysis, the voids volume percentage x, the top and sub-surface layer thicknesses d_1 and d_2 were allowed to vary, and a regression process was employed to minimize differences between the measured and calculated parameter values. The fitted value of volume voids percentage was then converted into an effective 2D voids density representing the surface layer ($d= d_1 + d_2$), as shown in Fig. 2 (a).

The physical meaning of the voids may be explained as following: (1) it can be used to describe the physical surface roughness of HgI_2 sample (i.e., on the very top surface); (2) the voids, especially in the sub-surface layer, may represent possible surface defects. It is shown, in Fig. 2 (a), different 2D voids densities associated with different initial surface conditions: the lowest 2D voids densities for cleaved surface, followed by higher voids densities for as-grown surface, and the highest 2D voids densities for 10% KI etched HgI_2 surface. The AFM surface images in Fig. 3 show the actual 3D surface pictures of two HgI_2 crystals, one with cleaved surface and one with as-grown surface, as a function of time after the crystal surfaces being exposed to air. It is obvious that the cleaved surface has the lowest aging rate by comparing the AFM surface images of Fig.3 (b), Fig. 3 (d) and Fig. 1 (c). The as-grown surface also presents a low surface aging. This is consistent with the VASE analysis results. The surface aging rates of HgI_2 surfaces are closely related with the 2D voids

densities: in general, the relative higher 2D voids density, the higher surface aging rate.

Parylene coated HgI_2 surface was made at TN Technologies and measured by AFM as a function of time, as shown in Fig. 4. The c-plane HgI_2 surface was subject to a parylene coating immediately after a 10% KI etching. Those AFM surface images at different hours, after the parylene coated surface being exposed to air, showed that very little changes took place even 1,612 hours after the coated surface being exposed to air. Continued AFM monitoring at extended hours (e.g., ~5,000 hours) showed some aging effects on the coated surface. It is convincing that a very low surface aging rate has been obtained by applying a parylene coating on the HgI_2 crystal surface. This indirectly supports the results of a HgI_2 stoichiometry study indicating that surface defects, related with surface aging, are possibly caused by evaporation of iodine from surface due to high iodine vapor pressure [7].

4. CONCLUSIONS

We have presented results of surface aging studies of HgI_2 crystals characterized by VASE and AFM. Three HgI_2 c-plane surfaces cut from the same crystal with different initial surface conditions, i.e., cleaved, as-grown and mechanically and chemically etched surfaces, were studied. The results indicated that the cleaved surface had the lowest aging rate among the three, while the chemically etched surface aged at the highest rate. A low aging rate was also observed from the as-grown surface. An effective 2D voids density representing the surface roughness and defects was obtained through VASE analysis. The surface aging rates of HgI_2 crystals were closely related with the 2D voids densities: in general, the relative higher 2D voids density, the higher surface aging rate. A very slow surface aging rate has been achieved by applying a parylene coating on HgI_2 surface.

ACKNOWLEDGMENTS

This work was supported by the Department of Energy via Sandia National Laboratories.

FIGURE CAPTIONS

1. Atomic force microscopy (AFM) images of a typical c-plane surface of HgI_2 crystal. (a) Before etching; (b) 12 minutes after etching; and (c) 545 hours after etching with 10% KI. The depth scale is shown on the right side of the figure.

2. (a) A comparison of VASE determined 2D voids densities in arbitrary units, as a function of aging time, of three different surface conditions: (●) as-grown; (*) cleaved; (❑) KI etched. (b) The surface model of HgI_2 crystal for VASE analysis including the top layer (d_1) and the sub-surface layer (d_2).

3. AFM surface images of the cleaved surface at (a) 49 hours after being exposed to air; and (b) 600 hours after exposure to air; AFM images of the as-grown surface at (c) 48 hours after being exposed to air; and (d) 600 hours after exposure to air.

4. AFM images of a parylene coated HgI_2 surface at (a) 247 hours; (b) 1,065 hours; (c) 1,612 hours after exposure to air;

REFERENCES

[1] W. R. Willig, Nucl. Instrum. Methods 96, (1971) 615.

[2] S. P. Swierkowski, G. A. Armantrout, and R. Wichner, IEEE Trans. Nucl. Sci. NS-21, (1974) 302.

[3] J. P. Ponpon, R. Stuck, P. Siffert, B. Meyer, and C. Schwab, IEEE Trans. Nucl. Sci. NS-22, (1975) 182.

[4] A. J. Dabrowski, W. M. Szymczyk, J. S. Iwanczyk, J. H. Kusmiss, W. Drummond, and L. Ames, Nucl. Instrum. Methods 213, (1983) 89.

[5] J. H. Howes and J. Watling, Mat. Res. Soc. Symp. Proc. 16, (1983) 207.

[6] H. Yao and B. Johs, Mater. Res. Soc. Symp. Proc. 302, (1993) 341.

[7] M. Schieber, M. Roth, H. Yao, M. DeVries, R. B. James, and M. Goorsky, J. Crystal Growth 146, (1995) 15.

[8] R. M. A. Azzam and N. M. Bashara, *Ellipsometry and Polarized Light*, North-Holland, Amsterdam, 1977.

[9] D. E. Aspnes, in *Handbook of Optical Constants of Solids*, edited by E. D. Palik Academic, New York, 1985, p. 89.

[10] X. J. Bao, T. E. Schlesinger, R. B. James, R. H. Stulen, C. Ortale, and A. Y. Cheng, J. Appl. Phys. 68, (1990) 86.

[11] D. E. Aspnes, J. B. Theeten, and F. Hottier, Phys. Rev. B 20, (1979) 3292.

[12] H. Yao and P. G. Snyder, Thin Solid Films 206, (1991) 283.

[13] H. Yao, B. Johs, and R. B. James, (to be published).

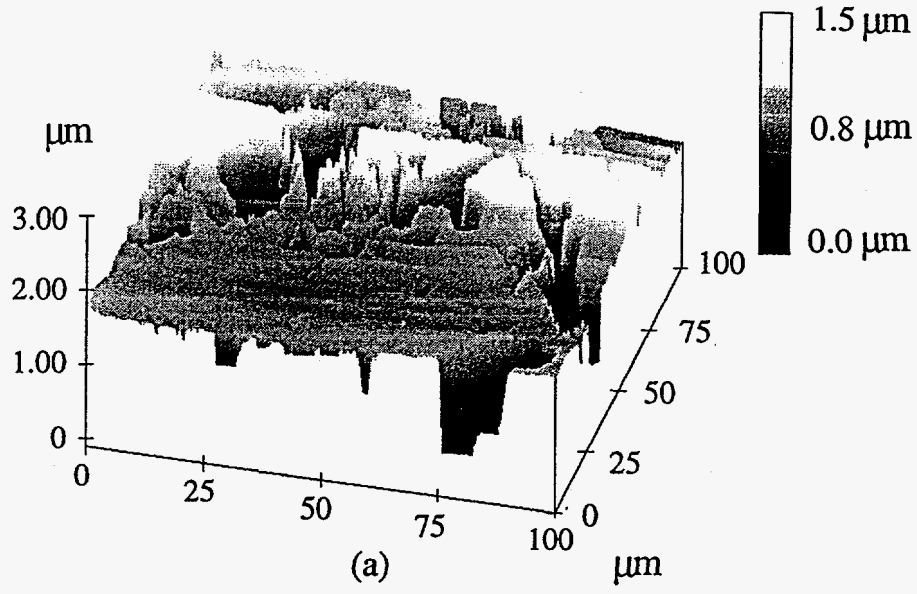
1.5 µm
0.8 µm
0.0 µm
µm
3.00
2.00
1.00
0
0
25
50
75
100
100
75
50
25
0
µm

(a)

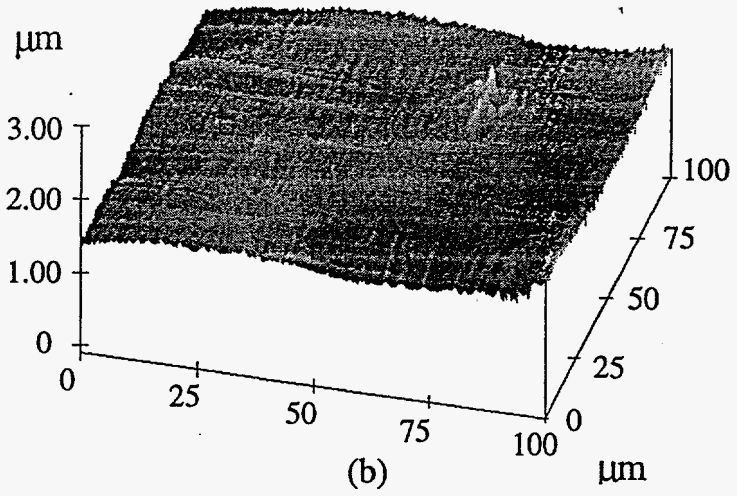
µm
3.00
2.00
1.00
0
0
25
50
75
100
100
75
50
25
0
µm

(b)

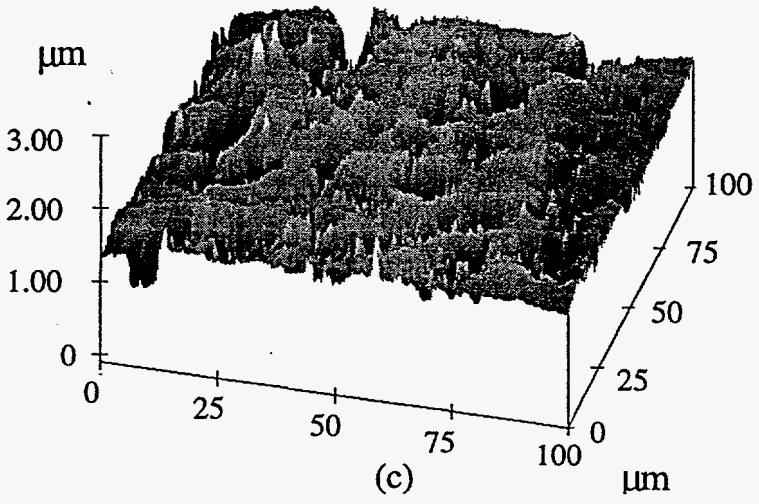
µm
3.00
2.00
1.00
0
0
25
50
75
100
100
75
50
25
0
µm

(c)

 Fig. 1

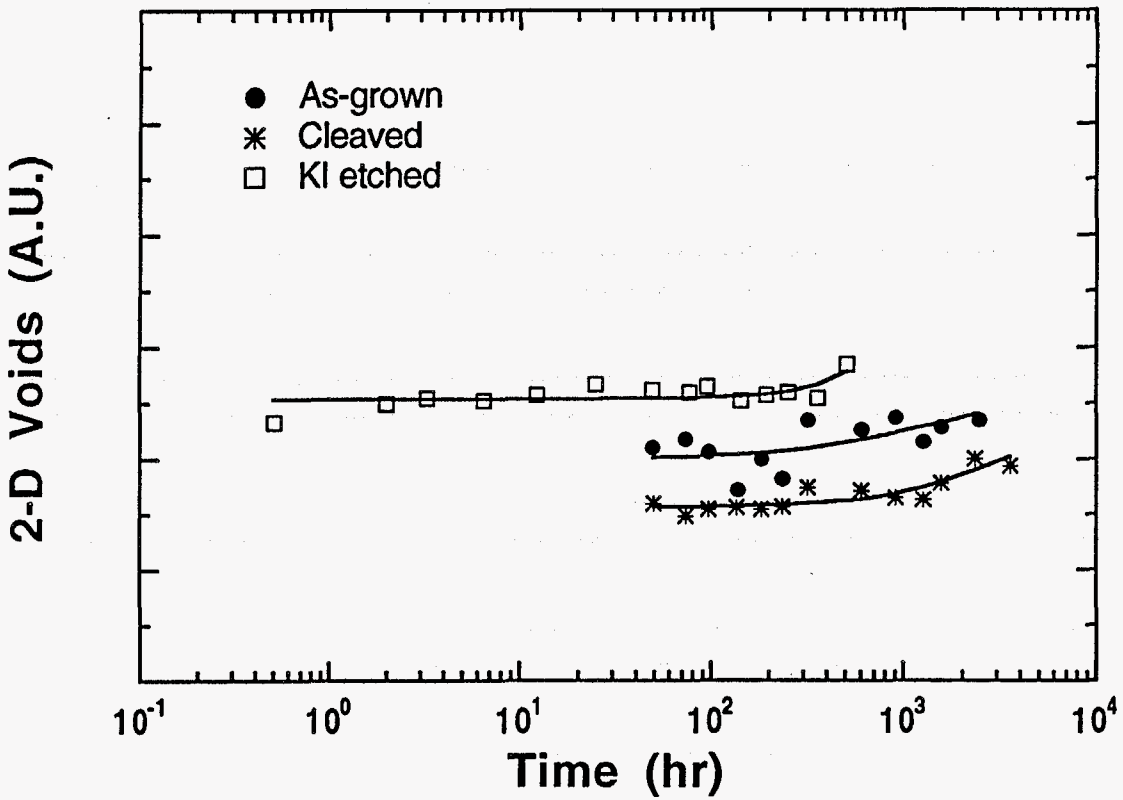
As-grown
Cleaved
KI etched
2-D Voids (A.U.)
10^{-1}
10^{0}
10^{1}
10^{2}
10^{3}
10^{4}
Time (hr)

(a)

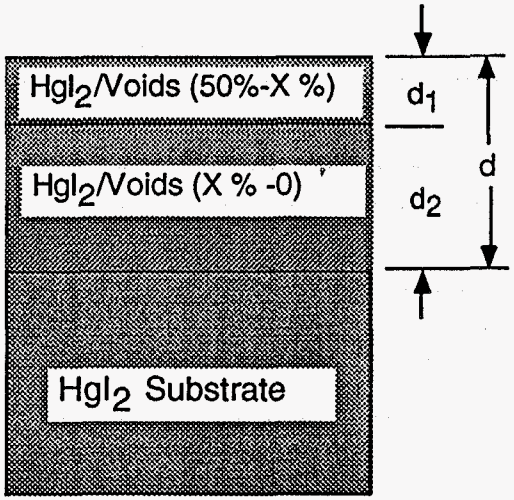
HgI_2/Voids (50%-X %)
HgI_2/Voids (X % -0)
HgI_2 Substrate
d_1
d_2
d

(b)

Fig. 2

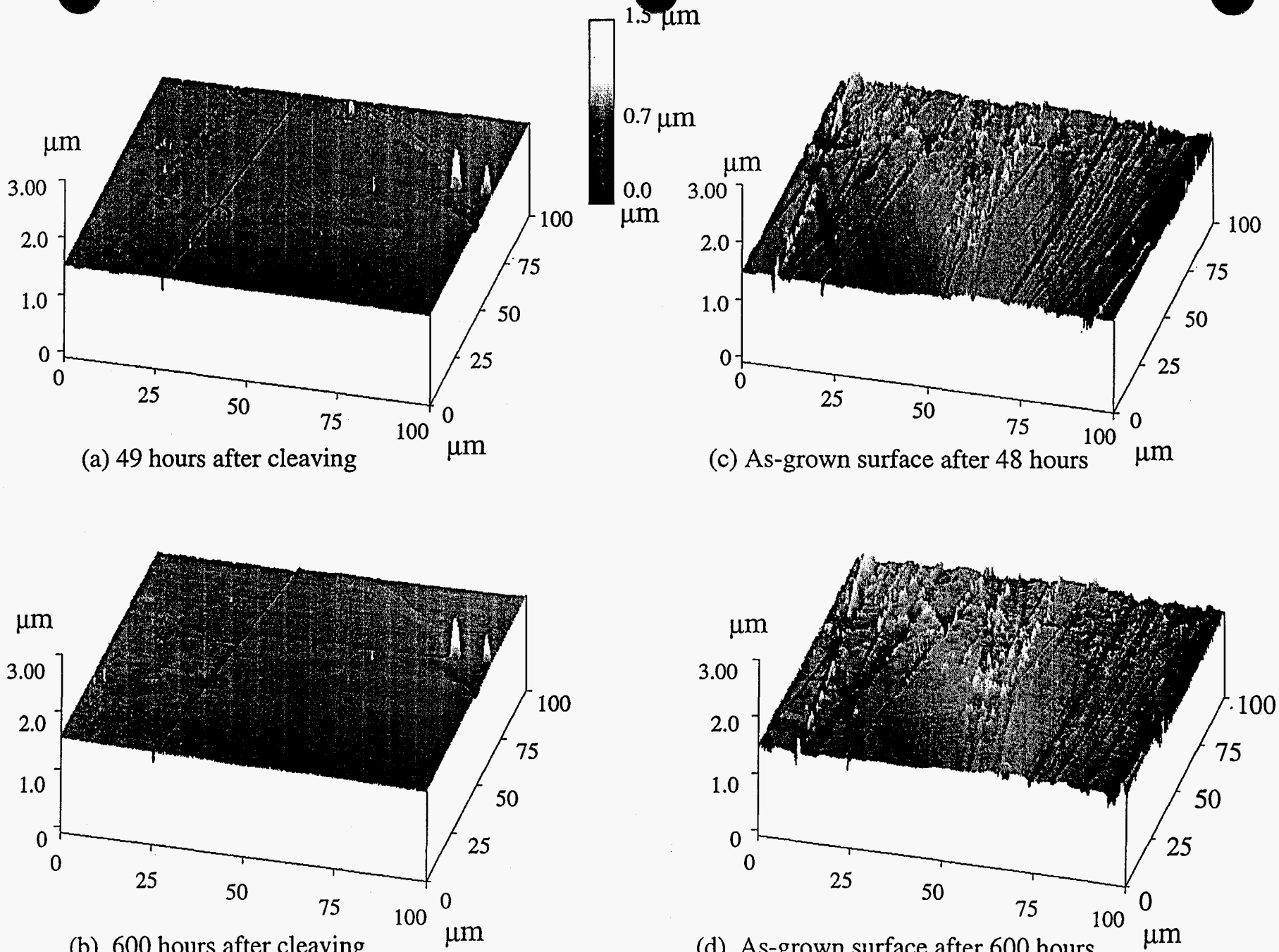

(a) 49 hours after cleaving

(c) As-grown surface after 48 hours

(b) 600 hours after cleaving

(d) As-grown surface after 600 hours

101

Fig. 3

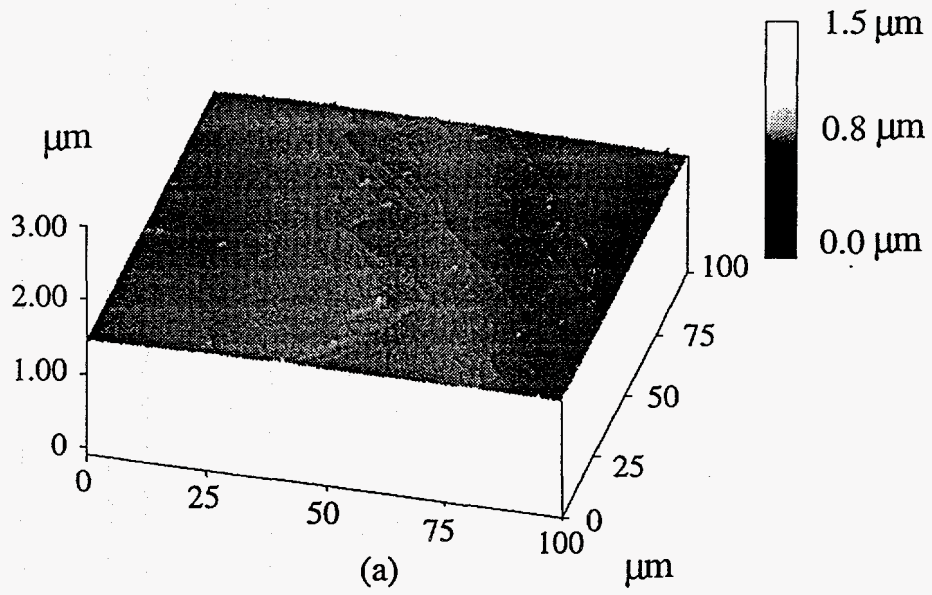
1.5 µm
0.8 µm
0.0 µm
µm
3.00
2.00
1.00
0
0
25
50
75
100
100
75
50
25
0
µm

(a)

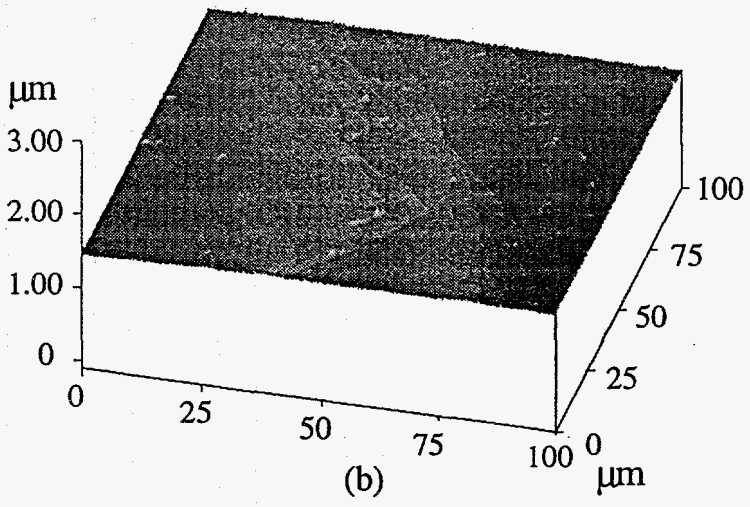
µm
3.00
2.00
1.00
0
0
25
50
75
100
100
75
50
25
0
µm

(b)

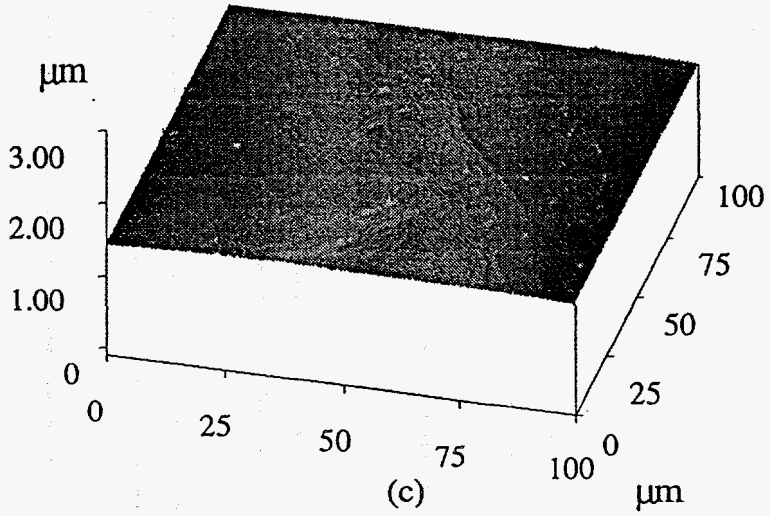
µm
3.00
2.00
1.00
0
0
25
50
75
100
100
75
50
25
0
µm

(c)

102 Fig. 4

Formation of PdHg by Reaction of Palladium Thin Film Contacts Deposited onto Mercuric Iodide (α-HgI_2) Radiation Detector Crystals.

D.L. Medlin[1], J. M, Van Scyoc[2], T. S. Gilbert[2], T. E. Schlesinger [2], D. Boehme[1], M. Schieber[1], M. Natarajan[3], and R.B. James[1]

[1]Sandia National Laboratories, Livermore California 94551

[2]Carnegie Mellon University, Department of Electrical and Computer Engineering, Pittsburgh PA.15213

[3]TN Technologies, Inc., Round Rock, TX 78680

Abstract

The microstructure and phase distribution of palladium thin films sputter deposited onto α-HgI_2 for use as electrical contacts in radiation detectors are investigated using electron microscopy. Our results show a limited reaction to form palladium mercuride (PdHg). It is shown that the formation of PdHg via several reaction pathways is thermodynamically feasible.

1. Introduction

Mercuric iodide (HgI_2) has applications as a room temperature γ- and x-ray detector. The material is highly reactive, though, which limits the set of materials suitable for thin film metallization in the fabrication of electrical contacts. Thin film palladium is commonly used as a contact material in HgI_2 devices and is generally considered to be chemically stable and reliable. Furthermore, previous calculations have suggested that palladium should be thermodynamically stable against a direct reaction with HgI_2 [1]. However, recent work provides evidence for a limited contact reaction. Van Scyoc and coworkers [2] monitored the time variation in four-point probe sheet resistance of a palladium contact immediately following thin film sputter deposition onto HgI_2. These results showed, unexpectedly, a transient increase in resistance that stabilized after roughly one hour. The increase in resistance was interpreted as resulting from an interaction of the palladium film with the substrate, either due to diffusion and dissolution of the film into the bulk of the substrate or a chemical reaction at the contact interface. To provide further insight into the contact material chemistry, this paper presents a study of the microstructure and phases present in a palladium film sputter deposited onto HgI_2. As we will discuss, the results of this study show a limited reaction to form palladium mercuride (PdHg).

2. Experimental

Palladium thin films, 750Å thick, were sputter deposited at room temperature onto single crystal [001] oriented α-HgI_2 (TN Technologies). The films were characterized both by x-ray diffraction and by electron microscopy using a JEOL 1200EX transmission electron microscope (TEM), operated at 120 kV, and a JEOL 4000EX high resolution transmission electron microscope (HRTEM), operated at 400 kV. Specimens of contact material were prepared for TEM examination by stripping away the HgI_2 substrate in

10% KI solution, giving a free-floating metal film that could be picked up and supported by a fine-meshed TEM grid.

3. Results

Figure 1 shows a low magnification transmission electron micrograph of a free standing palladium film after removal of the HgI_2 substrate. At the edges, where the film has torn, sections of the film have separated, folding up to reveal a thin underlying layer. A higher magnification image of a section of this exposed thin layer is shown in Figure 2. The electron diffraction results taken from these thin regions of the film (inset to Figure 2) are inconsistent with elemental palladium, but rather can be indexed in terms of the intermetallic compound PdHg. PdHg, also known as the mineral potarite, is a tetragonal compound with $L1_0$ (CuAu) crystal structure [3]. A comparison of the measured d-spacings with the expected reflections for the compound (JCPDS x-ray powder diffraction file #13-0149) is given in Table 1. A structure factor calculation of the expected relative diffraction intensities for PdHg (120 keV electrons) was also performed using the EMS package of electron microscopy routines [4]. This calculation shows that in addition to the reflections tabulated in the x-ray powder file, the {002} and {112} lines should also be present. The {002} and {112} lines are also noted in the original structure calculations by Terada and Cagle [3]. These reflections are quite close to the {111} and {201} lines (d_{111}=1.851 Å, d_{002}=1.846 Å and d_{201}=1.402 Å, d_{112}=1.399 Å) and are an order of magnitude more intense (see Table 1). As such, each of the {111}/{002} and {201}/{112} pairs would be resolved in electron diffraction as individual line, particular if there is line broadening due to fine grain size.

Additionally, the structure factor calculation indicates that the {102} and {210} reflections are quite weak, with intensities less than 1% of the {101}, which is likely why these are not detected in the observed pattern. The remaining rings correspond to d-spacings consistent to within about 5% of the tabulated values. Variations in lens focus

can lead to systematic calibration errors in electron diffraction analysis and so the data is also presented with the d-spacings normalized to the position of the {101} reflection. The normalized measurements are consistent within about 2%, which is comparable to the measurement error. Thus, the electron diffraction measurements provide strong evidence for the reaction of the palladium film with the HgI_2 substrate to form PdHg.

No crystallographic texture is apparent in the electron diffraction pattern indicating that the PdHg crystallites are randomly oriented. Broadening of the diffraction lines indicates a small grain size, which is confirmed by the TEM micrograph shown in Figure 2 and the HRTEM image shown in Figure 3. These micrographs show grain diameters typically less than 10 nm and furthermore suggest that the PdHg is discontinuous with amorphous material interspersed between the grains. The composition of the amorphous phase has not been identified in this study. The fringe spacings and angles observed in the HRTEM images can also be indexed in terms of PdHg, providing further confirmation of the phase identity. An example is shown by the indicated grain in Figure 3 and its indexed power spectrum (inset).

In the thicker regions of the film, that is where the film has not separated to reveal the thin underlying layer, the dominant phase is elemental palladium. Figure 4 shows a TEM image and selected area electron diffraction pattern obtained from one of these regions. The ring pattern spacings are consistent with elemental palladium. It is difficult to determine whether a thin PdHg layer is present as well in this region. The two strongest PdHg rings, {101} (d=2.34 Å) and {110} (d=2.14Å) straddle the position of the palladium {111} ring (d=2.25 Å) and this overlap would obscure detection if PdHg is a minor constituent. X-ray diffraction measurements from the film on the HgI_2 substrate detected only elemental palladium indicating that the reaction to form PdHg cannot be extensive through the thickness of the film. Determination of the through-thickness and lateral extent of the reaction will require cross-sectional microstructural examination.

It is interesting to note that the palladium diffraction intensity in Figure 4 is not azimuthally symmetric but rather has intensity variations, of four-fold symmetry, which indicate that the film is highly textured. Because the HgI_2 substrate has been removed, it was not possible in this study to experimentally relate the textured ring pattern to the crystallography of the underlying substrate. Nevertheless, the four-fold symmetry of the pattern and the 45° rotation between the intensity peaks in the {200} and {220} rings would be consistent with a limited topotactic relationship between the palladium film and the tetragonal c-axis oriented α-HgI_2 substrate. The lattice mismatch for $\{001\}_{Pd}\|\{001\}_{HgI2}$, $[100]_{Pd}\|[100]_{HgI2}$ is about 11%. If the reaction to form randomly oriented PdHg occurs uniformly at the interface, then the retention of a crystallographic relationship between the palladium and the HgI_2 substrate would indicate that the PdHg reaction occurs following deposition of the film rather than during the initial stages of deposition.

4. Discussion

Previous thermodynamic calculations [1] have suggested that palladium should be a stable contact material and that the direct reaction of palladium with HgI_2 (to form palladium iodide, PdI_2) is thermodynamically unfavorable; however, the reaction to form PdHg was not considered. Two studies of the thermochemical properties of PdHg have been performed. Jangg and Kroll [5] investigated the vapor pressure of mercury in equilibrium with PdHg to arrive at a free energy of formation, ΔG_f, of -72.0 kJ/mol. More recently, Baranski et al. [6] used electrochemical methods to arrive at a somewhat lower value for ΔG_f of -58.2 kJ/mol.

Table 2 shows the Gibbs free energy of reaction for several reactions of mercury compounds with palladium to form PdHg. Three of these reactions are thermodynamically favorable: (1) the reaction of palladium and HgI_2 to form PdHg and PdI_2, (2) the reaction of palladium and mercurous iodide (Hg_2I_2) to form PdHg and

iodine, and (3) the reaction of free mercury and palladium to form PdHg and iodine. The reaction of palladium and HgI_2 to form PdHg and free iodine (reaction 4) is not thermodynamically favorable ($\Delta G_{rxn} > 0$).

Reaction 1, then, allows for a direct reaction between the palladium film and the underlying HgI_2. Although we have identified PdHg, we have not detected PdI_2, the other product of this reaction. However, we note that PdI_2 is soluble in KI solution (as is HgI_2) and thus would have been etched away with the substrate during the TEM sample preparation. An indirect reaction pathway may also allow formation of PdHg. As shown in Table 2, a reaction of either mercurous iodide (Hg_2I_2) (reaction 2) or elemental mercury (reaction 3) with elemental palladium would produce PdHg with a negative free energy of reaction. Thus, if the surface of the HgI_2 crystal is iodine poor, then Hg_2I_2 would be formed, as has been identified previously in HgI_2 [8,9] and which is also consistent with aging experiments showing a surface roughening of HgI_2 that appears to be due to iodine depletion. Reaction 3, which requires the presence of free mercury, is less likely. Free mercury is found only in heavily doped Hg:HgI_2 samples, but not in undoped HgI_2 crystals. It is possible, though, that under the energetic particle bombardment encountered in sputter deposition some surface decomposition to free mercury and iodine may occur. In order to further distinguish between these different reaction pathways, films deposited using more benign thermal evaporation processes should be examined and methods to preferentially remove HgI_2 while retaining any possible PdI_2 should be devised.

5. Conclusions

In summary, we have provided electron diffraction and HRTEM evidence for the formation of PdHg in palladium thin film contacts sputter deposited onto α-HgI_2. The extent of the reaction is limited and in the thicker regions of the film elemental palladium is dominant. The PdHg consists of randomly oriented grains of nanocrystalline

dimensions (<10nm diameter). Although this layer may result from the reaction of sputter deposited Pd with traces of mercurous iodide or free mercury at the surface of the crystal, direct reaction of palladium with HgI_2 to form PdHg and PdI_2 is thermodynamically feasible and would be expected to occur over time. The gradual increase in contact resistance that has been observed following deposition [2] may be reflecting the occurrence of the reaction. These results may have implications for the long-term stability of palladium contacts on HgI_2-based devices.

References

[1] A.Y. Cheng, in *Semiconductors for Room Temperature Radiation Detector Applications* Materials Research Society Symposium Proceedings Vol. 302, eds. R.B. James et al. (MRS, Pittsburgh, 1993) 141.

[2] J.M. Van Scyoc, *et al.*, in *Diagnostic Techniques for Semiconductor Materials Processing*, Materials Research Society Symposium Proceedings Vol. 324, eds. O.J. Glembocki et al. (MRS, Pittsburgh, 1994).

[3] K. Terada and F. Wm. Cagle Jr., American Mineralogist **45**, (1960) 1093.

[4] P. Stadelman, Ultramicroscopy **21** (1987) 131.

[5] G. Jangg and W. Groll, Z. Metallkd. **56** (1965) 232, cited by Z. Galus, CRC Critical Reviews in Analytical Chemistry **4** (1975) 359.

[6] A. Baranski, A. Kryska and Z. Galus, Journal of Electroanalytical Chemistry **349** , (1993) 341.

[7] I. Barin, *Thermochemical Data of Pure Substances* (VCH Verlagsgesesellschaft, Germany, 1989).

[8] M. Schieber, H. Hermon, and M. Roth, in *Semiconductors for Room Temperature Radiation Detector Applications*, Materials Research Society Symposium Proceedings Vol. 302, eds. R.B. James et al. (MRS, Pittsburgh, 1993) 347.

[9] M. Schieber, M. Roth, H. Yao, R.B. James, and M Goorsky, J. Cryst. Growth **146** (1995 15.

Figure Captions

Figure 1. Low magnification transmission electron micrograph of free standing palladium film. Arrows indicate examples of thin regions from which PdHg was identified.

Figure 2. Electron micrograph taken from exposed thin section near edge of film. Selected area electron diffraction pattern (inset) from region is identified as palladium mercuride (PdHg) (see also Table 1). The position of the strong {101} ring is indicated.

Figure 3. High resolution transmission electron micrograph taken from region identified by SADP to be PdHg. Inset shows the indexed power spectrum calculated by fourier transforming image of grain indicated in the center of the figure. Pattern is consistent with a PdHg grain oriented along a $[11\bar{1}]$ zone axis.

Figure 4. Electron micrograph from thicker region of film. Selected area electron diffraction pattern (inset) detects only elemental palladium. The pattern indicates a strong four-fold texture. Additionally, note the 45° rotation between the intensity peaks in the {200) and {220} rings.

Table 1 Summary of Electron Diffraction Measurements for Phase Identified as Palladium Mercuride (PdHg)

PdHg (Potarite) JCPDS-13-0149 a=b=3.031 Å, c=3.692 Å				Observed	
hkl	d (Å)	d/d_{101}	Relative Intensity†	d (Å)	d/d_{101}
001	3.68	1.57	0.7	3.49	1.52
100	3.06	1.31	1.1	2.96	1.29
101	2.34	1.00	100.0	2.30	1.00
110	2.14	0.914	39.2	2.07	0.90
111	1.851	0.791	1.2		
002*	1.846*	0.789*	13.1	1.79	0.78
102	1.581	0.676	0.9	n.d.	--
200	1.513	0.647	14.1	1.47	0.64
201	1.402	0.599	0.7		
112*	1.399	0.598	22.1	1.35	0.59
210	1.355	0.579	0.6	n.d.	--
211	1.274	0.544	32.6	1.23	0.53

n.d. = not detected

†Relative intensities are determined from a structure factor calculation using 120 keV electrons.

*The {002} and {112} reflections are not explicitly listed in JCPDS-13-0149. A structure factor calculation for 120 keV electrons shows that these are allowed reflections and that these are relatively intense compared with the nearly overlapping {111} and{201} reflections.

Table 2. Gibbs Free Energies of Reaction for several reactions producing PdHg.

Reaction	ΔG_{rxn} (kJ/mol)
(1) $HgI_2(s) + 2Pd(s) = PdHg(s) + PdI_2(s)$	-28.0 (-40.7)
(2) $Hg_2I_2(s) + 2Pd(s) = 2PdHg(s) + I_2(s)$	-5.3 (-32.9)
(3) $Hg(l) + Pd(s) = PdHg(s)$	-58.2 (-72.0)
(4) $HgI_2(s) + Pd(s) = PdHg(s) + I_2(s)$	+44.0 (+30.2)

Notes: Gibbs Free Energies of Formation are taken at 298.15K and are: $HgI_2(s)$: -102.24 kJ/mol [7]; $Hg_2I_2(s)$: -111.14 kJ/mol [7]; $PdI_2(s)$: -70.98 kJ/mol [7]; PdHg(s): -58.2 kJ/mol [6] and -72.0 [5]. Gibbs Free Energy of Reaction is calculated using the ΔG_f values for PdHg taken from Ref. 6 and, in parentheses, Ref. 5.

Fig 1

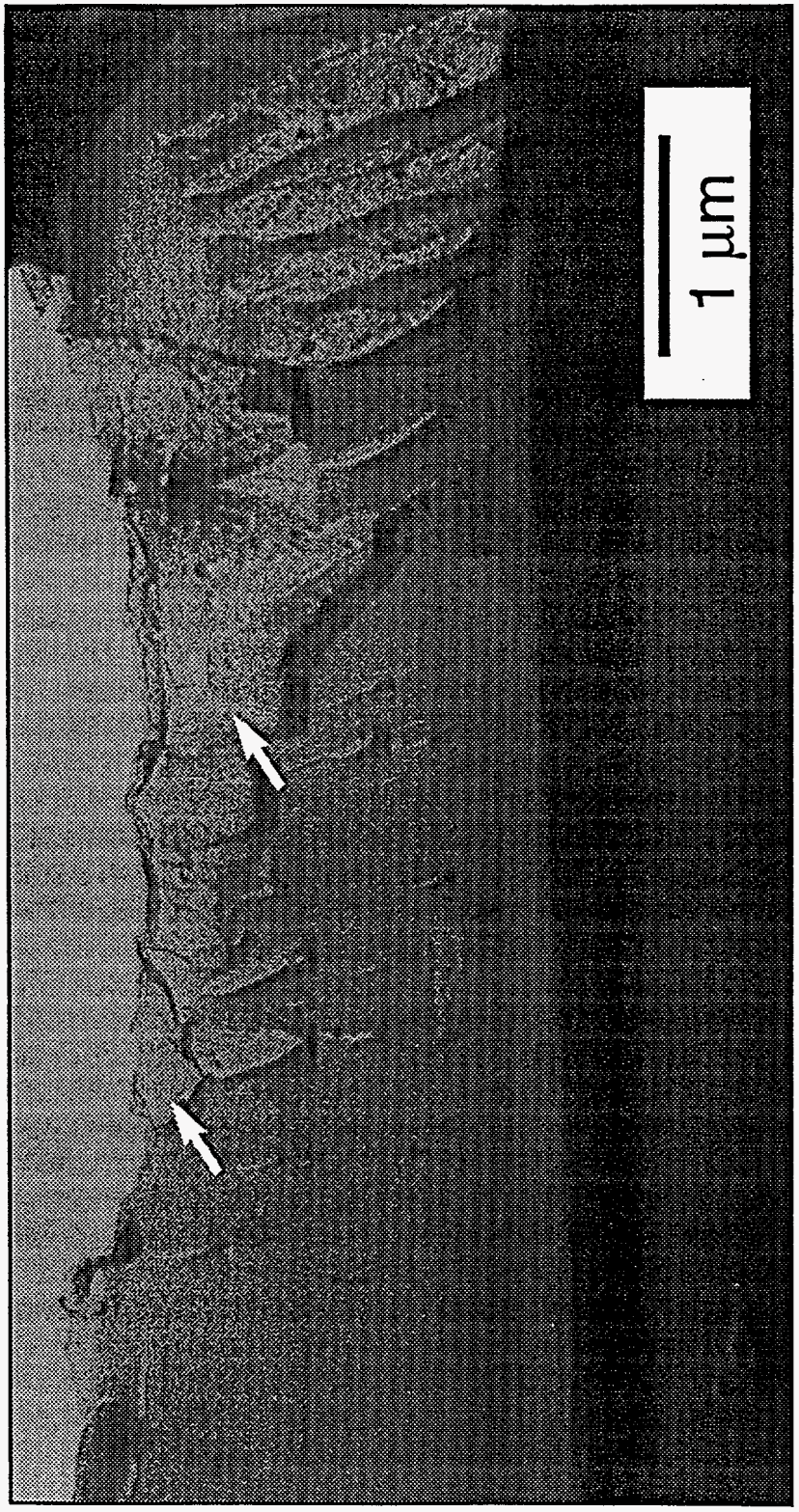

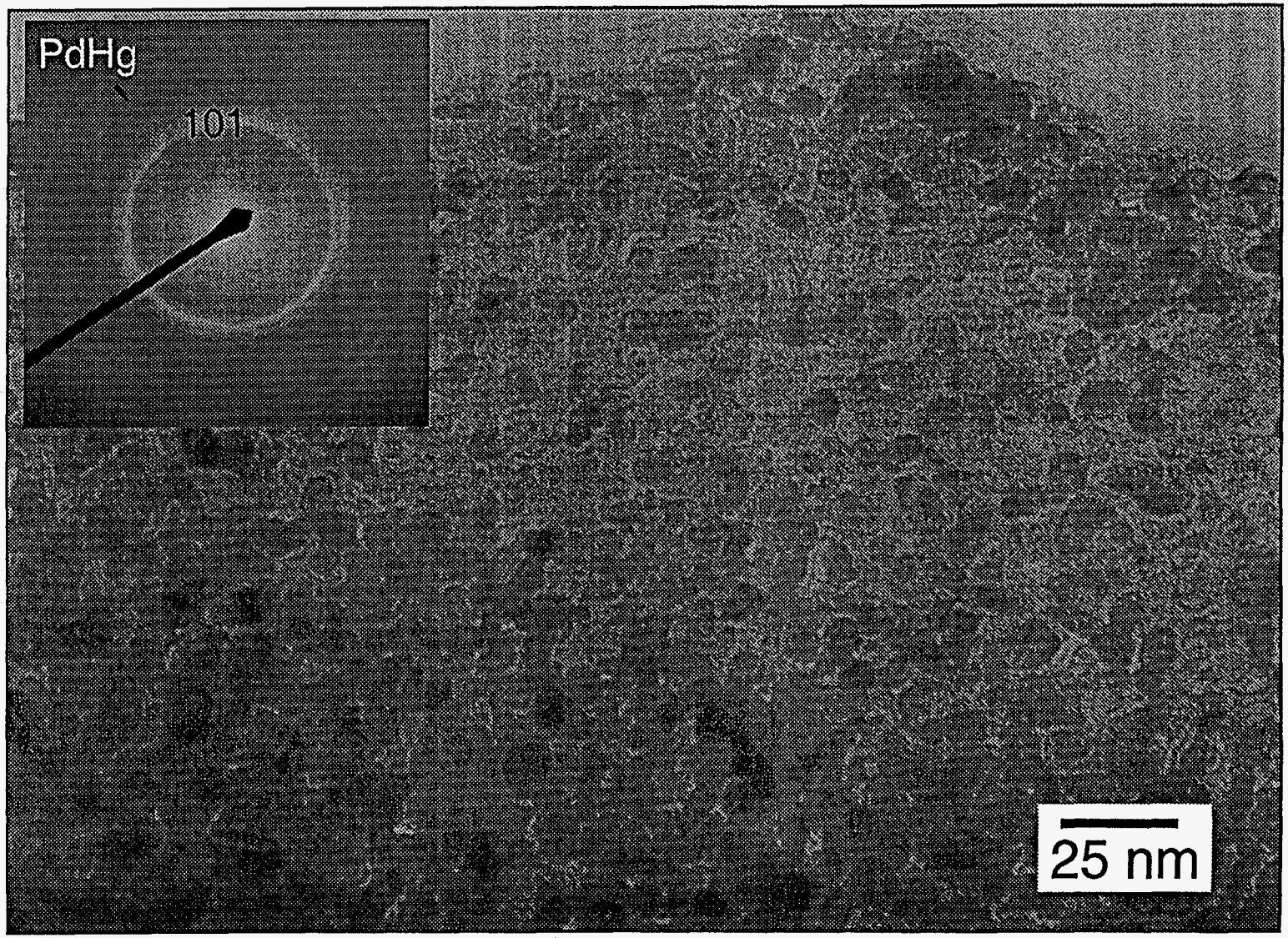
PdHg
101
25 nm

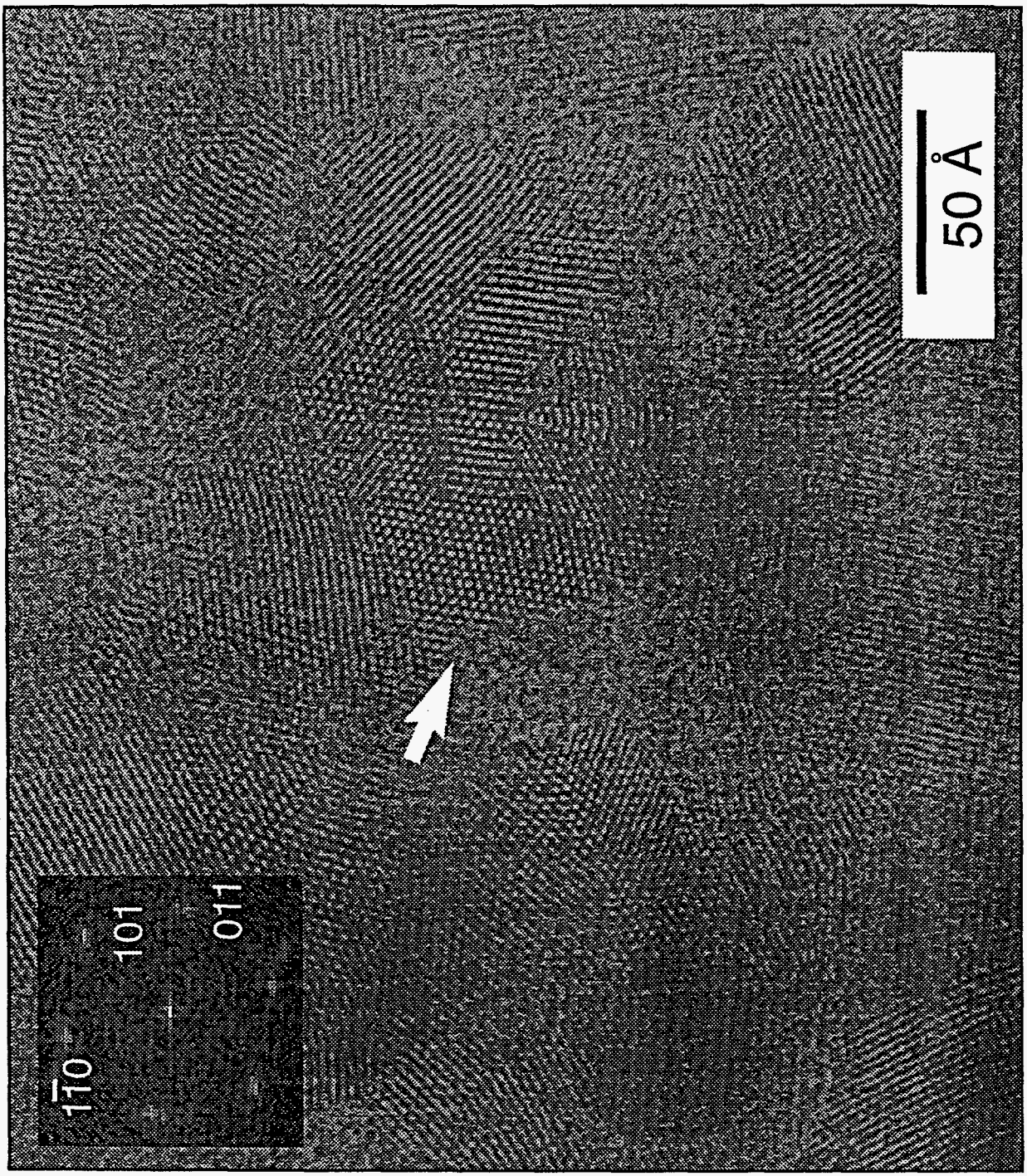

Fig 3

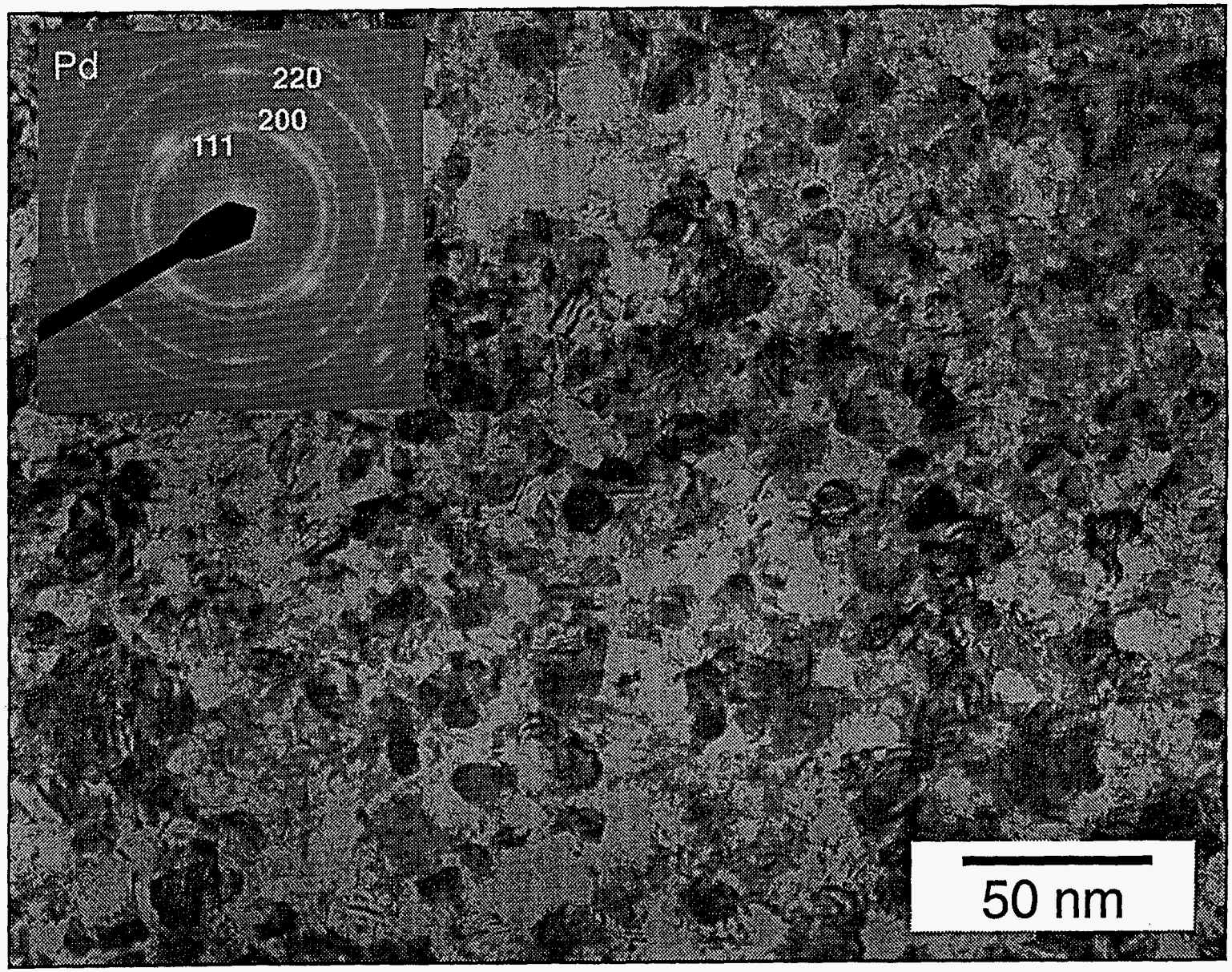
Pd
220
200
111
50 nm

Sent to Phys. Rev. B

Optical Anisotropic Dielectric Response of HgI_2

Huade Yao
University of Nebraska, Center for Microelectronic and Optical Materials Research, and Department of Electrical Engineering, Lincoln, NE 68588-0511;

Blaine Johs
J.A. Woollam Co., Inc., Lincoln, NE 68502;

Ralph B. James
Sandia National Laboratories, Livermore, CA 94551-0969

ABSTRACT

Anisotropic optical properties of HgI_2 were studied by variable angle spectroscopic ellipsometry (VASE). Angular dependent polarized reflectance and transmittance at three special optical-axis configurations, concerning the uniaxial anisotropic nature of the crystal, were derived to facilitate the VASE analysis. Two surface orientations of this tetragonal crystal were selected, i.e., an a-plane and a c-plane sample. Room temperature multiple-angle SE measurements from both samples with three different optical configurations along with polarized transmission measurements were jointly analyzed by the VASE analysis through multiple-sample, multiple-model methods. Anisotropic dielectric functions of single crystal HgI_2, $\varepsilon_\perp(\omega)$ and $\varepsilon_\parallel(\omega)$, for optical electric field vector oriented perpendicular and parallel to the c axis, respectively, were obtained in the range of 1.24 - 5.1 eV. Different absorption energy-band edges, at room temperature, were observed from the ordinary and extraordinary dielectric responses at 2.25 and 2.43 eV, respectively. This is consistant with the results related to the optical transitions between the conduction band and the heavy- and light-hole valence band indicated by theoretical studies. A surface model related to the surface roughness and defects of HgI_2 was established and characterized by the VASE analysis.

I. INTRODUCTION

Crystal mercuric iodide (HgI_2) is an important technological material for room-temperature radiation (i.e., gamma- and x-ray) detectors.[1-5] It also presents some interesting scientific issues regarding its tetragonal crystal structures. The optical anisotropic behavior was observed via the reflectance and absorption spectra of HgI_2 crystal when the optical electric field vectors E oriented parallel and perpendicular to the c axis.[6-11] The imaginary part of the dielectric functions $\varepsilon_{2\perp}(\omega)$ ($E \perp c$) were deduced from the reflectivity spectra by means of Kramers-Kronig relations under several assumptions.[10] However, the optical anisotropic dielectric response of this crystal, such as dielectric functions ($\varepsilon = \varepsilon_1 + \varepsilon_2$), have not been determined directly by precise optical measurements. Since HgI_2 crystal is tetragonal, it must be described by two dielectric response functions, $\varepsilon_\perp(\omega)$ and $\varepsilon_\parallel(\omega)$, for optical electric field vector oriented perpendicular (ordinary) and parallel (extraordinary) to the *c* axis, respectively. One frequently encountered difficulty is to calculate and analyze the optical measurement results in dealing with the uniaxial anisotropic nature of the crystal.

In this paper, we report, for the first time, determination of room temperature anisotropic dielectric functions, $\varepsilon_\perp(\omega)$ and $\varepsilon_\parallel(\omega)$, of HgI_2 crystal in the range of 1.24 - 5.1 eV, by variable angle spectroscopic ellipsometry (VASE). The optical functions were extracted from simultaneous analysis of VASE measurements of two HgI_2 crystal samples: one c-plane surface, to which the c-axis of the crystal is perpendicular; and another a-plane surface, to which the c-axis is parallel. An analytical angular dependent polarized reflectance and transmittance at three special optical-axis configurations, for the uniaxial anisotropic crystal were derived and a surface model concerning the roughness and possible near surface defects was established for the VASE analyses. Room-temperature energy-band absorption

edges of the HgI_2 crystal from the ordinary and extraordinary dielectric response will be discussed and presented.

II EXPERIMENTAL DETAILS

A. Sample Preparations

Two HgI_2 surfaces from this tetragonal crystal were prepared for the VASE measurements: a c-plane surface, to which the c-axis of the crystal is perpendicular, and an a-plane surface, to which the c-axis is parallel, as shown in Fig. 1. Three special optical configurations were chosen for the VASE measurements: a c-plane surface, i.e., the c-axis is normal to the sample surface, which we term here as c-p configuration, as shown in Fig. 2; an a-plane surface with c-axis is in the plane of sample surface and parallel to the plane of incidence, aEp configuration; and an a-plane surface with the c-axis perpendicular to the plane of incidence, aEs configuration.

Sliced and polished c-plane and a-plane HgI_2 samples were subjected to a chemical etching to ensure clean and fresh surface before the VASE measurements. In the etching process, the samples were immersed in a 10% KI (by weight) solution for about 2 min. After the KI etching, the samples were immediately rinsed with deionized water for ~2-3 min. This KI etching treatment removes a surface layer of about 60 μm thickness (i.e., a ~30 μm/min etching rate).[12] The fresh ruby red HgI_2 surfaces were blown in dry air to remove the excess water. VASE measurements were performed immediately on the new fresh surfaces.

B. VASE Measurements

The spectroscopic ellipsometry (SE) is designed to accurately determine the values of tan(ψ) and cos(Δ), which are the amplitude and projected phase of the complex reflectance ratio,

$$\rho = r_p / r_s = \tan(\psi) e^{i\Delta}, \tag{1}$$

where r_p and r_s are the reflectance coefficients of light polarized parallel to (p) or perpendicular to (s) the plane of incidence. The ψ and Δ are sensitive to changes of the surface conditions, overlayer thicknesses, dielectric functions and other parameters of the sample.[13, 14]

The pseudodielectric function <ε> is obtained from the ellipsometrically measured values of ρ, in a two-phase model (ambient/substrate):

$$< \varepsilon > = < \varepsilon_1 > + i < \varepsilon_2 > = \varepsilon_a \left[\left(\frac{1-\rho}{1+\rho} \right)^2 \sin^2 \Phi \tan^2 \Phi + \sin^2 \Phi \right], \tag{2}$$

regardless of the possible presence of surface overlayers.[13] The ε_a in Eq.(2) represents the ambient dielectric function (i.e. ε_a=1 in vacuum). Since the HgI_2 is a tetragonal crystal, it exhibits uniaxial anisotropy and must be described by two dielectric response functions $\varepsilon_\perp(\omega)$ and $\varepsilon_\parallel(\omega)$, representing optical electric field vector oriented perpendicular (ordinary) and parallel (extraordinary) to the c-axis of the crystal, respectively.

Ellipsometric Measurement of the complex ratio, ρ at a single wavelength and angle of incidence provides two quantities (ψ and Δ), which can be used to determine two parameters describing the sample, e.g., dielectric function ($\varepsilon=\varepsilon_1+i\varepsilon_2$) of a isotropic bulk sample with no overlayer complications. Spectroscopic (multiple wavelengths) ellipsometric measurements greatly increase the number of determined parameters of the sample, especially when measurements were made at more than one angle of incidence. Thus, the variable angle spectroscopic

ellipsometry (VASE) makes possible the detailed evaluation of crystals with tetragonal structures.

Multiple angle SE measurements of the two HgI_2 samples at the three special optical configurations, mentioned above, were taken in the range of 1.24 to 5.1 eV with an increment of 0.02 eV, at 5 different angles of incidence ranging from 67.5° to 77.5° with an increment of 2.5°. The VASE measurements were made using a Woollam Co. Variable Angle Spectroscopic Ellipsometer (VASE™), which was equipped with a beam-chopped, rotating analyzer to increase the stray light rejection and signal to noise ratio.

A surface model was assumed, for the VASE analysis, including a top surface rough layer and a graded subsurface layer representing the distribution of possible surface defects, as shown in Fig. 3. In this model, each surface layer contains more than one consitituent. The Bruggeman effective-medium approximation (EMA)[15] is employed to calculate the effective optical constants of the mixed layer. It can be expressed as:

$$f_A \frac{\varepsilon_A - \varepsilon}{\varepsilon_A + 2\varepsilon} + f_B \frac{\varepsilon_B - \varepsilon}{\varepsilon_B + 2\varepsilon} = 0, \tag{3}$$

where ε is the effective dielectric function of the mixed layer. The values of ε_A and ε_B are the dielectric functions of the material A and B, respectively, and f_A and f_B are the relative volume fractions. This is based on the assumption of a homogeneous mixture and a random-aggregate spherical microstructure (e.g. a HgI_2 layer with voids). A detailed application of this surface model is presented in later of this paper.

VASE data from the three different reflection geometries were numerically fitted simultaneously through a regression analysis of the assumed surface model, by varying the anisotropic optical constants of the crystal as well as the surface

roughness layer thicknesses and the voids volume percentage until the calculated and measured values match as closely as possible. This is done by minimizing the χ^2 error function defined as:

$$\chi^2 = \sum_{i,j} \left\{ \left[\frac{\psi(h\nu_i, \Phi_j) - \psi^c(h\nu_i, \Phi_j)}{\sigma_{i\psi}} \right]^2 + \left[\frac{\Delta(h\nu_i, \Phi_j) - \Delta^c(h\nu_i, \Phi_j)}{\sigma_{i\Delta}} \right]^2 \right\}, \quad (4)$$

where hν is the photon energy, Φ is the external angle of incidence, σ is the measured standard deviation of the measurement, and i and j are used to sum over all the photon energies and external angles of incidence, respectively. In all three configurations, the interface reflection Jones matrix r is diagonal.[16]

III. ANISOTROPIC REFLECTANCE AND TRANSMITTANCE

VASE analysis employs the coefficients of reflectance and transmittance as functions of spectral optical dielectric response of each media and the angle of incidence at the boundary of the two media. For isotropic materials, they are well known as Fresnel's equations. For anisotropic media, this issue has been theoretically studied. However, the practical analytical expression is not readily available. In this section, we present a derivation of the angular dependent polarized functions of reflectance and transmittance at the three special configurations, based on Maxwell's equations and the properties of uniaxial anisotropic media (crystals).

In an isotropic medium, the electric field E and displacement field vector D are in the same direction and always normal to the wave propagation and the velocity of a plane wave is a constant independent of the direction of propagation in the medium. Therefore, the refractive indices of an isotropic medium is a sphere corresponding to a constant frequency. These are no longer true in anisotropic media, except for certain perticular directions. For uniaxial anisotropic crystals, The

electric field vector **E** and displacement field vector **D** are in general not in the same direction. So does the wave propagation direction represented by the Poynting vector **S** and the direction of the wave vector **k**, as shown in Fig. 4. The wave velocity as the electric field vector **E** perpendicular to the optic axis (ordinary) is different from that as **E** parallel to the optic axis (extraordinary). The refractive indices n_e related to the extraordinary wave is an ellipsoid. Therefore, in general, a plane wave incident on the surface of an uniaxial crystal will be refracted into two waves: ordinary wave and extraordinary wave, as shown in Fig. 5.

Now we will look at refraction at the three special optical configurations at the interface of an isotropic medium and a uniaxial crystal.

A. Optic Axis Normal to the Boundary (C-P):

a. P-wave (extraordinary behavior):

The p-wave here refers to light vibrating in the plane of incidence. Since the vibration is neither perpendicular nor parallel to the optic axis, it is an extraordinary behavior. As shown in Fig. 6, the kinimatic condition requires that

$$k_1 \sin(\theta_1) = k_{2o} \sin(\theta_{2o}) = k_2(\theta_{2e}) \sin(\theta_{2e}) \tag{5}$$

for the refracted waves. Multiplication of equ. (5) by $\lambda_o/2\pi$ (where λ_o is the wavelength in vacuum) results in

$$n_1 \sin(\theta_1) = n_{2o} \sin(\theta_{2o}) = n_2(\theta_{2e}) \sin(\theta_{2e}) \tag{6}$$

where n_1 is the index of refraction of the incident medium (isotropic)) and n_2 is the index of refraction of the anisotropic uniaxial crystal. Equ (6) looks like the Snell's law. However, it is important to point out that n_2 is not, in general, constant. It varys with the directions of the wave vectors **k**. In this case, the index n_2 ellipsoid in the plane of incidence can be written as:

$$\frac{1}{(n_2)^2} = \frac{[\cos(\theta_{2e})]^2}{(n_{2o})^2} + \frac{[\sin(\theta_{2e})]^2}{(n_{2e})^2}, \tag{7}$$

where n_{2o} and n_{2e} are lengths of the two major ellipsoid axes. By rearranging equ. (7), n_2 can also be written as:

$$n_2(\theta_{2e}) = \frac{n_{2o}n_{2e}}{\sqrt{[n_{2e}\cos(\theta_{2e})]^2 + [n_{2o}\sin(\theta_{2e})]^2}}. \tag{8}$$

The equations of reflectance r_{12p} and transmittance t_{12p} of the p-wave were obtained by solving Maxwell equations and their boundary conditions. Due to the anisotropic nature of the uniaxial crystal, the results are tedious. For the purpose of simplisity and clear physical pictures, we adopt the format of Frensel's equations by replacing some constants with additional expressions.

The reflectance and transmittance then can be written as:

$$\boxed{r_{12p} = \frac{n_{2s}\cos(\theta_1) - n_1\cos(\alpha)}{n_{2s}\cos(\theta_1) + n_1\cos(\alpha)}} \tag{9}$$

$$\boxed{t_{12p} = \frac{2n_1\cos(\theta_1)}{n_{2s}\cos(\theta_1) + n_1\cos(\alpha)}} \tag{10}$$

where n_{2s} reflects the directional difference of the wave vector **k** and the Poynting vector **S**, as shown in Fig. 4, and is expressed as

$$n_{2s} = n_2\cos(\theta_{2e} - \alpha), \tag{11}$$

where

$$\tan(\theta_{2e}) = \frac{n_1\sin(\theta_1)}{n_{2o}\left[1 - \left(\frac{n_1\sin(\theta_1)}{n_{2e}}\right)^2\right]^{1/2}}, \tag{12}$$

and

$$\tan(\alpha) = -\left(\frac{n_{2o}}{n_{2e}}\right)^2 \tan(\theta_{2e}). \tag{13}$$

b. S-wave (ordinary refraction):

The s-wave here refers to light vibrating perpendicular to the plane of incidence. Since the vibration is perpendicular to the optic axis, we have ordinary behavior, where

$$n_2 = n_{2o} \tag{14}$$

Therefore, the expressions of reflectance and transmittance are straight forward:

$$\boxed{r_{12s} = \frac{n_1 \cos(\theta_1) - n_{2o} \cos(\theta_{2o})}{n_1 \cos(\theta_1) + n_{2o} \cos(\theta_{2o})}} \tag{15}$$

$$\boxed{t_{12s} = \frac{2n_1 \cos(\theta_1)}{n_1 \cos(\theta_1) + n_{2o} \cos(\theta_{2o})}}. \tag{16}$$

B. Optic Axis in the Boundary and in the Plane of Incidence (aEp):

a. P-wave (extraordinary behavior):

For the same reason as in the c-p configuration, the p-wave has an extraordinary behavior since it is vibrating in the plane of incidence. In this case, the Equ. (6) is still valid. The $n_2(\theta_{2e})$ in the plane of incidence is written as

$$\frac{1}{(n_2)^2} = \frac{[\cos(\theta_{2e})]^2}{(n_{2e})^2} + \frac{[\sin(\theta_{2e})]^2}{(n_{2o})^2}, \tag{17}$$

and can be rearranged as

$$n_2(\theta_{2e}) = \frac{n_{2o} n_{2e}}{\sqrt{[n_{2o} \cos(\theta_{2e})]^2 + [n_{2e} \sin(\theta_{2e})]^2}}. \tag{18}$$

Notice that the positions of the two major ellipsoid axes, n_{2o} and n_{2e}, have been stwitched compared with Equ. (7), due to the direction change of the optic axis.

Thus, we have

$$\boxed{r_{12p} = \frac{n_{2s}\cos(\theta_1) - n_1\cos(\alpha)}{n_{2s}\cos(\theta_1) + n_1\cos(\alpha)}} \tag{19}$$

$$\boxed{t_{12p} = \frac{2n_1\cos(\theta_1)}{n_{2s}\cos(\theta_1) + n_1\cos(\alpha)}}. \tag{20}$$

Same as in the c-p case, the n_{2s} is expressed as

$$n_{2s} = n_2\cos(\theta_{2e} - \alpha), \tag{21}$$

where

$$\tan(\theta_{2e}) = \frac{n_1\sin(\theta_1)}{n_{2e}\cos(\theta_{2o})} \tag{22}$$

$$\tan(\alpha) = -\left(\frac{n_{2e}}{n_{2o}}\right)^2\tan(\theta_{2e}). \tag{23}$$

b. S-wave (ordinary refraction):

For the same reason as in the c-p case, the s-wave here has the ordinary behavior since its vibration is perpendicular to the optic axis. Therefore,

$$n_2 = n_{2o}, \tag{24}$$

and we have

$$\boxed{r_{12s} = \frac{n_1\cos(\theta_1) - n_{2o}\cos(\theta_{2o})}{n_1\cos(\theta_1) + n_{2o}\cos(\theta_{2o})}} \tag{25}$$

$$\boxed{t_{12s} = \frac{2n_1\cos(\theta_1)}{n_1\cos(\theta_1) + n_{2o}\cos(\theta_{2o})}}. \tag{26}$$

C. Optic Axis in the Boundary and Normal to the Plane of Incidence (aEs):

a. P-wave (ordinary refraction):

The p-wave in this configuration vibrates perpenducular to the optic axis. Hence it is an ordinary refraction. Therefore, $n_2 = n_{2o},$, and we have

$$n_1 \sin(\theta_1) = n_{2o} \sin(\theta_{2o}), \tag{27}$$

and

$$\boxed{r_{12p} = \frac{n_{2o}\cos(\theta_1) - n_1\cos(\theta_{2o})}{n_{2o}\cos(\theta_1) + n_1\cos(\theta_{2o})}} \tag{28}$$

$$\boxed{t_{12p} = \frac{2n_1\cos(\theta_1)}{n_{2o}\cos(\theta_1) + n_1\cos(\theta_{2o})}}. \tag{29}$$

b. S-wave (extraordinary refraction):

The s-wave here vibrates parallel to the optic axis (perpendicular to the plane of incidence), resulting in extraordinary refraction. Therefore, we have

$$n_2 = n_{2e}, \tag{30}$$

and

$$n_1 \sin(\theta_1) = n_{2e} \sin(\theta_{2e}). \tag{31}$$

This condition leads to the results as:

$$\boxed{r_{12s} = \frac{n_1\cos(\theta_1) - n_{2e}\cos(\theta_{2e})}{n_1\cos(\theta_1) + n_{2e}\cos(\theta_{2e})}} \tag{32}$$

$$\boxed{t_{12s} = \frac{2n_1\cos(\theta_1)}{n_1\cos(\theta_1) + n_{2e}\cos(\theta_{2e})}}. \tag{33}$$

IV. RESULTS AND ANALYSIS

Figure 7 shows pesudodielectric response <ε> of an a-plane single crystal HgI_2 surface, measured by VASE with aEp and aEs configuration, respectively, at 5 different angles of incidence ranging from 67.5° to 77.5° with an increment of 2.5°.

The obviously different psudodielectric responses from the aEp and aEs geometries, and angular dispersions of $<\varepsilon_1>$ and $<\varepsilon_2>$ in both situations provide strong evidence of the uniaxial anisotropic nature of HgI_2 crystal. The c axis of this a-plane sample was at first assumed parallel to one of its cleaved edges. This assumption was proved to be correct in the later VASE analysis.

Polarized transmission measurements were made on the a-plane surface with optical electric field vector E oriented parallel ($E \parallel <c>$) and perpendicular ($E \perp <c>$) to the c axis, respectively, in a range from 1.24 - 2.5 eV with an increment of 0.02 eV, as shown in Fig. 8.

The graded subsurface, in the surface model as shown in Fig. 3, is constructed by varying voids volume percentage from 0 to x (a fitting parameter), representing the distribution of possible surface defects, which may related with surface aging of HgI_2. The top surface roughness was modeled through an EMA layer with a fixed 50% voids volume percentage. During the VASE regression analysis, optical constants of the HgI_2 crystal, ε_{1o}, ε_{1e}, ε_{2o}, ε_{2e}, and the thicknesses of the top (d_1) and subsurface (d_2) layers, plus the voids percentage x in the subsurface layer were varied to fit all the VASE data from two samples in c-p, aEp and aEs configurations and the polarized transmission data, simultaneously. Each sample was described by its own surface model, the numerical fitting was based on the assumption that the optical constants of the c-plane and a-plane samples are same and they were coupled together through a multi-sample VASE analysis. The multi-sample method allows us to analyze several independent VASE data simultaneously, and couple some of the common optical constants together during the numerical fitting. This method greatly increases the ratio of SE determined quantities to fitting parameters, so that reduce the possible coupling between fitting variables.

As an illustration, we show the results of multi-sample VASE analysis in Fig. 9 (a-plane) and Fig. 10 (c-plane). For the a-plane sample, 4 angles of incidence of

VASE data of each optical configuration (i.e., aEp and aEs respectively) were fitted, while 5 angles of incidence VASE data from the c-plane sample were used for analysis. As we can see that the model fit (the solid line) and the experimental data (the dotted or dashed lines) are matched very closely. The VASE analysis shows that this a-plane sample (N16-12) has a top roughness layer of ~46 Å followed by a subsurface layer of ~1039 Å, while the c-plane HgI_2 sample resulted in thicknesses of 42 Å and 1025 Å for the top and subsurface layer respectively. We believe the surface roughness layers described by EMA, especially the subsurface layer , are related to surface defects and surface aging of HgI_2 crystal. A detailed studies of the surface aging of HgI_2 crystal are reported in a separate paper.[17]

Figure 11 shows the room temperature (RT) anisotropic dielectric functions of HgI_2 crystal in a range of 1.24 - 5.1 eV, as results of the VASE analysis. It is noticeable that the absorption edges of the ordinary and extraordinary dielectric response ε_2 are different: ~2.25 eV for the ordinary and ~2.43 eV for the extraordinary response. This is consistant with the results related to the optical transitions between the conduction band and the heavy- and light-hole valence band indicated by theoretical studies.[18]

Kramers-kronig (k-k) transformation relation was employed to check the consistency of the anisotropic dielectric functions. The k-k transformation reflects the nature of relation between the real and imaginary part of the dielectric function $\varepsilon = \varepsilon_1 + i\varepsilon_2$, and can be written as:

$$\varepsilon_1(\hbar\omega) = 1 + \frac{2}{\pi} p \int_0^\infty \frac{x\varepsilon_2(x)}{x^2 - (\hbar\omega)^2} dx, \qquad (34)$$

where $\hbar w$ is the photon energy. By the k-k transformation, the real part of the dieletric function ε_1 can be obtained through the imaginary part ε_2. However, the k-k transformation integrates the entire spectral range, while our VASE

measurements are limited in the range of 1.24 to 5.1 eV. Two non-broadening oscillators were employed to cover the unmeasured spetral range. The modified k-k transformation is written as:

$$\varepsilon_1^{kk}(\hbar\omega) = \varepsilon_1^{offset} + \sum_{i=1}^{2} \frac{A_i}{(\hbar\omega)^2 - E_i^2} + \frac{2}{\pi} p \int_{1.24eV}^{5.1eV} \frac{x\varepsilon_2^{meas}(x)}{x^2 - (\hbar\omega)^2} dx, \qquad (35)$$

where A_i and E_i are the amplitude and center energy for the ith oscillator, respectively. An ε_1^{offset} was used to replace the unit value in the k-k relation. Thus, values of ε_{2o} (ordinary) and ε_{2e} (extraordinary) obtained through VASE analysis were used to calculate ε_{1o} (ordinary) and ε_{1e} (extraordinary) via the k-k relation Equ. (35), respectively. The calculated values were compared with the VASE determined ε_{1o} and ε_{1e}, through a regression analysis by varying the values of A_i, E_i and ε_1^{offset} until and calculated and measured values match as closely as possible. The results of the k-k fit are shown in Fig. 12 and Table I. It is obvious that good k-k fit was obtained by applying one oscillator on the higher energy side and one on the lower energy side for each set of ε , as indicated by the arrows in Fig. 12. The lower-energy-side oscillator is often not needed because of the simple non-absorbing behavior below the material band gap. However, one oscillator with low-center-energy is needed in this case because of the strong zone-center phonon absorption of HgI_2 crystal.[18]

Refractive indices (both ordinary, $\tilde{n}_o$ and extraordinary, $\tilde{n}_e$) can be derived respectively from the ε data by the following relations:

$$<\tilde{n}>^2 = (<n> + i<k>)^2 = <\varepsilon_1> + i<\varepsilon_2>, \qquad (36)$$

$$<n> = \left[\frac{<\varepsilon_1>}{2} + \frac{1}{2}\sqrt{<\varepsilon_1>^2 + <\varepsilon_2>^2}\right]^{1/2}, \qquad (37)$$

$$< k > = \left[- \frac{< \varepsilon_1 >}{2} + \frac{1}{2} \sqrt{< \varepsilon_1 >^2 + < \varepsilon_2 >^2} \right]^{1/2}, \tag{38}$$

as shown in Fig. 13. Notice that below ~3.55 eV, the HgI_2 is a negative uniaxial crystal ($n_o > n_e$), while above ~3.55 eV, it becomes a positive uniaxial crystal ($n_o < n_e$).

Figures 14 and 15 show polarized absorption and reflection coefficients of HgI_2 with optical electric field vector E oriented perpendicular (E ⊥ <c>) and parallel (E ∥ <c>) to the c axis, respectively. Those coefficients were calculated by using the refractive indices, shown in Fig. 13, through the normal-incidence absorption:

$$< \alpha > = 4\pi < k > / \lambda, \tag{39}$$

and reflection:

$$< R > = \frac{(< n > - 1)^2 + < k >^2}{(< n > + 1)^2 + < k >^2}. \tag{37}$$

V. CONCLUSIONS

In summary, we have studied the anisotropic optical properties of HgI_2 crystal, by variable angle spectroscopic ellipsometry. Polarized reflectance and transmittance at three special optical-axis configurations, concerning the uniaxial anisotropic nature of the crystal, were derived as functions of angles of incidence to facilitate the VASE analysis. Two surface orientations of the tetragonal crystal were chosen, i.e., an a-plane and a c-plane surface, for the study. Room-temperature anisotropic dielectric functions of HgI_2 crystal, both ordinary $\varepsilon_\perp(\omega)$ and extraordinary $\varepsilon_\parallel(\omega)$, in the range of 1.24 -5.1 eV, were extracted by the VASE measurements and multiple-sample and multiple-model analysis. Both dielectric functions satisfy the Kramers-kronig relation, respectively. Different energy-band absorption edges were observed,

at room temperature, from the ordinary and extraordinary dielectric responses at 2.25 and 2.43 eV, respectively. They are related with optical transitions between the conduction band and the heavy- and light-hole valence band.

ACKNOWLEDGMENTS

This work was supported by the Department of Energy via Sandia National Laboratories. A helpful discussion with Dr. G.E. Jellison, for checking the numerical results of the anisotropic Fresnel's equations, is greatly appreciated.

REFERENCES

1 W. R. Wing, Nucl. Instrum. Meethods **96**, 615 (1971).

2 S. P. Swierkowski, G. A. Armantrout, and R. Wichne, IEEE Trans. Nucl. Sci. **NS-21**, 302 (1974).

3 J. P. Ponpon, R. Stuck, P. Siffert, B. Meyer, and C. Schwab, IEEE Trans. Nucl. Sci. **NS-22**, 182 (1975).

4 A. J. Dabrowski, W. M. Szymczyk, J. S. Iwanczyk, J. H. Kusmiss, W. Drummond, and L. Ames, Nucl. Instrum. Methods **213**, 89 (1983).

5 J. H. Howes and J. Watling, Mat. Res. Soc. Symp. Proc. **16**, 207 (1983).

6 B. V. Novikov and M. M. Pimonenko, Sov. Phys. Semicond. **4**, 1785 (1971).

7 K. Kanzaki and I. Imai, J. Soc. Jpn. **32**, 1003 (1972).

8 A. Aneda, F. Raga, E. Grilli, and M. Guzzi, Nuovo Cimento **38**, 439 (1977).

9 P. D. Bloch, J. W. Hodby, C. Schwab, and D. W. Stacey, J. Phys. C **11**, 2579 (1978).

10 A. Anedda, E. Grilli, M. Guzzi, F. Raga, and A. Serpi, Solid State Commun. **39**, 1121 (1981).

11 T. Goto and A. Kasuya, J. Soc. Jpn. **50**, 520 (1981).

12 X. J. Bao, T. E. Schlesinger, R. B. James, R. H. Stulen, C. Ortale, and A. Y. Cheng, J. Appl. Phys. **68**, 86 (1990).

13 R. M. A. Azzam and N. M. Bashara, *Ellipsometry and Polarized Light* (North-Holland, Amsterdam, 1977).

14 H. Yao, P. G. Snyder, and J. A. woollam, J. Appl. Phys. **70**, 3261 (1991).

15 D. E. Aspnes,J. B. Theeten, and F. Hottier, Phys. Rev. B **20**, 3292 (1979).

16 A. Yariv and P. Yen, *Optical Waves in Crystals* (John Wiley & Sons, Inc., New York, 1984).

17 H. yao, L. A. Lim, R. B. James, M. Schieber, and M. Natarajan, Nucl. Instrum. Methods (to be published) (1996).

Intentionally Left Blank

[18] Y. C. Chang and R. B. James, Phys. Rev. B **46**, 15040 (1992).

[19] H. K. Sim and Y. C. Chang, Phys. Rev. B **49**, 4559 (1994).

FIGURE CAPTIONS

1. Tetragonal crystal structure of HgI_2.
2. Three special optical configurations: c-p, aEs and aEp as defined in the text.
3. Surface model for VASE analysis.
4. Extraordinary wave propagation in k-space.
5. Ray diagram for double refraction in uniaxial crystals. θ_{2o} and θ_{2e} stand for refraction angle of ordinary and extraordinary rays, respectively.
6. Kinematic condition for wave vectors of double refraction in uniaxial crystals. O and e stand for ordinary and extraordinary waves, respectively.
7. Pseudodielectric response $\langle\varepsilon\rangle$ of an a-plane single crystal HgI_2 surface, measured by VASE with aEp and aEs configuration, respectively, at 5 different angles of incidence ranging from 67.5° to 77.5° with an increment of 2.5°.
8. Polarized transmission of HgI_2.
9. VASE analysis of the model fit from the a-plane HgI_2. The solid line represents the best fit and the dashed lines are the experimental VASE and transmission data. The sketch at the lower right is the surface model for the analysis.
10. VASE analysis of the model fit from the c-plane HgI_2. This c-plane sample was analyzed simultaneously with the a-plane sample shown in Fig. 9 via multi-sample VASE analysis.
11. Anisotropic dielectric functions of HgI_2 with ordinary ($\mathbf{E} \perp c$) and extraordinary ($\mathbf{E} \parallel c$) responses, respectively.
12. The Kramers-kronig (k-k) fit of the dielectric functions of HgI_2. ε_o and ε_e refer to ordinary and extraordinary responses of dielectric functions, respectively
13. Refractive indices, both ordinary ($\mathbf{E} \perp c$) and extraordinary ($\mathbf{E} \parallel c$) responses, of HgI_2.

14. Polarized absorption coefficients of HgI_2 with optical electric field vector E oriented perpendicular (E ⊥ <c>) and parallel (E ∥ <c>) to the c axis, respectively.
15. Polarized reflection coefficients of HgI_2 with optical electric field vector E oriented perpendicular (E ⊥ <c>) and parallel (E ∥ <c>) to the c axis, respectively.

LIST OF TABLES

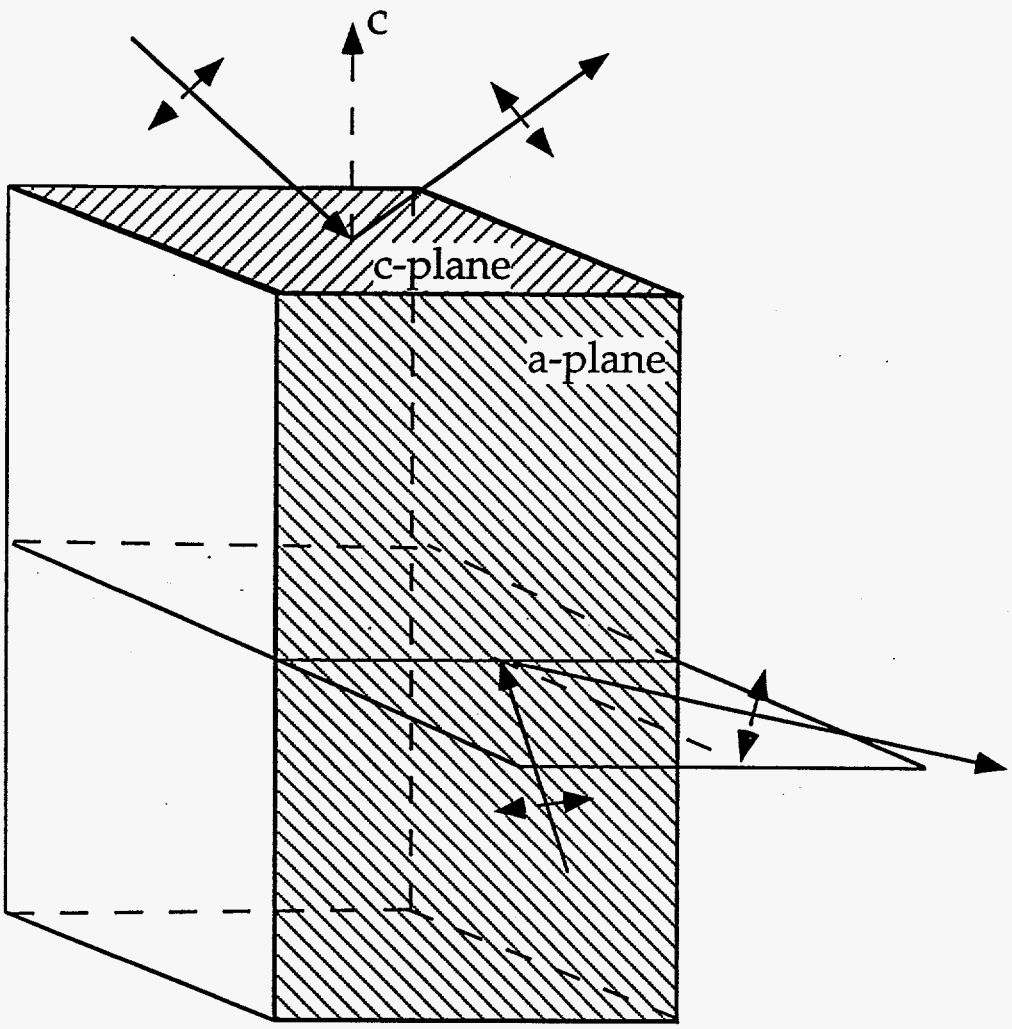

Figure 1

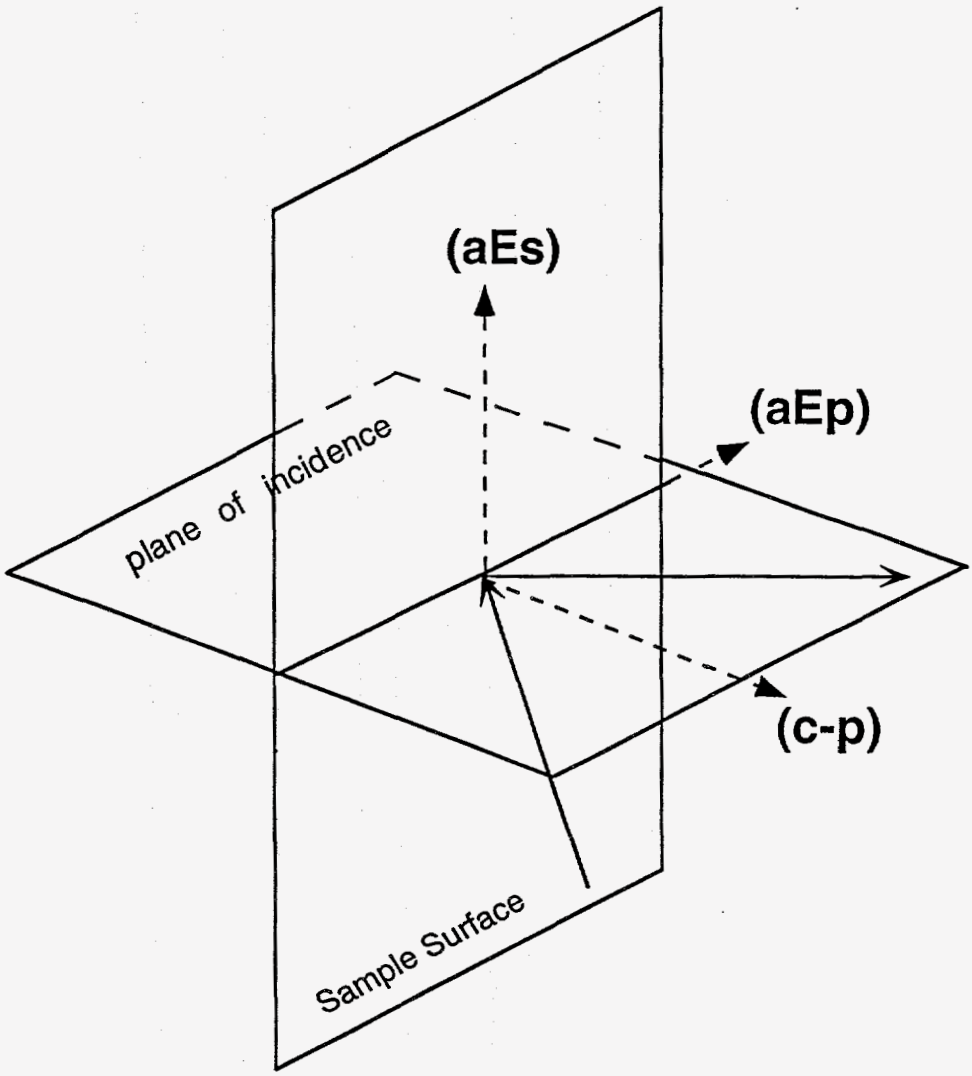

Figure 2

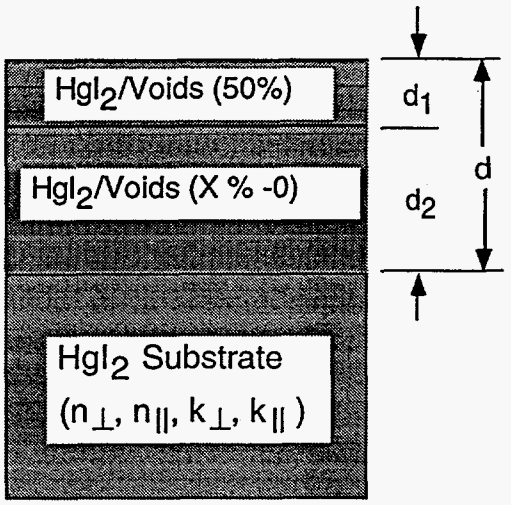
HgI_2/Voids (50%)
HgI_2/Voids (X % -0)
HgI_2 Substrate
($n_\perp$, $n_{||}$, $k_\perp$, $k_{||}$)
d_1
d_2
d

Figure 3

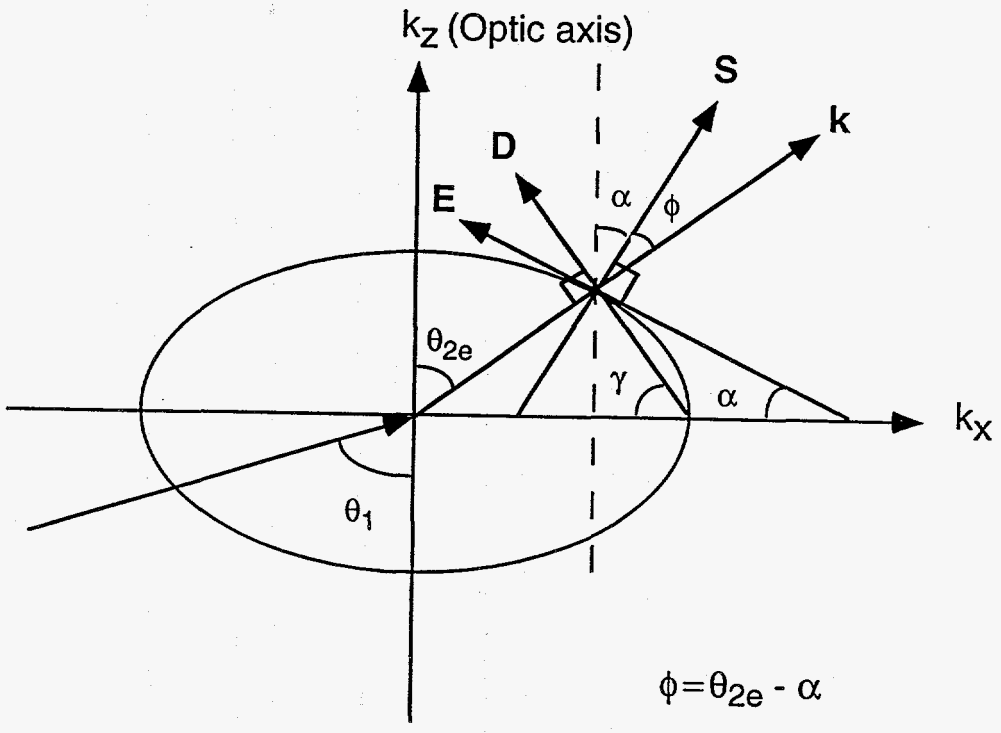

Figure 4

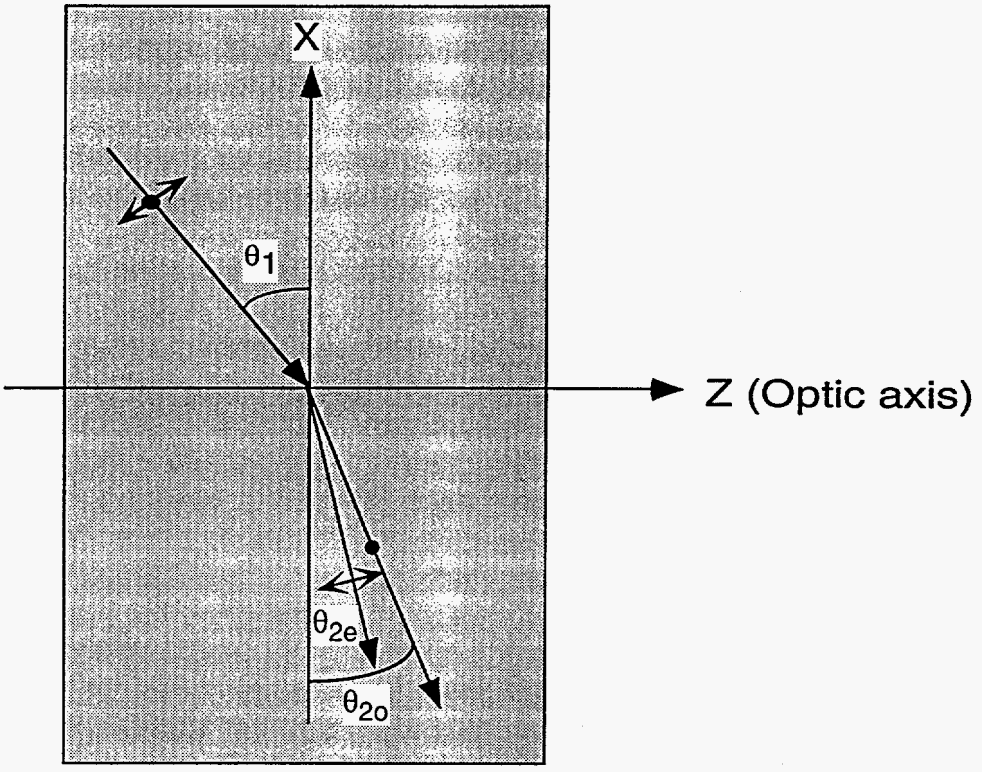

Figure 5

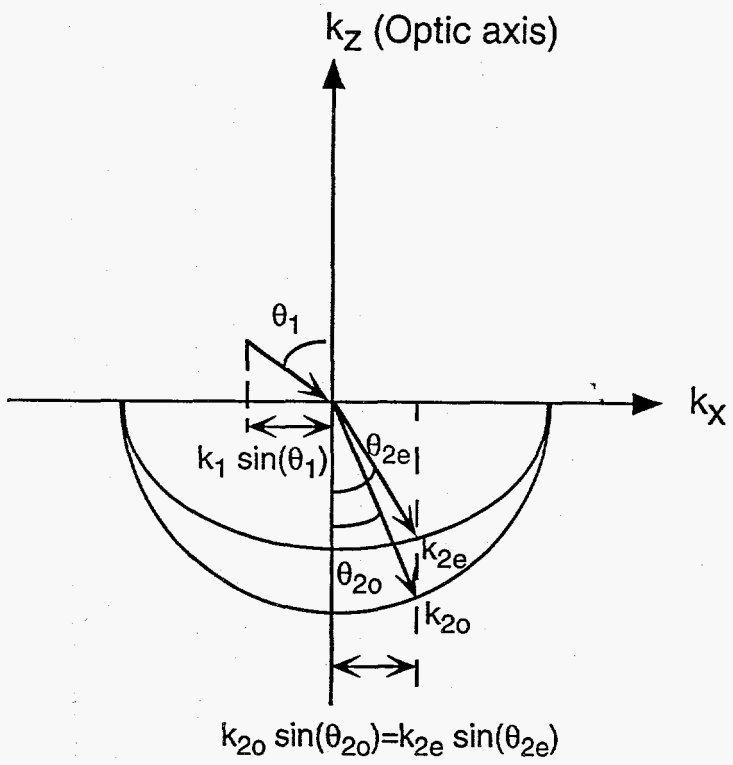
k_Z (Optic axis)
θ_1
k_X
$k_1 \sin(\theta_1)$
θ_{2e}
k_{2e}
θ_{2o}
k_{2o}
$k_{2o} \sin(\theta_{2o}) = k_{2e} \sin(\theta_{2e})$

Figure 6

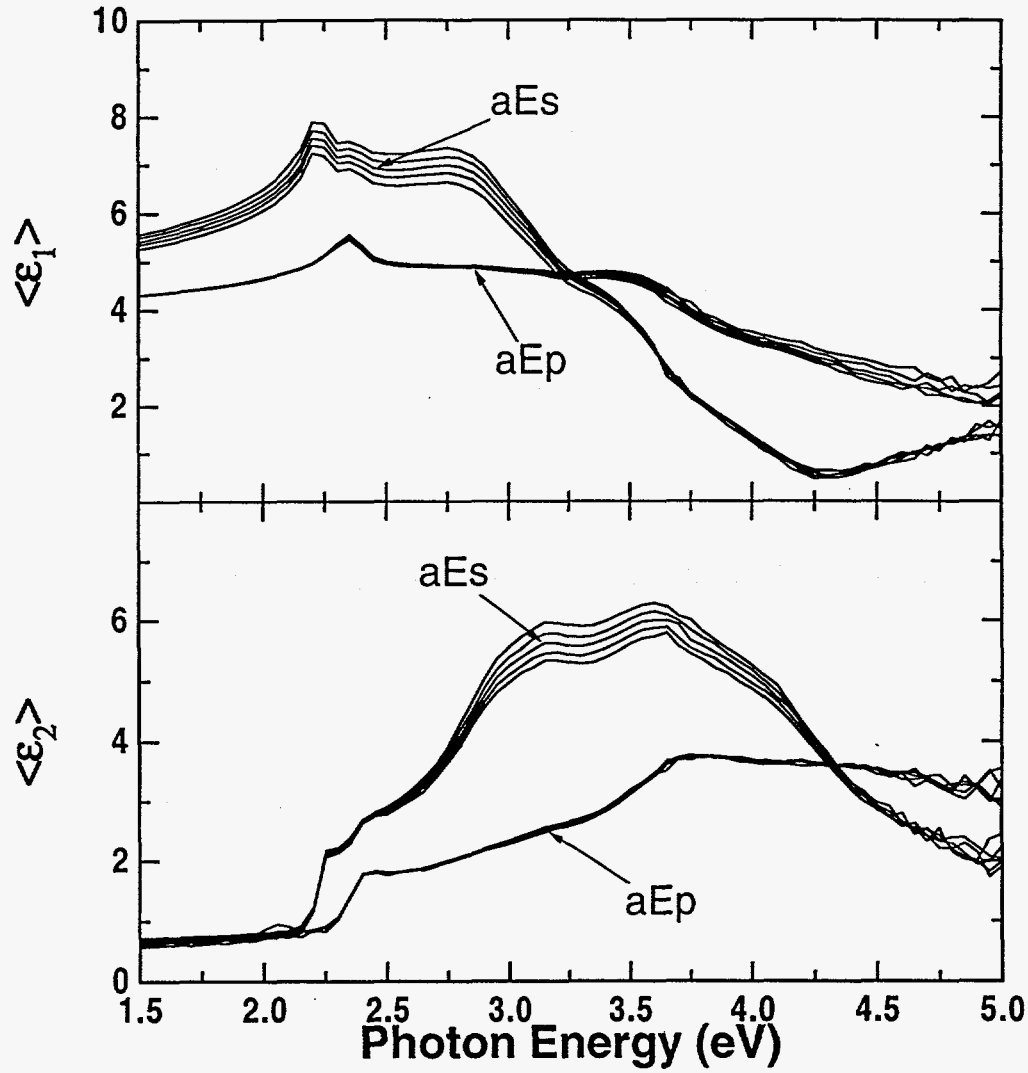
10
8
6
4
2
<ε1>
aEs
aEp
6
4
2
0
<ε2>
aEs
aEp
1.5
2.0
2.5
3.0
3.5
4.0
4.5
5.0
Photon Energy (eV)

Figure 7

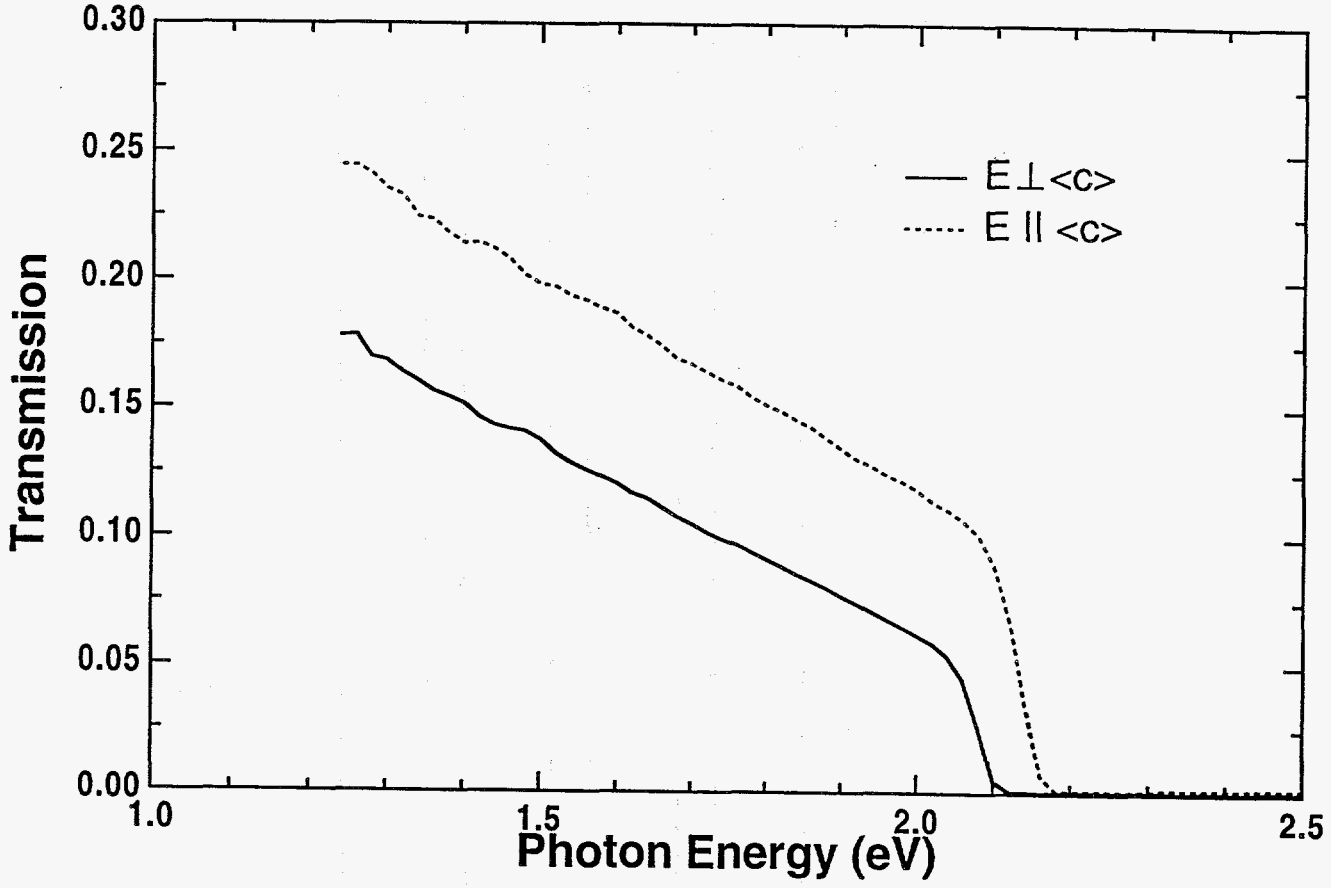
0.30
0.25
0.20
0.15
0.10
0.05
0.00
Transmission
1.0
1.5
2.0
2.5
Photon Energy (eV)
E⊥<c>
E || <c>

Figure 8

a-plane sample (N16-12):

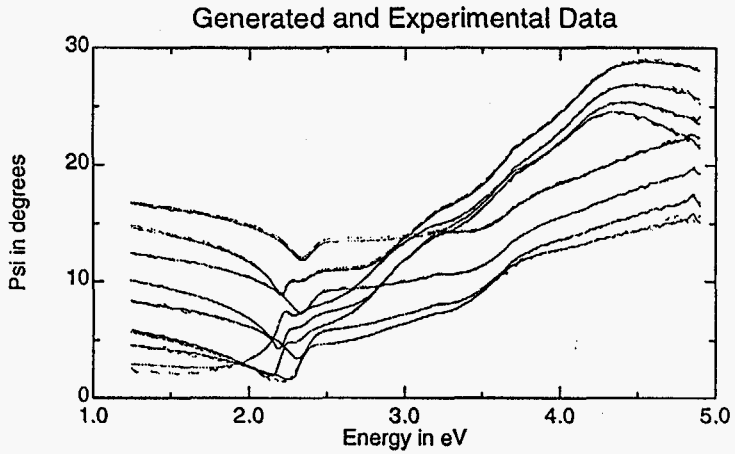

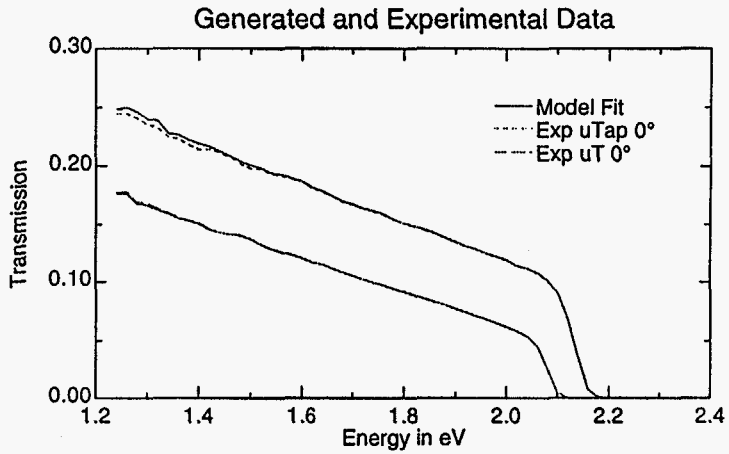

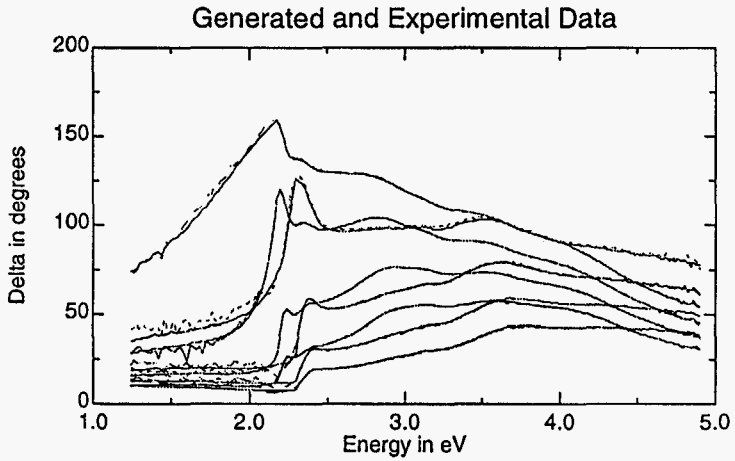

2	ema (hgi2hya)/50% void	46.53 Å
1	graded (hgi2hya)/void	1046.4 Å
0	hgi2hya	1.4 mm

c-plane sample (N15-21):

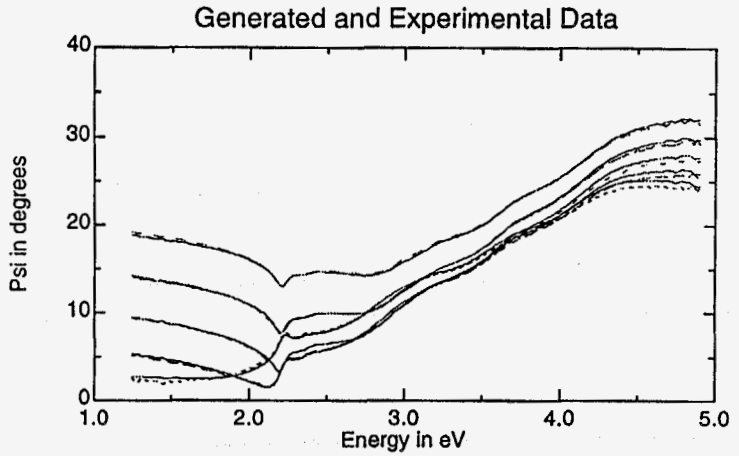

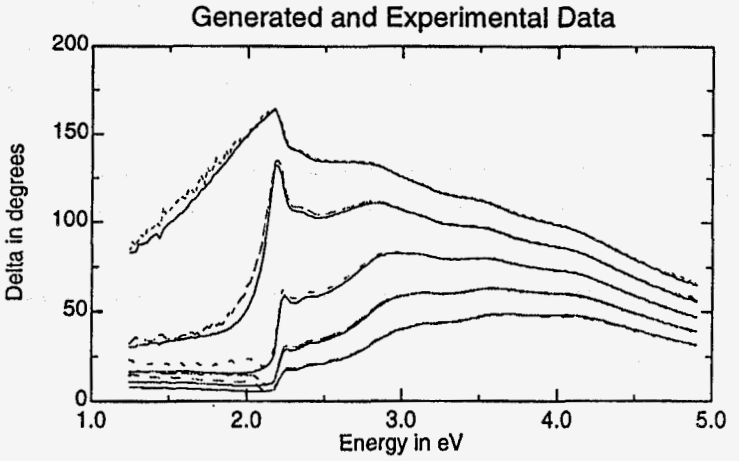

2	ema (hgi2hya)/50% void	41.283 Å
1	graded (hgi2hya)/void	1074.4 Å
0	(hgi2hya) Coupled to #0	1.138 mm

Fig. 10

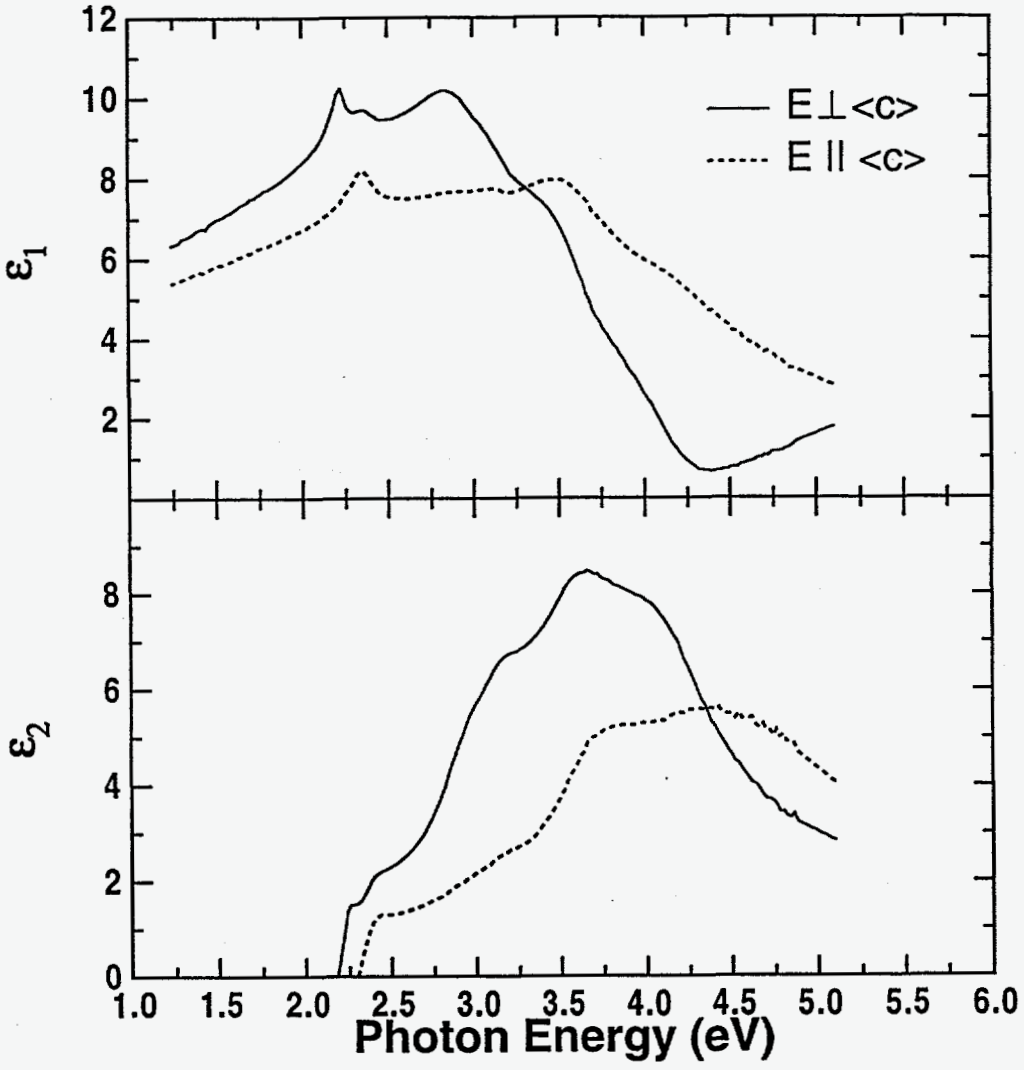
12
10
8
6
4
2
ε_1
E⊥<c>
E ∥ <c>
8
6
4
2
0
ε_2
1.0
1.5
2.0
2.5
3.0
3.5
4.0
4.5
5.0
5.5
6.0
Photon Energy (eV)

Figure 11

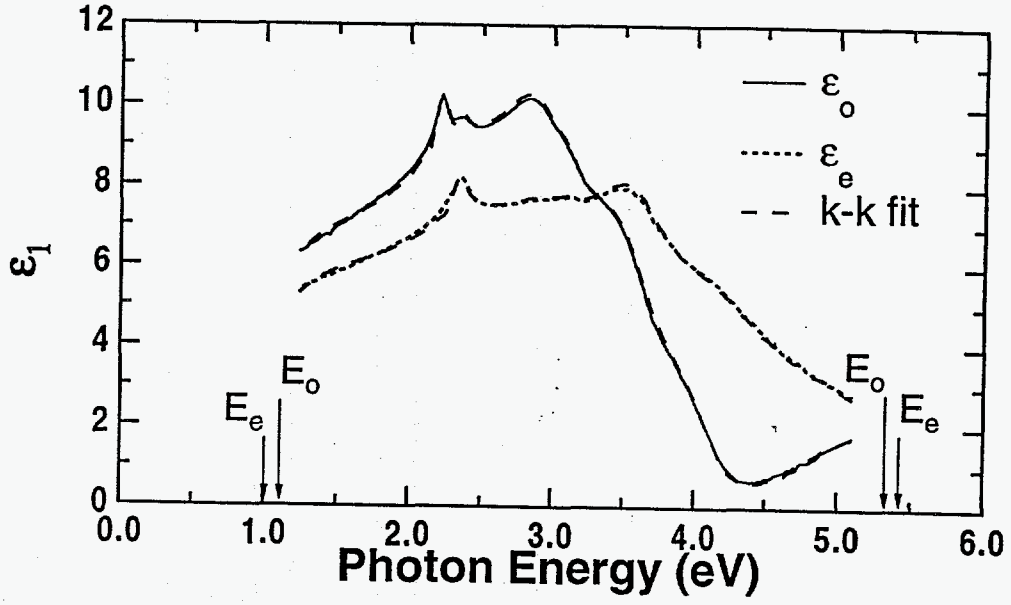
12
10
8
6
4
2
0
ε_1
0.0
1.0
2.0
3.0
4.0
5.0
6.0
Photon Energy (eV)
ε_o
ε_e
k-k fit
E_e
E_o
E_o
E_e

Figure 12

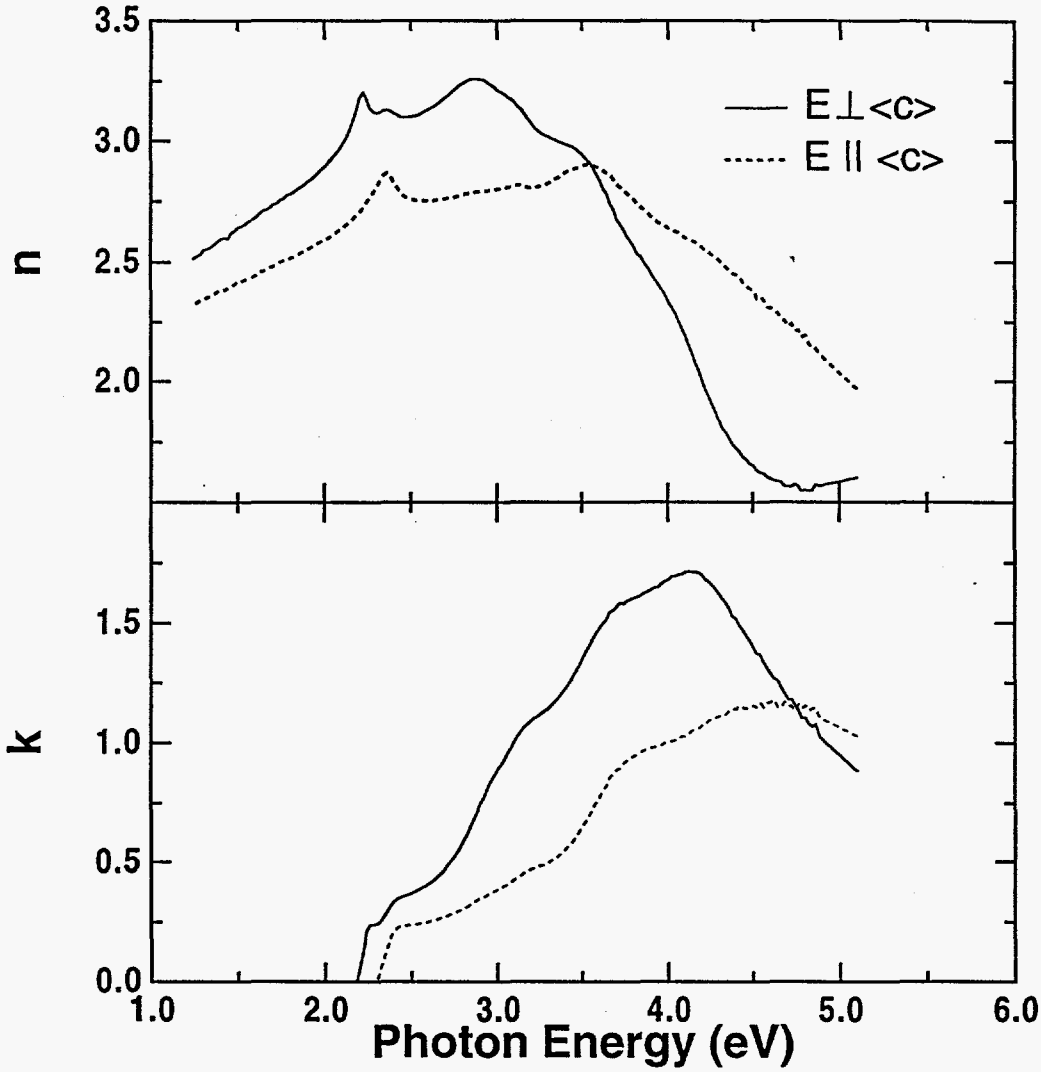

Figure 13

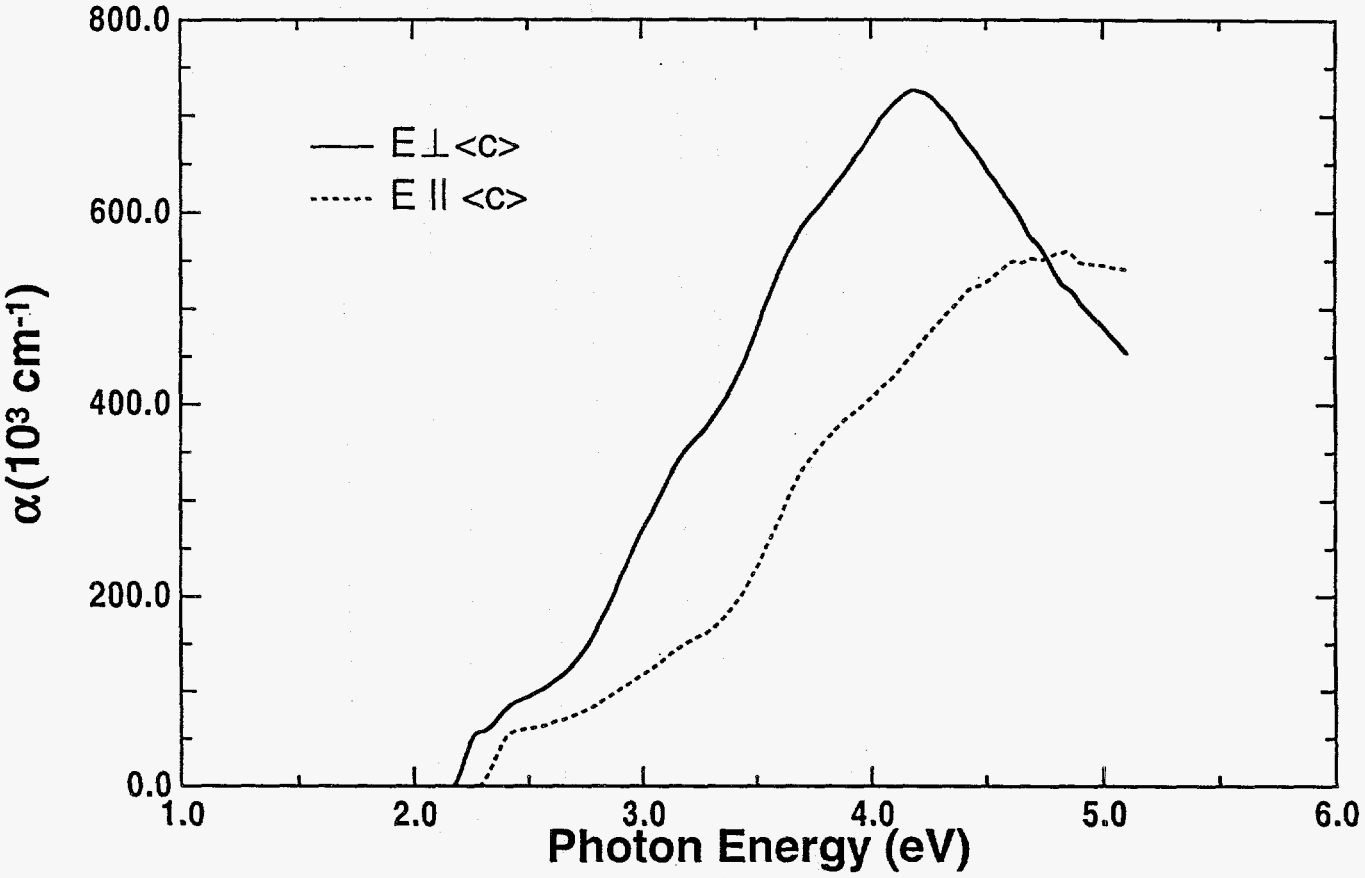
800.0
600.0
400.0
200.0
0.0
α(10³ cm⁻¹)
E⊥<c>
E || <c>
1.0
2.0
3.0
4.0
5.0
6.0
Photon Energy (eV)

Figure 14

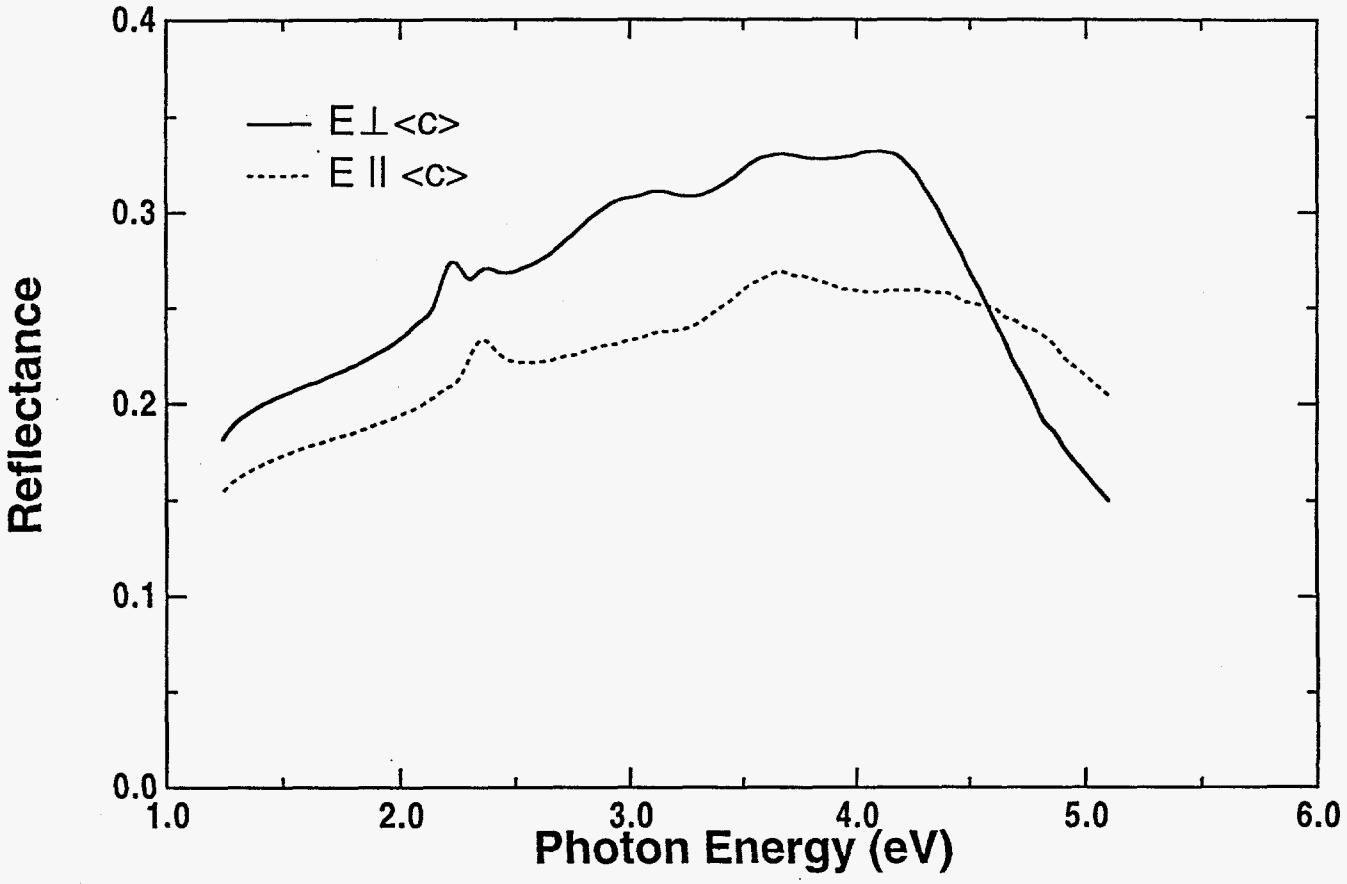
E⊥<c>
E || <c>
Reflectance
0.4
0.3
0.2
0.1
0.0
1.0
2.0
3.0
4.0
5.0
6.0
Photon Energy (eV)

Figure 15

Table I

	ε_1^{offset}	E_i (eV)	A_i
E_o	3.516	E_1=5.3228, E_2=1.1079	A_1=2.9958, A_2=0.3634
E_e	3.422	E_1=5.4225, E_2=0.9998	A_1=5.6906, A_2=0.68639

APPENDIX D

Deep Traps and Processing

Intentionally Left Blank

STUDY OF TRAPPING LEVELS IN DOPED HgI_2 RADIATION DETECTORS

H. Hermon[a], M. Schieber[a,b] and M. Roth[b]
[a] Sandia National Laboratories Org. 8347 MS 9162. Livermore, CA 94551, USA
[b] School of Applied Science, The Hebrew University of Jerusalem 91440 Jerusalem, ISRAEL

The transient charge technique, TCT, was used to measure the trapping levels of pure and doped HgI_2 detectors over the temperature range of 170K - 300K. The dopants were excess of Hg and I_2, naphthalene, butane, heavy paraffins, polyethylene and polyethylene glycol. The charge carriers were induced by α particles as well as by a U.V. nitrogen (337 nm) pulsed laser beam. The TCT determined trapping levels are compared with levels reported in literature from other solid state measurements.

1. INTRODUCTION

Charge carrier trapping, mainly of the holes, reduces significantly the charge collection efficiency of HgI_2 detectors. The main source of traps could be chemical defects e.g. non stoichiometry [1-2] and impurities [3], as well as mechanical defects mainly plastic deformations [4]. The layered structure of the HgI_2 crystal which consist of Van der Waals bonded I - I layers could facilitate the creation of these defects through the intercalation of impurities such as hydrocarbons. Large quantities of those impurities present in doped crystals could be found by changes in the unit cell of the crystal lattice [5].

It is known that the HgI_2 detectors are sensitive to impurities although some of the impurities may not be electrically active and on the contrary, could even be beneficial by strengthening mechanically the crystal. By doping with known impurities and correlating each of them to the trapping level found in the crystal, one can identify its specific contribution to the electrical properties in comparison with the best quality undoped crystal which is the subject of the present paper.

2. THE TCT METHOD

Transient charge technique (TCT) is used for the characterization of mobility μ and life time τ in mercuric iodide and is now used for measuring detrapping times and activation energies [5-9]. Other techniques have also been used to measure the activation energies of the traps in HgI_2, mainly deep level transient spectroscopy (DLTS) [10] and photoinduced current transient spectroscopy (PITS) [11] which are based on a similar mechanism as TCT, thermally stimulated currents (TSC) [12-18], photoconductivity in the IR region [16,17,19], dark currents measurements [20] and photo luminescence (PL) [21-23]. However, TCT (and DLTS) have some advantages over the other methods in that TCT detects both traps and recombination centers that is independent on the heating rate, the interpretation of TCT data is less complicated identifying traps for holes and electrons separately.

The most common ionization source used to introduce charge carriers in the crystal surface is ^{241}Am α particle source. A low energy 337nm N_2 pulsed laser was also used when poor quality crystals are tested which need higher intensity photon source for ionization. The intensity of the laser pulse was limited in order to maintain a space charge free (SCF) environment in the detector. The resulted current or voltage (depending on the electronic set-up) pulse shape obtained could easily be recorded on a digital oscilloscope.

Detrapping processes, which could be observed in HgI_2 at medium electrical fields of ~ 1000 V/cm depend much on the thermal process. Figure 1. exhibits the fast and slow component of the voltage transient, the fast component is due to trapping of charge carriers and the break point is the transient time T_R , the slow component ($t>T_R$) describes the detrapping process. It was found experimentally that $V_{(t)}$ at the average time required for a charge carrier to escape from the crystal- is 72% of the total pulse height, and this time is defined by t'. A simple regime for trapping analysis is given by

$$\tau<T_R<\tau_D \quad (1)$$

The mean time t' required for the charge carrier to be swept from the crystal is given by

$$t' = T_R(\tau+\tau_D)/\tau = T_R(1+\tau_D/\tau) \quad (2)$$

Under thermal equilibrium conditions τ and τ_D are given by:

$$\tau = (N_T V_{th} \sigma)^{-1} \quad (3)$$

$$\tau_D = (N_C V_{th} \sigma)^{-1} \exp(E_T/k_T) \quad (4)$$

And the ratio τ_D/τ is given by:

$$\tau_D/\tau = N_T/N_C \exp(E_T/k_T) \quad (5)$$

Where:

τ_D - Detrapping time
σ - Trapping cross section
N_C - Density of states in conduction band
k - Boltzman constant
τ - Trapping time
N_T - Density of trapping centers
V_{th} - Thermal velocity

After combining 2. and 5. we get

$$t'=T_R\{1+N_T/N_C \exp(E_T/k_T)\} \quad (6)$$

and

$$\ln(t'/T_R - 1) = \ln(N_T/N_C) + E_T/k_T \quad (7)$$

By measuring the temperature dependence of t', the trap activation energy E_T is obtained.

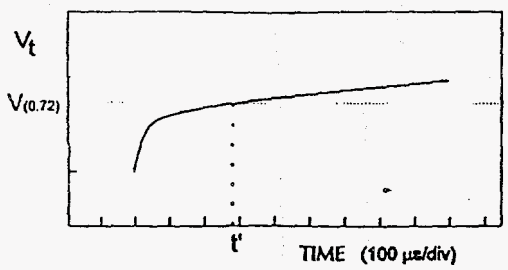

Fig. 1. Typical voltage transient measured on HgI_2 detector biased at -30V, t'=300µs

3. EXPERIMENTAL RESULTS and DISCUSSIONS

HgI_2 detectors were fabricated from vapor grown Hebrew University, (H.U.) crystals [27]. Some of the crystals were prepared from pure starting material, others were doped during growth with aromatic naphthalene up to 40 ppm, or with linear aliphatic paraffin (C_{23}) up to 180 ppm. Both dopants are characteristic of the various organic impurities found in mercuric iodide. The two other dopants used were excess of either iodine or mercury, used to check the defects induced by departure from stoichiometry. The detectors were 400 µm thick cleaved plates coated with transparent thin palladium contacts. Aquadag contacts could also be applied after drawing a fine transparent net on the HgI_2 surface.

The electronic set-up for the TCT measurements included high voltage power supply, low voltage power supply and storage oscilloscope connected to the output of the first stage of preamplification. The HgI_2 detector has been mounted in a cryostat built with feedthroughs for high voltage. When a laser source was used, an optical window was mounted on the test chamber. Fig. 2. shows TCT plots for both electrons and holes obtained from five different HgI_2 crystals tested.

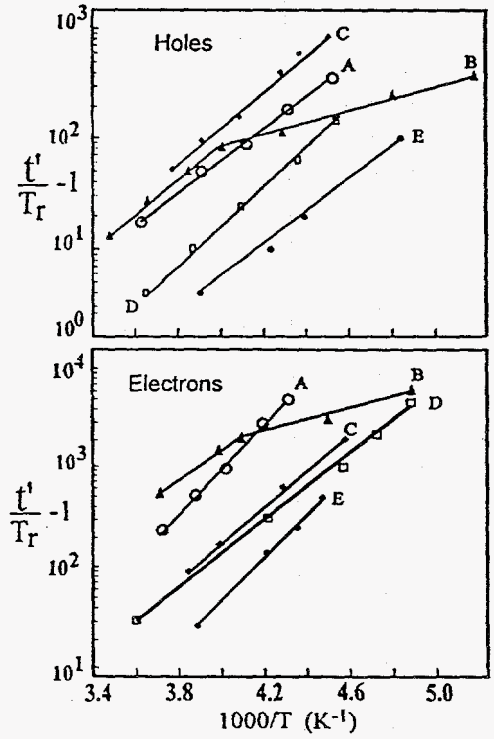

The detrapping times represented by the value t'/T_R - 1, were found to decrease with increasing temperature as expected from equation 7 and most of the points of the plot are straight lines, with the exception of sample B (mercury doped), which shows two slopes indicating two trapping levels for both electrons and holes. The appropriate trapping levels obtained from the plots are detailed in Fig. 2.

It is interesting to note that the two trapping energy levels found in the mercury doped crystal and shown in Fig. 2. are either shallow ~0.13 eV or medium ~0.40 eV. The concentration of the shallow trapping centers are in the same order of magnitude as the amount of doping introduced in the same crystal, indicating a possible large effect on the electrical properties of HgI_2 induced by the excess mercury which may be present as a Hg^+ found by Raman spectroscopy [25]. The other impurities did not show any obvious effects on the electrical properties and the only levels observed were in the 0.40-0.45 eV region levels which are common to HgI_2 crystals (see also Table 1). Therefore, it seems that the organic impurities as well as excess of iodine do not introduce new trapping levels to the crystal but it is possible that the present levels are due to a slight deviation from stoichiometry which may exist at thermal equilibrium. By comparing our with other published results [13-23] mostly not correlated with the chemical identity and concentration of the chemical impurity, one can speculate which of our added impurities may be responsible for the trapping levels mentioned in the literature. Table 1 lists the trapping levels identified by our TCT measurements and ascribed to a certain dopant from the shallow ~0.1 eV to the deepest levels mentioned in the literature of ~0.8 eV.

HgI_2 #	Dopant (ppm)	E_T (eV)	N_T (cm^{-3})
A	Naphthalene	0.51 e	$2x10^{16}$
	40	0.37 h	$1x\ 10^{16}$
B	Mercury	0.18	$5x10^{16}$
		0.41 e	$1x10^{18}$
	151	0.13,	$5x10^{18}$
		0.39 h	$1x10^{17}$
C	Paraffin	0.45 e	$6x10^{15}$
	180	0.40 h	$5x10^{15}$
D	Iodine	0.47 e	$3x10^{16}$
	55	0.42 h	$1x\ 10^{17}$
E	Pure	0.43 e	$2x10^{16}$
	-	0.46 h	$2x10^{15}$

Fig. 2. Temperature dependence of hole and electron detrapping times measured on five deferent mercuric iodide single crystals: A: naphthalene doped, B: mercury doped, C: paraffin doped, D: iodine doped and E: undoped. Activation energies (E_T) and trap densities (N_T) are listed.

Table 1. Comparison of energy levels in HgI_2 and dopants (if available) obtained from the literature.

Energy level	TCT Present work	PL [21-23]	TSC [13,22,28]	TSC [18]	TSC [12]	TSC [17]	DLTS [10]	PITS [11]
0.01-0.1		0.08 (Ag)	0.01 (Pd)			0.10-0.13 0.16-0.19	0.074	
0.1-0.2	0.13 (Hg) h 0.18 (Hg) e		0.19 (Ni)	0.16			0.15	0.19
0.2-0.3			0.20 (Au)	0.28		0.20-0.23 0.21-0.26 0.25-0.30		0.22
0.3-0.4	0.37 ($C_{10}H_8$) h 0.39 (Hg) h			0.32	0.34 0.38		0.31	0.32
0.4-0.5	0.40 (C_{23}) h 0.42 (I_2) h 0.43 (pure) e 0.45 (C_{23}) e 0.46 (pure) h 0.47 (I_2) e	0.48 (Cu) 0.49 (C)	0.48 (Ni)	0.40 0.45	0.45	0.40-0.44 0.43	0.46	0.44 0.49
0.5-0.6	0.51 ($C_{10}H_8$) e		0.54 (Pd) 0.57 (Al)	0.50 0.59	0.59	0.50-0.59		
0.6-0.7			0.61 (Al) 0.64 (Al)					
0.7-0.8					0.77		0.79	
0.8-1.0			0.92 (Ag)					

Our temperature dependent TCT measurements allowed us to probe only till ~0.5 eV and not to 0.9 reported in the literature. Analyzing the data shown in Table 1 one can see that levels attributed to specific impurities have been measured on specially doped HgI_2 crystals. The TCT identifies excess Hg, probably as Hg^+, to add a shallow level at 0.13 and 0.18 eV for holes and electrons respectively, and a similar level is found also for Ni at 0.19 eV by TSC. Naphthalene ($C_{10}H_8$) adds a shallower hole level at 0.37 and an electron level at 0.51 eV which has also been found by TSC but not identified as such. All other levels in the 0.4 to 0.5 eV found and identified by TCT and attributed to naphthalene, excess I_2 and found also in undoped HgI_2 have also been found by PL for Cu and C and by TSC for Ni.

This range of the trapping levels of 0.4 to 0.5 eV is well known and is found also by DLTS and PITS without attributing it to a specific impurity. Thus it can be concluded that doping experiments can help identify the contribution of a given impurity to the defect structure of HgI_2 and that the TCT helps also to distinguish between hole and electron trapping levels.

Since all doped crystals (especially the heavily doped>100ppm) did show a deterioration of the lifetimes of electrons and holes [2,24-27], one can speculate that most of the dopants, including inert hydrocarbons, affect the crystalline perfection and thereby degrade the nuclear spectral response of the detectors.

REFERENCES

1. M. Schieber, M. Roth and W. F. Schnepple, J. of Crystal Growth, 65 (1983) 353.
2. H. Hermon, M. Roth and M. Schieber, Nucl. Instr. and Meth. A322 (1992) 432.
3. M. Piechotka and E. Kaldis, Electrochem. Soc. 133 (1986) 200.
4 S. Steinberg, I. Kaplan, M. Schieber, C. Ortale, N Skinner and L. van den Berg, Nucl. Instr. Meth. A283 (1989) 123.
5. M. Schieber, H. Hermon and M. Roth, Mat. Res. Soc. 302 (1993) 347.
6. M. Roth, A. Burger, J. Nissenbaum and M. Schieber, IEEE Trans. Nucl. Sci. NS-34 (1987) 332.
7. G. Bartolini and A. Coche, Ed. "Semiconductors Radiation Detectors" (North Holland Amserdam, 1968).
8. M. Martini, J. W. Mayer and K. R. Zanio, in Applied Solid State Science, Ed. K. Wolf, Academic Press. NY (1972) Vol. 3.
9. J. W. Mayer, M. Nartini, K. R. Zanio and I. L. Fowler, IEEE Trans. Nucl. Sci. NS-17 (1970) 221.
10. V. Gerrish, EG&G private communication (1988).
11. F. Alvarez and J. Saura, J. Mat. Sci. 9 (1990) 569.
12. R. H. Bube, Phys. Rev. 106 (1957) 703.
13 X. J. Bao, T. E. Schlesinger, , R. B. James, A. Y. Cheng. C. Ortale and L. van den Berg, Mat. Res. Soc. Symp. Proc. 242 (1992) 767.
14. M. Schieber, I. Beinglass, G. Dishon, A. Holzer and G. Yaron, Nucl. Instr. and Methods A150 (1978) 71.
15. U. Gelbart, Y. Yacoby, I. Beinglass and A. Holzer, IEEE Trans. Nucl. Sci. NS-24 (1977) 135.
16. C. De Blasi, S. Galassni, C. Manfredotti, G. Micocci, L. Rogiero and A. Tepore, Nucl. Inst. Methods, A150 (1978) 103.
17. T. Mohammed-Brahim, A. Friant and J. Mellet, Phys. Stat. Sol. A79 (1983) 71.
18. A. Tadjin, D. Gosselin, J. M. Koebel and P. Siffert, Nucl. Instr. Meth. A213 (1983) 77.
19. J. L. Merz, Z. L. Wu, L. van den Berg and W. F. Schnepple, Nucl. Instr. and Methods A213 (1983) 51.
20. J. Nissenbaum, I. Shilo, A. Burger, A. Levy, M. Schieber, L. Keller and C. N. J. Wagner, Nucl. Inst. Methods, A213 (1983) 27.
21. X. J. Bao, T. E. Schlesinger, R. B. James, J. Markakis, A. Y. Cheng. C. Ortale, J. App. Phys. 66 (1989) 2578.
22. T. E. Schlesinger, X. J. Bao, R. B. James, A. Y. Cheng. C. Ortale and L. van den Berg, Nucl. Inst. Methods, A322 (1992) 414.
23. R. B. James, X. J. Bao, T. E. Schlesinger, C. Ortale, A. Y. Cheng. J. App. Phys. 67 (1990) 2571.
24. H. Hermon, M. Roth, J. Nissenbaum, M. Schieber and J. Shamir, J. Crystal Growth 109 (1991) 376.
25. H. Hermon, M. Roth, M. Schieber, and J. Shamir, Vibrational Spect. 2 (1991) 155.
26. H. Hermon, M. Schieber, M. Roth and J. Shamir. Analytica Chimica Acta. 259 (1992) 181.
27. H. Hermon, M. Roth and M. Schieber, Nucl. Instr. and Meth. A322 (1992) 442.
28. J. M. Van Scyoc, T. E. Schlesinger, R. B. James, A. Y. Cheng. C. Ortale, and L. Van den Berg, Mat. Res. Soc. Symp. Proc. 302 (1993) 115.
29. X. J. Bao, Ph.D. thesis, Carnegie Mellon University (1993).

PHOTOLUMINESCENCE STUDIES OF IMPURITIES AND DEFECTS IN MERCURIC IODIDE

X.J. BAO*,T.E. SCHLESINGER*,R.B. JAMES**,A.Y. CHENG*** AND C. ORTALE***
*Carnegie Mellon University, Department of Electrical and Computer Engineering, Pittsburgh, PA 15213
**Sandia National Laboratories, Advanced Materials Division, Livermore, CA 94450
***EG&G Energy Measurements, Inc., Goleta, CA 93116

ABSTRACT

We have studied the effects of chemical etching in potassium iodide(KI) aqueous solution, vacuum exposure and bulk heating on the photoluminescence(PL) spectra of mercuric iodide(HgI_2). Different contact materials deposited onto HgI_2 were also investigated, such as Pd, Cu, Al, Ni, Sn, In, Ag and Ta. These processing steps and the choice of a suitable electrode material are very important in the manufacturing of high-quality mercuric iodide nuclear detectors. Comparisons are made between the front surface photoluminescence and transmission photoluminescence spectra.

INTRODUCTION

Mercuric iodide has gained increasing attention because it can be used to fabricate high efficiency nuclear detectors operated at ambient temperature, as compared with conventional Si(Li) and Ge(Li) nuclear detectors that have to be kept cool at all times[1]. However, defects that are introduced during detector fabrication as well as due to the interaction of the contact material with the HgI_2 severely limit the manufacturing yield of high quality HgI_2 nuclear detectors[2]. Characterization of the processing steps and various contact materials can provide guidance in the optimization of fabrication processes and the proper choice of a contact material.

RESULTS AND DISCUSSIONS

HgI_2 has a bandgap of 2.4eV at 4.2K and produces strong PL at low temperatures. Many workers[3-6] have studied HgI_2 by PL measurement. In this work, an Argon-ion laser tuned to 4880Åwas used as an excitation source in the PL measurement. Several processing steps were separately studied by PL. These steps include KI etch, vacuum exposure and bulk heating. The effect of KI etching is shown in Fig.1. It can be seen that KI etch effectively exposes a fresh surface that is quite different from the "degraded" surface before the etch. This "degraded" surface can be formed within a day for samples stored in a dessicator. Since the PL spectra taken from a degraded surface resemble those taken from freshly etched samples that are relatively iodine poor (see Fig.2), the degradation was attributed to iodine loss due to sublimation and/or interaction of the HgI_2 with air. The effect of vacuum exposure was similar to KI etch in that it removes a layer of material from the surface. Instead of inducing a preferential loss of iodine or mercury, the vacuum does not produce a significant deviation of stoichiometry as measured with a PL technique. Bulk heating to 100^0C in a helium ambient for 10 to 60 minutes was found to decrease P2 to P3 and band 2 to P3 ratios. These changes were attributed to the creation of native defects at elevated temperatures. In Fig.2, P2 to P3 and band 2 to P2 ratios for nine different samples are plotted as a function of their color number. The color numbers come from the visual observation of the redness of the vapor in each ampoule during crystal growth, and it is qualitatively related to the abundance of iodine in the vapor. A larger color number is assumed to represent a larger iodine content in the crystal. It then appears that large P2 to P3 ratios can be roughly

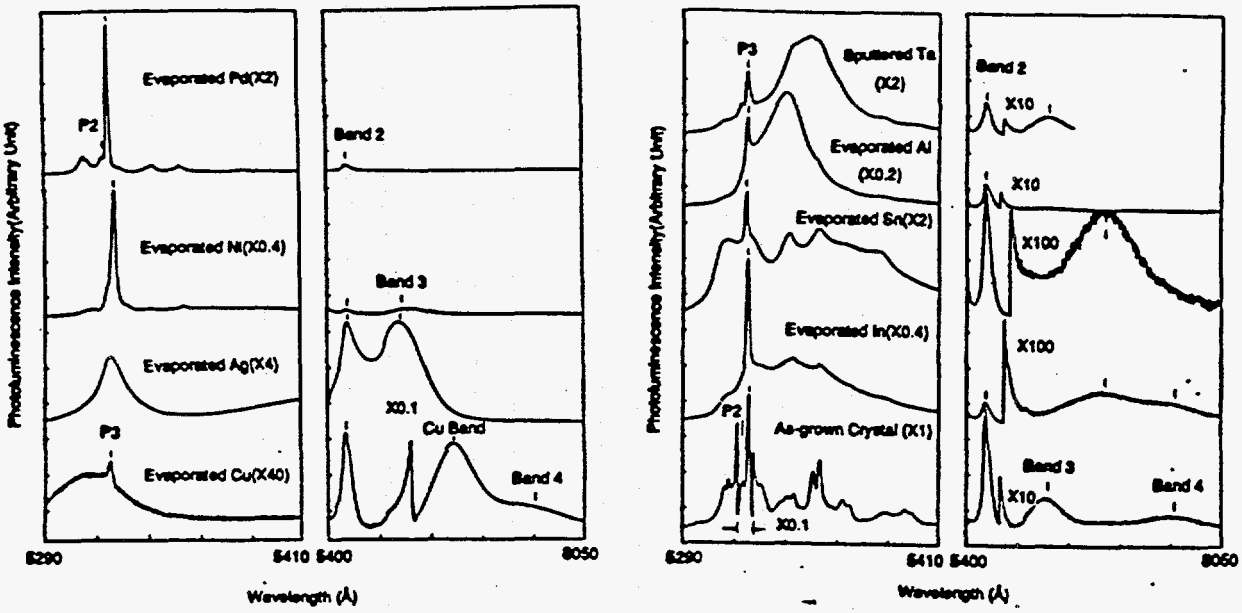

Figure 3: PL spectra taken from an as-grown HgI_2 crystal and from various semitransparent metal contacts deposited on HgI_2 substrates.

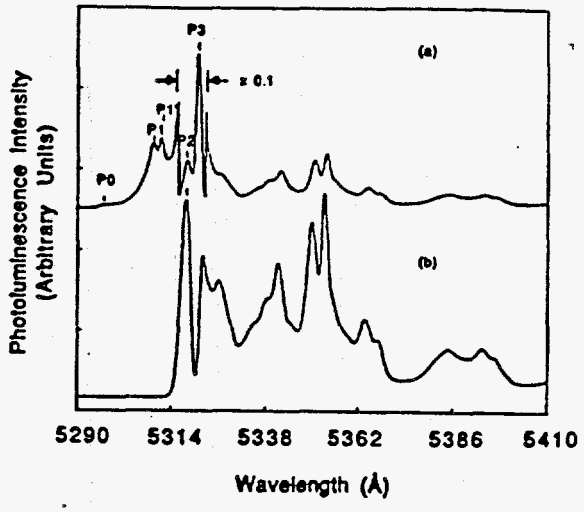

Figure 4: 4.2K PL spectra obtained in (a)reflection and (b)transmission mode.

suppress the overall band 1 emission considerably. Ag introduces a new broad band at about 5500Å. This band often appears as a shoulder on the shorter wavelength side of band 2. Cu contacts generate a very strong new band at about 6720Å, which we have labeled as the Cu band. From a back-doping experiment, it was found that Cu was a fast diffuser in bulk HgI_2. Nuclear detectors with Cu electrodes were tested and the performance indicated that Cu is unacceptable as a contact material for detector applications[4]. This is not surprising given the changes in PL spectra caused by Cu deposition. Ni induces little change in the PL spectra, except it may have slightly broadened P3. Ni-contacted nuclear detectors have yet to be tested. Pd contact is the "best" among these metals in that it produces the least changes in the PL spectra. In addition it is the most used contact material in the manufacture of nuclear detectors; although, problems related to Pd contacts do exist.

Fig.4 shows two PL spectra taken in two different configurations. Spectrum(a) was taken in the conventional way, as all of the other PL spectra shown above. Spectrum(b) was taken in a transmission configuration.

P2 and P3 have both been assigned as bound excitons by many workers[5,6]. From the

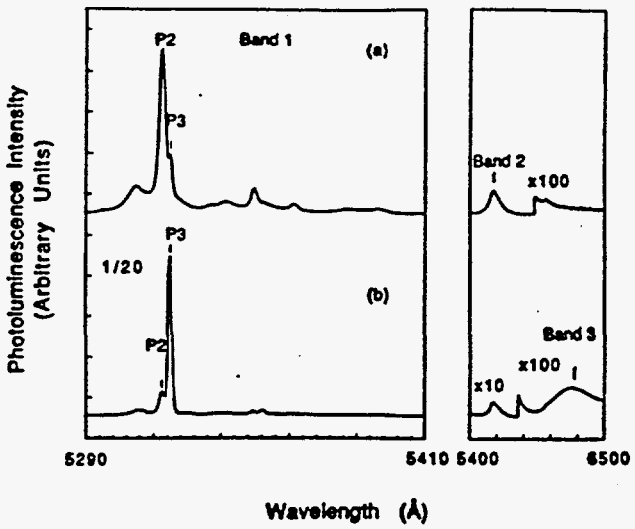

Figure 1: 4.2K PL spectra taken (a)before and (b)immediately after a 10% KI etch for about 3 minutes. The sample had been stored in a dessicator for 30 days prior to this experiment. P2 to P3 and band 2 to P3 ratios were decreased after KI etch primarily due to the increase of the absolute intensity of P3.

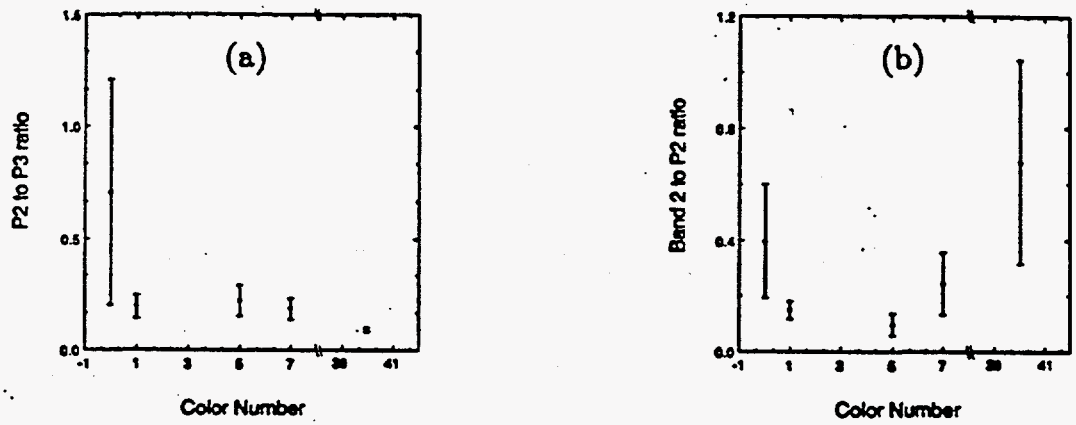

Figure 2: (a) P2 to P3 ratio and (b) Band 2 to P2 ratio as a function of color number for nine samples. All PL spectra were taken immediately after a KI treatment to expose a fresh surface. A larger color number is assumed to represent a larger iodine content. The P2 to P3 ratio is then related to the relative stoichiometry of the crystal.

correlated to an iodine deficiency in the crystal. The band 2 to P2 ratio clearly shows a U-shape with a minimum at 3 to 5.

Various contact materials were studied by depositing a semitransparent layer of the material onto HgI_2. PL spectra were then taken from the contacted area and compared with PL spectra taken from the as-grown crystal. The PL spectra from samples with semitransparent Pd, Cu, Al, Ni, Sn, In, Ag and Ta contacts as well as from an as-grown crystal are shown in Fig.3.

It is clear that almost every metal introduces some distinct feature in the PL spectra. As-grown crystals usually have a well-resolved band 1 in the near-bandgap photoluminescence (between 5290 and 5410Å), which we found consisted of at least 26 emission lines. At longer wavelengths there are three other broad bands labeled as band 2(5595Å), band 3(6200Å) and band 4(7550Å). In and Sn contacts introduce a similar broad band superimposed on band 1 and another broad band centered at about 6820Å. The broad band around band 1 was found to be detrimental to HgI_2 photodetectors with indium-tin-oxide(ITO) transparent contacts[3]. Al and Ta contacts introduce two different bands centered at about 5340 and 5350Å, respectively in the band 1 region. Ag and Cu metals

transmission spectrum, it is clear that P3 was almost completely re-absorbed and there is a deep valley at the wavelength position where P3 usually is observed in a reflection spectrum. On the other hand, P2 appeared as a well-resolved peak indicating a much smaller re-absorption than P3. The large absorption of P3 is readily explained if P3 is an exciton from a direct bandgap bound to an impurity. Since phonon participation is not required to conserve the crystal momentum in creating such an exciton, the emission from the radiative annihilation of this exciton can be re-absorbed. P2 must then be of a different origin. One possibility is that P2 is a phonon replica due to another line at a shorter wavelength. But no such line has been found. Another possibility is that P2 is due to an exciton from an indirect bandgap bound to an impurity. Since phonon participation is needed to conserve the crystal momentum for an indirect bandgap, the emission from the annihilation of such an exciton can not be re-absorbed. As a matter of fact, in the ordinary absorption spectra of HgI_2, continuous absorption was observed[5,7], which is characteristic of an indirect bandgap material. However in the extraordinary absorption spectra, sharp resonant absorption lines were observed[5,7], which are characteristic of a direct bandgap material. Therefore, we postulate that HgI_2 may have two conduction band minima that are very close in energy with one directly above and the other indirectly above the valence band maximum.

CONCLUSIONS

In conclusion, we found that processing steps can modify the defect structure of HgI_2 crystals. A degraded surface can be developed as quickly as one day, which can be removed by either KI etch or vacuum exposure. Heating to 100^0C appears to modify the concentration of native defects in the bulk. Different contact materials introduce distinct features in the PL spectra, which can be correlated to their capability as an electrode material for detector applications. The spectra also provide useful insights as to the nature of the interaction between the contact materials and HgI_2. Some of these features can be used as signatures to identify the existence of the corresponding metal as a dopant in HgI_2. Comparison between reflection and transmission PL spectra allows us postulate that HgI_2 may have two conduction band minima that are very close in energy.

The authors acknowledge the support of the U.S. Department of Energy for this work.

REFERENCES

1. M. Schieber, Nucl. Instr. Meth. 213, 1 (1983).

2. A. Holzer and M. Schieber, IEEE Trans. Nucl. Sci. NS-27, 266 (1980).

3. R.B. James, X.J. Bao, T.E. Schlesinger, J.M. Markakis, A.Y. Cheng and C. Ortale, J. Appl. Phys. 66, 2578 (1989).

4. X.J. Bao, T.E. Schlesinger, R.B. James, R.H. Stulen, C. Ortale, L. van den Berg, to be published.

5. B.V. Novikov and M.M. Pimonenko, Sov. Phys. Semicond. 4, 1785 (1971).

6. J.L. Merz, Z.L. Wu, L. van den Berg and W.F. Schnepple, Nucl. Instr. Meth. 213, 51 (1983).

7. I. Akopyan, B. Novikov, S. Permogorov, A. Selkin and V. Travnikov, Phys. Stat. Sol.(b) 70, 353 (1975).

INVESTIGATION OF DEEP LEVEL DEFECTS IN MERCURIC IODIDE BY THERMALLY STIMULATED CURRENT SPECTROSCOPY

X.J. BAO*, T.E. SCHLESINGER*, R.B. JAMES**, A.Y. CHENG***, C. ORTALE*** AND L. VAN DEN BERG***

*Carnegie Mellon University, Department of Electrical and Computer Engineering, Pittsburgh, PA 15213

**Sandia National Laboratories, Advanced Materials Division, Livermore, CA 94450

***EG&G Energy Measurements, Inc., Goleta, CA 93116

ABSTRACT

Mercuric iodide (HgI_2) single crystals deposited with semitransparent Pd, Al and Ag contacts were studied by thermally stimulated current spectroscopy (TSC). Distinct differences were found among spectra obtained from samples with different metal contacts, indicating that interactions between the metal contacts and mercuric iodide substrates have strong effects on the deep defect levels in mercuric iodide. The activation energies of some of these defect levels were estimated by taking TSC spectra with different heating rates. In addition, a pyroelectric effect was observed in Ag-contacted samples by thermally stimulated depolarization current technique (TSDC). The implications of these results in device applications of mercuric iodide are discussed.

INTRODUCTION

Mercuric iodide is an important semiconducting material for the fabrication of room temperature X-ray and γ-ray detectors[1-5]. Compared with conventional semiconductor nu-

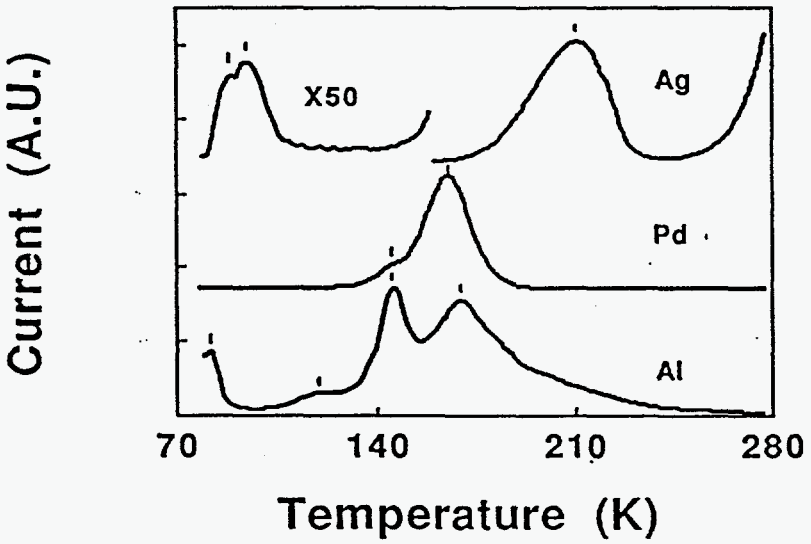

Figure 1: TSC spectra taken from samples contacted with semitransparent Ag, Pd, and Al metal layers. The spectra were scaled and displaced along the y-axis for comparison. TSC peaks are marked by the vertical bars.

clear detectors such as Si(Li), Ge(Li) and high purity Ge detectors, HgI_2 has the advantages of a larger bandgap (2.14eV at room temperature) and higher atomic numbers (80 and 53 for Hg and I, respectively). The wide bandgap results in a small dark current, which allows the device to be operated at room temperature. With the efficiency of the photoelectric

effect proportional to the fifth power of the atomic number, HgI_2 also has a higher stopping power for energetic photons and thus a higher detection efficiency. The ability to operate nuclear detectors at ambient temperature without the clumsiness of bulky cooling systems can greatly enhance the development of miniature nuclear detectors[2], X-ray imaging systems[3], and nuclear detection in space[4]. At present, HgI_2 nuclear spectrometers for X-ray detection have resolutions comparable to those of Si or Ge devices[5]. However, the manufacturing yield of high-performance HgI_2 detectors remains relatively low (about 20%)[6]. Defects introduced during crystal growth, device fabrication, and aging can all contribute to this low yield.

The choice of conducting electrodes is crucial in determining the quality of detectors. Pd and colloidal carbon have been empirically found to yield the best results, although reproducibility is still poor. Other metals such as Cu and Ag were found to be completely unacceptable[7,8]. Thus, understanding defects incorporated during the contact formation is important in optimization of the contact deposition process and also in searching for new contact materials. Previous low temperature photoluminescence (PL) measurements have shown that considerable changes can occur in the interfacial region between contact metals and HgI_2 substrates[7-9]. In this study, TSC is used to characterize Pd, Ag and Al contacts on HgI_2. Different defect structures were clearly observed for each of these contact materials.

RESULTS AND DISCUSSIONS

The HgI_2 samples used in this study were obtained from EG&G Energy Measurements, Inc. They were 1cmx1cm slices with thickness between 0.02 to 0.05cm. Each sample was chemically etched with 10% (by weight) KI aqueous solution prior to the contact deposition. A circular contact layer was thermally evaporated in a vacuum system with a pressure of

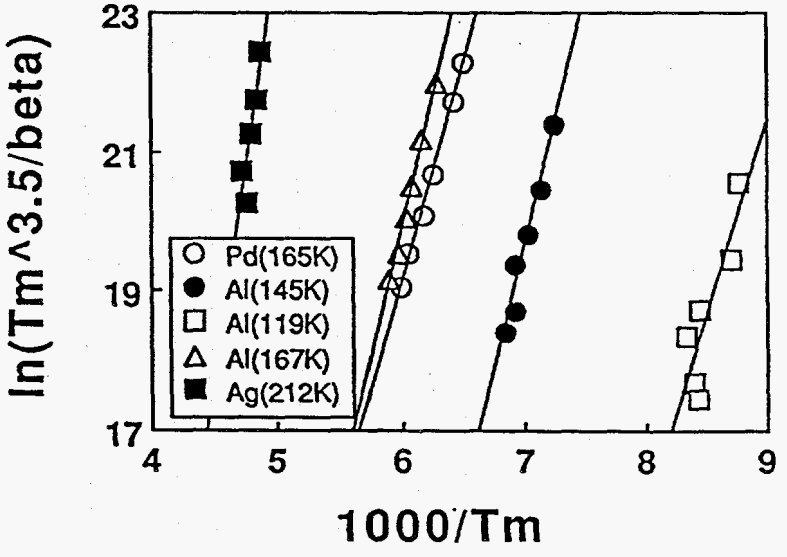

Figure 2: Arrehenius plots used to obtain trap activation energies. The temperatures in parenthesis in the legend refer to the average temperature of the traps, as tabulated in Table I.

about 10^{-6} Torr onto one side of the substrate using a shadow mask with a diameter of about 0.3cm. The contact has a transparency of about 50% in the visible light region as measured from a glass slide placed near the sample during contact deposition. Semitransparent contacts were necessary to make the TSC measurement. The sample was then mounted onto an alumina substrate with the semitransparent electrode facing up and using colloidal carbon

as the back contact. The TSC measurements were performed between 78K and 278K. The sample was first cooled to 78K in the dark and then illuminated through the semitransparent contact for 5 minutes with a 20mW argon laser beam (4880Å line). Current was then measured as a function of temperature as the sample was heated up and kept in the dark. A dc bias of 12V was applied to the sample all the time. To measure the activation energies of the traps, several TSC spectra were taken with different heating rates. If T_m is the temperature at which a current peak occurs, and $\beta(T_m)$ is the heating rate at temperature T_m, then the activation energy ΔE of the trap can be estimated from the slope of the plot of $\ln(\frac{T_m^{3.5}}{\beta(T_m)})$ vs. $1/kT_m$[9].

Table 1: TSC results for samples S8-21-5:Ag, V8-4-5:Pd, and N11-8-2:Al.

S8-21-5:Ag	1	2	3	4	5	6	7
T_m (K)		90	96				212
$\beta(T_m)$ (K/s)		0.27	0.39		-		0.14
ΔE (eV)							0.92
V8-4-5:Pd							
T_m (K)					146	165	
$\beta(T_m)$ (K/s)					0.23	0.19	
ΔE (eV)						0.54	
N11-8-2:Al							
T_m (K)	83			119	145	167	
$\beta(T_m)$ (K/s)	0.24			0.48	0.27	0.20	
ΔE (eV)				0.57	0.61	0.64	

Figure 1 shows three TSC spectra obtained from samples with semitransparent contacts of Ag, Pd, and Al. The Arrehenius plots used to obtain the trap activation energies are shown in Figure 2. The average TSC peak positions, the corresponding heating rates, and activation energies are tabulated in Table I.

From Figure 1, it is clear that all three spectra show distinctly different features. The TSC spectrum from the Pd sample has only two traps at temperatures of 145K and 165K. The Ag sample has three unique traps at temperatures of 90K, 96K and 212K. Also noticeable is the rapid increase of dark current as the temperature is increased. For the Al sample, there are four traps, two of them are at temperatures of 146K and 167K and are very similar to the two traps in the Pd sample, except that the peak at 145K is much more well resolved and the peak at 167K seems to be sitting on top of another peak (this may also be part of the reason why the activation energies for this trap differ so much as compared to the Pd samples). The other two traps are at 83K and 119K.

TSC measurements on HgI_2 have been performed by a number of researchers to investigate the correlations between TSC peaks and stoichiometry, aging, mechanical damage and detector performance[10-13]. In Ref. 10, three peaks at 81K, 89K, and 220K were related to iodine deficiency and one peak at 214K was related to mercury deficiency. Two peaks at 114K and 145K were believed to be cleavage-induced. One peak at 170K has been related to both good and poor detector performance by different authors[12,13]. From these results, we tentatively assign the peak at 83K from the Al sample and the peak at 90K from the Ag sample as due to iodine deficiency. The peak at 212K for the Ag sample may be either related to iodine deficiency or an impurity level. The two peaks at 119K and 146K from the Al sample may be due to native defects that are related to damage introduced by the

interaction of the Al contact with HgI_2 substrate. The peak at 165K appears to be not detrimental to device performance as it is the dominant peak in the sample contacted with Pd, which to date is the most commonly used contact material for HgI_2 detectors.

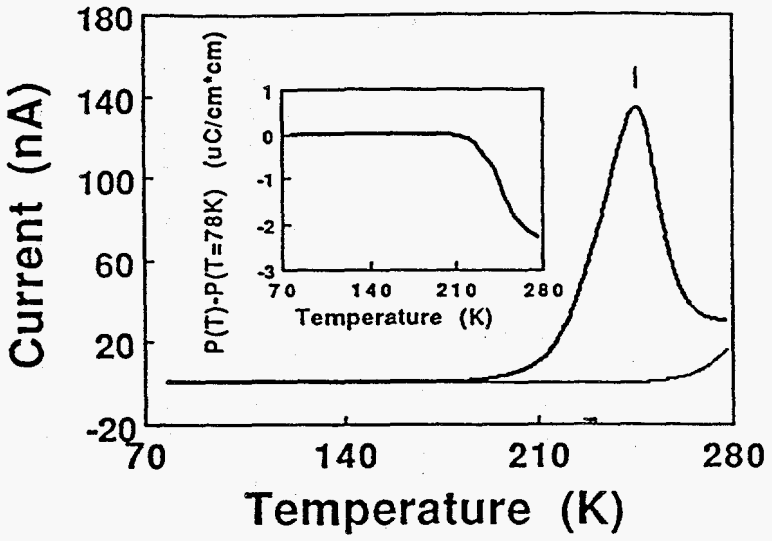

Figure 3: Thick line: TSDC spectrum from an Ag-contacted sample. Narrow line: dark current. The sample was biased with 12V during the measurement. The inset shows the polarization as a function of temperature.

These TSC results fit very well with previous PL measurements and calibration of detector performance[7-9,14,15]. Iodine deficiency has been found to be related to poor detector quality[14]. Cleaving was also believed to be detrimental to device quality if used in device fabrication, because HgI_2 is a soft material and mechanical damage can be easily introduced. Thus, both Al and Ag contacted devices probably will not be of high quality due to stoichiometry deviations near the interfacial region between the contacts and substrates. Indeed, Ag has been found not suitable as a contact material for HgI_2 nuclear detectors[8]. Al-contacted devices have yet to be tested. Furthermore, from PL measurements, Ag was found to diffuse fairly rapidly even at room temperature and to introduce a new radiative recombination center at a wavelength of about 5490Å[8]. Also, Ag has some doping effect as can be seen from Figure 1, by the increase in the dark current and therefore leakage current in detectors. On the other hand, PL spectra from Al samples show a broad radiative recombination center peaked at about 5340Å[15]. Similar broad bands have been observed from other samples that were deposited with Ta, In or Sn, even though they may be centered at slightly different wavelengths[15]. It is reasonable to believe that these bands may not be related directly to the impurities, but instead, are introduced indirectly due to the interaction between the metal and HgI_2. This will explain both the similarity in PL spectra from Al, Ta, In and Sn samples and the appearances of the two damage-related peaks at 119K and 145K in the TSC spectrum from the Al sample.

During the course of this study, we used TSDC to characterize a pyroelectric effect in Ag-contacted samples. TSDC has been extensively used to characterize pyroelectric and ferroelectric materials[16-18]. The measurements were performed as follows. The sample was kept in the dark all the time. First it was heated up to 278K, and a bias of 12V was applied prior to cooling the sample from 278K to 78K. Then, either the bias was reversed (as in Figure 3) or a short circuit (zero bias) was used (as in Figure 4). The sample was then heated up again and the current was measured by an electrometer as a function of temperature. Because of the pyroelectric effect, the polarization of the sample would change

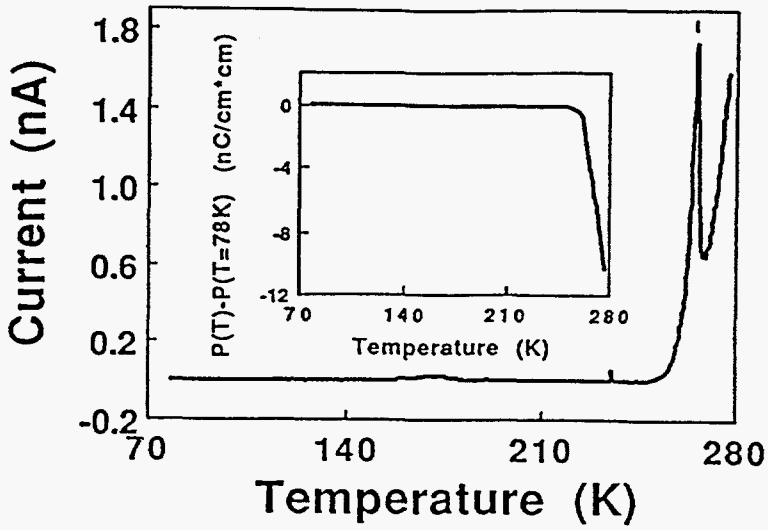

Figure 4: TSDC spectrum from an Ag-contacted sample. The sample was not biased during the measurement. The inset shows the polarization as a function of temperature.

as the temperature was increased. The change in polarization in turn would result in a change of polarization charge on the surface of the sample normal to the contacts (the sample can be treated as a dielectric material in a parallel plate capacitor). Since the voltage across the sample(capacitor) was fixed (either 12 or 0V), a current has to flow to neutralize the change of charge in the capacitor caused by the pyroelectric effect.

Figure 3 (a) shows TSDC and dark current with a dc bias of 12V. A current peak occurs at a temperature of about 246K. If we define polarization in the opposite direction of current flow, the measured current can be expressed as,

$$I = \frac{dQ_f}{dt} = -\frac{dQ_p}{dt} = -A\frac{dP_n}{dt}$$

where I is the current, Q_f is the free charge on the capacitor, Q_p is the polarization charge, P_n is the total polarization projected along the normal direction to the contacts of the parallel capacitor, A is the area of the contacts.

If we integrate with respect to time, the change of total polarization can be obtained as a function of temperature,

$$P_n(T) - P_n(T = 78K) = -\frac{1}{A}\int_0^{t(T)} I(t)dt$$

It is plotted as the inset of Figure 3.

Figure 4 shows the TSDC and change of polarization as a function of temperature obtained with zero bias (short circuited). The TSDC peak occurs at a higher temperature of 266K and is much narrower as compared with Figure 3. As a consequence, the change of polarization occurs in a much smaller temperature range as seen in the inset of Figure 4.

The pyroelectric effect can arise from several different mechanisms, (a) ion movement under an electric field, (b) space-charge polarization due to real charge storage such as carrier trapping[16], or (c) ferroelectric effect due to spontaneous polarization below the Curie temperature[18]. Which mechanism accounts for our observation of the pyroelectric effect in Ag-contacted HgI_2 is unknown. Further work is being done to answer this question and to investigate other related properties.

CONCLUSIONS

In conclusion, we have investigated semitransparent Ag, Pd and Al contacts on HgI_2 by TSC. The results indicate the TSC is an useful tool in characterizing electrical contact materials on HgI_2 detectors. The correlation between traps observed in TSC spectra and detector performance was discussed. A pyroelectric effect was also observed in Ag-contacted HgI_2.

ACKNOWLEDGEMENTS

~~We would like to thank the~~ Work supported by the U.S. Department of Energy ~~for financial support.~~ under Contract DE-AC 04 76DP00789

REFERENCES

1. H.L. Malm, IEEE Trans. Nucl. Sci. NS-19, 263 (1972).
2. S. Cain, A. Holzer, I. Beinglass, M. Schieber, and E. Lowenthal, IEEE Trans. Nucl. Sci. NS-25, 649 (1978).
3. B.E. Patt, A.G. Beyerle, R.C. Dolin, and C. Ortale, Nucl. Instr. Meth. Phys. Res. A283, 215 (1989).
4. J.S. Iwanszyk, Y.J. Wang, J.G. Bradley, J.M. Conley, A.L. Albee, and T.E. Economou, IEEE Trans. Nucl. Sci. 36, 841 (1989).
5. A.J. Dabrowski, W.M. Szymczyk, J.H. Kusmiss, W. Drummond, and L. Ames, Nucl. Instr. Meth. 213, 89 (1983).
6. N.L. Skinner, C. Ortale, M.M. Schieber, and L. van den Berg, Nucl. Instr. Meth. Phys. Res. A283, 119 (1989).
7. X.J. Bao, T.E. Schlesinger, R.B. James, J. Appl. Phys. 67, 7265 (1990).
8. R.B. James, X.J. Bao, T.E. Schlesinger, to be published.
9. X.J. Bao, T.E. Schlesinger, R.B. James, G.L. Gentry, A.Y. Cheng, and C. Ortale, J. Appl. Phys., in press.
10. R.C. Whited, and L. van den Berg, IEEE Trans. Nucl. Sci. NS-24, 165 (1977).
11. P. Suryanarayana, and H.N. Acharya, J. Electr. Mat. 18, 481 (1989).
12. T. Mohammad-Brahim, A. Friant, and J. Mellet, Phys. Stat. Sol.(a) 65, K1 (1981).
13. A. Tadjine, D. Gosseline, J.M. Koebel, and P. Siffert, Nucl. Instr. Meth. 213, 77 (1983).
14. J.L. Merz, Z.L. Wu, L. van den Berg, and W.F. Schnepple, Nucl. Instr. Meth. 213, 51 (1983).
15. X.J. Bao, T.E. Schlesinger, R.B. James, A.Y. Cheng, and C. Ortale, Mat. Res. Soc. Symp. Proc. 163, 1027 (1990).
16. G.M. Sessler, editor, Eletrets, 2nd ed. (Springer-Verlag, Berlin, 1987).
17. A.A. Bush, and A.G. Laptev, Sov. Phys. Sol. Stat. 31, 535 (1989).
18. E.P. Wohlfarth, editor, Ferroelectricity, 1st ed. (John Wiley & Sons Inc., New York, 1967).

Introduction of extrinsic defects into mercuric iodide during processing

C.-Y. Hung, X. J. Bao, and T. E. Schlesinger
Department of Electrical and Computer Engineering, Carnegie Mellon University, Pittsburgh, Pennsylvania 15213

R. B. James
Advanced Materials Research Division, Sandia National Laboratories, Livermore, California 94550

A. Y. Cheng, C. Ortale, and L. van den Berg
EG&G Energy Measurements, Incorporated, Goleta, California 93116

(Received 24 August 1992; accepted for publication 14 January 1993)

Low temperature (4.2 K) photoluminescence spectroscopy (PL) measurements were performed on mercuric iodide (HgI_2) crystals which were intentionally doped with copper or silver during KI etching. PL spectra obtained after these doping experiments show specific Cu and Ag features similar to those previously observed after deposition of Cu or Ag contacts on mercuric iodide crystals. The in-diffusion of Cu or Ag into bulk HgI_2 has also been confirmed a few days after doping. This diffusion introduces new recombination centers in the material. This work suggests that the processing steps used to fabricate mercuric iodide nuclear detectors can lead to the introduction of new defects which are detrimental to detector performance.

I. INTRODUCTION

Mercuric iodide (HgI_2), in its red tetragonal form, has many properties that make it well suited for use as a room temperature x-ray and γ-ray detector and spectrometer.[1–5] These properties include high atomic masses ($Z=80$ and 53 for Hg and I, respectively), low electron-hole creation energy (4.2 eV at 300 K),[3–5] and high resistivity (10^{13} Ω cm).[5]

There remain, however, many material and processing issues that are of concern for the further development of HgI_2 detectors. A low manufacturing yield of between 10% and 20% results in high cost, especially when one considers the long growth times for HgI_2 single crystals.[6] Defects introduced from the starting material for crystal growth and during processing may be partly responsible for limiting the yield of high quality detectors. Some possible defects are extrinsic impurities, as well as intrinsic defects such as vacancies, interstitials, antisite defects, defect complexes, and dislocations. These defects affect detector performance in several ways. They may be shallow dopants, thus increasing the dark current of the detector. If they are carrier traps, they may reduce the effective mobility of the charge carriers, decrease the charge collection efficiency (within the integration time of the amplifier circuit associated with the detector), redistribute the electric field inside the detector, or cause polarization effects. Defects may also change the properties of the electrical contact, for example, introducing a barrier to carrier collection. Investigation of these defects is of great importance, therefore, for the improvement of HgI_2 material and detectors.

Preparation of the material for fabricating detectors includes crystal growth, slicing the crystal, polishing and etching with KI solution, contact deposition, and mounting of the detectors on alumina substrates. Previously, it has been established that low temperature photoluminescence spectroscopy (PL) is a useful tool in studying the defects in HgI_2 introduced by processing steps such as crystal growth, chemical etching, annealing, and contact deposition,[7–9] and the signatures of several impurities were identified.[10–12] In particular, broad emissions centered at 5490 and 6270 Å appearing in the PL spectra were found to be associated with Ag and Cu impurities, respectively. It has also been established previously that both Ag and Cu can diffuse through the thickness of a typical wafer (approximately 0.5 mm) within a few hours even at room temperature.[10] Several features in the PL spectra were also correlated with detector quality.[13] Based on these results, we have performed PL measurements on HgI_2 crystals intentionally exposed to controlled quantities of either Cu or Ag during chemical etching. We show, in this article, that some impurities in the etching solution are introduced into the mercuric iodide crystal during the etching process. In particular, we focus our attention on Cu and Ag since these have well defined signatures in the PL spectra and because inductively coupled plasma (ICP) measurements have shown that both Cu and Ag are present in the KI etch in concentrations ranging from 1–50 and 1–500 ppb, respectively, depending on the vendor and lot. In fact, ICP measurements also reveal the presence of other impurities in the KI etch solution including Zn, Fe, Mn, Mg, Ca, Na, P, Se, and Al all in the 100 ppb range.

II. EXPERIMENTAL TECHNIQUE

Photoluminescence measurements were performed at 4.2 K with an argon ion laser as the excitation source. The laser was operated at 20 mW and tuned to 488 nm. This excitation source corresponds to an energy of 2.54 eV, which is above the band gap of HgI_2 (2.37 eV at 4.2 K). The PL was generated from a region beneath the surface of the sample extending to a depth of a few micrometers. The laser beam was modulated with a mechanical chopper at a frequency of 750 Hz. The spot size of the laser excitation on the specimen was about 1.5 mm in diameter. Samples

 0021-8979/93/094591-04$06.00

TABLE I. Samples used in this study along with crystal purification procedures, concentrations of Cu or Ag in KI solution, and storage times.

Sample ID	Purification procedures	Concentrations (by weight)	Storage period (days)
V5-11 JB-13	4XIX	0.19% Cu[a], 10% KI	3
N3-25-2	4XMXSXMXS	0.09% Cu[b], 10% KI	3
V5-11 JB-11	4XIX	0.09% Ag[c], 10% KI	3
V1-10-6	4XMXS	0.06% Ag[c], 10% KI	1.5

[a]From $CuCl_2.2H_2O$ solid powder.
[b]From Fisher Cu reference standard solution (1000 ppm).
[c]From Fisher Ag reference standard solution (1000 ppm).

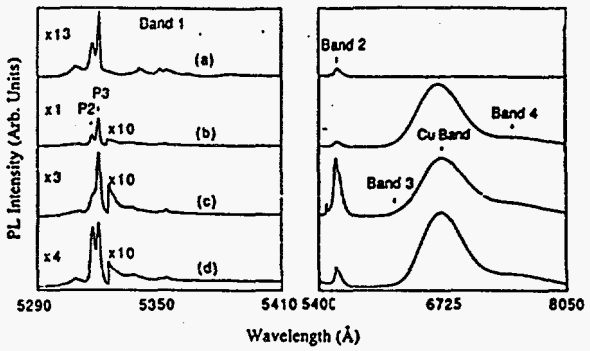

FIG. 1. 4.2 K photoluminescence spectra taken at nearly the same location from sample N3-25-2 (a) immediately after KI etch but before Cu doping, (b) immediately after KI etch in solution containing Cu, (c) after three days storage in a desiccator and before third KI etch, and (d) after three days storage and after third KI etch.

were cooled to a temperature of 4.2 K with liquid He in an optical cryostat. The liquid helium level was always kept below the specimen to obtain optimal light collection. The luminescence was collected by two collimating lenses and directed onto the entrance slits of a 0.85 m SPEX 1404 double pass spectrometer. The widths of the entrance and exit slits were set such that the spectral resolution was about 1 Å. The signal was detected with an S20 response photomultiplier tube and amplified by a Keithley 427 current amplifier, an EG&G 5207 lock-in amplifier, and recorded by a HP 9836 computer.

Slices of HgI_2 approximately 0.5 mm thick and with the *c*-axis normal to the plane were etched in a 10 wt % KI aqueous solution with mild agitation for about 1 min to remove any possibly degraded surface layer. This treatment removes a surface layer of about 30 μm in thickness. After etching, the samples were rinsed with deionized water for several minutes. PL spectra were then taken from four different locations on the sample. Measurements at various locations on each sample ensure statistically sound results since there is some variation in the PL spectra taken from different locations on a slice of HgI_2. The entire sample was then immersed for about 1 min in KI solution to which controlled amounts of Cu or Ag had been added and then rinsed in deionized water. PL spectra were then taken at approximately the same four locations as before to search for any Cu or Ag luminescence features that may have appeared. In Table I, we present the samples used in this study, including the amount of Cu or Ag included in the KI solution and the purification procedures employed in producing the starting material for crystal growth. These procedures are indicated by I, M, X, and S, indicating that the starting material had iodine added to it, was melted, was sublimed in an open tube, or was sublimed in a closed tube, respectively. In order to observe any diffusion of Cu or Ag into the bulk material, the samples were stored in a desiccator for a period of several days (also indicated in Table I) after the second set of PL spectra had been obtained. After the storage period, sets of PL spectra were taken both before and after a final KI etch to which no impurities were intentionally added.

Cu from both cupric chloride solid powder ($CuCl_2.2H_2O$) and Cu reference standard solution (Cu in diluted HNO_3 solution, 1 mg Cu per 1 ml) were used in the Cu doping experiments. Ag reference standard solution (Ag in diluted HNO_3 solution, 1 mg Ag per 1 ml) was used for the Ag doping experiments. After mixing Cu or Ag into the KI solution, any chemical reactions were allowed to stabilize by waiting for a period of a few hours. The etching solution was filtered to remove solid precipitates (Cu_2I_2 or AgI) and the filtered solution was used for etching. In principle, most of the Cu or Ag will have reacted with I in the KI solution and have been removed during filtration. However, HgI_2 crystals are found to be very sensitive to the presence of trace impurities and PL is capable of detecting extremely small concentrations of optically active centers.

III. RESULTS AND DISCUSSION

The PL spectrum of HgI_2 is generally divided into a number of wavelength regions. In the short wavelength region from 5290 to 5410 Å, the spectrum is collectively labeled as Band 1. It is composed of at least 26 narrow exciton-related emission lines and their phonon replicas.[14–17] In most spectra, the dominant peaks in the Band 1 region are two bound exciton lines at wavelengths of 5317.9 and 5320.8 Å and are labeled P2 and P3, respectively. In the long wavelength region from 5410 to 8050 Å, several broad emissions have been observed. The most common ones are centered at wavelengths of about 5595, 6200, and 7550 Å and are labeled as Bands 2, 3, and 4, respectively.[11] Several other emission bands have also been observed and correlated with specific impurities. In particular, bands at 5490 and 6720 Å have been correlated with Ag and Cu impurities, respectively.[10,11]

Figure 1 shows four PL spectra taken at nearly the same location on sample N3-25-2. Spectrum (a) was taken immediately after KI etching and before Cu doping. This spectrum is typical for undoped HgI_2 bulk material. Spectrum (b) was taken from the same location immediately after etching in the KI solution to which Cu had been introduced. The most dramatic difference in the spectra is the introduction of a new broad band centered at about 6720 Å between bands 3 and 4. This band has been observed in mercuric iodide on which a Cu contact had been deposited[10] and it was labeled as the "Cu band." Other

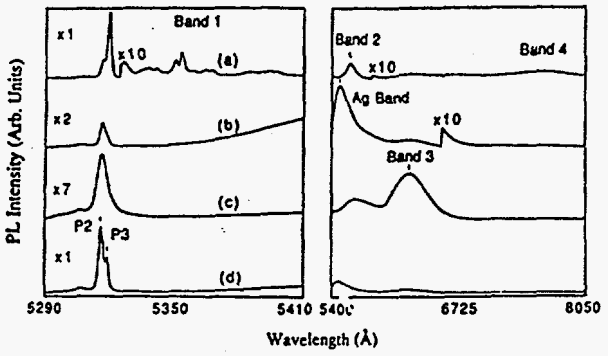

FIG. 2. 4.2 K photoluminescence spectra taken at nearly the same location from sample V5-11 JB-11 (a) immediately after KI etch but before Ag doping, (b) immediately after KI etch in solution containing Ag, (c) after three days storage in a desiccator and before third KI etch, and (d) after three days storage and after third KI etch.

changes in the spectra include the quenching of those peaks on the longer wavelength side of P3 in Band 1 and an increase of the absolute intensity of Band 4. The appearance of such a band is not observed in the case of Pd deposited onto HgI_2, which is generally employed as the electrode material in most detector applications.[18] The increase in Band 4 after Cu doping may indicate that it too is related to Cu impurities; however, since this band is also observed in nominally undoped material, it will not be assigned as a Cu band at this time.

Spectra (c) and (d) of Fig. 1 were taken at approximately the same location as (a) and (b) and were obtained after three days storage in a desiccator before and after KI etching. Chemical etching not only removes a surface layer (about 25 μm thick) but also allows for the investigation of bulk properties of the material by exposing a clean surface. One can therefore see that Cu has diffused into the bulk of the material since the Cu band is readily observed even after KI etching. Also, the decrease in intensity of the Cu band after storage is consistent with a decrease in concentration of Cu near the surface as it diffuses uniformly throughout the bulk.

A similar experimental procedure was followed on two samples selected for Ag doping and the spectra obtained from sample V5-11 JB-11 are presented in Fig. 2. Spectrum (a) was obtained immediately after the KI etch and before Ag doping, (b) immediately after etch with a KI solution spiked with Ag, (c) after three days storage and before a third KI etch, and (d) immediately after the KI etch that was not spiked with Ag. Spectrum (a) is, again, typical for undoped bulk HgI_2 with small Bands 3 and 4. After Ag doping, a new intense broad emission is observed centered at about 5490 Å as well as a significant increase in Band 3. Similar observations have been made for slices of HgI_2 on which a Ag layer had been deposited.[11] Since the band at 5490 Å is observed only after the introduction of Ag to the sample, it is identified as the "Ag band." It appears that the presence of Ag impurities tends to decrease P3 and also to broaden the emissions in the Band 1 region. The P3 intensity may be reduced relative to P2 due to the creation of an iodine deficiency in the crystal as a consequence of the formation of Ag/I compounds.[19]

In spectra (c) and (d) of Fig. 2, the Ag band is reduced in intensity after three days of storage, and we interpret this as being due to a decrease in the concentration of Ag in the near surface region as it diffuses into the bulk of the sample. The decrease in the Ag band is accompanied by an increase in both Bands 2 and 3. While the reasons for this latter observation are not clear, an increase in the Band 3 intensity is always observed in the spectra of Ag doped material. However, variations in the intensity of Band 3 have also been observed in as-received crystals, those contacted with other metals, and after surface treatments such as etching, annealing, vacuum exposure, or immersion in Hg or I. In spectrum (d) of Fig. 2, we also observe that P2 is the dominant peak, indicating I deficiency in the bulk, and we observe the Ag band shifted by about 10 Å to shorter wavelengths. This perhaps indicates some change in the Ag related center responsible for this band.

IV. CONCLUSION

In conclusion, we have employed low temperature PL measurements to study the intentional introduction of Cu and Ag defects to HgI_2 by adding small quantities of Cu and Ag to the KI etching solution used to process the HgI_2 slices. The presence of these impurities in KI etch solution has been verified by ICP measurements, as has the presence of a number of other impurities. The in-diffusion of both Cu and Ag from the KI solution has been confirmed. We infer that other impurities can, no doubt, be introduced into HgI_2 slice during the various steps employed to fabricated detectors and conclude that care needs to be employed to prevent the contamination of this material during processing. Since Cu and Ag are known to be detrimental to mercuric iodide detectors, performance and manufacturing yield improvements of HgI_2 detectors may therefore be realized if special care is taken to avoid contamination during processing.

ACKNOWLEDGMENTS

This work is supported by the U.S. Department of Energy. One of us (T. E. S.) acknowledges the support of the National Science Foundation through the Presidential Young Investigator Program.

[1] W. R. Willig, Nucl. Instrum. Methods 96, 615 (1971).
[2] H. L. Malm, IEEE Trans. Nucl. Sci. NS-19, 263 (1972).
[3] J. P. Ponpon, R. Stuck, and P. Siffert, Nucl. Instrum. Methods 119, 197 (1974).
[4] J. H. Howes and J. Watling, Mater. Res. Soc. Symp. Proc. 16, 207 (1983).
[5] H. L. Malm, T. W. Raudoff, M. Martina, and K. R. Zanio, IEEE Trans. Nucl. Sci. NS-20, 500 (1973).
[6] N. L. Skinner, C. Ortale, M. M. Schieber, and L. van den Berg, Nucl. Instrum. Methods Phys. Res. A 283, 119 (1989).
[7] X. J. Bao, T. E. Schlesinger, R. B. James, R. H. Stulen, C. Ortale, and A. Y. Cheng, J. Appl. Phys. 68, 86 (1990).

[8]R. B. James, X. J. Bao, T. E. Schlesinger, J. M. Markakis, A. Y. Cheng, and C. Ortale, J. Appl. Phys. 66, 2578 (1989).
[9]X. J. Bao, T. E. Schlesinger, R. B. James, G. L. Gentry, A. Y. Cheng, and C. Ortale, J. Appl. Phys. 69, 4247 (1991).
[10]X. J. Bao, T. E. Schlesinger, R. B. James, R. H. Stulen, C. Ortale, and L. van den Berg, J. Appl. Phys. 67, 7265 (1990).
[11]X. J. Bao, Ph.D. Dissertation, Carnegie Mellon University (1991).
[12]R. B. James, X. J. Bao, T. E. Schlesinger, C. Ortale, and A. Y. Cheng, J. Appl. Phys. 67, 2571 (1990).
[13]X. J. Bao, T. E. Schlesinger, R. B. James, S. J. Harvey, A. Y. Cheng, V. Gerrish, and C. Ortale, Nucl. Intrum. Methods Phys. Res. A 317, 194 (1992).
[14]X. J. Bao, T. E. Schlesinger, R. B. James, C. Ortale, and L. van den Berg, J. Appl. Phys. 68, 2951 (1990).
[15]B. V. Novikov and M. M. Pimonenko, Sov. Phys. Semicond. 4, 1785 (1971).
[16]B. V. Novikov and M. M. Pimonenko, Sov. Phys. Semicond. 6, 671 (1972).
[17]I. K. Akopyan, B. V. Bondarenko, B. A. Kazennov, and B. V. Novikov, Sov. Phys. Solid State 29, 238 (1987).
[18]T. E. Felter, R. H. Stulen, W. F. Schnepple, C. Ortale, and L. van den Berg, Nucl. Instrum. Methods Phys. Res. A 238, 195 (1989).
[19]X. J. Bao, T. E. Schlesinger, R. B. James, A. Y. Cheng, C. Ortale, and L. van den Berg (unpublished).

PROCEEDINGS
SPIE—The International Society for Optical Engineering

X-Ray Detector Physics and Applications

Richard B. Hoover
Chair/Editor

23–24 July 1992
San Diego, California

Sponsored and Published by
SPIE—The International Society for Optical Engineering

Cosponsoring Organization
Aviation Security R&D Service, FAA Technical Center

Volume 1736

Study of stoichiometry in mercuric iodide by low temperature photoluminescence spectroscopy

X.J. Bao*, R.B. James**, C.-Y. Hung*, T.E. Schlesinger*, A.Y. Cheng***, C. Ortale***, and L. van den Berg***

* Department of Electrical and Computer Engineering
Carnegie Mellon University, Pittsburgh PA 15213

** Advanced Material Research Division
Sandia National Laboratories, Livermore CA 94550

*** EG&G Energy Measurements, Inc.
Goleta, CA 93116

ABSTRACT

Low temperature (4.2 K) photoluminescence spectroscopy (PL) measurements were performed on mercuric iodide (HgI_2) crystals that were surface-doped with either iodine or mercury. Two methods of treatment were used to achieve the surface doping. The first is the direct immersion of HgI_2 samples into potassium iodide (KI) aqueous solution saturated with iodine or immersion into elemental mercury liquid. The second is the storage of HgI_2 crystals under either iodine or mercury vapor. Certain features in the PL spectra were correlated with the stoichiometry of the HgI_2 crystals modified by the surface doping. It was also found that if HgI_2 was exposed to air, an iodine deficient surface layer would form within a one-day period due to the preferential loss of iodine. Finally, the behavior of a broad emission band in the PL spectra and its implication in the fabrication of high quality HgI_2 nuclear detector is discussed.

2. INTRODUCTION

The most common semiconductor nuclear detectors such as lithium-drifted silicon (Si(Li)), lithium-drifted germanium (Ge(Li)), or high-purity germanium (HPG) suffer from several disadvantages. First, they have to be operated at cryogenic temperatures to reduce dark current. In some cases they have to be kept at low temperature at all times to avoid permanent damage to the Li profile in the detector. This makes the detector system bulky and inconvenient to use. Secondly the relatively low atomic numbers of Si and Ge (14 and 32, respectively) result in a low efficiency of the photoelectric interaction between the incident energetic photons and the semiconductor, since this interaction is proportional to the fifth power of the atomic number of the material. In an effort to find a suitable semiconductor that has a high atomic number and low dark current at room temperature, and which may be fabricated into nuclear detectors, many material systems have been investigated in the last two decades.[1-3]

0-8194-0909-X/93/$

HgI_2 is a semiconductor with a dark resistivity of about 10^{13} Ω-cm at room temperature. This is partly due to its relatively wide bandgap of 2.1 eV at room temperature. This property, along with the high atomic numbers of its constituent atoms (80 and 53 for Hg and I, respectively) have made HgI_2 one of the most promising materials for the fabrication of X-ray and γ-ray detectors operating at room temperature.[4–7] Currently, HgI_2 detectors operating at room temperature have similar energy resolution for X-rays of moderate energy when compared with Si(Li) detectors. For example, a full-width-at-half-maximum (FWHM) of 150 eV can now be achieved by HgI_2 detectors for the full energy peak of the K_α line of Mn (5.9 keV).[8]

Many material and processing issues are of concern for the further development of HgI_2 detectors. Low manufacturing yield of about 10% results in high cost in the fabrication of these detectors, especially given the difficulty and the length of time in growing HgI_2 single crystals.[9] Defects introduced from the starting material during crystal growth, and during processing are responsible for limiting the yield of high quality detectors. Some possible defects are extrinsic impurities, as well as intrinsic vacancy, interstitial, anti-site defects, defect complexes, and dislocation. These defects affect the detector performance in several ways. They may be shallow dopants, thus increasing the dark current of the detector. If they are carrier traps, they may reduce the effective mobility of the charged carriers, decrease the charge collection, redistribute the electric field inside the detector, and cause polarization effects. Defects may also change the properties of the electrical contact causing carrier injection or introducing a barrier to carrier. Investigation of these defects is of great interest therefore for the application of HgI_2.

Stoichiometry has a significant influence on the formation of defects in HgI_2 crystals and thus the quality of the detectors. Many workers have studied issues related to stoichiometry in HgI_2. There have been efforts to measure the absolute stoichiometry in HgI_2 crystals grown by different methods and with different starting materials and to correlate the detector quality with the stoichiometry.[10–13] Even though, the absolute stoichiometry in many of the materials studied remain unclear, it is generally believed that stoichiometric HgI_2 is the best for detector fabrications. For example, mobility-lifetime product measurements by van den Berg et al.[14] for crystals with various relative iodine and mercury contents have shown that excessive mercury doping will reduce the value of the mobility-lifetime product for holes while excessive iodine doping will reduce the value of mobility-lifetime product for electrons.

In this investigation, low temperature photoluminescence spectroscopy was employed to study stoichiometry in HgI_2. Previously, it has been established that PL is a useful tool in studying the defects in HgI_2 introduced by processing steps such as crystal growth, chemical etching, annealing, and contact deposition.[15–17] Signatures of several impurities were identified.[18–20] Several features in the PL spectra were also correlated with detector quality.[21] Based on these results, we have made PL measurements on HgI_2 crystals intentionally treated with either mercury or iodine in an effort to identify features in the PL spectra that are related to stoichiometry and also to relate them to detector quality. In addition, we studied the effect of aging since it has be suggested that HgI_2 tends to form a surface layer deficient of iodine due to the higher vapor pressure of iodine compared with mercury.[15]

3. EXPERIMENTAL TECHNIQUES

Table 1: Samples used in this study.

No.	Sample ID	Color	GPA	Starting Material	Experiment
1	N2-6-1	1	2.5	4XMS	Etch in KI saturated with I_2
2	V1-10-8	1	2.7	4XMXS	Storage with I_2
3	V8-5-3	5	2.4	4X2(MXS)	Immersion in Hg
4	V1-10-2	1	2.7	4XMXS	Storage with Hg
5	N13-13-1	0	3.3	4XMXS	Aging

HgI_2 slices of about 1 cm x 1 cm x 0.05 cm were obtained from EG&G Energy Measurements, Inc. They were cut with a thread dipped in KI aqueous solution from single crystals of HgI_2 grown by vapor transport. The preparation of starting material and the crystal growth have been in development for the last two decades and have been well documented in the literature.[22–26] Five samples were used in this study and are tabulated in Table I. Also listed in the table are color, grade point average (GPA), and purification procedures used for the preparation of the starting material. The color refers to the qulitative visual observation of the vapor color during crystal growth. The assigned numbers indicate the redness of the observed color of the vapor. These numbers correspond qualitatively to the relative concentration of iodine in the vapor during the crystal growth, where a higher number indicates a higher iodine content. These numbers range from 0 to 10. The GPA for each crystal was obtained as follows. Approximately ten to twenty detectors were fabricated from each crystal and their performance was evaluated in terms of their response to the 662-keV radiation from a ^{137}Cs source. A grade of A, B, C or D was assigned to each detector according to its energy resolution and peak-to-valley ratio, where grade A corresponds to the highest quality and grade D the lowest. GPA is determined by assigning weighting factors of 4, 3, 2 and 1 to grades A, B, C and D, respectively and then taking the weighted average. The starting materials were prepared in slightly different ways. "4X" indicates that the raw material was sublimed in an open tube four times. "M" indicates that the raw material underwent melting. "S" indicates that a closed-tube sublimation was used.

PL measurements were performed at 4.2 K with an argon ion laser as an excitation source. The laser was operated at 20 mW and tuned to 488 nm. The laser beam was modulated with a mechanical chopper at a frequency of 750 Hz. The spot size of the laser on the specimen was about 1.5 mm in diameter. The luminescence was collected by two collimating lenses into a Spex 1404 0.85 m-double pass spectrometer. The entrance and exit slit widths were set such that the spectral resolution is about 1 Å. The signal at the exit was detected by a photomultiplier with an S-20 response and amplified by a Keithley 427 current amplifier and an EG&G 5207 lock-in amplifier.

The experments proceeded as follows. First the sample was etched in a 10% (by weight) KI aqueous solution to remove any possibly degrade surface layer. 4.2 K PL spectra were then taken from several spots from the sample. Part of, or the entire sample was then treated with iodine or mercury. Finally, the PL spectra were taken from the treated region, and in the case of partly treated samples, also from untreated regions. Several spectra were taken each time from several spots to average over any nonuniformity across the sample. For the treatments, part of sample

N2-6-1 was immersed in a 10% KI aqueous solution saturated with iodine for one minute. Sample V1-10-8 was sealed in a petri dish with a small amount of iodine for six days. The sample was not in direct contact with the solid iodine. Part of sample V8-5-2 was immersed in mercury for a few seconds. Sample V1-10-2 was stored with Hg vapor for six days. Additionally, after the storage with mercury and the PL measurements, sample V1-10-2 was stored with iodine for two days and PL spectra were taken after this storage.

Sample N13-13-1 was used to investigate the effect of aging. PL spectra were taken from this sample after it was freshly etched in 10% KI solution, and after being exposed to air for twenty hours, one week, and twenty days.

4. RESULTS

PL spectra taken from HgI_2 crystals are generally divided into two wavelength regions. In the short wavelength region from 5290 to 5410 Å, the spectrum is collectively labeled as Band 1. It is composed of at least 26 narrow exciton-related emission lines, such as free exciton, bound exciton, and their phonon replicas due to longitudinal and transverse optical phonons.[27–30] In most spectra, the dominant peaks in Band 1 region are two bound exciton lines at wavelengths of 5317.9 and 5320.8 Å, and are labeled P2 and P3, respectively. In the long wavelength region from 5410 to 8050 Å, several broad emission bands have been observed. The most common ones are centered at wavelengths of about 5595, 6200, and 7550 Å, and are labeled as Band 2, 3, and 4, respectively.[20] Several other emission bands have been correlated with impurities in the crystals.

Fig. 1 shows two spectra taken from sample N2-6-1. Spectrum (a) was from an untreated region and spectrum (b) was from a region that was immersed in a 10% KI solution saturated with iodine. By comparing the two spectra, it can be found that the major difference is the overall higher PL intensity and smaller P2 to P3 ratio in spectrum (b). The smaller P2 to P3 ratio is mainly due to the increase in the absolute intensity of P3. Also it should be noted is that Band 3 was present in both spectra.

For samples stored under iodine vapor for six days, similar results were obtained and are shown in Fig. 2 for sample V1-10-8. Here spectrum (a) was taken before storage and spectrum (b) was taken at approximately the same spot after storage. The overall PL intensity was enhanced and P2 to P3 ratio was reduced after the sample was stored with iodine for six days. Another spectrum (not shown here) taken from the back of the sample showed similar changes but to a lesser extent. This is probably because the sample was placed on a glass slide and the back of the sample was therefore less exposed to the iodine vapor. In all spectra from this sample taken after a six-day storage, no significant sign of aging has occurred (refer to the effect of aging that will be mentioned later).

Two spectra taken from sample V8-5-2 are shown in Fig. 3. Spectrum (a) was from an untreated region and spectrum (b) was from a region that was immersed in mercury for a few seconds. Small droplets of mercury were visible on the surface of the sample due to wetting. It can be seen from the two spectra that overall PL intensity was greatly reduced in regions treated with mercury. Band 3 has disappeared in spectrum (b).

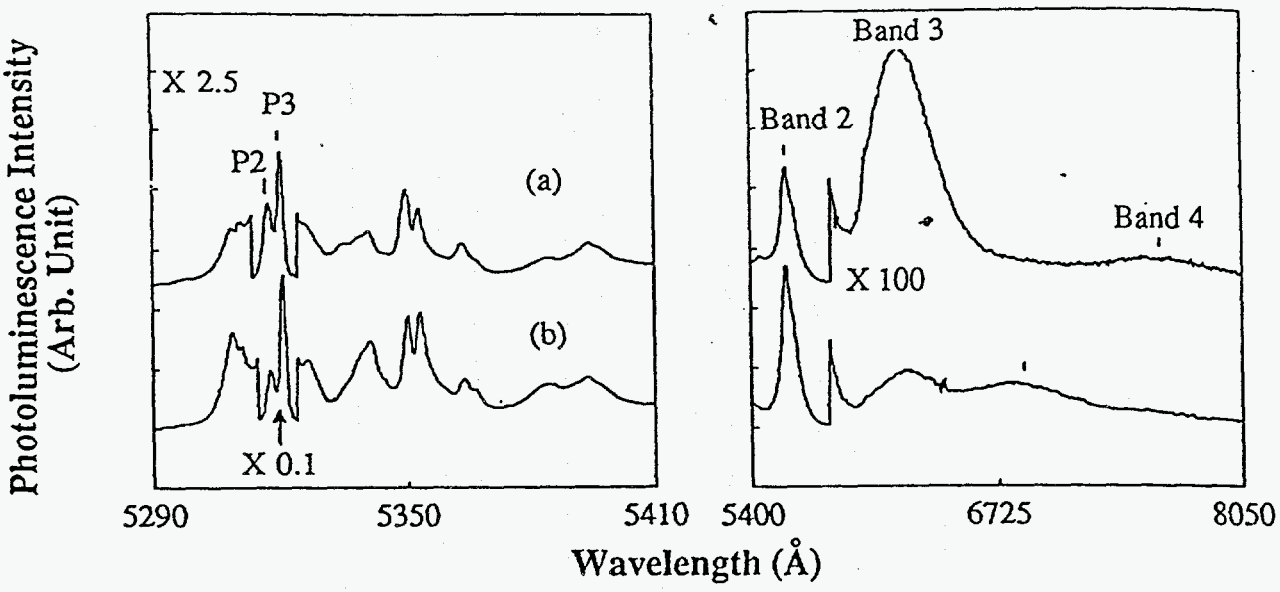

Figure 1: 4.2 K photoluminescence spectra taken from sample N2-6-1 from (a) an untreated region and (b) a region immersed in a 10% KI solution saturated with iodine for one minute.

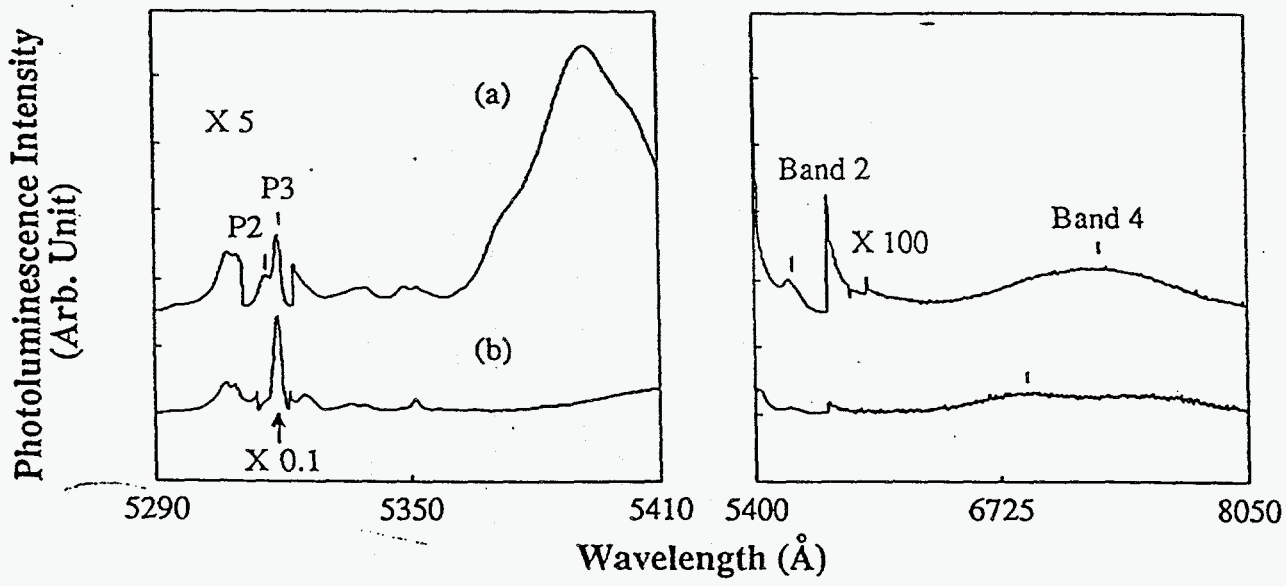

Figure 2: 4.2 K photoluminescence spectra taken from sample V1-10-8 (a) before and (b) after a six-day storage with vapor of iodine. The sample was KI etched before storage.

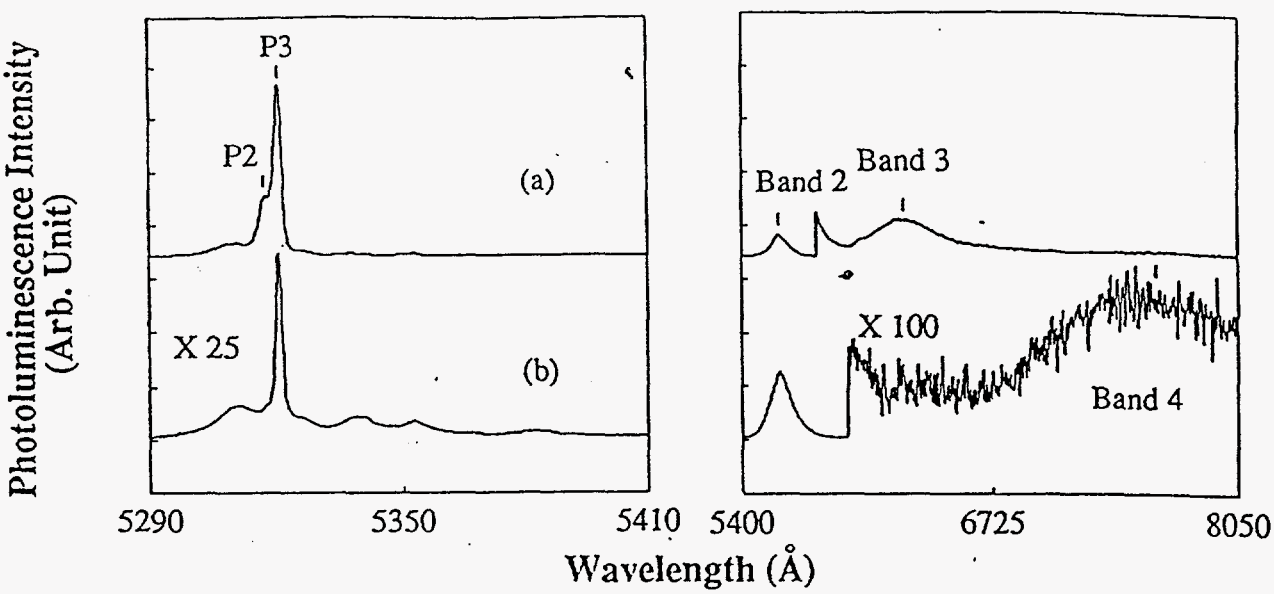

Figure 3: 4.2 K photoluminescence spectra taken from sample V8-5-2 from (a) an untreated region and (b) a region immersed in mercury for a few seconds.

Fig. 4 shows four spectra taken from sample V1-10-2. Spectrum (a) was taken after a KI etch. Spectra (b) and (c) were taken from the back and front surfaces after a six-day storage with mercury. It can be seen that after storage with mercury, the PL intensity was reduced, especially from the front surface, where the spectrum almost disappeared in the band 1 region. Visually, it was observed that a metallic sheet has formed on the surface of the HgI_2 sample. Spectrum (d) shows partly recovered PL intensity after storage with iodine vapor following the formation of the sheet of metallic mercury on the surface of the sample. Spectrum (d) in the band 1 region is broad and featureless (centered at the position of P2) and looks very similar to spectrum (a) of Fig. 5, where the sample had been exposed to air for twenty days.

The effect of aging is shown in Fig. 5. Four spectra were taken from sample N13-13-1 after different exposure times to air. From spectra (a) to (d), the spectra were taken twenty days, one week, twenty hours, and minutes after a 10% KI etch. As aging progresses, P3 decreases and gradually disappears while P2 becomes dominant. After about twenty days, the spectrum is predominantly a featureless broad strong peak slightly shifted away form P2 to P3. From the gradual change of the spectra, it appears that this broad peak derives from P2, even though it has been shifted several angstroms to longer wavelength. This shift may be related to a much higher concentration of the defect related to P2 as the surface of the crystal ages more. This also explains the enhanced intensity of this peak. Band 3 is present in spectra (d), but not in spectra (a), (b), and (c).

5. DISCUSSIONS

The treatments of HgI_2 by iodine or mercury in this study most likely introduce excess iodine or mercury near the surface region, rather than in the bulk. PL spectroscopy is a technique that probes the near-surface region. So these measurements can be regarded as surface-doping experiments.

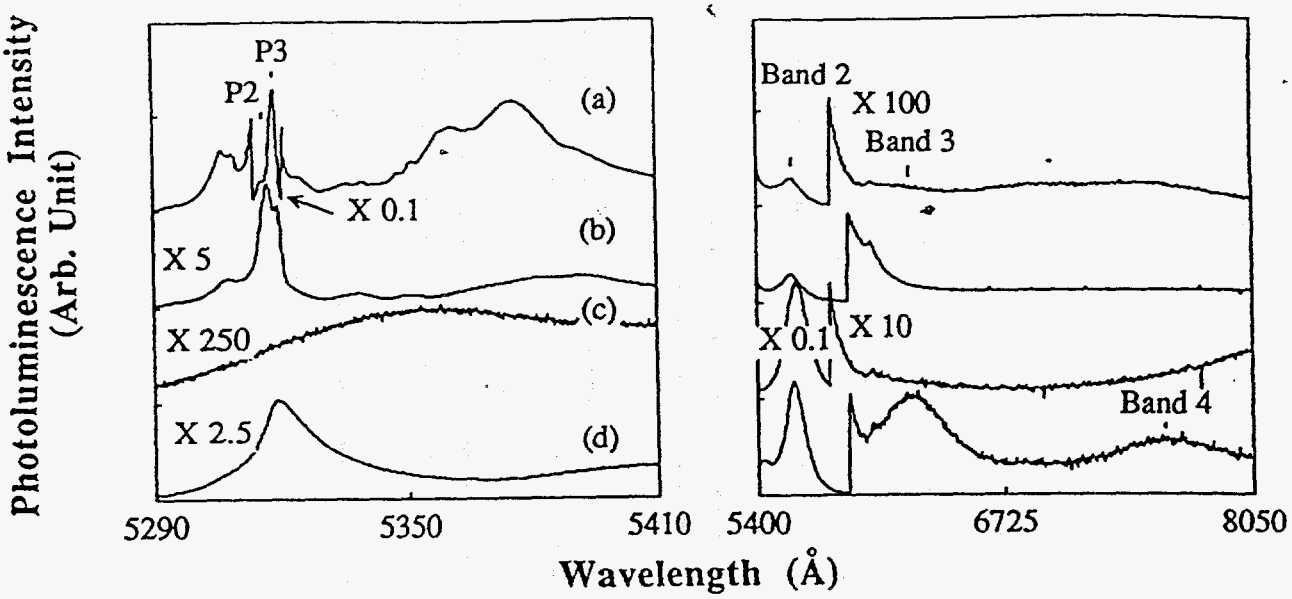

Figure 4: 4.2 K photoluminescence spectra taken from sample V1-10-2. They were obtained (a) before storage (b)from back after storage (c) from front surface after storage with mercury vapor for six days and (d) from front surface after storage with iodine vapor for two days following the storage with mercury.

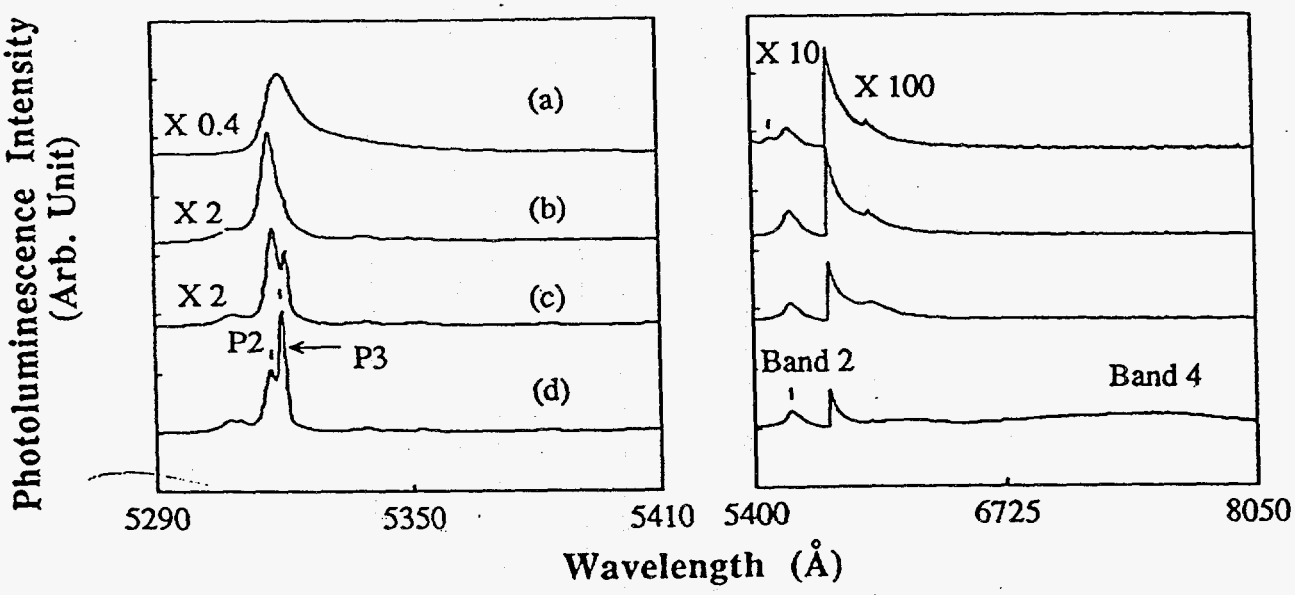

Figure 5: The effect of aging when the crystal is exposed to air. The spectra were taken from sample N13-13-1 (a) twenty days (b) one week (c) twenty hours and (d) minutes after KI etched.

From Figs. 1 and 2, it appears that treating HgI_2 crystals with iodine by the two different methods used in this study has similar effects on their PL spectra. The overall intensity of the PL intensity is enhanced in the Band 1 region and P2 to P3 ratio was decreased, primarily due to the increase of the absolute intensity of P3. From Figs. 3 and 4, P3 as well as the overall intensity of PL was greatly reduced by the excess mercury near the surface, indicating that the crystal may be damaged. In the case of storage with mercury, PL was barely detectable from the front surface. These results are consistent with a previous study of the effects of etching of HgI_2 in KI solution, exposure to vacuum, and heat treatment.[15] It was found that P3 was probably related to excess iodine in the HgI_2 crystals. Results from Figs. 1 to 4 demonstrate directly the effects of excess iodine or mercury on HgI_2.

Fig. 5 shows the effect of aging on the PL spectra of HgI_2. Based on the conclusion that P3 was related to mercury deficiency, it can be inferred that the aging process is due to the loss of iodine near the surface, resulting in the decrease of the absolute intensity of P3. As the aging progresses, P2 becomes the dominant peak. It was also found that a one-day period is the typical length of time before a sample will have a change in its spectra similar to that from spectra (d) to (c) in Fig. 5. This interpretation of the effect of aging on the PL spectra of HgI_2 is also consistent with the results of storage with iodine or mercury vapor. In the case of storage with iodine vapor, no effect of aging was observed even after six days (see Fig. 2). On the other hand, spectrum (b) in Fig. 4 looks exactly as if the surface has aged (compare with spectra (b) and (c) of Fig. 5).

It is also interesting to note the behavior of Band 3. It has been reported that crystals that produce higher quality detectors tend to have smaller Band 3 in their PL spectra.[21] Even though, there is evidence that the defect related to Band 3 is probably a metallic impurity, its chemical identity is unknown. How this defect is introduced and what can be done to eliminate it is not fully understood. In general, the behavior of Band 3 has been difficult to predict and characterize.

In this study, we have observed some fairly consistent behavior of Band 3. It seems that if this band occurs in a crystal, its absolute intensity is generally stronger in relative iodine rich conditions. In Fig. 3, Band 3 was present in spectrum (a) but disappeared after the mercury treatment as shown in spectrum (b). Spectrum (a) was obviously taken in an iodine rich condition compared with the mercury treated surface. In Fig. 4, spectrum (a) has a small amount of Band 3 but after storage with mercury vapor, both spectra (b) and (c) do not show any Band 3. However, after further storage in the presence of iodine vapor, Band 3 occurred in spectrum (d). In the aging experiment, it can also be seen that Band 3 disappeared as the sample ages (see Fig. 5). Band 3 appears in both of the spectra in Fig. 1 and has comparable intensity. Fig. 2 is the exception in this trend observed for Band 3. No Band 3 is present in any of the two spectra shown in Fig. 2.

In the early stage of the development of HgI_2 room temperature detectors, it was found that purification by sublimation was critical in producing HgI_2 raw materials of sufficient quality for crystal growth and detector fabrication.[32,33] The study of PL spectra has also shown that these purification procedures reduce the intensity of Band 3 considerably.[31,34] Before purification, Band 3 was usually the strongest emission in the spectra. After several sublimations, Band 3 almost disappeared. Since it is believed that the sublimation process results in iodine loss, the final purified materials are iodine deficient compared with the starting materials. This is consistent with our finding in this study.

It is not certain how the defect related to Band 3 is introduced and associated with iodine rich conditions. There are two most likely explanations. The defects may be present in iodine which was used for these treatment and in the KI used for etching. This can explain spectrum (d) of Fig. 4 but not Figs. 3 and 5. Alternatively, the incorporation of this defect may be facilitated by the excess iodine. Since excess iodine will increase the concentration of defects such as mercury vacancies, which may help metallic impurities get incorporated and diffused into HgI_2 crystals. This possibility will be able to explain the Band 3 in Figs. 3 and 5. It seems that both mechanisms for the incorporation of the defect associated with Band 3 may be present.

6. CONCLUSIONS

Low temperature photoluminescence spectroscopy was employed to study the effect of surface doping of HgI_2 crystals by iodine or mercury. Iodine-rich crystals show a stronger P3 and overall emission in the PL spectra. Excess mercury seems to induce damage to the crystal, and results in greatly reduced PL intensity. Based on these result, it was found that exposure to air results in the preferential loss of iodine near the surface region of HgI_2 with noticeable change in PL spectra within a one-day period. The behavior of Band 3 was also discussed because of its importance to detector applications. Band 3 was generally found to be stronger in the relative iodine-rich conditions.

7. ACKNOWLEDGEMENT

We would like to thank the U.S. Department of Energy for financial support. One of us (TES) would also like to acknowledge the support of National Science Foundation through a Presidential Young Investigator award.

8. REFERENCES

1. W.R. Willig, "Large Bandgap Mercury and Lead Compounds for Nuclear Particle Detection," *Nucl. Instrum. Methods,* 101, pp. 23-24, 1972.

2. S.P. Swierkowski, and G.A. Armantrout, "Prognosis for High-Z Semiconductor Detectors," *IEEE Trans. Nucl. Sci.,* NS-22, pp. 205-210, 1975.

3. G.A. Armantrout, S.P. Swierkowski, J.W., Sherohman, and J.H. Yee, "What Can be Expected from High-Z Semiconductor Detectors?" *IEEE Trans. Nucl. Sci.,* NS-24, pp.121-125, 1977.

4. W.R. Willig, "Mercuric Iodide as a Gamma Spectrometer," *Nucl. Instrum. Methods,* 96, pp. 615-616, 1971.

5. H.L. Malm, "A Mercuric Iodide Gamma-ray Spectrometer," *IEEE Trans. Nucl. Sci.,* NS-19, pp. 263-265, 1972.

6. W. Puschert, and H. Scholz, "γ-ray Spectra Detected with HgI_2 at Room Temperature," *Appl. Phys. Lett.,* 28, pp. 357-359, 1976.

7. J.S. Iwanczyk, A.J. Dabrowski, G.C. Huth, and W. Drummond, "Continuing Development of Mercuric Iodide X-ray Spectrometry," *Advances in X-ray Analysis,* Vol. 27, pp. 405-414, 1984.

8. A.J. Dabrowski, W.M. Szymczyk, J.S. Iwanczyk, J.H. Kusmiss, W. Drummond, and L. Ames, "Progress in Energy Resolution of Mercuric Iodide (HgI_2) X-ray Spectrometers," *Nucl. Instrum. Methods,* 213, pp. 89-94, 1983.

9. N.L. Skinner, C. Ortale, M.M. Schieber, and L. van den Berg, "Preparation and Evaluation of Mercuric Iodide for Crystal Growth," *Nucl. Instrum. Methods Phys. Res. A,* 283, pp. 119-122, 1989.

10. A. Burger, S. Morgan, C. He, E. Silberman, L. van defi Berg, C. Ortale, L. Frank, and M. Schieber, "A Study of Homogeneity and Deviations from Stoichiometry in Mercuric Iodide," *J. Crystal Growth,* 99, pp. 988-993, 1990.

11. G. Dishon, M. Schieber, L. Ben-Dor, and L. Halitz, "On the Stoichiometry in HgI_2," *Mat. Res. Bull.,* 16, pp. 565-574, 1981.

12. I.F. Nicolau, and G. Rolland, "Deviation from Stoichiometry in α-HgI_2," *Mat. Res. Bull.,* pp. 759-770, 1981.

13. M.C. DeLong, and Rosenberger, "Stoichiometry and Purity in HgI_2," *Mat. Res. Bull.,* 16, pp. 1445-1454, 1981.

14. R.C. Whited, and L. van den Berg, "Native Defect Compensation in HgI_2 crystals," *IEEE Trans. Nucl. Sci.,* NS-24, pp. 165-167, 1977.

15. X.J. Bao, T.E. Schlesinger, R.B. James, R.H. Stulen, C. Ortale, and A.Y. Cheng, "Incorporation of Defects during Processing of Mercuric Iodide Detectors," *J. Appl. Phys.,* 68, pp. 86-92, 1990.

16. R.B. James, X.J. Bao, T.E. Schlesinger, J.M. Markakis, A.Y. Cheng, and C. Ortale, "Low-temperature Photoluminescence Studies of Mercuric-iodide photodetectors," *J. Appl. Phys.,* 66, pp. 2578-2584, 1989.

17. X.J. Bao, T.E. Schlesinger, R.B. James, G.L. Gentry, A.Y. Cheng, and C. Ortale, "Studies of Semi-transparent Palladium Contacts on Mercuric Iodide by Photoluminescence and Thermally Stimulated Current Measurements," *J. Appl. Phys.,* 69, 4247-4252, 1991.

18. X.J. Bao, T.E. Schlesinger, R.B. James, R.H. Stulen, C. Ortale, and L. van den Berg, "Investigation of Copper Electrodes for Mercuric Iodide Detector Applications," *J. Appl. Phys.,* 67, pp.7265-7267, 1990.

19. R.B. James, X.J. Bao, T.E. Schlesinger, C. Ortale, and A.Y. Cheng, "Effects of Indium and Tin Overlayers on Photoluminescence Spectrum of Mercuric Iodide," *J. Appl. Phys.,* 67, pp. 2571-2575, 1990.

20. X.J. Bao, "Defects in Red Mercuric Iodide Related to Device Applications," *Dissertation for Ph.D.,* Carnegie Mellon University, 1991.

21. X.J. Bao, T.E. Schlesinger, R.B. James, R.H. Stulen, A.Y. Cheng, V. Gerrish, and C. Ortale, "Correlations Between Mercuric Iodide Photoluminescence Spectra and Nuclear Detector Performance," *Nucl. Instrum. Methods Phys. Res. A,* to be published.

22. M. Schieber, R.C. Carlston, H.A. Lammonds, P.T. Randtke, F.W. Schnepple, and J. Llacer, "Purification, Growth, and Characterization of Alpha Mercuric-Iodide Crystals for Gamma-ray Detection," *J. Crystal Growth,* 24/25, pp. 205-211, 1974.

25. J.S. Iwanczyk, "Advances in Mercuric Iodide X-ray Detectors and Low Noise Preamplification Systems," *Nucl. Instrum. Methods Phys. Res. A,* 283, pp. 208-214, 1989.

26. M. Schieber, M. Roth, and W.F., Schnepple, "Crystal Growth and Applications of Mercuric

Iodide," *J. Crystal Growth,* 65, pp. 353-364, 1983.

27. X.J. Bao, T.E. Schlesinger, R.B. James, C. Ortale, L. van den Berg, "High Resolution 4.2 K Photoluminescence Near Bandgap Photoluminescence Spectrum of Mercuric Iodide," *J. Appl. Phys.,* 68, pp. 2951-2954, 1990.

28. B.V. Novikov, and M.M. Pimonenko, "Exciton Absorption and Luminescence of Tetragonal HgI_2 at Low Temperatures," *Sov. Phys. Semicond.,* 4, pp. 1785-1789, 1971.

29. B.V. Novikov, and M.M. Pimonenko, "Influence of Temperature on the Exciton Luminescence of Tetragonal HgI_2 Single Crystals," *Sov. Phys. Semicond.,* 6, pp. 671-673, 1972.

30. I.K. Akopyan, B.V. Bondarenko, B.A. Kazennov, and B.V. Novikov, "Luminescence of α-HgI_2 Crystals," *Sov. Phys. Solid State,* 29, pp. 238-243, 1987.

31. J.L. Merz, Z.L. Wu, L. van den Berg, and W.F. Schnepple, "Low Temperature Photoluminescence of Detector-grade HgI_2," *Nucl. Instrum. Methods,* 213, pp. 51-64, 1983.

32. I Beinglass, G. Dishon, A. Holzer, and M. Schieber, "Improved Crystals of Mercuric Iodide Grown in a Horizontal Furnace from the Vapor Phase Using the Temperature Oscillation Method," *J. Crystal Growth,* 42, pp. 166-170, 1977.

33. M. Schieber, I. Beinglass, G. Dishon, A. Holzer, and G. Yaron, "State-of-the-art of Crystal Growth and Nuclear Spectroscopic Evaluation of Mercuric Iodide Radiation Detectors," *Nucl. Instrum. Methods,* 150, pp. 71-77, 1978.

34. S. Nikitine, and R. Kleim, "Some Properties of the Luminescence of the Red Mercuric Iodide," *Phys. Lett.,* 20, pp. 341-343, 1966.

Nuclear Instruments and Methods in Physics Research A322 (1992) 435–441
North-Holland

NUCLEAR
INSTRUMENTS
& METHODS
IN PHYSICS
RESEARCH
Section A

Photoluminescence investigations of defects introduced during processing of mercuric iodide nuclear detectors

R.B. James
Advanced Materials Research Division, Sandia National Laboratories, P.O. Box 969, Livermore, California 94550, USA

X.J. Bao and T.E. Schlesinger
Department of Electrical and Computer Engineering, Carnegie Mellon University, Pittsburgh, PA 15213, USA

A.Y. Cheng, C. Ortale and L. van den Berg
EG&G Energy Measurements, Inc., 130 Robin Hill Road, Goleta, CA 93116, USA

Low-temperature photoluminescence (PL) spectroscopy was performed on a variety of HgI_2 samples to determine the effects of chemical etching with KI and HNO_3 solutions and the modifications in the PL spectra due to the presence of carbon, chromium and parylene films. These investigations reveal that the processing steps used to manufacture HgI_2 nuclear detectors can lead to the incorporation of new defects into the near-surface region of the crystals. Moreover, correlations between the photoluminescence spectra and detector performance show that some of these defects are undesirable for producing high-quality devices.

1. Introduction

Mercuric iodide (HgI_2) has several properties that make it desirable for use as an X-ray and gamma-ray spectrometer [1–5]. Both the Hg and I have high atomic masses (i.e., $Z = 80$ and 53, respectively), so the material has superior ability to attenuate energetic photons. In its red tetragonal form, HgI_2 is photosensitive and the number of charge carriers produced in the crystal is proportional to the incident photon energy. The material also has a high bulk resistivity (about 10^{13} Ω cm), which ensures a low dark current for room temperature operation of the detectors. Although the potential for manufacturing state-of-the-art spectrometers from HgI_2 crystals has been clearly demonstrated [6], the production of consistently reliable devices continues to present significant challenges due to defects contained in the as-grown crystals and defects that are introduced during processing of the detectors. These defects often act as carrier traps, which reduce the charge collection in fabricated devices and degrade their performances. Most of the difficulties with processing stem from the fact that HgI_2 has a high vapor pressure and it is easily deformed, sensitive to heating and chemically very reactive.

The fact that there are crystals that never produced high-quality spectrometers and also crystals that produced both good and bad devices implies that both crystal growth and processing introduce defects that limit the performance of working detectors. The characterization of these defects has been pursued by many workers using a variety of techniques, both in bulk crystals and fabricated detectors [7–21]. The focus of this work is on the use of low-temperature photoluminescence (PL) spectroscopy to study defects incorporated during detector processing and the role of these defects on detector quality. Typical processing steps include chemical etching, vacuum exposure, surface heating, deposition of electrical contacts and encapsulation. The effects of vacuum exposure and surface heating have been covered in an earlier publication [12], and they will not be discussed further in this paper.

Photoluminescence measurements provide a nondestructive method to analyze those defects that act as radiative recombination centers in the material. Several studies of the PL spectra of HgI_2 have been previously conducted and some of the features in the spectra have been related to stoichiometry [9–12], contaminants [13,14], and detector performance [15–18].

2. Experiment

The photoluminescence measurements were conducted using an argon ion laser tuned to 4880 Å as an excitation source. The laser beam was chopped at a frequency of 750 Hz and operated at a power of 20

mW. The spot size of the laser excitation on the samples was about 1 mm in diameter. The HgI_2 crystals were cooled in an optical cryostat with liquid helium. The liquid helium was always kept below the specimen to obtain optimal light collection. The PL was dispersed by a SPEX 1404 double-pass spectrometer and detected by a Hamamatsu R943-02 photomultiplier with a S-20 response. The output of the photomultiplier was amplified by a Keithley 427 current amplifier and an EG&G 5207 lock-in amplifier. The spectral resolution of the PL spectrum in the near-band-edge region was about 0.5 Å. The photoluminescence was generated from a region with a depth of less than a few microns from the surface.

The HgI_2 crystals used in this study were grown at EG&G Energy Measurements, Santa Barbara Operations by a method described in a previous publication [22]. Slices of HgI_2 with a cross section of about 1×1 cm were cut along the crystallographic C plane [23] to a thickness of about 0.06 cm using a thread dipped into a KI aqueous solution. The slices were then polished on each side in a 10% KI solution, followed by a rinse in de-ionized water.

In the chemical etching experiments, samples were immersed in either a 10% aqueous solution (by weight) of KI or 10% solution (by volume) of reagent-grade HNO_3. The specimens were etched for 2 min, while the solutions were mildly agitated. The KI treatment removes a surface layer of about 54 μm as measured by a Tencor Instruments Alpha Step 200 profiler. After chemical etching, the samples were rinsed with de-ionized water for about 2 min, then loaded into the optical cryostat.

The experimental procedure was to first perform the photoluminescence on several different spots in the as-received samples, then to chemically etch the samples and repeat the PL measurements on approximately the same spots. Several samples were used in this experiment, some of which were first etched with KI solution followed by HNO_3 and others that were first etched with HNO_3 followed by KI. Data from many different spots on each sample were obtained to understand any spot to spot variation in the material.

After chemical etching of the HgI_2 crystals, electrical contacts were deposited on both the front and back sides. The contact deposition process typically involves the thermal evaporation or sputtering of elemental metals. Ideally, one would like an electrical contact to be conducting, stable in air, inert and well bonded to the HgI_2 substrate and for some applications, transparent to visible light. The process of depositing contacts is a crucial step regarding the introduction of defects, because the near-surface region of the crystal is subjected to heating while in vacuum and a significant amount of material loss occurs by way of sublimation. In addition, HgI_2 is known to be very reactive and temperature-sensitive, changing to the yellow orthorhombic phase at about 399 K [7]. Because of these problems, HgI_2 slices are extremely vunerable to damage during deposition of electrical contacts and only a few materials have been successfully used as contacts for detector applications. These materials include carbon, palladium, gold and indium–tin-oxide [4,24]. Although these contacts have yielded working detectors, there still remains a wide degree of variability in the performances of fabricated devices. Since the ideal contact material for each detector application has not yet been determined, measurements of contact chemistry, diffusion of contact materials into HgI_2 and device performance for detectors employing different contact materials continue to be of current interest.

In this paper we also report studies of the effects of carbon and chromium contacts on the photoluminescence of HgI_2. Similar investigations have been reported for palladium [11,25], indium–tin-oxide [16,17], indium [18], tin [18] and copper [14] films. Thin (~ 100 Å) semitransparent layers of carbon or chromium were deposited onto the front and back sides of several different mercuric iodide slabs. An alumina mask with a 0.5-cm diameter circular aperture was placed over each sample during the deposition, so that part of the HgI_2 slab would be covered by a thin layer of carbon or chromium and part of the slab would be bare HgI_2 crystal. By comparing the PL spectra from points beneath the electrical contact and adjacent to it, the effects of the contact deposition process on the radiative recombination centers were determined.

The semitransparent films of carbon were sputtered onto the HgI_2 and the chromium films were thermally evaporated from a tungsten wire basket. Each specimen was situated on top of a glass witness slide and the transparency of the film deposited onto the witness slide was used as an indicator of the transparency of the carbon or chromium film deposited onto the HgI_2 substrate. Most of the films used in this work had a transparency of between 30 and 50% on the glass witness slides.

After contact depositions, colloidal carbon is often used to attach a 1-mil palladium wire to the front and back contacts of each specimen, so that an electrical bias can be applied during detector operation. Detectors are next encapsulated in parylene to prevent the exposure of the crystal to air and hopefully reduce problems associated with aging. The parylene polymers were deposited from the vapor phase at a pressure of about 0.1 Torr. The mean free path of the gas molecules in the deposition chamber is about 0.1 cm, so that the deposition is not line-of-sight and all sides of the HgI_2 crystal are uniformly coated. Results for the effects of parylene coatings on the photoluminescence spectrum of HgI_2 are also investigated for samples that were aged for a period of approximately two years after the

coating was deposited. These results are compared to a different HgI_2 crystal that was also aged for about two years but did not receive a parylene coating.

3. Results and discussion

The top curves in fig. 1 display a typical photoluminescence spectrum at 4.2 K from a bare HgI_2 crystal that was stored in a dessicator for about 30 days after chemical etching with KI. There are approximately 26 emission lines between 5290 and 5410 Å, which lie slightly below the bandgap (5230 Å at 4.2 K) [26]. These emission lines are collectively labeled as Band 1, since they merge into a single band at higher temperatures. Although all of the emission lines are not clearly visible in fig. 1a, they can be resolved in many samples by simply magnifying the PL intensity in selected spectral regions. The Band-1 photoluminescence is usually dominated by two bound excitons (P2 and P3) at about 5317 and 5320 Å. The intensity of the bound exciton P3 has previously been related to mercury-deficient or iodine-rich material [12]. A more detailed discussion of the PL peaks in the Band 1 region is contained in ref. [26]. Fig. 1b shows the effect of chemical etching this sample in a 10% KI solution. In general, the overall PL intensity will increase after KI etching, although the amount of the increase is highly dependent on the degree of aging of the HgI_2 surface. This increase in the PL efficiency is due to a decrease in the surface recombination after etching and/or a reduction in the amount of nonradiative electron–hole recombination centers in the bulk. Another effect of KI etching is to greatly increase the magnitude of the P3 emission relative to the other emission lines. At longer wavelengths, the PL spectra also show the presence of a broad band emission peaked at about 7500 Å (labeled Band 4) after KI etching. The peak intensity of this band is about three orders of magnitude smaller than the peak intensity of P3.

The increase in the absolute intensity of P3 is often more than one order of magnitude, depending on the time elapsed after the previous KI etch and the stoichiometry of the as-grown crystal. Since P3 has been attributed to mercury-deficient material and P3 is greatly increased after removal of the surface layer, it can be inferred that the surface layer becomes mercury-rich upon aging in air. This is most likely due to the preferential loss of iodine from the surface during the time the specimens are stored in a dessicator, since iodine has a higher vapor pressure than mercury at 300 K [10]. The chemical etching effectively removes the mercury-rich surface layer, leading to an increase in the concentration of defects (e.g., mercury vacancies) responsible for the P3 emission.

Fig. 1c shows the effect of HNO_3 etching on a freshly KI-etched sample. The Band-1 spectral region was not noticeably changed by HNO_3 etching; however, the emission of a new broad band (labeled Band 3) peaked at 6200 Å was observed from every spot studied on this sample. The intensity of this broad emission band represented an appreciable (10–30%) percentage of the total photoluminescence intensity. Band 3 has previously been attributed to unknown contaminants contained in HgI_2, although earlier doping measurements have not led to a conclusive determination of the particular impurity [7,10]. The introduction of Band 3 after HNO_3 etching is especially important, because the intensity of its emission is correlated to device quality (see later section on relationships to detector performance).

Similar measurements were observed when the samples were first etched with HNO_3, followed by KI etching. A few general trends were noted during these

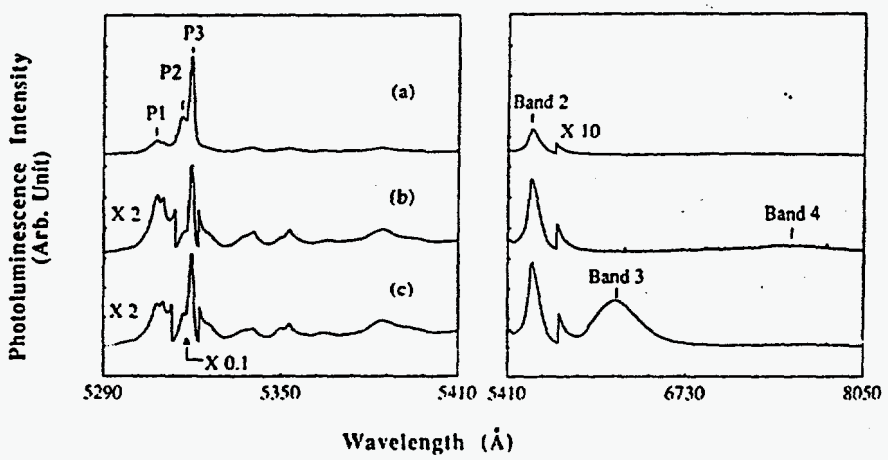

Fig. 1. 4.2-K photoluminescence spectra taken (a) after storage is a dessicator for about 30 days, (b) immediately after etching the aged sample in a KI solution, and (c) immediately after etching the specimen in HNO_3. Note the scale changes at about 5315, 5322 and 5750 Å.

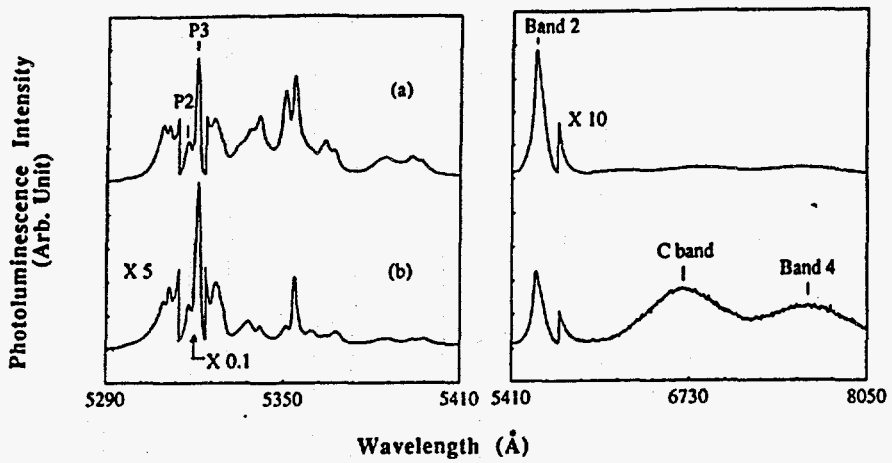

Fig. 2. Typical PL spectra obtained on a carbon-contacted HgI_2 sample at 4.2 K. The top and bottom spectra are for a point away from and beneath the semitransparent C film, respectively.

etching experiments. The Band-3 emission that was introduced after HNO_3 etching was greatly reduced after KI etching. This observation implies that Band 3 is predominantly incorporated into the near-surface region by the nitric acid etch and the subsequent KI etching of 50–60 μm of the surface effectively removes this contaminated layer. Nitric acid etching of aged HgI_2 was also found to increase the overall photoluminescence intensity, but the amount of increase was less than that observed after KI etching. This observation may be due to a slower rate of etching of 10% HNO_3 compared to 10% KI, so that a smaller amount of the aged, degraded surface layer was removed about the HNO_3 etch.

The next step for processing detectors is the attachment of electrical contacts onto both sides of the freshly etched HgI_2 slabs. At present, palladium and carbon are the most extensively used contact materials for manufacturing devices. Thus, understanding of palladium and carbon contacts on HgI_2 are of considerable practical interest, and it is also important in the optimization of the Pd and C contact deposition process. The effects of thermally evaporating palladium on the defect states in HgI_2 have been recently presented [25] and we report for the first time the effects of carbon contacts on the PL spectra of HgI_2. Figs. 2a and 2b show typical photoluminescence spectra at 4.2 K from points adjacent to and beneath a carbon contact, respectively. The Band-1 spectral region (5290–5410 Å) appears unaffected by the presence of the carbon film. The most dramatic difference in the PL is the introduction of a new broad band centered at about 6670 Å, which we label as a carbon band. The position of this band is close to a broad-band emission (peaked at 6720 Å) observed in copper-doped crystals [14]. Since the peak positions of the bands in C- and Cu-contacted HgI_2 are reproducible and distinguishable from each other, these bands are probably of different origins.

The temperature dependence of the carbon band has been studied for temperatures between 4 and 130 K. For temperatures exceeding about 130 K, the emis-

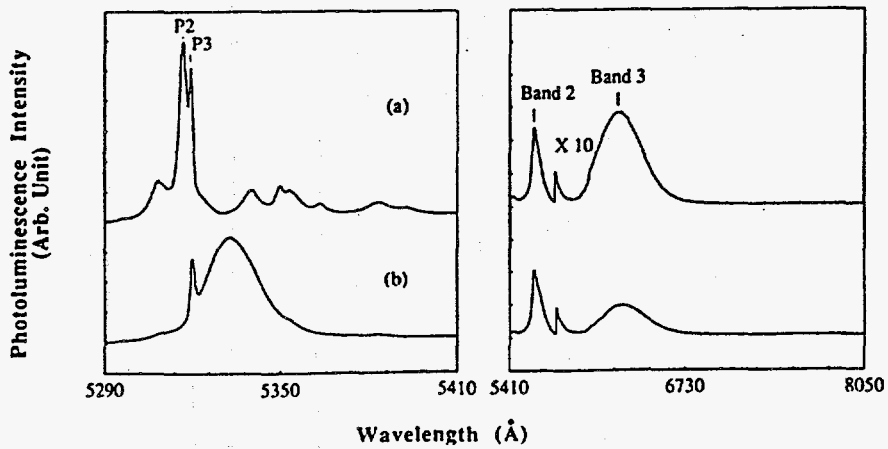

Fig. 3. The top and bottom curves show typical PL spectra obtained at 4.2 K from points away from and beneath a semitransparent Cr film, respectively.

sion of this band can no longer be resolved. An Arrhenius plot of the logarithm of the intensity of the carbon band versus the reciprocal temperature yields an activation energy for thermal dissociation of 44 meV, which is much smaller than the energy difference between the peaks of the free exciton line and carbon band (407 meV).

The results of similar measurements conducted on samples with semitransparent chromium contacts are shown in fig. 3. The top curve shows the PL spectrum from a typical point away from the Cr contact and the bottom curve shows the spectrum from a typical point beneath it. The most obvious difference between the two spectra is the appearance of a broad emission band on the long wavelength side of P3. The total intensity of this band represents a significant fraction of the total integrated luminescence. The peak of the broad band is found to vary from sample to sample and lies in the range of 5325 and 5373 Å for the four specimens studied. The variation in the peak position between different points on the same sample is only a few ångströms. This observation suggests that the Cr-deposition process (e.g., thickness of film and degree of surface heating) affects the peak position and relative magnitude of the new broad-band emission. Since a similar band has been observed for Al, Ge, Ta, In and Sn contacts [18,27], we believe that the presence of this band is associated with the interfacial chemistry between Cr and HgI_2, rather than point defects caused by Cr diffusion. Thermodynamic data for the ternary Hg–metal–I system show that Cr, Al, Ge, Ta, In and Sn all form iodides that are more stable than HgI_2 [28]. Given the similarities between the PL spectra beneath these different metal contacts, one can easily rationalize the existence of similar contact chemistry leaving the same type of defects in the metal/HgI_2 interfacial region.

Another consistent difference between the PL away from and beneath the Cr contact is that for points beneath the Cr the emission of the bound exciton P2 at 5317 Å is greatly reduced compared to bound exciton P3 at 5320 Å. The quenching of the P2 emission has also been observed beneath other metallic contacts, such as Al, Ge, Ta, In, Sn and indium–tin-oxide [16–18,27], and we believe it is also associated with similar contact chemistry between these different conducting overlayers and mercuric iodide.

After attachment of wires to the electrical contacts, the detectors are usually coated with parylene in an effort to reduce the rate of surface degradation. Fig. 4a shows the PL spectrum from a bare HgI_2 crystal that had been stored in a dessicator for approximately two years. The Band-1 emission is dominated by the bound exciton P2, and P3 is not resolved in the spectrum. Although the emission of P2 has clearly broadened upon aging, no new radiative recombination centers are manifested in the PL spectrum. Since iodine is believed to be preferentially lost from the HgI_2 surface during aging and P3 is associated with stoichiometry deviations (either mercury-deficient or iodine-rich material), it is not surprising that the emission of P3 is greatly reduced for a heavily aged crystal that has been exposed to air. Figs. 4b and 4c show typical spectra from a different HgI_2 detector that had been coated with parylene and then stored in a dessicator for about two years. The middle and bottom curves were taken from points away from and beneath the palladium contact, respectively. From fig. 4b it is clear that parylene coatings have a significant effect on the sites for radiative recombination in the near-surface region of HgI_2. Neither P2 or P3 are apparent in the spectrum and the broad emission peaked at 5329 Å resembles the luminescence feature observed beneath the Cr films (see fig. 3). The maximum intensity of this PL line

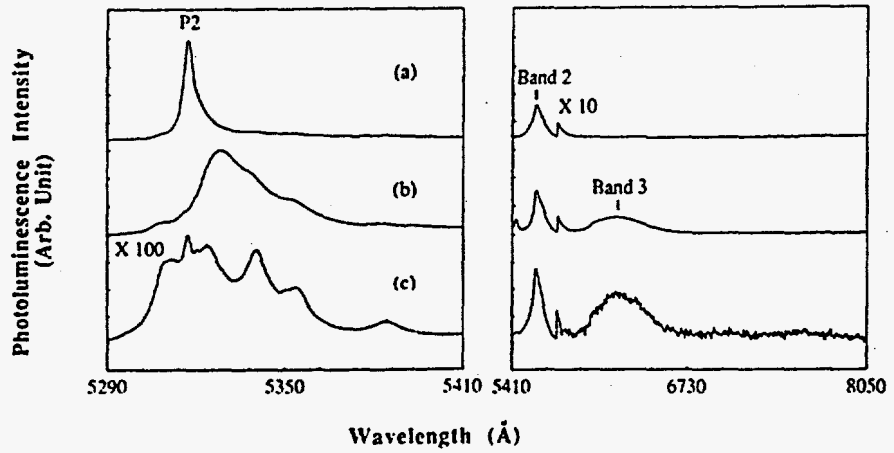

Fig. 4. Typical 4.2-K PL spectra from (a) a bare HgI_2 crystal, (b) the noncontacted region on a parylene-coated detector, and (c) beneath the Pd contact on a parylene-coated detector. Both the crystal and detector used in this experiment had been stored in a dessicator for about two years.

was found to vary between 5327 and 5345 Å for the different specimens studied. It appears that parylene also reacts chemically with HgI_2, which is useful for film adherence but often detrimental to carrier transport. Since no charge transport exists across the parylene/HgI_2 interface, it is possible the polymeric coating does not adversely affect device performance. Fig. 4c shows the PL spectrum beneath the parylene-coated Pd contact. The Pd contact on this detector is optically thick having a transparency of only a few percent. Thus, the overall PL intensity is quite weak and must be multiplied by 100. The main effect of Pd contacts on the PL is to considerably reduce the emission of both P2 and P3 without causing the introduction of new recombination centers [25]. This spectrum is typical of a freshly etched HgI_2 sample with an optically thick Pd contact, which implies that the parylene film has protected the Pd/HgI_2 interfacial region over the two-year storage period; however, it is also possible that the Pd overlayer itself is sufficient to prevent aging of the Pd/HgI_2 interface.

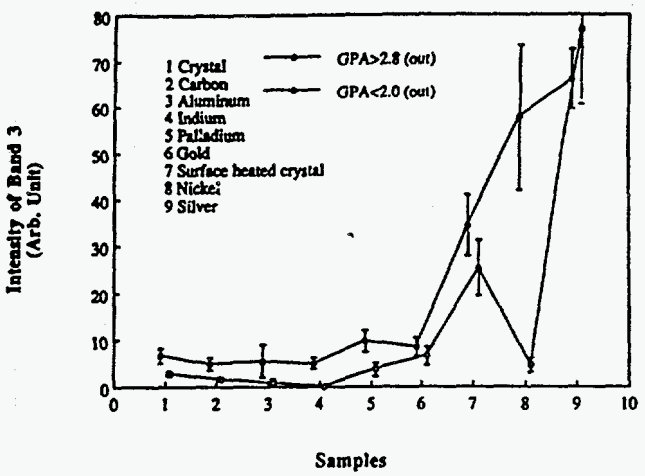

Fig. 5. Averaged peak intensities of the Band-3 luminescence for different sets of samples. The top curve is for crystals that produced detectors with GPAs less than 2.0 and the bottom curve is for those crystals with GPAs greater than 2.8.

4. Relationships to device performance

Photoluminescence data was obtained from 52 HgI_2 slices taken from fourteen different crystals. Approximately ten to twenty detectors were fabricated from each crystal and a grade of A, B, C or D was assigned according to its energy resolution and peak-to-valley ratio for ^{137}Cs radiation, where A designates the best detectors and D the worst [13]. A GPA was assigned to each crystal by using weighting factors of 4, 3, 2 and 1 for grades A, B, C and D, respectively and then taking the weighted average. Fig. 5 shows the results for the peak intensity of Band 3 for the groups of samples that have GPAs greater than 2.8 and less than 2.0. The error bars represent the standard deviation of the average intensity of the different points taken from different samples. Results for nine sets of samples are presented in the figure. The sets include bare crystals without surface treatment, bare crystals that have undergone surface heating under vacuum and crystals that have been deposited with various model contacts for studies of contact chemistry. The PL on the samples with model contacts were all taken from points adjacent to the contacted regions.

One obvious trend in fig. 5 is that the emission of Band 3 is larger in crystals that produced lower quality detectors. Although the physical identity and origin of the defect responsible for the Band-3 emission is not known, we have made several observations regarding this band that may be helpful in understanding its origin and useful in an effort to improve the processing technology used to manufacture HgI_2 devices. Three of these observations are discussed below. (1) The intensity of Band 3 varies for the as-received samples. For some crystals the intensity of Band 3 cannot be resolved and for a few crystals the Band-3 luminescence is the dominant radiative recombination center. Most specimens have a relatively weak Band 3 and the intensity of the band is usually a few percent of the total integrated PL. (2) Etching with reagent-grade HNO_3 introduces the defect responsible for Band 3 into the near-surface region of the crystals (see fig. 1). (3) The intensity of Band 3 is often modified after KI etching. Some specimens that do not show a Band-3 emission do so after KI etching [12], and others that show a significant Band-3 emission have a decrease in its intensity after the KI etch. The first observation implies that Band 3 is not solely associated with the process of chemical etching. Each of the three observations are consistent with assumption that Band 3 is due to a contaminant that can be incorporated during crystal growth or the etching process. The origin of Band 3 is probably a common impurity that is contained in the source material used to grow HgI_2 and the KI and HNO_3 etchants. Since both HgI_2 and KI contain I, it is possible that a contaminant contained in the I source material is responsible for the Band-3 luminescence. Some of the common impurities in the I source material include Cl, S, C, N, O, B, P, Si, Ni, Fe, Cr, Ca, Al, Cu, Zn and Na [29]. The particular impurity of interest must also be contained in the reagent-grade HNO_3. The primary contaminants in the HNO_3 are Cl, S, O, P, Ni, Fe and Cu. Additional studies of elemental analysis of the HgI_2 source material, HgI_2 single crystal, KI and HNO_3 need to be completed. In addition, efforts should also be placed on purification of the KI and HNO_3 used in the etching process or to consider another etchant of higher purity that can be used to

follow the KI or HNO_3 etch. A much more thorough discussion of the correlations between the HgI_2 PL spectra and nuclear detector performance will be contained in a future publication [30].

5. Conclusions

We have employed low-temperature photoluminescence spectroscopy to characterize defects introduced during chemical etching with KI and HNO_3 solutions, beneath carbon and chromium electrical contacts and beneath parylene coatings. Chemical etching is found to increase the overall photoluminescence efficiency by reducing the traps responsible for nonradiative recombination. Etching with reagent-grade HNO_3 introduces an emission band peaked at 6200 Å that is found to be detrimental to detector performance. Both carbon and chromium contacts modify the PL spectrum of HgI_2. Carbon contacts introduce a new luminescence feature peaked at about 6670 Å, which is most likely due to carbon diffusion. Chromium introduces a relatively large emission band peaked between 5225 and 5373 Å, which is probably due to the formation of chromium iodides at the Cr/HgI_2 interfacial region. Parylene coatings are also found to alter the electron–hole recombination in the near-surface region of HgI_2. In general, the photoluminescence results provide clear evidence that the processing procedures and choice of contact material play important roles in terms of incorporating new defects into HgI_2 detectors and that some of these defects have a direct influence on the quality of gamma-ray detectors.

Acknowledgements

We would like to acknowledge the U.S. Department of Energy for financial support. One of us (T.E.S.) would also like to acknowledge support from the National Science Foundation through a Presidential Young Investigator award. We would also like to thank A. Antolak, D. David and M. Khudatyan for many useful discussions.

References

[1] W.R. Willig, Nucl. Instr. and Meth. 96 (1971) 615.
[2] H.L. Malm, IEEE Trans. Nucl. Sci. NS-19 (1972) 263.
[3] J.P. Ponpon, R. Stuck and P. Siffert, Nucl. Instr. and Meth. 119 (1974) 297.
[4] J.H. Howes and J. Watling, Mater. Res. Soc. Symp. Proc. Vol. 16 (1983) 207.
[5] H.L. Malm, T.W. Raudoff, M. Martina and H.R. Zanio, IEEE Trans. Nucl. Sci. NS-20 (1973) 500.
[6] R.C. Whited and M. Schieber, Nucl. Instr. and Meth. 162 (1979) 119.
[7] R.H. Bube, Phys. Rev. 106 (1957) 703.
[8] B.N. Novikov and M.M. Pimonenko, Sov. Phys. Semicond. 4 (1971) 1785.
[9] Z.L. Wu, J.L. Merz, L. van den Berg and W.F. Schnepple, J. Lumin. 24 (1981) 197.
[10] J.L. Merz, Z.L. Wu, L. van den Berg and W.F. Schnepple, Nucl. Instr. and Meth. 213 (1983) 51.
[11] D. Wong, X.J. Bao, T.E. Schlesinger, R.B. James, A.Y. Cheng, C. Ortale and L. van den Berg, Appl. Phys. Lett. 53 (1988) 1537.
[12] X.J. Bao, T.E. Schlesinger, R.B. James, R.H. Stulen, C. Ortale and A.Y. Cheng, J. Appl. Phys. 68 (1990) 86.
[13] R.B. James, D.K. Ottesen, D. Wong, T.E. Schlesinger, W.F. Schnepple, C. Ortale and L. van den Berg, Nucl. Instr. and Meth. A283 (1989) 188.
[14] X.J. Bao, T.E. Schlesinger, R.B. James, R.K. Stulen, C. Ortale, and L. van den Berg, J. Appl. Phys. 67 (1990) 7265.
[15] D. Wong, T.E. Schlesinger, R.B. James, C. Ortale, L. van den Berg and W.F. Schnepple, J. Appl. Phys. 64 (1988) 2049.
[16] R.B. James, X.J. Bao, T.E. Schlesinger, J.M. Markakis, A.Y. Cheng and C. Ortale, J. Appl. Phys. 66 (1989) 2578.
[17] R.B. James, X.J. Bao, T.E. Schlesinger, J.M. Markakis, A.Y. Cheng and C. Ortale, in: Fluorescence Detection III, ed. E.R. Menzel, Proc. SPIE 1054 (1989) 103.
[18] R.B. James, X.J. Bao, T.E. Schlesinger, C. Ortale and A.Y. Cheng, J. Appl. Phys. 67 (1990) 2571.
[19] I.Kh. Akopyan, B.V. Bondarenko, B.A. Kazennov and B.V. Novikov, Sov. Phys. Solid State 29 (1987) 238.
[20] P.M. Petroff, Y.P. Hu and F. Milstein, J. Appl. Phys. 66 (1989) 2525.
[21] L.R. Williams and R.J. Anderson, in: Picosecond and Femtosecond Spectroscopy from Laboratory to Real World, ed. K.A. Nelson, Proc. SPIE 1209 (1990) 140.
[22] H.A. Lamonds, Nucl. Instr. and Meth. 213 (1983) 5.
[23] A. Jeffrey and M. Vlasse, Inorg. Chem. 6 (1967) 396.
[24] J.M. Markakis and A.Y. Cheng, Nucl. Instr. and Meth. A283 (1989) 232.
[25] X.J. Bao, T.E. Schlesinger, R.B. James, G.L. Gentry, A.Y. Cheng and C. Ortale, J. Appl. Phys. 69 (1991) 4247.
[26] X.J. Bao, T.E. Schlesinger, R.B. James, C. Ortale and L. van den Berg, J. Appl. Phys. 68 (1990) 2951.
[27] R.B. James, X.J. Bao and T.E. Schlesinger, unpublished.
[28] E.A. Brandes, Smithells Metals Reference Book, 6th ed. (Butterworths, London, 1983) pp. 8–58.
[29] Y.F. Nicolau, Nucl. Instr. and Meth., 213 (1983) 13.
[30] X.J. Bao, T.E. Schlesinger, R.B. James, R.H. Stulen, A.Y. Cheng, V. Gerrish and C. Ortale, Nucl. Instr. and Meth., in press.

Left Intentionally Blank

Nuclear Instruments and Methods in Physics Research A322 (1992) 414–420
North-Holland

NUCLEAR INSTRUMENTS & METHODS IN PHYSICS RESEARCH
Section A

Carrier traps and transport in mercuric iodide

T.E. Schlesinger and X.J. Bao
Department of Electrical and Computer Engineering, Carnegie Mellon University, Pittsburgh, PA 15243, USA

R.B. James
Advanced Materials Research Division, Sandia National Laboratories, P.O. Box 969, Livermore, CA 94550, USA

A.Y. Cheng, C. Ortale and L. van den Berg
EG&G Energy Measurements, Inc., 130 Robin Hill Road, Goleta, CA 93116, USA

Thermally stimulated current spectroscopy (TSC) was performed on a variety of mercuric iodide samples and detectors to determine the nature and origin of deep traps in this material. It is shown that the trap type and concentration is a function of the metal overlayer employed as a contact material. The energy barrier height as well as the type (electron or hole) of barrier at the metal/semiconductor interface has also been determined by internal photoemission measurements. When polarization effects are not present, as is the case in most Pd contacted samples, the barrier height can be accurately determined by this technique. A value of 1.05 eV was measured for a hole barrier at the Pd/HgI_2 interface.

1. Introduction

Many workers have focussed their attention on mercuric iodide (HgI_2) as a promising material for producing the highest sensitivity and resolution room temperature nuclear detectors. Indeed some extremely high quality X-ray and gamma-ray detectors have been fabricated using this material [1,2]. In an ideal situation, when using this material in this application, photogenerated carriers created in the semiconductor material will all be swept towards the contacts by a uniform electric field present in the detector due to the externally applied bias. These carriers will all be a collected at the contacts and thus both sensitivity and energy resolution would be limited only by the intrinsic material properties or underlying physical interactions between the radiation and the material. This ideal case does not describe existing detectors and the difference between an "ideal" and "real" detector is shown schematically in fig. 1. In the "real" detector one finds that detector performance is limited by the presence of surface states as well as intrinsic and extrinsic defects and impurities. In particular, the presence of energy barriers at the contacts may prevent complete charge collection, the presence of trapped charges creates non-uniform internal electric fields which also degrade charge collection, and the presence of deep traps which may capture and re-emit carriers further broads detector response. The primary goal of the studies reported in this paper is to characterize the deep traps present in mercuric iodide and to determine the energy barriers present at the metal/semiconductor interface. By determining the origin of the traps and nature of these energy barriers, contact materials as well as processing conditions can be suggested which will ultimately improve detector performance.

The electrical properties of HgI_2 have been studied by many workers using a variety of techniques [3–5]. Current–voltage and capacitance–voltage techniques provide measures of the barrier heights of electrical contacts and dielectric properties in certain frequency ranges. Often purely electrical measurements are limited by the extremely high resistivity of HgI_2 and thus many techniques are combined with some external excitation source such as photons or α-particles. α-particles have a very short absorption length in HgI_2 and are typically used to measure carrier lifetimes and mobility products [6]. Near-band-gap photons have been used to perform photocurrent and photoresponse measurements [7–9]. Below-band-gap photons can be used to measure barrier heights and also impurity conduction. Thermally stimulated current spectroscopy (TSC) and internal photoemission measurements are the two experimental tools which we have employed in this study. TSC reveals characteristics of deep traps in semi-insulating material including trap energy levels, relative concentrations, and whether the center is an electron or hole trap. Reviews and detailed descrip-

tions of this technique can be found in the literature [10–13]. Internal photoemission measurements provide a fairly direct measure of the barrier height at the metal/semiconductor interface.

Several researchers have performed TSC measurements on HgI_2. Some of them have tentatively related TSC peaks they have observed to stoichiometry, energy resolution, polarization effects in detectors, and structural imperfections such as dislocations. Mohammed-Brahim [14] has observed that HgI_2 crystals which show a 170 K peak in the TSC spectra are also able to make detectors that can resolve the 59.6 keV radiation from a ^{241}Am source. It is also observed that prolonged (24 h) illumination by near-band-gap monochromatic light (5900 Å) at room temperature enhances the magnitude of this peak and improves the energy resolution of the detectors. Whited and Van den Berg [15] performed TSC measurements on HgI_2 samples doped with mercury or iodine. They attributed an 81 K peak (observed in undoped samples) and an 89 K peak

Table 1
Summary of the results of thermally stimulated current measurements obtained from the literature. The comments associated with particular traps are explained in detail in the quoted references.

Ref.		T_1	T_2	T_3	T_4	T_5	T_6	T_7	T_8	T_9	T_{10}	T_{11}
[19]	T_m [K]	99	109	121	138	153	168	186	203			
	E_i [eV]	0.24	0.28	0.32	0.38	0.39	0.42	0.50	0.52			
	comments											
[20]	T_m [K]			129	142		172	196		222	267	293
	E_i [eV]			0.34	0.38		0.45	0.51		0.59	0.77	
	comments											
[15]	T_m [K]	81 and 89	98	102	138		162	180	214	220		
	E_i [eV]						0.32					
	comments	V_I and V_{I_2}	e	h	h		h	h	V_{Hg}^{2-},e	I_{Hg}^{2+},h		
[21]	T_m [K]		112						212			
	E_i [eV]		0.17						0.45			
	comments		h						h			
[22]	T_m [K]	95	116		132	144	168	178	200			
	E_i [eV]	0.15–0.23	0.19–0.28		0.12–0.29	0.27–0.35	0.36–0.49	0.37–0.51	0.43–0.54			
	comments	slow	fast		slow	fast	slow	slow	fast			
[23]	T_m [K]						170	180		230	252	280
	E_i [eV]						0.46	0.46		0.63	0.62	0.70
	comments							I-strg			aged	baked
[24]	T_m [K]						167			233		
	E_i [eV]						0.26			0.73		
	comments											
[9]	T_m [K]		102			143	159	170	196			
	E_i [eV]		0.28			0.36	0.40	0.43	0.51			
	comments											
[25]	T_m [K]	107	112	125		145	170	190	200	217	245	
	E_i [eV]											
	comments		e			h				h		
[16]	T_m [K]	100	110	125		155	173		205	225		
	E_i [eV]	0.16	0.28	0.32		0.40	0.45		0.50	0.59		
	comments						bad					
[18]	T_m [K]		114			145				217		
	W_i [eV]		0.19			0.22				0.45		
	comments		clv			clv				h		
[14]	T_m [K]	96(8)	112(5)	125	140	155(60)	170	185	204		252	275
	E_i [eV]	0.10–0.13	0.16–0.19	0.20–0.23	0.21–0.26	0.25–0.30	0.50–0.59	0.40–0.44	0.43			
	comments						good					

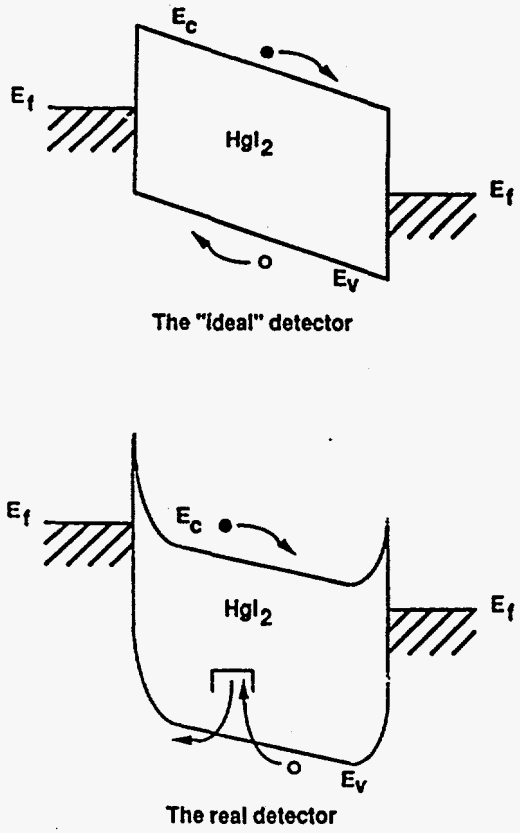

Fig. 1. Schematic representation comparing the operation of an "ideal" detector with that of a "real" detector. The "real" detector is subject to the presence of an energy barrier at the contacts, non-uniform electric fields, and deep traps.

(observed in heavily mercury doped samples) to V_I (iodine vacancy) and V_{I_2} levels respectively. Two TSC peaks at higher temperatures of 220 K and 214 K in mercury and iodine doped crystals, respectively, were assigned to V_{Hg}^{2-} (mercury vacancy, electron trap) and I_{Hg}^{2+} (mercury interstitial, hole trap). Tadjine et al. [16,17] found that an intense TSC peak at 173 K is related to fast polarization in detectors which degrades the energy resolution as tested by the 5.9 keV line of ^{55}Fe. This TSC peak was also observed to be more intense in crystals with strong stoichiometric deviations (iodine rich). Stuck et al. [18] observed a TSC peak at 217 K in etched samples. This was identified as a hole trap since it was present only when the illuminated electrode was positively biased. Two additional peaks at 114 K and 145 K were detected in cleaved samples and were attributed to dislocations. TSC results from the literature are summarized in table 1. A total of eleven TSC peaks have been observed and are labeled as T_I to T_{II}. The positions of these peaks agree fairly well among various authors even though there is some variation in the peak magnitudes. This latter variation is most likely due to differences in crystal growth, measurement configurations, illumination intensity, duration, and wavelength, or contacts used. The variation in thermal activation energy among various authors is most likely due to the different procedures used to obtain these values.

2. Experimental

HgI_2 crystals used in this work were grown at EG&G Energy Measurements Inc. by the temperature oscillation method. Slices about 0.5–1.0 mm thick and 1.0×1.0 cm in size were cut along the crystallographic c plane using a thread dipped in KI (aqueous) solution. The slices were next polished in a 20% KI solution, followed by a 30 s etch in a 10% KI solution and a 5 min rinse in deionized water. Semitransparent (for the TSC measurements) contacts were deposited by evaporation through a mask with a circular opening about 0.6 cm in diameter. Thus only a portion of the surface was contacted. The contacts for the TSC measurements were about 50% transparent as determined from films deposited at the same time on an adjacent glass slide. The samples were then mounted on an alumina substrate using Dow Corning 3140 RTV silicone rubber. A thermocouple placed near the substrate during the metal deposition was used to monitor the substrate temperature.

The TSC measurements were made by biasing the sample with a 12 V battery and measuring the current as a function of temperature. The traps were filled at the starting temperature (77 K or 4.2 K) by illuminating the semitransparent electrode with an argon laser for 5 min. The current was measured using a Keithly 619 electrometer. The temperature was measured by a miniature Si temperature sensor pressed against the alumina substrate near the HgI_2. Heating was provided by a 25 Ω resistive heater wire wrapped around a copper finger onto which the sample was attached. For each TSC spectrum, the heater voltage was fixed so that the heating rate was a slow monotonically decreasing function of temperature and thus the heating rate was calculated in the vicinity of each peak. Different average heating rates were obtained by applying different voltage to the heater.

For the internal photoemission measurements the samples were illuminated from the back surface. This surface was contacted at a small point using a colloidal carbon solution. The wavelength dependent illumination was provided by a 100 W halogen lamp which was directed through a SPEX spectrometer whose resolution was set to about 30 Å. The photoresponse was measured in the wavelength range 5000–10 000 Å without a bias being applied to the sample.

3. Results and discussion

3.1. TSC

Although the TSC traps are observed at temperatures below 200 K they may nonetheless play a significant role in determining detector performance at room temperature. As an example consider a trap with an activation energy of 0.54 eV and a capture cross section of 10^{-14} cm^2 (chosen as a reasonable number). The detrapping time of such a trap at room temperature would be about 400 μs which is greater than both the electron or hole lifetimes (typically 1 μs). Nuclear detectors are usually biased so that the transit time of carriers is less than their lifetimes, so that the majority of carriers are collected before they recombine. Thus a trap such as the one described above can lead to incomplete charge collection and degraded energy resolution since the trapping time is fast and the detrapping time longer than the acquisition time.

For Pd contacted samples three traps were observed at 10, 146, and 165 K. The activation energies obtained for the first and last of these traps were 0.01 eV and 0.54 eV, with the second trap not well enough resolved to obtain an activation energy. Our observations regarding these traps have been reported elsewhere [26]. For Ag contacted samples three major peaks were observed at temperatures of 90, 96, and 212 K. The resolution of these peaks only allowed for the determination of the activation energy of the trap at 212 K, and its activation energy was determined to be 0.92 eV. In the case of silver contacted samples there

Table 2
Summary of results of thermally stimulated current measurements in this work.

Contact		T_1	T_2	T_3	T_5	T_6	T_8	T_{10}
Cu	T_m [K]			116		161		
	β [K/s]			0.51		0.34		
	comments			h		h		
Ag	T_m [K]	90	96				212	
	β [K/s]	0.27	0.39				0.14	
	comments							
Al	T_m [K]	83		119	146	170		
	β [K/s]	0.24		0.48	0.38	0.30		
	comments							
Mg	T_m [K]				147	162	206	273
	β [K/s]				0.39	0.35	0.25	0.16
	comments					e		e
Au	T_m [K]						193	
	β [K/s]						0.28	
	comments						h	
Ni	T_m [K]	89			147	166	202	
	β [K/s]	0.21			0.39	0.33	0.24	
	comments				e	e	h	
In	T_m [K]	87		119	150	168		
	β [K/s]	0.24		0.56	0.39	0.33		
	comments							
Sn	T_m [K]				149	163		
	β [K/s]				0.44	0.40		
	comments							
Pd	T_m [K]				149	163		
	β [K/s]				0.44	0.40		
	comments					e		
Cr	T_m [K]				144	157	211	
	β [K/s]				0.10	0.086	0.058	
	comments							
ITO	T_m [K]		95	113	144	165	213	
	β [K/s]		0.59	0.61	0.35	0.35	0.29	
	comments			h		e		

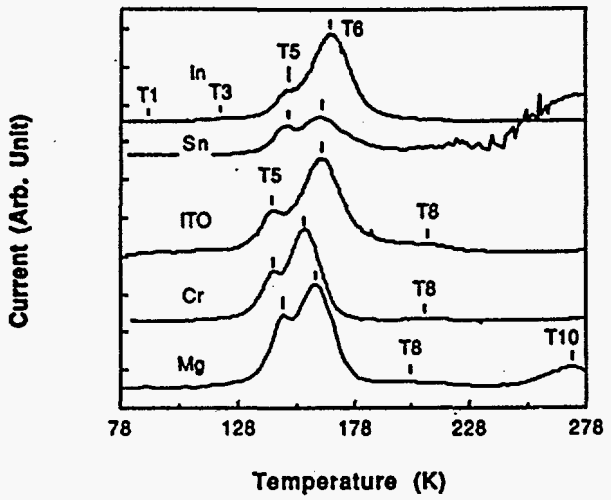

Fig. 2. TSC spectra for (a) In, (b) Sn, (c) ITO, (d) Cr, and (e) Mg.

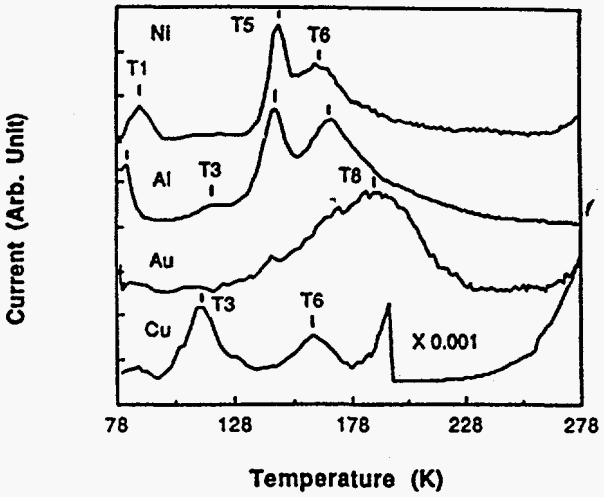

Fig. 3. TSC spectra for (a) Ni, (b) Al, (c) Au, and (d) Cu. There is a scale change in the spectrum of Cu where the dark current begins to rise dramatically at near room temperature.

was also observed a large increase in the background "dark" current at temperatures above 240 K indicating that Ag plays a role in lowering the resistivity of mercuric iodide. During the study of Ag contacted HgI_2 a pyroelectric effect was also observed. While the mechanism of this observed pyroelectric effect in Ag contacted mercuric iodide is not known, it is worth mentioning that silver ion movement is quite likely because α-AgI is a well known superionic conductor [27]. In superionic materials, ionic conductivity as high as 1.0 $(\Omega\,\mathrm{cm})^{-1}$ has been observed. In the case of AgI the ionic conductivity is due to the movement of Ag cations over the allowed positions in the rigid I sublattice. The possibility of ion movement also agrees with some rough estimates. Given the area of the Ag contact, the number of Ag atoms per monolayer is about 3.4×10^{14}, and it is believed that less than ten monolayers are deposited. The integrated number of charges we observe in this pyroelectric effect is about 3.0×10^{14} or about 10% of the total number of Ag atoms deposited. This is reasonable since we know from PL measurements that Ag is a fairly fast diffuser in HgI_2 both along the crystal surface and through the bulk.

TSC spectra performed on In, Sn, indium–tin-oxide, Cr, and Mg contacted material are shown in fig. 2. The common feature of all these spectra is that T_6 is the dominant peak followed by T_5. These spectra are similar to those obtained from Pd contacted material except that the intensities of the peaks are one to two orders of magnitude smaller. Ni and Al contacted samples produce spectra similar to each other shown in fig. 3. In these spectra T_5 is dominant and T_1 is also clearly observed. Al contacted samples have TSC peak intensities one order of magnitude greater than Ni-contacted samples. TSC spectra for Au and Cu contacted samples are presented in fig. 3 also. Only a very weak T_8 is observed in the spectrum of the Au contacted material while two weak peaks (T_3 and T_6) are observed in the Cu-contacted sample.

The TSC peaks observed in this work are summarized in table 1. As can be seen all the observed peaks are consistent with peaks previously observed in mercuric iodide. However, it is clear that the subset of peaks observed in any one sample strongly depends on the particular metal overlayer. It may be suggested that those traps which are observed consistently in nearly all the samples have intrinsic defects as their origin. It is also clear that continued systematic studies relating stoichiometry and processing details are necessary to firmly establish the relationship between particular centers and their origin.

3.2. Photoresponse

A room temperature photoresponse spectrum taken from a sample with Pd contacts is shown in fig. 4. In

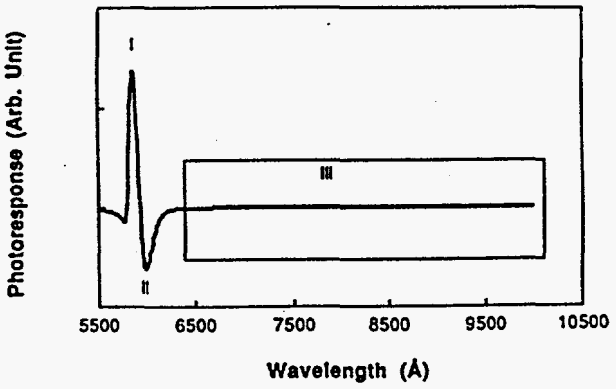

Fig. 4. Photoresponse from a Pd contacted HgI_2 sample measured at room temperature.

the near-band-gap region (labeled I and II), the current changes direction and shows maxima in both directions. The photoresponse in region III is in the negative direction and is about two orders of magnitude smaller than that in regions I and II. The photoresponse in the near-band-gap region can be qualitatively explained by referring to the band diagram in fig. 5. When the energy of the incident photon is large compared with the band gap of the semiconductor (short wavelengths) absorption takes place primarily near the surface, designated here as process I. In this process, if the bands bend as shown in this figure the current flows from right to left which may be defined as positive. The appearance of a current maximum is due to two factors; the surface recombination velocity and the absorption coefficient. At short wavelengths, a large surface recombination velocity will limit the photocurrent since most the carriers will recombine quickly near the surface. As the wavelength increases, absorption takes place further in the bulk and the importance of surface recombination is decreased, thus the photocurrent will tend to increase. At the same time the absorption coefficient decreases as the wavelength increases and the photocurrent would tend to decrease. These two competing effects produce a photoresponse maximum. As the wavelength is increased further and if there is some asymmetry in the two contacts (in size or barrier height) process II may dominate if the back contact is more efficient in collecting carriers. Thus the photocurrent can change sign at some wavelength. If the above explanation is qualitatively correct than we can infer that the bands bend as depicted in fig. 5 at both a free surface and Pd contacted surface. This is in agreement with results obtained using X-ray spectroscopy to determine the band bending in this material.

In the long wavelength region III, the photocurrent is generated by electrons excited into the metal contact and which leaves behind a hole in the semiconductor. These holes drift under the influence of the built-in electric field. Using the Fowler theory [28] one can plot

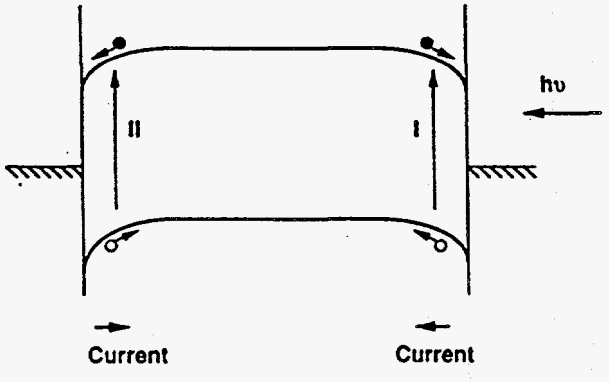

Fig. 5. Schematic band diagram of HgI_2 and metal contacts.

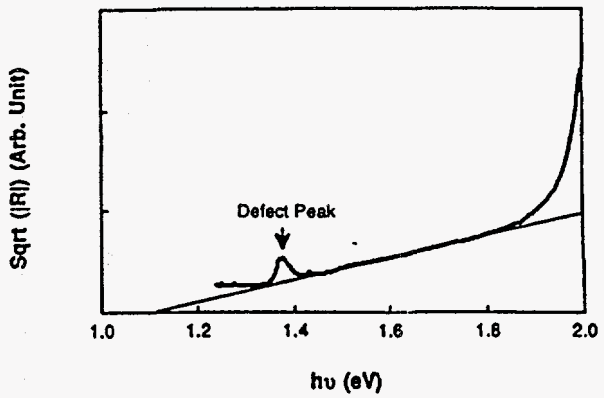

Fig. 6. Plot of the square root of the photoresponse as a function of photon energy to obtain the barrier height. The barrier height measured from the intercept of the straight line to the x-axis is 1.05 eV.

the square root of the photoresponse per incident photon to obtain the straight line plot shown in fig. 6. The barrier height is obtained by extrapolating the straight line portion of this graph to find the intercept on the horizontal axis. This yields a barrier height in the case of Pd of 1.05 eV. As can be seen, a large portion of this plot fits the straight line quite well. The observed photocurrent peak observed at 1.38 eV is due to the ionization of impurity levels.

Photoresponse measurements were also performed on HgI_2 samples contacted with other metals such as Ag, Au, Cu, etc. Both electron and hole barriers were observed and the barrier heights ranged from 0.3 eV to 1.2 eV. However, almost all samples showed a polarization effect, that is, the photoresponse spectra were a function of time. These spectra were also very sensitive to the polarity of the bias applied to the sample with the barrier height even changing type in some cases. This polarization effect may have as its origin the trapping of large numbers of photogenerated carriers. It would seem therefore that avoiding above-band-gap illumination may be necessary to obtain unambiguous data. At the same time the photoresponse technique may offer a method to study the origin of polarization effects.

4. Conclusions

TSC spectra clearly show that the concentration and type of traps which are found in mercuric iodide are a function of the metal overlayers used for contacting this material. The internal photoemission measurements allow one to measure the type (electron or hole) of barrier that exists at the metal/semiconductor interface as well as determine its value. By considering the information that these techniques provide it is possible

to determine appropriate processing conditions and contact material for optimal detector performance. This includes, as an example, the possible use of more than one contact material biased in such a manner so as to provide a hole collecting contact at the negative electrode and an electron collecting contact at the positive electrode. Further investigations relating process conditions to intrinsic and extrinsic deep trap concentrations should make it possible to minimize the deleterious effects of these centers.

Acknowledgements

This work was supported by the U.S. Department of Energy. One of us (T.E.S.) also acknowledges the support of the National Science Foundation through the Presidential Young Investigator Program.

References

[1] K. Hull, A. Beyerle, B. Lopez, J. Markakis, C. Ortale, W. Schnepple and L. van den Berg, IEEE Trans. Nucl. Sci. NS-30 (1983) 402.
[2] R.C. Whited and M.M. Schieber, Nucl. Instr. and Meth. 162 (1979) 113.
[3] J.L. Regolini and J. Saura, J. Appl. Phys. 54 (1983) 1528.
[4] P. Suryanarayana, H.N. Acharya and K.V. Rao, J. Mater. Sci. 3 (1984) 21.
[5] J. Mellet and A. Friant, Nucl. Instr. and Meth. A283 (1989) 199.
[6] J. Llacer, M.M.K. Watt, M. Schieber, R. Carlston and W. Schnepple, IEEE Trans. Nucl. Sci. NS-21 (1974) 305.
[7] F. Nix, Phys. Rev. 47 (1935) 72.
[8] M. Chester and C.C. Coleman, J. Phys. Chem. Solids 32 (1971) 223.
[9] J. Bornstein and R. Bube, J. Appl. Phys. 61 (1987) 2677.
[10] A.G. Milnes, Deep Impurities in Semiconductors (Wiley, New York, 1973).
[11] R.H. Bube, Photoconductiyity of Solids (Wiley, New York), 1960).
[12] P.L. Land, J. Phys. Chem. Solids 30 (1969) 1693.
[13] D. Look, Semiconductors and Semimetals 19 (chap. 2) (1983) 75.
[14] T. Mohammed-Brahim, Phys. Status Solidi A65 (1981) K1.
[15] R.C. Whited and L. van den Berg, IEEE Trans. Nucl. Sci. NS-24 (1977) 165.
[16] A. Tadjine, D. Gosselin, J. Koebel and P. Siffert, Mater. Res. Soc. Symp. Proc. 16 (1983) 217.
[17] A. Tadjine, D. Gosselin, J.M. Koebel and P. Siffert, Nucl. Instr. and Meth. 213 (1983) 77.
[18] R. Stuck, J.C. Muller, J.P. Ponpon, C. Scharager, C. Schwab and P. Siffert, J. Appl. Phys. 47 (1976) 1545.
[19] T. Mohammed-Brahim, A. Friant and J. Mellet, Phys. Status Solidi 79 (1983) 71.
[20] R.H. Bube, Phys. Rev. 106 (1957) 703.
[21] C.D. Blasi, S. Galassini, C. Manfredotti, G. Micocci, L. Ruggiero and A. Tepore, Nucl. Instr. and Meth. 150 (1978) 103.
[22] U. Gelbart, Y. Yacoby, I. Beinglass and A. Holzer, IEEE Trans. Nucl. Sci. NS-24 (1977) 135.
[23] P. Suryanarayana and H.N. Acharya, J. Electron. Mat. 18 (1989) 481.
[24] S.B. Hyder, J. Appl. Phys. 48 (1977) 313.
[25] J.C. Muller, A. Friant and P. Siffert, Nucl. Instr. and Meth. 150 (1978) 98.
[26] X.J. Bao, T.E. Schlesinger, R.B. James, G.L. Gentry, A.Y. Cheng and C. Ortale, J. Appl. Phys. 69 (1991) 4247.
[27] V.V. Gurevich and A.K. Ivanov-Shits, Semiconductors and Semimetals 26 (chap. 4) (1988).
[28] S.M. Sze, Physics of Semiconductor Devices (Wiley, New York, 1981) p. 683.

Left Intentionally Blank

ELECTRICAL CHARACTERIZATION OF IMPURITIES IN AND CONTACTS ON MERCURIC IODIDE

J. M. VAN SCYOC*, T. S. GILBERT*, and R. B. JAMES*
*Advanced Electronics Manufacturing Technologies Department, Sandia National Laboratories, Livermore, CA 94550

ABSTRACT

Mercuric iodide (HgI_2) is a semiconductor that has shown great promise for use in room-temperature high-resolution x-ray and gamma-ray spectrometers. Its widespread usage has been limited, however, by low yield and long-term reliability problems. The processing of this material is still in its infancy compared to silicon, so research efforts continue to pursue the root causes of device failures. Two likely sources of performance limitations are impurities and poor contacts. Significant efforts have been expended in developing and using various purification schemes. However, quantitative chemical analyses have shown that several metallic impurities still exist at the high ppb level. In addition, it has not yet been definitively determined which impurities are most problematic and at what level they have a detrimental effect. Leakage currents and current-voltage measurements have been used to study the movement of mobile impurity-related defect centers in the bulk mercuric iodide. In particular, this method has been used to quantify the drift of metallic impurities, such as Ag and Cu, which are known to or believed to degrade HgI_2 detectors. Four-point-probe sheet resistance measurements have been used to study the stability of contacts and the formation of reaction layers. In particular, such measurements have revealed that the Pd contacts currently used for the highest quality detectors are not as stable as previously thought, as the films of Pd react with the HgI_2 to form the amalgam PdHg.

INTRODUCTION

Red mercuric iodide, α-HgI_2, is a wide bandgap semiconductor that has been pursued as a material for room-temperature x-ray and gamma-ray spectrometers for over two decades. It has several advantages that make it well suited for such applications, but it has not yet found widespread usage because of several difficulties in its processing. Two such problems are considered here.

The first problem is with impurities that exist in the bulk semiconductor material. Several impurities are found to exist at the high part-per-billion or low part-per-million level in the precursors (mercuric chloride and potassium iodide), the raw mercuric iodide, freshly grown mercuric iodide crystals, and the final detectors [1]. Many of these impurities are known or expected to be detrimental to the performance of the radiation detectors. These impurities introduce defects which form carrier traps in the bulk of the detector. These traps then capture the x-ray or gamma-ray photo-generated electrons and holes as they drift in the device field. This stochastic loss of charge results in a variably diminished signal which degrades the spectral response. Significant effort has been expended on developing and utilizing purification schemes to remove these impurities. Current manufacturing processes involve a long and complex purification routine that includes multiple open- and closed-tube sublimations and melts. While the process does produce high quality detectors, the yield is low and there are long-term (two to three years) stability problems with the detectors. The devices also require continuous biasing in order to maintain their high performance.

The second problem is in the formation of electrical contacts for biasing and charge collection. Through trial and error, it has been found that palladium contacts produce the best detectors. The mercuric iodide has a high vapor pressure and is relatively reactive, such that making good contacts is difficult. Many metals, particularly copper and silver, readily diffuse into the mercuric iodide, leaving behind no conductive layer.

The work discussed in this paper uses electrical characterization methods to study these two sources of problems.

EXPERIMENTS AND RESULTS

Electrical Characterization of Impurities

Previous work has shown that many of the detrimental impurities in HgI_2, such as Ag and Cu, are mobile in the applied electric field and drift toward the electrodes. By biasing thin films of copper on one side of detector-like slabs of mercuric iodide, it was shown that the Cu impurity acts as a positive charge that drifts toward the negative electrode [2]. Similarly, it has been found that Ag also acts as a positive impurity [3]. In the work here, an unpurified rod of bulk polycrystalline HgI_2 was biased and the current monitored to study the movement of impurities. Figure 1 shows a schematic of the basic experiment. The samples of mercuric iodide used here were 7 mm in diameter and had a length of 39 mm.

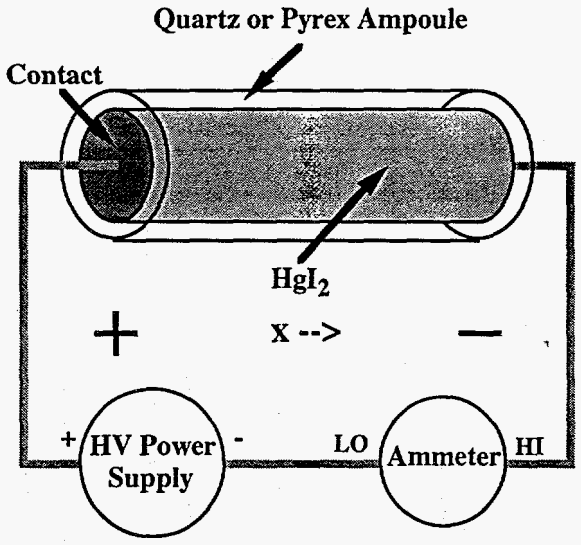

Figure 1. Schematic diagram of the setup used to study mobile impurities in HgI_2.

Prior to long-term biasing, the current-voltage characteristics of the sample were studied. Figure 2 shows an example I-V curve for voltages up to 500 V, or an equivalent uniform field of 128 V/cm, which is almost two orders of magnitude lower than the device fields of 10^4 V/cm. As can be seen in the plot, the current saturates at around 0.5 μA, or a current density of 1.3 $\mu A/cm^2$. In normal detectors at the bias field of 1 V/μm the current density is only on the order of 10 pA/cm^2. The significantly higher leakage current found here is the result of the impurities present. In particular, the saturation level is equivalent to $3x10^{12}$ single charges per second. The previous work cited above, and the results discussed below reveal that the bulk of this enhanced current level is from the movement of the impurities themselves, as opposed to free carriers from doping.

Following the initial I-V characterization, the sample was left under bias for several hundred hours to allow the movement of the impurities to reach completion. Figure 3 shows the current versus time data measured. As shown, the current quickly rises to the saturation level of about 0.5 μA. It then slowly decays back down to its final asymptotic value of about 1 nA. While the high peak current decays rapidly with in the first day, the tail stretches out over the 500 hours shown here. The large current pulse results from the rapid movement of the highly mobile impurities, such as Ag and Cu, while the long tail results from the movement of the much slower impurities.

While the movement of impurities in a detector produces significant degradation in the device response, this mobility can be used to benefit to purify the mercuric iodide material prior to crystal growth and detector fabrication. In particular, applying bias to the bulk material, as discussed above, results in the movement of positive impurities to the negative electrode, and negative impurities to the positive electrode. This should result in the piling up of one set of impurities at one end, and a complementary set of impurities at the opposite end, leaving a highly purified central section. By removing and using this central pure section for detector production, better

yield and devices should result. Table I shows some results for the impurities found in such an "electrodrift purification" experiment, as measured with inductively-couple plasma mass spectroscopy (ICP-MS) quantitative chemical analyses. Reference 4 discusses the ICP-MS technique as applied to HgI_2, and Reference 5 discusses more fully the use of the electrodrift phenomena as a purification method.

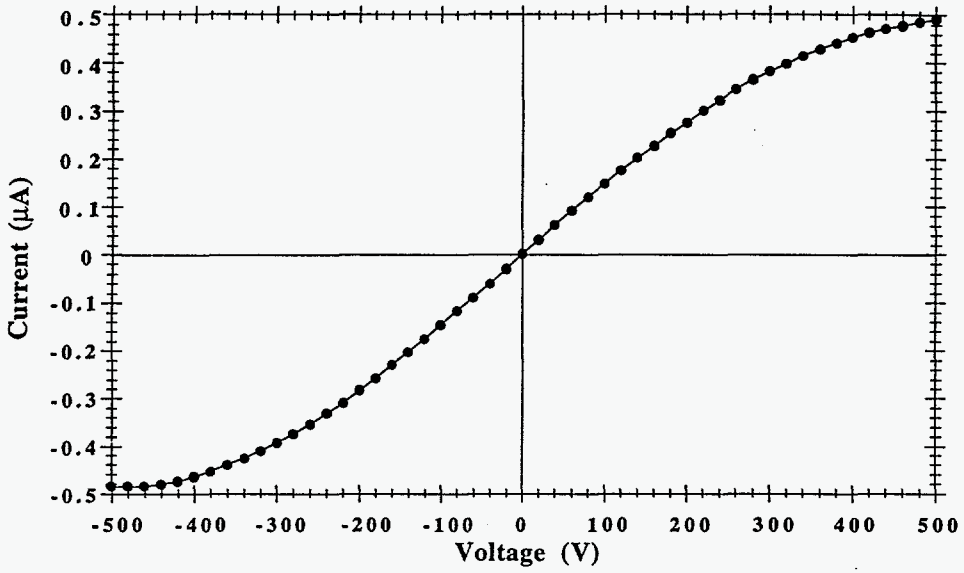

Figure 2. I-V characteristic for the mercuric iodide polycrystalline rod.

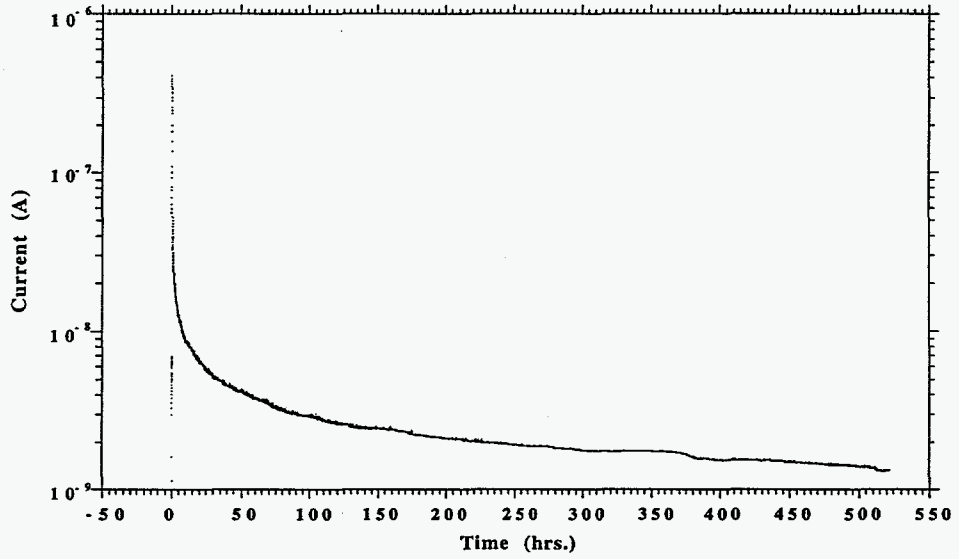

Figure 3. Leakage current versus time for the HgI_2 sample at a constant bias of 975 V.

Table I. ICP-MS quantitative chemical analyses results for electrodrift purification HgI_2 sample.

Impurity	Concentration in Material Before Electrodrift	Concentration in Positive Section After Electrodrift	Concentration in Center Section After Electrodrift	Concentration in Negative Section After Electrodrift
Ag	100 ppb	1 ppb	1 ppb	800 ppb
Cu	3.2 ppm	1.2 ppm	5.0 ppm	12 ppm
Cd	0.48 ppm	1.77 ppm	0.41 ppm	0.17 ppm

Electrical Characterization of Contacts

The quality of the electrical contacts that form the electrodes for the radiation detector is a critical factor in the performance of the device. Because mercuric iodide has such a high resistivity, on the order of 10^{13} Ω*cm, the detector structures used can be quite simple. In particular, the detector consists of a bulk slab of HgI_2, on the order of 1 mm thick and 1 cm^2 in area, with an electrode on each large face. The device is then biased at on the order of 1 kV and the detector connected to a charge sensitive preamplifier. The photo-generated charge in the bulk semiconductor drifts in the applied electric field and is collected at the contacts. The key requirement of the electrode layer is then that it provide a low resistivity ohmic contact, such that little of the electric field is dropped at the contacts.

As discussed above, palladium has become the contact material of choice, either evaporated or sputter-deposited. It is generally assumed that the palladium simply forms a stable low resistivity contact. However, the situation is more complicated. In the second set of experiments discussed here, four-point-probe sheet resistance measurements were used to quantify the evolution of the contact. Four point probe measurements are a very simple, common means for measuring the basic electrical properties of thin films. A fixed, known current is injected through two outer probe tips, and the resultant voltage measured on the two inner probe tips. In the case of mercuric iodide, there is an added complication in the fact that the material is mechanically very soft, and the probe tips easily deform and damage the thin film and HgI_2 surface. Therefore, great care is required in using the right amount of probe pressure. References 6 and 7 discuss previous work on studying contacts on HgI_2 with four point probes, particularly the rapid diffuser Cu and the more stable W.

For the present experiments three samples were studied. All of the samples studied were standard 1 cm^2 x 1 mm HgI_2 single crystal slabs with Pd thin films sputtered through shadow masks. For comparison, witness glass slides with the same mask were sputter-deposited at the same time. The first sample had a 6.4 mm diameter circular Pd film of nominal 1000Å, the second sample had a nominal 330Å film, and the third sample had a 6.4 mm square Pd film of 330Å nominal thickness.

The relation between measured sheet resistance and film resistivity and thickness is given by the following equation.

$$\rho\ [\Omega*cm] = R_S\ [\Omega] * t\ [cm] * C\ (d/s) \qquad (1)$$

where

ρ = film resistivity

R_S = sheet resistance

t = film thickness

C (d/s) = correction factor

d = film diameter (circular) or side length (square)

s = probe tip spacing = 1.0 mm

The correction factor C is a non-analytical function that depends upon many factors in general, but has been simplified for the geometries here to depend only upon d and s and whether the film is circular or square. Several assumptions are required to reach this equation, and it is likely that some of them are over simplifications.

Figure 4 shows the sheet resistance versus time for the thick circular film on both the HgI_2 and the glass slide. The film on HgI_2 both starts at a higher sheet resistance than the film on glass and changes over a period of a few hours. The higher initial value is a result of a thinner film being deposited on the mercuric iodide. Given the high vapor pressure of mercuric iodide, the surface of the sample sublimes away rapidly in the vacuum deposition system, and the Pd deposition process must compete with this process. The Pd film on glass has a sheet resistance of 0.594 Ω, and a profilometer measured thickness of 1000Å, which gives a resistivity of 2.2×10^{-5} Ω*cm. The film on mercuric iodide has an initial sheet resistance of 1.763 Ω. Because of the softness of the HgI_2,

it is not possible to use a profilometer to measure the thickness of the Pd, so it is estimated using the resistivity given by the glass film. This results in a film thickness of 337 Å. The final sheet resistance value of 1.793 Ω gives a thickness of 331 Å. Thus there is a change in film thickness of about 2% in the first two hours after deposition.

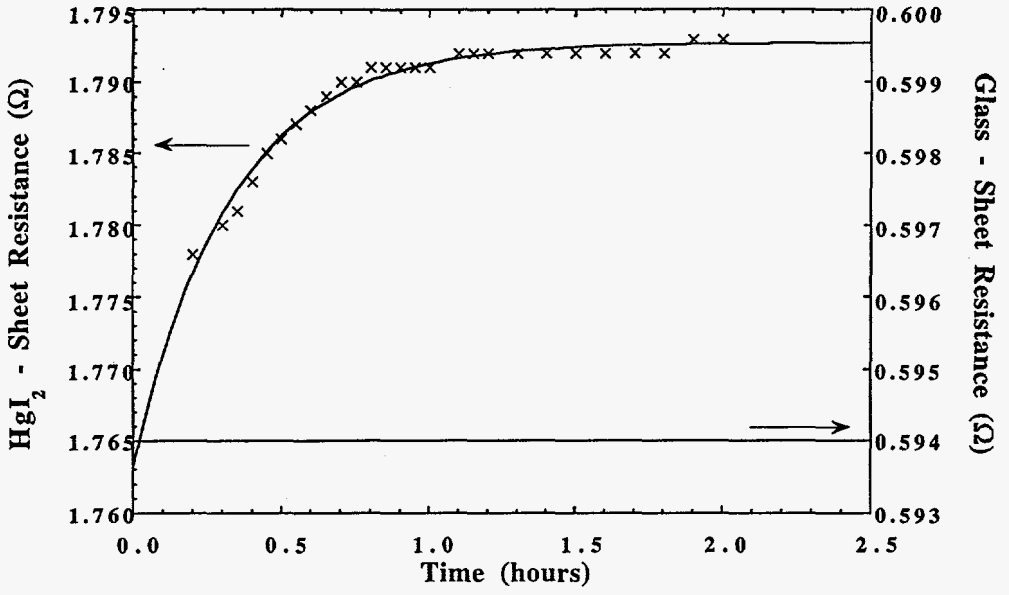

Figure 4. Sheet resistance versus time for 6.4 mm diameter circular nominal 1000Å Pd thin films on HgI_2 ("x" points on curve) and a glass slide (flat line).

The other two samples were used to study the effects of some of the parameters of the thin film contact. The second sample differs from the first only in the thickness of the layer. The glass sample had a film thickness of 333Å and a sheet resistance of 3.48 Ω which results in a resistivity of 4.3×10^{-5} Ω*cm. The difference in the computed resistivity from the two samples on glass results from errors caused by the assumptions made in deriving equation 1 above, which is consistent with the fact that the bulk resistivity of Pd is around 1.1×10^{-5} Ω*cm. Using the value here, the film on HgI_2 final sheet resistance value of 5.4 Ω results in a final thickness of 215 Å. The sheet resistance measurements were too unsteady to plot a curve of the change versus time in this sample.

The third and final sample was a square contact with the same nominal thickness as the second sample. Here the film on glass, with thickness of 333Å and sheet resistance of 3.93 Ω, gives a resistivity of 4.6×10^{-5} Ω*cm, consist with the second sample, as expected. The final value of sheet resistance for the film on HgI_2 is 13.0 Ω, which gives a thickness of 101 Å. The difference between the circular and square contact can be explained by the differences in edge length. The circular sample has an edge length of 20 mm, while the square sample has an edge of 26 mm. The effective reduction in film thickness results from the loss of Pd to the formation of PdHg, a higher resistivity almagam. This reaction occurs only with the Pd near the HgI_2 surface where excess Hg is usually available because of the preferential sublimation of I, which is the case at the edges of the film. Therefore, the sample with the greater amount of edge, i.e., the square one, has a higher loss of conductive Pd. Reference 8 discusses the study of the formation of PdHg on Pd-contacted HgI_2 using transmission electron microscopy.

SUMMARY AND CONCLUSIONS

In this work two sources of device failures in mercuric iodide room-temperature radiation detectors were studied. Current-voltage and leakage current versus time measurements were used to study the mobility of various metallic impurities in bulk mercuric iodide. In particular, it was found that some impurities, such as Ag and Cu, act as positive charges, while other impurities, such as Cd, act as negative charges. While the mobility of these impurities causes problems when

the impurities are present in HgI_2 detectors, the mobility can also be used to advantage as a means for purification of bulk material prior to crystal growth. Four-point-probe sheet resistance measurements were used to study the stability of the standard Pd electrical contacts on HgI_2. It was found that significantly less film is deposited on HgI_2 than glass, and that the film that is deposited actually decreases in thickness after deposition as Pd forms PdHg with excess Hg at the HgI_2 surface.

ACKNOWLEDGMENTS

This work was supported by the U. S. Department of Energy.

REFERENCES

1. E. Cross, E. Soria, and G. Buffleben, presented at the **9th International Workshop on Room Temperature Semiconductor X and γ-Ray Detectors, Associated Electronics, and Applications**, September 21, 1995, Grenoble, France, and submitted to *Nucl. Instr. and Meth. A.*

2. J. M. Van Scyoc, R. B. James, T. E. Schlesinger, and T. S. Gilbert, in **Defect and Impurity Engineered Semiconductors and Devices**, edited by S. Ashok, J. Chevallier, I. Akasaki, N. M. Johnson, and B. L. Sopori (*Mater. Res. Soc. Proc.* **378**, Pittsburgh, PA 1995), pp. 795 - 801.

3. J. M. Van Scyoc, R. B. James, T. E. Schlesinger, T. S. Gilbert, and M. Schieber, presented at the **International Conference on Crystal Growth XI**, June 22, 1995, Amsterdam, The Netherlands, and submitted to *J. Crys. Growth.*

4. E. S. Cross, E. Mroz, and J. A. Olivares, in **Semiconductors for Room-Temperature Radiation Detector Applications**, edited by R. B. James, T. E. Schlesinger, P. Siffert, and L. Franks (*Mater. Res. Soc. Proc.* **302**, Pittsburgh, PA 1993), pp. 61 - 65.

5. J. M. Van Scyoc, R. B. James, A. Burger, E. Soria, C. Perrino, E. Cross, M. Schieber, and M. Natarajan, presented at the **9th International Workshop on Room Temperature Semiconductor X and γ-Ray Detectors, Associated Electronics, and Applications**, September 21, 1995, Grenoble, France, and submitted to *Nucl. Instr. and Meth. A.*

6. J. M. Van Scyoc, T. E. Schlesinger, R. B. James, A. Y. Cheng, C. Ortale, and L. van den Berg, in **Semiconductors for Room-Temperature Radiation Detector Applications**, edited by R. B. James, T. E. Schlesinger, P. Siffert, and L. Franks (*Mater. Res. Soc. Proc.* **302**, Pittsburgh, PA 1993), pp. 115 - 120.

7. J. M. Van Scyoc, T. E. Schlesinger, H. Yao, R. B. James, M. Natarajan, X. J. Bao, J. S. Iwanczyk, B. E. Patt, and L. van den Berg, in **Diagnostic Techniques for Semiconductor Materials Processing**, edited by O. J. Glembocki, et al. (*Mater. Res. Soc. Proc.* **324**, Pittsburgh, PA 1994), pp. 65 - 71.

8. D. L. Medlin, J. M. Van Scyoc, T. S. Gilbert, T. E. Schlesinger, D. Boehme, M. Schieber, M. Natarajan, and R. B. James, presented at the **9th International Workshop on Room Temperature Semiconductor X and γ-Ray Detectors, Associated Electronics, and Applications**, September 1995, Grenoble, France, and submitted to *Nucl. Instr. and Meth. A.*

MATERIALS RESEARCH SOCIETY SYMPOSIUM PROCEEDINGS VOLUME 302

Semiconductors For Room-Temperature Radiation Detector Applications

Symposium held April 12-16, 1993, San Francisco, California, U.S.A.

EDITORS:

R.B. James
Sandia National Laboratories
Livermore, California, U.S.A.

T.E. Schlesinger
Carnegie Mellon University
Pittsburgh, Pennsylvania, U.S.A.

Paul Siffert
Laboratorie PHASE/CRN
Strasbourg, France

Larry Franks
EG&G Energy Measurements
Goleta, California, U.S.A.

MRS
MATERIALS RESEARCH SOCIETY
Pittsburgh, Pennsylvania

ANALYSIS OF HgI_2 AND PbI_2 CRYSTALS AND DETECTORS BY PARTICLE-INDUCED X-RAY EMISSION (PIXE) AND ION BACKSCATTERING SPECTROSCOPY (IBS)

G. S. BENCH†, A. J. ANTOLAK§, D. H. MORSE§, D. W. HEIKKINEN†,
A. E. PONTAU§, R. B. JAMES§, D. C. DAVID§, A. BURGER•, and L. VAN DEN BERG+
†Lawrence Livermore National Laboratory, Livermore, CA 94550
§Sandia National Laboratories, Livermore, CA 94551
•Fisk University, Nashville, TN 37208
+EG&G Energy Measurements, Goleta, CA 93116

ABSTRACT

The Ion Micro-Analysis Group (IMAG) in Livermore conducts quantitative trace elemental analysis with PIXE and depth profiling with IBS using an MeV ion microbeam. The system has the capability to produce two-dimensional trace element and IBS images. PIXE analyses have been conducted on HgI_2 and PbI_2 crystals and detector materials in order to identify and quantify near surface trace contaminants. IBS measurements have been conducted to investigate elemental depth distributions in various materials.' The results of measurements on several different samples are reported and a discussion of factors affecting quantitative *in vacuo* microanalysis of these materials is presented.

INTRODUCTION

The Ion Micro-Analysis Group (IMAG) in Livermore is an integrated group of scientists and engineers who use accelerator-based techniques to provide nondestructive materials characterization. Two of these techniques, particle-induced x-ray emission (PIXE) and ion backscattering spectrometry (IBS), are particularly useful for studies of near-surface impurity profiles, diffusion-mediated reactions, or minor and trace element compositions [1, 2]

PIXE's sensitivity for trace element detection is on the order of a few parts per million. When ions pass through matter, they interact with the electrons in the atoms producing vacancies. In an inner shell, the created vacancy can be filled by an electron from an outer shell and an x-ray photon of characteristic energy can be emitted. By measuring the photon energy, the element from which the x ray orginated can be determined and the amount of that element present can be determined from the number of x rays generated. For identification and quantification of trace elements, PIXE can be 100 times more sensitive than electron microanalysis due to the much reduced secondary electron bremsstrahlung background. Usually the measurements are made with protons, but heavier ions can be used to increase sensitivity in some instances since the cross section scales roughly as Z^2. IMAG has a dedicated PIXE beamline using 1-5 MeV/nucleon incident ions. The range of protons at these energies is between ten and a few hundred microns in HgI_2 so PIXE is primarily a tool for near surface analysis. Ions can be focused with a quadrupole lens system down to spot sizes of 10 μm at present. The ion beam can be rastered over the sample to provide two-dimensional spatial distributions of the elements. Characteristic x-rays are detected with a Si(Li) detector which has a resolution of 200 eV. The IMAG PIXE system uses approximately 10^{10} ions/s and data can be acquired simultaneously from elements with $Z \geq 11$ (typically a few minutes per spot). Final spectral data analysis is accomplished with a suite of IMAG-developed computer software.

High energy ion scattering is routinely used for obtaining elemental depth profiles. Utilizing the 10 MV tandem accelerator, IMAG has the capability to conduct ion backscattering spectroscopy (IBS) measurements with protons and high energy heavy ions. By measuring the energy of the recoiling ions, depth distributions of the elemental constituents can

Mat. Res. Soc. Symp. Proc. Vol. 302. ©1993 Materials Research Society

be determined which are useful for studying interfaces, thin films and multilayers. Quantitative data analysis is obtained using standard backscattering software on a computer workstation.

EXPERIMENT AND ANALYSIS

HgI_2's low sublimation energy requires that special sample preparation procedures must be followed before PIXE or IBS analysis can be done *in vacuo*. In order to minimize material removal under these conditions, samples are coated with a thin layer (< 5 μm) of either carbon or parylene. Use of this protective layer has enabled measurements to be made with current densities of up to 1 $\mu A/cm^2$ for 3-MeV protons with no observable damage to detector materials. Alternative methods such as using a cold stage in the analysis chamber or external beam techniques have not yet been fully explored. However, parylene coatings on HgI_2 are routinely used to encapsulate and protect fabricated detectors.

Figure 1 shows a typical 3-MeV PIXE spectrum from a 5 x 5 mm^2 HgI_2 detector-grade crystal which was partially covered by a 2 mm diameter thin contact layer of palladium. The sample was then coated by a 4 μm layer of parylene and then encased in a cadmium collar which exposed the contact layer. The beam spot was focused to a size of about 200 x 200 μm^2 and the spectrum was collected in 25 minutes. To attenuate the intense iodine L x rays, 0.76 mm of mylar was placed in front of the Si(Li) detector. Consequently, trace elements with atomic numbers less than 20 could not be detected in this experimental arrangement. The cadmium signal in the figure arises from the iodine K x rays fluorescing the cadmium collar.

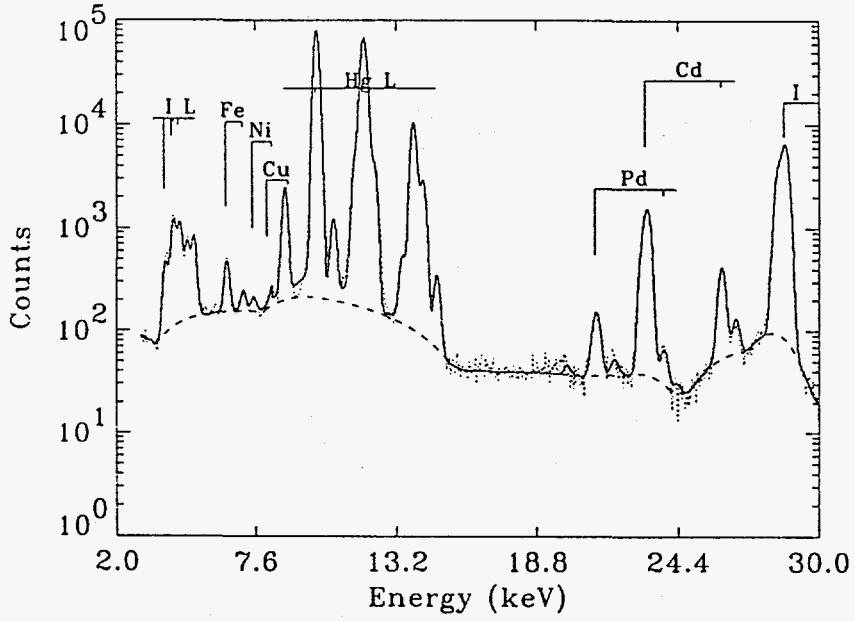

Figure 1. PIXE spectrum from a HgI_2 detector-grade crystal covered by a thin contact layer of palladium. The characteristic x ray lines for elements are labeled.

Secondary fluorescence from the iodine also contributes about 10% to the palladium signal. The PIXE analysis revealed that the crystal's stoichiometry, Hg:I, was 1:2.2±0.3. The palladium layer thickness in the examined region was determined to be 90±20 Å after secondary fluorescence corrections were applied (the nominal value was 125 Å). Small amounts of iron, copper and nickel were also observed although secondary fluorescence of impurities in the cadmium collar is the dominant contribution to these signals. Spot analyses

made on other non-encased HgI_2 samples have typically shown iron levels on the order of 100 ppm or less in the near surface region and smaller amounts of copper and nickel. Inductively coupled plasma mass spectrometry has also shown the presence of these elements in HgI_2. PIXE data for a two-dimensional spatial map over the palladium contact were collected after the cadmium collar was removed from the sample. The 3-MeV proton beam spot size was 200 μm and the data were acquired in 200 μm steps. The average palladium contact layer thickness was determined to be 99±18 Å. Figure 2a shows the 4 x 4.4 mm^2 pixel image obtained by setting an energy window around the palladium K-line. The line of high concentration (black pixels) is a palladium bias wire leading to the circular contact. Although the distribution of iron appeared to be uniform across the scanned region, the copper distribution was non-uniform as shown in Figure 2b. The copper level in one region (dark pixels) is about 0.5 weight %. Zinc is also present in the high copper containing region at a concentration of about 0.4 weight % but is below detectable limits (20 ppm) in the rest of the scanned area. Carbon paint was used to bond the palladium wire to the contact. Since PIXE measurements on a 2 x 2 mm^2 region of a carbon paint sample alone showed copper and zinc at less than 5 mg/kg, it is unlikely that the carbon paint used in the detector's fabrication is the source of the high localised level of copper and zinc.

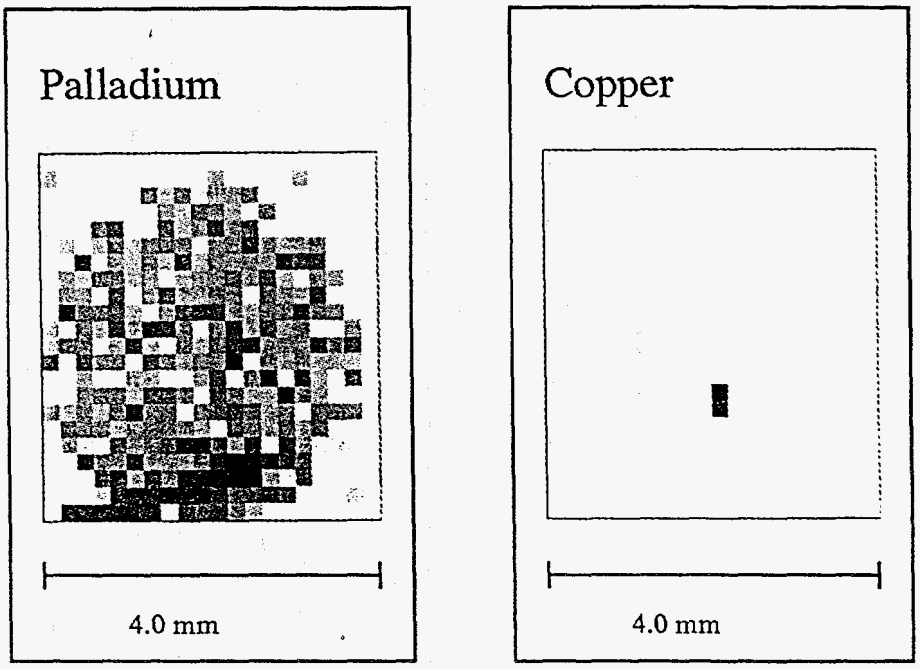

Figure 2. Two-dimensional PIXE maps of (a) palladium and (b) copper from the same HgI_2 crystal of figure 1 but with the cadmium collar removed.

A possible mechanism affecting detector performance is the presence of impurities in the as-grown detector crystals due to the fabrication process. One method of initially removing impurities from these materials is called zone refining. In this technique, a heating element is passed several times across an ampoule containing the grown crystals resulting in reduced impurity levels near the center of the ampule. PIXE measurements were conducted on several zone refined PbI_2 samples taken from both ends of the ampoule and around its center. The analysis showed that iron, copper and nickel concentrations could be significantly reduced near the ampule center.

Other possible means of introducing impurities into the crystals can be diffusion or electromigration of contaminants originating from the contact material. IMAG has conducted extensive PIXE and IBS measurements on several samples in order to identify and quantify

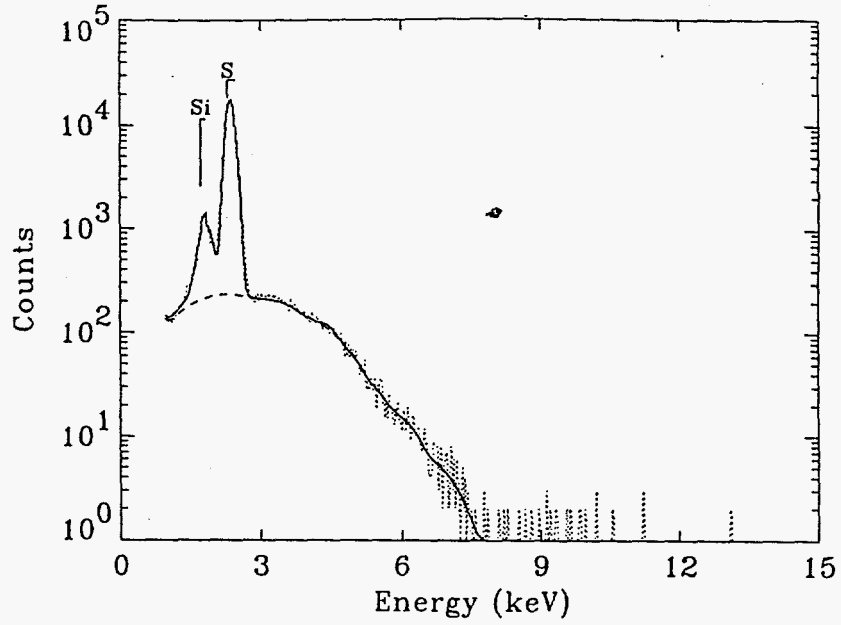

Figure 3. A PIXE spectrum from a self-supporting hydrogel sample. The x ray lines for silicon and sulphur are identified.

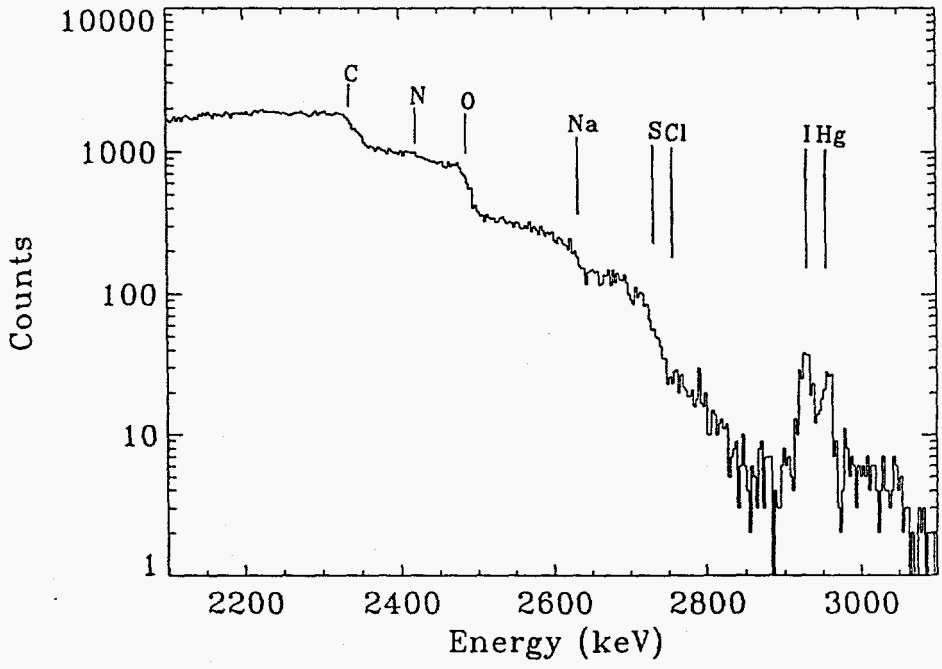

Figure 4. A backscattering spectrum from a 3-MeV proton beam incident on a hydrogel sample. The surface recoil energies of several elements are shown.

trace elements in contact materials. Figure 3 shows a 3-MeV PIXE spectrum from a self-supporting piece of a water-based hydrocarbon gel (hydrogel) commonly used as an electrical contact for photodetector applications. In this analysis, a 150 μm beryllium filter was placed in front of the detector to prevent backscattered ions from penetrating into the Si(Li) crystal. Consequently, only elements with atomic number greater than 12 were detectable. The impurities identified in this material were sulphur at a concentration of approximately 11g/kg and silicon at 5.3 g/kg. However, in other plastic-type contact materials concentrations of sodium up to 20 g/kg, chlorine to 20 g/kg, iron to 3 mg/kg and zinc up to 100 mg/kg have also been observed. Figure 4 shows a 3-MeV proton IBS spectrum of a 2 mm thick hydrogel layer on a portion of a bare HgI_2 crystal. Backscattered particles were collected with a silicon surface barrier charged particle detector at a scattering angle of 120°. This sample had been stored for two years prior to analysis. In this case, the purpose was to determine whether Hg and/or I diffuse directly through the hydrogel or if HgI_2 outside the hydrogel contact sublimes and then redeposits on the outer surface of the hydrogel. At this beam energy, protons can only penetrate approximately 100 μm into the hydrogel. The surface recoil energies of several elements are labeled in the figure. The two peaks between 2.9 and 3.0 MeV each have a FWHM equal to that of the detector resolution. The position of the lower energy peak corresponds to the iodine surface recoil energy, while the position of the higher energy peak corresponds to mercury's surface recoil energy.

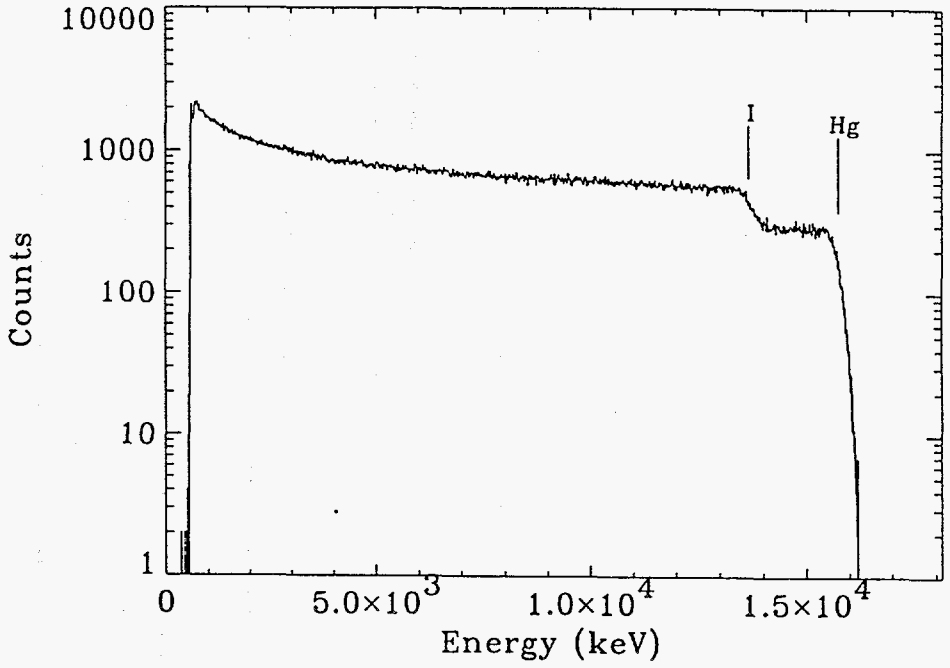

Figure 5. A backscattering spectrum from a 20-MeV oxygen beam incident on a thick HgI_2 sample. The surface recoil energies of mercury and iodine are clearly separated.

These data indicate that the only detectable Hg and I exist as a thin film on the hydrogel and/or are distributed within the first 0.3 μm below the surface (0.3 μm is the approximate depth resolution in the near surface region of the sample for this experiment). The Hg:I atomic ratio is determined to be 1:2.2±0.3. Consequently, it is most likely that the deposited Hg and I is caused by sublimation from the exposed parts of the crystal. This assumption gives a HgI_2 surface layer thickness of around 10 Å. The possibility also exists that this surface layer formed during the time the sample was in the analysis chamber's vacuum. The chamber was at a pressure of approximately 10^{-5} torr and the measurements were made at room temperature on a sample not protected by carbon or parylene. The backscattered spectrum in figure 4 also

shows the presence of sodium, sulphur and possibly some chlorine in the hydrogel in addition to C, N and O. The data indicates that the sodium and sulphur have a uniform depth distribution in the analyzed region.

Owing to the light mass of the bombarding particle, an IBS spectrum of 3-MeV protons on a bare HgI_2 crystal produces a spectrum with the Hg and I surface recoil energies separated by less than 50 keV. In this case, quantitative information can be difficult to extract since the energy resolution of the experiment is at least 15 keVusing silicon surface barrier charged particle detectors. It is more advantageous to use heavier ions in order to obtain greater differences in kinematic factors for moderate- to high-Z elements and to obtain better depth resolution within the sample. Figure 5 shows an IBS spectrum for a 20-MeV oxygen beam bombarding a HgI_2 crystal. The spectrum was collected with the particle detector located at a 120° scattering angle. The mercury and iodine surface recoil energies in figure 5 are separated by about 2 MeV (for 20 MeV protons, the difference would only be about 0.2 MeV). Quantitative analysis of Figure 5 yields a Hg:I ratio in the near surface of the sample as 1:2.04±0.09. Any other elements present were below minimum detection limits for this analysis. An additional advantage of using relatively low energy heavy ions is that the scattering cross section more closely follows conventional Rutherford scattering than does the analogous proton data. IMAG hopes to use such beams to study the diffusion and electromigration properties of elements such as palladium or silver into the near surface of HgI_2 materials.

SUMMARY

The Ion Micro-Analysis Group (IMAG) has conducted preliminary PIXE and IBS measurements on HgI_2 and PbI_2 radiation sensor materials. These ion beam techniques are useful for studying near surface contaminants and elemental depth distributions. Problems related to the low sublimation energy of HgI_2 and performing the measurements in vacuum have been overcome by coating the crystals with thin layers of carbon or parylene. Various trace elements have been identified and are consistent with measurements made by other methods. In the future, IMAG will continue to analyze these materials with PIXE and IBS by focusing on the effects of diffusion and electromigration of contaminants. In addition, another ion microbeam technique, ion channeling, may be used to investigate crystalline structure and defects in these materials.

ACKNOWLEDGEMENTS

This work was supported by the U.S. Department of Energy under SNL Contract No. DE-AC04-76P00789 and LLNL Contract No. W-7405-ENG-48.

REFERENCES

1. S. A. E. Johansson and J. L. Campbell, *PIXE A Novel Technique for Elemental Analysis*, (John Wiley and Sons, Chichester, 1988).
2. J. R. Bird and J. S. Williams, *Ion Beams for Materials Analysis*, (Academic Press, Sydney, 1989).

Left Intentionally Blank

MATERIALS RESEARCH SOCIETY SYMPOSIUM PROCEEDINGS VOLUME 302

Semiconductors For Room-Temperature Radiation Detector Applications

Symposium held April 12-16, 1993, San Francisco, California, U.S.A.

EDITORS:

R.B. James
Sandia National Laboratories
Livermore, California, U.S.A.

T.E. Schlesinger
Carnegie Mellon University
Pittsburgh, Pennsylvania, U.S.A.

Paul Siffert
Laboratorie PHASE/CRN
Strasbourg, France

Larry Franks
EG&G Energy Measurements
Goleta, California, U.S.A.

MRS
MATERIALS RESEARCH SOCIETY
Pittsburgh, Pennsylvania

DEFECTS IN SILVER-DOPED MERCURIC IODIDE CRYSTALS AND THEIR EFFECT ON X-RAY AND GAMMA-RAY DETECTOR PERFORMANCE

R. B. JAMES*, X. J. BAO**, T. E. SCHLESINGER**, A. Y. CHENG***, AND V. M. GERRISH***

*Advanced Materials Research Department, Sandia National Laboratories, Livermore, CA 94550

**Department of Electrical and Computer Engineering, Carnegie Mellon University, Pittsburgh, PA 15213

***EG&G Energy Measurements, Goleta, CA 93116

ABSTRACT

The processing steps associated with purification of source material, crystal growth, and attachment of electrical contacts can introduce defects into mercuric iodide (HgI_2) that degrade the performance of detectors. We have employed low-temperature photoluminescence (PL) spectroscopy to study radiative recombination centers in the interfacial region between a thin semi-transparent film of silver and mercuric iodide. The Ag film was found to introduce a new broad emission band centered at 5490 Å in the photoluminescence spectrum of HgI_2. This PL feature can be used as a signature to identify the existence of Ag as a contaminant in HgI_2 crystals and detectors. Experiments were also conducted on mercuric iodide surfaces that had been doped with silver, and the results showed that Ag is a rapid diffuser in bulk HgI_2. Detectors with silver electrodes were also fabricated and tested using an americium-241 gamma-ray source. Large increases in the leakage currents were observed for the Ag-doped HgI_2 devices, indicated that Ag impurities are electrically active in HgI_2. These measurements show that silver is unacceptable as an electrode material for mercuric iodide x-ray and gamma-ray detector applications. In addition, they reveal that caution must be taken during handling of mercuric iodide source material, crystals, and detectors to avoid contact with silver, silver compounds, or with any material that contains silver as a contaminant.

INTRODUCTION

Mercuric iodide (HgI_2) has several properties that make it desirable for use as an x-ray and gamma-ray spectrometer. [1-5] Both the Hg and I have high atomic masses, so the material has superior ability to attenuate energetic photons. In its red tetragonal from, HgI_2 is photosensitive and the number of charge carriers produced in the crystal is proportional to the incident photon energy. HgI_2 also has a high bulk resistivity (about 10^{13} Ω-cm), which ensures a low dark current and allows for room temperature operation of detectors fabricated from the material. Although the potential of HgI_2 for the manufacturing of state-of-the-art solid-state spectrometers has been clearly demonstrated [6], the production of consistently reliable sensors continues to present significant challenges related to defects in the as-grown crystals and defects introduced during detector processing. Most of the difficulties with crystal growth and processing of HgI_2 for detector applications stem from the fact that the material is difficult to purify, is easily deformed, has a high vapor pressure at room temperature, and is chemically very reactive.

The defects contained in HgI_2 devices often act as carrier traps, which degrade the energy resolution of the detectors. The trapping of photogenerated electrons and holes reduces the charge collected for each absorbed photon, and the unique relationship between the amount of charge collected for each gamma ray and its energy no longer exists. In addition, the trapped charge modifies the internal electric field within the detector and causes polarization effects. Several studies have been conducted in an effort to understand the introduction of stoichiometric defects and contaminants during the crystal growth [7-22], detector processing steps [13-14,16-20], and aging [14,20].

Because of problems associated with chemical reactions between HgI_2 and most conductors, only a few materials have been successfully used as electrical contacts for HgI_2 detector

Mat. Res. Soc. Symp. Proc. Vol. 302. ©1993 Materials Research Society

applications, such as carbon, palladium, gold, and indium-tin-oxide. [4,23] However, the performances of the detectors fabricated with each of these contact materials still show a wide degree of variability. Ideally, one would like an electrical contact to be conductive, stable in air, inert and well bonded to HgI_2, and for some applications, to be transparent to visible light. Since the ideal contact material for each detector application has not yet been identified, measurements of contact chemistry and device performance for detectors employing different electrode materials are currently of interest. [13-14,17-19] In some cases, investigations of the HgI_2/contact interfacial region also increase our understanding of the effect of impurities on the charge transport in devices, particularly for contact materials that diffuse into HgI_2 and dope the material.

In this work we use low-temperature photoluminescence spectroscopy, thermally stimulated current, and tests of gamma-ray response to study HgI_2 detectors with silver electrodes. Dark-current measurements of the electrical conductivity of HgI_2 devices with silver contacts are also reported. The experimental approach, results and discussion, implications for device fabrication, and conclusions are presented in the following sections.

EXPERIMENTAL APPROACH

The HgI_2 crystals used in this study were grown at EG&G Energy Measurements, Santa Barbara Operations by a method described in an earlier publication. [24] Slices of HgI_2 with a cross section of about 1 cm x 1 cm were cut along the crystallographic C plane [25] to a thickness of about 0.06 cm using a thread dipped into a KI aqueous solution. The slices were then polished on each side in a 10% KI solution.

During the silver depositions, an alumina mask with a 0.5-cm-diameter circular aperture was placed over each HgI_2 sample. Thin (~100 Å) semitransparent films of Ag were deposited onto the front side of several different mercuric iodide slabs. This step typically takes between 6 and 8 min from roughing to venting of the vacuum chamber. Each specimen was situated on top of a glass witness slide, and the transparency of the Ag film deposited on top of the witness slide was used as an indicator of the transparency of the Ag overlayer deposited onto the HgI_2 substrate.

A tungsten wire basket containing between 3 and 6 mg of silver was heated by passing current through the filament under moderate vacuum conditions (10^{-5}-10^{-6} Torr). This processing step is particularly important because both mercury and iodine have high vapor pressures (about 10^{-5} at 300 K) [26], and material loss occurs via sublimation. Furthermore, some heating of the HgI_2 surface occurs due to the radiation from the hot (~ 2000 K) tungsten basket, which further increases the rate of sublimation. This surface heating may also be important in terms of the interfacial chemistry between some electrode materials and the mercuric iodide substrate. The degree of surface heating was estimated by using a sensitive chromel-alumel (Type K) thermocouple that was spot welded to a 0.64-cm-diameter thin palladium foil. The thermocouple was placed adjacent to each HgI_2 specimen. For the silver depositions, the palladium foil was heated for approximately 15 seconds, and a maximum temperature of between 318 and 353 K was recorded for the different runs.

After the silver depositions, an aquadag electrical contact was painted on the other side of each HgI_2 slab. Colloidal carbon was used to attach a 1-mil palladium wire to the front and back contacts, so that an electrical bias could be applied. Each slab was next mounted onto an alumina substrate using Dow Corning 3140 silastic sealant.

The photoluminescence (PL) measurements were conducted using an argon ion laser (tuned to 4880 Å) as an excitation source. The laser beam was chopped at a frequency of 750 Hz. The power incident on the sample was about 15 mW, and the spot size of the laser beam was about 0.2 cm. The HgI_2 crystals were cooled in an optical cryostat with liquid helium. The PL was dispersed by a Spex 1404 double pass spectrometer and detected by a photomultiplier with a S-20 response. The output of the photomultiplier was amplified by a Keithley 427 current amplifier and an EG&G 5207 lock-in amplifier. The spectral resolution of the PL spectrum in the near-band-edge region was about 0.5 Å.

At a wavelength of 4880 Å (corresponding to a photon energy of 2.54 eV), the laser source is above the bandgap of mercuric iodide (2.37 eV at 0 K), and the beam is absorbed within a depth of about 1000 Å from the surface. The PL emitted from the sample is primarily determined by the location of defects at which radiative recombination occurs, rather than the penetration depth of the laser radiation. Accounting for the effects of carrier diffusion, the actual depth probed by this technique is on the order of 1 micron. By irradiating points beneath and adjacent to the Ag contact, comparisons between the photoluminescence spectra from the bare HgI_2 crystal and from the Ag/HgI_2 interfacial region were made.

Measurements of thermally stimulated current were next conducted to obtain further information on carrier traps in the crystals. The specimens were biased at 12 V, and the current was measured as a function of temperature. The traps were initially filled by illuminating the Ag/HgI_2 interfacial region with the argon laser for a period of 5 minutes. This illumination was performed at a temperature of either 4.2 or 77 K, depending on whether liquid helium or nitrogen was used as a cryogen. The samples were then heated slowly by a 25-W resistive wire heater that was wrapped around a copper finger onto which the HgI_2 slab and alumina substrate were mounted. Different heating rates were selected by varying the voltage to the heater. Temperatures were measured with a silicon sensor that was pressed against the alumina substrate at a position of about 0.2 cm from the HgI_2 slab.

After completion of the TSC measurements, detector tests were conducted using gamma-ray radiation from an Americium-241 source. Dark current measurements were also performed to gain insight into the origin of the unusually large leakage currents observed in the fabricated detectors.

RESULTS AND DISCUSSION

(a) Effect of Semi-transparent Silver Films on the 4.2-K Photoluminescence Spectra of HgI_2

The top curve of Fig. 1 displays a typical photoluminescence spectrum for specimen #1 at 4.2 K from a point 2-mm away from the silver film. This PL spectrum was taken 3 days after deposition of the Ag film, and it closely resembles spectra taken from other slabs of the same crystal that were not deposited with Ag. A vertical bar in Fig. 1a is drawn at the wavelength where there is an emission line. Although some of the labelled peaks are not clearly visible in this spectrum, they are definitely present and can be easily seen by magnifying the intensity in the selected wavelength region of interest. Table I is a list of these PL peaks and their wavelengths at maximum intensity.

For all of the spectra taken from points adjacent to the Ag film, the PL in the near-bandedge region consisted of two dominant peaks (P2 and P3) at about 5318.6 and 5321.5 Å with three smaller peaks on the shorter wavelength side and several other lines on the longer wavelength side. This group of photoluminescence peaks between 5295 and 5400 Å, which lie slightly below the bandgap (5230 Å at 4.2 K), are collectively labeled as band 1. Two broad emission bands at about 5595 and 6200 Å are also observed in typical spectra, and they are labeled as band 2 and band 3, respectively. For all the different HgI_2 crystals used in these studies, the peak intensities of bands 2 and 3 were about one order of magnitude smaller than the peak intensity of P3. A more thorough discussion of the PL spectrum in undoped HgI_2 can be found in Ref. [27]. The PL spectra taken from points away from the Ag contact were nearly identical to the spectrum reported in Ref. [27]. The primary difference is that the peaks observed in the Ag-contacted specimens are shifted to slightly longer wavelengths (by 0.4-1.0 Å).

For points beneath the silver film on each sample, the photoluminescence spectra were significantly different. Figure 1b shows the PL spectrum from a typical point beneath the Ag film at a time of 3 days following the Ag deposition. The emission in the Band-1 spectral region (5290-5400 Å) is dominated by a single feature peaked at about 5321.2±1.5 Å. Although the peak of the emission is located at about the same wavelength as P3, it is much broader than P3 (see figs. 1a and 1b). In addition, the intensity of the Band 3 emission at about 6200 Å is greatly reduced beneath the Ag film. Band 3 has been attributed to unspecified impurities in as-grown crystals by earlier investigators [10], and if this is the case, it is presently unclear why these impurities are no longer effective as centers for radiative recombination in the region immediately below the Ag film.

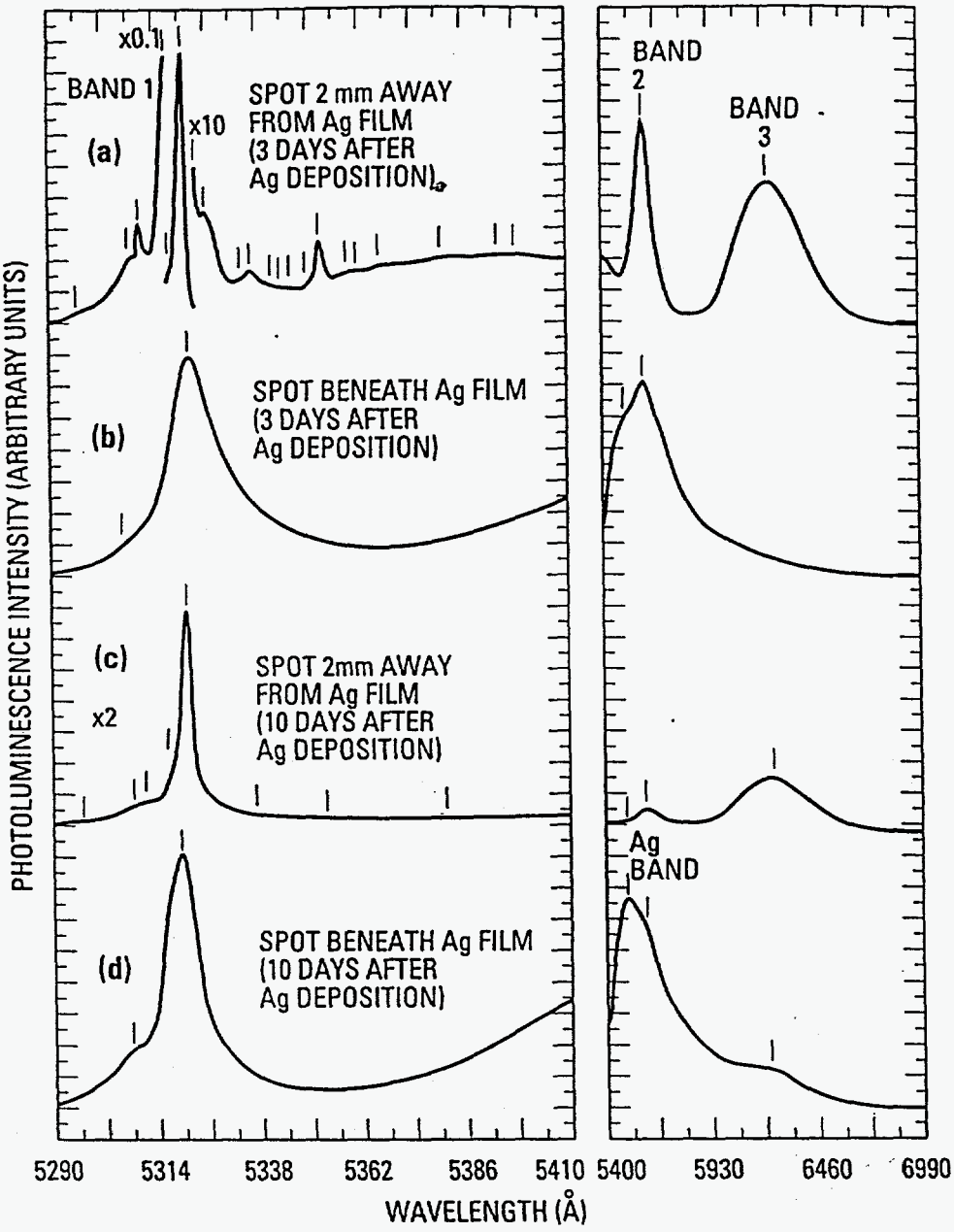

Figure 1. Photoluminescence spectra from spots that are either beneath or 2 mm away from the Ag film. The spectra in 1a and 1b were taken 3 days after the Ag film was deposited, and the spectra in 1c and 1d were taken 10 days after the film was deposited.

Another important difference between the PL from points beneath the Ag film and away from it is the presence of a new broad photoluminescence feature located at about 5490 Å. This emission peak typically appears as a distinct shoulder on the short wavelength side of Band 2 (see Fig. 1b). It has not been previously observed in undoped HgI_2. Since this peak is only observed in crystals with Ag impurities and it is the dominant photoluminescence feature in regions with high silver concentrations, we label the emission as "Ag Band". A similar emission band, which is located at 6720 Å, has been reported in copper-doped HgI_2 crystals. [20] These photoluminescence peaks now provide signatures for the presence of Ag and Cu contaminants in HgI_2 crystals and detectors.

Table I. Wavelengths and photon energies of the near-band-edge photoluminescence peaks of HgI_2 at 4.2 K.

Wavelength (Å)	Energy (eV)	Wavelength (Å)	Energy (eV)
5297.4	2.3398	5347.1	2.3181
5309.5	2.3345	5350.7	2.3165
5311.8	2.3335	5354.1	2.3151
5318.6	2.3305	5361.3	2.3120
5321.5	2.3293	5363.8	2.3109
5327.4	2.3267	5369.5	2.3084
5333.4	2.3241	5384.0	2.3022
5338.1	2.3220	5394.1	2.2979
5342.3	2.3202	5398.7	2.2959
5344.5	2.3192		

During the course of these investigations of the photoluminescence spectra of Ag-contacted HgI_2, it became clear that the results were dependent on the amount of time elapsed between the Ag deposition and the optical measurements. Figure 1d shows the PL spectra from the same spot beneath the Ag film as for Fig. 1b, but at a time of ten days after the film deposition, instead of three. The photoluminescence in the 5290-5410 Å region is still dominated by the same recombination center; however, the peak of the emission has shifted to a shorter wavelength (~5319±1Å), and it has narrowed in energy. After aging 100 days in a dessicator, the large emission in the Band-1 spectral region has moved to a slightly shorter wavelength (now peaked at 5318 Å), which is approximately the same peak position of the bound exciton P2 in undoped HgI_2. [27]

Based on these aging studies, it appears that the dominant emission beneath the silver contact, which is peaked at 5320±2 Å, is due to the bound exciton P2. Both the shift and narrowing of the energy of the P2 luminescence are probably caused by diffusion of the silver in the film and a reduction in the degree of stress within the Ag/HgI_2 interfacial region as the specimen ages. If this interpretation is correct, then the presence of the Ag contact quenches the emission of the bound exciton P3 located at about 5321 Å, which is usually the largest emission in the photoluminescence spectra of HgI_2. [8-14,16-20] Previous investigations of off-stoichiometric HgI_2 have led to the conclusion that P3 is associated with iodine-rich or mercury-deficient material. [18] Thus, the quenching of P3 beneath the Ag contact implies that Ag/I compounds are formed at the Ag/HgI_2 interface. The formation of Ag/I compounds would cause a reduction in the excess iodine contained in iodine-rich crystals or a filling of mercury vacancies in mercury-deficient crystals due to an accumulation of metallic Hg.

Other PL measurements on Ag-contacted HgI_2 samples that had been aged for 100 days showed that the broad-band emission peaked at about 5490 Å, labeled as "Ag band" in Fig. 1, was still clearly evident in the spectra. In addition the Band-3 luminescence, which was earlier quenched for points beneath the Ag film, has grown in intensity upon aging; although, it is still about three times less in intensity compared to points away from the Ag film. One possible explanation is that the Band-3 emission is associated with a defect located at (or near) the HgI_2 surface. It has been previously shown that the process of evaporating electrical contacts cleans the HgI_2 surface by sublimation during the vacuum exposure [18], which may account for the quenching of Band 3 in the region where Ag was deposited. The presence of the semi-transparent Ag film slows significantly the formation of the defect responsible for Band 3, as compared to the surfaces of bare HgI_2 crystals exposed to air. However, after an aging period of a few weeks, this particular defect reappears as an important center for radiative recombination for regions beneath the Ag contact. Both the thickness of the film (~100 Å) and the continued loss of Ag from the near-surface region via diffusion are probably important in this aging process.

Figure 1c shows a typical PL spectrum from a point about 2 mm away from the Ag film at a time of 10 days after the KI etch and Ag deposition. Comparing the results in Figs. 1a and 1c, we see that the aging of our Ag-contacted HgI_2 samples leads to a significant reduction in the overall

PL intensity, especially in the intensity of the bound exciton P3 (at ~5321 Å). These results on aged HgI_2 are for the most part consistent with an earlier study by Bao et al. [18] One important difference is associated with the emission at 5490 Å, which we labeled as "Ag Band" (see Fig. 1d). Several days after the Ag deposition we could detect the presence of this peak at all points on the 1cmx1cm HgI_2 surface, even though the 0.5-cm-diameter Ag film was deposited in only the central portion. Moreover, the intensity of this peak increased for spots that were closer to the Ag contact. These results provided conclusive evidence that Ag diffuses readily in HgI_2, and that the Ag diffusion was partly responsible for the temporal changes in the PL spectra for points beneath the Ag film and away from it (see figs. 1b and 1d).

Based on the measurements discussed above, there was some uncertainty as to whether silver diffusion in HgI_2 is a bulk or surface process. A separate experiment was performed on a 1cmx1cmx0.06cm HgI_2 slab with a semi-transparent 0.4-cm-diameter Ag film deposited on one side only. The specimen was loaded into the optical cryostat with the Ag-contacted side of the slab facing away from the laser excitation, and PL spectra were obtained from several spots on the backside of the sample. Figure 2a shows a typical spectra from a spot on the backside that was separated from the circular Ag film by 0.06cm of bulk HgI_2 (i.e., the sample thickness). The spectra was taken three days after the Ag deposition, and it looks indistinguishable from undoped HgI_2. [27] However, after a period of ten days, the PL spectrum from the same region exhibited the presence of Ag dopants (see figs. 1b and 2b). In particular, the emission observed at 5490 Å, which is an indicator of Ag impurities, is clearly resolved in the spectrum, and the Band-1 photoluminescence in the 5290-5410 Å region closely resembles the spectra from the Ag/HgI_2 interfacial region (see figs. 1b, 1d and 2b). The largest emission in the Band-1 spectral region is peaked at about 5318 Å, which is approximately the same location as the bound exciton P2 in undoped HgI_2. Figure 2c displays a typical spectrum from a point on the backside of the sample that was separated from the Ag film by 0.2cm of bulk HgI_2. This spectrum was also taken at a time of ten days following the Ag deposition. Photoluminescence results taken from several spots on the backside of the specimen showed that there was a smaller intensity of the "Ag Band" for regions that were farther separated from the Ag film by bulk HgI_2. These measurements reveal that silver diffuses through the bulk of the material, instead of by a surface diffusion process. The rate of diffusion at room temperature is estimated to be on the order of 10 μm/hr. A similar study was recently reported for copper contacts on HgI_2, and it revealed that copper was also a rapid diffuser in bulk HgI_2. [20]

(b) Effect of Vacuum Exposure on the 4.2-K Photoluminescence Spectra

Vacuum exposure experiments were conducted to determine the extent to which some of the features in the photoluminescence spectra are attributed to recombination centers residing at (or near) the HgI_2 surface. The vacuum exposure acts similar to a chemical etch in that it induces a rapid removal of material from the surface (~1 monolayer/s at 300 K). Figure 3a shows a typical spectrum from a point 2-mm away from the semi-transparent Ag film for a sample that had been stored in a dessicator for 3 days after the Ag deposition. The data were taken immediately after the specimen was exposed to 30 min of vacuum at a pressure of about $5x10^{-6}$ Torr. The spectrum looks similar to the one displayed in Fig. 1a, which was taken on a different slab from the same HgI_2 crystal at a time of 3 days after the Ag deposition. One notable difference is the broad emission at about 5835 Å, which is easily detected at most points in the vacuum-exposed specimens. This PL feature is typically not resolved for samples that have not been recently exposed to vacuum conditions. After several days of storage in air, this peak is either not resolved or observed at a much lower intensity (relative to Bands 2 and 3).

Figure 3b shows the photoluminescence spectrum from a typical point beneath the Ag film immediately after 30 min of vacuum exposure. The spectra was taken at a time of 3 days following the Ag deposition. The exposure of the specimen to vacuum also causes significant loss of material from the Ag-contacted region. Although the original location of the Ag film is still visually observable, the amount of Ag residing on the HgI_2 is greatly reduced. Since the material loss to uncoated HgI_2 is predicted to be on the order of 1 μm during the vacuum exposure, it is clear that the presence of the thin (~100 Å) silver film slows the loss of HgI_2 from the Ag/HgI_2 interfacial region. Comparing the results shown in Figs. 3b and 1b, several modifications due to the vacuum

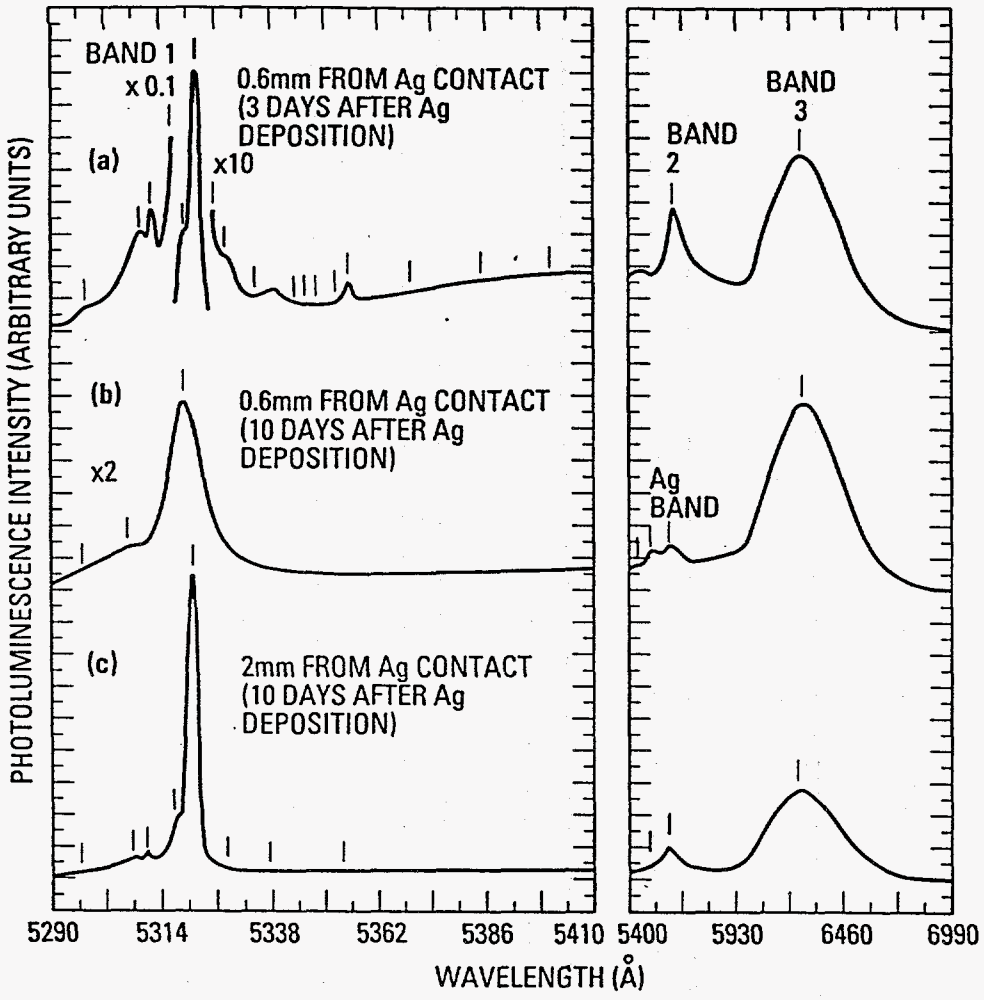

Figure 2. Photoluminescence spectra taken from different points on the backside of a Ag-contacted HgI_2 sample. The points were separated from the Ag film by either 0.6 or 2 mm of bulk HgI_2.

exposure are obvious. First, the single emission in the PL spectrum peaked at about 5320±2 Å is much narrower after the vacuum exposure. In addition, the two bound excitons P2 and P3 are easily resolved in the vacuum-exposed sample. These changes are attributed to a reduction in the amount of silver within the near-surface region of the HgI_2 after the vacuum exposure, which decreases the stress in this region. Another difference is that the Ag Band, which is located at 5490 Å, becomes the dominant peak in the photoluminescence spectrum for the vacuum-exposed specimens.

(c) Temperature Dependence of the PL Spectrum for the Ag/HgI_2 Interfacial Region

The temperature dependence of the photoluminescence of HgI_2 has been reported by several different investigators (see, for example, Refs. [8, 10 and 12]). Their results demonstrated a strong dependence of the PL on the lattice temperature. Figure 4 shows the PL spectra from the interfacial region of the HgI_2 crystal and Ag film in the temperature range of 1.5 to 95 K. These spectra were taken at a time of 13 days following the KI chemical etch and Ag deposition. The specimen was exposed to vacuum conditions for 30-min prior to the PL measurements in order to more clearly resolve the fine detail in the Band-1 spectral region. When the temperature was increased from 1.5 K, the intensities of the dominant bound excitons at 5318 and 5321 Å began to decrease, and these emissions were not resolved for temperatures exceeding about 45 K. The lines

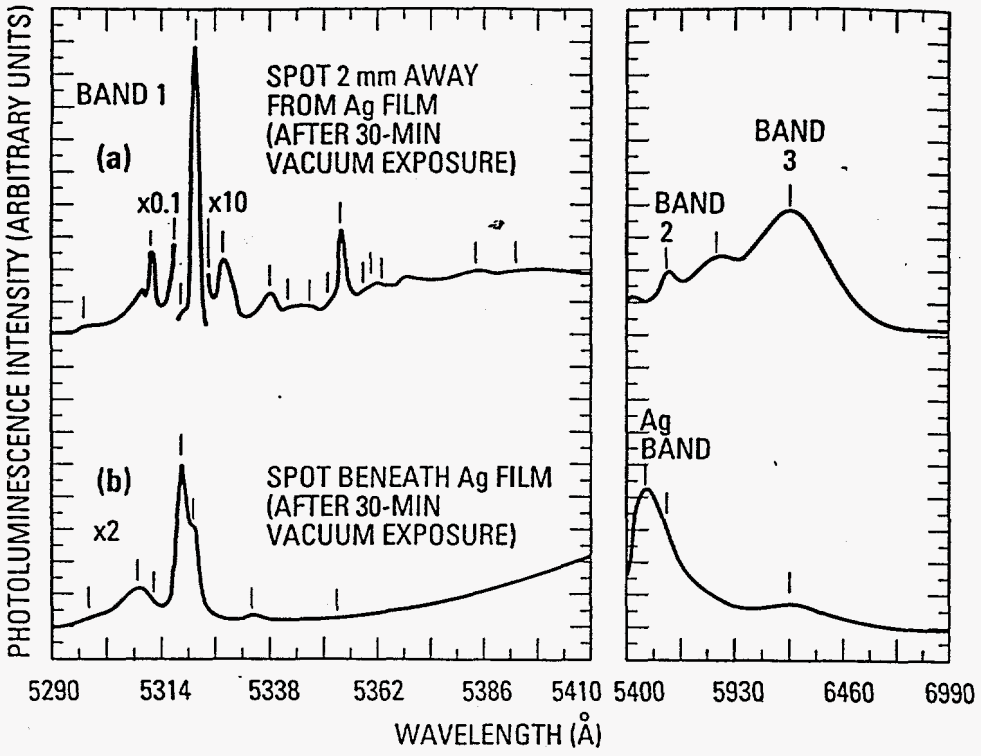

Figure 3. Photoluminescence spectra taken after a 30-min vacuum exposure from points either beneath or 2 mm away from the Ag film.

at 5309 and 5311 Å remained fairly constant up to about 12 K, then began to increase in the range of 12-35 K, and then decreased at higher temperatures. These two lines merged into a single symmetrical band at about 70 K. This band was still observable at temperatures up to 150 K, although the peak intensity was 2-3 orders of magnitude smaller than at 1.5 K. The intensity of the silver band at 5490 Å decreased monotonically with increasing temperature, and it was found to disappear at approximately 40 K. The intensities of Band 2 and Band 3 at 5600 and 6220 Å also decrease with temperature, and their emissions were measurable up to temperatures of approximately 95 and 150 K, respectively. All of these changes in the line intensities were accompanied by a shift of the spectrum to longer wavelengths due to the narrowing of the bandgap with increasing temperature.

The temperature dependences of the photoluminescence lines P2, P3, Ag band, Band 2, and Band 3 are typical of excitons bound to a point defect or a defect complex. The distribution of a bound exciton is proportional to $\exp(-E_{T,i}/kT)$, where $E_{T,i}$ is the energy for thermal dissociation of the ith bound exciton and T is the lattice temperature. Thus, the value of $E_{T,i}$ for the ith bound exciton is given approximately by the slope of the logarithm of the photoluminescence intensity versus reciprocal temperature over the temperature range where the line intensity is decreasing exponentially. For the temperature range in which the PL intensities were used in each numerical fit, the determination of $E_{T,i}$ by this method assumes that the binding energy of the exciton-defect complex varies weakly with T and that the population of each bound exciton is not increased significantly at higher temperatures due to thermal dissociation of a more weakly bound exciton or defect complex. The values of E_T for the emission lines P2, P3, Ag band, Band 2 and Band 3 are shown in Table II. The value of E_T shown in Table II for the Ag band was obtained from fitting PL spectra taken from points immediately below the Ag contact, and the other values for $E_{T,i}$ were obtained from spectra taken from points both away from and beneath the Ag contact. The value of $E_{T,i}$ for each recombination center must be considered as approximate, because the precise value depends on the range of temperature selected for the fit, and even for the same range of T there is typically a variation of ±20% for the different specimens studied. The thermal dissociation energy

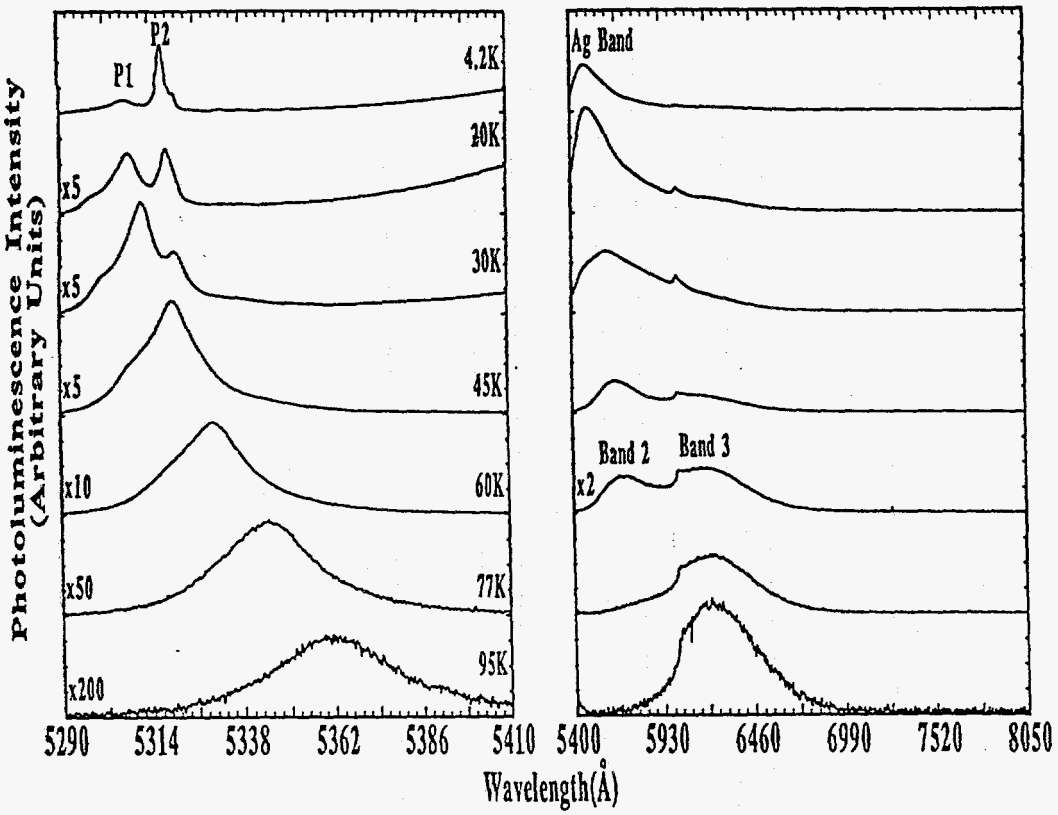

Figure 4. Temperature dependence of photoluminescence spectra.

Table II. Values for the thermal dissociation energies for several radiative recombination centers.

Spectral Line	Peak Position at 4.2 K (Å)	E_T (meV)	Temperature Range for Fit (K)	Energy below line at 5311 Å (meV)
P2	5318	4	20-35	2.9
P3	5321	6	20-35	4.1
Ag Band	5490	24	20-45	75.9
Band 2	5595	55	55-100	118.3
Band 3	6200	76	90-135	334.5

of the emission line P2 is very close to the value reported earlier [10]; however, our value of E_T for the line P3 is considerably smaller than the one shown in Ref. [10].

The temperature dependences of two PL lines, located at about 5309 and 5311 Å at 4.2 K, are markedly different from the other lines. The intensities of these two lines increase in the range of 12-35 K, which coincides with the decrease in the intensities of P2 and P3. These data suggest that the lines at 5309 and 5311 Å (at 4.2K) are associated with free excitons, and the intensity increases are caused by the thermal liberation of bound excitons P2 and P3 into free excitons. This interpretation agrees with the one reported in Ref. [10], but it is different than the interpretation proposed in Ref. [8]. Following Merz and Wu [10], we assume that the line at 5311 Å is the ground state of the free exciton. Table II shows the energy separation at 4.2 K between the line at 5311 Å (i.e., the free exciton) and some of the other PL lines at lower energies, which gives information on the binding energy of the excitonic state. The binding energies of P2 and P3 are in good agreement with the thermal dissociation energies, providing further evidence that P2 and P3 are excitons bound to a point defect. However, the predicted binding energies of the Ag band, Band 2, and Band 3 are much larger than their corresponding thermal dissociation energies. The

implication is that the Ag band, Band 2 and Band 3 are caused by donor-acceptor radiative recombination and that the values for E_T are attributed to the thermal dissociation of the more shallow donor or acceptor within the defect complex.

(d) Thermally Stimulated Current (TSC) Measurements

Figure 5 shows TSC spectra from 78 to 278 K for six different heating rates. Three traps are observed at temperatures of about 90, 96 and 212 K. Only one trap was observed at about 8 K in the temperature range of 4 to 78 K. The traps are different than those found in detectors with Al and Pd contacts, suggesting that interactions between the metal contact and mercuric iodide have strong effects on the deep level defects in HgI_2. [28] The activation energies of the defect states can be estimated by using the TSC taken at different heating rates. Following the analysis of Refs. [29-30], the trap depths are found to be 9.5, 82, 57 and 92 meV for the four traps peaked at temperatures of 8, 90, 96 and 212 K, respectively.

(e) Dark Current Measurements and Evaluation of Ag-contacted HgI_2 Detectors

The thermally stimulated current measurements also showed a rapid increase in the dark current as the lattice temperature was increased above 240 K (see Figure 5). For a Ag film having a thickness of about 100 Å, the increased dark current is about 3 orders of magnitude larger than that typically observed for Pd-contacted HgI_2 devices. We believe that the conduction mechanism is associated with the ionic movement of Ag, instead of the substitution of Ag on a Hg site to form a shallow electrically active defect. AgI is a well-known superionic material [31], in which case the material possesses intrinsic structural disorder with respect to Ag^+ ions. We know from photoluminescence measurements that Ag is a rapid diffuser in bulk HgI_2, and it is possible that the increased electrical conductivity of Ag-doped HgI_2 is associated with the movement of Ag over energetically allowed positions in a rigid I sublattice. It is also worth mentioning that Ag_2HgI_4 has been shown [32] to possess ionic conductivity of considerable magnitude, especially above a transition point at 324 K. Future experiments to study mass transport of Ag in HgI_2 during application of an external bias and the possible formation of a Ag_2HgI_4 ternary compound are planned.

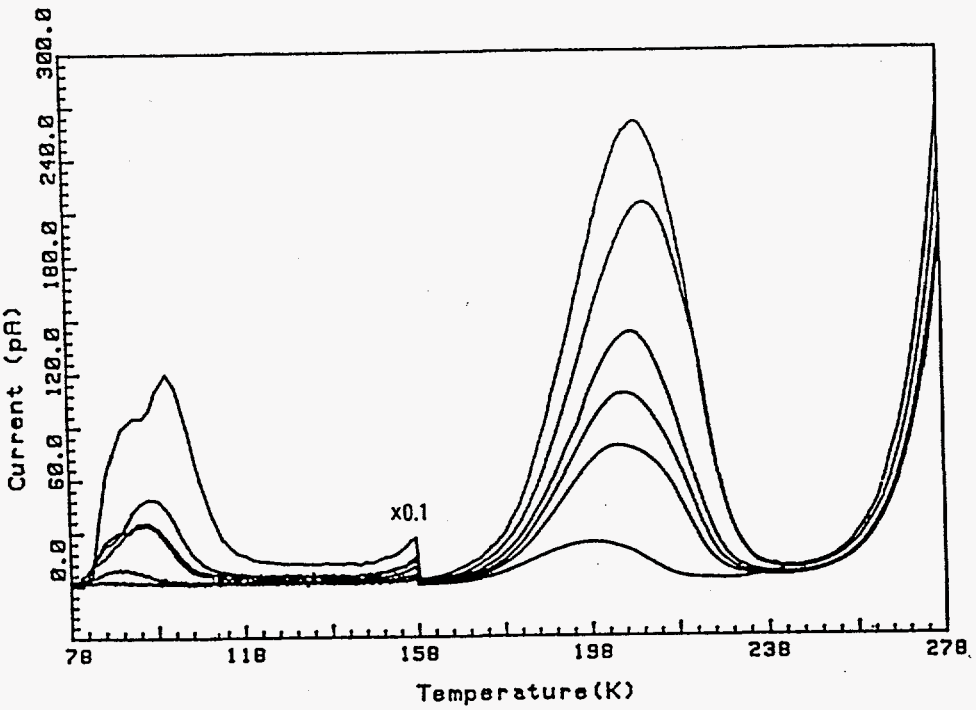

Figure 5. Thermally stimulated current spectra for Ag-contacted HgI_2 at six different heating rates.

HgI_2 nuclear spectrometers with Ag electrodes were fabricated and evaluated with an Am-241 x-ray source. Based on our measurements of Pd-contacted HgI_2 detectors, the 59.5-keV photon emitted from Am-241 shows a distinct photopeak with a full-width-at-half-maximum of about 3-6%. No photopeak was observed for Ag-contacted HgI_2 detectors due to the large leakage currents, confirming that Ag electrodes are unacceptable for HgI_2 detector applications.

Although Ag impurities are obviously detrimental to HgI_2 devices, it is possible that doping the material with excess Ag might allow one to perform new diagnostic tests with electron and ion beams. In this case one would intentionally add Ag to HgI_2 to reduce the resistivity of the specimen, and thus reduce the charging problems that typically exist when these techniques are used on bare undoped HgI_2. It is also possible that the solubility of Ag in HgI_2 crystals is fairly high, so that one can alter the bulk resistivity of HgI_2 by several orders of magnitude by doping HgI_2 with Ag.

CONCLUSIONS

We have completed a study of the effects of Ag dopants on the photoluminescence and thermally stimulated current spectra of HgI_2 crystals and have fabricated gamma-ray detectors with Ag electrodes. The results show that Ag is unacceptable as a contact material for x-ray and gamma-ray detector applications. They also show that special care must be taken to avoid contamination of HgI_2 with Ag during the purification of source materials, crystal growth, chemical etching, polishing, attachment of contacts, encapsulation, and handling practices.

ACKNOWLEDGMENTS

We would like to acknowledge the U. S. Department of Energy for financial support. One of us (T.E.S.) would also like to acknowledge support from the National Science Foundation through a Presidential Young Investigator award. We would also like to thank A. Antolak, D. David, S. Haney, and R. Anderson for many useful discussions.

REFERENCES

1. W. R. Willig, Nucl. Instrum. Methods **96**, 615 (1971).
2. H. L. Malm, IEEE Trans. Nucl. Sci. **NS-19**, 263 (1972).
3. J. P. Ponpon, R. Stuck, and P. Siffert, Nucl. Instrum. Methods **119**, 297 (1974).
4. J. H. Howes and J. Watling, Mat. Res. Soc. Symp. Proc. Vol. **16**, 207 (1983).
5. H. L. Malm, T. W. Raudoff, M. Martina, and K. R. Zanio, IEEE Trans. Nucl. Sci. **NS-20**, 500 (1973).
6. R. C. Whited and M. Schieber, Nucl. Instrum. Methods **162**, 119 (1979).
7. R. H. Bube, Phys. Rev. **106**, 703 (1957).
8. B. N. Novikov and M. M. Pimonenko, Sov. Phys. Semicond. **4**, 1785 (1971).
9. Z. L. Wu, J. L. Merz, L. van den Berg, and W. F. Schnepple, J. Lumin. **24**, 197 (1981).
10. J. L. Merz, Z. L. Wu, L. van den Berg, and W. F. Schnepple, Nucl. Instrum. Methods **213**, 51 (1983).
11. I. Kh. Akopyan, B. V. Bondarenko, B. A. Kazennov, and B. V. Novikov, Sov. Phys. Solid State **29**, 238 (1987).
12. D. Wong, T. E. Schlesinger, R. B. James, C. Ortale, L. van den Berg, and W. F. Schnepple, J. Appl. Phys. **64**, 2049 (1988).
13. D. Wong, X. J. Bao, T. E. Schlesinger, R. B. James, A. Y. Cheng, C. Ortale, and L. van den Berg, Appl. Phys. Lett. **53**, 1537 (1988).
14. R. B. James, X. J. Bao, T. E. Schlesinger, J. M. Markakis, A. Y. Cheng, and C. Ortale, J. Appl. Phys. **66**, 2578 (1989).
15. P. M. Petroff, Y. P. Hu, F. Milstein, J. Appl. Phys. **66**, 2525 (1989).
16. R. B. James, D. K. Ottesen, D. Wong, T. E. Schlesinger, W. F. Schnepple, C. Ortale, and L. van den Berg, Nucl. Instrum. Methods **A283**, 188 (1989).

17. R. B. James, X. J. Bao, T. E. Schlesinger, J. M. Markakis, A. Y. Cheng, and C. Ortale, in Fluorescence Detection III, edited by E. R. Menzel, Proc. SPIE **1054**, 103 (1989).
18. X. J. Bao, T. E. Schlesinger, R. B. James, R. H. Stulen, C. Ortale, and A. Y. Cheng, J. Appl. Phys. **68**, 86 (1990).
19. R. B. James, X. J. Bao, T. E. Schlesinger, C. Ortale, and A. Y. Cheng, J. Appl. Phys. **67**, 2571 (1990).
20. X. J. Bao, T. E. Schlesinger, R. B. James, R. H. Stulen, C. Ortale, and L. van den Berg, J. Appl. Phys. **67**, 7265 (1990).
21. L. R. Williams and R. J. Anderson, in Picosecond And Femtosecond Spectroscopy from Laboratory to Real World, K. A. Nelson, Editor, Proc. SPIE **1209**, 140 (1990).
22. L. R. Williams, R. J. Anderson, and M. J. Banet, in Ultrafast Phenomena VII, E. Ippen, Editor (Springer-Verlag, New York, 1990).
23. J. M. Markakis and A. Y. Cheng, Nucl. Instrum. Methods A**283**, 232 (1989).
24. H. A. Lamonds, Nucl. Instrum. Methods **213**, 5 (1983).
25. A. Jeffrey and M. Vlasse, Inorg. Chem. **6**, 396 (1967).
26. E. A. Brandes, Smithells Metals Reference Book, 6th ed. (Butterworths, London, 1983), p. 8-58.
27. X. J. Bao, T. E. Schlesinger, R. B. James, C. Ortale, and L. van den Berg, J. Appl. Phys. **68**, 2951 (1990).
28. T. E. Schlesinger, X. J. Bao, R. B. James, A. Y. Cheng, C. Ortale, and L. van den Berg, Nucl. Instrum. Methods A**322**, 414 (1992).
29. A. G. Milnes, Deep Impurities in Semiconductors (Wiley-Interscience, New York, 1963), p. 230.
30. S. B. Hyder, J. Appl. Phys. **48**, 313 (1977).
31. Y. Y. Gurevich and A. K. Ivanov, Semiconductors and Semimetals **26**, 229 (1988).
32. J. A. A. Ketelaar, Z. Physik. Chem. B**26**, 327 (1934).

Left Intentionally Blank

MATERIALS RESEARCH SOCIETY SYMPOSIUM PROCEEDINGS VOLUME 302

Semiconductors For Room-Temperature Radiation Detector Applications

Symposium held April 12-16, 1993, San Francisco, California, U.S.A.

EDITORS:

R.B. James
Sandia National Laboratories
Livermore, California, U.S.A.

T.E. Schlesinger
Carnegie Mellon University
Pittsburgh, Pennsylvania, U.S.A.

Paul Siffert
Laboratorie PHASE/CRN
Strasbourg, France

Larry Franks
EG&G Energy Measurements
Goleta, California, U.S.A.

MRS
MATERIALS RESEARCH SOCIETY
Pittsburgh, Pennsylvania

INCORPORATION OF EXTRINSIC DEFECTS IN HgI_2 DURING DETECTOR FABRICATION

J.M. Van Scyoc*, T.E. Schlesinger*, R.B. James**, A.Y. Cheng***, C. Ortale***, And L. van den Berg***
*Department of Electrical and Computer Eng., Carnegie Mellon University, Pittsburgh, PA
**Sandia National Laboratories, Livermore, CA
***EG&G Energy Measurements, Goleta, CA

ABSTRACT

The incorporation of extrinsic defects into mercuric iodide substrates during detector fabrication can be extremely detrimental to device performance. In particular, extrinsic defects can act as trapping and recombination centers, and they can reduce charge collection efficiencies, decrease $\mu\tau$ product, or contribute to polarization effects in nuclear detectors. In this paper we present results of processing, photoluminescence, and electromigration experiments that clearly show that extrinsic defects can be incorporated in mercuric iodide during detector fabrication. By observing the luminescence features characteristic of Cu and Ag in mercuric iodide, we show that both these materials are taken up by mercuric iodide crystals during etching with KI if the etching solution is contaminated with these elements. The migration of material from contacts into the crystal, as shown by resistance measurements, is also presented. We infer from this work that other defects which are detrimental to device performance may also be incorporated in mercuric iodide if insufficient care is taken during device fabrication. Suggestions are therefore made as to some of the precautions that must be taken in order to realize the highest quality detectors.

INTRODUCTION

Red mercuric iodide (α-HgI_2) is well suited for use in room temperature radiation detectors because of many of its properties [1-5]. These properties include high atomic numbers (Z_{Hg}=80 and Z_I=53), low electron-hole creation energy (4.2eV at 300K) [3-5], and high resistivity ($10^{13}\Omega$*cm) [5]. However, detector quality is still limited by many material and processing issues, resulting in low manufacturing yields, high production costs [6], and long term instability. Defects introduced from the starting material and during the processing are possibly responsible for these problems.

Several steps are required to produce mercuric iodide detectors. After purification of the starting material and crystal growth, slices are cut from the larger crystal and polish etched in KI solution. Then contacts are deposited, and the detectors are mounted on alumina substrates. During this production many individual processes are involved. Chemical etching, material heating, and vacuum exposure are encountered throughout detector formation. It has been shown that these steps can have noticeable effects on the material properties [7]. The contacting process is also critical in detector fabrication. Choice of contact material and method of deposition have a large impact on the quality and stability of the detector. Several materials have been studied for use as contacts, although palladium has been standardized as the current metal of choice. Evaporation or sputter deposition of the metal requires vacuum

Mat. Res. Soc. Symp. Proc. Vol. 302. ©1993 Materials Research Society

exposure, and can result in heating of the mercuric iodide, leading to material degradation.

As mentioned before, all of the processing steps involved in detector formation can re in defects in the mercuric iodide. These defects can be extrinsic or intrinsic to the merc iodide crystals. These defects affect detector performance by increasing the dark curren shallow dopants, or acting as carrier traps and degrading the long term reliability v polarization effects. Therefore, characterization of the defects and their origins is of g importance. Determining how specific processing steps introduce particular defects, and w can be done to prevent this is of utmost importance in increasing the viability of merci iodide as a detector material. In this paper we consider the introduction of defects during etching process and the introduction of defects from the detector contacts.

EXPERIMENTS

Ag and Cu Doped Etches

Several times during the production of mercuric iodide detectors chemical etching involved. Chemical etching is used to prepare the material surfaces for subsequent processir The etching removes the exposed surface to reveal fresh crystal, smoothes the surfaces, a removes mechanical damage. However, this etch can also introduce defects. Contaminants the etch can be transported into the mercuric iodide during the etching.

One method of materials characterization that has been shown to be applicable to the stuc of mercuric iodide is photoluminescence spectroscopy (PL). PL is a useful tool for findir defects [7-9] and impurities [10-12] introduced during processing. Regarding the latter, c interest here, broad emissions at 5490Å and 6720Å in the PL spectra are associated with A and Cu impurities, respectively.

In this work we introduced controlled amounts of Ag or Cu into the etching solutions, an studied the resultant PL spectra for characteristic peaks. Ag and Cu are of interest becaus both can be present in the KI crystals used to produce the etching solutions. As revealed b inductively coupled plasma mass spectroscopy (ICP-MS), Ag is present in the 1 - 50ppl range, and Cu in the 1 - 500ppb range in typical vendor lots.

Photoluminescence measurements were performed at 4.2K with an argon ion laser as the excitation source. The laser was operated at 20mW and tuned to 488nm, corresponding to an excitation energy of 2.54eV, which is above the bandgap of HgI_2 (2.37eV at 4.2K). The PL was generated from a region beneath the surface of the sample extending to a depth of a few microns. The laser beam was modulated at 750Hz by a mechanical chopper and had a spot size of about 1.5mm diameter. Samples were cooled in an optical cryostat with liquid helium below the sample and out of the optical path. The luminescence was collected by two collimating lenses and directed into a 0.85m SPEX 1404 double pass spectrometer. The entrance and exit slits on the spectrometer were set to give a spectral resolution of 1Å. The signal was detected with an S20 photomultiplier tube, amplified by a Keithley 427 current amplifier and an EG&G 5207 lock-in amplifier, and recorded by an HP 9836 computer.

Prior to any PL measurements, the HgI_2 samples were etched in 10% by weight KI solution to remove degraded surface layers. Mild agitation in the KI for 1min. removes the

top 30μm of material. The samples were then rinsed in deionized water for several minutes. Measurements were made at four locations on samples to ensure statistically sound results. Samples were then introduced to the Ag or Cu doped KI solution and etched for 1min., followed by a DI rinse. Both solutions had an impurity concentration of 0.09% by weight, obtained from Fisher 1000ppm standard reference solutions. The resultant KI/impurity solutions were mixed, allowed to sit for several hours, then filtered to remove the solid precipitates (AgI or Cu_2I_2). PL spectra were then taken on each sample at the same four points as before the etch.

PL spectra are typically divided into several wavelength regions of interest. The short wavelengths from 5290Å to 5410Å are considered Band 1. The longer wavelengths from 5400Å to 8050Å contain several broad emission bands, including Band 2 at 5595Å, Band 3 at 6200Å, Band 4 at 7550Å, and the Ag and Cu impurity bands mentioned above. Figure 1 below shows the PL spectra of a sample before and after etching in the Ag-doped KI solution. The peak that appears at 5490Å in the PL spectrum after the Ag-doped etch appears only after Ag has been introduced to samples. Therefore, it is considered to indicate the presence of defects caused by Ag and is labeled the "Ag Peak". Figure 2 below shows the PL for the Cu-doped etched sample. The peak that appears at 6720Å in the PL spectrum after the Cu-doped etch appears only after Cu introduction, as with the Ag-doped etch. Similarly, it is considered to indicate the presence of Cu impurity defects and is labeled the "Cu Peak".

As these two spectra demonstrate, the presence of contaminants in the solution used to etch HgI_2 samples during detector processing can cause defects to appear in the material, which can lead to degraded detector performance.

Contact Electromigration

In order to collect charge photogenerated in the HgI_2, good electrical contacts must be

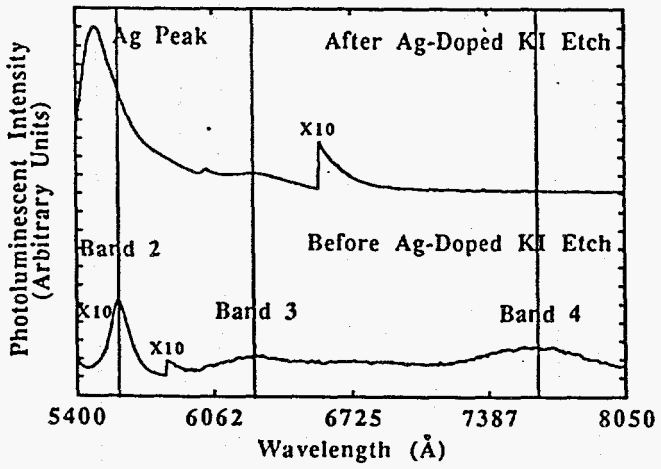

Figure 1. Photoluminescence spectrum of HgI_2 sample before and after etching in 10% KI solution doped with 0.09% Ag.

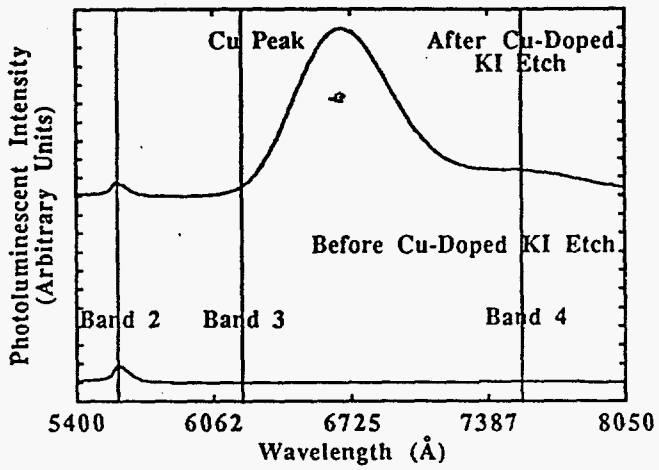

Figure 2. Photoluminescence spectrum of HgI_2 sample before and after etching in 10% KI solution doped with 0.09% Cu.

deposited on the surfaces. However, the material used for contacts can have negative effects on the quality of the underlying material. The contact metal can migrate into, or react with the mercuric iodide, resulting in defects in the mercuric iodide, and degradation of the contact.

One possible way to study the movement of contact material into the mercuric iodide is to monitor the sheet resistance of the contact itself. As material leaves the contact, the effective thickness decreases and the measured sheet resistance increases. By characterizing this change with respect to time, it is possible to obtain a measure of the rate of transport of material into the mercuric iodide. By biasing the samples during the time of interest, an indication of the polarity of contact material ions can be determined. For example, if the resistance increases faster with the contact under study more positively biased, then positive metal ions are leaving the contact.

Another possible method is to monitor the effective resistivity of the bulk mercuric iodide. As the mobile contact ions move into the mercuric iodide, they decrease its resistance by increasing mobile carrier concentrations. The polarity of particles entering the HgI_2 can be determined by reasoning similar to the method considered above.

In this work we deposited contacts of Cu and W onto HgI_2 samples. As discussed above, Cu can easily be introduced during the detector processing, and is detrimental to material and detector quality. In contrast, PL indicates that W is relatively stable as a contact material on HgI_2 [11]. All contact films were sputtered at ambient temperature in 5mT argon pressure using a Kurt J. Lesker Company Mini-Supersystem. The first Cu films were 500Å thick, but were found to react with the HgI_2 too rapidly, and to be too thin to probe because of the softness of the HgI_2 underneath. Cu films of 2000Å were found to be satisfactory for preliminary measurements. Since W is a hard refractory metal, 500Å W films were solid enough to probe. All of these preliminary samples were not biased, and were stored in desiccator cabinets in ambient room light.

Figure 3 below shows the sheet resistivity for a 2000Å Cu film. The graph also shows the results from the same film on a glass slide. Since the resistance of the film on glass is stable, the change in resistance of the film on mercuric iodide must be related to either the diffusion of contact Cu into the substrate, or the reaction of the two materials. The resistance follows an exponential form, except for the first few points. The cause of this initial flat portion is as yet unclear, but it could be related to limitations in the measurement setup, or some incubation period phenomenon. Figure 4 below shows the W results. The W results are clearly much more stable, yet the film on the HgI_2 did exhibit a slight linear rise not found in the film on glass. Therefore, there is some activity associated with the W, but it is not nearly as severe as that of the copper. Visual inspection of the samples agreed with this, as the Cu contact appeared to be "swallowed up" by the mercuric iodide substrate, while the W film appeared unchanged.

Future measurements of this nature will expand upon the sample biasing conditions and ambient environment.

CONCLUSIONS

In conclusion, we have shown how the details of the processing of mercuric iodide for detectors can have a significant affect on the quality of the material and hence the detectors produced. In particular, impurities in the chemical etchants can be introduced into the bulk material and contact material can also diffuse in. Therefore, careful examination of processing procedures is required. The purity of all materials used during processing and the choice of appropriate contact materials must be considered in order to achieve good quality devices with long term reliability.

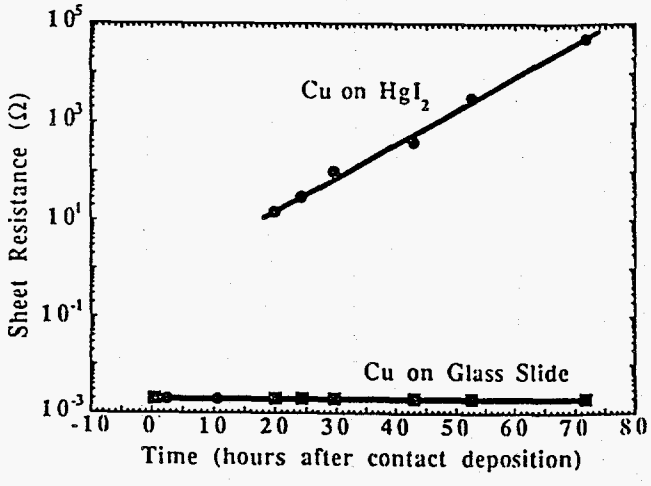

Figure 3. Sheet resistivity versus time for a 2000Å Cu film sputtered on HgI_2 compared to the same on a glass slide.

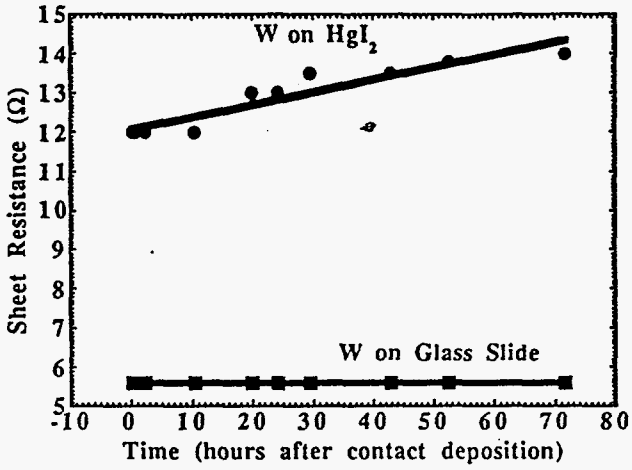

Figure 4. Sheet resistivity versus time for a 500Å W film sputtered on HgI_2 compared to the same on a glass slide.

AKNOWLEDGMENTS

This work was supported by the U.S. Department of Energy. One of us [T.E.S.] would like to acknowledge the support of the National Science foundation through the Presidential Young Investigator Program.

REFERENCES

1. W.R. Willig, *Nucl. Instrum. Meth.* **96**, 615 (1971).
2. H.L. Malm, *IEEE Trans. Nucl. Sci.* **NS-19**, 263 (1972).
3. J.P. Ponpon, R. Stuck, and P Siffert, *Nucl. Instrum. Meth.* **119**, 197 (1974).
4. J.H. Howes and J. Watling, *Mat. Res. Soc. Symp. Proc.* **16**, 207 (1983).
5. H.L. Malm, T.W. Raudoff, M. Martina, and K.R. Zanio, *IEEE Trans. Nucl. Sci.* **NS-20**, 500 (1973).
6. N.L. Skinner, C. Ortale, M.M. Schieber, and L. van den Berg, *Nucl. Instrum. Meth. Phys. Res.* **A283**, 119 (1989).
7. X.J. Bao, T.E. Schlesinger, R.B. James, R.H. Stulen, C. Ortale, and A.Y. Cheng, *J. Appl. Phys.* **68**, 86 (1990).
8. R.B. James, X.J. Bao, T.E. Schlesinger, J.M. Markakis, A.Y. Cheng, and C. Ortale, *J. Appl. Phys.* **66**, 2578 (1989).
9. X.J. Bao, T.E. Schlesinger, R.B. James, G.L. Gentry, A.Y. Cheng, and C. Ortale, *J. Appl. Phys.* **69**, 4247 (1991).
10. X.J. Bao, T.E. Schlesinger, R.B. James, R.H. Stulen, C. Ortale, and L. van den Berg, *J. Appl. Phys.* **67**, 7265 (1990).
11. X.J. Bao, Ph.D. thesis, Carnegie Mellon University, 1991.
12. R.B. James, X.J. Bao, T.E. Schlesinger, C. Ortale, and A.Y. Cheng, *J. Appl. Phys.* **67**, 2571 (1990).

Left Intentionally Blank

MATERIALS RESEARCH SOCIETY
SYMPOSIUM PROCEEDINGS VOLUME 378

Defect and Impurity Engineered Semiconductors and Devices

Symposium held April 17-21, 1995, San Francisco, California, U.S.A.

EDITORS:

S. Ashok
The Pennsylvania State University
University Park, Pennsylvania, U.S.A.

J. Chevallier
CNRS
Meudon, France

I. Akasaki
Meijo University
Nagoya, Japan

N.M. Johnson
Xerox Palo Alto Research Center
Palo Alto, California, U.S.A.

B.L. Sopori
National Renewable Energy Laboratory
Golden, Colorado, U.S.A.

PITTSBURGH, PENNSYLVANIA

DEFECTS AND IMPURITIES IN MERCURIC IODIDE PROCESSING

J. M. VAN SCYOC*, R. B. JAMES*, T. E. SCHLESINGER**, AND T. S. GILBERT**
*Advanced Materials Research Department, Sandia National Laboratories, MS 9162, P.O. Box 969, Livermore, CA 94551
**Department of Electrical and Computer Engineering, Carnegie Mellon University, 5000 Forbes Avenue, Pittsburgh, PA 15213

ABSTRACT

In the fabrication of mercuric iodide (HgI_2) room temperature radiation detectors, as in any semiconductor process, the quality of the final device is very sensitive to the impurities and defects present. Each process step can change the effects of existing defects, reduce the number of defects, or introduce new defects. In HgI_2 detectors these defects act as trapping and recombination centers, thereby degrading immediate performance and leading to unstable devices. In this work we characterized some of the defects believed to strongly affect detector operation. Specifically, we studied impurities that are known to be present in typical HgI_2 materials. Leakage current measurements were used to study the introduction and characteristics of these impurities, as such experiments reveal the mobile nature of these defects. In particular, we found that copper, which acts as a hole trap, introduces a positively charged center that diffuses and drifts readily in typical device environments. These measurements suggest that Cu, and related impurities like silver, may be one of the leading causes of HgI_2 detector failures.

INTRODUCTION

Red mercuric iodide (α-HgI_2) has been researched for almost three decades for use as a room-temperature radiation detector material. It has several properties which make it an extremely attractive material for this purpose. The high average atomic number of the constituent atoms (Z_{Hg}=80, Z_I=53, or Z_{avg}=62) results in a high efficiency for stopping photons into the low MeV range. The electron-hole pair creation energy of 4.2eV at room temperature leads to a sufficiently large signal response per photon. And finally, the room temperature bandgap of 2.13eV results in a resistivity on the order of $10^{14}\Omega$*cm and a dark current on the order of picoamps for typical device structures. These properties combine to give a material that has been used to produce some of the highest resolution room-temperature x-ray and gamma-ray detectors [1-4]. In addition, the capability for room temperature operation results in the possibility of compact spectrometer field instruments for applications such as environmental monitoring or special nuclear materials (SNM) monitoring.

However, these positive properties are balanced by several negative properties. Some of the basic properties of HgI_2 cause many of the problems. The fact that it is a compound semiconductor immediately leads to stoichiometry issues. The material has a relatively high vapor pressure at room temperature, and in addition, the iodine is generally preferentially sublimed at a faster rate, yielding mercury rich surfaces. The red tetragonal α-HgI_2 phase undergoes a phase transition around 125°C to the yellow orthorhombic β-HgI_2 phase which destroys the crystallinity of the material upon return to room temperature. Finally, the material is mechanically very soft and also delaminates easily at the iodine layers.

The extrinsic factors that degrade mercuric iodides' usefulness are related to carrier trapping centers that are introduced into the material. These can arise from structural damage to the crystal or stoichiometric changes during the crystal growth and device fabrication processes. Of interest here, however, are the impurities that are introduced into the material, either from the original starting materials (generally mercuric chloride and potassium iodide), or further along in the fabrication. Several impurities are believed to play a role in mercuric iodide detectors, ranging from hydrocarbons to metallic elements. The impurities of interest here are copper and related metals.

Mat. Res. Soc. Symp. Proc. Vol. 378 © 1995 Materials Research Society

These factors all lead to problems in the initial yield of high quality detectors, and the long term reliability of the detectors. These two problems combine to limit the applications of these sensors particularly in the commercial arena. Given that the basic intrinsic material properties cannot be changed, one of the primary ways to improve the material is to identify the impurities that are deleterious to the detector performance, and work to reduce their presence. In this work we studied how copper and related impurities can be a prime source of problems in mercuric iodide detectors.

EXPERIMENTS AND RESULTS

Mercuric Iodide Detector Response

Mercuric iodide and other high resistivity room temperature semiconductor radiation detector materials allow for a very simple device structure. A bulk slab of material has simple ohmic contacts applied to opposite faces and a bias applied. The incoming x-ray or gamma-ray photon interacts with the semiconductor material yielding a number of electron hole pairs proportional to the photon energy. These carriers then drift in the applied field. This motion of carriers, or current pulse, is converted to a voltage pulse via a charge-sensitive preamplifier. This voltage pulse is then pulse-height-analyzed (PHA) and a count placed into the memory channel corresponding to the pulse magnitude. Therefore, the spectrum of event counts versus channel number, or pulse height is directly proportional to the energy spectrum of the radiation seen by the detector, and the system can be thusly calibrated.

For this work a standard x-ray/gamma-ray detector characterization setup was used to measure the spectral response of a HgI_2 detector. A high voltage power supply was used to provide negative bias to the entrance electrode. A custom-built box housed the detector under test and connected to a Tennelec TC170 charge sensitive preamplifier, modified for DC coupling, by way of a BNC connector. A Tennelec TC241 spectroscopy amplifier was used to shape the pulse from the preamplifier, and a The Nucleus MCA card and software were installed in a PC to collect the spectra. For the detector itself, a $1cm^2$ by 2mm thick slab of mercuric iodide had 200Å thick 6.35mm diameter palladium contacts sputtered on each side and Pd wire leads aquadagged on. This is representative of the actual devices used in spectrometer systems. The detector was biased at -1000V and irradiated with a 1μCi Americium-241 source placed about 2cm above the entrance electrode. Each spectrum was collected over a 1000s livetime. ^{241}Am has a gamma photon at 59.54keV and several x-ray escape peaks in the 14 to 21keV range. The gamma photopeak energy lies roughly in the center of the range of energies of interest for HgI_2 detector applications.

The previously given description of detector operation is an idealized model, in which the photopeak would be a one channel wide delta function at the appropriate pulse height for the number of carriers created by an incident photon (for example, the 14,176 electron-hole pairs for 59.54keV gamma-ray). However, even in a "perfect" detector, i.e. one with complete charge collection, the peak would still be broadened to a gaussian shape because of carrier statistics. The more critical problem, however, is that many other processes degrade the spectral response more seriously. Anything that leads to a change in the voltage pulse height at the PHA greater than the digitization step size will lead to an error in the spectrum. The simplest possibility is that there is a constant amount of charge that is not collected, because it is trapped. This means that all of the pulses are reduced in magnitude, and the spectrum is thus shifted to lower channels. A constant change like this, although resulting in a reduction of the signal to noise in the system, can be "corrected" by simply recalibrating the energy scale. The more serious problem lies in the variable effects of real trapping processes. The trapping process is stochastic, such that the amount and timing of charge trapping is statistically broadened. Thus, events will have pulse heights reduced by different amounts. Therefore the photopeak is broadened on the low channel side. This is generally called "hole-tailing" as holes are usually the carriers trapped which lead to diminished pulses. Figure 1 shows the detector response of the mercuric iodide device above, which exhibits this hole-tailing problem. If the carriers that were trapped are released after the original pulse collection time, the pulse heights of subsequent events can actually be larger than expected, though this rarely is visible in spectra, as the probability for the timing to be correct is low.

Finally, the problem of particular interest here, if the trapping process itself is changing, the effects on spectral response will be changing. Mercuric iodide detectors all exhibit this effect to some degree, particularly in the initial biasing characteristics. When a detector has been completely fabricated and is biased for the first time, the spectral response is very poor and changes significantly over time. It generally requires hours of bias for a device to stabilize to its high performance level. Figure 2 shows the evolution of the energy spectrum for the above detector, which actually required almost 200 hours to stabilize, as it was fabricated from material of lower than usual quality.

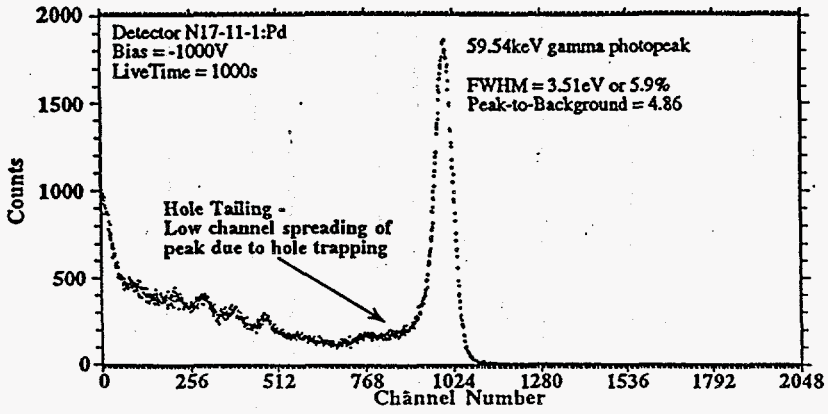

Figure 1. ^{241}Am spectrum from mercuric iodide detector exhibiting hole tailing.

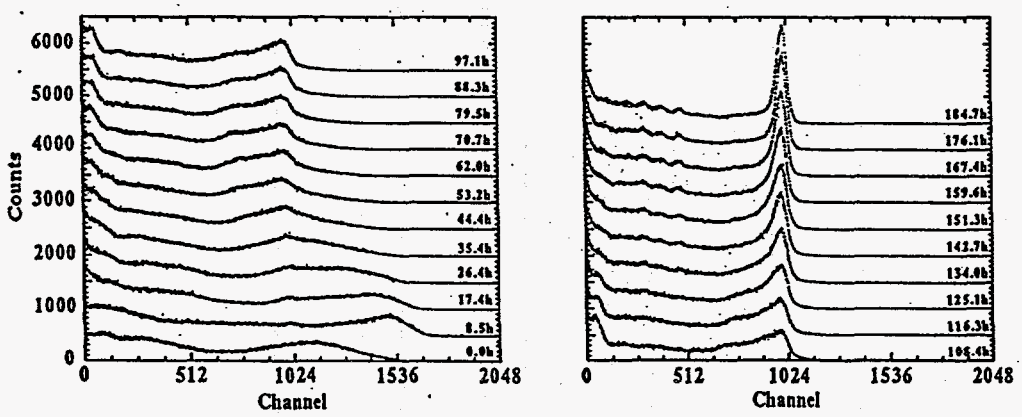

Figure 2. ^{241}Am spectrum versus time after initial biasing for mercuric iodide detector.

From Figure 2 one can study the detailed spectral evolution. After three days of biasing, the spectrum is just increasing in total counts and decreasing in peak widths. However, in the initial period, the first day in particular, the spectrum undergoes more substantial changes. There appear to be at least two separate peaks arising in the region of the expected gamma photopeak. One of these becomes the photopeak, while the peak at higher pulse height eventually disappears. As mentioned above, this higher than expected pulse height peak could be related to detrapping coincident with later events. However, the processes underlying this initial biasing behaviour require further study.

Impurities in Mercuric Iodide

Given that mercuric iodide is a somewhat primitive technology in semiconductor terms, impurities still tend to be present at significant levels. One set of methods for quantifying the elemental impurities are the Inductively Coupled Plasma Optical Emission and Mass Spectroscopy (ICP-OES and ICP-MS, respectively), which vaporize and ionize a sample solution with a plasma and measure the presence of a range of elements. The ICP-OES technique can generally measure down to the high ppb range, while the ICP-MS method can reach the high ppt region. Both of these techniques have been used on many HgI_2 samples, from initial material to purified material ready for crystal growth to completed crystals, as readily detectable levels of impurities are common. For example, copper is seen in the 100ppb to 1ppm level over a wide variety of samples, and therefore, it is fairly well accepted that copper is indeed present in most material [5]. Many of these impurities, such as copper, are electrically active, and thus are believed to be a prime cause of hole trapping. The presence of such an electrically active impurity would lead to a smaller signal and the distortion of the energy spectrum as seen in Figure 1 above.

Other experiments have shown that the impurities, as expected, can be equally well introduced during subsequent processing of the crystal for detector fabrication. Another good method for locating and identifying impurities present in a sample is low temperature photoluminescence (PL). PL has been used extensively on HgI_2, and the material has a rich PL spectrum. In general, impurities can be detected down to the ppt level, but can rarely be quantified. One common step used throughout the fabrication process is the wet chemical etch in a dilute solution of potassium iodide (KI). The KI etch is used to remove mechanical damage from cutting, etc., and to remove the "aging" from the surface that results from the high vapor pressures of the Hg and I. Previous experiments have shown, however, that impurities in the KI solution are readily incorporated into the HgI_2, and that these impurities readily diffuse throughout the sample in a matter of days. In addition sheet resistance measurements of thin film metal layers of copper have been conducted which showed that a large fraction of the Cu "disappears" into the HgI_2. Therefore, copper can be introduced into the bulk material during the detector fabrication process as it readily diffuses throughout the sample, and it has been shown to degrade detector performance [6-10].

Leakage Currents Characterization

The existence of these mobile impurities complicates the carrier collection situation further. First, there is a current associated with the movement of any charged impurity itself, which leads to a heightened noise level. Secondly, the trapping effects of the impurity center varies unpredictably as the impurity moves in the bulk material. The previous work cited above demonstrated the high diffusivity of copper in HgI_2. The experiment here demonstrates the mobility of the copper impurity in an electric field in mercuric iodide. In this experiment we intentionally doped a sample with a charge of copper. We then monitored the leakage current, or dark current, versus time to determine the movement of the copper-related centers.

The measurement system consisted of several instruments controlled and monitored by a personal computer via a GPIB (IEEE-488) interface. The sample was biased using a high voltage power supply capable of supplying up to 10mA at 500V. The sample bias voltage was monitored with a standard digital multimeter and stable within +/-1V. The leakage current was measured with a Keithley Instruments 485 picoammeter, with resolution down to 0.1pA. Finally, a switching assembly was fabricated that allowed for computer controlled reversal of bias direction, and removal of bias for other measurements. With this setup the copper doped/contacted devices were biased and monitored over a period of days to capture the "transients" in the leakage currents.

The first set of samples used in this experiment were two similar $1cm^2$ by 0.1mm thick HgI_2 crystals. A 6.35mm diameter, 2500Å thin film of high purity copper was sputter deposited onto one face of the sample, and a palladium lead was attached with aquadag. This translates to a doping level of about 2800ppm if the copper is distributed uniformly throughout the bulk of the HgI_2. On the reverse side, an aquadag contact of similar area was made. The samples were then placed in a dark desiccator cabinet and connected to the measurement circuit. One sample had a positive 350V bias applied to the front, doping contact, while the other had the positive bias applied to the back contact, effectively giving a negative bias to the doping contact. In both cases

this translates to an electric field on the order of 3.5V/μm, which is higher than the normal detector fields of 1V/μm. This higher field accelerates the mobile processes. Figure 3 shows the results obtained for these two samples.

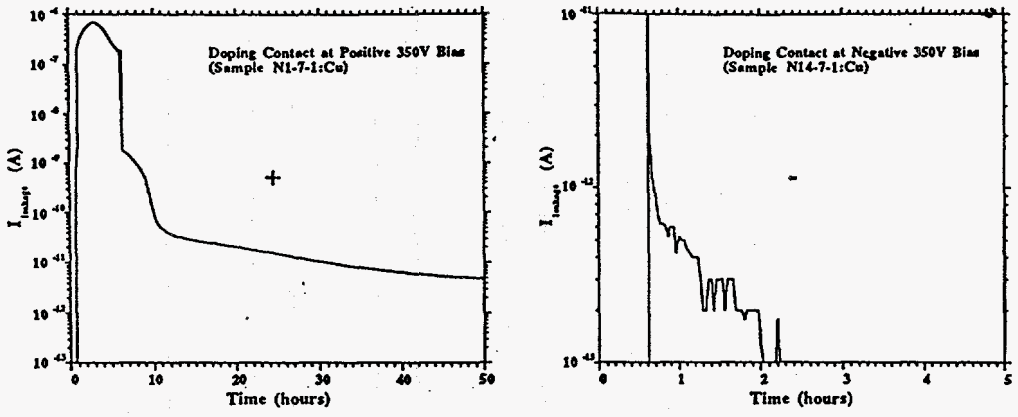

Figure 3. Leakage currents versus time for positively and negatively biased copper doping contacts on HgI_2.

The leakage current for the positively biased sample exhibited a peak that sharply rose from the initial leakage current of 0.1pA to 0.7μA. The peak decayed more slowly to a background leakage current of 5pA. This higher leakage level possibly indicates that the material had been damaged by the presence and movement of the high level of impurities, as the very initial leakage current was closer to the typical value for detectors.

Integrating the current gives the total charge moved, which should be representative of the impurities moved, as the intrinsic electron conductivity in the mercuric iodide is very low. The majority of the impurities, over 99%, appear to move in the first six hours. The total charge moved was 8.5×10^{-3}C, or 5.3×10^{16} single charges. This represents about 8% of the total number of atoms present in the deposited Cu film, assuming a singly charged impurity.

The negatively biased sample exhibited only a very small and brief current transient. Here 2.5×10^{-9}C or 1.5×10^{10} single charges were moved. This is consistent with the view that the Cu forms a positively charged center, which is held at the negative contact. The transient that does occur is the movement of the few impurities that had diffused into the substrate back into the contact area.

These results show that the copper impurity, which may be a copper iodide (CuI) or something related, exhibits a single positive charge. The impurity drifts in the field as a positively charge carrier with an ionic mobility. For the second set of leakage current measurements one, different sample had the applied field periodically reversed. This experiment was done to confirm the above conclusions, and more importantly, to see if the copper impurities remain mobile after traversing the bulk of the mercuric iodide.

This sample was a $1cm^2$ by 1mm thick HgI_2 crystal, with a 6.35mm diameter, 250Å thin film sputtered onto one face. This translates to a doping level of about 28ppm, which is two orders of magnitude lower than the first two samples. This sample also had a 350V bias which now translates to an electric field on the order of 0.35V/μm, which is one order of magnitude lower than before. Figure 4 shows the results obtained for this sample.

The leakage current for this sample exhibited a peak that sharply rose from the initial leakage current of 0.1pA to about 2nA. The peak decayed more slowly to a background leakage current of 0.2pA. The leakage current this time had returned more-or-less to its initial level, indicating that the material had not been damaged in this case because of the much lower level of impurities flowing through the sample. The majority of the impurities, over 97%, appear to move in the first four hours. The total charge moved was 4.3×10^{-6}C, or 2.7×10^{13} single charges. This represents about 0.04% of the total number of atoms present in the deposited Cu film. This amount is significantly lower than that of the first samples, most likely because of the lower field.

When the bias is reversed after one day a similar transient develops. Here 2.8×10^{-6}C or 1.7×10^{13} single charges were moved, with 98% in the first two hours. This means that only 64% of the impurities moved back across. The remainder were either pinned somewhere in the bulk, or removed or stabilized at the back contact.

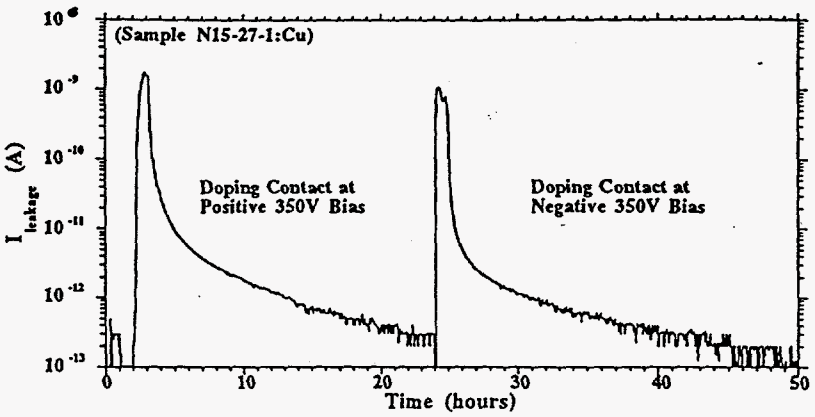

Figure 4. Leakage currents versus time for reversing field on copper doped HgI_2.

CONCLUSIONS

Detector characterizations were used to highlight the degradation in performance frequently seen in mercuric iodide room temperature radiation detectors. This work sought to understand some of the causes of these failures by studying the copper impurities that are present in mercuric iodide and that are introduced during processing. Previous measurements revealed the high diffusivity of copper in mercuric iodide at room temperature. The leakage current measurements on doped samples shown here were used to demonstrate that the copper impurity is charged and mobile, and can easily be swept back and forth through the bulk crystal by an applied electric field. These measurements show how copper can affect the operation of detectors. In particular, the copper presents two means of detector failure. First, the presence of the copper introduces a defect center that traps carriers associated with the incoming photons, and leads to decreased and statistically broadened pulse heights. Secondly, the copper is seen to be mobile, which leads to changes in detector performance, particularly as the bias is changed. The movement of copper and similar impurities, such as silver, may actually be the cause of the needed conditioning time. When a detector is first biased, a fraction of the impurities are swept through the sample and remain at the back contact until the bias is removed when diffusion becomes the dominant mechanism. These results suggest that copper must be removed from and kept away from the mercuric iodide crystal and detector. Purifications are required to remove it from starting material, and the subsequent processing must be "clean".

ACKNOWLEDGMENTS

This work was supported by the U.S. Department of Energy

REFERENCES

1. L. van den Berg, Nucl. Inst. & Meth. in Phys. Res. A A322, 453 (1992).
2. A. J. Dabrowski, J. S. Iwanczyk, Y. J. Wang, M. Madden, and M. Szawlowski, Proc. of the SPIE 2007, 19 (1993).
3. V. Gerrish and L. van den Berg, Nucl. Inst. & Meth. in Phys. Res. A A299, 41 (1990).

4. P. Olmos, G. Garcia-Belmonte, J. M. Perez, and J. C. Diaz, Nucl. Inst. & Meth. in Phys. Res. A **A299**, 45 (1990).
5. E. Soria, (private communication).
6. C. Y. Hung, X. J. Bao, T. E. Schlesinger, R. B. James, A. Y. Cheng, C. Ortale, and L. van den Berg, J. Appl. Phys. **73**, 4591 (1993).
7. X. J. Bao, T. E. Schlesinger, R. B. James, R. H. Stulen, C. Ortale, and A. Y. Cheng, J. Appl. Phys. **68**, 86 (1990).
8. X. J. Bao, Ph.D. Thesis, Carnegie Mellon University 1991.
9. R. B. James, X. J. Bao, T. E. Schlesinger, A. Y. Cheng, and V. M. Gerrish in *Semiconductors for Room-Temperature Radiation Detector Applications*, edited by R. B. James, T. E. Schlesinger, P. Siffert, and L. Franks (Mat. Res. Soc. Symp. Proc. **302**, Pittsburgh, PA, 1993) pp. 103-114.
10. J. M. Van Scyoc, T. E. Schlesinger, R. B. James, A. Y. Cheng, C. Ortale, and L. van den Berg in *Semiconductors for Room-Temperature Radiation Detector Applications*, edited by R. B. James, T. E. Schlesinger, P. Siffert, and L. Franks (Mat. Res. Soc. Symp. Proc. 302, Pittsburgh, PA, 1993) pp. 115-120.

Photoionization investigation of defect traps in mercuric iodide room-temperature x-ray spectrometers

J. M. Van Scyoc, T. S. Gilbert, T. E. Schlesinger

Carnegie Mellon University, Department of Electrical and Computer Engineering
5000 Forbes Avenue, Pittsburgh, PA 15213-3890

R. B. James

Sandia National Laboratories, Advanced Materials Research Division 8347
7011 East Avenue, Livermore, CA 94550

ABSTRACT

Impurities in mercuric iodide (HgI_2) x-ray spectrometers are investigated by photoionization (PI) spectroscopy. The observed spectrum is shown to be a function of the particular impurities present in the material both in as-grown material and in material intentionally doped with Cu and Ag. The effect of contaminants on detector performance is also explicitly demonstrated as is the need for high purity starting materials and carefully controlled processing conditions.

Keywords: mercuric iodide, defects, traps, contacts, photoionization

1. INTRODUCTION

Radiation spectrometers are finding increased application in fields as diverse as national security and treaty verification, medical imaging, industrial process monitoring, environmental monitoring and remediation, and basic science. Spectrometers and detectors employing high purity germanium (HPGe) or lithium-drifted silicon (Si(Li)), while offering excellent performance in terms of energy resolution, require cooling well below room temperature, necessitating bulky apparatus that is fragile and that requires constant attention.[1-6] By contrast room temperature nuclear spectrometers offer the advantages of compact portable systems capable of unattended operation.

Mercuric iodide (α-HgI_2) has several properties that make it an ideal material for the fabrication of room temperature spectrometers. The high atomic number of the elements (Z_{Hg}=80 and Z_I=53) results in a large photoelectric interaction in this material and hence a high stopping power for photon energies into the MeV range. The relatively low electron-hole pair creation energy (4.2 eV at room temperature) allows for a large response per incident photon, and the large bandgap of 2.13eV at 300K results in a high intrinsic resistivity ($10^{14}\Omega$*cm), and low dark current (10^{-12}A). These properties make this material suitable for some of the highest resolution and highest sensitivity room temperature radiation spectrometers.[2, 5-7]

Although mercuric iodide has great potential, there are a number of practical problems that currently limit actual spectrometer performance and fabrication yield. Red mercuric iodide has a tetragonal unit cell and forms a layered structure. These layers are connected at iodine planes by

0-8194-1629-0/94/$6.00

weak van der Waal bonds, and thus the material is easily delaminated. The material is soft and plastic deformation can occur under the sample's own weight if not properly supported thus this material is sensitive to mechanical handling and can be easily damaged. The material is also very sensitive to heating and at about 125°C red tetragonal α-HgI_2 undergoes a phase transformation to the yellow orthorhombic β-HgI_2 phase. The mercury and iodine have sufficiently high vapor pressures that the surface of an unencapsulated sample will degrade within hours. Finally, mercuric iodide is strongly reactive with many materials. All of these complications make mercuric iodide crystal growth and device fabrication non-trivial and extreme care is required in the entire device fabrication process.

One primary problem encountered in spectrometers is that of incomplete charge collection. This results in a broadening of photopeaks and hence a decrease in both energy resolution and sensitivity. An additional problem is the lack of long term stability in some detectors in which the spectral quality degrades over time with both peak height and resolution decreasing. These problems have as their origin the presence of carrier traps and recombination centers in the material. These traps and recombination centers may originate from both extrinsic impurities or intrinsic defects that are present in the as-grown material or are introduced during fabrication. The low fabrication yield of high quality detectors which can result as a consequence of the presence of these traps and recombination centers leads to high unit costs and thus can limit the application of these spectrometers in many areas where compact hand-held spectrometers would be useful.[8-13] Therefore, materials characterization measurements which allow for the characterization of carrier traps and recombination centers are extremely important. This paper presents the results of photoionization spectroscopy (PI) investigations of undoped mercuric iodide and mercuric iodide doped with Cu and Ag.

2. EXPERIMENT

2.1 Photoionization

In this technique a sample maintained at a constant temperature is illuminated with photons of increasing energy. Carriers are excited from traps into the conduction/valence bands with the absorption of a photon. These carriers then drift or diffuse through the sample resulting in a photocurrent, or photoresponse. The resulting peaks in the photocurrent versus wavelength spectrum, for below bandgap excitation, are directly related to trap energy levels. Varying the temperature gives further detailed information regarding these traps. Figure 1 shows the measurement technique schematically.

2.2 Radiation Detector Characterization

A typical spectrometer structure is usually quite simple. Thin (~250Å) palladium contacts are deposited on the large faces of a HgI_2 slab of the order of 1cm x 1cm x 1mm. The charge created by the incident photons are separated by an applied bias and then measured by a system consisting of a charge-sensitive preamplifier, a spectroscopic amplifier, and a multi-channel analyzer. These spectrometers are generally used in the measurement of x-ray and γ-ray emissions. Figure 2 shows an example spectrum collected with a small (5mm x 5mm x 0.5mm) HgI_2 detector of fair quality, whose design was optimized for x-rays.

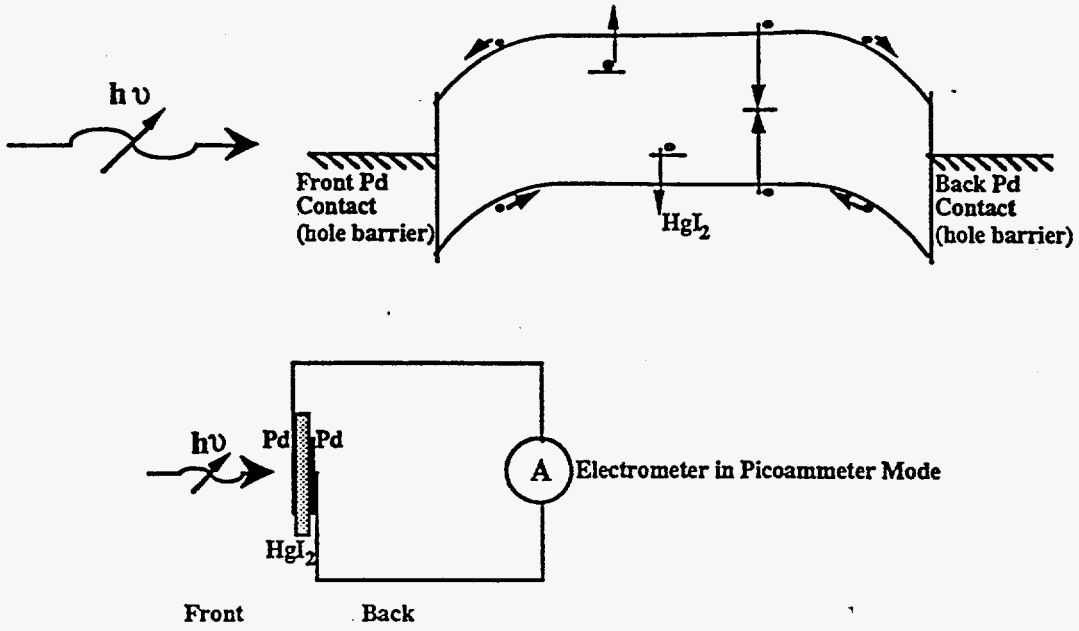

Figure 1. Diagram of photoionization experimental setup.

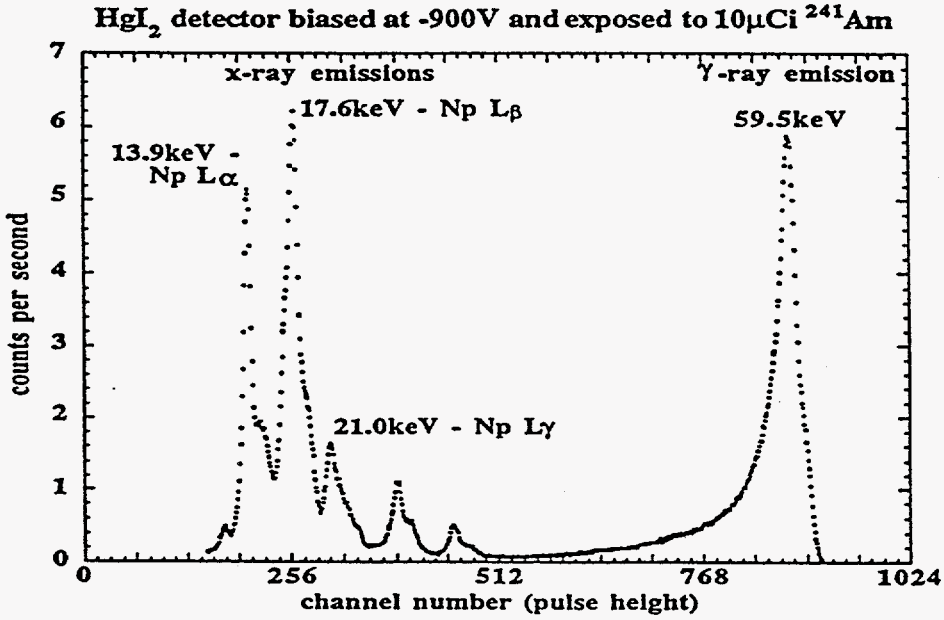

Figure 2. Example mercuric iodide x-ray/γ-ray spectrum.

3. MEASUREMENTS

3.1 Photoionization

As discussed above, one of the primary processing related problems in mercuric iodide spectrometer fabrication is the unintentional doping of the material with contaminants. Two impurities that are often present in typical samples of mercuric iodide, and believed to be a serious problem for spectrometer performance are silver and copper. Thus, these dopants are a focus of the present study.

For this work two mercuric iodide samples were studied. Each measured approximately 10mm x 10mm x 2mm, and was grown by a similar process. On each slab palladium contacts of ~250Å thickness were sputter deposited in the configuration shown in Figure 3. Photoionization was performed on these two samples at a low temperature of 80K (LT), and at room temperature (RT). The bandgap of mercuric iodide at LT is around 2.32eV (5340Å) and at RT is 2.13eV (5820Å). The samples were illuminated with a quartz tungsten halogen lamp source whose emission was directed through a double pass spectrometer and onto the sample of interest. The following wavelength/energy ranges were studied.

Long wavelength (LW) - 15000Å (0.83eV) to 6500Å (1.91eV)
Near-band-edge (NBE) - 6500Å (1.91eV) to 5000Å (2.48eV)

The two samples were then intentionally doped with either Ag or Cu. Both were doped by sputtering a 125Å thick film in the configuration shown in Figure 3. Assuming that all the sputtered metal diffuses uniformly into the bulk of the mercuric iodide, this results in a doping level on the order of 1ppm, which is about an order of magnitude higher than the level of contamination found in typical mercuric iodide materials.

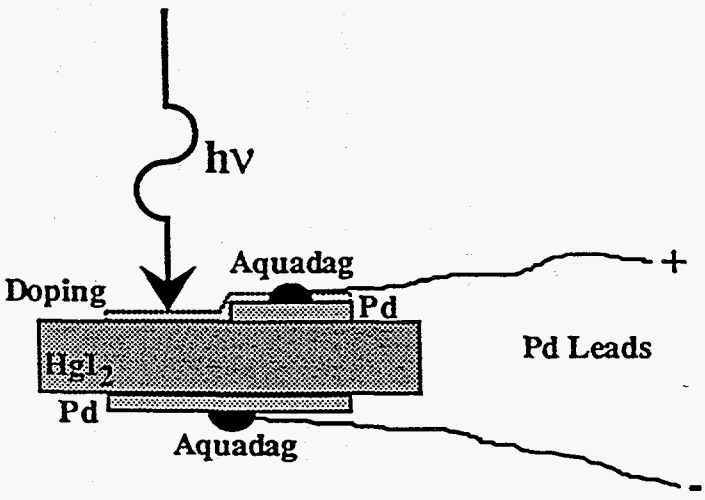

Scale: 1cm = 1mm (Film thicknesses exaggerated x20)

Figure 3. Configuration of photoionization samples.

3.2 Radiation Detector Characterization

To investigate the effects of the dopants on detector performance, a detector was fabricated in the configuration described above. The time evolution of the spectra obtained with this undoped spectrometer were studied to allow for the identification of changes in the spectra resulting from the presence of the dopants. The detector was then doped with Ag in a similar manner to that described above and the time evolution of the spectra carefully measured

4. RESULTS

4.1 Photoionization

For all of the samples studied, the LW range did not show any photopeaks above the background noise level. This may be a result of a somewhat high noise level, and a low illumination level, both related to limitations in the measurement system. However, the noise level was near the leakage current level of typical mercuric iodide detectors (pA range), and the light source was sufficient to cause large currents in the NBE region. Therefore, it seems reasonable to believe that any photopeaks in the LW region were extremely weak, and further discussions here relate only to the NBE results.

Figure 4 shows the low temperature and room temperature PI spectra for the two samples. The NBE spectra for these samples, before doping, although fairly similar, do show differences. This suggests that there are some differences in the material between these two samples. This is reasonable given that there often is significant inhomogeneity in mercuric iodide even within a sample. The photoionization spectrum can be understood qualitatively as follows assuming hole barriers at both contacts as shown above. At the longest wavelengths the light penetrates the mercuric iodide and excites carriers in the metal at the back of the sample creating the observed photoresponse. As wavelength is decreased (energy increased) more and more of the light is absorbed towards the front of the sample. The photocurrent generated near the front contact is opposite in sign to that generated at the back. Eventually this photocurrent dominates the spectrum.

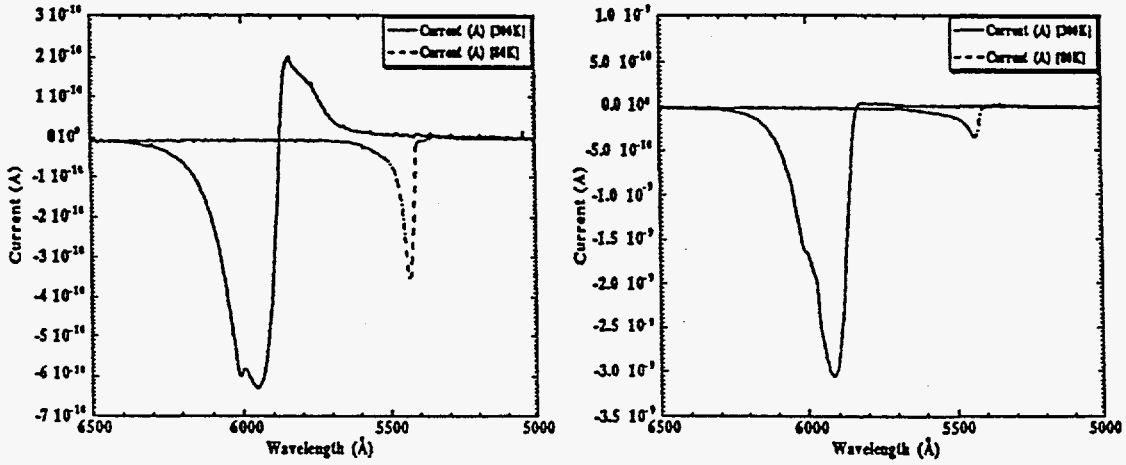

Figure 4. PI spectra of two Pd contacted mercuric iodide samples.

Figure 5 shows the spectra obtained from the doped samples. After doping with Cu and Ag much stronger differences are observed. Both dopants radically change the photoresponse in that the primary peak is now in the positive current direction. However, the peak in the Cu doped sample is an order of magnitude stronger and occurs at a somewhat longer wavelength. It has been shown that Cu diffuses most readily into the mercuric iodide thus the observation of a stronger photopeak in the Cu doped sample is consistent with that fact that a greater concentration of Cu dopants probably results from this doping method.

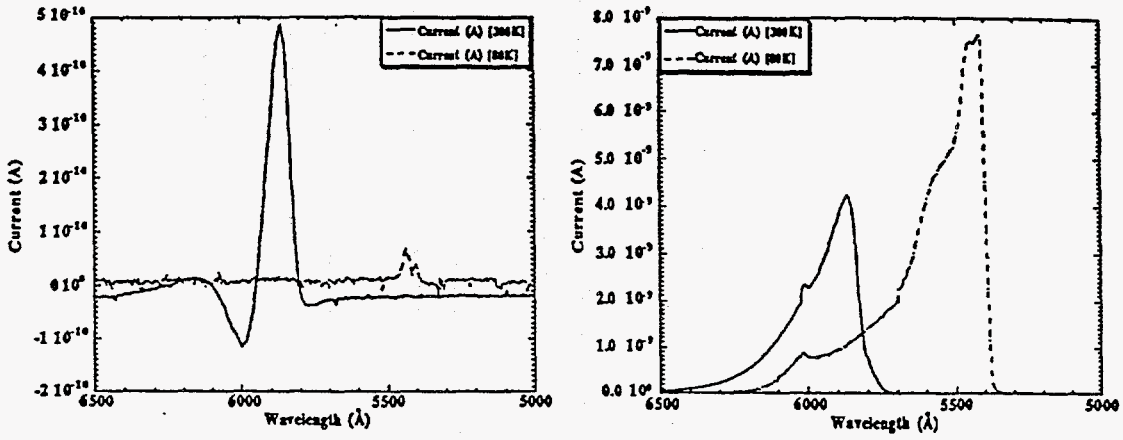

Figure 5. PI spectra of Ag-doped sample (left) and PI spectra of Cu-doped sample (right).

4.2 Radiation Detector Characterization

Figure 6 shows the effects of applying and reapplying bias (-1000 V) on the x-ray spectrum obtained with a mercuric iodide spectrometer. The bias was reapplied after waiting the amount of time required to dope the sample (about 3 hours). After about 200 hours under bias the detector spectrum ceases to change appreciably (only the first 100 hours are shown in figure 6 on the left) and the resolution and photopeak intensity is the same as the best seen in figure 6 on the right. When rebiased after being off bias for about 3 hours the spectrum recovers in about five hours to the same level of performance as initially observed after 200 hours. Figure 7 shows the time evolution over a 200 hour period of the spectrum obtained with the same spectrometer after doping with silver. In this spectrum the photopeak intensity and energy resolution is greatly reduced as compared to that obtained with the undoped spectrometer. Further, the position of the photopeak (channel number) is shifted to apparently lower energies. Both of these effects can result from severe charge trapping, and hence incomplete charge collection, in the spectrometer. We conclude that the Ag related defect center observed in the PI spectrum is responsible for this degradation in performance.

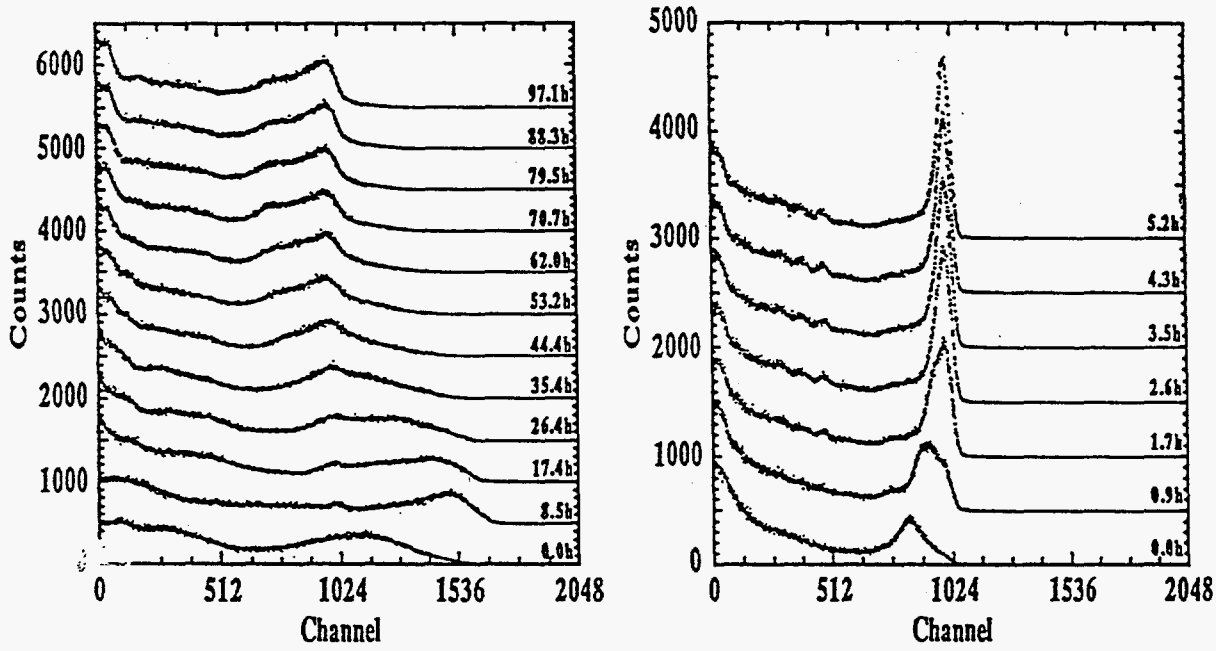

Figure 6. Original biasing effects on detector spectra (left) rebiasing effects on detector spectra (right).

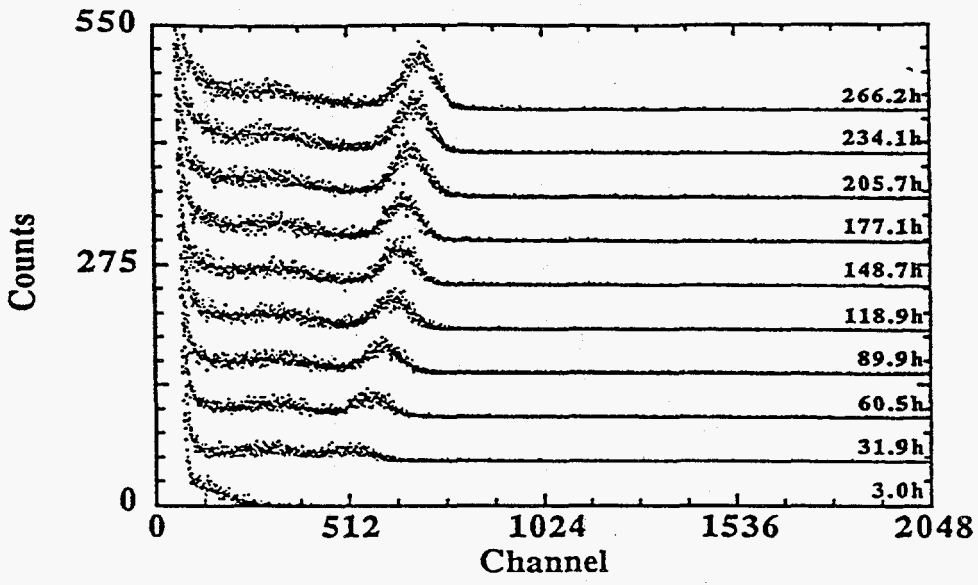

Figure 7. Effects of silver doping on detector spectra.

5. CONCLUSIONS

The measurements presented here demonstrate that photoionization can be used to effectively study defect-related traps in mercuric iodide. These measurements suggest that the contaminants introduced during processing can have a significant effect on detector performance. Particular care must be exercised including the use of high purity starting materials and processing chemicals, and the proper choice of contact material.

6. ACKNOWLEDGEMENTS

This work was supported by the U. S. Department of Energy. One of us (T. E. S.) would like to acknowledge the support of the National Science Foundation through the Presidential Young Investigator Program.

7. REFERENCES

1. R. Arlt, D. E. Rundquist, D. Bot, P. Siffert, M. Richter, A. Khusainov, V. Ivanov, A. Chrunov, Y. Petuchov, F. Levai, S. Desi, M.Tarvainen, and I. Ahmed, "Use of room temperature semiconductor detectors for the verification of nuclear material in international safeguards - recent advances", *Mat. Res. Soc. Symp. Proc.*, Vol. 302, pp. 19-29, 1993.

2. P. Olmos, G. Garcia-Belmonte, J. M. Perez, and J. C. Diaz, "Use of thick HgI_2 detectors as intelligent spectrometers", *Nucl. Inst. & Meth. in Phys. Res. A*, Vol. A299, pp. 45-50, 1990.

3. J. S. Iwanczyk, Y. J. Wang, N. Dorri, A. J. Dabrowski, T. E. Economou, and A. L. Turkevich, "Use of mercuric iodide x-ray detectors with alpha backscattering spectrometers for space applications", *IEEE Trans. on Nucl. Sci.*, Vol. 38, pp. 574-579, 1991.

4. R. Cesareo, G. E. Gigante, J. S. Iwanczyk, and A. Dabrowski, "The use of a mercuric iodide detector for x-ray fluorescence analysis in archaeometry", *Nucl. Inst. & Meth. in Phys. Res. A*, Vol. A322, pp. 583-590, 1992.

5. L. van den Berg, "Recent developments in mercuric iodide technology at EG&G Energy Measurements, Inc. Santa Barbara Operations", *Nucl. Inst. & Meth. in Phys. Res. A*, Vol. A322, pp. 453-456, 1992.

6. A. J. Dabrowski, J. S. Iwanczyk, Y. J. Wang, M. Madden, and M. Szawlowski, "Recent advances with mercuric iodide x-ray detectors and large area silicon avalanche photodiodes", *Proceedings of the SPIE*, Vol. 2007, pp. 19-29, 1993.

7. V. Gerrish, and L. van den Berg, "Improved yield of high resolution mercuric iodide gamma-ray spectrometers", *Nucl. Inst. & Meth. in Phys. Res. A*, Vol. A299, pp. 41-44, 1990.

8. V. Gerrish, "Polarization and gain in mercuric iodide gamma-ray spectrometers", *Nucl. Inst. & Meth. in Phys. Res. A*, Vol. A322, pp. 402-413, 1992.

9. C. Y. Hung, X. J. Bao, T. E. Schlesinger, R. B. James, A. Y. Cheng, C. Ortale, and L. van den Berg, "Introduction of extrinsic defects into mercuric iodide during processing", *J. Appl. Phys.*, Vol. 73, pp. 4591-4594, 1993.

10. X. J. Bao, T. E. Schlesinger, R. B. James, R. H. Stulen, C. Ortale, and A. Y. Cheng, "Incorporation of defects during processing of mercuric iodide detectors", *J. Appl. Phys.*, Vol. 68, pp. 86-92, 1990.

11. N. L. Skinner, C. Ortale, M. M. Schieber, and L. van den Berg, "Preparation and evaluation of mercuric iodide for crystal growth", *Nucl. Inst. & Meth. in Phys. Res. A*, Vol. A283, pp. 119-122, 1989.

12. J. M. Van Scyoc, T. E. Schlesinger, H. Yao, R. B. James, M. Natarajan, X. J. Bao, J. S. Iwanczyk, B. E. Patt, and L. van den Berg, "Process monitoring for fabrication of mercuric iodide room temperature radiation detectors", *Mat. Res. Soc. Symp. Proc.*, Vol. 324, pp. 65-71, 1994.

13. R. B. James, X. J. Bao, T. E. Schlesinger, A. Y. Cheng, and V. M. Gerrish, "Defects in silver-doped mercuric iodide crystals and their effect on x-ray and gamma-ray detector performance", *Mat. Res. Soc. Symp. Proc.*, Vol. 302, pp. 103-114, 1993.

Left Intentionally Blank

MATERIALS RESEARCH SOCIETY SYMPOSIUM PROCEEDINGS VOLUME 324

Diagnostic Techniques for Semiconductor Materials Processing

Symposium held November 29–December 2, 1993, Boston, Massachusetts, U.S.A.

EDITORS:

O.J. Glembocki

Naval Research Laboratory
Washington, DC, U.S.A.

S.W. Pang

University of Michigan
Ann Arbor, Michigan, U.S.A.

F.H. Pollak

Brooklyn College of CUNY
Brooklyn, New York, U.S.A.

G.M. Crean

National Microelectronics Research Centre
Cork, Ireland

G. Larrabee

Booz, Allen & Hamilton
Dallas, Texas, U.S.A.

MRS

MATERIALS RESEARCH SOCIETY
Pittsburgh, Pennsylvania

PROCESS MONITORING FOR FABRICATION OF MERCURIC IODIDE ROOM TEMPERATURE RADIATION DETECTORS

J. M. Van Scyoc[1], T. E. Schlesinger[1], H. Yao[2], R. B. James[3], M. Natarajan[4], X. J. Bao[4], J. S. Iwanczyk[5], B. E. Patt[5], and L. van den Berg[6]

1 Carnegie Mellon University, Department of Electrical and Computer Engineering, Pittsburgh, PA 15213
2 University of Nebraska, Center for Microelectronic and Optical Materials Research, and Department of Electrical Engineering, Lincoln, NE 68588
3 Sandia National Laboratories, Advanced Materials Research Division, Livermore, CA 94550
4 TN Technologies, Inc., Round Rock, TX 78680
5 Xsirius, Inc., Camarillo, CA 93012
6 EG&G Energy Measurements, Goleta, CA 93116

ABSTRACT

In the fabrication of mercuric iodide room temperature radiation detectors, as in any semiconductor process, the quality of the final device can be very sensitive to the details of the processing steps. Each processing step can either reduce the intrinsic defects and those extrinsic defects introduced by earlier steps, or it can introduce new defects. In mercuric iodide these defects can act as trapping and recombination centers, thereby degrading immediate device performance or leading to long-term reliability problems. With careful study and monitoring of each step, the process can be modified to improve the end product. In this work we used several techniques to study processing steps and their effects. Photoluminescence spectroscopy and photoionization revealed defects introduced during processing. One critical step is the formation of electrical contacts, as both the material choice and deposition method have an impact. Four point probe sheet resistance methods were used to characterize the loss of material from the contact as it reacted with or moved into the bulk semiconductor. Ellipsometry was used to characterize the intrinsic optical functions of the material, and to study the effects of surface aging on these functions. Results from this work provide suggestions for the modification and monitoring of the detector fabrication process.

INTRODUCTION

Many diverse applications currently utilize, or could possibly utilize, nuclear radiation detection and spectroscopy. One major field currently of interest is the close monitoring of nuclear materials, for the verification of non-proliferation treaties, or the tracking of unauthorized, concealed materials. Environmental monitoring and remediation is another large field that is in its early stages. Concealed weapons and contraband detection, nuclear medicine and imaging, industrial process gauging, and basic science also have a need for such measurements. For all of these applications a compact, portable, low-maintenance instrument would be extremely useful. However, traditional detectors, such as high purity germanium (HPGe) or lithium-drifted silicon (Si(Li)), require cooling well below room temperature, necessitating a bulky apparatus that is fragile and that requires continued attention.

The semiconductor red mercuric iodide (α-HgI_2) has several properties that make it an ideal material for room temperature use, therefore allowing the production of the desired portable instruments [1-5]. In particular, the high atomic number of the elements (Z_{Hg}=80 and Z_I=53) means that the material has a high stopping power for photon energies into the MeV range, the relatively low electron-hole pair creation energy of 4.2eV at room temperature allows a large response per incident photon, and the large bandgap of 2.13eV at 300K results in a high intrinsic resistivity ($10^{14}\Omega$*cm), and low dark currents (10^{-12}A). These properties result in a material suitable for some of the highest resolution and sensitivity room temperature radiation detectors [6].

Mat. Res. Soc. Symp. Proc. Vol. 324. ©1994 Materials Research Society

The detector device structure used is usually quite simple, with thin (~250Å) palladium contacts deposited on the large faces of a HgI_2 slab around 1cm x 1cm x 1mm. The charge created by the incident photons and separated by an applied bias is then measured by means of a system composed of a charge-sensitive preamplifier, a spectroscopic amplifier, and a multi-channel analyzer. These sensors are generally applied to the spectroscopic examination of x-ray and γ-ray emissions. Figure 1 shows an example spectrum collected with a small (5mm x 5mm x 0.5mm) HgI_2 detector whose design was optimized for x-rays.

Although mercuric iodide has great potential in theory, there are many practical problems that currently limit the actual device performance achieved [7]. One primary problem is that not all charge that is generated by incoming photons is collected at the contacts. This incomplete charge collection effect is demonstrated by the left-side tailing of the 59.5keV peak in the spectrum of Figure 1, as the "lost" charge results in a lower pulse height than is expected. This leads to a loss of resolution by the broadening of peaks, and a loss of sensitivity as there are fewer counts at the location of the photopeak. Another problem is the long term unreliability and instability of some detectors. The spectral quality from such a detector will degrade over time, with peak height and sharpness decreasing. Third, the material is very sensitive to mechanical handling, and can be easily damaged. Finally, all of these factors lead to a low final yield of high quality detectors, which means that the unit cost is prohibitive for many of the potential applications where a compact, hand-held spectrometer would be useful.

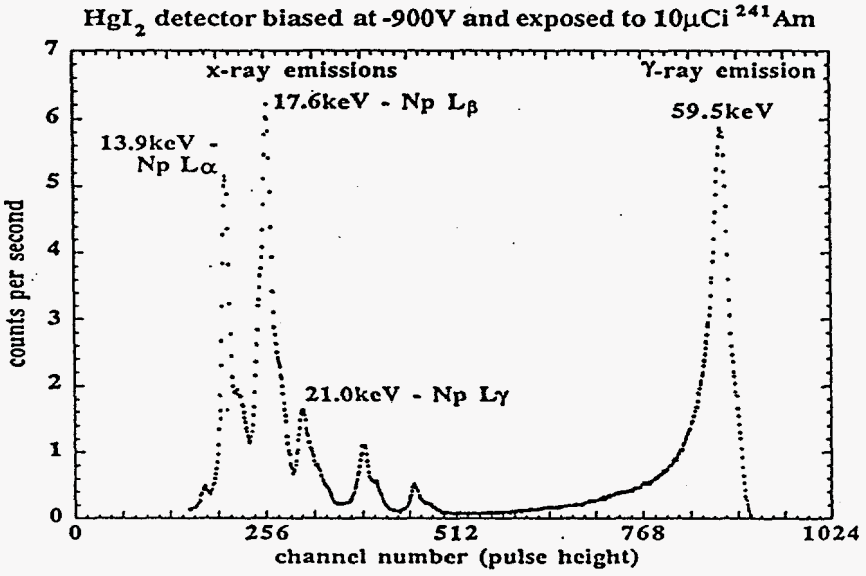

Figure 1. Example x-ray/γ-ray spectrum from a room temperature HgI_2 detector.

The underlying cause of all of these problems, of course, is the material properties. The largest limitations are related to charge traps and recombination centers. These centers trap charges and may release them at unpredictable times, potentially over the scale from sub-seconds to years, and lead to the observed degradation of performance. One source of these traps is impurities that are present in the material, either from the start, or introduced during processing. Other sources include intrinsic defects in the crystal structure from growth or processing. The other prime material problems are physical and chemical in nature. Red mercuric iodide has a tetragonal unit cell, and forms a layered structure. These layers are connected at iodine planes only by weak van der Waal bonds, and thus the material is easily delaminated. Overall, the material is simply soft, and plastic deformation can occur under a sample's own weight, if not properly supported. The material is also very sensitive to heating, as at around 125°C the red tetragonal α-HgI_2 phase

undergoes an phase transition to the yellow orthorhombic β-HgI_2 phase, which has inferior detector properties. Finally, mercuric iodide is strongly reactive with many agents, and the mercury and iodine have sufficient vapor pressures that the surfaces of an unencapsulated sample will degrade within hours.

All of these complications lead to the situation that mercuric iodide crystal growth and device fabrication are non-trivial. Extreme care is required in the entire fabrication and handling process. Therefore, processing diagnostics are useful to identify problems and point toward solutions. Off-line procedures allow further time to fully study the process and allow for recommendations of large-scale changes. On-line diagnostics allow for the rapid detection of problems arising during actual fabrication, and allow for adjustments to compensate. This paper discusses measurements that were primarily developed as cases of the former, but some of which are applicable (with some simplifications) for on-line diagnostics.

EXPERIMENTS AND RESULTS

Photoluminescence

Photoluminescence (PL) has been shown to be a good technique for the detection and identification of defect states in many materials. In mercuric iodide, much work has been done to determine and understand the rich spectra found in most samples.

PL involves exciting a sample optically with above bandgap illumination, and collecting and measuring the resulting luminescence spectrum as the excited electrons return to lower energy states. Generally mercuric iodide PL is done using an argon ion laser (4880Å line) in CW mode, with a power of 20mW, and the sample is cooled in liquid helium to around 4.2K. The resultant peaks in the spectrum relate to the band edge and the defect states, or phonon replicas of these. With these parameters, the excitation penetrates only a few micrometers, so the spectra relates to the near-surface layers. In HgI_2 PL there are two regions of interest, the near band edge region of 5290 to 5410Å, and the deep level region of 5400 to 8500Å. From the extensive characterization that has been done previously, correlations between relative peak intensities and locations, and associated process steps have been found for items such as impurities, sample aging, vacuum exposure, stoichiometry changes, and contact materials [8-13].

The technique is non-destructive, except for the required thermal cycling and extra material handling required. It can therefore be done on samples in the middle of processing, although a simplified version would be required for real-time online measurements.

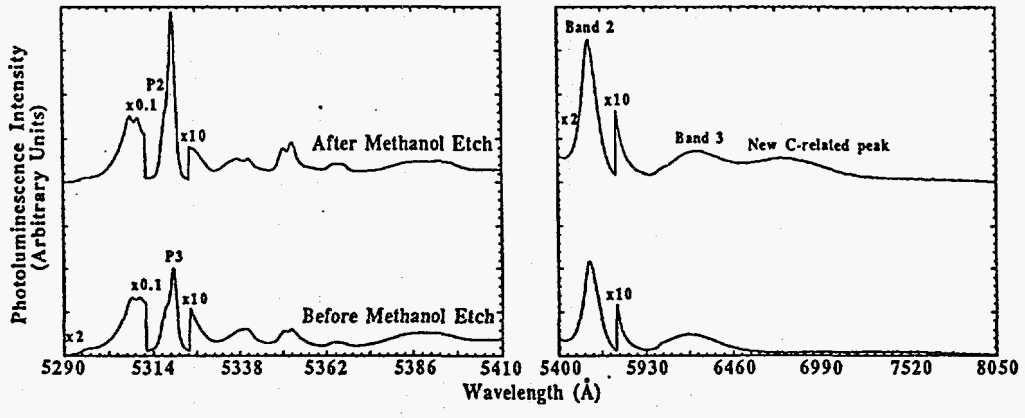

Figure 2. Photoluminescence spectrum before and after methanol etching of a HgI_2 crystal sample, showing the introduction of an impurity-related defect state at ~6700Å.

One example of a processing problem revealed by PL is shown in Figure 2. These PL spectra are from a sample immediately before and after a methanol etch. This work was done primarily as a test of alternative etchants, as the current usual etchant of choice is 10% by weight of potassium iodide in deionized water solution; however, in fabrication the sample could also be exposed to solvents such as methanol during cleaning and rinsing steps. The spectra here show that even though a high purity semiconductor grade methanol was used, a new defect level appears after the etch. In particular, this level appears to be a C-related impurity defect. It has been shown in other work that such defects severely degrade the resultant detector performance because of charge trapping effects.

Photoionization / Photoresponse

Another method that is useful for studying traps in mercuric iodide is photoionization (PI). In this newly developed technique a temperature controlled sample is illuminated with photons of increasing energy and the photocurrent, or photoresponse, is measured. The resultant peaks in the spectrum as a function of wavelength, for below bandgap excitation, relate to the trap levels. Varying the temperature gives further detailed information regarding these traps.

Figure 3 shows an example of a PI spectrum. The sample here is a piece of mercuric iodide that was intentionally doped with copper to a concentration on the order of 10ppm before the application of the palladium electrodes. The peak at around 2.05eV is seen only in the Cu-doped samples, and therefore it most likely relates to a trap introduced by the presence of this impurity.

Another parameter that can be obtained from this measurement is the barrier height of the metal/semiconductor interface. Extrapolating the linear portion of the square root of the response per incident photon to its zero-response value gives the barrier height; and the direction of the current gives the type of barrier (hole/electron).

This technique can be considered non-destructive when applied to partially fabricated detectors, as the contacts applied for the detector can be used for the PI/PR measurement. Again, the issues are merely those of thermal cycling and materials handling, and the limitations of the time and equipment needed for a measurement on-line.

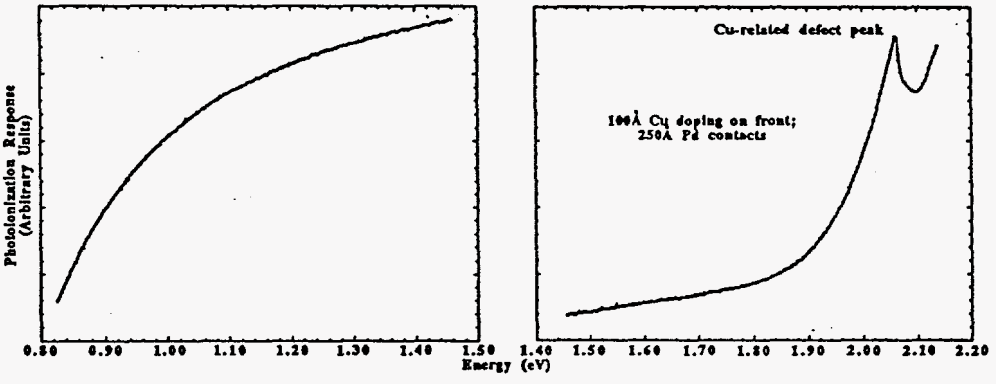

Figure 3. Photoionization spectrum of a Cu-doped Pd-contacted HgI_2 sample at 300K.

Four-point Probe Sheet Resistance

One area of the mercuric iodide detector fabrication that has not been fully studied is the choice of contact material and deposition method. Given the reactive nature of mercuric iodide, it is likely that any materials brought into contact for use as an electrode is going to change the substrate and be changed itself. Besides the formation of new products by reaction, mobile species from the

contact can move into the bulk of the mercuric iodide, thereby introducing further charge trapping centers.

A simple technique that can be used to characterize the quality of the contact and its interface with the mercuric iodide is the four-point probe sheet resistance measurement [13]. Four tungsten carbide tips in a linear arrangement are brought into contact with the sample and a known current is injected through the outer two. The voltage measured between the inner two probes is directly related to the resistance of the sample film, which is related to the effective thickness of the conductive film. Monitoring this resistance versus time reveals changes in the contact film.

Copper contacts showed an exponentially increasing resistance, as expected, since copper is known to diffuse rapidly into mercuric iodide. Figure 4 shows the more unexpected results. Palladium and the refractory metal tungsten are generally considered relatively stable on mercuric iodide. However, it appears that these materials move into and/or react with the mercuric iodide, as the resistance does increase. Both do form a reaction barrier, though, as the resistance eventually stabilizes, leading to the apparently stable contact that is generally assumed. Pd does this rapidly, and this is why the contacts have been generally thought to be stable. The W change is somewhat slower, but still stabilizes within a few days.

The technique is a somewhat destructive technique, as the probing mechanically damages the extremely soft mercuric iodide. In fact, in order to obtain stable resistance readings, relatively thick films (~1000Å), and very careful probe tip application are required. Otherwise, the tips simply poke through the film and measure the very high resistance of the bulk mercuric iodide.

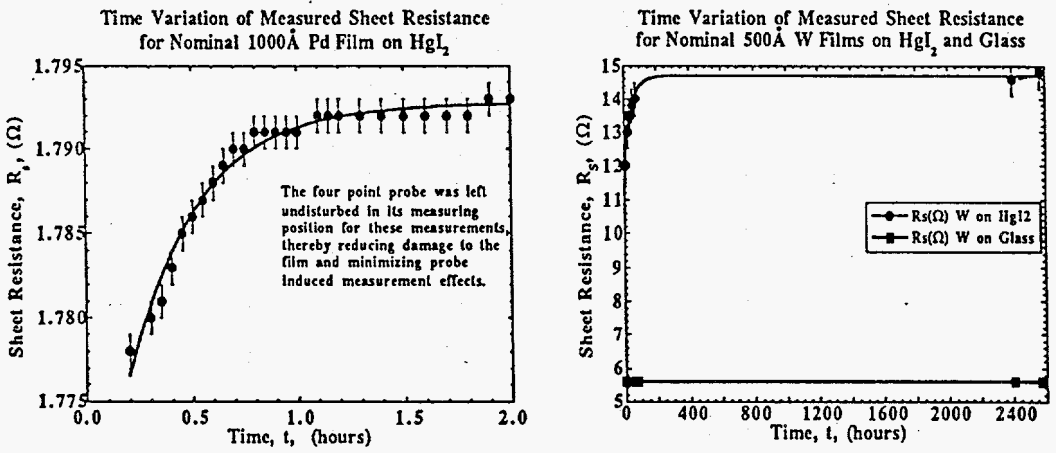

Figure 4. Four-point probe sheet resistance measurements of Pd and W contacts on HgI_2.

Variable Angle Spectroscopic Ellipsometry (VASE)

One final technique was employed to study the optical functions of bare mercuric iodide. Variable angle spectroscopic ellipsometry (VASE) can give detailed information about the dielectric functions of the material [14]. Since the HgI_2 structure is anisotropic, separate functions are required for the c-axis and a,b-axes.

Ellipsometry in general determines the ratio of complex reflectance r_p to r_s, with r_p and r_s the reflection coefficients of light polarized parallel to and perpendicular to the plane of incidence, respectively. This complex ratio is traditionally determined as an amplitude and an angle.

$$\rho = r_p / r_s = \tan(\psi) * \exp(i*\Delta)$$

with Δ and ψ the calculated values. The pseudo-dielectric and optical constants are obtained from these values by further calculations. Using variable angles of incidence and wavelengths, one can obtain further data which gives greater information about the optical functions of the sample.

Once these functions are characterized for bare, unadulterated mercuric iodide, they can be used

to study the effects of certain processing steps. One inevitable processing step is aging. Mercuric iodide left exposed to air (or even in other ambients) exhibits a large change in the surface. This surface degradation is know as aging. This phenomenon is possibly related to the sublimation of material from the surface, since the vapor pressure of the mercury and iodine are rather high at room temperature. Figure 5 shows the optical functions for an aging sample. These spectra show that there is indeed a change in the optical characteristics related to aging. It is believed that this change is caused by an increase in the amount of "voids" present in the near surface region, which fits with the picture of material subliming away.

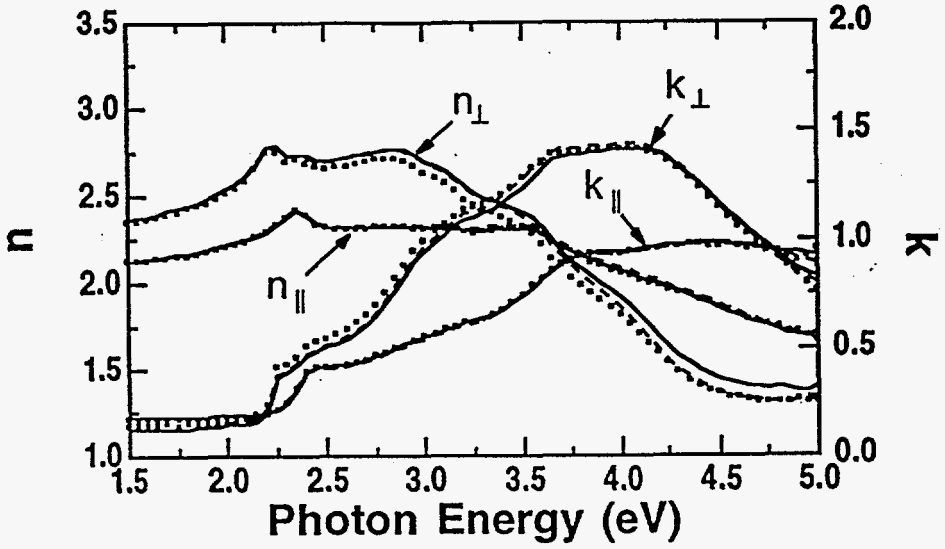

Figure 5. HgI_2 surface aging effects, characterized by the VASE measurements, via the changes of anisotropic refractive indices. The solid lines represent measurements right after the 10% KI etching, and the dashed and dotted lines are results, from the same sample, measured ~20 hours and ~548 hours after the etching, respectively.

Fabrication Modifications

These measurements all lead to the conclusion that certain processing steps can be improved. These measurements show where in the process sequence defects are introduced. Particular changes that are suggested include the use of high purity starting materials and processing chemicals, the proper choice of contact material, and the minimization of material aging. Also, some of these methods, the PL, PI, and VASE, in particular, can be simplified enough to incorporate into real-time online diagnostic tools. With these tools, acute or chronic changes in the amount of defects present in a detector under production could be detected, and conditions changed before too much material, time, and effort is wasted. This could potentially increase yield enough to lower the per unit cost to a point where other applications of detectors become feasible.

SUMMARY AND CONCLUSIONS

Various measurements, including photoluminescence, photoionization, four-point probe sheet resistance, and variable angle spectroscopic ellipsometry have been conducted on mercuric iodide samples subjected to the processing steps required for room temperature x-ray and γ-ray spectroscopic detector fabrication. These measurements highlight the effects of different steps and show correlations between the presence of defects and detector problems. These measurements, therefore, suggest changes required in the processing steps. Finally, some of these techniques can be incorporated into online fabrication diagnostics to more rapidly correct yield problems.

ACKNOWLEDGEMENTS

This work was supported by the U. S. Department of Energy. One of us (T. E. S.) would like to acknowledge the support of the National Science Foundation through the Presidental Young Investigator Program.

REFERENCES

1. W. R. Willig, Nucl. Instrum. Methods **96**, 615 (1971).
2. H. L. Malm, IEEE Trans. Nucl. Sci. **NS-19**, 263 (1972).
3. J. P. Ponpon, R. Stuck, and P. Siffert, Nucl. Instrum. Methods **119**, 297 (1974).
4. J. H. Howes and J. Watling, Mat. Res. Soc. Symp. Proc. **16**, 207 (1983).
5. H. L. Malm, T. W. Raudoff, M. Martina, and K. R. Zanio, IEEE Trans. Nucl. Sci. NS-20, 500 (1973).
6. R. C. Whited and M. Schieber, Nucl. Instrum. Methods **162**, 119 (1979).
7. N. L. Skinner, C. Ortale, M. M. Schieber, and L. van den Berg, Nucl. Instrum. Meth. Phys. Res. **A283**, 119 (1989).
8. X. J. Bao, T. E. Schlesinger, R. B. James, R. H. Stulen, C. Ortale, and A. Y. Cheng, J. Appl. Phys. **68**, 86 (1990).
9. R. B. James, X. J. Bao, T. E. Schlesinger, J. M. Markakis, A. Y. Cheng, and C. Ortale, J. Appl. Phys. **66**, 2578 (1989).
10. X. J. Bao, T. E. Schlesinger, R. B. James, G. L. Gentry, A. Y. Cheng, and C. Ortale, J. Appl. Phys. **69**, 4247 (1991).
11. X. J. Bao, T. E. Schlesinger, R. B. James, R. H. Stulen, C. Ortale, and L. van den Berg, J. Appl. Phys. **67**, 7265 (1990).
12. R. B. James, X. J. Bao, T. E. Schlesinger, C. Ortale, and A. Y. Cheng, J. Appl. Phys. **67**, 2571 (1990).
13. J. M. Van Scyoc, T. E. Schlesinger, R. B. James, A. Y. Cheng, C. Ortale, and L. van den Berg, Mat. Res. Soc. Symp. Proc. **302**, 115 (1993).
14. H. Yao and B. Johs, Mat. Res. Soc. Symp. Proc. **302**, 341 (1993).

Semiconductors for Room Temperature Nuclear Detector Applications

SEMICONDUCTORS
AND SEMIMETALS

Volume 43

Volume Editors

T. E. SCHLESINGER

DEPARTMENT OF ELECTRICAL AND COMPUTER ENGINEERING
CARNEGIE MELLON UNIVERSITY
PITTSBURGH, PENNSYLVANIA

RALPH B. JAMES

ADVANCED MATERIALS RESEARCH DEPARTMENT
SANDIA NATIONAL LABORATORIES
LIVERMORE, CALIFORNIA

ACADEMIC PRESS
San Diego Boston New York
London Sydney Tokyo Toronto

CHAPTER 5

Optical Properties of Red Mercuric Iodide

X. J. Bao

DEPARTMENT OF ANALYTICAL INSTRUMENTS
TN TECHNOLOGIES, INC.
ROUND ROCK, TEXAS

R. B. James

ADVANCED MATERIALS RESEARCH DEPARTMENT
SANDIA NATIONAL LABORATORIES
LIVERMORE, CALIFORNIA

T. E. Schlesinger

DEPARTMENT OF ELECTRICAL AND COMPUTER ENGINEERING
CARNEGIE MELLON UNIVERSITY
PITTSBURGH, PENNSYLVANIA

I. Introduction

Mercuric iodide (HgI_2) in its red tetragonal form has many properties that make it well suited for fabricating x-ray and gamma ray detectors that can be

operated without cryogenic cooling. These properties include a high bulk resistivity ($\sim 10^{13}$ Ω-cm), which ensures a low dark current during detector operation; large atomic masses of the constituent components of HgI_2 (i.e., $Z = 80$ and 53 for Hg and I, respectively), which allows for a high stopping power for x-rays and gamma rays; and high photosensitivity so that the number of electron–hole pairs generated in the crystal is proportional to the energy of the incident photon. Although the potential for manufacturing high resolution spectrometers has been clearly demonstrated, problems continue to be associated with incomplete charge collection, in which case the amount of charge collected for each photon is no longer uniquely proportional to its energy, and with device polarization, in which case the channel numbers corresponding to particular photopeaks or count rate are found to change with time. These problems with charge transport have motivated considerable research in the intrinsic and extrinsic optical properties of HgI_2 crystals, particularly those properties that appear to be related to detector quality.

Optical spectroscopy is a powerful technique to characterize the intrinsic and extrinsic energy levels in many semiconducting crystals. It has been shown that many of the detrimental carrier traps in mercuric iodide crystals and detectors can be probed using optical techniques. However, one difficulty frequently encountered in interpreting the optical measurements is the lack of knowledge of the electronic band structure of the undoped material and the energy levels corresponding to particular contaminants. The next part of this chapter focuses on calculations of the energy bands of mercuric iodide, density of states, momentum matrix elements, and anisotropic dielectric functions. Comparisons with measured values of the bandgap, effective masses, and absorption are made. The remaining portion of the chapter emphasizes numerous experimental reports on the optical properties, such as absorption, reflection, phonon spectrum, and defect states in as-grown and doped mercuric iodide crystals that can be studied by optical spectroscopy.

II. Band Structure

Angular resolved photoemission can be used to probe the electronic levels of HgI_2. By studying the energy of the photoelectrons, it is possible to obtain the energy of the initial (occupied) and final states, the wave vector **k**, and the spin. However, the relatively high vapor pressures of Hg and I complicate use of a photoemission technique and require that the material be cooled to low temperatures to eliminate loss of material from the surface via sublimation. Since photoemission measurements have not yet been used to map the dispersion of the energy bands of HgI_2, the current state of knowledge of the band structure relies primarily on theoretical work, and these investigations are reviewed in this section.

The space group for mercuric iodide is D_{4h}^{15}. The primitive tetragonal unit cell consists of two Hg atoms and four I atoms, as shown in Fig. 1. The nearest neighbor Hg-I spacing is about 2.78 Å. The crystal has inversion symmetry about the

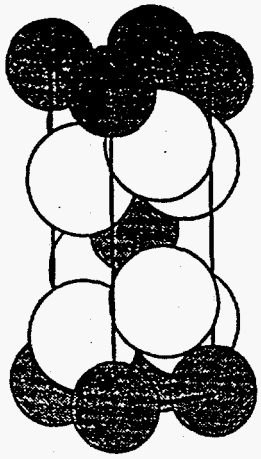

FIG. 1. The primitive tetragonal unit cell for HgI_2. (Reprinted with permission from D. E. Turner and B. N. Harmon, *Phys. Rev. B* **40**, 10516. ©1989 The American Physical Society.)

midpoint between the two Hg atoms. If one chooses the midpoint between the two Hg atoms as the origin of the coordinate system, the atomic positions of the two Hg atoms are $(-a/4, -a/4, -c/4)$ and $(a/4, a/4, c/4)$ and those of the four I atoms are $(-a/4, a/4, -0.111c)$, $(a/4, -a/4, 0.111c)$, $(-a/4, a/4, 0.389c)$, and $(a/4, -a/4, -0.389c)$. The values of a and c are 4.37 Å and 12.44 Å, respectively. The tetrahedral coordination of the mercury atoms in the unit cell is more clearly shown in Fig. 2.

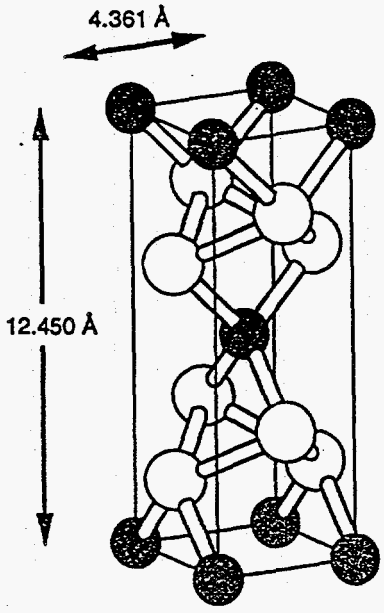

FIG. 2. The primitive HgI_2 unit cell drawn to emphasize the tetrahedral coordination of the mercury atoms. (Reprinted with permission from D. E. Turner and B. N. Harmon, *Phys. Rev. B* **40**, 10516. ©1989 The American Physical Society.)

Yee, Sherohman, and Armantrout, (1976) reported the first empirical pseudopotential calculation of mercuric iodide. In their calculation there was no self-consistency to allow for charge transfer, and no relativistic effects were included. Yee *et al.* (1976) predicted that the bottom of the conduction band did not occur at the same point in k-space as the top of the valence band. The fundamental bandgap was calculated to be indirect with the smallest energy gap occurring in the Γ–M direction of [110]. The prediction of an indirect fundamental bandgap was noted in several experimental reports, and it was often used to interpret optical measurements. Several years later Turner and Harmon (1989) pointed out that the crystal structure used in the work of Yee *et al.* (1976) was incorrect and the calculated results bear little relation with reality.

The report by Turner and Harmon (1989) was the first self-consistent calculation of the electronic band structure of HgI_2. A local density approximation was used, and both spin–orbit interaction and relativistic effects were included. Significant differences in the electronic bands were found between Yee *et al.* (1976) and Turner and Harmon (1989); for example, a direct rather than an indirect bandgap was found. Turner and Harmon also predicted that covalent bonding was dominant in HgI_2 crystals, and an ionicity of less than $Hg^{+0.1}$ was assigned. Figure 3 shows the calculated bands near the energy gap along high symmetry lines. The direct bandgap was calculated to have a value of 0.52 eV and found to be located at the zone center. The calculated value of 0.52 eV is much less than the experimental value of 2.37 eV (Novikov and Pimonenko, 1971), and the predicted bare electron and hole effective masses were also too small. Most of the discrepancy in the bandgap and effective masses is due to self-energy corrections for the excited states of the material, and the overall band structure calculated in Turner and Harmon (1989) appears qualitatively correct.

A few years after the calculations of Turner and Harmon (1989), an empirical nonlocal pseudopotential calculation of mercuric iodide in its red tetragonal form was reported by Chang and James (1992). Spin–orbit interaction and relativistic effects were also included, and the correct unit cell was used. Values for the electron and hole effective masses, optical matrix elements, absorption spectra, and complex dielectric function were reported. The local and nonlocal pseudopotentials were adjusted to fit the experimental value of the bandgap and qualitatively agree with the overall band structure obtained by the first principles calculation of Turner and Harmon (1989). Approximately 620 planewaves with energies less than 8 Rydberg were included in the diagonalization procedure. Figure 4 shows the calculated band structure of HgI_2. The calculated fundamental bandgap is direct at the zone center with a value of 2.37 eV, and the splitting between the first two valence bands (i.e., the heavy and light hole bands) is about 0.2 eV, both of which agree with the measured values at 4.2 K (Novikov and Pimonenko, 1971; Kanzaki and Imai, 1972).

Figure 5 shows a magnified view of the band structure of Chang and James (1992) near the zone center. The left side shows the electronic structure with wave vector $\mathbf{k}$ along the [110] direction, and the right-hand side shows the bands along

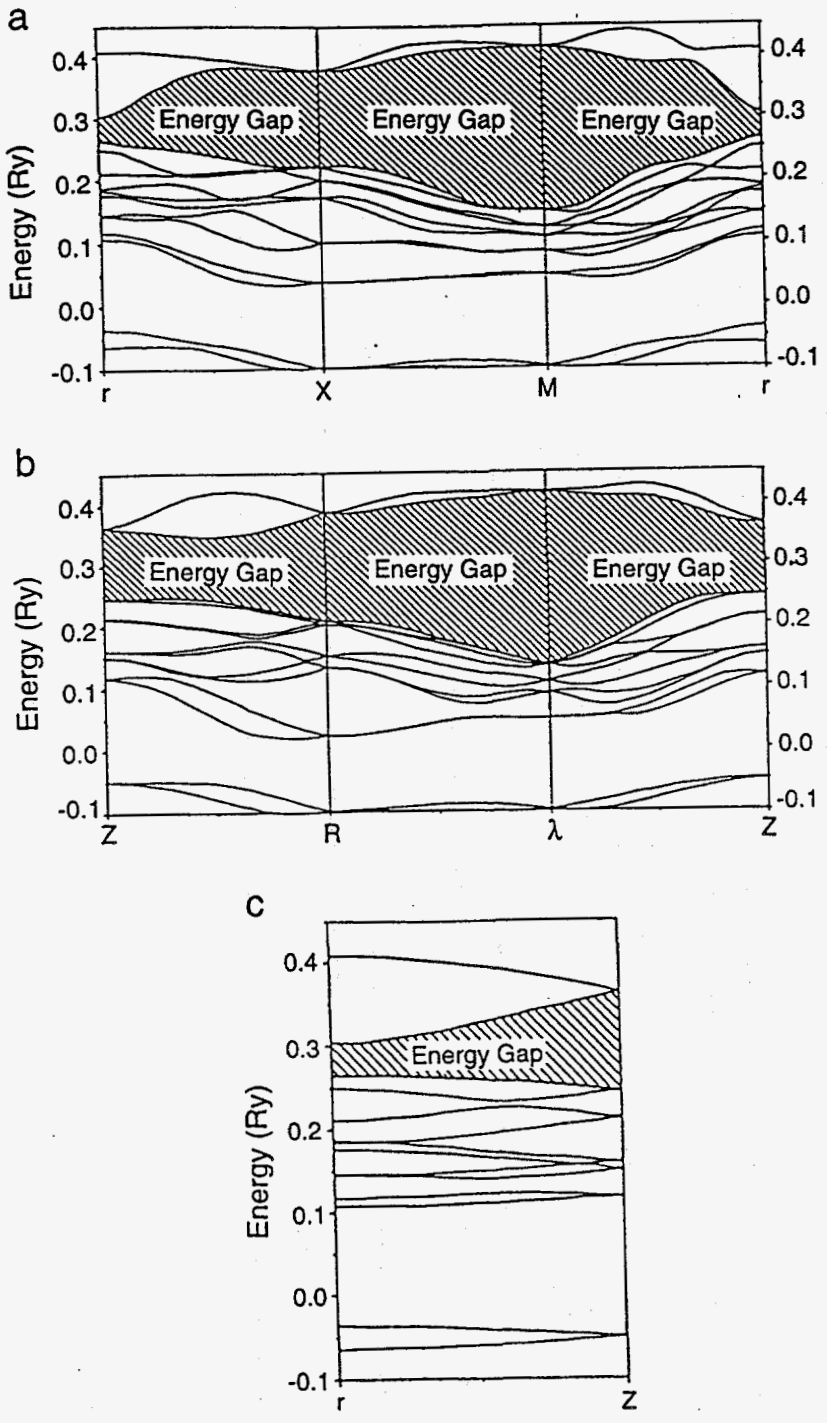

FIG. 3. Calculated bands of mercuric iodide near the energy gap along high symmetry lines. (Reprinted with permission from D. E. Turner and B. N. Harmon, *Phys. Rev. B* 40, 10516. ©1989 The American Physical Society.)

the [001] direction. The unit of k is in $2\pi/a$. The conduction band is found to be nearly isotropic and the valence band to be much more anisotropic. The effective masses and reduced effective masses are shown in Table I, along with the mea-

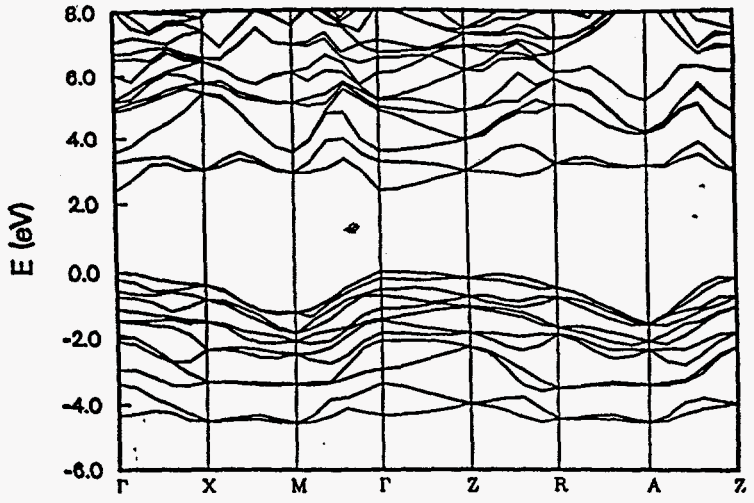

FIG. 4. Calculated band structure of mercuric iodide. (Reprinted with permission from Y. C. Chang and R. B. James, *Phys. Rev. B* **46**, 15040. ©1992 The American Physical Society.)

sured values. Table I also shows the polar masses (m^e and m^h), which were calculated by Chang and James using an intermediate coupling polaron theory.

Figure 6 shows the squared optical matrix elements P^2 for transitions between

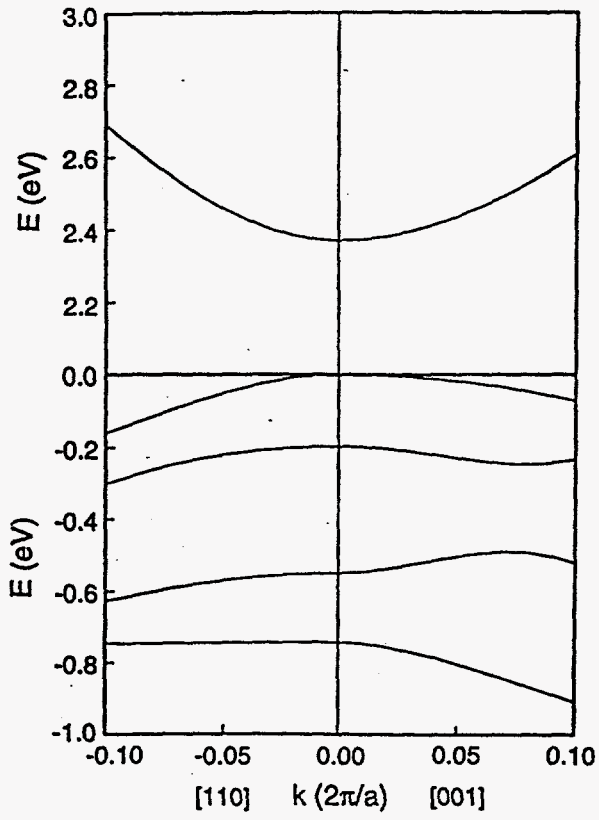

FIG. 5. Magnified view of the band structure of Fig. 4. (Reprinted with permission from Y. C. Chang and R. B. James, *Phys. Rev. B* **46**, 15040. ©1992 The American Physical Society.)

TABLE I

EFFECTIVE MASSES FOR MOTION PERPENDICULAR TO ($m_\perp$) AND PARALLEL TO THE C-AXIS ($m_\parallel$). THE SUBSCRIPTS AND SUPERSCRIPTS e AND h DENOTE ELECTRON AND HOLE, RESPECTIVELY. THE SUBSCRIPTS APPLY TO THE BARE EFFECTIVE MASSES AND THE SUPERSCRIPTS APPLY TO THE POLARON EFFECTIVE MASSES

	$m_{e,\perp}$	$m_{e,\parallel}$	$m^e_\perp$	$m^e_\parallel$	$m_{h,\perp}$	$m_{h,\parallel}$	$m^h_\perp$	$m^h_\parallel$	$\mu_\perp$	$\mu_\parallel$
Theory	0.22[a]	0.30[a]	0.29[a]	0.37[a]	0.59[a]	1.02[a]	0.89[a]	1.43[a]	0.22[a]	0.29[a]
Experiment	0.29[b]	0.25[b]	0.37[b]	0.31[b]	0.56[b]	1.72[b]	1.03[b]	2.06[b]	0.24[c]	0.31[c]

(Reprinted with permission from Y. C. Chang and R. B. James, *Phys. Rev. B* 46, 15040. © 1992 The American Physical Society.)

[a] Chang and James (1992)

[b] Schluter and Schluter (1974)

[c] Goto and Kasuya (1981)

the valence and conduction bands near the zone center (Chang and James, 1992). The curves shown in the figure are for transitions from the topmost five valence bands to the lowest energy conduction band. Here, P^2 is defined as

$$P^2_{ij} = 2/m\ |\langle k, i|e \cdot p|k, j\rangle|^2$$

The labels $v1$, $v2$, $v3$, $v4$, and $v5$ denote transitions between the first to fifth valence bands, respectively, and the lowest conduction band. The solid curves are for the in-plane polarization (i.e., e perpendicular to the z direction) and the dashed curves are for polarization along the c-axis (i.e., e parallel to z). For optical

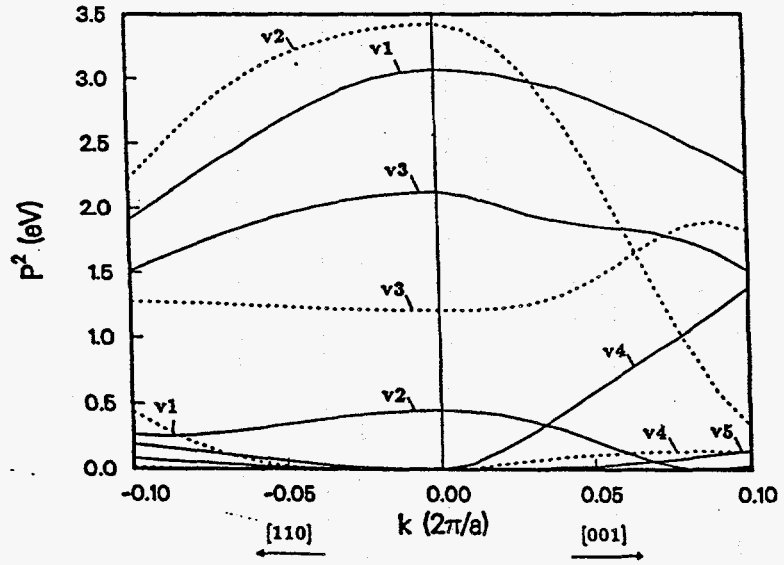

FIG. 6. Calculated squared optical matrix elements of P^2 for transitions between the valence and conduction bands near the zone center. (Reprinted with permission from Y. C. Chang and R. B. James, *Phys. Rev. B* 46, 15040. ©1992 The American Physical Society.)

absorption at wavelengths at the fundamental band edge, only the $v1$ transitions are resonant. The matrix elements for linearly polarized light perpendicular to the **z** direction are large at the zone center, whereas for **z** polarized light the matrix elements vanish at the zone center and are very weak for all values of **k**. These results for P^2 are consistent with the character of the heavy hole band, since the heavy hole state transforms like $(x + iy)\uparrow$. Here, the symbol $\uparrow$ denotes a spin up. For the $v2$ matrix elements, light polarized along the **z** direction is strongly absorbed, and the matrix elements are about six times larger at the zone center than the matrix elements for polarization perpendicular to **z**. This is consistent with the character of the light hole band, since the light hole state is a linear combination of states that transform like $(x + iy)\downarrow$ and $z\uparrow$ with the majority component having $z\uparrow$. Given the dependence of P^2 on the direction of light polarization, it is clear that the depth of penetration of light for photon energies near the fundamental bandgap depends strongly on the orientation of the crystal with respect to the direction of propagation of the linearly polarized light.

Using calculated values for the electronic band structure and optical matrix elements, one can model the absorption coefficient as a function of the incident photon energy. Chang and James (1992) used an effective mass approximation to obtain values for the real and imaginary parts of the complex dielectric constant of HgI_2 for photon energies near the fundamental bandgap. The calculation also included effects of excitons on the absorption spectrum. The solid curve in Fig. 7 shows the values for the absorption coefficient for unpolarized light, and the dotted curve shows the absorption coefficient for incident light polarized parallel to the **z** direction. Fig. 7 also shows the experimental absorption coefficient for thin HgI_2 films at temperatures of 4.2 and 79 K (Kanzaki and Imai, 1972). Since the films were polycrystalline, comparisons should be made between the experimental data at 4.2 K and the calculated results for the case of unpolarized light. The calculations by Chang and James (1992) predict that the heavy hole exciton absorption is significant only for light polarized perpendicular to the c-axis, and the light hole exciton absorption is nonzero for both polarizations with the absorption for light polarized parallel to **z** much stronger than for light polarized perpendicular to **z**. These predictions are also in agreement with reflectivity measurements of Kanzaki and Imai (1972).

The calculations by Turner and Harmon (1989) and Chang and James (1992) have significantly advanced the level of knowledge of the electronic bands and absorption spectrum of HgI_2. Using measured values for the phonon dispersion curves, it is now possible to model the electron–phonon and hole–phonon matrix elements and determine the scattering rates for carriers as a function of their wave vector **k**. By integrating the carrier–phonon scattering rates over the distribution of free carriers, one can in principle determine the electron and hole mobilities and their dependences on the lattice temperature. Although these calculations have not been reported to date, the task is a tractable one with modern supercomputers. The values for mobilities due to intrinsic scattering mechanisms (i.e., carrier–phonon) can then be used to determine the fundamental limits for the carrier mo-

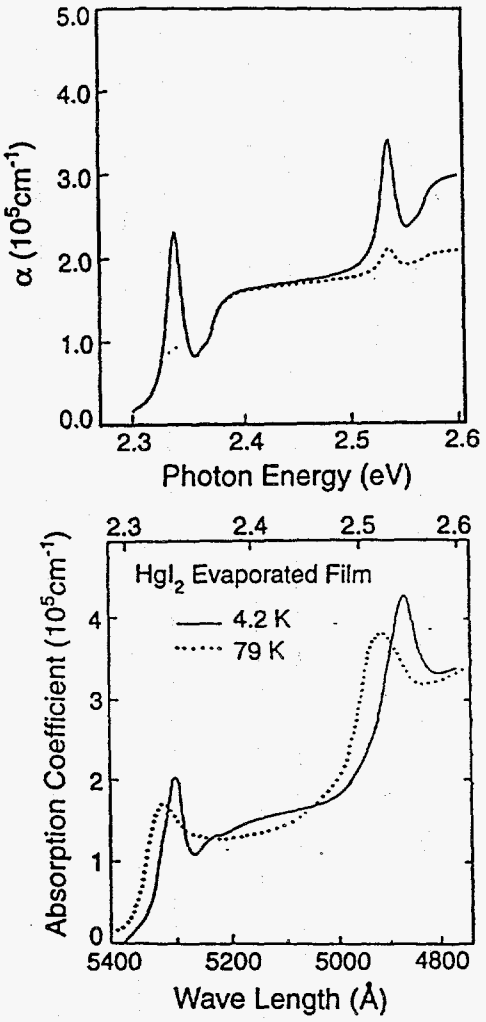

FIG. 7. Absorption spectra of HgI_2 near the fundamental absorption edge. Top, theoretical prediction; the solid curve is for unpolarized light and the dotted curve is for light polarized perpendicular to the c-axis. (Reprinted with permission from Y. C. Chang and R. B. James, *Phys. Rev. B* 46, 15040. ©1992 The American Physical Society.) Bottom, experimental absorption coefficient of thin mercuric iodide films at 4.2 and 79 K, both curves are for unpolarized light (Kanzaki and Imai, 1972).

bilities and ideally explain the wide variation in the reported values of the hole mobility of HgI_2 at 300 K.

III. Experimental Techniques and Measured Values for Optical Constants

1. MEASUREMENT OF BANDGAP AND SHIFT WITH TEMPERATURE

The energy of the bandgap and its temperature dependence is vital to understanding the performance of the radiation detectors fabricated from mercuric iodide. When HgI_2 photocells and x-ray and gamma ray spectrometers are used over

a range of temperatures, the performance of the devices will shift slightly due to changes in the optical and electrical properties of HgI_2. In some cases this change in the amount of photogenerated charge makes it difficult to spectrally resolve elements that have x-rays of similar energies, and temperature control of the detectors is typically required for stable signals. The temperature controllers reduce slightly the portability and compactness of the instruments, which may limit their usefulness in certain applications. Independent of the demands on temperature control for each application, it is clear that the understanding of the temperature dependence of detectors requires knowledge of the change in the bandgap, E_G. Measurements of $E_G(T)$ have been reported by a number of investigators using a variety of techniques. In one of the earliest studies, Bube (1957) used reflection measurements on polycrystalline samples to obtain a value of 2.14 eV for E_G at room temperature. Burger and Nason (1992) used excitonic reflection to obtain a direct bandgap of 2.292 eV at 300 K, which is considerably larger than the bandgap reported by Bube (1957). Since the measurements of Burger and Nason do not rule out the existence of an indirect bandgap at lower energy, it is possible that the measurements of Bube (1957) and Burger and Nason (1992) are not in conflict. At 77 K Chester and Coleman (1971) measured a value for E_G of 2.331 eV, and Bube (1957) obtained a value of 2.334 eV. At 4.2 K Goto and Nishina (1978) obtained a value of 2.3707 eV by emission, and Novikov and Pimonenko (1971) measured 2.369 eV by absorption. Anedda *et al.* (1977) reported 2.397 eV using wavelength modulated reflection at 2 K. Lopez-Cruz (1989) performed an analysis based on photoconductivity measurements and concluded that at 0 K, HgI_2 has a direct bandgap at 2.27 eV and an indirect gap of 2.203 eV. The measurements by Lopez-Cruz (1989) and Burger and co-workers (1992) suggest that the indirect and direct bandgaps of mercuric iodide are close together. If this is indeed the case, it might account for the photoluminescence (Novikov and Pimonenko, 1971) data, absorption (Kanzaki and Imai, 1972) measurements, and band structure calculations (Turner and Harmon, 1989; Chang and James, 1992) that predict a direct gap material, and the photoconductivity (Lopez-Cruz, 1989) and electroabsorption measurements (Chester and Coleman, 1971) that suggest an indirect gap material.

The temperature coefficient of the bandgap has also been reported by several investigators. Bube (1957) reported a coefficient of -14×10^{-4} eV/K in the temperature range of 330 to 400 K, Burger and Nason (1992) observed a value of -3.9×10^{-4} eV/K from 285 to 400 K, and Harbeke and co-workers (1974) reported -6.5×10^{-4} eV/K in the same temperature range. At low temperatures, Novikov and Pimonenko (1972) quoted a value of -2.6×10^{-4} eV/K from 20 to 77 K, and Merz *et al.* (1983) measured -1.13×10^{-4} eV/K from 32 to 45 K. Nason and Burger (1991) used the location of peaks in the reflectance spectrum to infer a value of the surface temperature during the growth of HgI_2 crystals.

Significant differences in the values for E_G and its temperature dependences are apparent. Some of the discrepancy may be attributed to the different techniques used to measure E_G and differing role of excitonic effects in the experiments. Further work needs to be done to more fully understand the details of the band

TABLE II

REFRACTIVE INDICES OF HgI_2 FOR POLARIZATION PERPENDICULAR TO C

Wavelength	n	R
Na D-line 589 nm	2.71 ± 0.04	21.4%
He–Ne laser 632 nm	2.62 ± 0.01	20.0%

(Reprinted with permission from Kanzaki and Imai, 1972 and the Physical Society of Japan.)

structure of HgI_2 and role of crystalline perfection and purity on the measured results for $E_G(T)$.

a. *Excitation near and above the Fundamental Band Edge*

The reflectance spectrum of single crystal and polycrystalline mercuric iodide over the region of 2 to 6 eV was studied by Kanzaki and Imai (1972), and several peaks were detected. Ellipsometry measurements have also been performed by Yao, Johs, and James, (1993), and values for the optical properties of HgI_2 have been reported.

i. The Ordinary Spectrum. Refractive indices were measured at room temperature using incident photon energies of 2.10 and 1.959 eV from Na and He–Ne lasers, respectively. Table II shows the measured values for the refractive indices of single crystal HgI_2 for the case of polarization perpendicular to the c-axis.

Figure 8 shows the reflectivity spectrum of HgI_2 at 4.2 K for photon energies

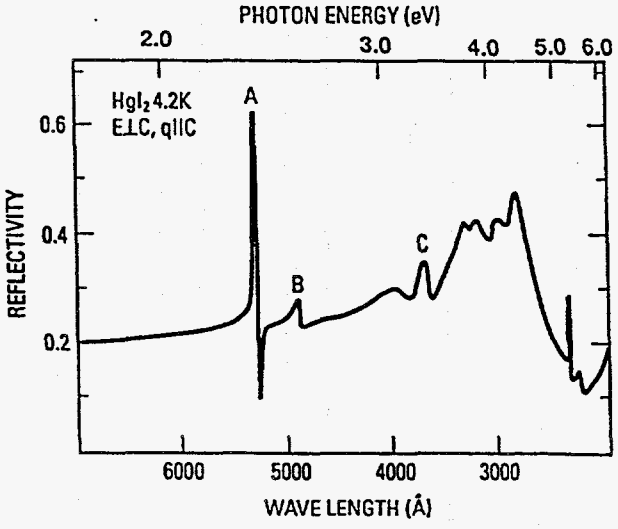

FIG. 8. Reflectance measurements at 4.2 K. (Reprinted with permission from Kanzaki and Imai, 1972 and the Physical Society of Japan.)

TABLE III

THE SHARP REFLECTIVITY PEAKS NEAR THE FUNDAMENTAL EDGE OF HgI_2. A DASH INDICATES VALUES NOT MEASURED BY KANZAKI AND IMAI (1972)

	$q \parallel c$	$E \perp c$	$q \perp c$	$E \perp c$	$q \perp c$	$E \parallel c$
	4.2 K	79 K	4.2 K	79 K	4.2 K	79 K
A	2.339	2.320	2.338	2.320	—	—
B	2.538	2.505	2.538	2.505	2.538	2.505
C	3.35	3.31	—	—	—	3.32

between 2 and 6 eV. Here the polarization of the light is perpendicular to the c-axis and the photon wave vector q parallel to c. The peaks at 2.339 (5301 Å) are sharp and large. For photon energies less than 2.339 eV, the material is transparent, indicating that the peak at 2.339 eV is due to formation of an exciton. The peaks of the reflectance spectrum are listed in Tables III and IV.

Figure 9 shows the reflectance spectrum at 4.2 K in the region near the bandgap. The circles show the measured reflectivities in a configuration with the light polarization perpendicular to the c-axis and the photon wave vector parallel to c, and the dotted line shows the measured results for light polarized perpendicular to the c-axis and the photon wave vector perpendicular to c. As shown in the figure, the observed values of reflectivities in both configurations agree with each

TABLE IV

THE REFLECTIVITY PEAKS OF HgI_2 FOR POLARIZATION PERPENDICULAR TO THE C-AXIS AND PHOTON WAVE VECTOR PARALLEL TO C

$T = 4.2$ K			$T = 79$ K	
eV	Å	Remarks	eV	Å
2.339	5301	Very sharp A	2.320	5343
2.368	5236	Very weak		
2.538	4885	Sharp B	2.505	4955
3.10	4000	Broad	3.06	4050
3.351	3700	Sharp C	3.306	3750
3.73	3325		3.71	3340
3.84	3230		3.83	3240
4.13	3000			
4.38	2830		4.35	2850
5.29	2345	Very sharp	5.25	2360
5.38	2305			
5.46	2270	Broad	5.44	2280

(Reprinted with permission from Kanzaki and Imai, 1972 and the Physical Society of Japan.)

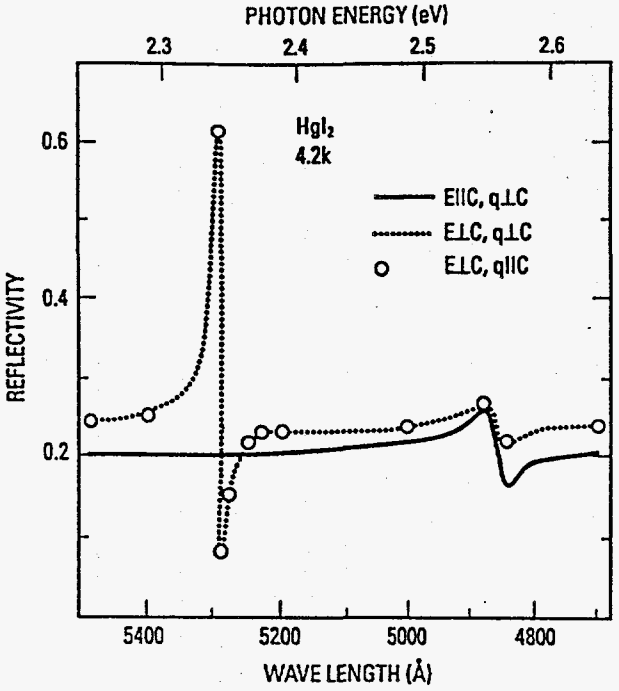

FIG. 9. Reflectivity spectra of HgI_2 at 4.2 K near the fundamental absorption edge: $\mathbf{E}\perp\mathbf{c}$, $\mathbf{q}\perp\mathbf{c}$ (dotted line); $\mathbf{E}\perp\mathbf{c}$, $\mathbf{q}\parallel\mathbf{c}$ (circles); $\mathbf{E}\parallel\mathbf{c}$, $\mathbf{q}\perp\mathbf{c}$ (solid line). (Reprinted with permission from Kanzaki and Imai, 1972 and the Physical Society of Japan.)

other. The configurations with $\mathbf{E}\perp\mathbf{c}$ correspond to the ordinary spectrum of HgI_2. Figure 10 shows the details of the reflectivity spectrum at 4.2 K for $\mathbf{E}\perp\mathbf{c}$ and $\mathbf{q}\parallel\mathbf{c}$ for photon energies in the 5 to 6 eV range.

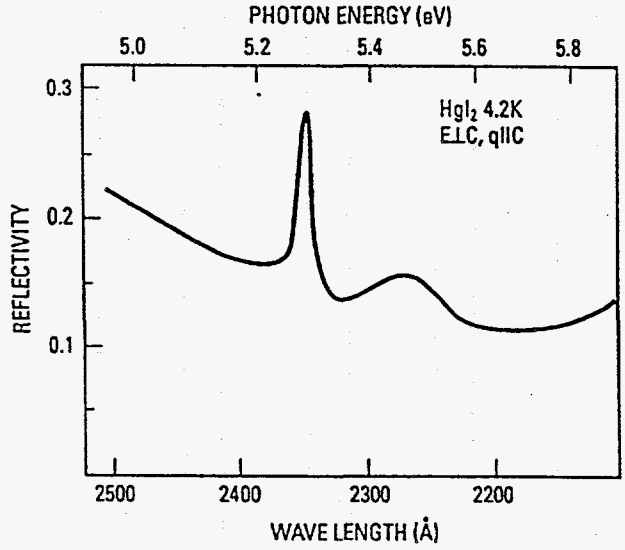

FIG. 10. Reflectivity spectrum of HgI_2 at 4.2 K at the 5 ~ 6 eV region, $\mathbf{E}\perp\mathbf{c}$, $\mathbf{q}\parallel\mathbf{c}$. (Reprinted with permission from Kanzaki and Imai, 1972 and the Physical Society of Japan.)

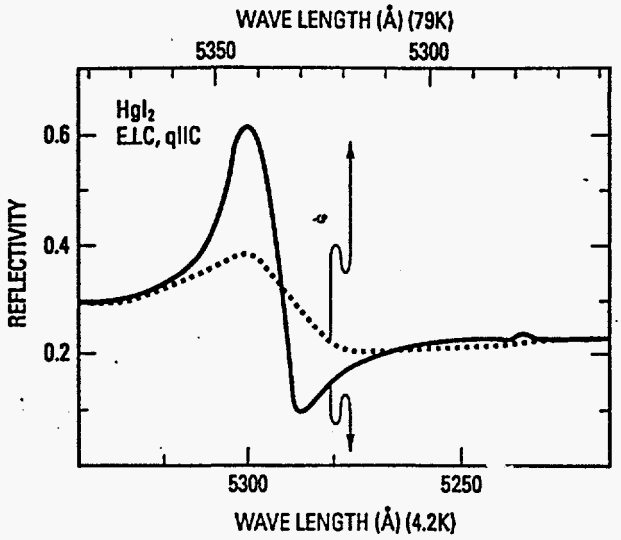

FIG. 11. Reflectivity spectra of HgI_2 at 4.2 K (solid line) and at 79 K (dotted line) near the fundamental edge in enlarged scale, $\mathbf{E}\perp\mathbf{c}$, $\mathbf{q}\parallel\mathbf{c}$. (Reprinted with permission from Kanzaki and Imai, 1972 and the Physical Society of Japan.)

Figure 11 shows reflectance spectra on an enlarged scale for wavelengths close to the band edge and temperatures of 4.2 and 79 K. The configuration used in this experiment is $\mathbf{E}\perp\mathbf{c}$ and $\mathbf{q}\parallel\mathbf{c}$. As the temperature is increased, the spectrum is shifted to longer wavelengths and becomes less sharp, which is primarily due to the reduction of the bandgap at higher temperatures. Figure 12 shows the reflectance of HgI_2 at 100 K for $\mathbf{E}\perp\mathbf{c}$ and for photon energies up to 10 eV, as measured by Anedda and coworkers (1977).

ii. The Extraordinary Spectrum. The extraordinary reflectance spectrum (i.e, $\mathbf{E}\parallel\mathbf{c}$ and $\mathbf{q}\perp\mathbf{c}$) was also measured by Kanzaki and Imai (1972). The results

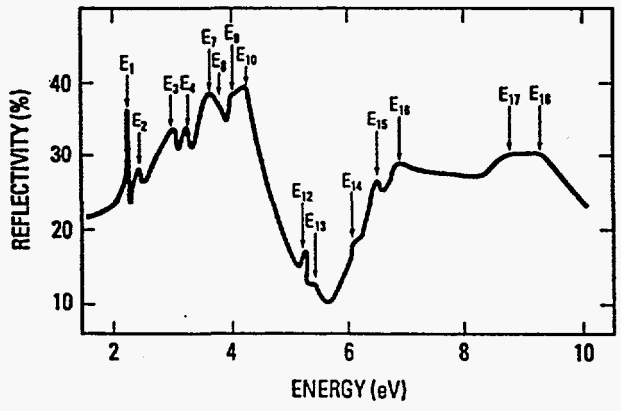

FIG. 12. Reflectivity spectrum of red HgI_2 at 100 K ($\mathbf{E}\perp\mathbf{c}$ and $\mathbf{k}\parallel\mathbf{c}$). (Reprinted from Anedda *et al. Solid State. Commun.* **39**, 1121 ©1981 with kind permission from Elsevier Science Ltd., The Boulevard, Langford Lane, Kidlington, OX5 1GB.)

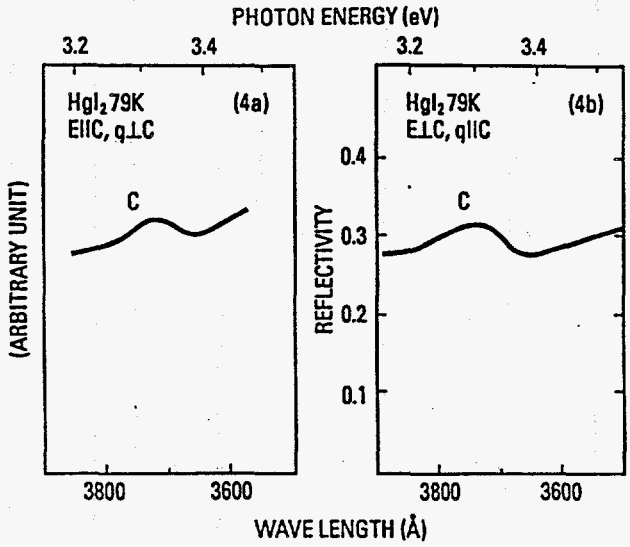

FIG. 13. Reflectivity spectra of HgI_2 at 79 K near 3.3 eV: $E \perp c$, $q \perp c$ (a); $E \perp c$, $q \| c$ (b). (Reprinted with permission from Kanzaki and Imai, 1972 and the Physical Society of Japan.)

are shown in Figure 9 by the solid curve. The extraordinary spectrum of HgI_2 has no peak near 5300 Å, and the first peak occurs at about 4885 Å (2.538 eV), which coincides with the second peak in the ordinary spectrum. The absence of the peak near 5300 Å in the extraordinary reflectivity spectrum is explained by the near zero optical matrix elements calculated by Chang and James (1992) (see Fig. 6).

Figure 13 shows the reflectance spectrum at 79 K for photon energies near 3.3 eV (Kanzaki and Imai 1972). A peak at about 3730 Å (3.32 eV) is observed in both the ordinary and extraordinary configurations. This peak corresponds to the peak at 3700 Å (3.351 eV) observed at 4.2 K (see Figure 12).

2. ABSORPTION

For photon energies exceeding the bandgap of HgI_2, the absorption coefficient is quite large ($>10^5$ cm^{-1}), and transmission measurements must be performed on thin films. It is difficult to polish and etch HgI_2 to submicron thicknesses, but thin films can be easily prepared by evaporating mercuric iodide in vacuum and depositing the evaporated material onto a cooled substrate. Kanzaki and Imai (1972) prepared thin polycrystalline films by evaporation in vacuum onto glass plates. Optical microscopy revealed that polycrystals of about 10 μm size were formed, and the c-axes of the domains were typically random in direction. The polycrystalline nature of the films requires that both the ordinary and extraordinary absorption occur in the film. The results of Kanzaki and Imai (1972) are shown in Fig. 7, along with the theoretical predictions for the absorption coefficient. The features of the transmittance measurements are consistent with reflectivity measurements (Kanzaki and Imai, 1972) and theory (Chang and James, 1992; Chang, Sim, and James, 1993).

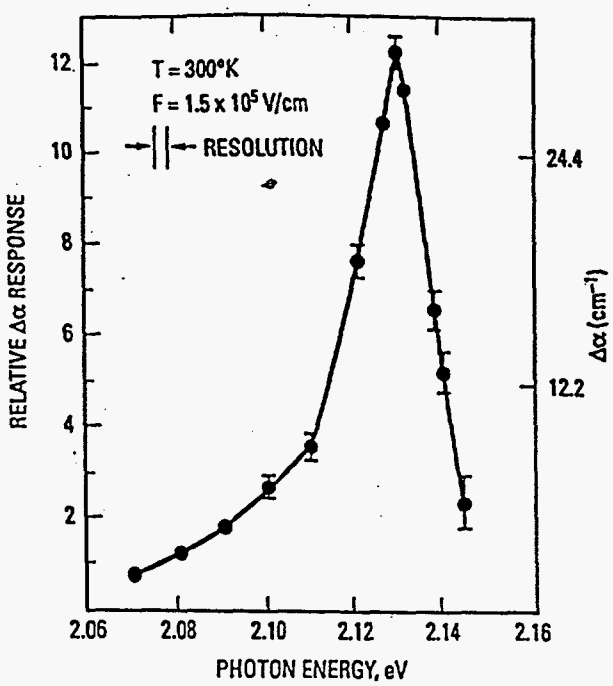

FIG. 14. Electroabsorption signal in HgI_2 at 300 K. (Reprinted from M. Chester and C. C. Coleman, *J. Phys. Chem. Solids* 32, 223 ©1971 with kind permission from Elsevier Science Ltd., The Boulevard, Langford Lane, Kidlington, OX5 1GB.)

The electroabsorption spectrum of HgI_2 has been investigated by Chester and Coleman (1971) as a function of temperature and electric field. The physical quantity determined by the measurements of Chester and Coleman (1971) is the change in the optical absorption coefficient induced by an electric field. Figure 14 shows typical results at 300 K for a field of 1.5×10^5 V/cm. The electroabsorption peak occurs at a spectral energy of 2.127 eV, which is slightly less than the bandgap of 2.14 ± 0.005 eV at 300 K.

Electroabsorption (EA) data were taken by Chester and Coleman (1971) at several temperatures. Figure 15 shows the dependence of the electroabsorption peak on the applied field for photon energies of 2.127 eV (coinciding with peak at 300 K) and 2.313 eV (location of peak at 88 K). The form of the EA spectrum did not change with the applied field, and the magnitude of the peak varies approximately as the 4/3 power of the field. A 4/3 power of the EA signal with the electric field is expected for an indirect bandgap material (Chester and Coleman, 1971), whereas a 1/3 power is expected for an allowed direct bandgap excitation. However, the theory that predicts a 4/3 power dependence for indirect bandgap materials does not include the case when exciton absorption is involved. Moreover, the EA peak observed by Chester and Coleman (1971) always occurred approximately 0.010 eV below the bandgap. There exists an exciton at an energy of about 0.010 eV below the bandgap (Bao *et al.*, 1990b), which suggests strongly that the EA signal at each temperature is associated with exciton absorption.

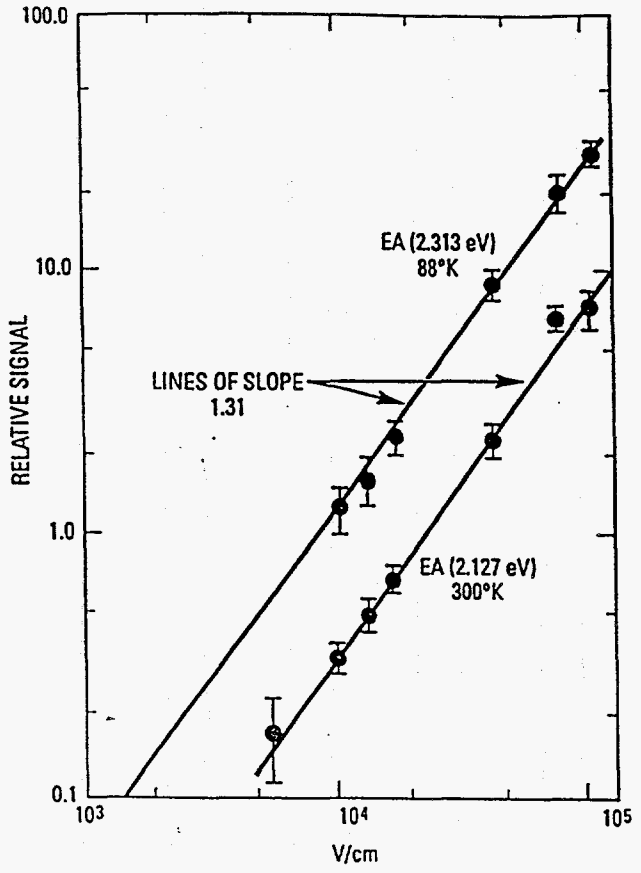

FIG. 15. Electroabsorption signal voltage dependence. (Reprinted from M. Chester and C. C. Coleman, *J. Phys. Chem. Solids* 32, 223 ©1971 with kind permission from Elsevier Science Ltd., The Boulevard, Langford Lane, Kidlington, OX5 1GB).

3. ELLIPSOMETRY MEASUREMENTS OF OPTICAL CONSTANTS

The imaginary part of the dielectric constant was first measured by Anneda and co-workers (1977), and the results are shown in Fig. 16 for energies between 2 and 10 eV. More recent measurements of the optical properties of HgI_2 were measured by Yao and Johs (1993), Schieber *et al.* (1994), and Yao *et al.* (1994) using variable angle spectroscopic ellipsometry (VASE). Figure 17 shows values for the room temperature anisotropic dielectric functions, ϵ_1 and ϵ_2, as measured by VASE (Schieber *et al.*, 1994; Yao *et al.*, 1994) for electric fields perpendicular and parallel to the c direction. Figure 18 shows measured values for the absorption coefficient in the energy range of 2–5 eV at 293 K, and Fig. 19 shows measured values for the reflectance in the 1–5 eV range (Yao *et al.*, 1994) at 293 K. Based on the VASE measurements, one sees that the depth of penetration of light and its reflectance are strongly dependent on the polarization of the radiation and the orientation of the crystal. Surface aging effects of HgI_2 crystals have also been studied by monitoring the changes in the dielectric constants after chemical etch-

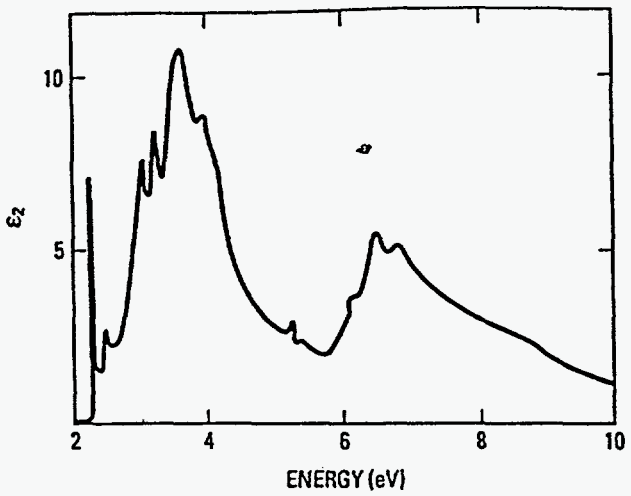

FIG. 16. Imaginary part of the dielectric constant versus energy. (Reprinted from Anedda *et al. Solid State. Commun.* 39, 1121 ©1981 with kind permission from Elsevier Science Ltd., The Boulevard, Langford Lane, Kidlington, OX5 1GB.)

ing and as a function of time (Schieber *et al.*, 1994; Yao and Johs, 1993). Some of the surface aging effects appear to be related to excess iodine contained in the crystals.

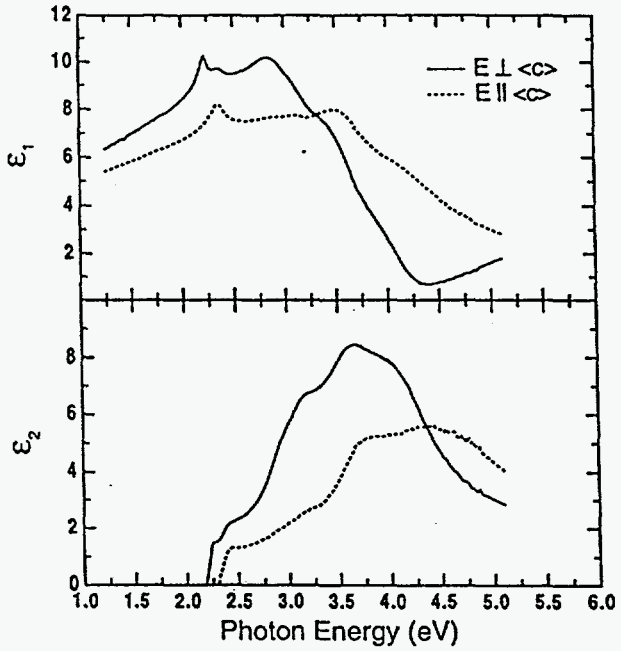

FIG. 17. Anisotropic optical constants of HgI_2 as measured by VASE (from Yao *et al.*, 1994).

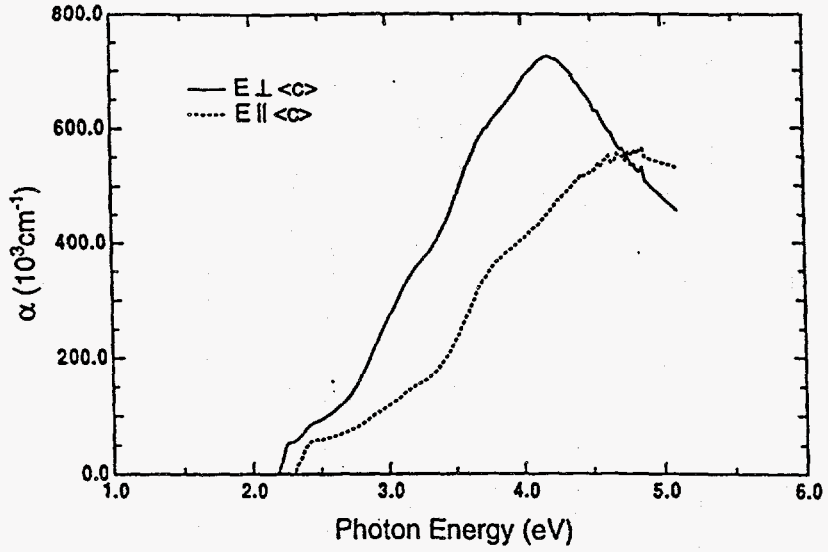

FIG. 18. Absorption of HgI_2 as measured by VASE (from Yao *et al.*, 1994).

4. OPTICAL PROPERTIES NEAR AND BELOW THE BANDGAP

Since HgI_2 is more optically transparent at photon energies near and below the bandgap, studies of the absorption coefficient at these wavelengths can be performed on thicker single crystals. The nature of the absorption still depends on the orientation of the light polarization with respect to the c axis of HgI_2. Figure 20

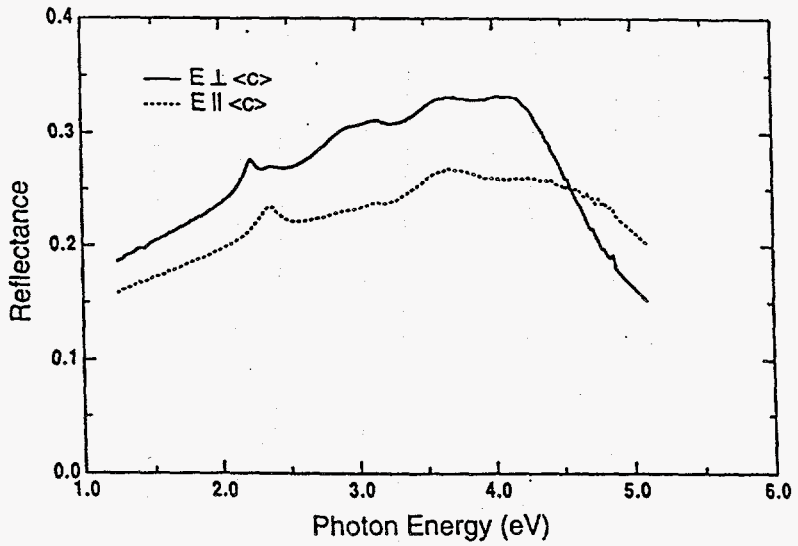

FIG. 19. Polarized reflectance of HgI_2 (from Yao *et al.*, 1994).

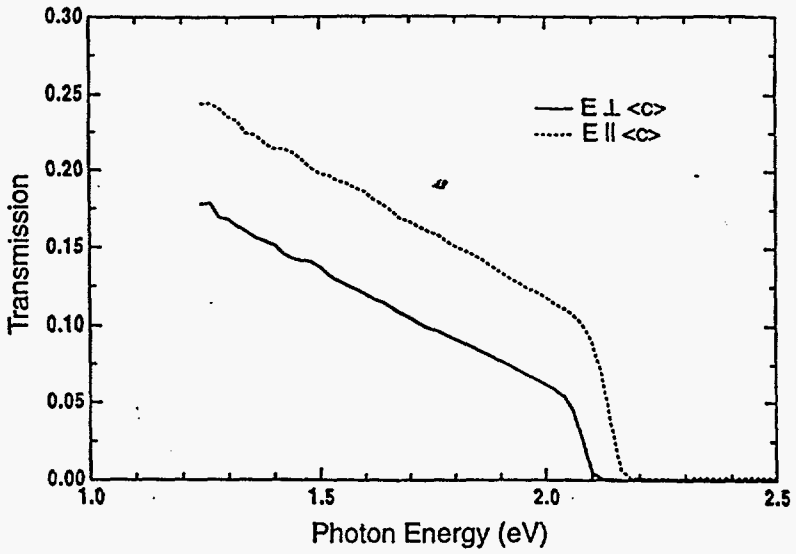

FIG. 20. Polarized transmission of HgI_2 (from Yao *et al.*, 1994).

shows room temperature values for the polarized transmission of HgI_2 for photon energies in the 1.2 to 2.2 eV range (Yao *et al.*, 1994).

Reflectivity in the ordinary configuration (i.e., $\mathbf{E}\perp\mathbf{c}$) at 4.2 K has been reported by Akopyan *et al.* (1975). At this temperature, the ordinary absorption ($\mathbf{E}\perp\mathbf{c}$) shows continuous absorption (Novikov and Pimonenko, 1971). However, in the extraordinary absorption spectrum (i.e., $\mathbf{E}\|\mathbf{c}$) at 4.2 K, the absorption consists of discrete resonant peaks (Novikov and Pimonenko, 1971) (see Fig. 21). The strongest peak (labeled as λ_0) occurred at 5297 Å and two weaker lines were measured at 5246 Å and 5239 Å. The continuous absorption at shorter wavelengths was attributed to interband transitions, and the bandgap was inferred to be 5230 Å (= 2.369 eV). On the long wavelength side of the large peak at 5297 Å, two narrow lines were observed at 5310 and 5321 Å, whose intensities varied from sample to sample. These same lines are also observed with varying intensities in the photoluminescence spectrum of HgI_2 (Novikov and Pimonenko, 1971) and have been described as excitonic in nature.

Akopyan *et al.* (1975) also observed these absorption peaks and assigned slightly different values for the peak positions and linewidths. They measured an absorption peak at 5309.1 Å and found the FWHM of the peak to be much less than that of the emission line at 5308 Å ($\mathbf{E}\perp\mathbf{c}$). To further investigate this line, the authors (Akopyan *et al.*, 1975) measured its behavior under a uniaxial stress with $\mathbf{P}\perp\mathbf{c}$. The shift of the bandgap with pressure was reported earlier by Zahner and Drickamer (1959). As stress was applied, the absorption line at 5309 Å became more intense than the line at 5297 Å. Such behavior is characteristic of a forbidden exciton transition, with the increase in the absorption at 5309 Å being due to the mixing of forbidden and allowed transitions by the uniaxial stress. A similar stress dependence was observed for the A_F line in CdS crystals (Hopfield and Thomas,

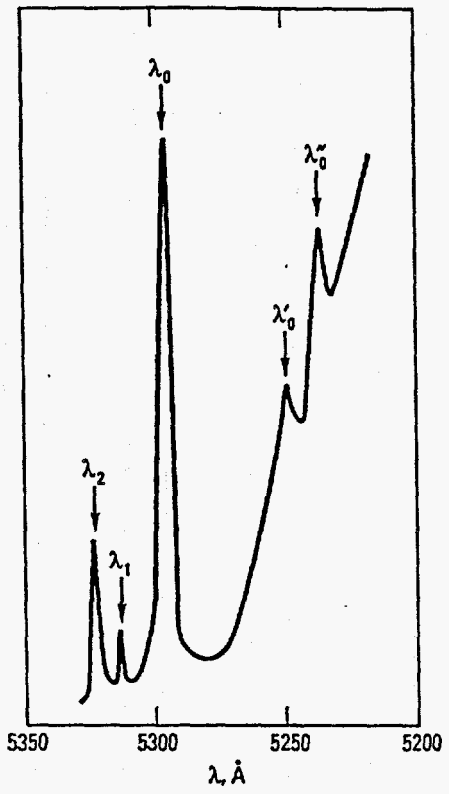

FIG. 21. An absorption spectrum of HgI_2 single crystal with its optic axis in the plane of the platelet. The spectrum was recorded at 4.2 K. The scale of the long wavelength part of the spectrum is magnified along the ordinance to show the structure. (Reprinted with permission from Novikov and Pimonenko, 1971 and the American Institute of Physics.)

1960, 1961; Thomas and Hopfield, 1959). The line in CdS was interpreted to result from transitions into an optically forbidden component of the ground state exciton level, which is split from the main allowed component by exchange interaction.

In a magnetic field ($H = 30$ kOe) in the orientation $\mathbf{H} \| \mathbf{c}$, the 5309 Å absorption line splits into a doublet, but it is not affected for $\mathbf{H} \perp \mathbf{c}$. The A_F line in CdS shows the same magnetic field dependence (Hopfield and Thomas, 1960), which gives further confidence in the assignment of the 5309 Å of HgI_2 to transitions into an optically forbidden component of the ground exciton state. The amount of exchange splitting depends on the ratio of the exciton Bohr radius to the lattice constant; and for exciton states of large radius (relative to the lattice constant), the exchange splitting is typically only a few tenths of a meV (Akopyan *et al.*, 1975).

At higher temperatures, the large absorption peak at 5297 Å broadens, and it gradually shifts to lower energies because of bandgap narrowing. At 77 K this line is located near 5328 Å and its full-width at half-maximum has increased by greater than 4. At this temperature the continuous absorption attributed to band to band transitions began at 5260 Å (Novikov and Pimonenko, 1971). The two narrow absorption lines (located at 5310 and 5321 Å at 4.2 K) disappear at about 30 K.

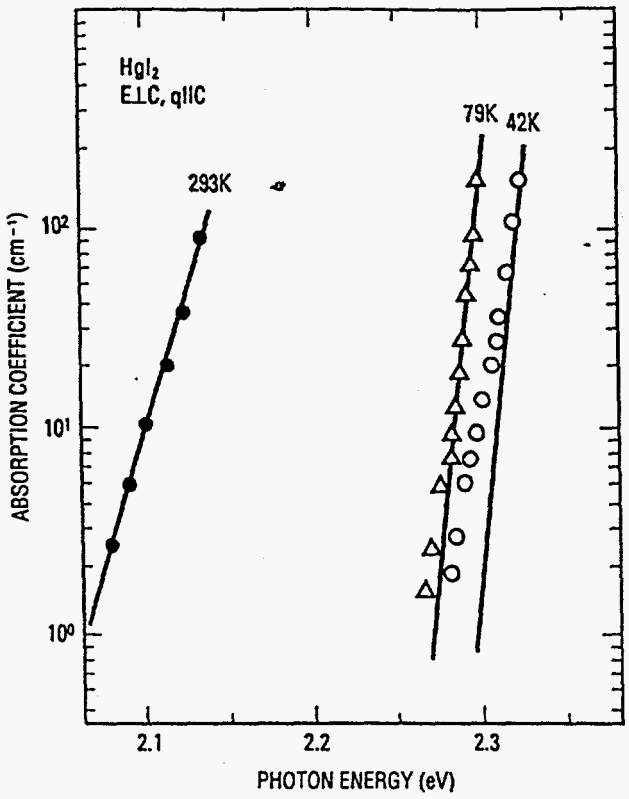

FIG. 22. Absorption spectra of HgI_2 single crystals in the tail part of the fundamental absorption edge. (Reprinted with permission from Kanzaki and Imai, 1972 and the Physical Society of Japan.)

Figure 22 shows data by Kanzaki and Imai (1972) on polycrystalline samples for the absorption coefficient on the low energy side of the fundamental bandgap at temperatures of 4.2, 79, and 293 K. Since the absorption coefficient has approximately an exponential dependence on the incident photon energy, the spectrum of HgI_2 is well described by Urbach rule (Urbach, 1953). At lower temperatures the deviations from Urbach rule are larger, which may be due to the excitonic effects (Novikov and Pimonenko, 1971). In addition, there may be increased contributions at lower temperatures from photoionization of carriers bound to impurities. As pointed out by Chester and Coleman, internal electric fields may be present in HgI_2, which can produce an internal Franz–Keldysh shift and lead to a larger tail in the absorption coefficient (Redfield, 1965).

The refractive index for ordinary absorption (i.e., $\mathbf{E} \perp \mathbf{c}$) for photon energies less than the bandgap is shown in Fig. 23. For even longer wavelengths, the material becomes much more transparent and thicker crystals are preferred for transmission measurements. Photoconductivity measurements have been performed on palladium contacted HgI_2 detectors, and an absorption peak was observed at about 9373 Å (Bao, 1991). This peak was attributed to photoionization of an electron or hole carrier bound to an impurity. Since mercuric iodide crystals do not naturally contain palladium (Soria *et al.*, 1994) and this peak was not seen on detectors with

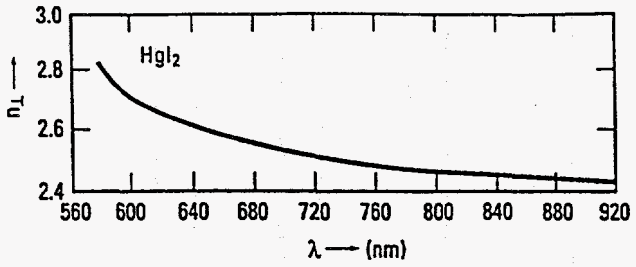

FIG. 23. The refractive index for ordinary absorption (i.e., $E \perp c$) for photon energies less than the bandgap. (Reproduced with permission from Seiskind, 1960.)

contacts other than Pd, it was believed due to Pd impurities. If this belief is indeed correct, it indicates that Pd either diffuses into HgI_2 during detector processing or aging or that Pd can migrate into the bulk due to the influence of an applied bias. Since Pd is the contact material of choice for most HgI_2 detector applications, the presence of diffusion or electrodrift phenomenon of Pd into HgI_2 is the subject of further investigation. Moreover, the movement of carrier traps not limited to Pd related defects in the material can lead to polarization effects, which are detrimental to device performance. Recent optical and electrical measurements have revealed that some elements (e.g., Cu and Ag) do indeed move under the application of an electric field (James *et al.*, 1993; Van Scyoc *et al.*, 1993).

For infrared wavelengths, most of the absorption is associated with impurities, although lattice absorption is significant for photon energies in the restralen region. For photon energies greater than the restralen region, two possible mechanisms for infrared absorption are the excitation of vibrational modes associated with contaminants and excitation of free carriers in the material. Several absorption bands associated with the presence of impurities have been observed in transmission infrared spectra experiments (James *et al.*, 1989a) (see Fig. 24). The strength of the absorption in these bands varies between samples due to differences in the amounts of impurities contained in the crystals. Attempts by James *et al.* (1989a) to identify the impurities associated with the absorption have been partly successful. For example, some specimens displayed a narrow absorption peak at about 1600 cm^{-1}, which corresponds to the measured energy for absorption by the H-O-H bending mode of water (Nyquist and Kagel, 1971). The absorption measured at about 2850, 2915, and 2970 cm^{-1} is due to the presence of aliphatic hydrocarbons in the bulk material. A broad absorption band peaked at about 3240 cm^{-1} was also detected by James *et al.* (1989a) and attributed to presence of free water or a water of hydration. Since HgI_2 has not been shown previously to form a hydrate, the water is probably bonded to a contaminant. Both calcium and sodium iodate are possible choices because they have infrared absorption spectra that resemble the measured results of James *et al.* (1989a) and Ca and Na are present in the HgI_2 crystals in the 1–10 ppm range (Schieber, Roth, and Schnepple, 1983; Soria, Natarajan, and James, 1994). Another absorption band observed by James *et al.* (1989a) was peaked at about 3500 cm^{-} . Since

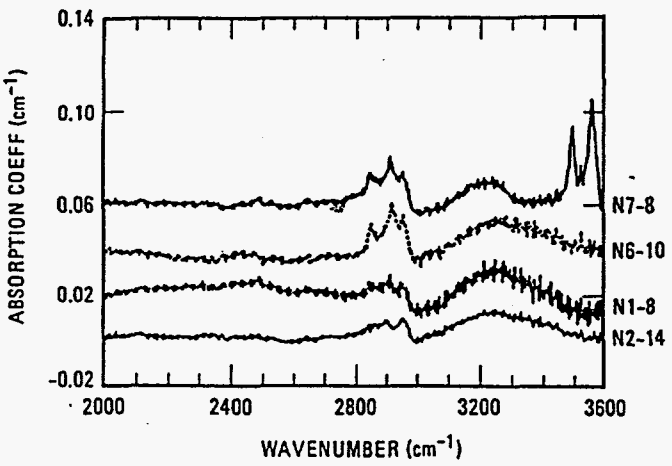

FIG. 24. FTIR spectra of four HgI_2 samples in the 2000–3600 cm^{-1} range. (Reprinted with p mission from James *et al.*, 1989a and Elsevier Science Publishers.)

strong absorption associated with the OH stretching vibrations of water and t hydroxyl group occur between 3200 and 3700 cm^{-1} (Nyquist and Kagel, 197 it was concluded by James *et al.* that the mercuric iodide samples studied in th work contained a significant amount of both oxygen and hydrogen and that mu of the oxygen and hydrogen was chemically bonded as H_2O and possibly OH. F excitation in the 600–900 cm^{-1} range, several weak narrow absorption ban were detected by James *et al.* (1989). The mostly likely candidates for these we absorption bands included mercurous iodide, calcium iodate, sodium iodate, a compounds containing a carbonate anion (Schieber *et al.*, 1983; Nyquist a Kagel, 1971).

The contribution from free carriers depends on the carrier density, and sin undoped HgI_2 is an insulating material, negligible free-carrier absorption is e pected. Furthermore, few impurities have been demonstrated to be electrical active in the material. However, it was recently shown that Cu and Ag dopants a electrically active in HgI_2 (Bao *et al.*, 1990a; James *et al.*, 1993). At present, i infrared transmission measurements have been reported on Cu- or Ag doped HgI and the role of free-carrier absorption has not been determined. It is also possib that the large increase in the conductivity of Cu and Ag doped HgI_2 is due to ion conduction instead of Cu or Ag acted as an electrically active substitutional in purity. Since many electron and ion probe diagnostic techniques demonstra charging problems on insulating materials like HgI_2, further investigations c HgI_2 crystals that have been intentionally doped with Cu or Ag (to greatly low the sample resistivity) are expected in the near future.

5. PHONON STRUCTURE OF RED MERCURIC IODIDE

The vibrational frequencies of the transverse and longitudinal modes of Hg have been obtained from the polarized far-infrared reflection spectrum (Prevc

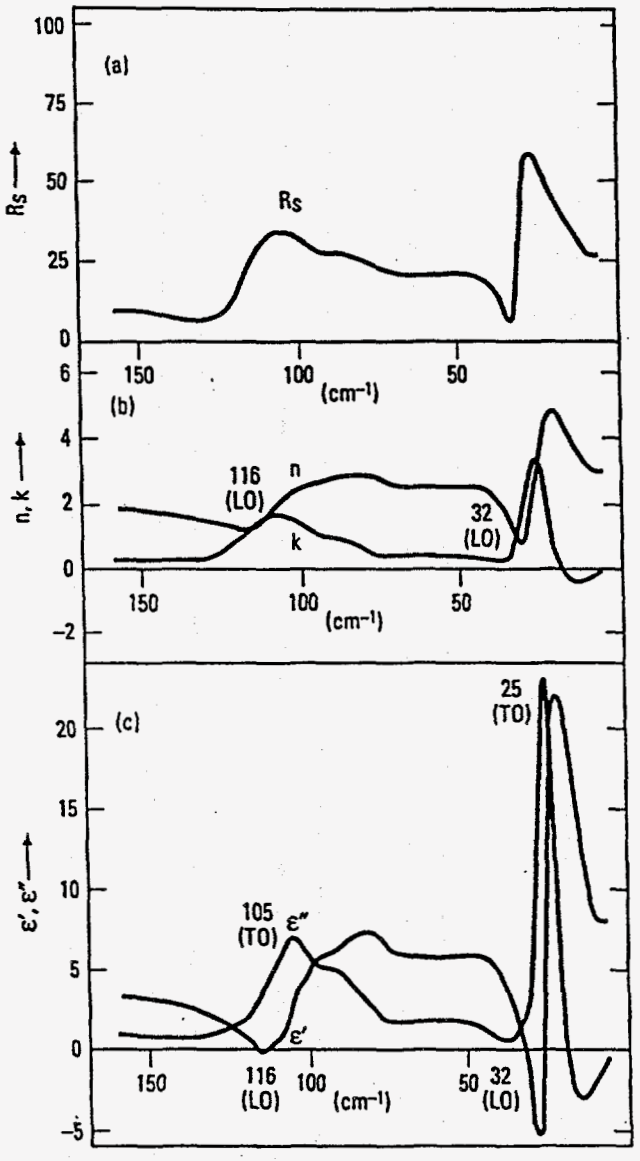

FIG. 25. Reflectivity and the optical and dielectric constants. (Reprinted from Y. Ogawa *et al.*, *Spectrochimica Acta* **32A**, 49 ©1976 with kind permission from Elsevier Science Ltd., The Boulevard, Langford Lane, Kidlington, OX5 1GB.)

Schwab, and Dorner, 1978). Figure 25 shows the reflectivity and the optical and dielectric constants as measured by Mikawa, Jacobsen, and Brasch, (1966). The reflectivity R_s was measured for light polarized perpendicular to the c-axis. The incidence angle was fixed at 20° in the experiment. The refractive index n, the absorption coefficient κ, and the real and imaginary parts of the complex dielectric constant, ϵ' and ϵ'', were obtained according to the model given by Roessler (1965, 1966) and Nakagawa (1971).

Raman measurements have also been conducted to measure the energies of the LO_1, LO_2, and LO_3 longitudinal optical phonon energies near the zone center (Nakashima, Mishima, and Mitsuishi, 1973; Adams and Hooper, 1970; Haisler

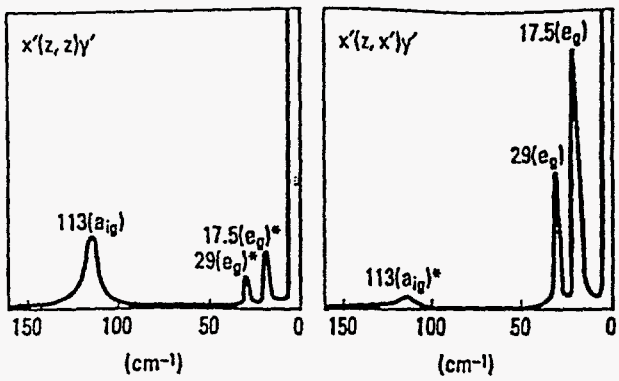

FIG. 26. The polarized Raman spectra. The experimental axes x' and y' are related to the crysta x- and y-axes by a 45° rotation about z(c). The appearance of the bands with asterisks is ascribed tc imperfections in the crystal. (Reprinted from Y. Ogawa *et al., Spectrochimica Acta* 32A, 49 ©197(with kind permission from Elsevier Science Ltd., The Boulevard, Langford Lane, Kidlington, OX5 1GB.)

et al., 1984; Prevot and Biellmann, 1979). Strong Raman bands are observed by several investigators at 17.5, 29, and 113 cm^{-1} (see Fig. 26, Ogawa *et al.*, 1976). Weaker bands were also reported by Melveger *et al.* (1968) at 46, 142 and 246 cm^{-1}. Further discussions on the assignments for the Raman bands are contained in Biellmann and Prevot (1980) and the references noted therein.

Phonons with a nonnegligible wave vector **q** can also participate in radiative transitions, such as excitation and photoluminescence. For indirect bandgap materials, phonon participation is typically required to conserve crystal momentum for photon energies near the bandgap. Radiative recombination can result in either the creation or destruction of a phonon, although phonon absorption can be usually ignored for measurements conducted at low temperatures. The energy of the photon emitted by a radiative transition that involves one or more phonons will be altered from the "no phonon" energy by the amount of energy corresponding to the phonon(s).

The lower section of Fig. 27 shows phonon dispersion curves of HgI_2 at room temperature (Prevot *et al.*, 1978). The full (open) symbols show acoustic (optic) vibrations either in transverse (squares) or longitudinal (circles) geometries for polarizations within the layer plane. The triangles in the figure refer to modes with polarization parallel to the principal axis. The upper section of Fig. 27 shows calculations of the phonon modes using a rigid ion model (Sim, Chang, and James, 1994). Additional phonon dispersion curves are predicted by Sim *et al.* (1994) that were not measured by Prevot *et al.* (1978). The absence of these curves in the experimental measurements has been explained based on the crystal symmetry of HgI_2. Higher energy phonon dispersion curves, along with values for the sound velocities and frequencies of infrared active modes have been predicted, and they are in accord with available experimental data (Sim *et al.*, 1994). Further discussions of the angular dispersion of the phonon frequencies and the infrared active modes can be found in the paper by Sim *et al.* (1994).

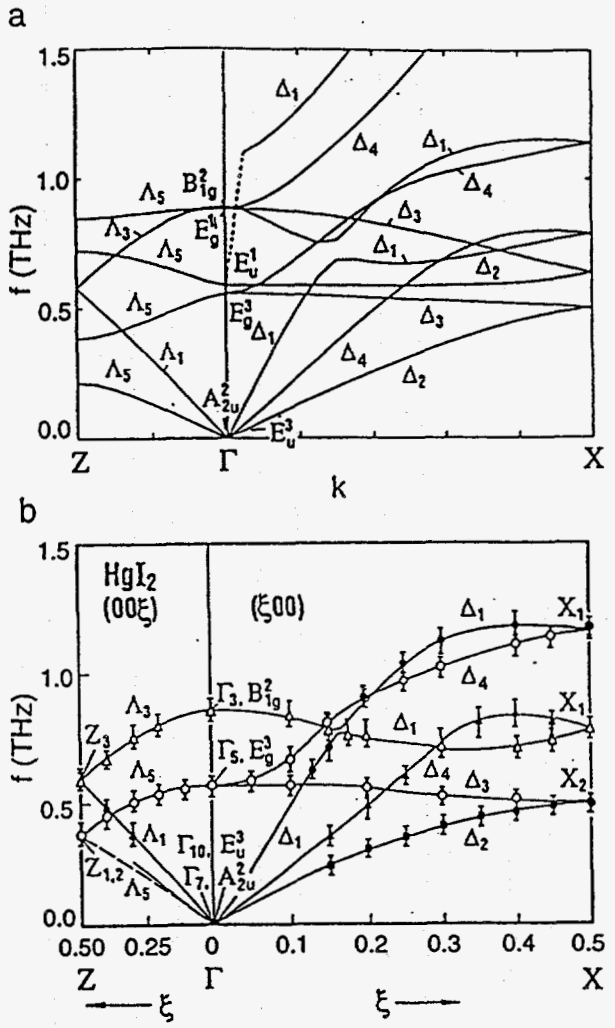

FIG. 27. Low energy phonon dispersion curves measured in red HgI_2 at room temperature. The full (open) symbols show acoustic (optic) vibrations either in transverse (squares) or longitudinal (circles) geometries for polarizations within the layer plane. The triangles in the figure refer to modes with polarization parallel to the principal axis. (From Prevot *et al.*, reprinted with permission by VCH Publishers ©1978.)

6. RADIATIVE RECOMBINATION OF NONEQUILIBRIUM ELECTRON–HOLE PAIRS

Excitation of mercuric iodide detectors by above band gap excitation leads to the creation of nonequilibrium electron–hole pairs. These photogenerated carriers move under the influence of the applied bias and are scattered by phonons, impurities, native defects, and dislocations. At zero bias and open circuit conditions, the electrons and holes eventually recombine to establish equilibrium. The recombination can be divided into three primary categories: (1) direct recombination in the bulk material, (2) recombination by way of traps, and (3) surface recombination. For direct recombination a free electron in the conduction band recombines

with a hole state in the valence band in a single transition. Energy conservation considerations requires that an amount of energy be given up that corresponds to the energy difference between the conduction and valence band states. One mechanism for disposing of this excess energy is by emission of radiation. In some cases the emitted radiation will involve the creation or annihilation of one or more phonons.

Prior to recombination, a free electron and hole can first be bound together by their electrostatic attraction to form an exciton. All excitons are unstable against a recombination process in which the electron drops into the hole. This process often involves the emission of radiation at an energy slightly less than the bandgap of the material, because the formation of excitons leads to a lowering of energy by an amount corresponding to the binding energy of the exciton. Free excitons are electrically neutral and move through the crystal transporting their excitation energy. At low temperatures free excitons in HgI_2 are trapped at a rate that exceeds the free exciton lifetime. This trapping further lowers the excitation energy of the excitons by an amount equal to the binding energy of the free exciton to its trapping sites. These trapping sites can be impurities, stoichiometric deviations, and extended defects. By monitoring the energy of the emitted recombination luminescence, one can determine information on the energy levels of the electrons, holes, free excitons, and bound excitons involved in the recombination process. Free and bound exciton luminescence are often in the form of sharp lines that are clearly separated in energy from the continuous band to band radiation and from other excitonic lines. Since the information gained on bound–exciton recombination assists in constructing an energy level diagram of the dominant traps, photoluminescence is a particular useful technique in characterizing defects in HgI_2 crystals. The exciton lifetimes in HgI_2 can also be studied by measuring the rate of decay of the emitted photoluminescence with fast exciting pulses (Williams, Anderson, and Banet, 1991).

Another recombination mechanism involves an electron that combines with a hole in the valence band in a two step process, which may be separated by a relatively long amount of time. Here, an electron can become captured by a deep trap; and some time later, a hole is influenced by the potential of this occupied electron trap. The trap can also capture the hole leading to the eventual recombination of the two carriers. This type of process can be more probable than a single step one, because the probability of a radiative recombination process increases greatly as the radiated energy is decreased.

The third area for recombination mentioned previously also involves traps, but in this case, the traps are located in the near-surface region of the crystal or detector. In this case, electrons and holes generated in the bulk of the material diffuse to the surface. The recombination rate depends on the quality of the surface, and it is often much larger than the recombination rate in the bulk. In some cases surface recombination may dominate and thereby reduce the advantages associated with long carrier lifetimes in bulk material.

Recombination at surfaces often involves only phonons to conserve energy, in

which case no radiation is emitted. This process has been shown to be important in mercuric iodide crystals and devices (Levi *et al.*, 1983, 1985), although the precise mechanism for recombination (multiphonon or Auger) has not been conclusively determined. It has been shown that the techniques employed for treating HgI_2 surfaces have an important influence on defects at the surface (David *et al.*, 1993), on leakage currents (Jayatirtha *et al.*, 1993), and on the rate of surface recombination (Levi *et al.*, 1983).

Photoluminescence and cathodoluminescence spectroscopy has been extensively used to study the radiative recombination of HgI_2 crystals and detectors (Novikov and Pimonenko, 1971, 1972; Merz *et al.*, 1983; Akopyan *et al.*, 1987; Bao *et al.*, 1990a, b, c; James *et al.*, 1989b; Petroff, Hu, and Milstein, 1989). Although the origin and nature of some of the emission lines have been identified, a complete description of all of the photoluminescence features is yet to emerge. Several reasons explain the difficulties in identifying each defect manifested in the photoluminescence spectrum. First, the absorption of electromagnetic waves in HgI_2 depends on the geometric relationship between the direction of the light polarization, the wave vector of the incident wave, and the c-axis of the crystal. Thus, the light penetrates to different depths in the material, depending on the geometrical configuration of the experiment. The reabsorption of the emitted photons depends on their wavelengths, so the relative intensities of the photoluminescence peaks will change as the depth of penetration of the exciting beam changes. Second, the crystals used in various studies were grown using different purification procedures and growth techniques, and the crystals contained different levels of impurities and deviations from stoichiometry. Third, handling practices have a significant effect on the dominant recombination centers, because HgI_2 is soft, highly reactive, sensitive to temperature changes, and has a high vapor pressure. It also develops a degraded surface layer for samples stored in air over a period of a few days, and this aged layer is different from a freshly etched HgI_2 surface. Fourth, HgI_2 is difficult to systematically dope with impurities, and efforts to intentionally dope a crystal during growth often lead to other changes in the sample, such as deviations from stoichiometry. Finally, the photoluminescence spectrum of HgI_2 at energies near the fundamental band edge consists of many sharp spectral lines that are spaced close together and often difficult to resolve. These lines vary in intensity due to differences in crystalline perfection and surface conditions. Confusion arises when comparing reported values for peak positions and relative magnitudes by different groups of investigators, especially when these groups also have different spectral resolutions for their experimental setups.

The remainder of this section focuses on measurements of the radiative recombination in HgI_2 crystals and the effects of the electrical contacts on the incorporation of new carrier traps. Bube (1957) reported the first low temperature photoluminescence spectrum of HgI_2, and three emission bands with peaks located at 5360, 5675, and 6200 Å were reported at 77 K. These bands were labeled 1, 2, and 3, respectively. By cooling the crystal to 4.2 K, Novikov and Pimonenko (1971) found that the band at 5360 Å observed by Bube actually consisted of

many narrow lines. All of the lines reported in by Novikov and Pimonenko (1971 were assigned as free or bound exciton emissions and their phonon replicas. Mer *et al.* (1983) reported similar results for the photoluminescence spectrum, but wit different assignment to a few lines. As more data became available and the qualit of the crystals continued to improve, Wong *et al.* (1988a) pointed out that som of the emission lines assigned earlier as phonon replicas did not have the correc peak positions. Goto and Nishina (1978) was the first to observe several weal steplike emissions between 5230 and 5290 Å, which they designated phonon as sisted indirect recombination of free electron–hole pairs. Akopyan *et al.* (1975) carefully studied many properties of the first three exciton lines, including thei polarization and changes under the influence of magnetic field and uniaxial stress.

The highest resolution photoluminescence spectrum existing today on undoped HgI_2 was obtained by Bao *et al.* (1990b). Although their experiments were conducted with relatively high instrument resolution, the primary reason that more emission peaks were resolved by Bao *et al.* (1990b) is probably due to additional improvements in the crystalline purity and quality, thus allowing the dominant peaks to be much narrower in energy and the relatively weaker peaks nearby in energy to be more clearly resolved from the background. Figure 28 shows the 4.2 K photoluminescence for photon energies near the fundamental bandgap. Bao *et al.* (1990b) found that many lines previously reported as singlets were actually composed of more than one line, which explained some of the earlier inconsistencies in peak positions. A total of 26 photoluminescence lines were reported between 5290 and 5400 Å, and several lines were observed for the first time. Some of the peaks are not well resolved in Fig. 28, but were much more clearly resolved

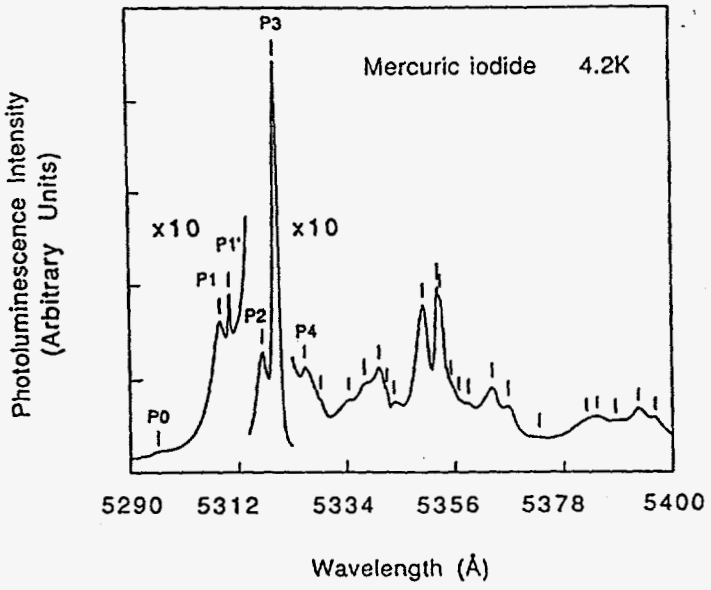

FIG. 28. A 4.2 K near-band edge photoluminescence spectrum of HgI_2 between 5290 and 5400 Å. Vertical bars indicate the positions of the emission lines. The spectral resolution of the spectrometer was 0.35 Å. (Reproduced with permission from Bao *et al.*, 1990b and the American Institute of Physics.)

TABLE V

WAVELENGTHS AND PHOTON ENERGIES OF BAND EDGE PHOTOLUMINESCENCE PEAKS OF HgI_2 BETWEEN 5290 AND 5400 Å

4.2 K[a]			4.2 K[b]		1.6 K[c]	
Wavelength (Å)	Energy (eV)	Notation	Energy (eV)	Notation	Energy (eV)	Notation
5296.9	2.3400	$P0$	2.340	λ_0	2.3402	1A*
5309.1	2.3347	$P1$	2.335	λ_1	2.3349	1A
5311.2	2.3337	$P1'$			2.3332	
5317.9	2.3308	$P2$	2.331	λ_x	2.3300	1B
5320.8	2.3296	$P3$	2.329	λ_2	2.3286	1C
5326.4	2.3271	$P4$	2.326	λ_0-LO	2.3262	1A*-LO
5329.6	2.3257					
5335.3	2.3232		2.323	λ_0-LO-TO		
5338.8	2.3217				2.3214	1A-LO
5341.6	2.3205					
5343.3	2.3197				2.3198	
5344.7	2.3191		2.319	λ_1-LO		
5350.8	2.3165		2.317	λ_x-LO	2.3162	1B-LO
5353.5	2.3153					
5354.1	2.3150		2.315	λ_2-LO		
5356.3	2.3141				2.3144	1C-LO
5358.4	2.3132					
5359.8	2.3126		2.313	λ_0-2LO	2.3120	1A*-2LO
5364.5	2.3106		2.310	λ_0-2LO-TO	2.3105	1A-2LO
5367.8	2.3092		2.308	λ_1-2LO	2.3083	
5374.2	2.3064					
5383.5	2.3024		2.303	λ_2-2LO	2.3022	1B-2LO
5383.3	2.3016				2.3012	1C-2LO
5390.1	2.2997					
5394.1	2.2979		2.298	λ_0-3LO	2.3977	1A*-3LO
5397.3	2.2966		2.296	λ_0-3LO-TO	2.2959	1A*-3LO-TO

Reproduced with permission from Bao *et al.*, 1990 and the American Institute of Physics.
[a] Bao *et al.*, 1990b
[b] Novikov and Pimenko, 1971
[c] J. L. Merz *et al.*, 1983

in other spectra. Table V lists these 26 peaks along with their wavelengths and photon energies. Peaks and their assignments reported by Novikov and Pimonenko (1971) and Merz *et al.* (1983) are shown for comparison.

The first five lines shown in Fig. 28 with wavelengths of 5296.9, 5309.1, 5311.2, 5317.9, and 5320.8 Å (labeled $P0$, $P1$, $P1'$, $P2$, and $P3$) are generally accepted to be free or bound exciton emission lines, although there is some uncertainty on the exact assignments (Bao *et al.*, 1990b). Table VI shows the FWHM of these five lines (Bao *et al.*, 1990b), along with their observations in the ordinary and extraordinary absorption and emission spectra (Novikov and Pimonenko, 1971; Akopyan *et al.*, 1975; Tubbs, 1972). From the table one finds that the lines

TABLE VI

OBSERVATIONS OF THE FIRST FIVE LINES BETWEEN 5290 AND 5400 Å IN THE ORDINARY (E⊥c) AND EXTRAORDINARY (E∥c ABSORPTION AND EMISSION SPECTRA WITH THEIR FWHM AS MEASURED IN THE 4.2 K EMISSION SPECTRA FROM THIS WORK

Lines[a] (4.2 K)		5296.9 Å *P*0	5309.1 Å *P*1	5311.2 Å *P*1′	5317.9 Å *P*2	53
Absorption (4.2 K)	E⊥c		Continuous, strong absorption[c,d]			
	E∥c	5297 Å[b,d]		5310 Å[c,d]		532
Emission (4.2 K)	E⊥c		5308 Å[b,c]	5318 Å[b]		
	E∥c	5297 Å[c]			5320 Å[b]	
FWHM (4.2 K)		0.88 meV	1.6 meV	0.19 meV	1.3 meV	0.6

Reproduced with permission from Bao *et al.*, 1990b and the American Institute of Physics.
[a]Bao *et al.*, 1990b
[b]Tubbs, 1972
[c]Akopyan *et al.*, 1975
[d]Novikov and Pimenko, 1971

at 5296.1 (*P*0), 5311.2 (*P*1′), and 5320.8 Å (*P*3) can be grouped together because each has relatively narrow line widths and they appear as well resolved peaks in both the emission and absorption spectra (E∥c). In addition, the relative intensity of the line at 5320.8 Å (*P*3) follows closely the line at 5311.2 Å (*P*1′), suggesting that the origin of the two lines is the same or strongly correlated. On the other hand, the lines at 5309.1 Å (*P*1) and 5317.9 Å (*P*2) fall into a separate group, in which they both appear in the ordinary emission (E⊥c) spectra while the ordinary absorption spectra show only a continuum. Furthermore, the two lines have distinctly larger FWHMs than lines *P*0, *P*1′, and *P*3. It has also been clearly demonstrated that the intensity of the line at 5317.9 Å (*P*2) follows the intensity of the line at 5309.1 Å (*P*1), which further supports the idea of a relationship between the two lines. The energy difference between *P*2 and *P*1 is approximately equal to the LO_2 phonon at 3.9 meV, although *P*2 has not been previously reported as a phonon replica of *P*1.

Akopyan and co-workers (1975) concluded that *P*0 is due a longitudinal free exciton transition, *P*1 is associated with a transverse free exciton transition, and *P*1′ is due to a spin forbidden free exciton transition (i.e., electron and hole spin in the same direction). The longitudinal–transverse exciton splitting would then be given by the difference in energy between the peaks of *P*0 and *P*1, which is approximately equal to 5.3 meV. Akoypan and co-workers (1975) conclude that continuum absorption is observed in the E⊥c configuration because the absorption is too strong to observe the weaker excitonic effects. Since the absorption is much less in the E∥c configuration, Akoypan *et al.* (1975) argue that the *P*0 resonant excitation can be observed. A pure longitudinal exciton cannot be excited by an electromagnetic wave, so it is speculated that *P*0 is due to the interaction of the

transverse exciton with the incident electromagnetic wave to form a polariton he crystal. If these assignments of $P0$, $P1$, and $P1'$ are correct, it is likely that is related to a transverse exciton and $P3$ to a longitudinal exciton. The temature dependence of the $P2$ and $P3$ emissions suggests that they are bound :iton emissions, in which case it can be postulated that $P2$ is a transverse bound :iton transition and $P3$ is a longitudinal bound exciton. Further discussions of bound excitons $P2$ and $P3$ will be presented later in this section.

The peaks on the long wavelength side (i.e., between 5321 and 5400 Å) will w be discussed. The three dominant optical phonons in the Raman spectra have ıe center phonon energies of 2.3, 3.9, and 14.3 meV. Novikov and Pimonenko)71) and Merz *et al.* (1983) have attributed the rest of the lines on the long velength side of $P3$ as phonon replicas of 2.3 and 14.3 meV phonons. No onon replicas have been assigned to the 3.9 meV. Wong *et al.* (1988a) argued ıt some of the lines identified as phonon replicas cannot be so, because the ergy separation from their no phonon parent line was not quite correct. Bao *al.* (1990b) later explained much of the discrepancy between different authors garding the peak positions of several photoluminescence emissions. Bao *et al.*)90b) showed that many of emission lines that were previously assumed to singlets were actually composite lines. Moreover, many of the other photoninescence peaks reported by Bao *et al.* (1990b) had asymmetric shapes sugsting that they too had multiline compositions.

Several difficulties are encountered when one tries to assign numerous lines to citon emissions and their phonon replicas. First, if only the 2.3 and 14.3 meV onons are used in assigning phonon replicas, many lines simply cannot be exained because their peak positions do not correspond to a combination of zone nter phonons. Second, if the phonon at 3.9 meV is also included, the assignents become somewhat arbitrary because many of the emission lines are closely aced, and they could be assigned to either different parent lines or different mbinations of emitted phonons. In theory, the ratio between the different bound :citon lines and their phonon replicas should be constant, so that measurements the relative intensities should be helpful in organizing all of the lines into oups and thus lead to their identification as phonon replicas. However, in prac:e, one observes that the bound exciton emissions vary in intensity from sample sample due to different concentrations of impurities or defects to which the :citons are bound. Moreover, the potential list of phonon replicas are so closely ıaced that there is significant overlap between adjacent emissions, which makes impossible to precisely determine the relative intensities of most of the photominescence peaks. Given these difficulties, assignment of most of the weaker nissions as phonon replicas is highly speculative. Nonetheless, there appears to general agreement in the literature that the intensities of the lines at 5350.8 and 353.5 Å (see Table V) follow closely in intensity the lines at 5317.9 ($P2$) and 320.8 Å ($P3$), respectively. In addition, the two sets of peaks differ from each ther by 14.3 meV, which corresponds to the LO_3 optical phonon energy. The vidence seems convincing that the lines at 5350.8 and 5353.5 Å are indeed the rst LO_3 phonon replica of the lines at 5317.9 ($P2$) and 5320.8 Å ($P3$).

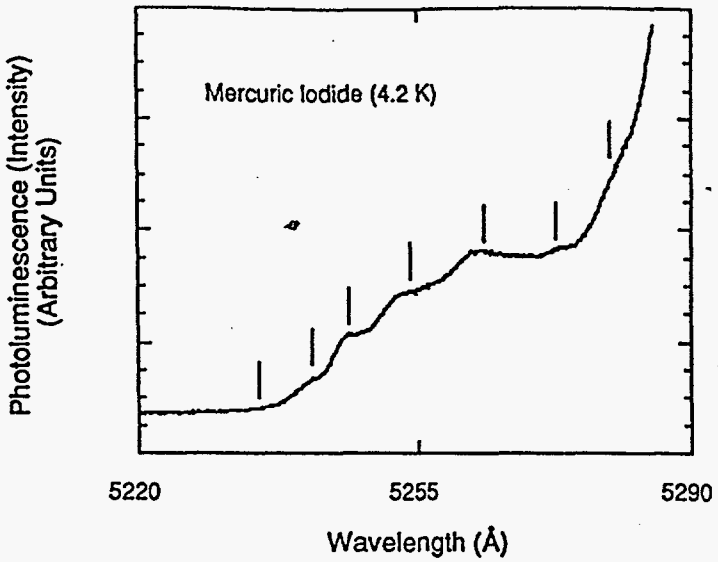

FIG. 29. A 4.2 K near-band edge photoluminescence spectrum of HgI_2 between 5220 and 5290 Å. Vertical bars indicate the positions of the emission lines. The spectral resolution of the spectrometer was 2.0 Å. (Reproduced with permission from Bao *et al.*, 1990b and the American Institute of Physics.)

7. PHONON–ASSISTED ELECTRON–HOLE PAIR PHOTOLUMINESCENCE

Figure 29 shows a typical 4.2 K spectrum at wavelengths between 5220 and 5290 Å. These lines are usually about three orders of magnitude weaker in intensity than the emission lines between 5290 and 5400 Å discussed earlier. They have been attributed to phonon assisted indirect radiative recombination of free electron–hole pairs. The peak positions were first measured by Goto and Nishina (1978) and later by Bao and co-workers (1990b). Table VII shows the measured peak position by the two groups of investigators. It is obvious that there is considerable difference between the peak positions reported. Bao and co-workers (1990b) observe two more peaks on the longer wavelength side, and Goto and Nishina (1978) report two more peaks on the shorter wavelength side. Part of the difficulty in assigning peak positions results from the weak intensities and stepwise nature of these lines, which makes it very difficult to determine the peak positions to better than about 1 Å.

8. EFFECTS OF GEOMETRICAL CONFIGURATION ON PHOTOLUMINESCENCE SPECTRA

Although most photoluminescence measurements on HgI_2 have been conducted in a reflection mode, one measurement has been made in which the laser beam excited the back side of the slab and the luminescence was collected from the front surface in a direction parallel to the normal (Bao *et al.*, 1990c). Figure 30

TABLE VII

WAVELENGTHS AND PHOTON ENERGIES OF BAND EDGE PHOTOLUMINESCENCE PEAKS OF HgI_2 BETWEEN 5220 AND 5290 Å

Wavelength (Å)[a] 4.2 K	Energy (eV)	Energy (eV)[b] 4.2 K	Notation
		2.3707	E_g
5235.0	2.3677	2.3684	$-LO_1$
		2.3662	$-2LO_1$
5241.5	2.3648	2.3639	$-3LO_1$
5246.4	2.3626	2.3614	$-4LO_1$
5253.0	2.3596	2.3589	$-5LO_1$
5263.1	2.3551	2.3562	$-LO_3$
5273.3	2.3505		
5280.7	2.3472		

Reproduced with permission from Bao *et al.*, 1990b and the American Institute of Physics.

[a] Bao *et al.*, 1990b

[b] Goto and Nishina, 1978

shows 4.2 K PL spectra taken in the reflection and transmission modes for a slice with the c-axis perpendicular to the normal of the sample. Comparisons between the spectra reveal that $P0$, $P1$, $P1'$ and $P3$ are almost completely reabsorbed for spectra taken in the transmission mode. This observation is consistent with absorption measurements.

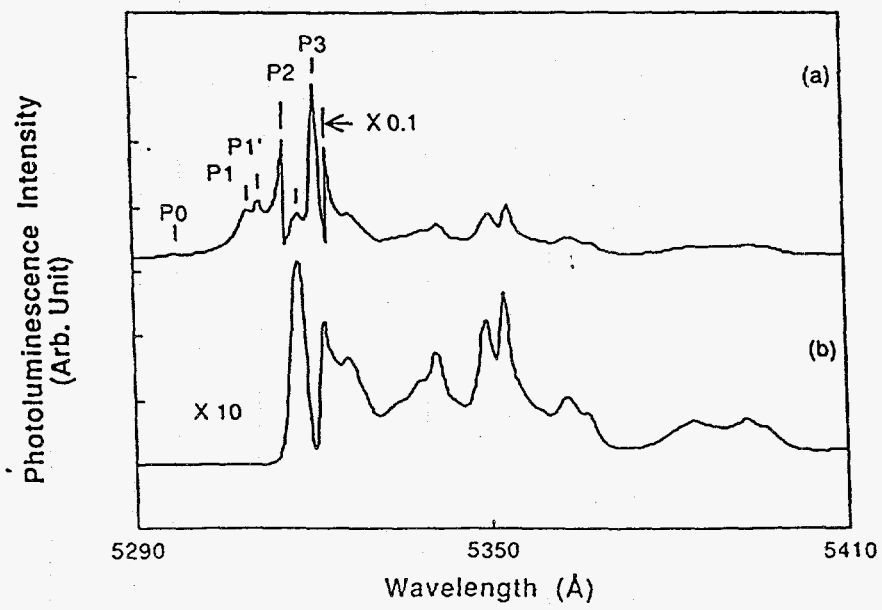

FIG. 30. 4.2 K photoluminescence spectra obtained in (a) reflection and (b) transmission modes. (Reproduced with permission from Bao *et al.*, 1990c and the American Institute of Physics.)

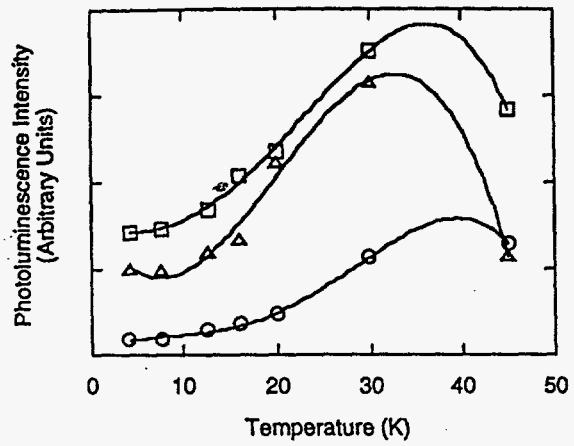

FIG. 31. Photoluminescence intensities of $P0$, $P1$, and $P5338.8$ as a function of temperature (from Bao, 1991). -⊖-, $P0$; -⊟-, $P1$; -△-, $P5338.8$.

9. TEMPERATURE DEPENDENCE OF THE PHOTOLUMINESCENCE SPECTRUM

The temperature dependence of photoluminescence spectrum may provide clues for the identification of spectral lines in addition to bandgap shift with temperature (see the previous subsections). The temperature behaviors of the first several photoluminescence lines were studied by several investigators (Novikov and Pimonenko, 1972; Merz *et al.*, 1983; Bao, 1991). It was found that the intensities of $P0$ and $P1$ increase with temperature below about 30 K (Bao, 1991; Novikov and Pimonenko, 1972; Merz *et al.*, 1983). Above 30 K, the intensities of $P0$ and $P1$ start to decrease with temperature. The intensities of $P0$ and $P1$ as a function of temperature are shown in Figure 31. This temperature behavior of $P0$ and $P1$ leads to their assignments as free exciton lines, which is consistent with discussions in the previous subsections on the origin of these emission lines. The intensities of $P2$ and $P3$, on the other hand, decrease with temperature, and their thermal activation energies can be obtained from the temperature dependence. Since these lines were believed due to bound excitons, the thermal activation energies were then the binding energies of these bound excitons. The measured thermal activation energies for $P2$ and $P3$ are tabulated in Table VIII. The peak positions of $P2$ and $P3$ relative to $P1$ and $P0$ are also listed. These measurements seem to agree with the assignment of these lines as discussed in the previous sections.

Figure 32 shows the temperature dependence of the three commonly observed broad photoluminescence bands label $B2$ (5595 Å), $B3$ (6200 Å), and $B4$ (7550 Å) (Merz *et al.*, 1983; Bao *et al.*, 1990a; Bao, 1991). The intensity of $B2$ decreases with temperature. The intensities of $B3$ and $B4$ increase with temperature below about 50 K and decrease above 50 K. The behavior of $B3$ and $B4$ has yet to be explained. More discussion on these bands will be provided in the next section on processing of HgI_2 detectors.

TABLE VIII

SUMMARY OF THERMAL ACTIVATION ENERGIES FOR $P2$ AND $P3$ BY DIFFERENT WORKERS (Novikov and Pimonenko, 1972; Merz *et al.*, 1983; Akopyan *et al.*, 1987; Bao, 1991)

Peak	E_T (meV)[a]	E_T (meV)[b]	E_T (meV)[c]	E_T (meV)[d]	Peak Position
$P2$	4.9	4		2.4	$P1$, 3.9 meV
$P3$	9.3	6	12	11.4	$P0$, 10.4 meV

[a] Bao, 1991
[b] Akopyan *et al.*, 1987
[c] Novikov and Pimenko, 1972
[d] Merz *et al.*, 1983

IV. Study of Processing by Photoluminescence Spectroscopy

1. PURIFICATION AND STOICHIOMETRY

Using low temperature photoluminescence spectroscopy, Merz *et al.* (1983) first studied the processes commonly employed to purify raw materials for vapor phase crystal growth. These processes include open tube sublimation, closed tube sublimation, and melting (Merz *et al.*, 1983). Figure 33 shows the effect of sublimation on the 77 K photoluminescence spectra of HgI_2 powders (Merz *et al.*, 1983). It can be seen that the intensity of band 2 relative to band 1 increases with each sublimation run. Band 3 practically disappeared after the first sublimation run. Chemical analyses show that the sublimation process significantly reduces the concentration of impurities in HgI_2, indicating that Band 3 is probably associated with impurities (Soria *et al.*, 1994). It is also suspected that sublimation reduces the iodine concentration by preferential removal of the more volatile species, which suggests that the band 2 to band 1 ratio is an indicator of the relative

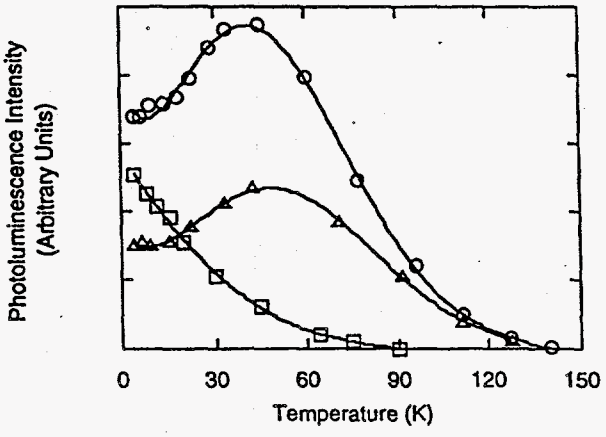

FIG. 32. Photoluminescence intensities of bands 2 (-⊟-), 3 (-⊖-), and 4 (-△-) as a function of temperature (from Bao, 1991).

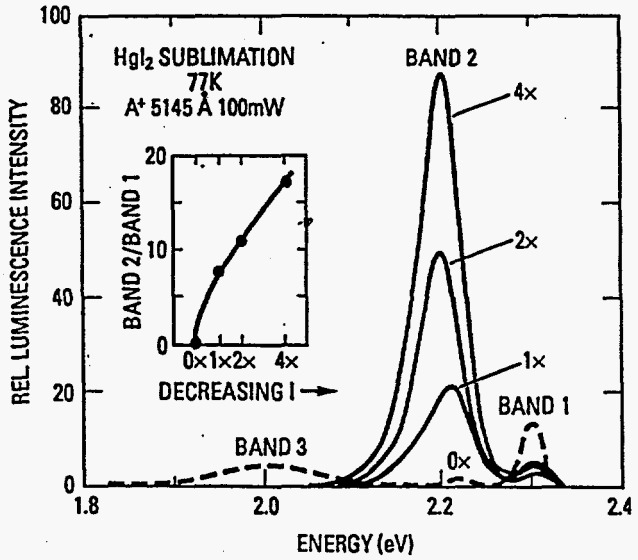

FIG. 33. Photoluminescence spectra of HgI_2 powder at 77 K, after various sublimation steps. The designations $N\times$ ($N = 0, \ldots, 4$) refer to the number of times the powder is passed along the sublimation tube. The inset shows the intensity ratio of band 2/band 1 for successive sublimation runs, using an arbitrary scale along the horizontal axis. (Reprinted with permission from Merz *et al.*, 1983 and Elsevier Science Publishers.)

concentration of iodine in the material. Subsequent doping experiments with iodine or mercury appear to agree with the hypothesis (Bao *et al.*, 1992a). Figure 34 shows 77 K photoluminescence spectra from six single crystals grown from materials doped with either iodine or mercury. Crystal *A* is heavily doped with iodine, *B* is lightly doped with iodine, *C* is undoped, *D* is lightly doped with mer-

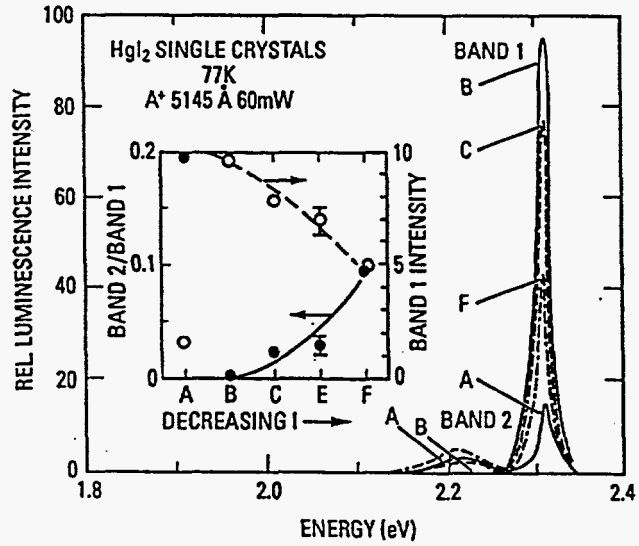

FIG. 34. Photoluminescence of doped HgI_2 single crystals at 77 K. Inset shows band 2/band 1 ratios, and intensity of band 1 for samples doped with Hg and I_2. (Reprinted with permission from Merz *et al.*, 1983 and Elsevier Science Publishers.)

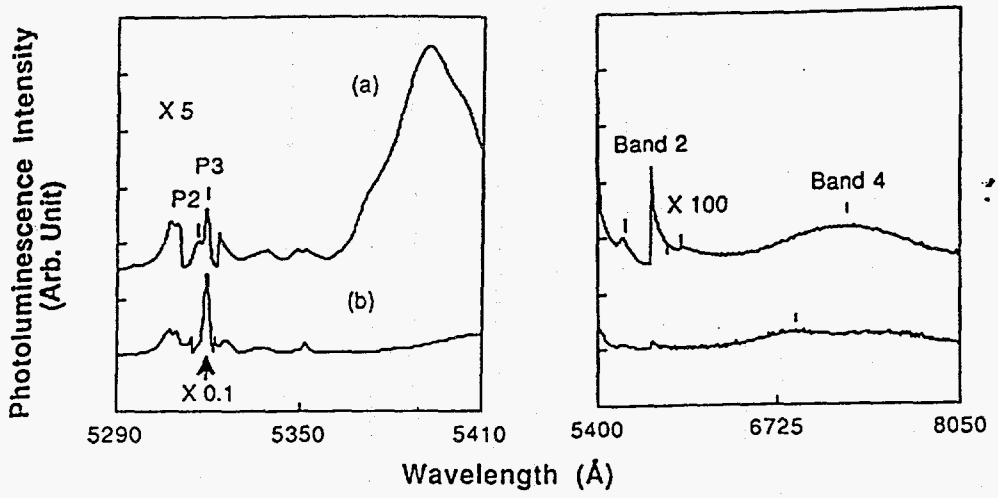

FIG. 35. 4.2 K photoluminescence spectra taken from a HgI_2 crystal (a) before and (b) after a six day storage with vapor of iodine. The sample was etched with 10% KI before storage. (Reprinted with permission from Bao *et al.*, 1992a and the American Institute of Physics.)

cury, *E* is moderately doped with mercury, and *F* is heavily doped with mercury. As can be seen from the figure, with the exception of sample *A*, which shows abnormally weak luminescence intensity, the band 2 to band 1 ratio increases with decreasing iodine content, and the absolute intensity of band 2 also increases with decreasing iodine content.

The effect of stoichiometry was further studied by Bao *et al.* (1992a). HgI_2 samples were stored in the presence of either iodine or mercury vapor and photoluminescence spectra were taken before and after the storage. Figure 35 shows the effect of storage in iodine vapor for six days. It is observed that the intensity of *P*3 will increase in the presence of iodine vapor. The effect of storage with mercury is shown in Fig. 36. The sample was sitting on a glass slide with the front surface exposed. After six days, the front surface looked metallic. And as can be seen from Fig. 36, spectrum (c) taken from the front surface has degraded dramatically with little intensity in the band 1 region. The back surface, which was not directly exposed to the vapor, however, changed less (spectrum (b) of Fig. 36). Nevertheless, there is a drastic decrease in the intensity of *P*3 after storage (compare spectra (a) and (b)). Further storage of the sample with iodine vapor recovers some of the luminescence intensity, but the spectrum (d) is still of low quality. The results of these experiments seem to be consistent with results of Merz *et al.* (1983) in that a low band 1 intensity relative to band 2 is an indication of iodine deficiency, since *P*3 usually dominates the band 1 region.

2. ETCHING AND VACUUM EXPOSURE

Etching of HgI_2 by aqueous solution of KI has been used extensively in the fabrication of HgI_2 detectors for sawing, polishing, and reducing crystal size.

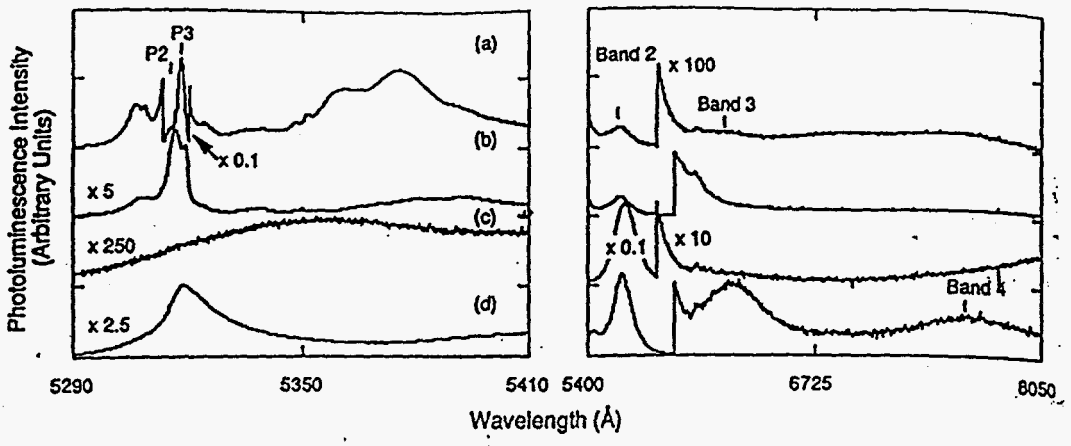

FIG. 36. 4.2 K photoluminescence spectra taken from a HgI_2 sample. They were obtained (a) before storage (b) from back of the sample after storage (c) from the front surface after storage with mercury vapor for six days, and (d) from front surface after storage with iodine vapor for two days following the storage with mercury. (Reprinted with permission from Bao *et al.*, 1992a and the American Institute of Physics.)

Figure 37 shows the effect of chemical etching by 10% KI aqueous solution (Bao *et al.*, 1990d). The intensity of $P3$ is enhanced after the etching. As a matter of fact, $P2$ was the dominating line before the etch, but $P3$ became dominant after the etch. The explanation is that the etching removes a surface layer that has degraded during storage. This surface layer will form in about 24 hr under typical storage conditions, such as in a desiccator (more discussion later with aging). It is further speculated that the degraded surface is due primarily to preferential removal of iodine species because of its relatively high vapor pressure. Therefore, a spectrum with relatively low intensity of $P3$ is probably related to iodine deficiency, which is consistent with stoichiometry study in the previous subsection. Several other etchants have also been studied such as nitric acid and methanol (Bao *et al.*, 1991; David *et al.*, 1993). It was found that in general all etchants have similar effect on the near-bandgap photoluminescence. However, there may

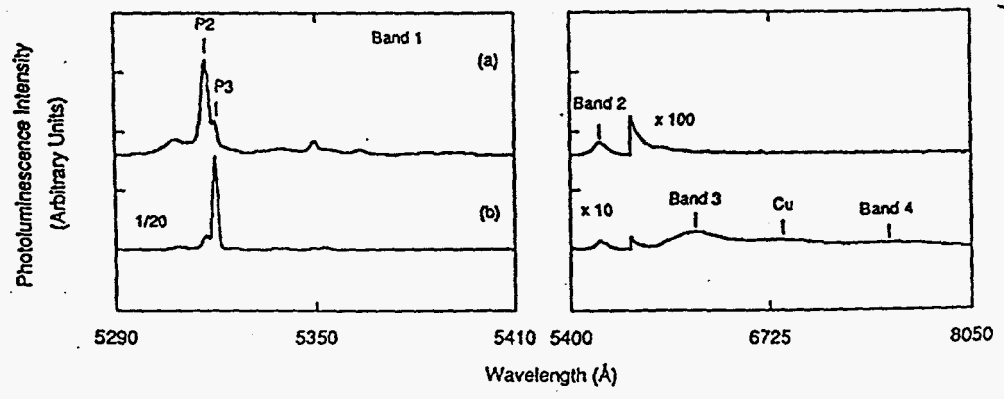

FIG. 37. A 4.2 K photoluminescence of a HgI_2 single crystal before and after a 10% KI etch for about 3 min. (Reprinted with permission from Bao *et al.*, 1990b and the American Institute of Physics.)

be variations in the emission lines in the long wavelength region, which are associated with the purity of the etchant and contaminations of the crystal during etching. The possible incorporation of impurity defects during etching has been verified for Ag and Cu by doping experiments, where a known amount of the impurities was intentionally added into the etching solution (Van Scyoc *et al.*, 1993).

Mercuric iodide surfaces change upon exposure to air (Schieber *et al.*, 1994; Yao *et al.*, 1994). The top photo in Fig. 38 shows the surface of a HgI_2 sample

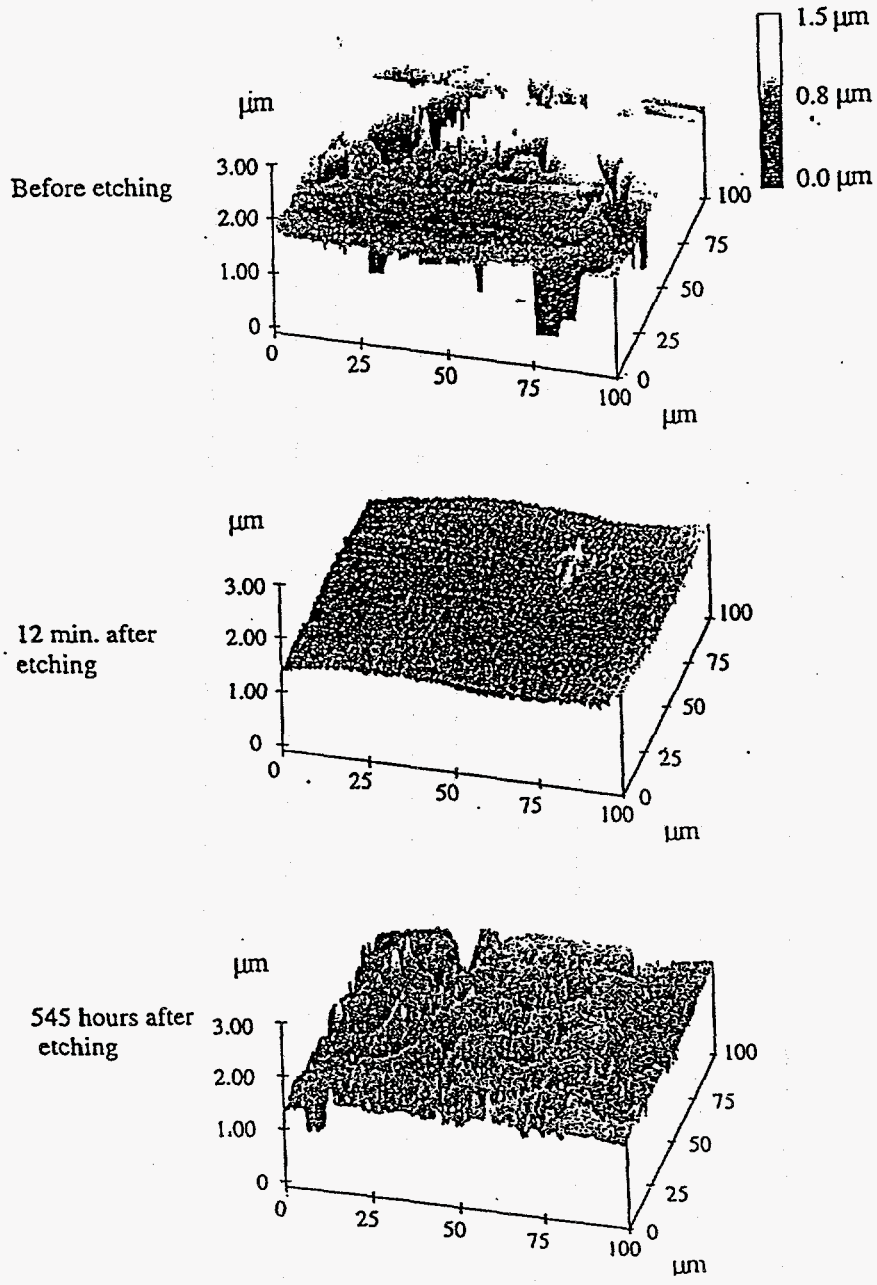

FIG. 38. Atomic force microscopy images showing effects of chemical etching and aging on the roughness of HgI_2 surfaces (from Yao *et al.*, 1994).

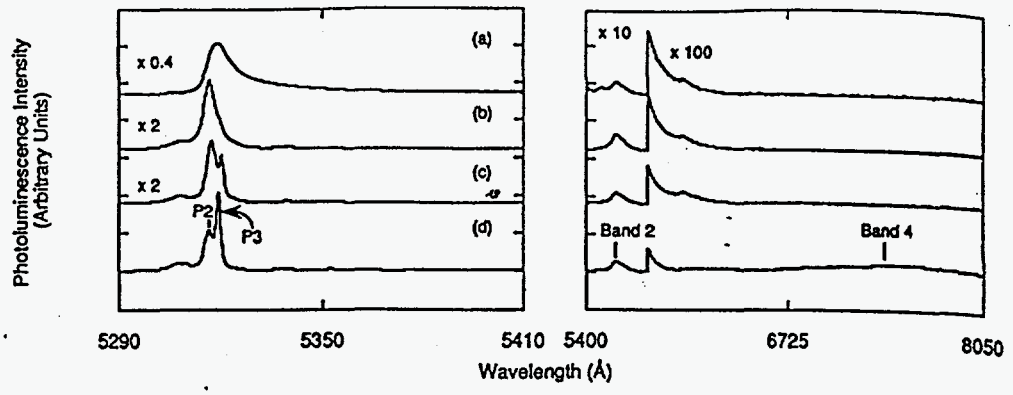

FIG. 39. The effect of aging when the crystal is exposed to air. The spectra were taken (a) 20 days, (b) 7 days, (c) 20 hr, and (d) minutes after a 10% KI etch. (Reprinted with permission from Bao *et al.*, 1992a and SPIE.)

that has been stored in a dessicator for a few months. The surface is quite rough with ridges that are several microns higher than the valleys. The middle photo shows the same surface after it has been chemically etched for 2 min in a 10% KI solution. The chemical etching removes most of the surface roughness, but this roughness returns with continued exposure of the sample to air. The bottom photo of Fig. 38 shows the surface at 545 hr after etching (Yao *et al.*, 1994).

The effect of aging on the low temperature photoluminescence of HgI_2 is shown in Fig. 39 (Bao *et al.*, 1992a). As aging progresses, $P3$ decreases and gradually disappears while $P2$ becomes dominant. This is exactly the reverse process as seen in the etching study. After about 20 days, the spectrum is predominantly a featureless broad strong peak slightly shifted away from $P2$ toward $P3$. From the gradual change of the spectra, it appears that this broad peak derives from $P2$. From a large number of measurements, it was found that typically the effect of aging can be observed within about 24 hr for a freshly etched sample stored in air. Changes in the stoichiometry of the near-surface region and roughening upon aging are expected to contribute to the photoluminescence spectra.

The effect of vacuum exposure on the near-bandgap photoluminescence spectra of HgI_2 is very similar to that of chemical etching (Bao *et al.*, 1990d). Unlike aging during storage, where there seem to be a preferential loss of iodine, the vacuum exposure removes the surface layer congruently. This is probably due to the high rate of removal of the HgI_2 molecules under vacuum. The effect of vacuum exposure is thus more like an etching than an aging effect.

3. CONTACTS

Currently the most widely used contact materials are Pd and colloidal carbon. Transparent contacts such as indium–tin oxide and hydrogel contacts have also been used for fabrication of HgI_2 photodetectors. This is primarily because most metals react with HgI_2 (Cheng, 1993). Since the ideal contact material for each

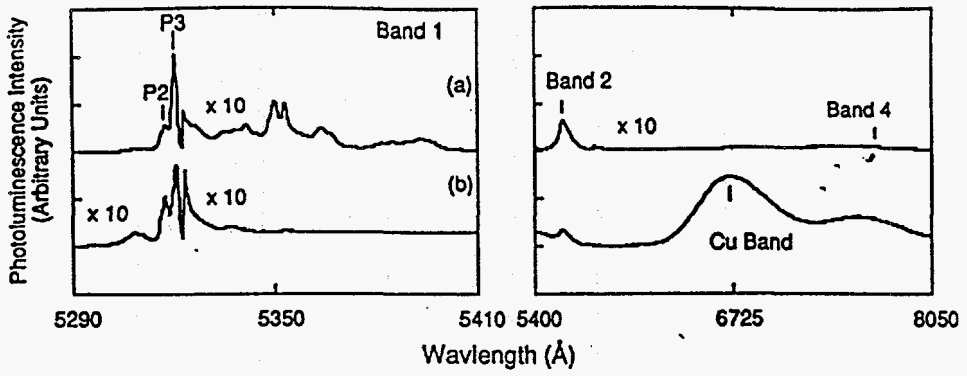

FIG. 40. A 4.2 K photoluminescence spectra of HgI_2 taken from the same spot (a) before and (b) a semitransparent Cu layer was deposited. (Reprinted with permission from Bao *et al.*, 1990a and the American Institute of Physics.)

detector application has yet to be identified, measurements of contact chemistry and device performance for detectors employing different electrode materials are currently of interest. In some cases, investigations of HgI_2–contact interfacial region also increase our understanding of the effect of impurities on the charge transport in devices, particularly for contact materials that diffuse into HgI_2 and dope the materials.

Several contact materials were studied carefully with optical and electrical techniques. They include materials that are currently in use such as Pd, C, In, and Sn and materials of potential use such as Cu, Ag, W, Au, Pt. Results for Cu and Ag will be discussed here. Interested readers can refer to the references for more details and for discussions on other contact materials (James *et al.*, 1989b, 1990, 1992; Schlesinger *et al.*, 1992; Wong *et al.*, 1988b; Bao *et al.*, 1990a, c, d, 1991; Bao, 1991; George *et al.*, 1993). Figure 40 shows two photoluminescence spectra taken from the same spot on a HgI_2 crystal obtained before and after a semitransparent Cu layer is deposited (Bao *et al.*, 1990a). Several changes can be observed. The most dramatic difference is the introduction of a new broad band centered at about 6720 Å between band 3 and band 4. This band has never been observed before and is apparently due to the incorporation of Cu into the HgI_2 crystal and is thus labeled the "Cu" band. Photoluminescence spectra were also taken from spots that were masked off during the Cu deposition. The spots were 2 mm away from the Cu layer. All of these spectra showed emission associated with the Cu band, which indicates that Cu diffuses easily along the crystal surface. A back-doping experiment was performed to study the bulk diffusion of Cu in HgI_2. Figure 41 shows the absolute intensities of the Cu band as a function of position. Four spectra were taken along each of the three directions *A*, *B*, and *C*. The excitation spots were first moved toward the Cu dot from position 1 to 2 and then away from the Cu dot from position 3 to 4. From the plot, it can be seen that the spots close to the Cu dot have stronger Cu band intensity than those farther away. Because the Cu dot was deposited on the other side of the sample (the sample is about 1 mm thick), it is concluded that Cu also diffuses readily through the

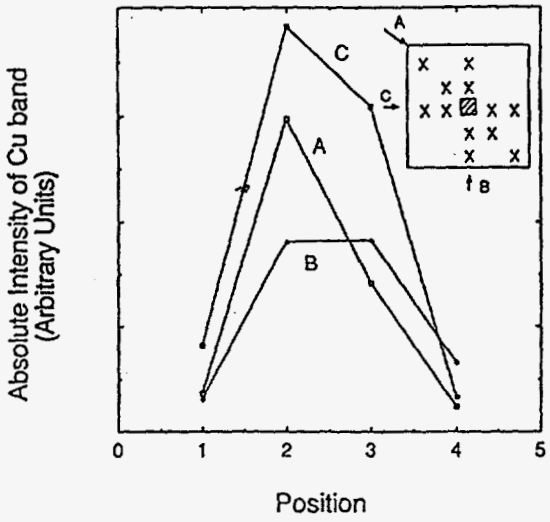

FIG. 41. Absolute intensities of the Cu band (at about 6720 Å) in the 4.2 K photoluminescence spectra as a function of the approximate position from the back-doping experiment. The insert shows the approximate location of points on a HgI_2 substrate (about 1 cm × 1 cm in size) from which the spectra were taken. The small square in the middle indicates the Cu film deposited on the back side. (Reprinted with permission from Bao *et al.*, 1990a and the American Institute of Physics.)

bulk of the material. It should be noted that the HgI_2 samples were never intentionally annealed to enhance the diffusion. The only time the sample may have been expose to momentary heating is during the contact deposition by thermal evaporation.

Nuclear detectors were also made with Cu as electrodes (Bao *et al.*, 1990a). These detectors had very poor performance and high leakage current. Further electrical measurements of Cu contacts also showed fast diffusion of Cu in HgI_2. These investigations revealed and that Cu atoms in HgI_2 are electrically active since the resistivity of HgI_2 was lowered by several orders of magnitude by Cu doping (Van Scyoc *et al.*, 1993). Copper is also believed to significantly degrade the hole transport in devices.

Similar experiments were performed for Ag (James *et al.*, 1993). The top curve of Figure 42 displays a typical photoluminescence spectrum from a point 2 mm away from the silver film. This spectrum was taken 3 days after deposition of the Ag film, and it closely resembles spectra taken from other slabs of the same crystal that were not deposited with Ag. For points beneath the silver film, the spectra were significantly different. Figure 42b shows the spectrum from a typical point beneath the Ag film. The emission in the band 1 spectral region is dominated by a single feature peaked at about 5321.2 ± 1.5 Å. The intensity of band 3 was greatly reduced. Another important difference between the photoluminescence spectra from points beneath the Ag film and away from it is the presence of a new broad feature located at about 5490 Å. This emission peak typically appears as a distinct shoulder on the short wavelength side of band 2 (see Fig. 42b). Since this

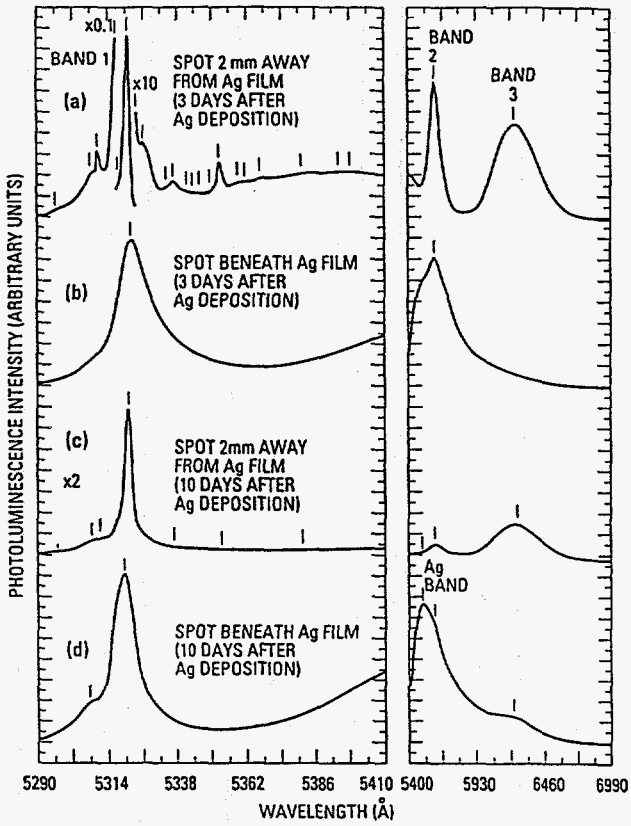

FIG. 42. A 4.2 K photoluminescence spectra from spots that are either beneath or 2 mm away from the Ag film. Spectra in 1a and 1b were taken 3 days after the Ag film was deposited, and the spectra in 1c and 1d were taken 10 days after the film was deposited. (Reprinted with permission from James *et al.*, 1993 and the Materials Research Society.)

peak is only observed in crystals with Ag impurities and it is the dominant photoluminescence feature in regions with high silver concentrations, it is labelled "Ag band." A separate experiment was performed on a 1 cm × 1 cm × 0.06 cm HgI_2 slab with a semitransparent 0.4 cm diameter Ag film deposited on one side only. Photoluminescence spectra were obtained from several spots on the back side that was separated from the circular Ag film by 0.06 cm of bulk HgI_2. Spectra were taken 3 days after the Ag deposition, and it looks indistinguishable from undoped HgI_2. However, after a period of 10 days, the spectrum from the same region exhibited the presence of Ag dopants. In particular, the emission observed at 5490 Å, which is an indicator of Ag impurities, is clearly resolved in the spectrum (see Fig. 43a and b). Figure 43c displays a typical spectrum from a point on the

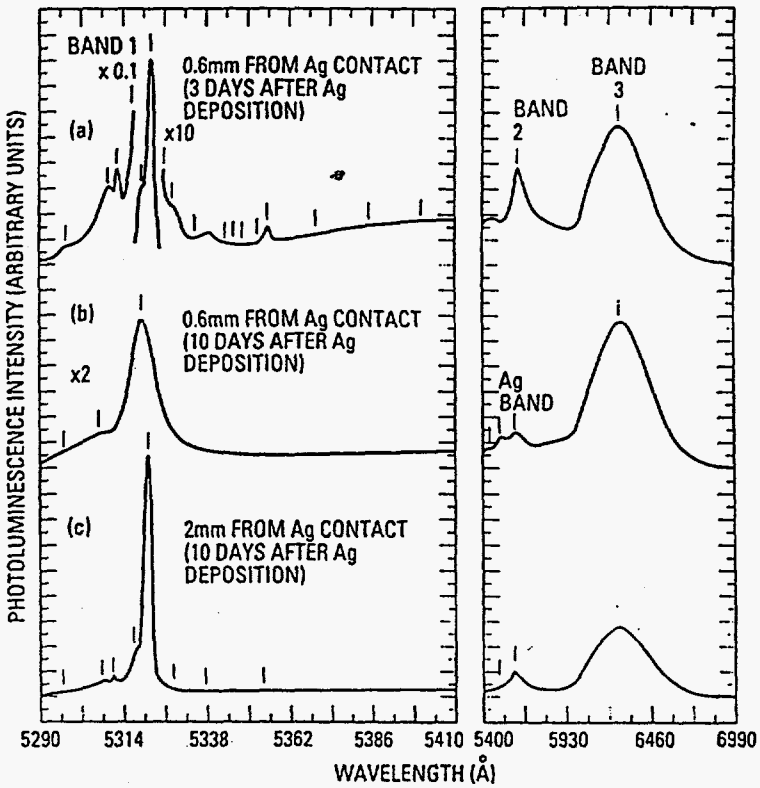

FIG. 43. A 4.2 K photoluminescence spectra taken from different points on the backside of a contacted HgI_2 sample. The points were separated from the Ag film by either 0.6 or 2 mm of b HgI_2. (Reprinted with permission from James *et al.*, 1993 and the Materials Research Society.)

back side of the sample that was separated from the Ag film by 0.2 cm of the bu HgI_2. The spectrum was also taken 10 days following the Ag deposition. Tl spectrum showed a smaller intensity of the "Ag band" for regions that were sep rated farther from the Ag film by bulk HgI_2. These measurements reveal that silv diffuses through the bulk of the material instead of surface diffusion only. The ra of diffusion at room temperature is estimated to be on the order of 10 μm/hr.

4. DETECTOR PERFORMANCE

For gamma ray applications, the detector performance is usually quantified l the photopeak resolution and peak to valley ratio (Gerrish, 1993). Figure 44 sho a pulse height spectra of the 662 keV gamma ray from a Cs-137 source. T resolution is 1.7% and the peak to valley ratio is 15:1. Merz *et al.* (1983) fi observed that crystals that produce better detectors tend to have higher intensi of luminescence in the band 1 region. Since the band 1 region corresponds to t near-band edge wavelength, it is reasonable to believe that higher intensities fro this region indicate higher quality crystals. Photoluminescence spectra taken fro

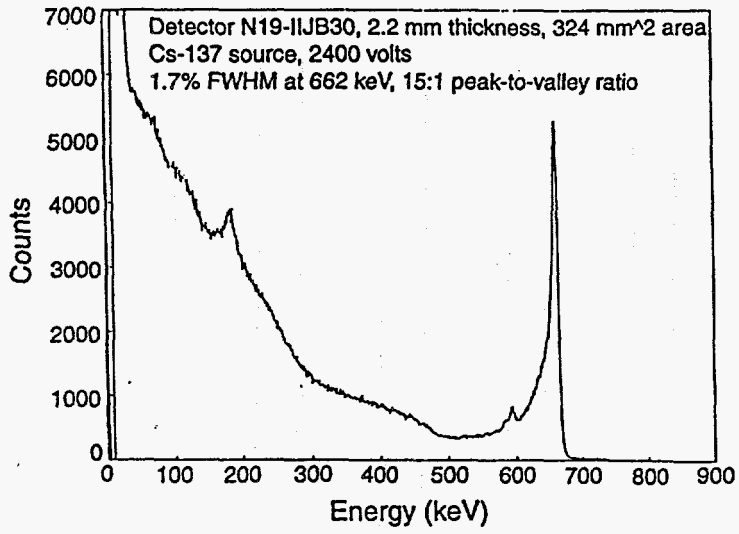

FIG. 44. A spectrum of the 662 keV gamma ray from a Cs-137 source taken with a HgI_2 detector at room temperature.

working detectors also show that better detectors have higher band 1 to band 2 ratio, as shown in Fig. 45. In addition, it is found from a large number of measurements that band 3 is also detrimental for detector performance (Bao *et al.*, 1992; James *et al.*, 1992). Based on these measurements it appears likely that larger emission from the deeply bound states (i.e., at wavelengths greater than ~5400 Å) are indicators of poor detector grade crystals.

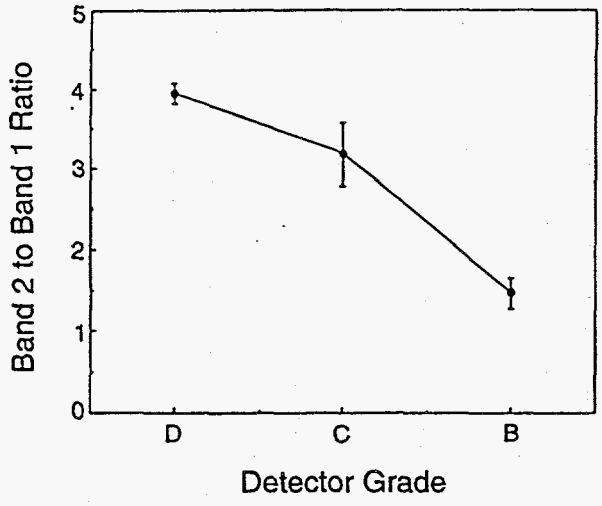

FIG. 45. Band 2 to band 1 ratios of three working detectors graded *B*, *C*, and *D*. The intensities of band 1 and band 2 were obtained by integrating from 5290 to 5410 Å and from 5410 to 5690 Å, respectively using 4.2 K photoluminescence spectra. The error bars are the standard deviation of the means from several measurements on each sample. (Reproduced with permission from Bao *et al.*, 1992b and Elsevier Science Publishers.)

V. Conclusions

Since the fabrication of the first HgI_2 nuclear detectors more than two decades ago, there have been much progress in several major aspects of HgI_2 sensor technologies. With advances in device processing (including purification, growth, fabrication, contacts, passivation, and testing) of HgI_2 and associated pulse processing electronics, the first commercial products were realized in 1988 in the form of field portable x-ray fluorescence systems designed and manufactured by TN Technologies, Inc. At the same time, fundamental research in the material properties of HgI_2 has increased the knowledge base of this material tremendously, which in turn helps the development of improved crystal growth and device processing procedures. In addition, developments of applications for HgI_2 in many other areas are keenly pursued by many researchers in the world. Better understanding of the optical properties of HgI_2 and development of new techniques will certainly become more important in the future. First, the application of HgI_2 in nuclear detection is fundamentally related to its photosensitivity. Therefore HgI_2 device behavior and performance will be better understood with greater knowledge of its fundamental electrical and optical properties. Second, given the high resistivity of HgI_2, the majority of characterization techniques used to study the electrical properties of HgI_2 utilize light sources for excitation. Third, as the technology is becoming more commercialized, rapid and cost effective testing in the manufacturing environment will be in demand for nondestructive characterization of materials, crystals, and detectors for sorting, grading, and process control. These analytical techniques will be derived from the research efforts that emphasize the relationships of crystalline purity, structural perfection, contact quality, with measurements of detector performance and manufacturing yield.

REFERENCES

Adams, D. M., and Hooper, M. A. (1970). *Astr. J. Chem.* **24**, 885.

Anedda, A., Raga, F., Grill, E., and Guzzi, M. (1977). *Il Nuovo Cimento* **38B**, 439.

Anedda, A., Grilli, E., Guzzi, M., Raga, F., Serpi, A. (1981). *Solid State. Commun.* **39**, 1121.

Akopyan, I., Novikov, B., Permogorov, S., Selkin, A., and Travnikov, V. (1975). *Phys. Stat. Sol. (b)* **70**, 353.

Akopyan, I. K., Bondarenko, B. V., Kazennov, B. A., and Novikov, B. V. (1987). *Sov. Phys. Solid State* **29**, 238.

Bao, X. J. (1991). Ph.D. thesis, Carnegie Mellon University.

Bao, X. J., Schlesinger, T. E., James, R. B., Stulen, R. H., Ortale, C., and van den Berg, L. (1990a). *J. Appl. Phys.* **67**, 7265.

Bao, X. J., Schlesinger, T. E., James, R. B., Ortale, C., and ven den Berg, L. (1990b). *J. Appl. Phys.* **68**, 2951.

Bao, X. J., Schlesinger, T. E., James, R. B., Cheng, A. Y., and Ortale, C. (1990c). *Mat. Res. Soc. Symp. Proc.* **163**, 1027.

Bao, X. J., Schlesinger, T. E., James, R. B., Stulen, R. H., Ortale, C., and Cheng, A. Y. (1990d). *J. Appl. Phys.* **68**, 86.

Bao, X. J., Schlesinger, T. E., James, R. B., Gentry, G. L., Cheng, A. Y., and Ortale, C. (1991). *J. Appl. Phys.* **69**, 4247.

Bao, X. J., James, R. B., Hung, C. Y., Schlesinger, T. E., Cheng, A. Y., Ortale, C., and van den Berg, L. (1992a). *SPIE Proc.* **1736**, 60.

Bao, X. J., Schlesinger, T. E., James, R. B., Harvery, S. J., Cheng, A. Y., Gerrish, V., and Ortale, C. (1992b). *Nucl. Instr. Meth. Phys. Res.* **A317**, 194.

Biellman, J., and Prevot, B. (1980). *Infrared Phys.* **20**, 99.

Bube, R. (1957). *Phys. Rev.* **106**, 703.

Burger, A., and Nason, D. (1992). *J. Appl. Phys.* **71**, 2717.

Burger, A., Morgan, S. H., Silberman, E., Nason, D., and Cheng, A. Y. (1992). *Nucl. Instr. Methods. Phys. Res.* **A322**, 427.

Chang, Y. C., and James, R. B. (1992). *Phys. Rev. B* **46**, 150404.

Chang, Y. C., Sim, H. K., and James, R. B. (1993). In *Semiconductors for Room-Temperature Radiation Detector Applications*, ed. R. B. James *et al.* Mat. Res. Soc. Symp. Proc. **302**, 121.

Chelikowsky, R. J., and Cohen, M. L. (1976). *Phys. Rev. B* **14**, 556.

Cheng, A. Y. (1993). In *Semiconductors for Room-Temperature Radiation Detector Applications*, ed. R. B. James *et al.* Mat. Res. Soc. Symp. Proc. **302**, 141.

Chester, M., and Coleman, C. C. (1971). *J. Phys. Chem. Solids* **32**, 223.

David, D. C., Van Scyoc, J., Khudatyan, M., James, R. B., Anderson, R. J., and Schlesinger, T. E. (1993). In *Semiconductors for Room-Temperature Radiation Detector Applications*, ed. R. B. James *et al.* Mat. Res. Soc. Symp. Proc. **302**, 147.

Gerrish, V. M. (1993). In *Semiconductors for Room-Temperature Radiation Detector Applications*, ed. R. B. James *et al.* Mat. Res. Soc. Symp. Proc. **302**, 129.

George, M. A., Azoulay, M., Burger, A., Biao, Y., Silberman, E., and Nason, D. (1993). *Thin Solid Films* **236**, 180.

Goto, T., and Kasuya, A. (1981). *J. Soc. Jpn.* **50**, 520.

Goto, T., and Nishina, Y. (1978). *Sol. Stat. Commun.* **25**, 123.

Haisler, V. A., Zaletin, V. M., Kravchenko, A. F., and Yashin, G. Y. (1984). *Phys. Stat. Sol. (b)* **121**, K13.

Harbeke, G., and Tosatti, E. (1974). *Proceedings of the 12th International Conference on the Physics of Semiconductors*. Stuttgart, 626.

Hopfield, J. J., and Thomas, D. G. (1960). *J. Phys. Chem. Solids* **12**, 276.

Hopfield, J. J., and Thomas, D. G. (1961). *Phys. Rev.* **122**, 35.

James, R. B., Ottesen, D. K., Wong, D., Schlesinger, T. E., Schnepple, W. F., Ortale, C., and van den Berg, L. (1989a). *Nucl. Instr. Meth. Phys. Res.* **A283**, 188.

James, R. B., Bao, X. J., Schlesinger, T. E., Markakis, J. M., Cheng, A. Y., and Ortale, C. (1989b). *J. Appl. Phys.* **66**, 2578.

James, R. B., Bao, X. J., Schlesinger, T. E., Ortale, C., and Cheng, A. Y. (1990). *J. Appl. Phys.* **67**, 2571.

James, R. B., Bao, X. J., Schlesinger, T. E., Chang, A. Y., Ortale, C., and van den Berg, L. (1992). *Nucl. Instr. Meth. Phys. Res.* **A322**, 435.

James, R. B., Bao, X. J., Schlesinger, T. E., Cheng, A. Y., and Gerrish, V. M. (1993). In *Semiconductors for Room-Temperature Radiation Detector Applications*, ed. R. B. James *et al.* Mat. Res. Soc. Symp. Proc. **302**, 103.

Jayatirtha, H. N., Azoulay, M., George, M. A., and Burger, A. (1993). In *Semiconductors for Room-Temperature Radiation Detector Applications*, ed. R. B. James *et al.* Mat. Res. Soc. Symp. Proc. **302**, 161.

Kanzaki, K., and Imai, I. (1972). *J. Phys. Soc. Jnp.* **32**, 1003.

Levi, A., Burger, A., Nissenbaum, J., and Schieber, A. (1983). *Nucl. Instr. Meth.* **213**, 35.

Levi, A., Schieber, M., and Burshtein, Z. (1985). *J. Appl. Phys.* **57**, 1944.

Lopez-Cruz, E. (1989). *J. Appl. Phys.* **65**, 874.

Melveger, A. J., Khanna, R. K., Guscott, B. R., and Lippincott, E. R. (1968). *Inorganic Chem.* **7**, 1630.

Merz, J. L., Wu, Z. L., van den Berg, L., and Schnepple, W. F. (1983). *Nucl. Instr. Meth.* **213**, 51.
Mikawa, Y., Jakobsen, R. J., and Brasch, J. W. (1966). *J. Chem. Phys.* **45**, 4528.
Nakagawa, I. (1971). *Bull. Chem. Soc. Japan* **44**, 3014.
Nakashima, S., Mishima, H., and Mitsuishi, A. (1973). *J. Raman Spectr.* **1**, 325.
Nason, D., and Burger, A. (1991). *Appl. Phys. Lett.* **59**, 3550.
Novikov, B. V., and Pimonenko, M. M. (1971). *Sov. Phys. Semicond.* **4**, 1785.
Novikov, B. V., and Pimonenko, M. M. (1972). *Sov. Phys. Semicond.* **6**, 671.
Nyquist, R. A., and Kagel, R. O. (1971). *Infrared Spectra of Inorganic Compounds.* Academic Press, New York.
Ogawa, Y., Harada, I., Hiroatsu, M., Takehiko, S., and Hiraishi, J. (1976). *Spectrochimica Acta* **32A**, 49.
Petroff, P. M., Hu, Y. P., and Milstein, F. (1989). *J. Appl. Phys.* **66**, 2525.
Prevot, B., and Biellmann, J. (1979). *Phys. Stat. Sol. (b)* **95**, 601.
Prevot, B., Schwab, C., and Dorner, B. (1978). *Phys. Stat. Sol. (b)* **88**, 327.
Redfield, D. (1965). *Phys. Rev.* **140A**, 2056.
Roessler, D. M. (1965). *Brit. J. Appl. Phys.* **16**, 1359.
Roessler, D. M. (1966). *Brit. J. Appl. Phys.* **17**, 1313.
Schieber, M., Roth, M., and Schnepple, W. F. (1983). *J. Cryst. Growth* **65**, 353.
Schieber, M., Roth, M., Yao, H., DeVries, M., James, R. B., Goorsky, M. (1994). *J. Cryst. Growth,* in press.
Schlesinger, T. E., Bao, X. J., James, R. B., Cheng, A. Y., Ortale, C., and van den Berg, L. (1992). *Nucl. Instr. Meth. Phys. Res.* **A322**, 414.
Schluter, I. C., and Schluter, M. (1974). *Phys. Rev. B* **9**, 1652.
Sieskind, M. (1960). *Rev. Opt. Theor. Intrum.* **39**, 239.
Sim, H. K., Chang, Y. C., and James, R. B. (1994). *Phys. Rev. B* **49**, 4559.
Soria, E., Natarajan, M., and James, R. B. (1994). Unpublished.
Thomas, D. G., and Hopfield, J. J. (1959). *Phys. Rev.* **116**, 573.
Tubbs, M. R. (1972). *Phys. Stat. Sol. (b)* **49**, 11.
Turner, D. E., and Harmon, B. N. (1989). *Phys. Rev. B* **40**, 10516.
Urbach, F. (1953). *Phys. Rev.* **92**, 1324.
Van Scyoc, J. M., Schlesinger, T. E., James, R. B., Cheng, A. Y., Ortale, C., and van den Berg, L. (1993). In *Semiconductors for Room-Temperature Radiation Detector Applications,* ed. R. B. James *et al.* Mat. Res. Soc. Symp. Proc. **302**, 115.
Williams, L. R., Anderson, R. J. M., and Banet, M. J. (1991). *Chem. Phys. Lett.* **182**, 422.
Wong, D., Schlesinger, T. E., James, R. B., Ortale, C., van den Berg, L., and Schnepple, W. F. (1988a). *J. Appl. Phys.* **64**, 2049.
Wong, D., Bao, X. J., Schlesinger, T. E., James, R. B., Cheng, A., Ortale, C., and van den Berg, L. (1988b). *Appl. Phys. Lett.* **53**, 1536.
Yao, H., and Johs, B. (1993). In *Semiconductors for Room-Temperature Radiation Detector Applications,* ed. R. B. James *et al.* Mat. Res. Soc. Symp. Proc. **302**, 341.
Yao, H., Johs, B., and James, R. B. (1994). Unpublished.
Yee, J. H., Sherohman, J. W., and Armantrout, G. A. (1976). *IEEE Trans. Nucl. Sci.* **NS-23**, 117.
Zahner, J. C., and Drickamer, H. G. (1959). *J. Phys. Chem. Solids* **11**, 92.

Left Intentionally Blank

Semiconductors for Room Temperature Nuclear Detector Applications

SEMICONDUCTORS
AND SEMIMETALS

Volume 43

Volume Editors

T. E. SCHLESINGER

DEPARTMENT OF ELECTRICAL AND COMPUTER ENGINEERING
CARNEGIE MELLON UNIVERSITY
PITTSBURGH, PENNSYLVANIA

RALPH B. JAMES

ADVANCED MATERIALS RESEARCH DEPARTMENT
SANDIA NATIONAL LABORATORIES
LIVERMORE, CALIFORNIA

ACADEMIC PRESS
San Diego Boston New York
London Sydney Tokyo Toronto

CHAPTER 4

Electrical Properties of Mercuric Iodide

X. J. Bao

DEPARTMENT OF ANALYTICAL INSTRUMENTS
TN TECHNOLOGIES, INC.
ROUND ROCK, TEXAS

T. E. Schlesinger

DEPARTMENT OF ELECTRICAL AND COMPUTER ENGINEERING
CARNEGIE MELLON UNIVERSITY
PITTSBURGH, PENNSYLVANIA

R. B. James

ADVANCED MATERIALS RESEARCH DEPARTMENT
SANDIA NATIONAL LABORATORIES
LIVERMORE, CALIFORNIA

List of Symbols

A	area of contact	$c_{e,h}$	capture probability of electron and hole
C	capacitance		

E	electric field
E_{ph}	x-ray photon energy
e	2.718 . . .
$e_{e,h}$	thermal emission probability of electron and hole
h	Planck's constant
I_d	detector leakage current
i	transient current density
J_{PF}	Poole–Frenkel current
J_S	Schottky current
k	Boltzman's constant
L	detector thickness
ln	natural logarithm
log	logarithm with a base of 10
m_0	electron rest mass
$m^*_{e,h}$	effective mass of electron and hole
$N_{c,v}$	effective density of states in the conduction and valence bands
N_t	density of carrier trap
n_t	density of carrier trap occupied
n	density of free electrons
Q	collected charge
Q_0	total charge generated
p	density of free holes
s	surface recombination velocity
T	absolute temperature
t_r	carrier transit time
V	applied voltage
v_d	drift velocity
v_{th}	thermal velocity of free carrier
β	heating rate
ΔE_t	activation energy of carrier trap
ΔE	FWHM of x-ray peak
ϵ	average energy to generate one electron-hole pair
ϵ_0	permittivity in vacuum
ϵ_r	dielectric constant
η	charge collection efficiency
$\mu_{e,h}$	mobility of electrons and holes
μ_{ph}	photoelectric absorption coefficient
ν	photon frequency
ρ	resistivity
$\sigma_{e,h}$	carrier capture cross section of electron and hole trap
τ_d	detrapping time
$\tau_{\text{dielectric}}$	dielectric relaxation time
$\tau_{e,h}$	lifetime of electron and hole
τ_t	trapping time
ϕ_{PF}	Poole–Frenkel barrier height
ϕ_S	Schottky barrier height

I. Introduction

Even with the progress made since its first use as a nuclear spectrometer in 1971 (Willig, 1971), HgI_2 technologies are still far from being fully developed. Compared with other semiconductors commonly employed in various applications, the relationships between most defects and the electronic properties are still either poorly understood or unknown. The potential of HgI_2 nuclear detector technologies will certainly be more fully realized as more progress is made toward the understanding of the material properties responsible for the wide variability in detector performances. The electrical properties of HgI_2 in many instances determine the performance of the x-ray and γ-ray spectrometers and photodetectors

fabricated from this material. Broadly speaking, the performance of a nuclear spectrometer is characterized by its energy resolution, peak to background ratio, efficiency, reliability, response speed, active volume, and the ease with which it can be handled. The electrical properties of importance include the dark resistivity of the material, mobility and lifetime of free carriers, effective masses of free carriers, behavior of traps, and surface effects. This chapter will be devoted to the description of the electrical properties of red HgI_2, particularly those important in using this material for x-ray and γ-ray detector applications. Other topics discussed in this chapter include the relationship of carrier traps to fabrication processes and device performance, measurement techniques used to characterize the electrical properties of HgI_2, and the theoretical background required to evaluate the data.

II. Carrier Transport

1. DARK RESISTIVITY AND I–V CHARACTERISTICS

HgI_2 detectors are exclusively biased along the crystallographic c-axis for carrier collection, and transport properties do depend on the crystallographic direction. Therefore, the discussion of transport properties for crystals and detectors will refer to values along the c-axis, unless otherwise noted. Dark resistivity determines the leakage current in HgI_2 x-ray and γ-ray spectrometers. A large leakage current is undesirable mainly because it reduces the energy resolution of the detector. Leakage current contributes to the FWHM (full width at half maximum) of the detector system according to the relation (Dabrowski and Huth, 1978)

$$\Delta E_d = (2.355\epsilon e)\sqrt{\frac{I_d \tau}{4q}} \tag{1}$$

where ΔE_d is the FWHM in eV due to leakage current, ϵ is the mean energy in eV required to create one electron–hole pair, e is 2.718, q is the electron charge in coulombs, I_d is the leakage current in amperes, and τ is the time constant of the shaping network in seconds.

One advantage of HgI_2 detectors is that their dark resistivity is many orders of magnitude greater than that of most other semiconductors, such as Si, Ge, III–V, and II–VI materials. While Si and Ge nuclear detectors are usually operated at cryogenic temperatures to reduce the leakage current, HgI_2 detectors have a high enough resistivity ($\sim 10^{13}$ Ω-cm) to be operated at room temperature. This advantage is not solely a matter of convenience, since it results in many new applications where cryogenic cooling is difficult or impossible and a compact portable system is essential (see the discussion in Chapter 1).

Dark resistivity in HgI_2 can be estimated by measuring the dark current and noting the sample geometry. Contacts are typically deposited on opposite faces of

HgI_2 slices to form a sandwich structure. The resistivity is then calculated accor ing to the equation: $\rho = VA/I_dL$, where ρ is the resistivity in Ω-cm, V is tl applied voltage in volt, I_d is the dark current in amperes, A is the area of tl contact in cm^2, and L is the thickness in cm. Other commonly used technique such as the four point probe method or Hall effect measurement, are difficult t use on HgI_2 because of its very high resistivity.

When a high voltage is applied, the dark current in HgI_2 usually decrease slowly with time (Braatz and Zappe, 1984; Levi, Schieber, and Burshtein, 1985 The estimated dark resistivity at 295 K is about 10^{11} Ω-cm initially and reaches saturation value of (0.6 to 20) $\times$ 10^{13} Ω-cm within 200 min. of applied bia (Braatz and Zappe, 1984). This decrease of dark current with time is believed t be due to the release of carriers from traps and is therefore described by a sum o exponentially decaying currents, each with a time constant corresponding to the detrapping time of a particular trap level. Investigations of this behavior have been used to understand carrier traps in HgI_2, and they will be discussed in Subsection III.2. The dependence of dark current on applied field is not linear over the entire range of voltages employed in detector operation (Braatz and Zappe, 1984; Mellet and Friant, 1989). The dark resistivity obtained, therefore, is only a rough estimate. Near room temperature, the dark current is very sensitive to temperature and increases rapidly with increasing temperature (Braatz and Zappe, 1984). For a HgI_2 detector of 1 cm^2 area, lowering the operating temperature to 0° C will reduce the dark current to below 1 pA compared to a dark current of about 10 pA at 300 K. The noise contribution from this source is then negligible when compared to the contribution from currently available preamplifiers (Levi *et al.*, 1985).

The mechanism of dark conductivity in HgI_2 has not been thoroughly studied. Ionic conductivity due to the movement of iodine vacancies was observed in HgI_2 single crystals and polycrystals at a temperature of 120° C (Kitajima and Wagner, 1988). Since HgI_2 devices are usually operated near or below room temperature, ionic conductivity probably is not dominant under these conditions. The dark electronic conductivity in a dielectric material is generally due to thermal emission or tunneling, both of which may be further divided into either bulk controlled or electrode controlled (Yeargan and Taylor, 1968). Tunneling in HgI_2 is unlikely given the typical device configurations employed. For the case of thermal emission, the bulk controlled current is determined by the Poole–Frenkel effect, which is associated with barriers in the bulk of the material. The electrode controlled current is determined by the Schottky effect, which is associated with the barrier at the metal–semiconductor interface. Both of these effects are controlled by the lowering of the barrier by an applied electric field (Yeargan and Taylor, 1968). The barrier lowerings are given by

$$\Delta\phi_{PF} = \sqrt{\frac{q^3E}{\pi\epsilon_e\epsilon_0}} = \beta_{PF}\sqrt{E} \tag{2}$$

and

$$\Delta\phi_S = \sqrt{\frac{q^3E}{4\pi\epsilon_r\epsilon_0}} = \beta_S\sqrt{E} \tag{3}$$

and $\Delta\phi_{PF}$ and $\Delta\phi_S$ are the barrier lowerings due to the Poole–Frenkel and Schottky effects, respectively, E is the electric field at the barrier (which may be different from the applied field), ϵ_0 is the vacuum permittivity, and ϵ_r is the high frequency relative dielectric constant. The Poole–Frenkel and Schottky currents (for electrons) are given by (Yeargan and Taylor, 1968)

$$J_{PF} = q\mu_n n_o E \exp\left(-\frac{\phi_{PF} - \Delta\phi_{PF}}{rkT}\right) \tag{4}$$

and

$$J_S = A_S T^2 \exp\left(-\frac{\phi_S - \Delta\phi_S}{kT}\right) \tag{5}$$

where r is a parameter between 1 and 2 depending on the position of the Fermi level, and ϕ_{PF} and ϕ_S are the Poole–Frenkel and the Schottky barriers, respectively. In the Poole–Frenkel model, the concentration of free carriers generally takes the form

$$n = n_o \exp\left(-\frac{\phi_{PF}}{rkT}\right) \tag{6}$$

where both n_o and ϕ_{PF} are functions of donor, acceptor and trap concentrations and their energy positions in the bandgap. The constant A_S is given by

$$A_S = \frac{2qk^3m_e^*}{(2\pi)^2h^3} \tag{7}$$

where m_e^* is the electron effective mass, k is the Boltzman constant, and h is the Planck constant. Given the similarities in the functional forms of Eqs. (4) and (5), it is difficult to identify whether the dark current in HgI_2 is due to the Poole–Frenkel or the Schottky effects unless systematic studies are performed to measure the dependence of the dark current on the applied electric field and the effect of polarity, temperature, and contacts with different work functions (Yeargan and Taylor, 1968).

Braatz and Zappe (1984) have interpreted their measured dark currents in HgI_2 as due to the Poole–Frenkel mechanism, and a linear region in the plot of $\ln(J_{PF})$

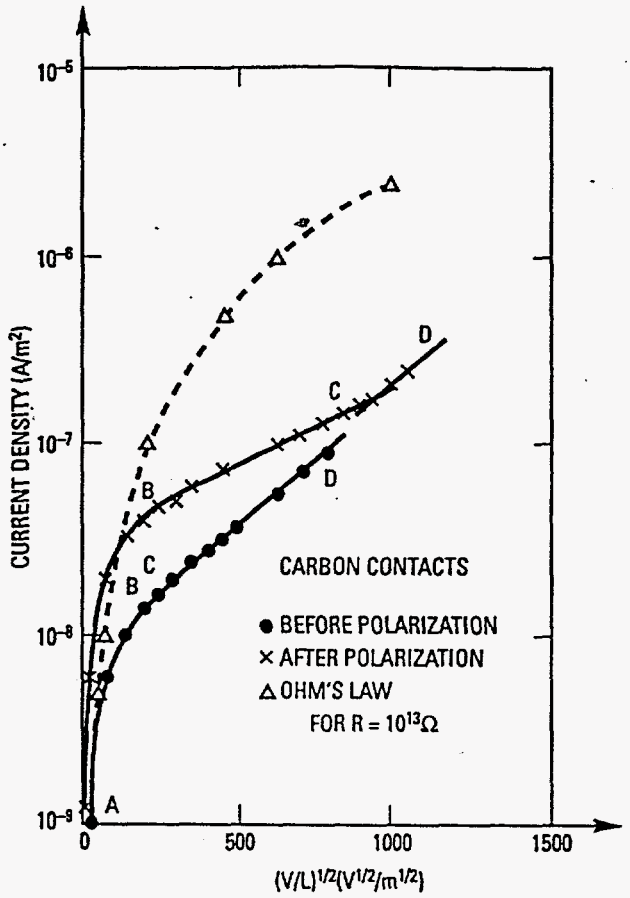

FIG. 1. Log(J) vs. $\sqrt{V/L}$ for a sample showing polarization after 24 hr under bias. (Reprinted from Mellet and Friant, 1989. ©1989 IEEE.)

vs. $\sqrt{E}$ was identified. From the slope of the linear region and the assumed Poole–Frenkel model, several parameters can be inferred such as trap concentration and trap energy levels. Figure 1 shows the plots of J_S vs. $\sqrt{V/L}$ obtained by Mellet and Friant (1989) for a sample before and after polarization. Ohm's law for $10^{13}\ \Omega$ is also shown for comparison. The data can be divided into three regions. In the AB region, the curve follows Ohm's law. The BC and CD regions are linear and were interpreted as Schottky current. The polarization effect will reduce the slope in the BC region. The electric field in the expression for the Schottky current (Eq. (5)) was taken to be proportional to the applied bias

$$E = \gamma \frac{V}{L} \tag{8}$$

where V is the applied field, L is the sample thickness, and γ is a number that characterizes the electrode. An injecting contact has $\gamma < 1$, and a blocking contact has $\gamma > 1$. From the CD region in the plot of $\log(J_S)$ vs. $\sqrt{V/L}$, the parameter γ may be determined from the slope. The barrier height ϕ_S without bias can be

calculated from the intercept with the y-axis. Further discussion of the electrical contacts can be found in Subsection V.1.

Another observation related to the I–V characteristics of HgI_2 was made by Levi *et al.* (1985). After a sample of HgI_2 has reached equilibrium, either by resting the sample in the dark under short circuit conditions for several hours or by illumination with an incandescent lamp for several minutes followed by a resting period in the dark (this latter procedure shortens the resting time to about half an hour), the dark current decays with time when a voltage is applied to this sample. This has also been observed by other workers (see Fig. 2a). If the applied voltage is then reversed, the dark current shows a current peak superimposed on a decaying current transient as shown in Fig. 2b. The position and magnitude of this current peak is a function of the preparing voltage V_P (the applied voltage before the reversal of bias), preparation time (the duration of the applied voltage before the reversal of the bias), and applied voltage V_R (the magnitude of the reversed bias). The explanation provided by Levi *et al.* (1985) is that the current peak is due to the trap controlled motion of holes. If the position of the peak t_m is assumed to be the transit time of the trap controlled charges, it will be related to the applied voltage by

$$t_m = \frac{L^2}{\mu_{\text{eff}} V_R} \tag{9}$$

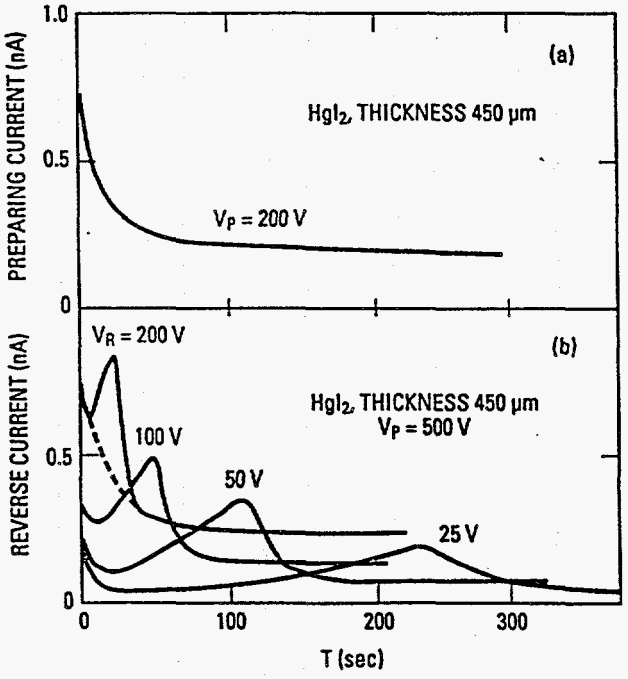

FIG. 2. Room temperature current vs. time transients under various conditions: (a) when the sample has reached thermal equilibrium before voltage application, (b) when the sample was subject to a voltage of 500 V for 10 min. before reversing the voltage. (Reprinted from Levi *et al.*, 1985, with permission.)

where μ_{eff} is the effective mobility of the trapped charges. The effective mobility is related to the trap parameters by (Nissenbaum, Schieber, and Burshtein, 1987)

$$\mu_{\text{eff}} = \mu_h \left(\frac{N_v}{N_t}\right) \exp\left(\frac{\Delta E_t}{kT}\right). \tag{10}$$

Indeed a plot of t_m vs. $1/V_R$ yields a straight line. The effective mobility determined from the slope is about 3.8×10^{-7} cm^2/V-sec. This value is many orders of magnitude lower than the electron or hole mobilities and can be accounted for by trap controlled motion where the charged carrier undergoes multiple trapping and detrapping processes (Rose, 1951). The integrated amount of charge under the current peak was found to be much greater than the charge on the detector electrodes (capacitance times applied voltage). It was argued that this excess current superimposed on the decaying component of current is provided by free electrons that screen the space charges produced by the trap controlled motion of holes, instead of a space charge limited current of holes. Therefore, the average electron concentration is related to the total collected charge under the current peak by (Levi *et al.*, 1985)

$$n_{\text{av}} = \frac{Q}{t_m A} \frac{L}{q\mu_n V_R} = \frac{Q}{qLA} \frac{\mu_{\text{eff}}}{\mu_e} \tag{11}$$

where Q is the total collected charge under the current peak obtained by integrating the current with time and subtracting the contribution due to the decay component and μ_e is the electron mobility. A plot of n_{av} vs. t_m is shown in Fig. 3. The time constant obtained from this plot is then the dielectric relaxation time, which is given by

$$\tau_{\text{dielectric}} = \frac{\epsilon_r \epsilon_0}{q\mu_e n} \tag{12}$$

where n is the dark electron density in HgI_2. The contribution of free holes to the conductivity is ignored here. The relaxation time thus obtained by Levi *et al.* (1985) at room temperature is about 25 sec. From Eq. (12), using $\epsilon_r = 9.75$ and $\mu_e = 100$ cm^2/V-sec, an electron concentration of $n = 2 \times 10^3$ cm^{-3} was obtained, which corresponds to a resistivity of about 3×10^{13} Ω-cm. Similar measurements of dark current in SbI_3-doped HgI_2 crystals (Nissenbaum *et al.*, 1987) resulted in a much smaller effective mobility of holes of 10^{-8} cm^2/V-sec, which was attributed to a shallower trap with a higher concentration. The trap activation energy obtained for SbI_3-doped crystals was 0.5 eV compared with 0.7 eV for undoped HgI_2. These activation energies were obtained with Eq. (10) by using measured values for the effective mobility as a function of temperature. The trap density in the SbI_3-doped HgI_2 was related to the doping level and found to be

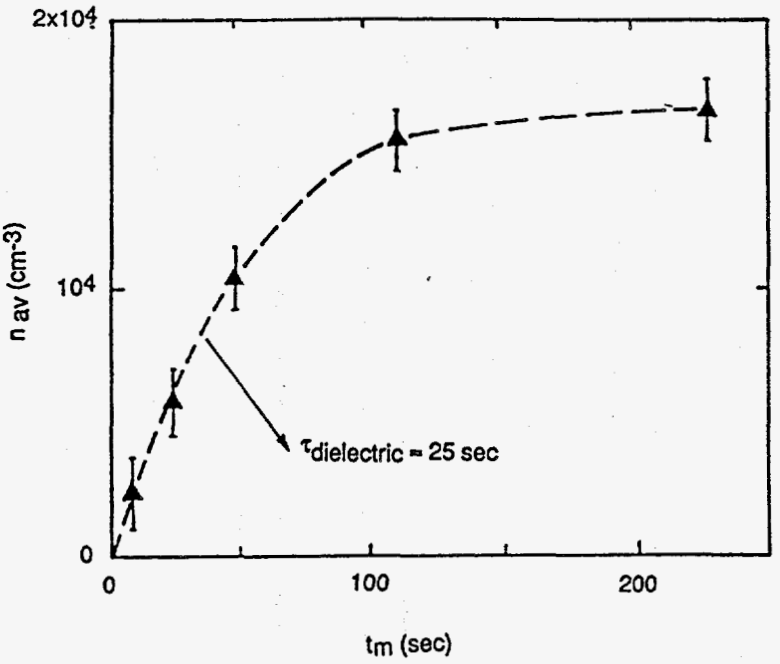

FIG. 3. Average electron density during a reversed current transient vs. reversed current peak time. (Reprinted from Levi *et al.*, 1985, with permission.)

2×10^{19} cm^{-3} for the 1.5 weight% SbI_3-doped sample and 2×10^{18} cm^{-3} for the 0.1 weight% SbI_3-doped sample.

Marschall and Milstein (1991) have studied the behavior of dark conductivity during plastic deformation. An increase in dark current of 15 to 140% was observed during plastic deformation, and it was attributed to the freeing of trapped charges with the motion of glide dislocations.

2. MOBILITY AND LIFETIME

a. Definition of Lifetime

Several characteristic times will be defined here for clarity. Transit time is the time it takes for a carrier to traverse the entire thickness of the detector. Trapping time is the average time it takes for a free carrier to be captured by a trap. After a carrier is trapped, it may contribute to conduction when it is detrapped. Detrapping time is the average time it takes for a carrier to escape from the trap. Lifetime is the average time it takes for a free carrier to recombine with an electron–hole either directly or through recombination centers. In semiinsulating materials, trapping and detrapping very often dominate the carrier transport, and it is difficult to distinguish between trapping time and lifetime. For instance, if an electron is trapped and remains trapped longer than the time of interest, it will have the same effect as if it has recombined with a hole (except for some long term effects such

as polarization and nonuniform electric fields). On the other hand, if the time of interest is longer than the detrapping time, then this electron is likely to be released into the conduction band and contribute to the conductivity. In the latter case, the effect of trapping is to produce an effective mobility of the carriers that is lower than the intrinsic mobility, as was discussed earlier in Section I. In this chapter, lifetime is loosely used as the average time it takes for the carriers to recombine or be trapped and remained trapped during the time of interest. In x-ray or gamma ray detection, the time of interest is usually the time constant of the shaping network, which defines the time the electronic system will spend collecting any charges induced by an incident x-ray or gamma ray photon.

b. *Relationship with Detector Performance*

The charge collection efficiency, η, is one of the most important factors to consider when designing x-ray or gamma ray spectrometers. It is related to peak broadening in x-ray spectra by the equation (Slapa *et al.*, 1976)

$$\Delta E_{\text{col}} = \alpha(1 - \eta)(E_{\text{ph}})^{1/2} \tag{13}$$

where ΔE_{col} is the FWHM of the x-ray peak in eV contributed by incomplete charge collection, α is a constant equal to 4.7×10^5 $(\text{eV})^{1/2}$, and E_{ph} is the energy of the incident x-ray photon in eV.

When nuclear radiations are detected by semiconductor detectors, carrier mobility and lifetime of the material determine the charge collection efficiency and carrier mobility and electric field determine the transit time. The charge collection efficiency is given by (Schieber *et al.*, 1978)

$$\eta = \frac{\lambda_e}{L}\left[1 - \exp\left(-\frac{L - x}{\lambda_e}\right)\right] + \frac{\lambda_h}{L}\left[1 - \exp\left(-\frac{x}{\lambda_h}\right)\right] \tag{14}$$

where x is the distance from the negative electrode of the charge sheet generated by the incident energetic photon and $\lambda_{e,h}$ are the mean drift lengths of electrons and holes, respectively. For electrons, λ_e is defined as

$$\lambda_e = \frac{\mu_e \tau_e V}{L}. \tag{15}$$

For gamma rays that penetrate deeply in HgI_2 detectors (x may be anywhere between 0 and L), the charge collection efficiency is close to unity only when the mean drift lengths of both types of carriers are much longer than the detector thickness. For shallow penetrating x-rays, most of the carriers are generated close to one electrode and only one type of carrier must traverse the detector. In this case, the thickness of the detector has to be smaller than the mean drift length of

the relevant carrier to achieve charge collection efficiency close to 1. In HgI_2 crystals, electrons have much higher mobilities than holes, and although electron lifetime is usually not very different from that of holes, the entrance electrodes of HgI_2 x-ray detectors are always biased negatively so that the electrons traverse the detector. The transit time (for electrons) is approximately given by

$$t_r = \frac{L^2}{\mu_e V}. \tag{16}$$

To reduce peak broadening and shifting due to incomplete charge collection, either the applied voltage is increased or the detector thickness is reduced. Thus there is a tradeoff between detector active volume (or efficiency) and the energy resolution of the detector. Present day HgI_2 detectors have been limited to a thickness of about 0.4–5 mm primarily because of the short mean drift length of holes. Finally, the charge collection efficiency given in Eq. (14) assumes that the shaping network has a time constant longer than the transit time of electrons and holes.

c. *Summary of Experimental Techniques*

Several techniques have been employed to measure electron and hole mobilities, lifetime, and mobility–lifetime products; and some of the results are summarized here. The techniques can be divided into transient and nontransient methods. The transient methods are basically time of flight measurements, and they can be further categorized into current and charge transient techniques. Several sources of excitation have been used, such as α particles, x-ray photons, electron bursts, or photoexcitation by lasers. In the current transient method, high level excitation sources such as electron bursts or laser pulses are used, so it is possible to have space charge limited (SCL) current as well as space charge free (SCF) current. All the transient techniques can potentially determine the electron and hole mobilities and lifetimes.

The nontransient methods include x-ray or α particle spectra methods, photocurrent, photo-Hall effect measurements, and the photomagnetoelectric (PME) effect. The energy spectrum and photocurrent methods can only determine the mobility-lifetime product. Photo-Hall effect measurements can determine the Hall mobility of carriers if the conduction is primarily by one type of carrier. HgI_2 is highly resistive, and although Ag and Cu dopants can lower the resistivity by a few orders of magnitude, the resistivity is still too large for conventional Hall effect measurements. As a result, most studies of Hall mobility employ carrier generation by photons. This technique is thus limited by the availability of single carrier conduction, which can be achieved by suitable excitation wavelength and intensity. The photomagnetoelectric measurement can determine the dependence of carrier lifetime on the illumination intensity and anisotropy of carrier transport.

In the current transient method, an above bandgap excitation source is used to generate a certain amount of charge near one electrode. A current transient can

then be measured as the charges traverse the thickness of the device under the influence of the applied voltage. If the generated charge is near the positively biased electrode, only holes will flow under the influence of the electric field and contribute to the current transient. In this case, the carrier transport properties of holes can be studied. Similarly, if the charge is generated near the negatively biased electrode, the transport properties of electrons can be studied. From an analysis of the waveform of the current transient, the carrier mobility and lifetime are determined. Currents in a semiinsulating material can be divided into space charge free and space charge limited currents. The criteria to determine whether a current is SCF or SCL is the total number of charges in the material. If the total charge in the material is much smaller than the charge on the electrode of the device (capacitance times applied voltage), it will not affect the electric field significantly and the current is considered space charge free. On the other hand, if the total charge in the material is much greater than the capacitor charge, the electric field in the device is determined mainly by the distribution of these charges and the current is space charge limited. Cho *et al.* (1975) have summarized the theoretical background which describes a current transient in a semiconductor under the assumption of uniform applied electric field.

i. Space Charge Free. Without trapping,

$$i(t) = \begin{cases} \dfrac{Q_0}{t_r} & 0 < t < t_r \\ 0 & t > t_r \end{cases}. \tag{17}$$

With trapping but negligible detrapping,

$$i(t) = \begin{cases} \dfrac{Q_0}{t_r} \exp\left(-\dfrac{t}{\tau}\right) & 0 < t < t_r \\ 0 & t > t_r \end{cases}. \tag{18}$$

With both trapping and detrapping,

$$i(t) = \begin{cases} \dfrac{Q_0}{t_r}\left[\tau + \tau_d \exp\left(-\dfrac{\tau_d + \tau}{\tau_d \tau} t\right)\right] & 0 < t < t_r \\ \dfrac{Q_0 t_r}{2\tau_d \tau} \exp\left(-\dfrac{t}{\tau_d}\right) & t > t_r \end{cases} \tag{19}$$

where $i(t)$ is the current as a function of time, Q_0 is the total charge generated, τ_d is the detrapping time, and τ is the lifetime of the carriers.

Current pulse shapes for the three SCF cases are shown in Fig. 4. Since SCF current is easy to establish and interpret, most of the measurements of current transient belong to this regime. As can be seen from Fig. 4, it is possible to determine the carrier transit time if the lifetime is not very short compared with the transit time so that the leading edge of the pulse is well defined. From the transit

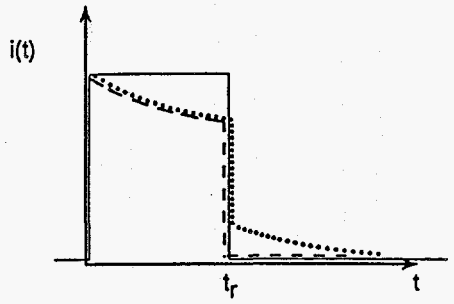

FIG. 4. Space charge free current pulse shapes: trap free case (solid line); trapping without detrapping (dashed line); trapping with detrapping (dotted line). (Reprinted with permission from Cho *et al.* 1975. ©1975 IEEE.)

time, the carrier drift velocity can be calculated by $v_d = L/t_r$. When the applied bias is varied, the drift velocity can be measured as function of the applied electric field. The slope of a plot of v_d vs E, in the linear region, gives the carrier mobility. It is also possible to determine the lifetime from the current pulses if there is considerable decay of the current magnitude within the transit time. From Eq. (18), the current decays exponentially if detrapping is negligible. If $\ln[i(t)]$ vs. Δt is plotted, the lifetime can be determined from the slope.

ii. Space Charge Limited. The SCL currents can be divided into two cases, those with infinite reservoirs and those with finite reservoirs of carriers. Examples of waveforms are drawn in Fig. 5 for the cases of infinite and finite reservoirs. It

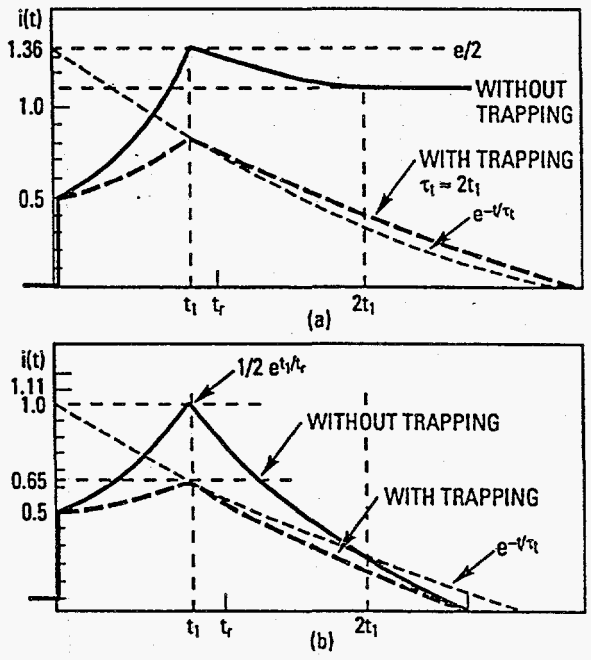

FIG. 5. Space charge limited current pulse shapes: trap free case (solid lines); trapping case (dashed lines); (a) infinite reservoir, (b) finite reservoir just sufficient to make the electric field zero at the electrode where the injection takes place at $t = 0$. (Reprinted with permission from Cho *et al.* 1975. ©1975 IEEE.)

should be noted that the current reaches maximum at a time of $t_1 \cong 0.787t_r$. Under typical bias conditions, it is possible to satisfy the SCL condition only with intense excitation such as photoinjection with laser pulses or electron beam bursts. For example, for a detector with a capacitance of 10 pF and bias of 100 V, the number of charges on each electrode is about 10^{10}. If it is assumed that an energy of 5 eV is necessary to generate an electron–hole pair by an incident α particle, a 5.8 MeV (^{244}Cm) α particle can only generate about 1×10^6 electron–hole pairs. Thus typical x-ray and gamma ray photons to be detected by HgI_2 spectrometers can generate only SCF current pulses.

From the pulse shape of the SCL current, it is also possible to measure the transit time, since the current peaks at $t_1 \cong 0.787t_r$. Determination of lifetime from SCL current is more difficult. It should be noted, however, that identifying whether a current is SCF or SCL is important, because if t_1 in the SCL current is mistaken as the transit time, an error of more than 20% may be introduced.

In the charge transient method, the charge induced by the transient current is measured. The properties of electrons and holes can be studied separately depending on the polarity of the bias in a manner similar to the current transient method. The advantage of this method is that it is closely related to x-ray detection. The technique simply uses a digital storage oscilloscope to monitor the output transient of a charge sensitive preamplifier. The excitation is usually either α particle or x-ray, and the current is SCF under typical experimental conditions. The charge transient is given by the integration of the current transient with respect to time. Using the current of the SCF case (without detrapping), the collected charge as a function of time is given by

$$Q(t) = \begin{cases} Q_0 \dfrac{\tau}{t_r}\left[1 - \exp\left(-\dfrac{t}{\tau}\right)\right] & t < t_r \\ Q_0 \dfrac{\tau}{t_r}\left[1 - \exp\left(-\dfrac{t_r}{\tau}\right)\right] & t > t_r \end{cases} \tag{20}$$

If the transit time is shorter than the lifetime, there is a sharp turn in the charge transient when the charges reach the electrode. Thus, the carrier drift velocity may be obtained by applying a voltage high enough so that transit time is short compared with lifetime and can be measured. On the other hand, if the applied field is small enough so that the lifetime is much shorter than the transit time, the lifetime may be determined by plotting $\ln[1 - Q(t)/Q(\infty)]$ vs t.

The x-ray spectra and photocurrent methods are able to give a rough estimate of mobility–lifetime product, either by analyzing the charge collection efficiency as a function of the applied electric field or the shape of x-ray photopeaks as discussed later. If the excitation is near one electrode, electrons or holes can be studied separately by varying the polarity of the applied bias. In an energy dispersive spectrum of x-rays, the position of the peak will initially increase with an increasing applied field because of increased charge collection efficiency and then

saturate to a constant value as the charge collection efficiency approaches unity. The charge collection efficiency at a given applied field is calculated by taking the ratio of the peak position to the saturated peak position in the x-ray spectrum. In photocurrent measurements, the current is measured as a function of the applied voltage. The current is assumed to be directly proportional to the charge collection efficiency and will thus saturate as the applied field is increased, in a similar manner as the measured position of the x-ray photopeak increases with the applied field. If the charges are generated close to one electrode and surface recombination is negligible, the charge collection efficiency is given by

$$\eta = \frac{\mu\tau E}{L}\left[1 - \exp\left(-\frac{L}{\mu\tau E}\right)\right]. \tag{21}$$

Since L is known, the measured η as a function of applied bias can be fit with Eq. (21) using $\mu\tau$ as a parameter. The best fit will thus give an estimate of mobility–lifetime product. A simpler method can also be used to roughly estimate the mobility–lifetime product. If the applied electric field is $E_{\eta=0.5}$ when the charge collection efficiency is 0.5, the mobility–lifetime product is then

$$\mu\tau = 0.63\frac{L}{E_{\eta=0.5}}. \tag{22}$$

This method has been widely used to estimate mobility–lifetime product in HgI_2 detectors. However, if surface recombination is present and significant, the mobility–lifetime product obtained with this technique will be underestimated (Levi, Schieber, and Burshtein, 1983a). When surface recombination is present, the charge collection efficiency is given by

$$\eta' = \frac{\mu E}{\mu E + s}\frac{\mu\tau E}{L}\left[1 - \exp\left(-\frac{L}{\mu\tau E}\right)\right] \tag{23}$$

where s is the surface recombination velocity. In the general case, $E_{\eta=0.5}$ is related to the surface recombination velocity and mobility–lifetime by

$$E_{\eta=0.5} \approx \frac{s}{\mu} + 0.63\frac{L}{\mu\tau}. \tag{24}$$

If the surface recombination is negligible $L/\tau >> s$, Eq. (24) reduces to Eq. (22). If the surface recombination dominates $L/\tau << s$, then

$$E_{\eta=0.5} = \frac{s}{\mu}. \tag{25}$$

It can be seen that, if surface recombination is significant, it is not possible to determine the mobility–lifetime product from the charge collection efficiency measured as a function of the applied field alone.

Another method to estimate the mobility–lifetime product from x-ray spectra is by examining the shape of an x-ray peak (Llacer *et al.*, 1974). An x-ray peak in the energy dispersive spectrum can be calculated as follows. The charge collection coefficient is a function of the position of interaction x as shown in Eq. (14). The probability of an x-ray photon interacting with the detector at x is given by (assuming the x-ray is incident from the negative electrode)

$$P(x) = \mu_{ph} \exp(-\mu_{ph} x) \tag{26}$$

where μ_{ph} is the photoelectric absorption coefficient. If $P(x)$ is plotted as function of η, one obtains the calculated x-ray spectrum (without pulse shaping). Note that in general η is a function of x (position) in contrast to the special case discussed in Eqs. (21) and (23). For HgI_2 under typical bias (Llacer *et al.*, 1974), the electron is completely collected and the only parameter in the plot is the mobility–lifetime product of holes (assuming μ_{ph} is known). By fitting the calculated spectrum to the measured one, the $\mu\tau$ product for holes can be obtained. Since the calculation actually fits the energy peak broadening due to incomplete collection of holes, the x-ray used should have a high enough energy that it penetrates into the bulk so that surface recombination is small.

The conventional measurement of Hall mobility in materials of high resistivity is difficult in both measurement and data interpretation (Look, 1983). Modified techniques (photo-Hall effect) have been employed to study carrier mobility in photoconducting insulators such as diamond and alkali halides (Redfield, 1954; Klick and Maurer, 1951). In these techniques, illumination is used to generate charge carriers. However, measurements of mobilities are limited to those conditions where single carrier conduction can be achieved by the illumination. Photomagnetoelectric experiments involve the measurement of photocurrents with and without the presence of a magnetic field as a function of excitation wavelength (Roosbroeck, 1956; Gartner, 1957; Zitter, 1958).

d. Room Temperature Measurements and Effects of Excitation Intensity

Measurements of mobility, lifetime and their product for electrons and holes at room temperature are summarized in Table I. The mobility generally agrees among different workers and techniques. The lifetime measured by different techniques varies considerably, sometimes by orders of magnitude. The measured values of lifetime obtained from the current transient method are usually smaller than those measured by the charge transient method. One likely reason for the large variation in values for lifetime is the varying quality of the crystals used. Another more subtle explanation for this variation is that lifetime is a function of carrier

TABLE I

SUMMARY OF MEASUREMENTS OF MOBILITY AND LIFETIME IN HgI_2 AT ROOM TEMPERATURE

Reference	μ_e (cm^2/V-sec)	τ_e (μsec)	$\mu_e\tau_e$ (cm^2/V)	μ_h (cm^2/V-sec)	τ_h (μsec)	$\mu_h\tau_h$ (cm^2/V)	Method
Martin, Bach, and Guetin, 1974	75-90	>0.1	$>6 \times 10^{-6}$	15	0.03	5×10^{-8}	a
Minder *et al.*, 1974	100	0.1	1×10^{-5}	4	0.01	4×10^{-6}	a
Ottaviani, Canali, and Quaranta, 1975	100						a
Watt and Cho, 1976	100			3.5	0.15	5.3×10^{-7}	b
Malm, 1972	70		$1-10 \times 10^{-5}$	4		$1-10 \times 10^{-6}$	b
Ponpon *et al.*, 1974	100			3			b
Swierkowski, Armantrout, and Wichner, 1974	94		1×10^{-4}	1		1×10^{-5}	b
Llacer *et al.*, 1974	120				3	1.1×10^{-6}	b, c
Beyerle *et al.*, 1983	100	>200	$>2 \times 10^{-2}$	6	15	9.10^{-5}	b
Roth *et al.*, 1987	97	3	2×10^{-4}	4	4.3	1.7×10^{-5}	b
Schieber *et al.*, 1978			4×10^{-5}			4×10^{-6}	c
Burshtein, Akujieze, and Silberman, 1986			3×10^{-4}			2.8×10^{-4}	d

Methods: a. current transient method; b. charge transient method; c. energy spectra method; d. photocurrent method.

concentration, which varies significantly in semiinsulating materials where the densities of both types of carriers generated by extrinsic excitation are much higher than those at equilibrium. A strong dependence of lifetime on injection level has actually been confirmed by photomagnetoelectric measurements. The lifetime of electrons was found to depend on the excess electron density with an exponent varying between -0.33 and -0.63 (Manfredotti *et al.*, 1977a; Adduci *et al.*, 1977). The lifetime of holes was found to depend on the excess hole density with an exponent of -1 (Adduci *et al.*, 1977). In a current transient measurement, the number of charges generated is most likely larger than that generated by a single α particle or x-ray photo used in the charge transient method so that the preceding explanation seems reasonable. Since the measurements in which α particle or x-ray excitation is used are more closely related to the operation of HgI_2 detectors, the values obtained from these measurements are probably more meaningful.

e. *Effects of Temperature, Crystallographic Orientation, and Stoichiometry*

Minder *et al.* (1974) measured electron and hole mobilities as a function of temperature using an electron excited current transient method. Both electron and hole mobilities were found to decrease with increasing temperature, and the experimental results are shown in Fig. 6. For electrons, the temperature dependence

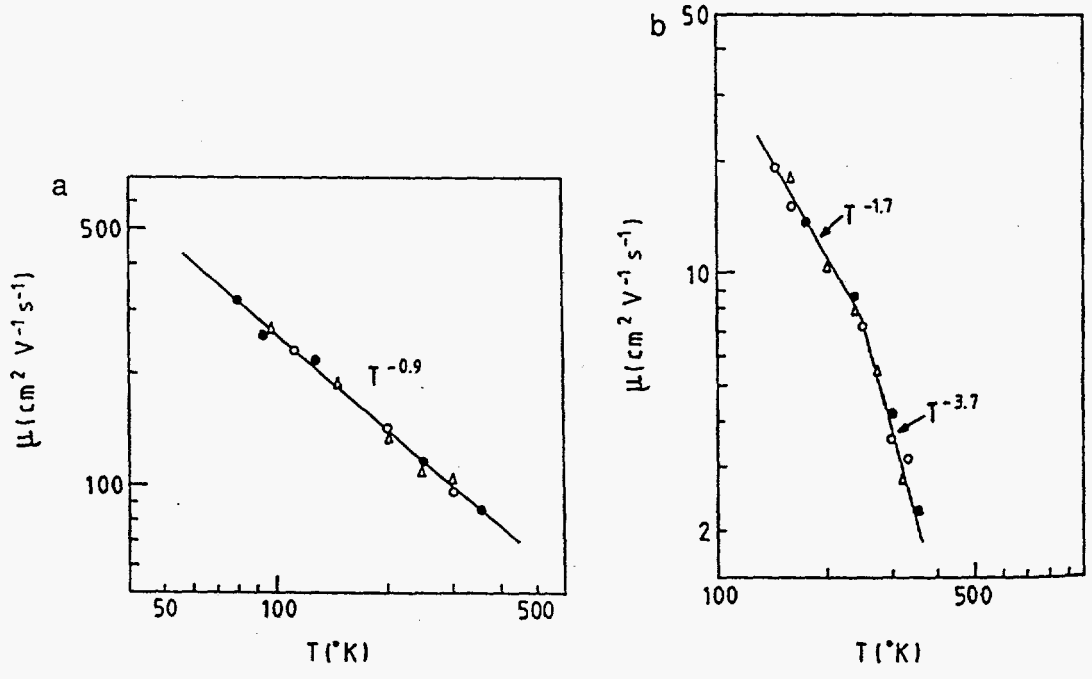

FIG. 6. Temperature dependence of the (a) electron [o, 243μ; Δ, 55μ; •, 260μ] and (b) hole [o, 30μ; •, 40μ; Δ, 55μ] mobility parallel to the c-axis. (Reprinted with permission from Minder *et al.*, 1974 and the American Institute of Physics.)

is given by

$$\mu_{e\parallel} \propto T^{-0.9} \qquad 114 < T < 300 \text{ K} \tag{27}$$

where $\mu_{e\parallel}$ is the electron mobility in the direction parallel to the c-axis. For holes, the temperature dependence is given by

$$\mu_{h\parallel} \propto \begin{cases} T^{-1.7} & 140 < T < 240 \text{ K} \\ T^{-3.7} & 240 < T < 350 \text{ K} \end{cases} \tag{28}$$

Using photo-Hall measurement, Bloch *et al.* (1977) found that above a temperature of 40 K, their samples always showed electron conduction irrespective of the wavelength of illumination. The Hall mobility of electrons measured as a function of temperature agrees well with the drift mobility of electrons measured by Minder *et al.* (1974). This indicates that the drift mobilities measured by the transient techniques probably reflect the intrinsic properties of the crystal with no trap controlled motion. The intrinsic mobilities of free carriers in a compound semiconductor like HgI_2 are typically controlled by scattering of carriers by non-polar optical phonons, polar optical phonons, and acoustic phonons. From the temperature dependence of the electron and hole mobilities, Minder, Ottaviani, and Canali, (1976) proposed that electrons are scattered mainly by polar optical phonons, while holes are mainly scattered by non-polar optical phonons. Below 15 K, single carrier conduction by holes was identified if the illumination wavelength was shorter than 5300 Å. Hole mobility decreases with temperature from 3 to 10 K by about one order of magnitude. Because of the low density of phonons at low temperatures, the scattering of carriers is either by neutral or ionized impurities. Hole mobility as high as 60,000 cm^2/V-sec was measured at low temperatures (Bloch *et al.*, 1977).

HgI_2 crystals have a layered structure (perpendicular to c-axis) with very weak bonding between layers (T. W. James and Milstein, 1983). It is therefore expected that the carrier mobilities will also depend on the crystallographic orientation. Ottaviani *et al.* (1975) and Minder *et al.* (1976) measured electron mobility using electron excited current transients in the direction parallel and perpendicular to the crystallographic c-axis at various temperatures. The electron mobility parallel to the c-axis was found to be always greater than that perpendicular to the c-axis. The mobility of electrons perpendicular to the c-axis has a slightly different temperature dependence with a value of 65 cm^2/V-sec at room temperature (Minder *et al.*, 1976). The data was well described by the expression

$$\mu_{e\perp} \propto T^{-0.8} \qquad 80 < T < 300 \text{ K} \tag{29}$$

where $\mu_{e\perp}$ is the electron mobility in the direction perpendicular to the c-axis. From photomagnetoelectric measurements at room temperature, Manfredotti *et al.* (1977a,b) calculated the hole mobility perpendicular to the c-axis to be about

23 cm^2/V-sec, which is higher than the value of 4 cm^2/V-sec typically observed parallel to the c-axis. From Hall measurements at low temperature (below 15 K), Bloch *et al.* (1977) also found that, for specimens of high purity where the scattering is due to neutral impurities, the Hall mobility of holes in HgI_2 is higher in the direction perpendicular to the c-axis. Even though the absolute value varies considerably, the mobility of holes along the c-axis was always measured to be about a factor of 2 smaller than that perpendicular to the c-axis. The higher mobilities perpendicular to the c-axis suggests fabricating detectors with charge transport in this direction. However, we have found that this leads to prohibitively high leakage currents possibly due to a high level of injection from the contacts.

Using current transient methods and taking precautions to ensure a high field existing in the sample, Martin *et al.* (1974) observed a maximum electron drift velocity at an applied field of 80 kV/cm and a negative differential electron mobility of about -5 cm^2/V-sec after 80 kV/cm. The maximum differential electron mobility is at 50 kV/cm. However, Ponpon *et al.* (1974) observed no negative differential electron mobility up to 100 kV/cm in their measurements using an α particle charge transient method.

Electron and hole transport properties in HgI_2 with deviations from stoichiometry were studied in an attempt to establish correlations between detector quality and stoichiometry. Whited and van den Berg (1977) measured the mobility–lifetime product of electrons and holes in undoped HgI_2 and crystals doped with iodine or mercury. It was found that iodine doping deteriorates the mobility–lifetime product of electrons and mercury doping decreases the mobility–lifetime product of holes. The results are shown in Table II. It should be noted, however, that these composition variations are only relative. The exact stoichiometric point is not known. Hermon *et al.* (1991) have also attempted to correlate the lifetime

TABLE II

MOBILITY–LIFETIME PRODUCT OF ELECTRONS AND HOLES IN HgI^2 WITH VARIOUS DEVIATIONS FROM STOICHIOMETRY[a]

Stoichiometry	$\mu_n\tau_n$ (cm^2/V)	$\mu_p\tau_p$ (cm^2/V)
Heavily I_2	3×10^{-6}	3×10^{-7}
Lightly I_2	4×10^{-6}	8×10^{-7}
Typical	7×10^{-5}	4×10^{-7}
Lightly Hg	3×10^{-4}	$<10^{-7}$
Lightly Hg	5×10^{-4}	$<10^{-8}$
Heavily Hg	4×10^{-4}	$<10^{-7}$
Best	2×10^{-4}	1.5×10^{-5}
High Purity	1×10^{-4}	2.6×10^{-6}

[a]Reprinted with permission from Whited and van den Berg, 1977. ©1977 IEEE.

TABLE III

DEVIATIONS FROM STOICHIOMETRY AND CHARGE TRANSPORT PROPERTIES OF HgI_{2+x} CRYSTALS[a]

Hg Excess ±7 (mole ppm)	I_2 Excess ±5 (mole ppm)	τ_n (μsec)	τ_p (μsec)	FWHM at 6 keV (eV)	FWHM at 660 keV (keV)
0	143	3.0	2.4	660	>30
0	134	2.8	2.0	572	>30
0	55	6.6	2.6	425	>30
0	13	7.0	3.8	444	<30
0	0	5.4	1.7	393	>30
0	0	12.0	4.5	358	<30
0	0	15.0	3.5	385	<30
0	0	3.6	2.5	460	>30
14	0	6.3	6.1	402	<30
32	0	5.3	1.4	362	>30
619	0	1.2	0.65	876	>30
652	0	1.2	0.40	984	>30

[a]Reprinted with permission from Hermon *et al.*, 1991 and Elsevier Science Publishers.

of electrons and holes with stoichiometry and energy resolution of detectors. The stoichiometry was measured by Raman spectroscopy for excess mercury and by spectrophotometric methods for excess iodine. Their findings are summarized in Table III. Excess mercury was found to reduce both electron and hole lifetimes. Excess iodine decreases the electron lifetime but does not have a significant effect on holes.

3. EFFECTIVE MASS

Effective mass is another important parameter pertaining to carrier transport. The calculation of effective conduction and valence band densities of states and carrier thermal velocities requires the knowledge of the effective masses of electrons and holes. Effective masses are also expected to depend on crystallographic orientation because of the anisotropy of HgI_2 crystals. Also related to the effective masses of electrons and holes is the reduced effective mass. Values of the effective masses of electrons, holes, and reduced mass vary considerably in the literature, depending on the methods used to obtain these values. Cyclotron resonance measurements, optical spectra of excitons, and band structure calculations have all been employed.

Using cyclotron resonance measurements at 1.2 K, Bloch *et al.* (1977, 1978) have obtained values of effective masses for electrons and holes in the direction perpendicular to the c-axis. The reported $m_{n\perp} = (0.37 \pm 0.02)m_0$, and $m_{p\perp} = (1.03 \pm 0.10)m_0$. From the anisotropy of the mobilities, the effective masses of

electrons and holes parallel to the c-axis may be deduced, since the mobility and effective mass are related by

$$\frac{\mu_\parallel}{\mu_\perp} = \left(\frac{m_\parallel}{m_\perp}\right)^n \tag{30}$$

where n depends on the nature of scattering. Bloch *et al.* (1978) used $\mu_{h\parallel}/\mu_{h\perp} = 0.5$ (below 15 K). They also used a value of $n = -1$ for holes since the scattering by neutral impurities is dominant at low temperature and the matrix elements for neutral impurity scattering are isotropic. For electrons, $\mu_{e\parallel}/\mu_{e\perp} = 1.4$ (80 to 300 K) (Minder *et al.*, 1976) was used. Since the temperature dependence of electron mobility suggests the presence of both polar optical phonon scattering and acoustic deformation potential scattering, n may range between -1.5 for the former and -2.5 for the latter. The inferred effective masses of electrons and holes in the direction parallel to the c-axis are $m_{e\parallel} = (0.31 \pm 0.03)m_0$ and $m_{h\parallel} = (2.06 \pm 0.50)m_0$.

Exciton masses may be deduced from optical spectra; however, these values vary among authors. This may be due to the different dielectric constant used in obtaining the exciton masses from the Rydberg constant or due to the polaron nature of the excitons in HgI_2, which makes the interpretation of the optical spectra more difficult. Anedda *et al.* (1977) performed wavelength modulated reflectivity spectra at 2 K to study the exciton properties of HgI_2. By using low frequency indices of refraction of $n_\perp = 2.39$ and $n_\parallel = 2.23$, exciton masses obtained from the optical spectra are $m_{r\perp} = 0.3m_0$, and $m_{r\parallel} = 0.51m_0$. Goto and Nishima (1979) obtained the following exciton masses: $m_{r\perp} = (0.68 \pm 0.1)m_0$, and $m_{r\parallel} = (1.2 \pm 0.1)m_0$ from resonant Brillouin scattering measurements. Novikov and Pimonenko (1971) obtained an exciton mass of $0.13m_0$ from ordinary ($E\|c$) absorption spectra.

Turner and Harmon (1989) computed the effective masses to be $m_{e\perp} = 0.11m_0$, $m_{e\parallel} = 0.15m_0$, $m_{p\perp} = 0.17m_0$, and $m_{p\parallel} = 0.78m_0$ based on band structure calculations. Yee, Sherohman, and Armantrout (1976) obtained $m_{e\perp} = 0.4m_0$, $m_{e\parallel} = 0.4m_0$, $m_{p\perp} = 3.5m_0$, and $m_{p\parallel} = 1.2m_0$ from pseudopotential calculations of band structure, although an incorrect unit cell was used in their calculation. Bloch *et al.* (1978) pointed out that the measured effective mass may be different from those calculated because of the strong interaction between carriers and phonons to form polarons. Additional comments regarding the effective masses of HgI_2 as obtained from optical techniques are contained in Chapter 5 on optical properties of HgI_2.

III. Deep Levels

Since no dopants have been found that can lower the resistivity of HgI_2 considerably, shallow levels in HgI_2 are either highly compensated or they do not exist. Cu and Ag can reduce the resistivity of HgI_2 by a few orders of magnitude from 10^{13} Ωcm but this is still extremely high compared with resistivities on the order

of 10^4 Ωcm or lower in typical doped semiconductors. Deep levels are therefore more important in affecting the performance of HgI_2 nuclear spectrometers. Recombination centers will reduce the lifetime of charged carriers while deep donor or acceptor levels may cause large variations in the electrical properties of HgI_2 from sample to sample. Defects in general also scatter carriers and reduce their mobility, especially at the lower temperatures, where carrier phonon scattering is smaller. Trap levels affect device performance in several important ways. First, if the trapped carrier remains trapped for longer than the charge collection time of the electronic system of the detector, then incomplete charge collection results. Second, even if the trapped carriers are released within the charge collection time and therefore collected, the effective mobility is lowered due to the trap controlled motion. This leads to an increase in the transit time, which in turn means that longer charge collection times are required to obtain complete charge collection. Third, trapped carriers modify the electric field in the device, which can cause polarization effects, giving rise to reliability problems in detectors. Polarization effects are typically observed as a change of efficiency, energy resolution, or charge collection efficiency with time. Finally, trapping near the metal contact–HgI_2 interface may alter the characteristics of the electrode and the charge transport across the electrode–HgI_2 interface.

A number of experimental techniques have been employed to study deep levels and their effects on device performance. A majority of these studies utilize thermally stimulated current (TSC) methods. Other techniques used include dark current transient methods, I–V measurements, photocapacitance measurements, photoresponse, and photoinduced transient spectroscopy (PITS).

1. THERMALLY STIMULATED CURRENT TECHNIQUE

The TSC technique has been widely used to characterize carrier traps in semi-insulating or dielectric materials (Bube, 1960; Milnes, 1973; Look, 1983). The measurements are performed as follows. The sample is biased and cooled to a low temperature (usually to liquid nitrogen temperature of 77 K) while in the dark. The sample is then illuminated by an optical excitation source such as a laser or an incandescent lamp to generate electron–hole pairs and fill the carrier traps to be studied. After illumination, the temperature of the sample is raised gradually while the dark current is measured. As the temperature is increased, the trapped carriers are more likely to be released into their respective bands and contribute to the dark current, while at the same time, the number of trapped carriers is decreased. The competition of these two processes results in peaks in the dark current when measured as a function of temperature. The TSC processes can be described by carrier rate equations. If there is no direct transfer of carriers between traps, the equations are (for electrons) (Look, 1983)

$$\frac{dn_{ti}}{dt} = -n_{ti}\left(\frac{g_{i0}}{g_{i1}}\right)N_c\sigma_{ei}v_{th}\exp\left(-\frac{\Delta E_{ti}}{kT}\right) + n(N_{ti} - n_{ti})\sigma_{ei}v_{th} \quad (31)$$

and

$$\frac{dn}{dt} = -\frac{n}{\tau_e} - \sum_i \frac{dn_{ti}}{dt} \tag{32}$$

where n_{ti} is the density of electrons trapped in the ith trap, N_{ti} is the density of the ith trap, σ_{ei} is the capture cross section of the ith trap, and g_{i0} and g_{i1} are the degeneracy factors of the ith traps when they are empty and occupied, respectively. These last parameters are generally assumed to be unity and thus ignored.

If the TSC peaks are well resolved so that each peak can be analyzed separately, the summation can be ignored (the index i can also be dropped), and simplified equations can be applied to each trap. Assuming the lifetime of the carrier is much smaller than the time scale over which the carrier density actually changes, i.e., $|dn/dt| << |n/\tau_n|$, the two simultaneous differential equations can be simplified to

$$n = \frac{\tau_e e_e n_t}{1 + \frac{\tau_e}{\tau_t}\left(1 - \frac{n_t}{N_t}\right)} \tag{33}$$

$$\frac{dn_t}{dT} = -\frac{1}{\beta} \frac{e_e n_t}{1 + \frac{\tau_e}{\tau_t}\left(1 - \frac{n_t}{N_t}\right)} \tag{34}$$

where β is the heating rate. The trapping and detrapping times are defined as the reciprocal of capture and emission probabilities (c_e and e_e), and they are given by

$$\tau_t = \frac{1}{c_e} = \frac{1}{N_t \sigma_e v_{\text{th}}} \tag{35}$$

$$\tau_d = \frac{1}{e_e} = \frac{1}{N_c \sigma_e v_{\text{th}} \exp\left(-\frac{\Delta E_t}{kT}\right)}. \tag{36}$$

a. Methods to Analyze TSC Spectra

Many methods have been developed over the years to analyze TSC data with the goal of obtaining relevant information such as activation energy, carrier capture rate, and trap concentration. A summary of these methods follows.

i. Heating Rate Method. Equations (33)–(34) may be solved for two limiting cases (Bao *et al.*, 1991a). Since the temperature dependence of τ_e, σ_e, and μ_e are

generally not very strong, it can be assumed that their temperature dependences follow a power law; i.e., $\tau_e = \tau_{e0}T^{\lambda}$, $\sigma_e = \sigma_{e0}T^{\alpha}$, and $\mu_e = \mu_{e0}T^{\gamma}$. The temperature dependences of the effective density of states of the conduction band and the thermal velocity are $N_c = N_{c0}T^{1.5}$ and $v_{th} = v_{th0}T^{0.5}$, where N_{c0} and v_{th0} are functions of electron effective mass.

In the first case, if the trapping time is much longer than lifetime (slow trap), i.e., $\tau_t >> \tau_e$, it can be shown that the temperature T_m at which the current peak occurs is related to the trap parameters and heating rate β by

$$\ln\left[\frac{T_m^{4+\alpha}}{\beta(T_m)}\right] = \frac{\Delta E_t}{kT_m} - \ln\left[\frac{kN_{c0}\sigma_{e0}v_{th0}}{\Delta E_e + kT_m(2 + \alpha + \gamma + \lambda)}\right]. \quad (37)$$

In the second case, if the trapping time is much shorter than the lifetime (fast trap), i.e., $\tau_t << \tau_e$, the solution for T_m can be shown to satisfy the following equation

$$\ln\left[\frac{T_m^{3.5-\lambda}}{\beta(T_m)}\right] = \frac{\Delta E_t}{kT_m} - \ln\left[\frac{\frac{kN_{c0}}{N_t\tau_{e0}}}{\Delta E_t + kT_m(2 + \alpha + \gamma + \lambda)}\right]. \quad (38)$$

To obtain Eqs. (37)–(38), the derivation does not require the heating rate to be constant. It suffices to know the heating rate where each current peak occurs, as long as the heating rate is not too irregular a function of temperature so as to give multiple solutions for T_m. To utilize Eqs. (37)–(38), several TSC curves have to be obtained with different heating rates. Since a constant heating rate for the entire TSC spectrum is not required, it is more practical to vary the heating power and record the temperature where the current peak occurs and the heating rate at this temperature. By plotting the left-hand side of Eqs. (37)–(38) vs $1/kT_m$, the activation energy of the trap may be obtained from the slope. From the intercept of the plot with the x-axis, σ_e and $N_t\tau_e$ can be obtained for the fast and slow traps, respectively. The temperature dependences of lifetime and capture cross section and whether a trap is fast or slow, however, are usually not known. If the temperature dependences of lifetime and capture cross section are not very strong, it is generally acceptable to ignore them altogether. It can be shown that if $\Delta E_t > 20\ kT_m$ (usually true), a variation of α or λ by 2 results in about a 10% uncertainty in ΔE_t. As for the determination of $N_t\tau_e$ and σ_e, they appear in Eqs. (37)–(38) in a logarithm term. The values obtained for $N_t\tau_e$ and σ_e, usually contain a very large uncertainty due to small errors in the temperature measurements, and the effects of temperature dependences are small and can be ignored. In general it is not known whether a trap is fast or slow. The best that can be done is to obtain both $N_t\tau_e$ and σ_e by assuming the trap is either slow or fast, respectively, and then check the values obtained. If one of the parameters obtained this way is unreasonable, then one trapping speed of the center can be ruled out and the other parameter can typically be accepted. This illustrates the difficulty of obtaining parameters

such as $N_t\tau_e$ and σ_e from TSC data. In many cases, they are obtained under certain assumptions that may not be justified, and even if the assumptions are justified, the values contain large uncertainties simply due to the nature of the mathematical equations governing the TSC process.

ii. Delayed Heating Method. In this method, the traps are initially filled and the sample is held at some temperature for varied lengths of time so that some number of the traps are emptied. The TSC measurements are then performed (Stuck *et al.*, 1976) as a function of time after excitation. The total charge under the TSC peak is then a function of the waiting time and related to the detrapping time by

$$Q_{\mathrm{TSC}} \propto \exp\left(-\frac{t}{\tau_d}\right). \tag{39}$$

Since the detrapping time is related to the activation energy by Eq. (36), the activation energy and carrier capture cross section can be obtained by measuring τ_d at different temperatures and plotting $\ln(\tau_d)$ vs. $1/kT$.

iii. Initial Rise Method. From Eq. (33), it can be seen that if the trapping time and lifetime are not strong functions of temperature, then the carrier density is a strong function of temperature through the emission rate. Therefore, at the onset of a TSC peak, when n_t has not changed very much, the activation can be obtained by plotting $\ln(n)$ vs $1/kT$ regardless of whether the trap is fast or slow (Gelbart *et al.*, 1977). When using this method, it is sometimes necessary to employ a "cleaning" technique. This technique is useful when two TSC curves are close together in temperature so that the initial rise of the high temperature peak is superimposed with the falling edge of the lower temperature peak. It is possible to significantly reduce the interference of the lower temperature peak by holding the sample at a temperature just below the high temperature peak for a period of time, so that the carriers trapped in the centers related to the low temperature peak are released. The TSC spectrum taken after this cleaning procedure will include less of the low temperature peak and the initial rise of the high temperature peak can be measured with greater accuracy.

iv. Fermi Level Method. In this method, the trap is assumed to be in equilibrium with its corresponding band (fast trap). The trap energy level is assumed to be at the Fermi level and the activation energy can then be obtained by (Bube, 1957)

$$\Delta E_t = kT_m \ln\left(\frac{N_c}{n_{\max}}\right) \tag{40}$$

where n_{max} is the carrier density at the current peak. After the activation energy is obtained this way, the capture cross section can then be calculated using Eq. (37).

v. Grossweiner's Method. If retrapping is ignored (slow trap) and $\Delta E_t / kT_m > 20$, $N_c \sigma_n v_{th} > 10^7$/sec, the trap parameters can be estimated by (Grossweiner, 1953)

$$\Delta E_T = \frac{1.51 kT_m}{T_m - T_-} \tag{41}$$

where T_- is the temperature where the TSC is half of its maximum on the low temperature side. In this method, β should be constant over the TSC current peak. The capture cross section can then be calculated by

$$\sigma_e = \frac{3T_- \beta \exp\left(\frac{\Delta E_t}{kT_m}\right)}{2N_c T_m (T_m - T_-)}. \tag{42}$$

vi. Luschick's Method. If retrapping is assumed dominant, the trap activation energy may be estimated by (Stuck *et al.*, 1976)

$$\Delta E_t = \frac{kT_m^2}{T_+ - T_m} \tag{43}$$

where T_+ is the temperature where TSC is half of its maximum on the high temperature side.

vii. Numerical Method. From Eqs. (33)–(34), it can be seen that the shape of TSC curve for n/N_t is a function of only the heating rate β, activation energy ΔE_t, capture cross section σ_e, and trap density and lifetime product $N_t \tau_e$. Since a TSC curve is not symmetric about its maximum, T_-, T_m, and T_+ can be measured and used to obtain ΔE_t, σ_e, and $N_t \tau_e$ numerically. In this method, the heating rate is measured as a function of temperature and used in Eqs. (33)–(34) to solve the TSC curve numerically with three parameters: ΔE_t, σ_e, and $N_t \tau_e$. The temperatures at which the TSC current reaches maximum (T_m^c), and half-maximum on the low (T_-^c) and high (T_+^c) temperature side of the peak can be obtained from this calculation as a function of the trap parameters (Bao *et al.*, 1992):

$$\begin{aligned} T_-^c &= T_-^c (\sigma_e, \Delta E_t, N_t \tau_e) \\ T_m^c &= T_m^c (\sigma_e, \Delta E_t, N_t \tau_e) \\ T_+^c &= T_+^c (\sigma_e, \Delta E_t, N_t \tau_e). \end{aligned} \tag{44}$$

From the TSC spectrum, temperatures at which the measured TSC current is maximum and half-maximum can also be obtained and are labeled as T_-^m, T_m^m, and T_+^m. With these values, a three dimensional root finding problem is set up using the Newton–Raphson method (Press *et al.*, 1988) with three unknowns: σ_e, ΔE_t, and $N_t\tau_e$. The three equations are

$$\begin{aligned} T_-^c(\sigma_e, \Delta E_t, N_t\tau_e) - T_-^m &= 0 \\ T_m^c(\sigma_e, \Delta E_t, N_t\tau_e) - T_m^m &= 0 \\ T_+^c(\sigma_e, \Delta E_t, N_t\tau_e) - T_+^m &= 0. \end{aligned} \tag{45}$$

It should be noted that if a trap is either slow or fast, the TSC curve is dependent on only two trap parameters, ΔE_t and σ_e for the former and ΔE_t and $N_t\tau_e$ for the latter. In these situations, Eq. (45) will result in overdetermination, and care should be taken to identify which of the three trap parameters cannot be determined. A limit can then be established for this parameter, and the nature of the trap (i.e., fast or slow) can also be identified.

b. TSC Spectra of Mercuric Iodide

Stuck *et al.* (1976) made TSC measurements on samples prepared by chemical etching in an aqueous KI solution and cleaving. In the samples prepared by etching, one peak at 217 K was found and attributed to a hole trap since it was present only when the bias polarity of the illuminated contact was positive (see Fig. 7a). After comparing several techniques, a mean value of 0.45 eV for the activation energy and 4×10^{-15} cm^2 for the capture cross section were obtained. In the samples prepared by cleaving, two more peaks at 114 and 145 K were observed under both polarities of bias as shown in Fig. 7b. The activation energies for these two traps were estimated to be about 0.19–0.22, and 0.22–0.24 eV, respectively.

The effects of iodine and mercury doping on the TSC spectra of HgI_2 were investigated by Whited and van den Berg (1977). Figure 8 shows TSC spectra from undoped (a), iodine doped (b), and mercury doped (c) samples. Several traps were observed at 81 K, 98 K (electron), 102 K (hole), 138 K (hole), 162 K (hole), and 180 K (hole). TSC peaks that appear in only one kind of sample were then attributed to native defects due to deviation from stoichiometry. A peak at 81 was observed in undoped samples, and it was attributed to iodine vacancy V_I. Two peaks at 89 and 220 K observed in heavily Hg doped samples were attributed to iodine vacancy V_{I2} and mercury interstitial I_{Hg}. A peak at 214 K in iodine doped samples was assigned to mercury vacancy V_{Hg}.

Tadjine *et al.* (1983) found seven peaks in their TSC spectra at temperatures of 100, 110, 125, 155, 173, 205, and 225 K. By correlating with the detector performance, it was found that the samples with an intense peak at 173 K exhibit fast polarization and poor resolution. A TSC spectrum is shown in Fig. 9a for such a

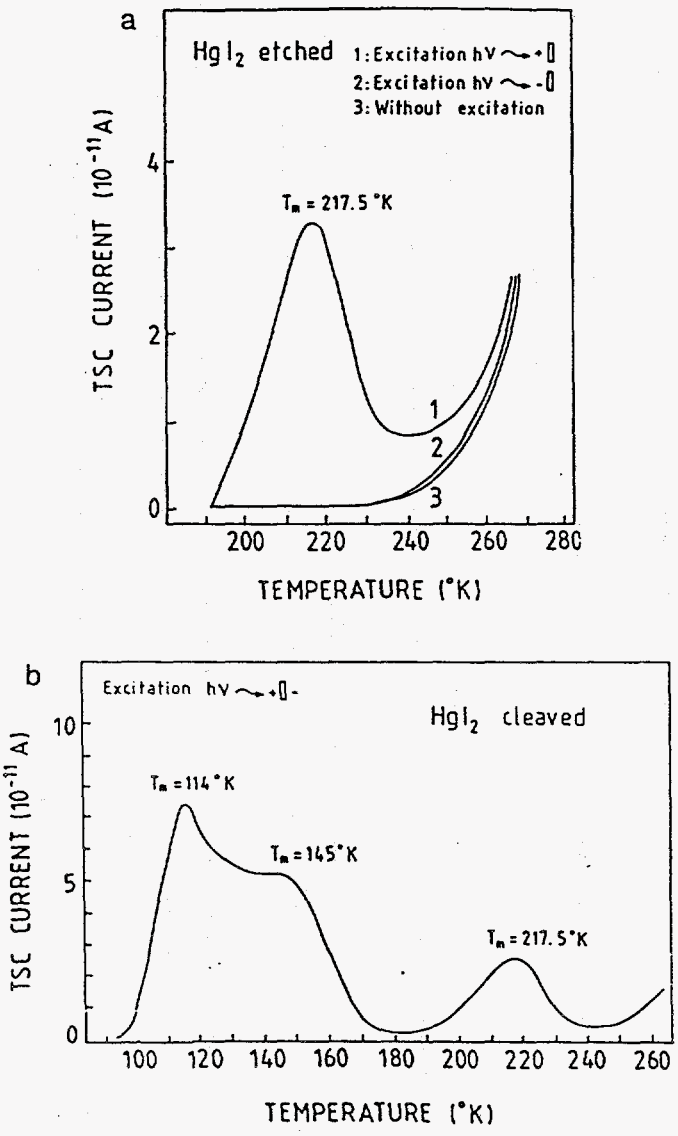

FIG. 7. TSC current in (a) etched and (b) cleaved HgI_2 samples. (Reprinted with permission from Stuck *et al.*, 1976 and the American Institute of Physics.)

sample. Samples with a low intensity peak at 173 K were found to produce good detectors (see the TSC spectrum shown in Fig. 9b).

Suryanarayana and Acharya (1989) have studied the effects of aging, baking, storage in I_2 vapor, and application of bias on TSC spectra of HgI_2. From Fig. 10a, as-grown crystals show two TSC peaks at 170 and 230 K. The crystals show two peaks at 170 and 252 K for aged samples and two peaks at 170 and 280 K for the baked samples. As can be seen in Fig. 10b, if a bias of 500 V is applied to the aged sample for 12 hr, the peak at high temperature disappears and the intensity of the peak at low temperature increases. For samples stored in iodine vapor, there is only one peak at 180 K in the TSC spectrum. The activation energies and capture cross section were obtained using the Fermi level method.

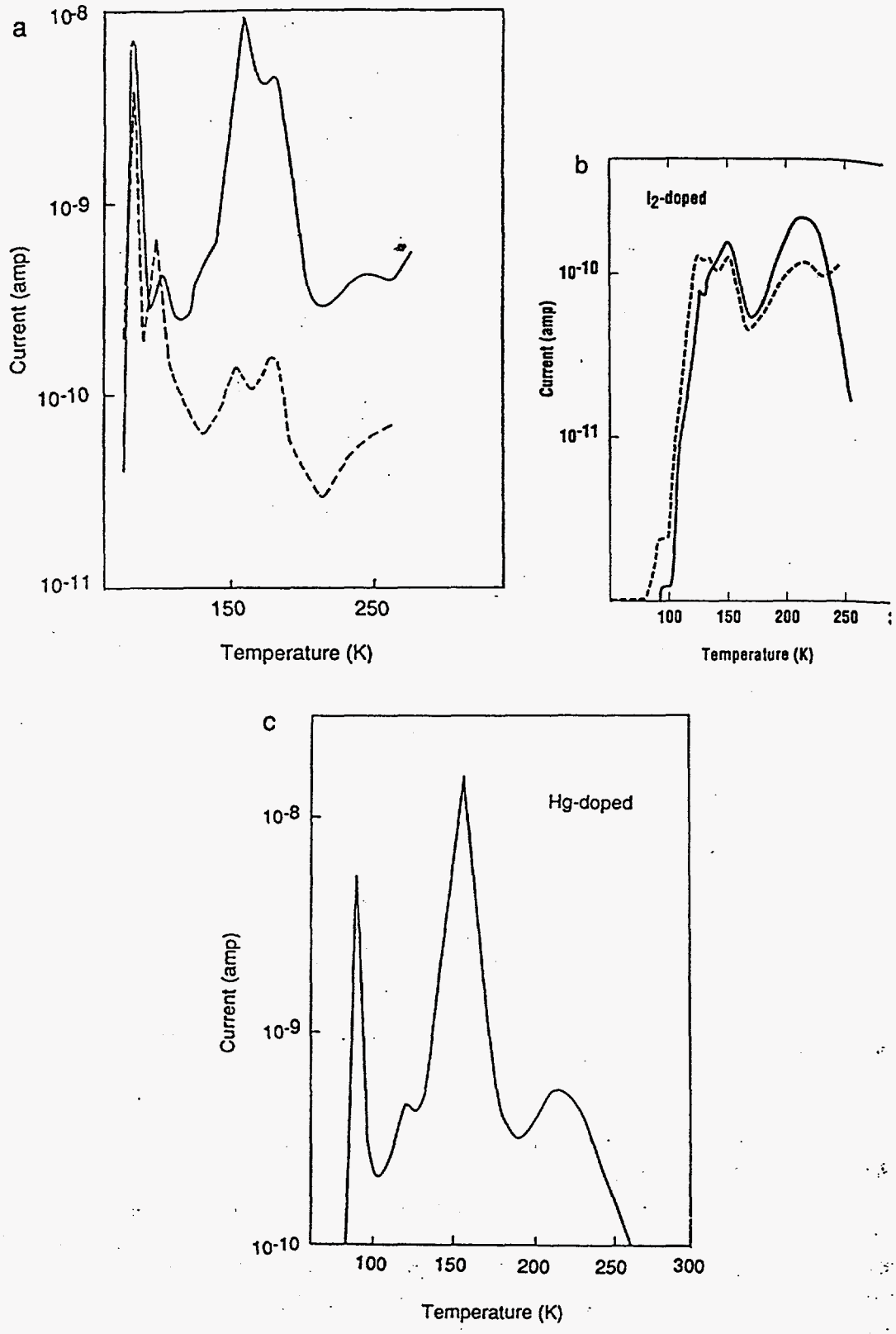

FIG. 8. (a) TSC of undoped crystal for both hole and electron traps (—, hole traps; ---, electron traps); (b) TSC of heavily iodine doped crystals for both hole and electron traps (---, hole traps; —, electron traps); (c) TSC of heavily mercury doped crystal. (Reprinted with permission from Whited and van den Berg, 1977. ©1977 IEEE).

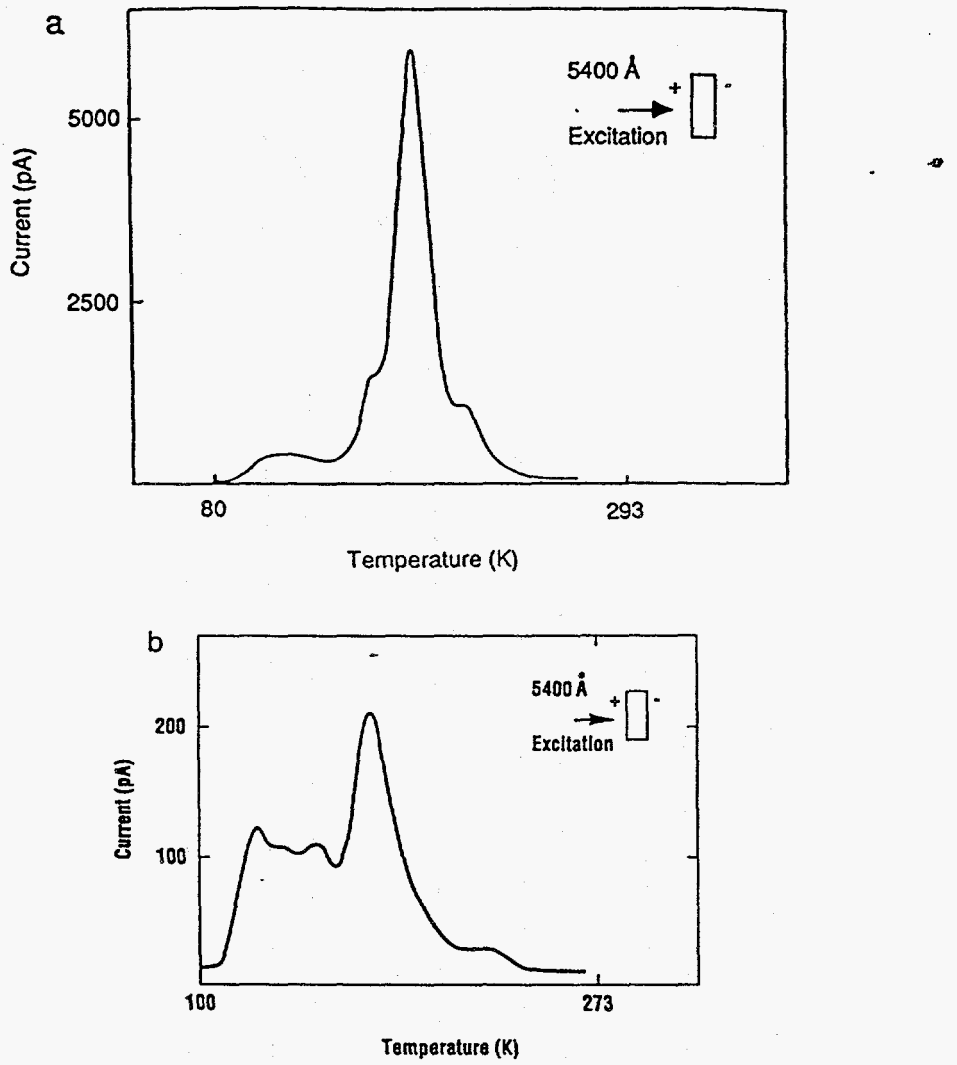

FIG. 9. (a) TSC spectrum of a crystal that makes detectors with fast polarization and very poor energy resolution; (b) TSC spectrum of a crystal that makes detectors with no polarization effect and very good energy resolution at values below 60 keV. (Reprinted with permission from Tadjine *et al.*, 1983 and Elsevier Science Publishers.)

Prolonged (~24 hr) illumination by monochromatic light (~5900 Å) at room temperature reduced the 203 K peak and increased the 170 K peak dramatically in the TSC spectra measured by Mohammed-Brahim (1981) (see Fig. 11). Accompanied by the emergence of the peak at 170 K, the x-ray detector will resolve the 59.6 keV photon from an Am-241 source. It was concluded that a direct correlation between the 170 K peak and improvement of nuclear detection exists.

Gelbart *et al.* (1977) have tried to identify whether a trap is fast or slow. The activation energy was obtained by the initial rise method and then compared with those obtained assuming retrapping is fast (Fermi level method) or slow (Grossweiner's method). Among the traps observed, those at 95, 132, and 178 K were

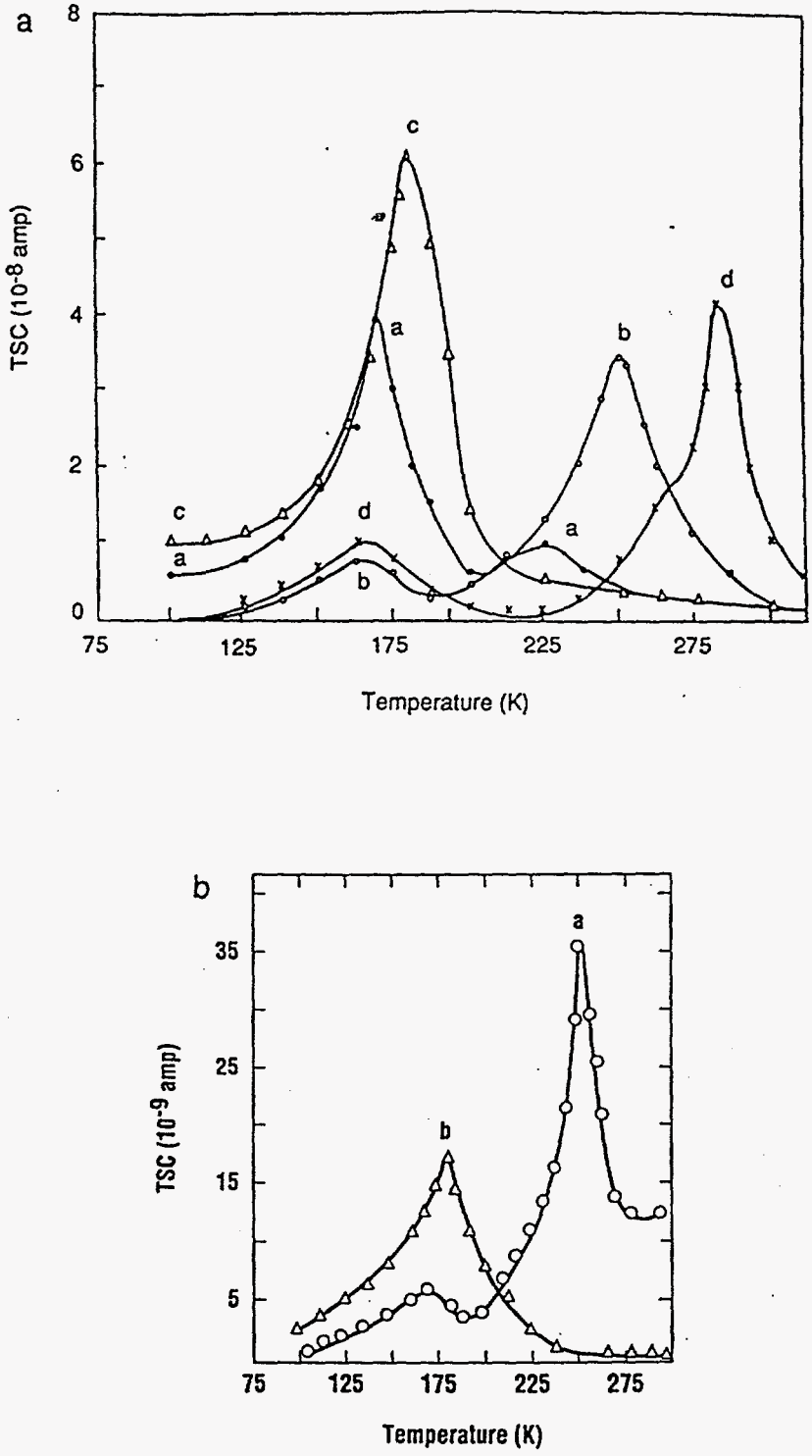

FIG. 10. (a) TSC spectra of HgI_2 crystals: *a* as-grown crystals, *b* aged samples, *c* as-grown crystal stored in iodine chamber, *d* as-grown crystal after baking at 350 K for 30 minutes; (b) TSC spectra of HgI_2 crystals: *a* aged samples, *b* same as *a* after application of dc bias 500 V for 12 hr. (Reprinted with permission from Suryanarayana and Acharya, 1989 and JOURNAL OF ELECTRONIC MATERIALS, a publication of the Minerals, Metals & Materials Society, Warrensdale, PA 15086.)

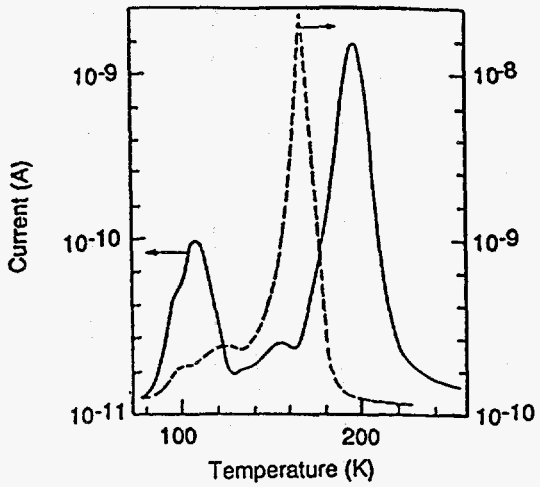

FIG. 11. Illumination effect on TSC spectra of a solution grown sample (from Mohammed-Brahim, 1981).

identified as slow traps, and those at 116, 144, and 200 K were identified as fast traps.

Blasi *et al.* (1978) have used the integrated area under each TSC peak to estimate the concentration of traps. If it is assumed that the traps are completely filled at low temperature, then the trap density may be estimated by

$$N_t = \frac{A_c}{qVG} \tag{46}$$

where A_c is the total integrated charge under a TSC peak in coulomb, V is the volume of the sample, and G is the photoconductive gain calculated for the steady state excitation of a photocurrent with magnitude equal to the TSC average current. The trap densities estimated for the two traps observed by the authors at 112 and 212 K are 3.5×10^{15} and 8.3×10^{15} cm^3. Hyder (1977) observed two TSC peaks at about 167 and 233 K in samples doped with Ag (about 3 ppm).

The effects of different contact materials on TSC were studied by Bao (1991). As can be seen in Table IV, the contacts have a dramatic effect on the TSC spectra. With the exception of samples contacted with Cu and Ag, where fast diffusion into HgI_2 bulk has been observed even at room temperature and therefore the effect may be due to the bulk, the variation of the TSC spectra with different contact materials is most likely due to the difference in the defects introduced by the interaction of the contact material with HgI_2 in the near-surface region. In fact, low temperature photoluminescence spectroscopy studies (Bao *et al.*, 1990, 1991a; R. B. James *et al.*, 1989, 1990) have shown that most of these contact layers modify the defect structure in the near surface region.

TABLE IV

EFFECT OF CONTACTS ON TSC SPECTRA OF HgI_2 (from Bao, 1991)

Contact		T_1	T_2	T_3	T_5	T_6	T_8	T_{10}
Cu	T_m(K)			116		161		
Ag	T_m(K)	90	96				212	
Al	T_m(K)	83		119	146	170		
Mg	T_m(K)				147	162	206	273
Au	T_m(K)						193	
Ni	T_m(K)	89			147	166	202	
In	T_m(K)	87		119	150	168		
Sn	T_m(K)				149	163		
Pd	T_m(K)				149	163		
Cr	T_m(K)				144	157	211	
ITO	T_m(K)		95	133	144	165	213	

Because the TSC data can be analyzed so many ways and TSC measurements themselves are very sensitive to experimental conditions such as excitation power, wavelength, sample geometry, illumination time, waiting time, heating rate, sample preparation, or contacts, it is difficult to compare results obtained from different workers. In addition, among the four parameters of activation energy, capture cross section, trap density, and lifetime product, it is possible to determine activation energy with only reasonable accuracy. The other parameters depend exponentially on activation energy and thus small uncertainties in the value of this parameter lead to large uncertainties in the other parameters. The reported values should be viewed as rough estimates in terms of order of magnitude and hence be used with caution. Peaks in TSC spectra obtained from several workers are summarized in Table V.

2. OTHER TECHNIQUES

Several other techniques have been employed to study deep levels in HgI_2. These techniques have not been correlated as well as TSC measurements to detector fabrication and performance. Brief reviews of isothermal current, photoinduced current transient spectroscopy, and photocapacitance spectroscopy follow.

a. Isothermal Current

When a voltage is applied to a HgI_2 sample, the dark current will decrease with time (Braatz and Zappe, 1984). This decay of current has been explained as due to the release of trapped carriers, which then drift under the applied electric field and are collected by the electrodes (Mellet and Friant, 1989). If retrapping is ig-

nored, the current is then given by (Micocci *et al.*, 1983)

$$I_d = \sum_i A_i \exp\left(-\frac{t}{\tau_{di}}\right). \tag{47}$$

By best fitting the decay of the dark current with time using Eq. (47), several detrapping times may be obtained. From the detrapping time, and assuming a typical capture cross section, the trap activation energy (assuming electron traps) can be estimated by

$$\Delta E_t = kT \ln(N_c \sigma_e v_{th} \tau_d). \tag{48}$$

Using this technique, Mellet and Friant (1989) studied the detrapping time in HgI_2 crystals grown either by solution or vapor phase and also crystals prepared with various surface treatments and deposited with a variety of contacts. Detrapping times from 0.68 to 40,000 seconds have been observed in these crystals, which correspond to trap activation energies from 0.67 to 0.96 eV.

b. Photoinduced Current Transient Spectroscopy

Alvarez and Saura (1990) have employed PITS to study traps in HgI_2. The technique and the interpretation of the data are very similar to deep level transient spectroscopy (DLTS), used widely in characterizing carrier traps and recombination centers in semiconductors. Instead of the typical boxcar integrators employed in DLTS, a two phase lock-in amplifier was used (Pons, Mooney, and Bourgoin, 1980). The basic idea, however, is still the same, in that a rate window is created and the transients are measured as a function of temperature. A peak will occur in the spectrum when the emission probability corresponding to the rate window was reached at a certain temperature. This corresponds to a measurement of the emission probability (related directly to the rate window) at the peak temperature. The position of the peak in terms of temperature will vary as the rate window is changed. A measurement of the shift in peak temperature as a function of rate window gives the emission probability as a function of temperature. By proper data analysis using Eq. (36), the trap activation energy and the capture cross section can be obtained. Using a modulated light source to create the necessary trap filling, Alvarez and Saura (1990) have observed five traps with activation energies 0.19, 0.22, 0.32, 0.44, and 0.49 eV. The capture cross sections range from 3.4×10^{-16} to 3.3×10^{-13} cm^2. The densities of the traps estimated from the amplitude of the current decay are from 4×10^{13} to 8×10^{14} cm^{-3}.

c. Photocapacitance Spectroscopy

Photocapacitance spectroscopy involves the measurement of ac capacitance under illumination as a function of the illumination wavelength. When the photon

TABLE V

TSC RESULTS FROM VARIOUS WORKERS

Reference		T_1	T_2	T_3	T_4	T_5	T_6	T_7	T_8	T_9	T_{10}	T_{11}
Bube, 1957	T_m(K)			129	142		172	196		222	267	293
	ΔE_t(eV)			0.34	0.38		0.45	0.51		0.59	0.77	
	Comments											
Whited and van den Berg, 1977	T_m(K)	81, 89	98	102	138		162	180	214	220		
	ΔE_t(eV)	V_1 & V_{22}					0.32					
	Comments		*e*	*h*	*h*		*h*	*h*	V_{Hg}, *e*	I_{Hg}, *h*		
Blasi *et al.*, 1978	T_m(K)		112						212			
	ΔE_t(eV)		0.17						0.45			
	Comments		*h*						*h*			
Gelbart *et al.*, 1977	T_m(K)	95	116		132	144	168	178	200			
	ΔE_t(eV)	.15–.23	.19–.28		.12–.29	.27–.35	.36–.49	.37–.51	.43–.54			
	Comments	Slow	Fast		Slow	Fast	Slow	Slow	Fast			
Suryanarayana and Acharya, 1989	T_m(K)						170	180		230	252	280
	ΔE_t(eV)						0.46	0.46		0.63	0.63	0.70
	Comments							I-strg			*Aged*	*Baked*

Hyder, 1977	T_m(K)						167			233		
	ΔE_t(eV)						0.26			0.73		
	Comments											
Bornstein and Bube, 1987	T_m(K)		102			143	159	170	196			
	ΔE_t(eV)		0.28			0.36	0.40	0.43	0.51			
	Comments											
Muller, Friant, and Siffert, 1978	T_m(K)	107	112	125		145	170	190	200	217	245	
	ΔE_t(eV)											
	Comments		*e*			*h*				*h*		
Tadjine *et al.*, 1983	T_m(K)	100	110	125		155	173		205	225		
	ΔE_t(eV)	0.16	0.28	0.32		0.40	0.45		0.50	0.59		
	Comments						Bad					
Stuck *et al.*, 1976	T_m(K)		114			145				217		
	ΔE_t(eV)		0.19			0.22				0.45		
	Comments		clv			clv				*h*		
Mohammed-Brahim, Friant, and Mellet 1983	T_m(K)	96(8)	112(5)	125	140	155(60)	170	185	204		252	275
	ΔE_t(eV)	.10–.13	.16–.19	.20–.23	.21–.26	.25–.30	.50–.59	.40–.44	0.43			
	Comments						Good					

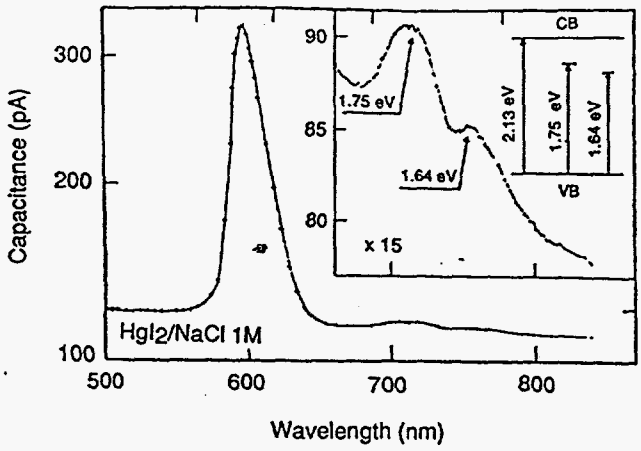

FIG. 12. Electrochemical photocapacitance spectroscopy spectrum and associated energy transitions for single crystal HgI_2 in 1 M NaCl. The back electrode is biased at +1 V. (Reprinted with permission from Burger *et al.*, 1989 and Elsevier Science Publishers.)

energy is equal to the activation energy of a deep center, the carriers are liberated from this deep center into the corresponding band edge. These carriers will redistribute under the bias either as free carriers or as trapped carriers in a different center or location. This changes the polarization of the sample and a capacitance peak is observed. Burger *et al.* (1989) observed three peaks using electrochemical photocapacitance spectroscopy (EPS). A NaCl electrolyte cell was used and the back carbon contact was biased +1 V. The measurement frequency was 1 kHz. The spectrum is shown in Fig. 12 along with an interpretation of the levels and transitions involved. The three peaks appear at photon energies of 2.13, 1.75, and 1.64 eV. Photocapacitance in a longer wavelength region was measured by Zolotarev *et al.* (1970). Three peaks at 0.54, 0.69, and 0.89 eV were observed. Since photo quenching also occurs at 0.69 and 0.89 eV (see the next section), these peaks are explained as due to the liberation of holes from traps.

IV. Photoconductivity

HgI_2 was one of the first materials used for studies of photoconductivity study (Nix, 1935). Bube (1957) reported a systematic investigation of photoconductivity of HgI_2. The high resistivity of HgI_2 makes many typical semiconductor characterization techniques difficult to perform and many measurements of the electrical properties of HgI_2 have relied on the application of light. These experimental techniques include current transient measurements, photocurrent, internal photoemission, photoresponse, TSC, PITS, photomagnetoelectric effect, photo-Hall effect, cyclotron resonance measurements, photoelectrochemical measurements, and photocapacitance measurements, many of which have been discussed above. In addition, illumination by light affects the performance of detectors, the length of time for HgI_2 to reach equilibrium, and the photocurrent generated by a primary

source (quenching effect). This section focuses on the use of photocurrent techniques to characterize HgI_2.

1. BEHAVIOR OF PHOTOCURRENT

Photocurrent measurements of HgI_2 show a maximum at wavelengths near the bandgap (see Fig. 13). Several explanations for this peak have been reported. The peak may be a result of significant surface recombination (Adduci *et al.*, 1977; Burshtein *et al.*, 1986; Bornstein and Bube, 1987) that reduces the photocurrent for the highly absorbing photon energies. As the wavelength of the incident light decreases near the bandgap, the photocurrent will first increase due to an increase in the absorption, and as the wavelength continues to decrease, more and more carriers will be generated near the surface region. Here they recombine quickly through surface states due to the high carrier density and do not contribute to the photocurrent. A second explanation is that the peak in photocurrent is due to exciton formation, which causes a resonant absorption at a wavelength slightly below the bandgap (Manfredotti *et al.*, 1977a,b). The exciton energy measured by

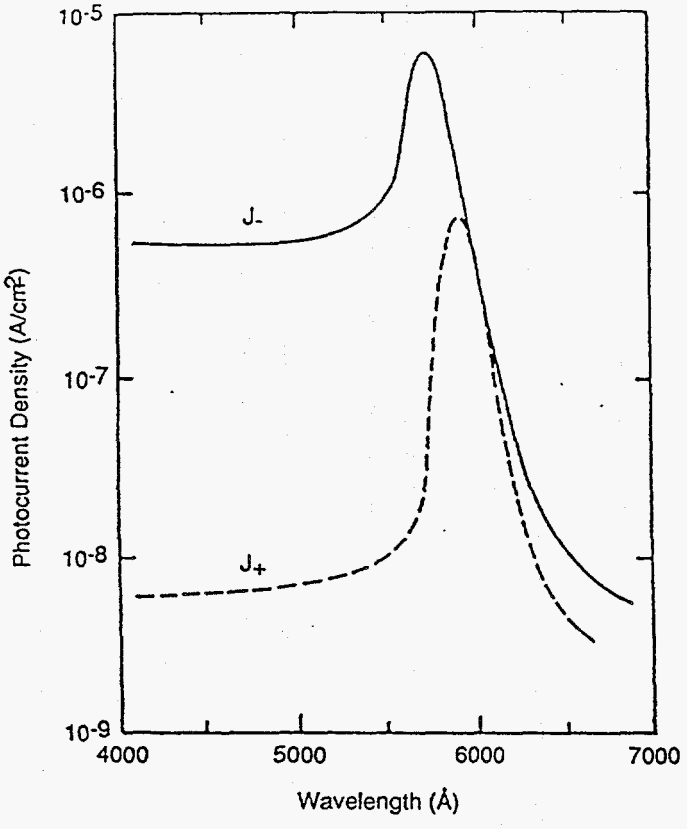

FIG. 13. Spectral response of photocurrent density for the photodetector cell with transverse geometry in which light and electric field are parallel; J^- is the photocurrent density when the illuminated surface is negative, and J^+ is the photocurrent density when the illuminated surface is positive. (Reprinted with permission from Borstein and Bube, 1987 and American Institute of Physics.)

Novikov and Pimonenko (1971) is about 29 meV, which is comparable to thermal energy at room temperature. However, for the excitons to contribute to the photocurrent, they have to dissociate and produce free carriers. The most likely process is to give their energy to trapped carriers that are then liberated to the corresponding band edge to contribute to the photocurrent.

Light spot scanning measurements conducted by Bube (1957) found that the photocurrent is limited mainly to a small region at or near the cathode; i.e., as the light spot is moved between the cathode and anode, the current is maximum when the spot is near the cathode. The voltage drop also occurs mostly near the cathode. This probably indicates that the photocurrent is due mainly to an electron contribution. When the light spot is near the cathode, more electrons will move toward the anode, resulting in more electrons in the active region and a higher photocurrent.

When photovoltaic short circuit current is measured as a function of wavelength, another interesting phenomenon has been observed (Bao, 1991). The setup for this measurement is shown in Fig. 14, where the direction of the current is also displayed. This configuration is used to measure the barrier height of the back contact and will be discussed in Subsection V.1. The current spectral response is shown in Fig. 15. It can be noted that the short circuit current reverses its direction twice as the wavelength of the excitation light increases. At short wavelengths, the current is negative (region I); as the wavelength increases, the current reverses its direction to positive (region II); and then changes back to a negative direction for all long wavelength responses (regions III and IV). These observations can be explained in terms of the dependence of carrier lifetime on the excess carrier density (or excitation intensity) (also refer to Subsection II.2.d). If the lifetimes of electrons and holes depend on the excess carrier with the form $\tau_e \propto \Delta n^{\alpha}$ and $\tau_h \propto \Delta p^{\lambda}$, then the excess carrier density will be related to the carrier generation rate per unit volume G by

$$\Delta n \propto G^{1/(1-\alpha)} \qquad \Delta p \propto G^{1/(1-\lambda)}. \tag{49}$$

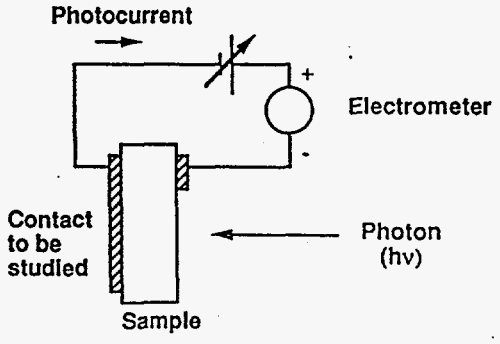

FIG. 14. Experimental setup for the photoresponse measurements. The configuration is designed to measure the barrier height of the back contact.

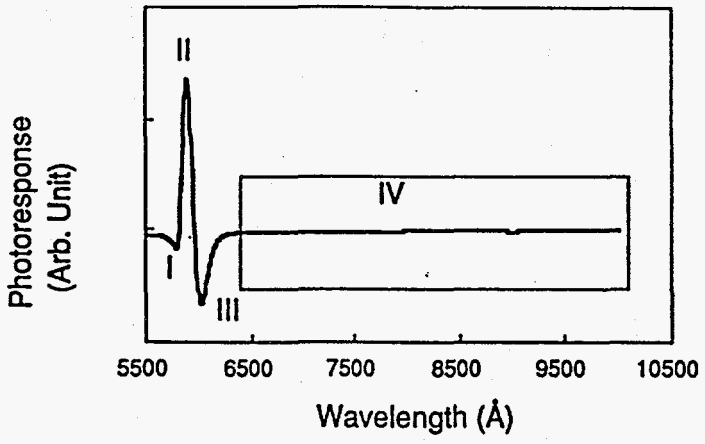

FIG. 15. Photoresponse from a palladium contacted sample measured at room temperature. The four regions labeled I, II, III, and IV are believed to arise from different processes in the sample.

If $\alpha > \lambda$, then $\Delta n < \Delta p$ at low G, and $\Delta n > \Delta p$ at high G. If $\alpha < \lambda$, the opposite is true. From photomagnetoelectric measurements by Adduci *et al.* (1977) and Manfredotti *et al.* (1977a), $\alpha = -0.33$ to -0.63, and $\lambda = -1$, thus, the contribution to the photocurrent is expected to be by holes in the low intensity excitation region and by electrons in the high intensity excitation region. Figure 15 can be explained as follows, using the band diagram shown in Fig. 16. In region I, absorption is primarily near the surface because of the above bandgap excitation; thus the generation rate is relatively high and the conduction is primarily by electrons. The sample then behaves like an n-type semiconductor and a positive space charge will be formed near the front surface. This results in a band bending as shown in Fig. 16 and causes the current to be negative. As the wavelength increases to region II, the absorption is still mainly near the front surface, but the generation rate per volume decreases as the absorption coefficient is reduced. The conduction becomes p-type and the band bending and current reverses its direction. As the wavelength is further increased to region III and IV, the excitation is more uniform across the sample, and the conduction is p-type. Because of the configuration of the measurements setup shown in Fig. 14, the back contact is more efficient than the front contact, which is away from the illumination spot. The short circuit current is then a result of the band bending near the back contact as shown in Fig. 16, and the current will reverse its direction again. At even longer wavelengths in region IV, the carriers are no longer generated from band to band transition but from transition between the band edge and the electrical contact as shown in Fig. 16. A similar observation was made when the intensity of the illumination is changed (Blasi *et al.*, 1978). The current reverses its sign as the intensity of the illumination is increased. The conduction was found to be p-type at low intensity and n-type at high intensity.

When photocurrent is measured (with above bandgap light) as a function of temperature, several things were observed. Below 15 K, the photocurrent de-

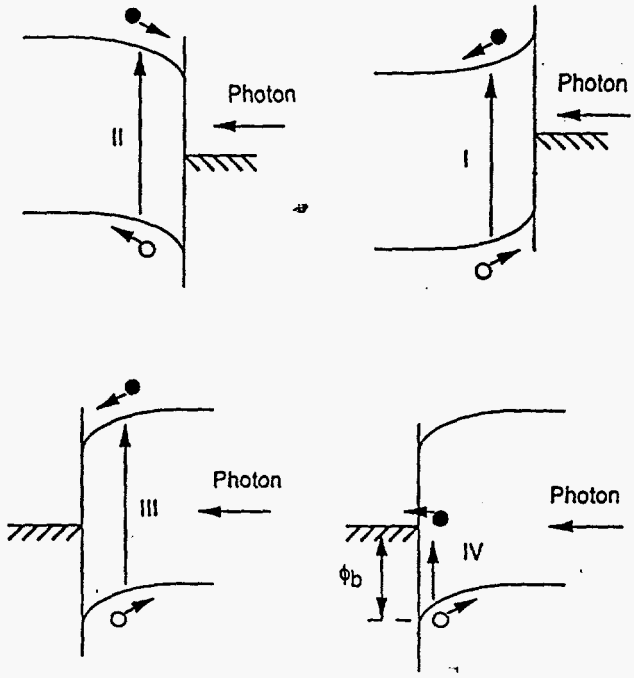

FIG. 16. Band diagrams illustrating the four processes that result in the short circuit current photocurrent.

creased rapidly with increasing temperature. At this temperature, the photocurrent was due mainly to holes, whose mobility also decreases rapidly with increasing temperature. Thus, the decrease in photocurrent is controlled by mobility, not carrier lifetime (Bloch *et al.*, 1977). At higher temperatures (>15 K), the photocurrent usually shows current peaks at several temperatures. These changes can not be accounted for by the temperature dependence of the mobility only, rather, the lifetime of carriers also changes. Bube (1957) has attributed the current peaks as due to the changeover of certain centers from the role of recombination centers to trapping centers as the Fermi level moves toward the center of the bandgap and crosses these centers. This changeover may decrease the hole occupancy on this level and the holes are redistributed to other more efficient recombination centers, thereby reducing the lifetime of the conducting carriers (electrons in this case). The decrease in photocurrent with increasing temperature is referred to as a "thermal quenching" effect. The activation energy of the center and the temperature of the peaks is related to the carrier density by

$$\ln(n_{\max}) = \ln\left(\frac{N_v \sigma_n}{\sigma_e}\right) - \frac{\Delta E_t}{kT_m}. \tag{50}$$

It can be seen that, if the carrier density is varied, the current maximum will appear at a different temperature. Since the carrier density can be varied by changing the excitation power, it is possible to obtain information of the trap by measuring the current peak position as a function of illumination power. The photocurrent

peaks are shifted to higher temperatures as the excitation power is increased. Bube (1957) obtained an excitation energy of 0.51 eV and a σ_h/σ_e ratio of 10^3 for the photocurrent peak at about 193 K. Mohammed-Brahim *et al.* (1983) observed several photocurrent peaks at 80, 120, and 200 K with corresponding excitation energies of 0.21, 0.36, and 0.5 eV.

2. PHOTOCURRENT QUENCHING

Photoquenching was observed in HgI_2 by Zolotarev *et al.* (1970), Mohammed-Brahim *et al.* (1983) and Saura and Tognetti (1975). In these studies, a photocurrent was first measured using a primary excitation near the bandgap. A secondary illumination with below bandgap photon energy was then applied, and the photocurrent was measured and compared with the one obtained without secondary illumination. For some photon energies of the secondary illumination, the photocurrent will be quenched. If the photon energy of the secondary illumination is varied, the spectral response of photo quenching (percentage of photocurrent loss due to the secondary illumination) can be measured.

As shown in Fig. 17, Saura and Tognetti (1975) observed a sharp decrease as the photon energy of the secondary light source increases to 0.56 eV. A second quenching was observed as the photon energy of the secondary light source approaches 0.75 eV. The quenching disappeared when the photon energy of the secondary source was increased beyond 1.75 eV. The authors explained the spectra

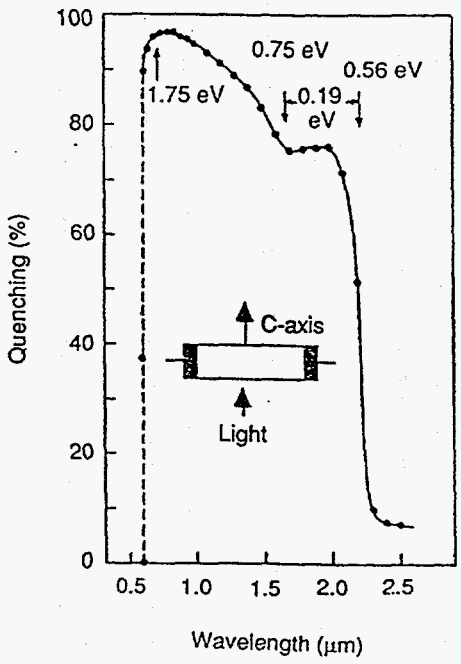

FIG. 17. Infrared quenching spectrum of HgI_2 at 77 K. The number of quenching photons was the same at all wavelength: $V = 70$ V, $\lambda_{prim} = 5400$ Å (from Saura and Tognetti, 1975).

as due to a center 0.56 eV above the valence band edge. The first rise in quenching is due to the transfer of a hole from this trap to the valence band. The second rise is attributed to the transfer of holes from the same center to the second valence band located 0.19 eV below the valence band maximum. The onset of the disappearance of photo quenching at 1.75 eV corresponds to the beginning of transfer of electrons from this center to the conduction band edge. A similar quenching effect was observed by Mohammed-Brahim *et al.* (1983), except for the location of the onset of quenching. Mohammed-Brahim *et al.* (1983) observed the first rise in quenching at 0.4 eV and the second one at 0.48 eV. The second quenching was present up to photon energies of about 1.77 eV. The quenching peaks observed by Zolotarev *et al.* (1970) are located at 0.60 and 0.89 eV. These two photon energies correspond to two of the three photocapacitance peaks observed by the same authors.

The photo quenching effect may be explained in a similar way as the thermal quenching effect. It is due to the transfer of trapped carriers into the corresponding band edges and the capture by a more efficient recombination center, which leads to a reduction in the lifetime of the free majority carriers of the other type. Since the photoconductivity is most likely to be due to electron conduction (especially when the excitation power is not too low), the energies levels obtained by these quenching measurements are most likely relative to the valence bands.

V. Surface Effects

Surface effects play an important role in the applications of HgI_2 nuclear detectors. Injecting contacts and surface conduction increase the leakage current and are undesirable for HgI_2 detectors. The recombination rates near the surface are generally very different from the bulk of a crystal because of the presence of surface states. This effect influences performance considerably, since high recombination rates result in incomplete charge collection. Therefore, proper choice of the electrical contact material, method of contact deposition, and surface treatment are extremely important in the fabrication of HgI_2 detectors.

1. Electrical Contacts

The nature of the charge transport across the contact–semiconductor interface depends on the work functions of the metal and semiconductor. It is also very sensitive to the presence of surface states, which are often created by chemical interactions between the metal and the semiconductor and by various processing procedures used to attach the electrical contacts. Contacts made from a variety of materials have been tried on HgI_2 detectors. Several of them have been successfully used for fabricating HgI_2 nuclear detectors or photodetectors. These include

palladium, colloidal carbon, gold, germanium, transparent indium–tin oxide (ITO), conducting hydrogel, and saltwater. Palladium and carbon are usually the contact materials of choice for most x-ray and gamma ray detector spectrometers. With the exception of carbon, which is often applied to HgI_2 in the form of colloidal carbon, hydrogel, or saltwater, these contact materials are deposited either by thermal evaporation or sputtering. During thermal evaporation or sputtering a HgI_2 crystal is exposed to vacuum and heat treatment, and it often interacts with the contact material of choice during the deposition procedures. Because HgI_2 is a soft, reactive material with a high vapor pressure, all of the processing conditions are potential sources of defects in the near-surface region, leading to the incorporation of undesirable surface states.

Metals that form barriers to carrier transport on HgI_2 have been measured by two methods, internal photoemission and a dark current method. Other techniques such as the capacitance method are difficult to apply to HgI_2 due to its high resistivity.

The experimental setup for the internal photoemission measurement has already been shown in Fig. 14. To avoid absorption in the contact, the illumination is shone through the opposite site of the contact to be studied. The photocurrent under a bias or in a short circuit condition is measured as function of incident photon energy. In the long wavelength region (labeled as IV in Fig. 15), the photocurrent is due to the photoelectric effect where carriers are excited from the electrical contact into the semiconductors (see Fig. 16). The photoresponse per photon is related to the incident photon energy and the barrier height by (Sze, 1981)

$$\sqrt{R} \sim h\nu - \phi_b \qquad \text{if} \quad h\nu - \phi_b > 3kT \tag{51}$$

where R is the photocurrent per incident photon, $h\nu$ is the energy of the photon, ϕ_b is the barrier height.

Figure 18 shows the photoresponse as a function of photon energy for a palladium contacted HgI_2 sample for photon energies in the range of 1.1 to 2.0 eV (i.e., using the long wavelength photoresponse from about 0.5 to 1 μm, region IV of Fig. 15). The current was measured in a short circuit configuration to avoid any influence of the dark current. The measured value of barrier height of the palladium contact was found to be 1.1 eV. From the direction of the current flow in the short circuit configuration, the barrier was found to be a hole barrier (p-type conduction). A current peak due to photoionization of a defect level occurs at 1.38 eV (see Fig. 18).

Similar measurements have also been performed on contacts made from a variety of other metals. Almost all of these showed some degree of polarization effect, that is, the results of measurements depended on time and sample history, thereby making the measured value unreliable. This is not surprising since palladium contacts are now widely used as the contact material of choice, due to its relatively good performance and the high quality of detectors that can be fabricated with Pd contacts.

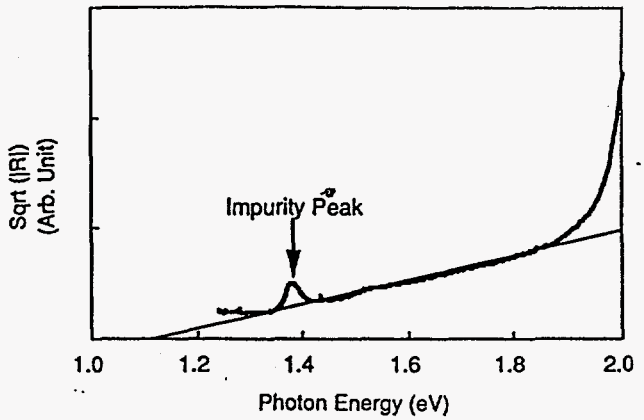

FIG. 18. Plot of the square root of the photoresponse as a function of photon energy to obtain the barrier height. The barrier height measured for the palladium contacted is 1.05 eV from the intercept of the straight line with the x-axis. A defect peak at 1.38 eV can also be seen.

The dark current technique has also been used to measure the barrier height, by assuming that the dark current in HgI_2 arises from thermal emission from the contact (Mellet and Friant 1989). By measuring the dark current as a function of applied electric field and using Eqs. (3) and (5), the barrier height was determined to be about 1.2 eV, for both palladium and carbon contacts. Mellet and Friant (1989) also studied the correlations between the contact parameter γ (defined in Eq. (8)) and the detector performance. It was found that γ (from Eq. (8)) ranges from 26 to 70 and higher values are usually related to higher energy resolution in the detectors. Crystals grown from the vapor phase tend to have higher γ values than those grown from solution.

2. SURFACE RECOMBINATION

Surface recombination also influences the performance of the HgI_2 devices. It directly affects the amount of charges that are separated and eventually collected by the electrical contacts. The surface recombination is characterized by a surface recombination velocity and is defined as $s = N_{st} v_{th} \sigma$, where N_{st} is the area density of recombination centers near the surface. For the purposes of this discussion, recombination also includes any trapping processes that hold charge for a time longer than the charge collection time of the detector electronics.

Using Eqs. (23)–(24), Levi *et al.* (1983a) have studied surface recombination in HgI_2 detectors. As can be seen from Eq. (24), if the electric field $E_{\eta=0.5}$ (when the charge collection efficiency is half) is plotted vs. the detector thickness, it is possible to determine whether the surface recombination is significant. Figure 19 shows such plots for electrons and holes (Levi *et al.*, 1983a). From the plot for electrons, there is hardly any dependence on the detector thickness. Therefore, Eq. (25) holds and the surface recombination for electrons is significant and

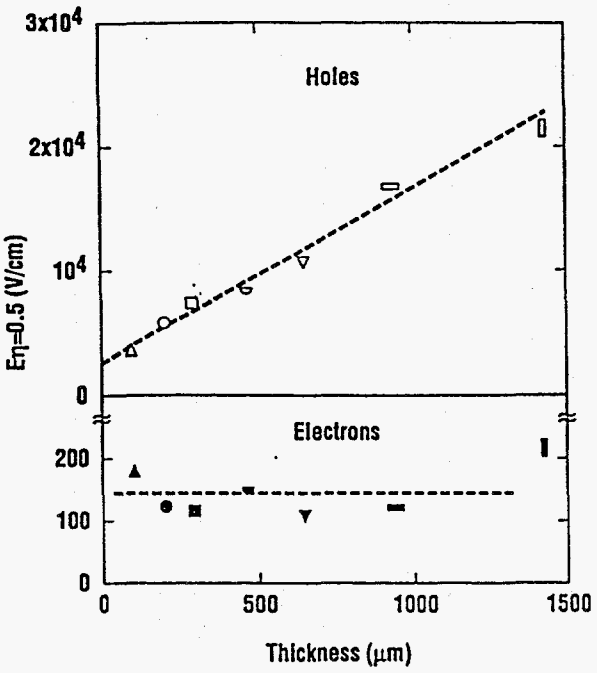

FIG. 19. Half-maximum collection field vs. detector thickness for holes (top) and electrons (bottom). (Reprinted with permission from Levi *et al.*, 1983a and the American Institute of Physics.)

greater than bulk trapping (i.e., $s_n >> L/\tau_n$). The value of s_n was calculated to be about 1.5×10^4 cm/sec using an electron mobility of 100 cm^2/V-sec and lifetime of electrons $\tau_n >> 10^{-5}$ sec. The plot for holes is quite different from that for electrons. From the intercept with y-axis and using a hole mobility of 4 cm^2/V-sec, the surface recombination for holes (s_p) is about 10^4 cm/sec. From the slope a lifetime τ_p for holes of about 10^{-6} sec is obtained. In this case, the hole surface recombination is negligible.

This method used to determine the surface recombination velocity requires the fabrication of several detectors with different thicknesses. It is possible, however, to measure surface recombination velocity using only one device. In their measurements, Roth *et al.* (1987) first used the charge transient method to determine the mobilities and lifetimes of electrons and holes, and the charge collection efficiency η (Eq. (21)) was calculated assuming no surface effect. The actual charge collection efficiency η' is then related to the surface recombination velocity by

$$\frac{\eta}{\eta'} - 1 = \frac{s}{\mu E}. \tag{52}$$

The surface recombination velocity may be obtained from the slope of the plot ($\eta/\eta' - 1$) vs. $1/\mu E$. For electrons, the surface effect was also found to be important and $s_n = 2 \times 10^4$. The hole surface recombination was found to be negligible, in agreement with Levi *et al.* (1983a).

The effect of surface treatment on surface recombination was studied by Levi *et al.* (1983b). The surface recombination velocity of electrons was measured with the sample treated with potassium iodide (KI) aqueous solutions at different temperatures, concentrations, and waiting times before contact deposition. It was found that the lowest surface recombination was achieved by etching with 20% KI solution at temperatures between 0 to 10° C, and the contact deposition made about 24 hr after etching. Mellet and Friant (1989) have found that nitric acid treatment of solution grown HgI_2 improved the low-energy response of the detectors considerably.

VI. Detector Performance

The qualities of radiation detectors are characterized by their energy resolution, peak to background (peak to valley) ratio, efficiency, active volume, response time, radiation damage resistance, and reliability. Most of these qualities are closely related to the electrical properties of the detector material, as discussed in various sections of this chapter and related chapters in this book. This section will be devoted to the discussion of background counts in HgI_2 x-ray and gamma ray detectors, and polarization effects.

1. PEAK-TO-BACKGROUND RATIO

When an x-ray spectrum is taken from a HgI_2 detector, a certain amount of background counts occurring in channels below the photo peak can be observed even though the incident x-rays are monoenergetic. In spectroscopy applications, these background counts may impose a detection limit when x-rays of different energies are present. These background counts cover all energies below the photo peak and are not due to x-ray escapes, which usually produce sharp peaks in the low energy region. To quantify this continuous background, the peak to background ratio can be measured and used as a figure of merit to describe this aspect of the detector performance. Continuous backgrounds have been observed in Si and Ge detectors and have traditionally been related to a dead layer beneath the entrance contact.

The origins of the dead layers for Si and Ge detector with x-ray energies below a few keV have been associated with photogenerated carriers moving to the entrance surface against the applied field and not contributing to the charge collection. The carriers may move to the entrance either through diffusion, which is a multiple scattering process, or as hot carriers that escape to the surface without scattering (Caywood, Mead, and Mayer, 1970; Llacer, Haller, and Cordi, 1977). Estimated dead layer thicknesses for Si and Ge x-ray detectors are not very different from measured values at x-ray energies below a few keV (Goulding, 1977; Musket and Bauer, 1973; Llacer *et al.*, 1977). In the case of HgI_2 detectors, the

estimated dead layer thickness due to hot carriers is much less than the measured value and can be ignored. The dead layer thickness due to diffusion is a function of the applied field and is approximately given by (Dabrowski *et al.*, 1981)

$$d = \frac{kT\mu}{4v_d} \tag{53}$$

where μ is the carrier mobility and v_d is the carrier drift velocity. Since the electron drift velocity will not saturate under bias typically applied to HgI_2 detectors (also see Subsection II.2), the dead layer due to the carrier diffusion is a function of the electric field through the drift velocity. It should be pointed out that the electric field used to calculate the drift velocity should be that near the entrance contact, which may not be equal to the applied electric field.

Dabrowski *et al.* (1981) measured the dead layer thicknesses for HgI_2 detectors using Al and Mg x-rays. The dead layer thicknesses were found to depend both on the x-ray energy and on the contact materials. For a detector with palladium contacts, the dead layer thicknesses are 0.24 μm for the 1.49 keV Al x-rays and 0.15 μm for the 1.25 keV Mg x-rays. For a detector with carbon contacts, the dead layer thicknesses are 0.08 μm for the Al x-rays and 0.05 μm for the Mg x-rays. The large difference between the detectors with different contacts was attributed to the difference in band bending near the entrance electrodes, resulting in different total electric field strength even under the same applied field.

Dead layer thicknesses measured from a large number of HgI_2 detectors are about 0.091 μm at 5.89 keV (Mn x-rays from a Fe-55 radioactive source) and 1.6 μm at 22.16 keV (Ag x-rays from a Cd-109 radioactive source). These values do not vary very much among good detectors (good energy resolution, minimum tailing, etc.) and are not very sensitive to the applied electric field above a certain bias. Figure 20 shows the peak to background ratio (inversely proportional to the dead layer thickness) at 5.89 keV measured as a function of the applied bias. As can be seen, the peak to background ratio changes very little with the applied field above about 300 V. The rapid decrease of peak to background ratio below 300 V is due to the incomplete depletion of the detector at low bias. If Eq. (53) is used to estimate the electric field near the entrance electrode, the obtained value will be much smaller than a typical applied bias, which is difficult to account for even if there is certain band bending near the surface. It appears then that the origins of the dead layer may be more than just the diffusion mechanism in HgI_2. One likely source of the background counts is the energetic electrons generated by the incident x-rays through the photoelectric effect. These electrons will gradually lose their energy by ionization of more electrons along the path. If the energetic photoelectrons are generated near the entrance surface, they may deposit only part of their energy before reaching the surface and thus product counts in lower energy channels. The ranges of these electrons can be estimated from the Katz–Penfold formula (Katz and Penfold, 1952; Manfredotti and Nastasi, 1984). They are about 0.082 μm and 1.3 μm at 5.89 keV and 22.16 keV, respectively, for HgI_2. These

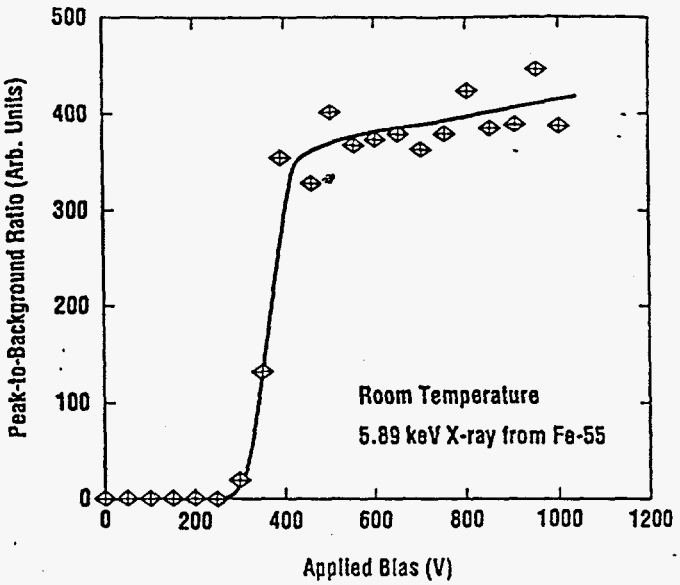

FIG. 20. The peak to background ratio measured at 5.89 keV as a function of the applied bias for a HgI_2 detector. The thickness of the detector is about 400 μm.

values are reasonably close to the measured values of dead-layer thicknesses given the simplicity of the calculation. The dead layer due to such an effect will not depend on the electric field and will provide the lower limit for the thickness (more accurate values may be obtained with more elaborate calculations taking into account the details of interaction and the directional dependence of photoelectrons). Therefore dead layer in HgI_2 x-ray detectors may come from both carrier diffusion and energetic photoelectrons. At low electric fields, the dead layer due to diffusion may dominate and is a function of the electric field. At higher electric fields, the dead layer comes mainly from the energetic photoelectron escape and is an intrinsic property of the material and independent of the electric field.

2. POLARIZATION EFFECT

In the application of semiconductors in x-ray and gamma ray detections, the polarization effect is defined as the time dependence of the detector performance. Possible causes of polarization include trapping, detrapping, and change of defect structure in the detector. The trapping and detrapping of carriers will change the space–charge distribution in the detector and thus modify the electric field profile. The charge collection efficiency will be altered correspondingly through the changes in the average drift length of carriers (see Eq. (14)) or the effectiveness of moving carriers away from surface recombination centers (see Eq. (23)). Since the time constants such as trapping and detrapping times may vary considerably among different traps, time dependent detector performances can be observed with quite different time scales. The polarization may have drastically different

effects on the x-ray spectra. The x-ray spectra may either improve or degrade, and the time constant may vary from seconds to several years. These differences come from the different defect structures in the detectors, which may be related to different crystal growth techniques, different impurities and native defect in the detectors, different contact materials and deposition techniques, different detector fabrication procedures, etc. The detector behaviors can be further complicated by the simultaneous presence of both trapping and detrapping, detrapping through other mechanisms such as Auger recombination (Gerrish 1992), and other factors such as radiation energy, flux, penetration depth, and detector temperature. Therefore, the observed behaviors of polarization effects in HgI_2 can be quite different among researchers (Whited, Schieber, and Randtke, 1976; Holzer and Schieber, 1980; Mohammed-Brahim, Friant, and Mellet, 1985; Squillante, Shah, and Moy, 1990; Gerrish, 1992; Natarajan, Scoopo, and Henderson, private communication, 1992).

a. Trapping

The effect of carrier trapping on the x-ray spectra is shown in Fig. 21 (Natarajan, Scoopo, and Henderson, private communication, 1992). The gradual degra-

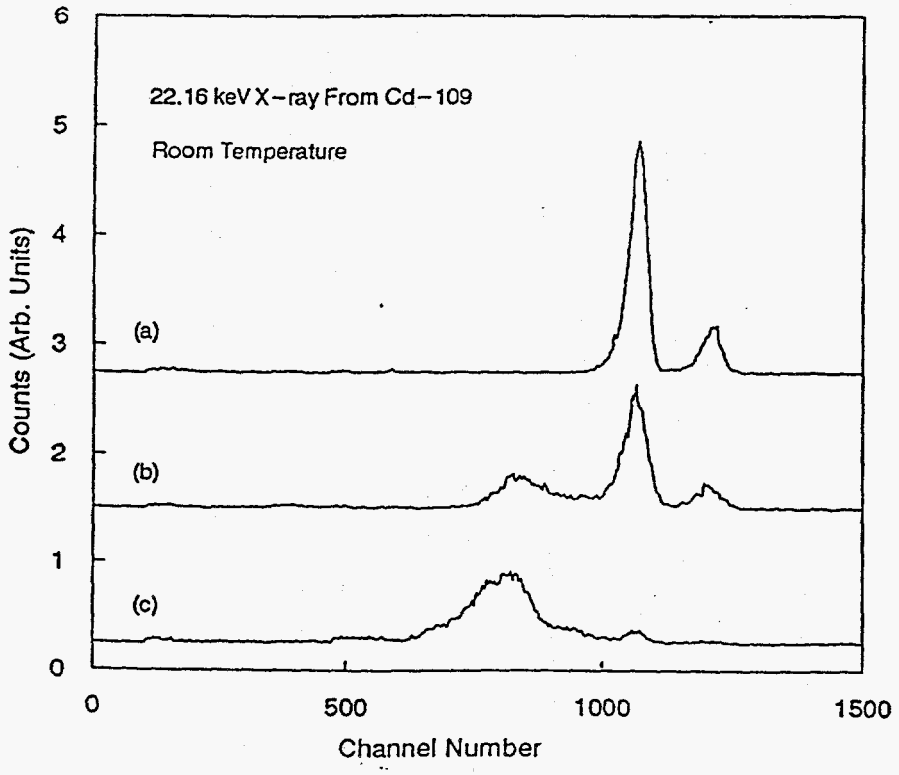

FIG. 21. X-ray spectra of 22.16 keV showing the polarization effect due to electron trapping in the HgI_2 detectors; spectrum (a) was taken before polarization and spectra (b) and (c) were taken at increased levels of polarization (trapping) (from Natarajan, Scoopo, and Henderson, private communication, 1992).

dation of the x-ray spectra form (a) to (c) is caused by increased concentration of trapped electron carriers. This polarization effect is attributed to trapping for several reasons. First, the changes in the x-ray spectra can be induced only in the presence of excitation. Second, the changes are completely reversed if the excitation source is removed. Third, the reversal in the absence of excitation is slowed down considerably if the detector is cooled to about $-5°C$, indicating that the reversal process is thermally activated (release of the trapped carriers from the defect states responsible for the polarization effect). In Fig. 21, the trapped carriers are believed to be electrons because the polarization effect degrades the x-ray spectra. This is due to reduced electric field near the entrance electrode (negatively biased), which can be produced only by the accumulation of more negative space charge in the detector. It is entirely possible, however, for a trapping process to improve the x-ray spectra, if the trapped carriers are holes instead of electrons. Such a polarization effect will then have all the characteristics behaviors as described for Fig. 21, except that the x-ray spectra will improve as the trapping (degree of polarization) increases (Mohammed-Brahim *et al.*, 1985). Holzer and Schieber (1980) studied the effects of radiation on the count rate, energy resolution, and the position of the photo peak. As the radiation flux or energy increases, detectors that polarize will deteriorate faster indicating a trapping process is responsible for the observed degradation.

b. Detrapping

Since the electric field in the detector can also be modified by a change in space charge due to detrapping of carriers, detrapping may also lead to a polarization effect. The reversal process described in the previous paragraph is one form of such a polarization effect. If polarization is due to detrapping, it will not need excitation and the time constant related to the polarization will become very temperature sensitive (for thermally activated detrapping) as observed for the reversal process just described. Another polarization effect in HgI_2 detectors due to detrapping is observed after a bias is first applied to the detector. Figure 22 shows a group of 5.89 keV x-ray spectra taken at different time intervals after the bias is applied. Even after 8 hr, the spectrum is still improving. Spectrum (e) has a peak-to-background ratio about twice as large as spectrum (d). The changes in the x-ray spectra shown in Fig. 22 were attributed to the detrapping process after the bias was applied and the depletion region was being established. This detrapping process is also responsible for the dark current transient as described by Eq. (47). In reality, it is more likely to have several different traps detrapping at the same time after the application of bias. Some of these traps may be electron traps and some may be hole traps. Thus, even though Fig. 22 shows a case in which the electron detrapping dominates over the hole detrapping because the x-ray spectrum improves, it is also possible to have a dominant hole detrapping process; in which case, the x-ray spectrum will degrade. The detector may reach an optimal

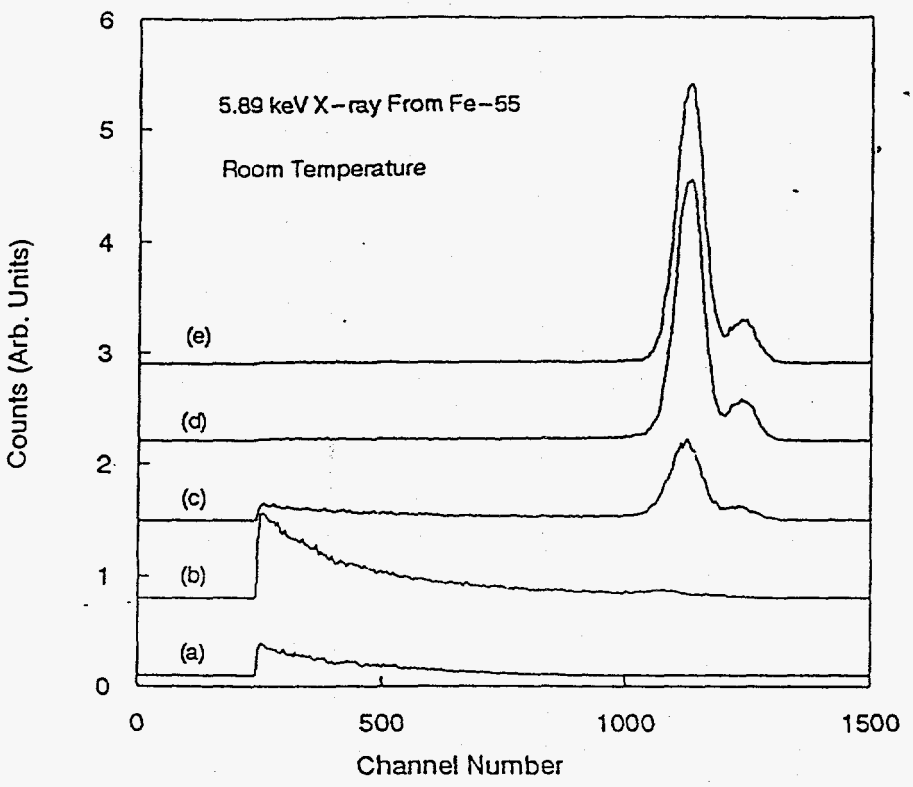

FIG. 22. X-ray spectra at 5.89 keV showing polarization effect due to electron detrapping in the HgI_2 detectors after the application of the bias. (Spectra (a) to (e) were taken 0, 1, 2, 8, and 24 hr after the bias was applied. The detector was not irradiated with the x-rays between these measurements.

(or worst) performance at a certain time if both electron and hole detrapping is present and these can dominate at different times because of differing detrapping times.

c. *Others*

Auger recombination of holes in HgI_2 gamma ray detectors has been observed by Gerrish (1992). In this process, trapping of the holes results in the ejection (detrapping) of electrons. The ejection of electrons is not thermally activated and may show different behaviors as described in Subsection VI.1.b. In this process, the trapping affects the detection of the energy of the incident x-rays because of the gain created by the ejected electrons (Gerrish 1992). On the other hand, as the electron trap empties, the space charge will be more positive and the rate of the Auger recombination will be less. Hence, a time dependent detector performance (improvement of energy resolution for gamma rays in this case) was observed that may take up to several weeks to stabilize after application of bias.

Polarization effects due to trapping and detrapping are reversible processes. Permanent changes in defect structure may also result in time-dependent changes

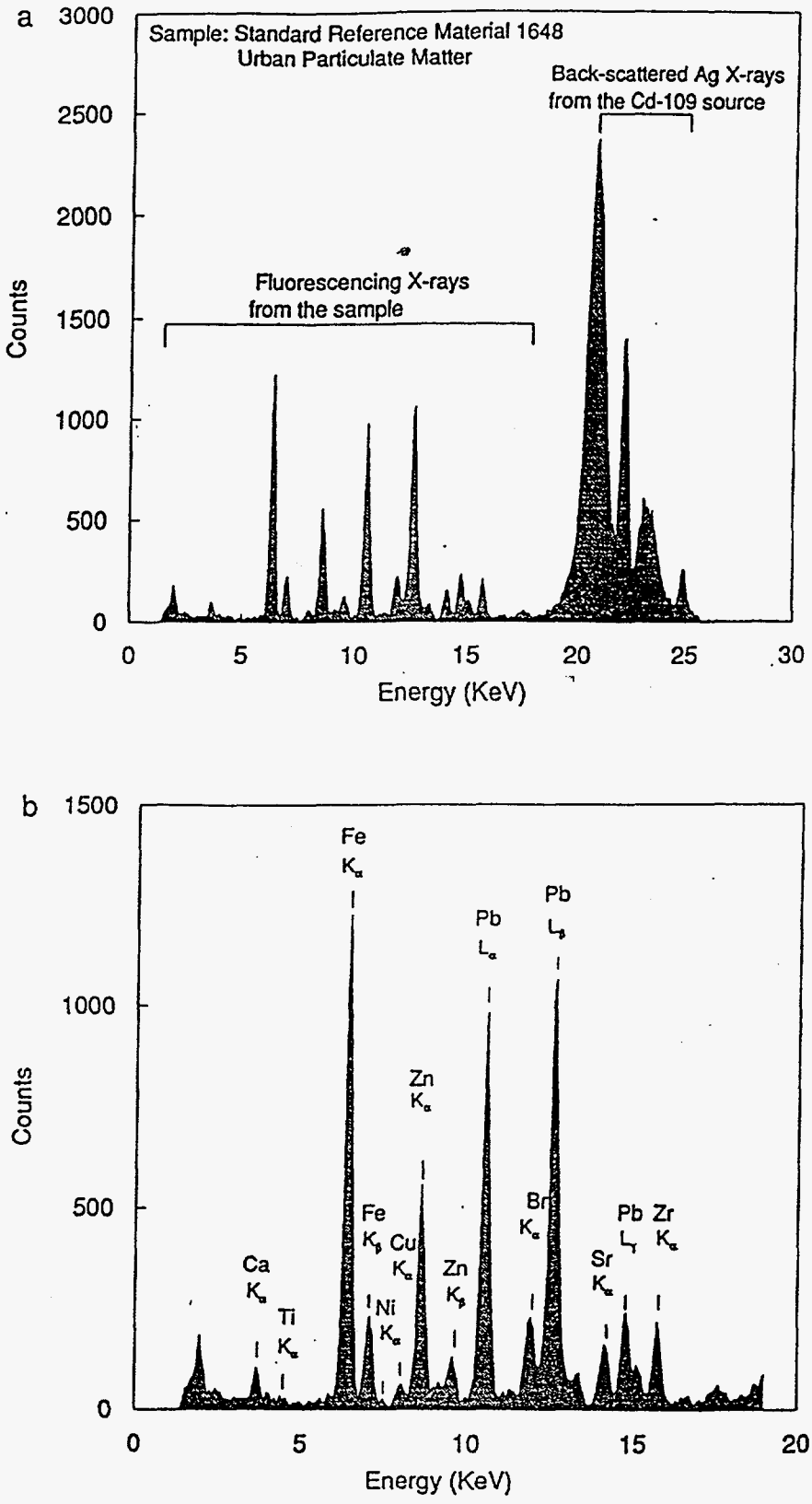

FIG. 23. (a) An x-ray spectrum taken with the battery-powered field portable XRF system: Spectrace-9000, manufactured by TN Technologies, Inc.; (b) the fluorescence portion of the spectrum with identifications of the observed elements by their characteristics x-ray emissions (from Berry and Voots, private communication, 1992).

in the detector performance. Most of the permanent degradations observed in HgI_2 detectors are related to its relatively high vapor pressure (Swierkowski *et al.*, 1974; Squillante *et al.*, 1990). Advances in the encapsulation techniques for HgI_2 detectors, especially with the use of parylene coatings, have greatly alleviated these problems (Iwanczyk *et al.*, 1990).

VII. Conclusions

The electrical properties of mercuric iodide most relevant to x-ray and gamma ray detection were discussed in this chapter. Several techniques that have been extensively used to characterize HgI_2 crystals and detectors were discussed in detail. These techniques include current and charge transient measurements, TSC, and photoconductivity. Two of the present challenges in HgI_2 sensor technology are to increase control of the detector fabrication processes and to modify the detector processing strategy in such a way so as to increase the manufacturing yield of high quality detectors. HgI_2 detectors have been successfully utilized in commercial field portable x-ray fluorescence (XRF) systems used for alloy analysis and other general-purpose applications (TN Technologies 1992). These XRF systems are the first field portable XRF instruments with energy resolution approaching that of a laboratory (Si) system and far exceeding that of a gas-filled proportional analyzer. The full-width at half-maximum of these systems at 5.89 keV employing HgI_2 detectors cooled to $-5°C$ by Peltier coolers is about 270 eV as compared with 150 eV for a Si detector (cooled by liquid nitrogen) and 800 eV for a gas-filled proportional counter. Figure 23a shows an x-ray spectrum taken with such a portable system, Spectrace-9000 (TN Technologies 1992) from a standard reference material and excited by one of the three built-in excitation sources (Cd-109 radioactive source emitting 22.16 keV Ag x-rays) (Berry and Voots, private communication, 1992). Figure 23b shows the fluorescence portion of the spectrum in Figure 23a with the identification of the observed elements (Berry and Voots, private communication, 1992). The superb spectroscopic capabilities are demonstrated in Fig. 23b with the well-resolved characteristic x-rays very close in energies. With the three excitation sources employed by the Spectrace-9000, the 19 lb. battery powered field portable instrument is capable of performing quantitative analysis of elements from S to U. Progress in optimizing the various material parameters and processing steps, such as crystal growth, stoichiometry, impurity control, surface treatment, choice of contact, deposition method, and encapsulation, will determine the future of this technology.

REFERENCES

Adduci, F., Cingolani, A., Ferrara, M., Lugara, M., and Minafra, A. (1977). *J. Appl. Phys.* **48**, 342.
Alvarez, F., and Saura, J. (1990). *J. Mat. Sci. Lett.* **9**, 569.

Anedda, A., Raga, F., Grill, E., and Guzzi, M. (1977). *Il Nuovo Cimento* **38B,** 439.
Bao, X. J. (1991). Ph.D. thesis, Carnegie Mellon University.
Bao, X. J., Schlesinger, T. E., James, R. B., Stulen, R. H., Ortale, C., and van den Berg, L. (1990). *J. Appl. Phys.* **67,** 7265.
Bao, X. J., Schlesinger, T. E., James, R. B., Gentry, G. L., Cheng, A. Y., and Ortale, C. (1991a). *J. Appl. Phys.* **69,** 4247.
Bao, X. J., Schlesinger, T. E., James, R. B., Cheng, A. Y., Ortale, C., and van den Berg, L. (1991b). *Mat. Res. Soc. Symp. Proc.* **170,** 541.
Bao, X. J., Schlesinger, T. E., James, R. B., Cheng, A. Y., Ortale, C., and van den Berg, L. (1992). *Mat. Res. Soc. Symp. Proc.* **242,** 767.
Beyerle, A. G., Hull, K. L., Markakis, J., Schnepple, W., and van den Berg, L. (1983). *Mat. Res. Soc. Symp. Proc.* **16,** 191.
Blasi, C. D., Galassini, S., Manfredotti, C., Micocci, G., Ruggiero, L., and Tepore, A. (1978). *Nucl. Instr. Methods* **150,** 103.
Bloch, P. D., Hodby, J. W., Jenkins, T. E., Stacey, D. W., and Schwab, C. (1977). *Il Nuovo Cimento* **38B,** 337.
Bloch, P. D., Hodby, J. W., Schwab, C., and Stacey, D. W. (1978). *J. Phys. C* **11,** 2579.
Bornstein, J., and Bube, R. H. (1987). *J. Appl. Phys.* **61,** 2676.
Braatz, U., and Zappe, D. (1984). *Phys. Stat. Sol. (a)* **86,** 407.
Bube, R. (1957). *Phys. Rev.* **106,** 703.
Bube, R. (1960). *Photoconductivity of Solids.* John Wiley & Sons, New York.
Burger, A., Shi, W., Silberman, E., Franks, L., and Schnepple, W. F. (1989). *Nucl. Instr. Methods Phys. Res. A* **283,** 232.
Burshtein, Z., Akujieze, J. K., Silberman, E. (1986). *J. Appl. Phys.* **60,** 3182.
Caywood, J. M., Mead, C. A., and Mayer, J. W. (1970). *Nucl. Instr. Meth.* **79,** 329.
Cho, Z. H., Watt, M. K., Slapa, M., Tove, P. A., Schieber, M., Davies, T., Schnepple, W., Randtke, P., Carlston, R., and Sarid, D. (1975). *IEEE Trans. Nucl. Sci.* **NS-22,** 229.
Dabrowski, A. J., and Huth, G. C. (1978). *IEEE Trans. Nucl. Sci.* **NS-25,** 205.
Dabrowski, A. J., Iwanczyk, J. S., Barton, J. B., Huth, G. C., Whited, R., Ortale, C., Economou, T. E., and Turkevich, A. L. (1981). *IEEE Trans. Nucl. Sci.* **NS-28,** 536.
Gartner, W. (1957). *Phys. Rev.* **105,** 823.
Gelbart, U., Yacoby, Y., Beinglass, I., and Holzer, A. (1977). *IEEE Trans. Nucl. Sci.* **NS-24,** 135.
Gerrish, V. (1992). *Nucl. Instr. Methods Phys. Res.* **A322,** 402.
Goto, T., and Nishima, Y. (1979). *Solid State Commun.* **31,** 751.
Goulding, F. S. (1977). *Nucl. Instr. Meth.* **142,** 213.
Grossweiner, L. I. (1953). *J. Appl. Phys.* **24,** 1306.
Hermon, H., Roth, M., Nissenbaum, J., and Schieber, M. (1991). *J. Cryst. Growth* **109,** 376.
Holzer, A., and Schieber, M. (1980). *IEEE Trans. Nucl. Sci.* **NS-27,** 266.
Hyder, S. B. (1977). *J. Appl. Phys.* **48,** 313.
Iwanczyk, J., Barton, J. B., Dabrowski, A. J., Kusmiss, J. H., and Szymczyk, W. M. (1983). *IEEE Trans. Nucl. Sci.* **NS-30,** 363.
Iwanczyk, J., Dabrowski, A. J., Markakis, J. M., Ortale, C., and Schnepple, W. F. (1984). *IEEE Trans. Nucl. Sci.* **NS-31,** 336.
Iwanczyk, J. S., Wang, Y. J., Bradley, J. G., Albee, A. L., and Schnepple, W. F. (1990). *IEEE Trans. Nucl. Sci.* **NS-37,** 2214.
James, R. B., Bao, X. J., Schlesinger, T. E., Markakis, J. M., Cheng, A. Y., and Ortale, C. (1989). *J. Appl. Phys.* **66,** 2578.
James, R. B., Bao, X. J., Schlesinger, T. E., Ortale, C., and Cheng, A. Y. (1990). *J. Appl. Phys.* **67,** 2571.
James, T. W., and Milstein, F. (1983). *J. Mat. Sci.* **18,** 3249.
Kanel, H. V., Wachter, P., and Gerischer, H. (1984). *J. Electrochem. Soc.* **131,** 77.
Katz, L., and Penfold, A. S. (1952). *Rev. Mod. Phys.* **24,** 28.

Kitajima, K., and Wagner, J. B. Jr. (1988). *Solid State Ionics* **28–30,** 1146.
Klick, C. C., and Maurer, R. J. (1951). *Phys. Rev.* **81,** 124.
Levi, A., Schieber, M. M., and Burshtein, Z. (1983a). *J. Appl. Phys.* **54,** 2472.
Levi, A., Burger, A., Nissenbaum, J., Schieber, M., and Burshtein, Z. (1983b). *Nucl. Instr. Methods* **213,** 35.
Levi, A. Schieber, M. M., and Burshtein, Z. (1985). *J. Appl. Phys.* **57,** 1944.
Llacer, J., Watt, M. M. K., Schieber, M., Carlston, R., and Schnepple, W. (1974). *IEEE Trans. Nucl. Sci.* **NS-21,** 305.
Llacer, J., Haller, E. E., and Cordi, R. C. (1977). *IEEE Trans. Nucl. Sci.* **NS-24,** 53.
Look, D. C. (1983). *Semiconductors and Semimetals* **19,** 75.
Malm, H. L. (1972). *IEEE Trans. Nucl. Sci.* **NS-19,** 263.
Manfredotti, C., and Nastasi, U. (1984). *Nucl. Instr. Meth. Phys. Res.* **A225,** 138.
Manfredotti, C., Murri, R., Quirini, A., and Vasanelli, L. (1977a). *IEEE Trans. Nucl. Sci.* **NS-24,** 158.
Manfredotti, C., Murri, R., and Vasanelli, L. (1977b). *Solid State Commun.* **21,** 53.
Markakis, J. M. (1988a). *IEEE Trans. Nucl. Sci.* **35,** 356.
Markakis, J. M. (1988b). *Nucl. Instr. Methods Phys. Res.* **A263,** 499.
Marschall, J., and Milstein, F. (1991). *Appl. Phys. Lett.* **58,** 1422.
Martin, G. M., Bach, P., and Guetin, P. (1974). *Appl. Phys. Lett.* **25,** 286.
Mellet, J., and Friant, A. (1989). *IEEE Trans. Nucl. Instr. Methods Phys. Res.* **A283,** 199.
Micocci, G., Rizzo, A., Tepore, A., and Zuanni, F. (1983). *Phys. Stat. Sol. (a)* **80,** 263.
Milnes, A. G. (1973). *Deep Impurities in Semiconductors.* John Wiley & Sons, New York.
Minder, R., Majni, G., Canali, C., Ottaviani, G., Stuck, R., Ponpon, J. P., Schwab, C., and Siffert, P. (1974). *J. Appl. Phys.* **45,** 5074.
Minder, R., Ottaviani, G., and Canali, C. (1976). *J. Phys. Chem. Solids* **37,** 417.
Mohammed-Brahim, T. (1981). *Phys. Stat. Sol. (a)* **65,** K1.
Mohammed-Brahim, T., Friant, A., and Mellet, J. (1983). *Phys. Stat. Sol. (a)* **79,** 71.
Mohammed-Brahim, T., Friant, A., and Mellet, J. (1985). *IEEE Trans. Nucl. Sci.* **NS-32,** 581.
Muller, J. C., Friant, A., and Siffert, P. (1978). *Nucl. Instr. Methods* **150,** 97.
Musket, R. G., and Bauer, W. (1973). *Nucl. Instr. Meth.* **109,** 593.
Nissenbaum, J., Schieber, M., and Burshtein, Z. (1987). *J. Appl. Phys.* **61,** 2921.
Nix, C. (1935). *Phys. Rev.* **47,** 72.
Novikov, B. V., and Pimonenko, M. M. (1971). *Sov. Phys. Semicond.* **4,** 1785.
Ottaviani, G., Canali, C., and Quaranta, A. A. (1975). *IEEE Trans. Nucl. Sci.* **NS-22,** 192.
Ponpon, J. P., Stuck, R., Siffert, P., and Schwab, C. (1974). *Nucl. Instr. Methods* **119,** 197.
Pons, D., Mooney, P. M., and Bourgoin, J. C. (1980). *J. Appl. Phys.* **51,** 2038.
Press, W. H., Flannery, B. P., Teukoslky, S. A., and Vetterling, W. T. (1988). *Numerical Recipes in C.* Cambridge University Press, New York.
Redfield, A. (1954). *Phys. Rev.* **94,** 526.
Rose, A. (1951). *RCA Rev.* **12,** 362.
Roosbroeck, W. V. (1956). *Phys. Rev.* **101,** 1713.
Roth, M., Burger, A., Nissenbaum, J., and Schieber, M. (1987). *IEEE Trans. Nucl. Sci.* **NS-34,** 465.
Saura, J., and Tognetti, N. P. (1975). *Phys. Stat. Sol. (a)* **31,** K125.
Schieber, M., Beinglass, I., Dishon, G., Holzer, A., and Yaron, G. (1978). *IEEE Trans. Nucl. Sci.* **NS-25,** 644.
Slapa, M., Huth, G. C., Seibt, W., Schieber, M. M., and Randtke, P. T. (1976). *IEEE Trans. Nucl. Sci.* **NS-23,** 102.
Squillante, M. R., Shah, K. S., and Moy, L. (1990). *Nucl. Instr. Meth. Phys. Rev.* **A288,** 79.
Stuck, R., Muller, J. C., Ponpon, J. P., Scharager, C., Schwab, C., and Siffert, P. (1976). *J. Appl. Phys.* **47,** 1545.
Suryanarayana, P., and Acharya, H. N. (1989). *J. Electr. Mat.* **18,** 481.
Swierkowski, S. P., Armantrout, G. A., and Wichner, R. (1974). *IEEE Trans. Nucl. Sci.* **NS-21,** 302.
Sze, S. M. (1981). *Physics of Semiconductor Devices,* 2nd ed. Wiley-Interscience, New York.

Tadjine, A., Gosselin, D., Koebel, J. M., and Siffert, P. (1983). *Nucl. Instr. Methods* **213**, 77.
TN Technologies. (1992). Product brochures for Metallurgist-XF and Spectrace-9000.
Turner, D. E., and Harmon, B. N. (1989). *Phys. Rev. B* **40**, 10516.
Van den Berg, L. (1992). *Nucl. Instr. Methods Phys. Res.* **A322**, 453.
Watt, M. K., and Cho, Z. H. (1976). *IEEE Trans. Nucl. Sci.* **NS-23**, 124.
Whited, R. C., and van den Berg, L. (1977). *IEEE Trans. Nucl. Sci.* **NS-24**, 165.
Whited, R. C., Schieber, M. M., and Randtke, P. T. (1976). *J. Appl. Phys.* **47**, 2230.
Willig, W. R. (1971). *Nucl. Instr. Methods* **96**, 615.
Yeargan, J. R., and Taylor, H. L. (1968). *J. Appl. Phys.* **39**, 5600.
Yee, J. H., Sherohman, J. W., and Armantrout, G. A. (1976). *IEEE Trans. Nucl. Sci.* NS-23, 117.
Zitter, R. N. (1958). *Phys. Rev.* **112**, 852.
Zolotarev, V. F., Kikineshi, A. A., Semak, D. G., Fedak, V. V., and Chepur, D. V. (1970). *Sov. Phys. Semicond.* **4**, 802.

Intentionally Left Blank

APPENDIX E

Devices

Intentionally Left Blank

Investigation of copper electrodes for mercuric iodide detector applications

X. J. Bao and T. E. Schlesinger
Department of Electrical and Computer Engineering, Carnegie Mellon University, Pittsburgh, Pennsylvania 15213

R. B. James and R. H. Stulen
Advanced Materials Division, Sandia National Laboratories, Livermore, California 94450

C. Ortale and L. van den Berg
EG&G Energy Measurements, Inc., Goleta, California 93116

(Received 11 January 1990; accepted for publication 2 March 1990)

Copper diffusion in mercuric iodide was studied by low-temperature photoluminescence (PL) spectroscopy and Auger electron spectroscopy. A broad radiative emission band at a wavelength of about 6720 Å in the PL spectra was found to be related to Cu incorporation in the crystal. PL spectra obtained from surface doping experiments indicate that Cu is a rapid diffuser in HgI_2 bulk material. Auger electron spectroscopy performed as a function of depth from the crystal surface confirms the rapid bulk diffusion process of Cu in HgI_2. Fabrication of HgI_2 nuclear detectors with Cu electrodes indicates that Cu is not acceptable as an electrode material, which is consistent with the fact that it diffuses easily into the bulk crystal and introduces new radiative recombination centers.

INTRODUCTION

Mercuric iodide in its red tetragonal form has many properties that make it well suited for use as a room-temperature x-ray and gamma-ray detector and spectrometer.[1-5] These properties include high atomic masses (i.e., $Z = 80$ and 53 for Hg and I respectively), photosensitivity, low-hole electron creation energy (4.2 eV at 300 K)[3-5] and high resistivity (10^{13} ohm cm).[5] However, low charge collection efficiencies, primarily because of hole trapping, severely limit the yield of high-performance detectors. Native defects and impurities introduced during crystal growth,[6-8] fabrication processes[9-11] and aging[9,12] are believed to contribute to the formation of these trapping centers. One of the steps in fabricating HgI_2 into nuclear detectors is the deposition of electrical contacts. So far, only a few materials have been successfully used, such as carbon, gold, germanium, and palladium.[2,4,10] These materials were mainly selected by a trial and error process, in which the detectors were used to demonstrate their superiority to other materials. But even among these materials, the quality of the detectors varies significantly. The lack of understanding of the formation of the electrical contact has lead to studies of defects associated with different contact materials and processing procedures.[9-11,13]

In this work we studied the deposition of copper on HgI_2, using 4.2-K photoluminescence (PL) spectroscopy and Auger electron spectroscopy (AES). Nuclear detectors were also fabricated with Cu electrodes and their performance measured. The experimental techniques, results, and discussions will be provided in the next two sections.

EXPERIMENT

For the PL measurements, an argon ion laser tuned to 488 nm was used as the excitation source at a power level of 5 mW, and the beam was chopped at a frequency of 750 Hz. The samples were cooled to a temperature of about 4.2 K in an optical cryostat with liquid helium. Photoluminescence was dispersed by a Spex 1404 double-pass spectrometer and detected by a photomultiplier with an S-20 response. The current output of the photomultiplier was amplified by a Keithley 427 current amplifier and then an EG&G 5207 lock-in amplifier. Because the excitation source has a photon energy of 2.54 eV, which is above the band gap of HgI_2 (2.37 eV at 4.2 K), the PL was generated from a region within a depth of less than a few microns from the surface.

AES spectra were taken using a 3-keV primary electron beam and a double-pass CMA spectrometer (PHI Model No. 15-255G). Specimens were inserted into the vacuum system through a rapid sample insertion interlock and cooled to prevent material loss. The samples were sputtered with an argon plasma, and the Auger signal was obtained as a function of depth as referenced to the etch rate for tantalum oxide.

Cu was deposited onto HgI_2 substrates by evaporation in a vacuum of about 5×10^{-6} Torr. The HgI_2 substrates (about 1.0 cm × 1.0 cm × 0.05 cm in dimension) were etched for a few minutes in a 10% (by weight) KI aqueous solution to clean the surface prior to the deposition.[9] In the first doping experiment, PL spectra were taken from several spots immediately after the KI etch. A semitransparent layer of Cu was then deposited onto part of the substrate, with the other part covered by an alumina mask. PL spectra were then taken again from both the masked-off region and the region that was deposited with Cu. In the second "back-doping" experiment, a small dot (about 0.15 cm × 0.15 cm) of Cu was deposited in the middle on one side of the substrate, and PL spectra were taken from the other side at locations that were at different distances from the Cu dot. For the Auger profiling experiment, spectra were first taken at the Cu-contacted surface, then a layer of about 75 Å was removed by a plasma etch. This process was repeated four times with a total thickness of about 300 Å removed.

The performance calibration of nuclear detectors was

 0021-8979/90/127265-03$03.00

carried out with an ^{241}Am radiation source. The emitted x-rays were incident on the negative electrode of each HgI_2 detector, which was biased with 400 V.

RESULTS AND DISCUSSIONS

Figure 1 shows two PL spectra from HgI_2 obtained in the first doping experiment. Spectrum (a) was taken before the Cu deposition and is typical of PL spectra taken from undoped HgI_2 bulk material. There are about 26 emission peaks between 5290 and 5410 Å, which have been collectively called band 1.[9] Among these peaks, P2 and P3 (with wavelengths of about 5318 and 5321 Å, respectively) have been assigned as bound exciton emissions and have received much more attention than the others since they are usually the dominant peaks. In a previous publication,[9] a large P2-to-P3 ratio was related to iodine deficiency in the sample. In the wavelength region between 5400 and 8050 Å, three broad bands can usually be detected in undoped samples. They are labeled as band 2 (at a wavelength of about 5600 Å), band 3 (at a wavelength of about 6200 Å), and band 4 (at a wavelength of about 7550 Å). Note that band 3 is relatively weak in this sample and is not well resolved in Fig. 1. Spectrum (b) was taken from the same spot but after a semitransparent Cu layer was deposited. Several changes can be observed. The most dramatic difference is the introduction of a new broad band centered at about 6720 Å between band 3 and band 4. This band is apparently due to the incorporation of Cu into the HgI_2 crystal and was thus labeled as the "Cu" band. Other changes include the increase in the P2-to-P3 ratio, the quenching of the peaks to the longer wavelength side of P3 in band 1, and an increase of the absolute intensity of band 4.

The increase of P2 relative to P3 can be explained as a stoichiometry change due to iodine deficiency, which may be caused by iodine loss in the process of evaporating Cu onto the crystal and/or the formation of Cu/I compounds[14] near the interfacial region. However, this increase of the P2-to-P3 ratio was not observed for all the samples that we have measured. One possible explanation is that since there are variations in the evaporation times and evaporation temperature, the deposited films will have different thicknesses and also the deposition process will modify the HgI_2 substrates to different degrees, especially if there are two competing factors that have opposite effects on the P2-to-P3 ratios. For instance, while reaction of Cu with I and iodine sublimation induce iodine deficiency and may increase the P2-to-P3 ratio, excessive exposure to heat will reduce the P2-to-P3 ratio.[9] Furthermore, a thicker contact may help to prevent material loss by acting as a barrier layer. We have observed similar effects for Pd contacts when the deposition temperature was varied.[9]

The quenching of those peaks to the longer wavelength side of P3 further indicates the degraded interface between the Cu contact and HgI_2. This phenomenon was not observed for semitransparent Pd contacts, which have been successfully used as electrodes for HgI_2 nuclear detectors.[10] The increase of band 4 after Cu deposition implies that band 4 may also be related to the Cu impurities. Since this band is often observed in undoped HgI_2, we will not assign it as a Cu band.

PL spectra were also taken from spots that were masked off during the Cu deposition. All of these spectra showed the new band at 6720 Å, which indicates that Cu diffuses easily along the crystal surface.

The back-doping experiment was designed to study the bulk diffusion properties of Cu in HgI_2. Figure 2 shows the absolute intensities of the Cu band as a function of position. Four spectra were taken along each of the three directions *A*, *B*, and *C*. The excitation spots were first moved towards the Cu dot from position 1 to position 2 and then away from the Cu dot from position 3 to position 4. From the plot, it can be seen that the spots closer to the Cu dot have a stronger Cu band intensity than those further away from the Cu dot. Because the Cu dot was deposited on the other side of the sample, it can be concluded that the Cu band comes mainly from the Cu diffusion through the bulk of the material.

Figure 3 shows the Auger signals of Hg, I, and Cu as a

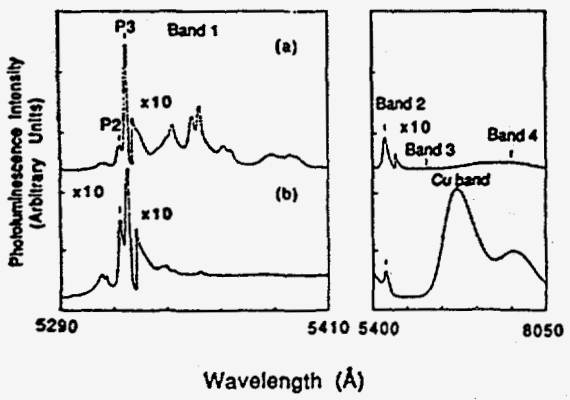

FIG. 1. 4.2-K PL spectra of HgI_2 taken from the same spot (a) before and (b) after a semitransparent Cu layer was deposited.

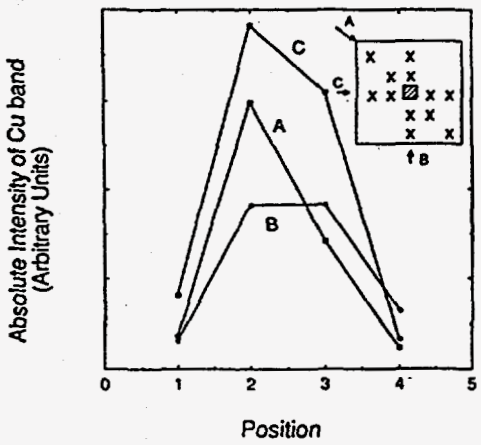

FIG. 2. Absolute intensities of the Cu band (at about 6720 Å) in the PL spectra as a function of the approximate position from the back-doping experiment. The insert shows the aproximate location of points on a HgI_2 substrate (about 1 cm × 1 cm in size) from which PL spectra were taken. The small square in the middle indicates the Cu film deposited on the back side.

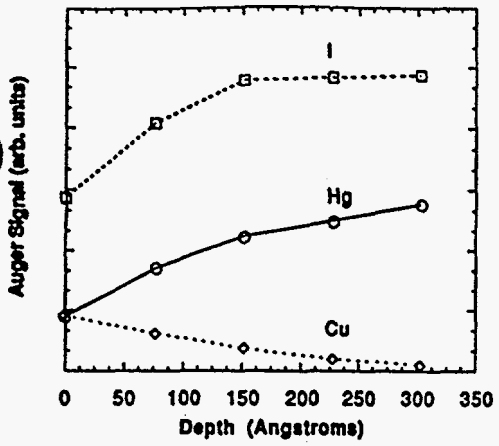

FIG. 3. Auger signals of Cu, I, and Hg as a function of depth from the AES profiling experiment.

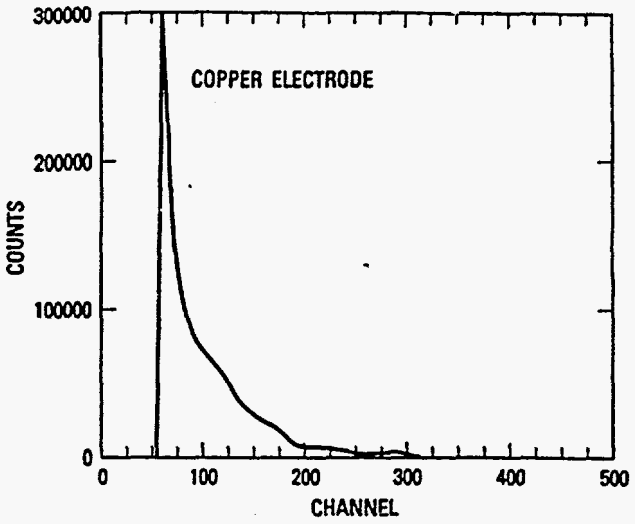

FIG. 4. Test of a HgI_2 nuclear detector with Cu electrodes using a ^{241}Am source. The 59.5-keV photon, which is often used to grade detector performance and should be peaked at a channel number of about 350, was not resolved.

function of depth. In addition to these major species, signals for C and Cl were also observed and are likely due to contamination. Both I and Hg signals increase while Cu decreases with increasing depth. The Auger signals plotted in this figure are the peak-to-peak signal values recorded directly in the Auger spectra and have not been corrected for differing elemental sensitivity. This correction would require Auger measurements on well-characterized mercury and iodine containing compounds using a 3-keV excitation beam, and these have not yet been performed. The ratio of the amplitude of the Auger signals for the different elements thus does not directly give stoichiometry or phase information. The variation of the signals with depth, however, does accurately represent change in composition. In the absence of diffusion, one would expect no Hg and I signals at the surface and a Cu signal that is fairly uniform to a certain depth and then decreases abruptly to near zero. The drop in the iodine and mercury signals near the surface is due to the presence of both Cu and residual impurities, most notably C and Cl. While carbon is a common surface contaminant, the presence of Cl may be due to sample preparation and handling. The primary result from the depth profiling shown in Fig. 3 is that the initially formed metallic Cu film has clearly diffused into the bulk mercuric iodide, leaving a near-surface region that is a mixture of Cu, Hg, and I.

HgI_2 nuclear spectrometers were fabricated with Cu electrodes and calibrated with a ^{241}Am source. The detected x-ray spectrum for a ^{241}Am source is shown in Fig. 4. Based on our measurements of Pd-contacted HgI_2 detectors, the 59.5-keV photon, which is often used to grade detector performance, should be peaked at a channel number of about 350. This peak is not resolved in our tests on Cu-contacted HgI_2 detectors, which confirms that Cu electrodes are unacceptable for HgI_2 spectrometer applications. Furthermore, the measurements provide further evidence that the introduction of new recombination centers, observed by PL, is detrimental to detector performance.

CONCLUSIONS

We have identified a broad emission band centered at about 6720 Å in the PL spectra of HgI_2 as due to Cu impurities in the crystal. To our knowledge, this is the first time an emission band in the PL spectra of HgI_2 has been positively assigned to a specific impurity. Cu was found to be a fast diffuser in bulk HgI_2, which explains why Cu is not acceptable as an electrode material for detector applications.

ACKNOWLEDGMENTS

We would like to acknowledge D. Wong, T. E. Felter, Larry Frank, and G. Gentry for many useful discussions. We would also like to thank the U.S. Department of Energy under Contact No. DE-AC08-88NV10617 for financial support.

[1]W. R. Willig, Nucl. Instrum. Meth. 96, 615 (1971).
[2]H. L. Malm, IEEE Trans. Nucl. Sci. NS-19, 263 (1972).
[3]J. P. Ponpon, R. Stuck, and P. Siffert, Nucl. Instrum. Meth. 119, 197 (1974).
[4]J. H. Howes and J. Watling, Mat. Res. Soc. Symp. Proc. 16, 207 (1983).
[5]H. L. Malm, T. W. Raudoff, M. Martina, and K. R. Zanio, IEEE Trans. Nucl. Sci. NS-20, 500 (1973).
[6]M. Schieber, W. F. Schnepple, and L. van den Berg, J. Cryst. Growth 33, 125 (1976).
[7]J. P. Ponpon, R. Stuck, and P. Siffert, IEEE Trans. Nucl. Sci. NS-22, 182 (1975).
[8]M. R. Squillante, S. Lis, T. Hazlett, and G. Entine, Mat. Res. Soc. Symp. Proc. 16, 199 (1983).
[9]X. J. Bao, T. E. Schlesinger, R. B. James, C. Ortale, and L. van den Berg (unpublished).
[10]T. E. Felter, R. H. Stulen, W. F. Schnepple, C. Ortale, and L. van den Berg, Nucl. Instrum. Methods A 238, 195 (1989).
[11]D. Wong, X. J. Bao, T. E. Schlesinger, R. B. James, A. Cheng, C. Ortale, and L. van den Berg, Appl. Phys. Lett. 53, 1537 (1988).
[12]P. Suryanarayana and H. N. Acharya, J. Electron. Mater. 18, 481 (1989).
[13]R. B. James, X. J. Bao, T. E. Schlesinger, C. Ortale, and A. Y. Cheng, J. Appl. Phys. 66, 2578 (1989).
[14]*Handbook of Chemistry and Physics*, 58th ed. (CRC Press, Cleveland, 1977/78).

Intentionally Left Blank

DEVELOPMENT OF HIGH-RESOLUTION CADMIUM ZINC TELLURIDE AND MERCURIC IODIDE GAMMA-RAY DETECTORS FOR USE IN NON-PROLIFERATION

Richard Olsen*,**, Ralph B. James*, Arlyn J. Antolak*, and Ching Wang**
*Sandia National Laboratories, Livermore, CA 94550
**Detectronics, Livermore, CA 94550

ABSTRACT

There is a widespread need for light-weight, portable gamma-ray spectrometers suitable for nuclear proliferation, treaty verification, special nuclear materials control, and IAEA-like applications. The detectors should have high energy resolution and sensitivity, and ideally they would be operable at room temperature. The focus of the present work is to increase the sensitivity of the devices by increasing the active volume of the detectors. The scope of this work has been limited to cadmium zinc telluride (CdZnTe) and mercuric iodide (HgI_2) detectors, because they are two of the most promising candidate materials at this time. Data obtained from single detectors show that the response of independent detectors is slightly different. An RC correction cicuit is presented to adjust for the different charge induced at the preamp input from the different detectors in the array, so that the response from each detector is identical. This allows a number of small semiconductor detectors to be stacked vertically or horizontally in order to greatly increase the overall system sensitivity. Moreover, the output of each detector can be added prior to the preamp, and multiple preamps are not required. A small amount of unwanted noise does occur due to the increased system capacitance, but this is offset by the increased absorption efficiency of the detector assembly. Nuclear spectroscopic data on horizontal and vertical CdZnTe detector cascades and on thick CdZnTe detectors are presented.

INTRODUCTION

Special nuclear materials (SNM) have radiological signatures associated with the emission of gamma rays and the emission of alpha, beta, and neutron particles. The alpha and beta particles are completely attenuated by thin layers of shielding, but the gamma rays, which have principal radiations in the 100 keV to 2 MeV range, are much more difficult to shield and can be directly measured to determine the presence of weapons-grade nuclear materials. One of the simplest ways to monitor the presence of radiation is based on scintillator/photomultiplier systems. Unfortunately, these systems have poor energy resolution, and in many cases, they do not give spectral data of sufficient quality to uniquely determine the presence of SNM thereby leading to problems with false alarms. Typical energy resolution of portable scintillators is about 8-14%, and elaborate schemes are taken to utilize the limited spectral data. Germanium detectors can give the necessary spectral information to identify the source(s), but these systems require cryogenic cooling, which makes them more difficult to operate, heavier, and require regular maintenance for operation. They are simply unable to operate in an "anywhere/anytime" mode, and the cryogen restricts their use in many monitoring scenarios.

There is a clear and obvious need for gamma-ray detectors that operate at ambient conditions and have the energy resolutions required to identify the unique characteristics of SNM. This requirement for room-temperature detectors has motivated the search for new compound semiconductors which have large bandgaps, high cross sections for x-rays and gamma-rays, good carrier transport properties, and are physically rugged and stable. Until now, most of these detectors have not been able to meet system requirements for sensitivity due to limitations on the detector volumes. In order to obtain high energy resolution, it has been necessary to limit the thicknesses to a few millimeters and the cross-sectional areas to a few square centimeter. Additional improvements in the charge collection properties of the devices are required if one wants to fabricate room-temperature gamma ray spectrometers having volumes of 10 cm^3 and larger.

Several approaches are underway to increase the sensitivity of high-resolution, room-temperature semiconductor detectors. The emphasis has been largely placed on

increasing the mobility-lifetime products for electron and hole charge carriers, which would allow one to fabricate larger and thicker detectors, and on improving the crystal growth and detector processing strategies. The three most promising materials for large-volume semiconductor detectors are currently cadmium zinc telluride (CdZnTe), cadmium telluride (CdTe) and mercuric iodide (HgI_2). Recent work has shown that room-temperature CdZnTe spectrometers having thicknesses of 1 cm can be fabricated, and the technological feasibility for 2.5-cm thick CdZnTe detectors has also been demonstrated. HgI_2 gamma-ray detectors having thicknesses up to 1 cm have also been produced (Ref. 1). The sensitivity of these devices still falls short of that achieved with scintillators, and further enhancements in range of detector operation are desirable.

The goal of this work is to improve the state-of-the-art for the sensitivity of room-temperature gamma sensors by arraying several smaller detectors, both in vertical and horizontal geometries. CdZnTe and HgI_2 detectors have been used but the technological approach is not limited by the detector material nor the detector geometry. The detector arrays allow for a significant increase in the sensitivity compared to the best room-temperature gamma detectors available today, and they can be designed and engineered to meet critical system requirements in terms of energy resolution, portability, ruggedness, low maintenance, and ability to operate in an unattended mode. In the case of CdZnTe, the arrayed detectors are found to be stable at temperatures up to about 70 ^{o}C, which allows their use in relatively hot desert-like environments.

RESULTS AND DISCUSSION

Several CdZnTe (and HgI_2) detectors were chemically etched and polished to reduce surface damage. Gold electrodes were deposited on the CdZnTe crystals, and 1-mil palladium wires were attached for application of a bias. Each detector was evaluated in terms of sensitivity, energy resolution, and dark current. Spectra were obtained for the detectors using several different gamma-emitting radionuclides and varying data collection times.

Figure 1 shows spectra for a 5x5x1.5 mm CdZnTe detector using a barium-133 source. The Ba-133 source has gamma-ray emissions that are in the same energy range as Pu-239. The detector had a bias voltage of 250 V, and the entrance electrode was negatively biased. The data collection time for the experiment was selected to be 2000 seconds. The four dominant gamma-ray peaks at energies of 300-400 keV are easily observed in the figure. Data taken on other CdZnTe detectors showed that not all detectors have the same carrier collection efficiencies, which causes the location of the photopeaks to vary between different detectors. This variation in peak positions complicates the use of vertical and horizontal stacking of detectors as a way to increase the effective sensitivity of the detector assembly.

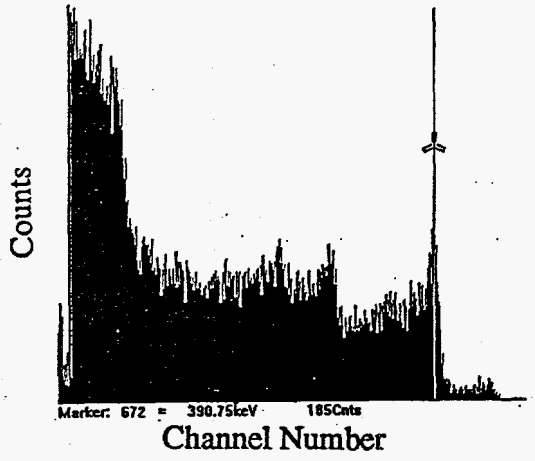

Figure 1. Spectrum for a 5x5x1.5 mm CdZnTe detector using Ba-133 radiation. The FWHM for the pulser is 3.1 keV.

An electronic scheme has been devised that adjusts the energy scale of each detector independently so that the peak positions are aligned for the different detectors. Figure 2 shows a schematic of the spectrum shift circuit in the case of vertical coupling of three detectors. The circuit involves simple RC networks, and it allows the detectors to be added together before the preamplification stage. The circuit is designed to discard a fraction of the charge for pulses from each detector, so that the charge induced on the preamplifier input is decreased. The fraction of the charge discarded is given by the ratio $C_{D,i}/(C_{D,i}+C_i)$ where $C_{D,i}$ is the capacitance of the i^{th} detector and C_i is the capacitance of

the detector's associated series capacitor. An alternative scheme for shifting the energy scale of each detector is to independently vary the voltage bias applied to each detector, since the charge collection efficiency of each device is dependent on the bias.

The electronic circuit shown in Figure 2 has been incorporated into our CdZnTe detector arrays. Excitation of one (or more) of the detectors by gamma or x-rays creates charge in the corresponding detector. A charge pickup by any detector creates a voltage offset at the preamplifier input. The preamp tries to return its input to its quiescent state by developing a current pulse through its feedback capacitor. This restoring current forces the charge collected in the detector to divide between the detector capacitance and the series capacitors. A few percent of the collected charge is intentionally lost to the series capacitor and its resistor, and this small amount of charge does not contribute to charge induced at the preamp input. The RC time constant (> 100 μs) must be longer than the time constant of the pulse amplifier.

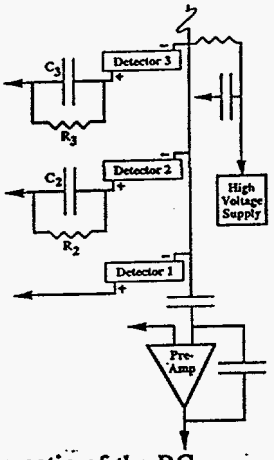

Figure 2. Schematic of the RC energy correction circuit showing how multiple room-temperature gamma-ray detectors can be connected in series to a single preamplifier and subsequent amplification stage.

There is a small penalty in using the electronic scheme discussed above to array several small detectors, in that it contributes to increases in the overall leakage current and capacitance of the system. This increased leakage current and capacitance leads to an increase in the system noise, which slightly degrades the energy resolution of the detector assembly. However, we find that the small decrease in energy resolution is more than offset by the increased sensitivity of the detector array. This increased sensitivity is manifested by larger photopeaks, which allows for an improved detectability to the characteristic gamma-ray emissions associated with SNM.

Figure 3 shows a spectrum using a Ba-133 radioisotope for a CdZnTe detector, which has the energy correction circuit activated. The response of this detector is also shown in Figure 1 for the case in which the circuit is off. Comparing Figures 1 and 3, we note that the RC network shifts the peak positions to lower channel numbers, because a fraction of the charge generated in the detector no longer contributes to the preamplifier output.

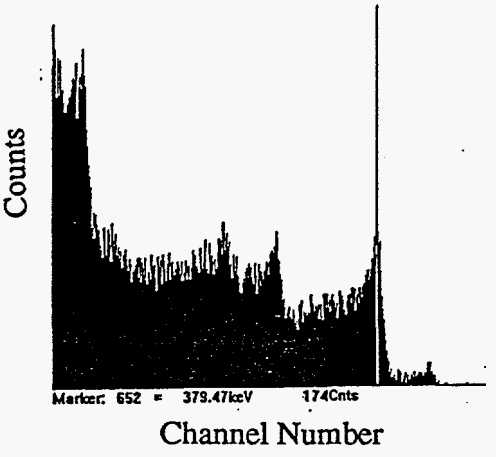

Figure 3. Spectrum for a 5x5x1.5 mm CdZnTe detector using Ba-133 radiation and the RC energy correction circuit. The detector was biased at 250 V and the data were acquired over a period of 2000 s. The FWHM for the pulser was measured to be 3.1 keV. Note the position of the photopeaks at the lower channel numbers compared to the spectrum in figure 1.

When multiple detectors are to be connected together, each detector is evaluated separately for its response to a particular gamma-emitting radionuclide, and the positions of the photopeaks are noted. The detector with the peak positions at the lowest channel numbers is selected, and each of the remaining detectors is connected to an RC circuit in such a way that the charge induced on the preamp by absorption of a gamma ray in any detector is identical. In a detector assembly, the entrance

electrode of the detector is typically biased negatively, because for most room-temperature semiconductors (e.g., CdZnTe and HgI_2) the hole mobility is substantially less than the electron mobility, and it is preferable to minimize the hole transit distance. For high-energy gamma rays that readily penetrate the bulk of the detectors, the direction of the electric field is less important.

Figure 4a shows a spectrum for two 5x5x1.5-mm thick CdZnTe detectors connected in a side-by-side lateral array geometry without an energy correction circuit. The presence of double peaks is obvious in the measured spectrum. Although this two-element detector array increases the sensitivity of the detector to SNM, it can actually lower the detectability of the instrument, because of the difficulty in uniquely determining the energy of the incident gamma ray based on the position of the photopeaks. In the event of other background radiation, significant problems with false alarms would be expected. Figure 4b shows a spectrum for the same CdZnTe detectors, except that an RC corrective circuit has been connected to one of the detectors. Here, the RC circuit on one of the detectors has been designed so that the positions of the photopeaks are aligned with the other detector. Using this approach, several smaller detectors can be connected together so that effective cross-sectional areas of 50-100 cm^2 are achievable. The performance of an array of small detectors would be approximately equal to that of a single detector with the same surface area. Moreover, if there are inhomogeneities in the single large-area detector which produce spot-to-spot variations in the spectra, then the performance of a number of small detectors would be expected to be significantly better than that of the single large detector. At present, detectors having cross-sectional areas of 50-100 cm^2 are not available, and in the event they are produced in the future, it is still possible to array these detectors to further enhance the sensitivity of the instrument.

Besides two-dimensional lateral arrays, it is also possible to vertically stack detectors to increase their absorption to high energy gamma-rays. We have found much better spectra can be obtained by wiring the vertical stack assembly so that the positive (negative)

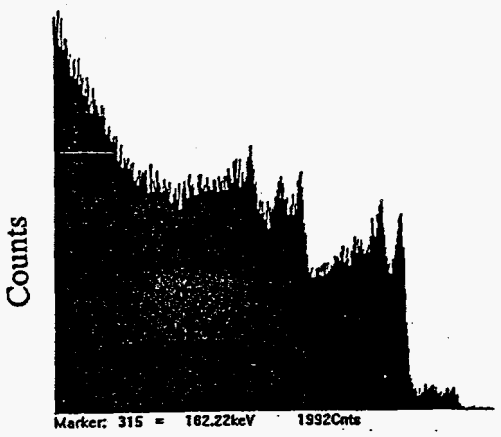

(a)

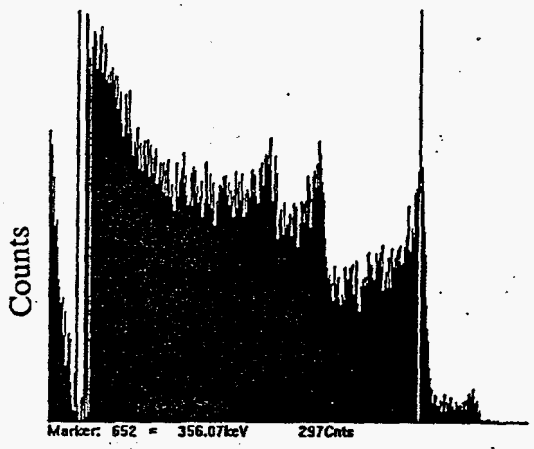

(b)

Figure 4. Spectra for two 5x5x1.5 mm CdZnTe detectors connected in parallel using a Ba-133 radioactive source. Figure 4a is a spectrum using no energy correction circuit and figure 4b is with the energy correction circuit activated. Note the double peaks in 4a associated with two different detector responses to the incident radiation are aligned in 4b to produce the same photopeaks.

face of one detector faces the positive (negative) face of the adjacent one. A thin insulator must be placed between the detectors to avoid a short circuit. Spectral data obtained for the alternative stacking scheme where the positive electrode of one detector faces the negative electrode of the adjacent detector was not as good because the thin insulators effectively act as capacitors thereby producing a large amount of unwanted noise. In the positive-to-positive face arrangement, the voltage difference between the faces of adjacent electrodes is small, and it does not significantly contribute to the input capacitance as seen by the preamp. For low energy gammas incident from the top of the vertical stack, most of the excitation will take place in only the top detector, but for high energy gammas the sensitivity of the vertical array will be much greater than a single detector due to the increased absorption of the incident gammas. An alternative geometry is to illuminate the detector cascade from the side so that radiation impinges equally on each detector.

It is possible to continue adding detectors into the vertical stack to effectively stop gamma rays with energies of 1000 keV and larger. For example, Figure 5a shows spectra for three 5x5x2 mm CdZnTe detectors connected in a vertical stack, but in this case no energy corrective circuitry has been included. This particular spectrum was taken with Na-22 radiation, which has a principal gamma-ray emission at 511 keV. Three distinct photopeaks are observed due to the differing response of each detector in the stack. Without changing any other experimental conditions, the corrective circuit is switched on, and some of the charge normally induced at the preamp input is now dissipated into the RC networks. In this setup the detector having photopeaks at the lowest channel numbers is connected directly between the preamp and ground, and the other two detectors are connected to RC circuits so that all detectors have photopeaks in the same positions. Figure 5b shows a Na-22 spectrum for the same detector assembly, but in this measurement the energy corrective circuit has been switched on. The FWHM for the 511-keV photopeak is about 13 keV (or 2.6%), and the FWHM of the pulser is 8.2 keV. Both the sensitivity and peak-to-valley ratio of the detector assembly is better than any one of the smaller detectors.

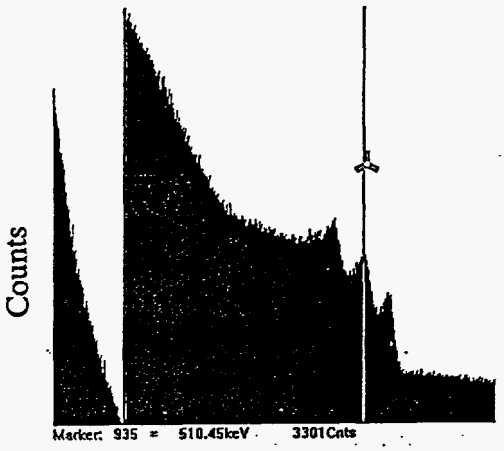

(a)

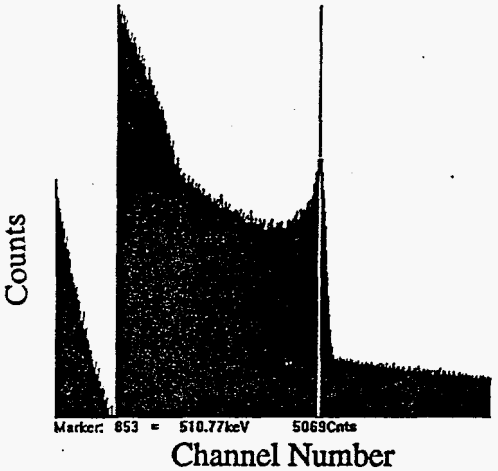

(b)

Figure 5. Spectra taken with Na-22 radiation incident on three 5x5x2 mm CdZnTe detectors stacked vertically and connected in parallel. Data were collected over a time of 3600 s. The detector assembly was irradiated from the side and each detector in the stack sees the same gamma-ray source. Figure 5a shows the collected spectrum without the energy corrective circuit and figure 5b shows the spectrum with the circuit connected so that the 511-keV photopeaks associated with each detector are aligned.

Thicker detectors are desirable for gamma-ray energies above about 100 keV, particularly if the sources of radiation at the measurement location are weak. Several attempts have been made to fabricate thick (> 10 mm) CdZnTe and HgI_2 detectors with good energy resolution [Refs. 1-3]. Figure 6 shows a spectrum using Na-22 radiation for a 10-mm thick CdZnTe detector, which was irradiated from the negatively biased entrance electrode. The bias voltage was 1000 V. The FWHM of the 511-keV photopeak is about 7 keV (or 1.4%). This particular

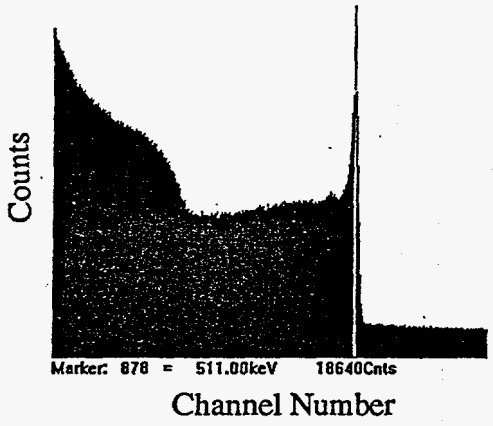

Figure 6. Spectrum taken with Na-22 radiation incident on a relatively large-volume 10x10x10 mm CdZnTe detector. Data were collected over a time of 3600 s.

10x10x10 mm CdZnTe detector is not typical of those readily available today, and it represents one of the best thick (10 mm or more) room-temperature semiconductor detectors ever produced. We anticipate that large volume detectors of this quality will be readily available in a few years, and using the electronic scheme discussed in this paper, it will be straightforward to array these large volume detectors.

CONCLUSIONS

A circuit has been devised to connect several room-temperature semiconductor gamma-ray detectors of slightly different responses to a single preamp. The detector arrays have significantly greater sensitivity than the individual detectors, and the elimination of multiple preamps greatly simplifies the portability of the instrument. This approach is useful because room-temperature semiconductor gamma detectors are currently limited to relatively small areas and thicknesses, and system requirements of portable instruments for searching and monitoring SNM require sensors with improved detectability. Future improvements in the fabrication of arrays of gamma-ray detectors are expected to reduce the counting times by more than an order of magnitude compared to the state-of-the-art for single room-temperature semiconductor detectors.

REFERENCES

1. V. M. Gerrish, "Electronic Characterization of Mercuric Iodide Gamma-Ray Spectrometers", in *Semiconductors for Room-Temperature Radiation Detector Applications*, edited by R. B. James, T. E. Schlesinger, P. Siffert, and L. Franks (Materials Research Society, Pittsburgh, PA, 1993), p. 129.

2. G. F. Knoll and D. S. McGregor, "Fundamentals of Semiconductor Detectors for Ionizing Radiation", in *Semiconductors for Room-Temperature Radiation Detector Applications*, edited by R. B. James, T. E. Schlesinger, P. Siffert, and L. Franks (Mat. Res. Soc., Pittsburgh, PA, 1993), p. 3.

3. Bruce Glick, E. Eissler, K. Parnham, S. Cameron, and C. Johnson, "Large Volume/ Large Area CdZnTe Radiation Detectors", Presentation at 1994 Symposium on Radiation Measurements and Applications, Ann Arbor, MI, unpublished.

Characterization of silver impurities in mercuric iodide and their relationship to gamma-ray detector performance

J. M. Van Scyoc[a], R. B. James[a,*], T. E. Schlesinger[b], T. S. Gilbert[b], and M. Schieber[a]

[a]Advanced Materials Research Department, Sandia National Laboratories, MS 9162, Livermore, CA 94551, USA
[b]Department of Electrical and Computer Engineering, Carnegie Mellon University, Pittsburgh, PA 15213, USA

Abstract

Red mercuric iodide (α-HgI_2) has been studied extensively for use as a room-temperature radiation detector material. Although it has several properties which make it an extremely attractive material for such applications, it has not seen large-scale deployment, particularly in the commercial market, because of several continuing problems. These problems arise, in part, from some of the intrinsic properties of the material. However, the primary limiting factors at this point are related to the phenomena of incomplete charge collection and device polarization. This paper examines one purported cause for both the carrier trapping and the device instability. In particular, silver is an elemental impurity that is known to exist in typical HgI_2. Leakage current experiments demonstrate how this electrically active impurity is mobile in bulk HgI_2. Detector characterization shows how the presence of the silver degrades the performance and affects the spectral properties of the device over time. These results are combined with related work on impurities in HgI_2 to develop a picture of the effects of silver on detectors and the processing requirements for detector fabrication.

*Corresponding author.

1. Introduction

Red mercuric iodide (α-HgI_2) has been investigated for almost three decades for use as a room-temperature radiation detector material. It has several properties which make it an extremely attractive material for this purpose. The high average atomic number of the constituent atoms (Z_{Hg}=80, Z_I=53, or Z_{avg}=62) results in a high efficiency for stopping photons into the low MeV range. The electron-hole-pair creation energy of 4.2 eV at room temperature leads to a sufficiently large signal response per photon. Finally, the room-temperature bandgap of 2.13 eV results in a resistivity on the order of 10^{14} Ω*cm and a dark current on the order of picoamps for typical device structures. These properties combine to give a material that has been used to produce some of the highest resolution room-temperature x-ray and gamma-ray detectors [1-4]. In addition, the capability for room-temperature operation results in the possibility of compact spectrometer systems that can be used in the field for applications ranging from environmental monitoring to special nuclear materials (SNM) monitoring.

All of these positive properties noted above are coupled to and offset by several negative properties of the material. Some basic properties of HgI_2 cause some of the problems. The fact that it is a compound semiconductor immediately leads to issues of crystal stoichiometry. The material has a relatively high vapor pressure at room temperature, and in addition, the iodine is preferentially sublimed at a faster rate, yielding mercury-rich surfaces. The red tetragonal α-HgI_2 phase undergoes a phase transition around 125 °C to the yellow orthorhombic β-HgI_2 phase which destroys the crystallinity of the material upon returning to room temperature. In addition, the material is mechanically very soft and also delaminates easily along the iodine layers.

The extrinsic factors that degrade mercuric iodides' usefulness are related to carrier-trapping centers that are introduced into the material at some point in the process. These can arise from structural damage to the crystal or stoichiometric changes during the crystal growth and device fabrication processes. Of interest here, however, are the impurities that are introduced into the material, either from the original starting materials or further along in the fabrication process.

Several impurities are believed to play a role in mercuric iodide, ranging from hydrocarbons to metallic elements. One particular example of the latter is silver.

These factors all lead to problems in the initial yield of high-quality detectors and the long-term reliability of the detectors. These two problems combine to limit the applications of these sensors, particularly in the commercial arena. Given that the intrinsic material properties can only be sidestepped, one of the primary ways to improve the material is to identify the impurities that are deleterious to the detector performance and work to reduce their presence. In this paper we quantify how silver degrades mercuric iodide detectors.

2. Experiments

2.1 Leakage Currents

Electrically active impurities in a semiconductor detector trap some of the carriers generated by a photon event, thereby leading to a decreased amount of charge collected at the device contacts and a diminished signal amplitude. The trapping process is stochastic, and therefore the effect on the measured signal is random. Accordingly, the mere presence of an electrically active impurity leads to a smaller signal and a "smearing" of the energy spectrum. The presence of a mobile impurity complicates the situation further. There is a current associated with the movement of the impurity itself, which leads to a heightened noise level, and the trapping effects of the impurity center vary unpredictably as the impurity moves in the bulk material. The first experiment described here demonstrates the mobility of the silver impurity in mercuric iodide. In this experiment we intentionally doped a sample with an amount of silver. We then monitored the leakage (or dark) current versus time to determine the movement of the silver.

The sample used in this experiment was a standard detector piece cut from a vapor-grown HgI_2 crystal, with dimensions of 1 cm^2 by 1 mm thick. A 6.35 mm diameter, 200 Å thin film of high-purity silver was sputter-deposited onto one face of the sample, and a palladium lead was attached with aquadag (colloidal carbon suspension). This translates to a doping level of 15 ppm if the silver is distributed uniformly throughout the bulk of the HgI_2. On the reverse side, an aquadag

contact of similar area was made. The sample was then placed in a dark dessicator cabinet and connected to the measurement circuit.

The measurement circuit consisted of several instruments controlled and monitored by a personal computer via a GPIB (IEEE-488) interface. The sample was biased using a high-voltage power supply capable of supplying up to 10 mA at 500 V. The sample bias voltage was monitored with a standard digital multimeter and was stable within +/-1 V. The leakage current was measured with a Keithley Instruments 485 picoammeter with a resolution of 0.1 pA. Finally, a switching assembly was fabricated that allowed for computer-controlled reversal of the bias direction and removal of bias for other measurements. With this setup the silver-doped/contacted device was biased and monitored for several days to capture "transients" in the leakage current.

2.2 Detector Characterization

A standard x-ray/gamma-ray detector-characterization setup was used to measure the spectral response of the HgI_2 detectors. A high-voltage power supply was used to provide a negative bias to the entrance electrode. A custom-built box housed the detector under test and was connected to a Tennelec TC170 charge-sensitive preamplifier, modified for DC coupling, by way of a BNC connector. A Tennelec TC241 spectroscopy amplifier was used to shape the pulses from the preamplifier, and a The Nucleus MCA card and software were installed in a PC to collect the spectra.

For this set of experiments, a 1 cm^2 by 2 mm-thick slab of mercuric iodide had 200 Å thick 6.35 mm-diameter Pd contacts sputtered on each side and Pd wire leads aquadagged on. The detector was then characterized to determine its "undoped" performance. Then a 400 Å thick 7.94 mm-diameter film of silver was sputtered on top of the entrance electrode to dope the sample. Assuming that the entire silver film in contact with the material was evenly distributed throughout the bulk HgI_2, this would result in a concentration on the order of 8 ppm.

Because HgI_2 detectors always require a conditioning time when bias is initially applied, we characterized this effect first in order to separate out the doping effects. The sample was irradiated with a 1 μCi ^{241}Am source placed about 2 cm above the entrance electrode. ^{241}Am has a gamma

photon at 59.54 keV and several x-ray escape peaks in the 14 to 21 keV range. The energy of the primary gamma photopeak lies near the middle of the range of energies of interest for most HgI_2 detector applications.

3. Results and Discussion

3.1 Previous Related Work

There have been extensive efforts in recent years to quantify the amount of various types of impurities present in mercuric iodide materials. It is useful to know the impurities present at various stages of the process in order to see, for example, if sublimation- or melt-purification schemes actually reduce the level of impurities as desired. One set of methods for quantifying the elemental impurities is Inductively Coupled Plasma Optical Emission and Mass Spectroscopy (ICP-OES and ICP-MS, respectively), which vaporize and ionize a sample solution with a plasma and measure the presence of a range of elements. The ICP-OES technique can generally measure down to the high ppb range, while the ICP-MS method can reach the ppt region. Both of these techniques have been used to quantify the silver in many HgI_2 samples, ranging from the initial material to purified material ready for crystal growth to completed crystals. Typically, silver is seen in the 100-300 ppb level over a wide variety of samples [5]. Therefore, it is fairly well accepted that silver is indeed present in most material.

Other experiments have shown that the impurities, as expected, can be equally well introduced during subsequent processing of the material for detector fabrication. Another good method for locating and identifying impurities present in a sample is low-temperature photoluminescence (PL). PL has been used extensively on HgI_2, and the material has a rich PL spectrum. In general, impurities can be detected down to the ppt level, but can rarely be quantified. One common step used throughout the fab process is a wet-chemical etch in a dilute solution of potassium iodide (KI). The KI etch is used to remove mechanical damage from cutting, polishing, and related operations, and to remove the "aging" from the surface that results from the high vapor pressures of the Hg and I. Earlier experiments have shown, however, that impurities in the KI solution are readily incorporated into the HgI_2 and that these impurities readily diffuse throughout the sample in

a matter of days. Therefore, silver can certainly be introduced into samples during the detector fabrication process, and it has been shown to degrade detector performance [6-9].

3.2 Leakage Currents

The leakage currents experiments, as described above, were conducted on a mercuric iodide sample with the silver overlayer. The sample was initially biased with the doping contact at a positive bias. Previous work had suggested that the silver impurity exhibits a positive charge, therefore this positive initial bias is expected to drive the silver impurities into the bulk of the mercuric iodide. Fig. 1 shows the results of the leakage current evolution over time for a period of several days. The leakage current exhibited a peak that slowly decayed to the background leakage current of 1 nA, which is higher than that found in typical detector structures. This may indicate that the material had been damaged by the presence and movement of the high level of impurities, since the very initial leakage current was closer to the typical value of picoamps.

The majority of the impurities, over 90%, appear to move in the first hour. The total charge moved, as determined by the integration of the current over time, was 3.8×10^{-3} C, or 2.4×10^{16} single charges. The entire silver film had about 3.5×10^{16} atoms, so about 70% of the silver atoms present resulted in mobile impurities in the HgI_2, assuming a singly charged impurity.

After the leakage current had stabilized (after about three days), the bias was reversed. Once again, the current had a peak that decayed similarly, with about 84% of the movement in the first hour. In this case about 2.0×10^{16} single charges moved, meaning that 18% of the initial group of mobile impurities were much less mobile. This tends to indicate that the majority of the silver impurities are "pulled back" through the HgI_2 towards the now-negative front contact. Once again, the background level is around 1 nA.

As alluded to above, the silver impurity, which may be a silver iodide (AgI) or something related, exhibits a single positive charge. The impurity drifts in the field as a positively-charged carrier with low, ionic mobility.

3.3 Detectors

In general, mercuric iodide detectors require at least several hours of biasing at the operating voltage before the spectral performance stabilizes. To characterize this for the detector to be doped with silver, we measured the spectral response at set time intervals over a period of several hours. As seen in Fig. 2, the ^{241}Am spectrum undergoes significant changes during the conditioning process. In particular, the initial few hours show the development of a peak that later disappears and that is at a higher channel than the actual photopeak. Once the photopeak develops, it continues to shift slightly to higher channels and decreases in linewidth. It took about 200 hours under bias for this detector to stabilize in terms of spectral response, and at that point it had a photopeak FWHM of about 3.51 keV or 5.9% and a peak-to-valley ratio around 4.9. While these figures are far from the state-of-the-art, the detector can be considered a "spectrometer".

In order to do the doping experiment, it was necessary to remove the detector from biasing for a few hours during the deposition process. The detector will then lose some of its conditioning and will need to be biased again for a period to allow the response to stabilize. Fig. 3 shows the results of removing the detector from bias for 3 hours and then rebiasing it. It shows that after about 10 hours the detector has recovered.

The sample was then doped as discussed above and the spectra acquired as before. Fig. 4 shows the results. As can be seen, the detector takes close to 300 hours to stabilize, and the spectral performance has degraded significantly. First, the pulse height of the photopeak has shifted from around channel 1001 to around channel 706, meaning a decrease in the charge-collection efficiency. The peak-to-valley ratio has only decreased somewhat (to about 4.3), but the resolution has degraded to 7.31 keV or 12%.

These results show that the presence of the silver impurity does indeed have a strong deleterious effect on the operation of HgI_2 detectors. The overall achievable performance seems to have been irreversibly degraded. In addition, the conditioning time required has increased from about 10 hours to almost 300 hours. Combined with the leakage current results above, this suggests that the silver impurities move through the detector and also leave behind trapping centers. The long conditioning time is connected with the time it takes to remove all of the silver

impurities by pulling them through the bulk and to the back contact. The overall degradation indicates that the silver leaves behind a trap, most likely a hole trap, that captures some of the photo-generated charge leading to a reduction in the pulse-height, and broadening of the peak.

4. Conclusions

This work has demonstrated that silver impurities are present in mercuric iodide, are introduced during processing, and that they affect detector performance. Leakage current measurements on doped samples were used to demonstrate that the silver impurity is mobile and can easily be swept back-and-forth through the bulk crystal by an applied electric field. Detector characterization on doped detectors was used to show the actual degradation in performance.

These two measurements show how silver affects the operation of detectors. In particular, the silver presents two means of detector failure. First, the presence of the silver introduces a defect center that traps carriers associated with the incoming photons and leads to decreased and statistically-broadened pulse heights. Second, the silver is seen to be mobile, which leads to changes in detector performance -- particularly as the bias is changed. Actually, the movement of silver and similar impurities may be the cause of the required conditioning time. When a detector is first biased, a fraction of the impurities are swept through the sample and remain at the back contact until the bias is removed, at which time diffusion becomes the dominant mechanism.

These results suggest that silver must be removed from and kept from entering the mercuric iodide crystals and detectors. Purification is required in order to remove silver from the starting material, and the subsequent processing must be "clean".

References

[1] L. van den Berg, Nucl. Inst. & Meth. in Phys. Res. A A322 (1992) 453.

[2] A. J. Dabrowski, J. S. Iwanczyk, Y. J. Wang, M. Madden, and M. Szawlowski, Proc. of the SPIE 2007 (1993) 19.

[3] V. Gerrish and L. van den Berg, Nucl. Inst. & Meth. in Phys. Res. A A299 (1990) 41.

[4] P. Olmos, G. Garcia-Belmonte, J. M. Perez, and J. C. Diaz, Nucl. Inst. & Meth. in Phys. Res. A A299 (1990) 45.

[5] E. Soria, internal communications.

[6] C. Y. Hung, X. J. Bao, T. E. Schlesinger, R. B. James, A. Y. Cheng, C. Ortale, and L. van den Berg, J. Appl. Phys. 73 (1993) 4591.

[7] X. J. Bao, T. E. Schlesinger, R. B. James, R. H. Stulen, C. Ortale, and A. Y. Cheng, J. Appl. Phys. 68 (1990) 86.

[8] X. J. Bao, Ph.D. Thesis, Carnegie Mellon University (1991).

[9] R. B. James, X. J. Bao, T. E. Schlesinger, A. Y. Cheng, and V. M. Gerrish, Mat. Res. Soc. Symp. Proc. 302 (1993) 103.

Figure Captions

Fig. 1 Leakage current versus time for the silver-doped detector sample.

Fig. 2 Initial detector response variation versus time for 0 to 184.7 hours after biasing. The bias voltage was -1000 V and the counting time was 1000 s for each spectrum.

Fig. 3 Variation of detector response with time after removing the bias for three hours. The bias voltage was -1000 V and the counting time was 1000 s for each spectrum.

Fig. 4 Detector response after silver doping versus time for 0 to 263.2 hours. The bias voltage was -1000 V and the counting time was 1000 s for each spectrum.

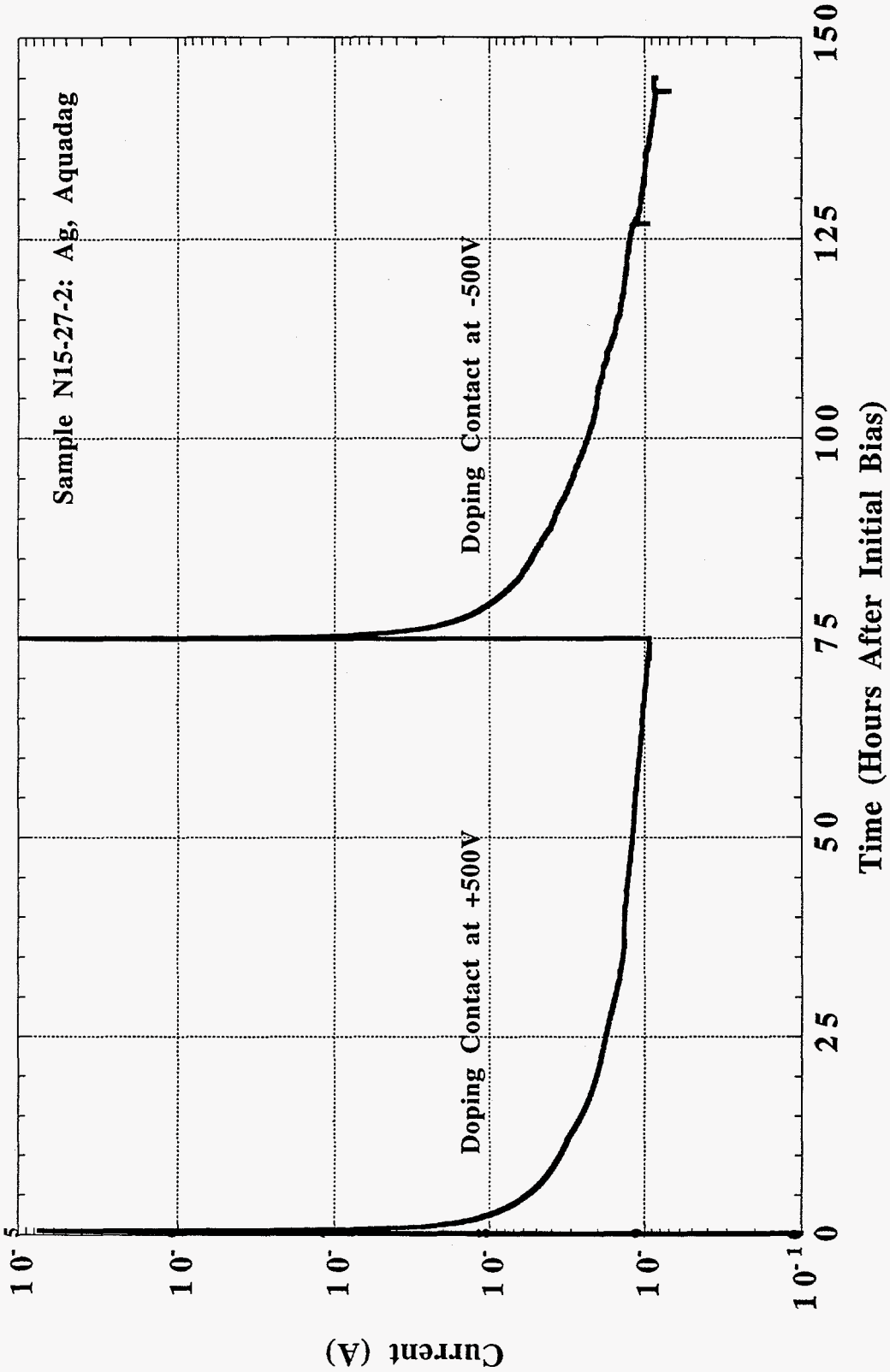
Sample N15-27-2: Ag, Aquadag
Doping Contact at -500V
Doping Contact at +500V
Current (A)
Time (Hours After Initial Bias)
10^-5
10^-6
10^-7
10^-8
10^-9
10^-10
0
25
50
75
100
125
150

Fig. 1

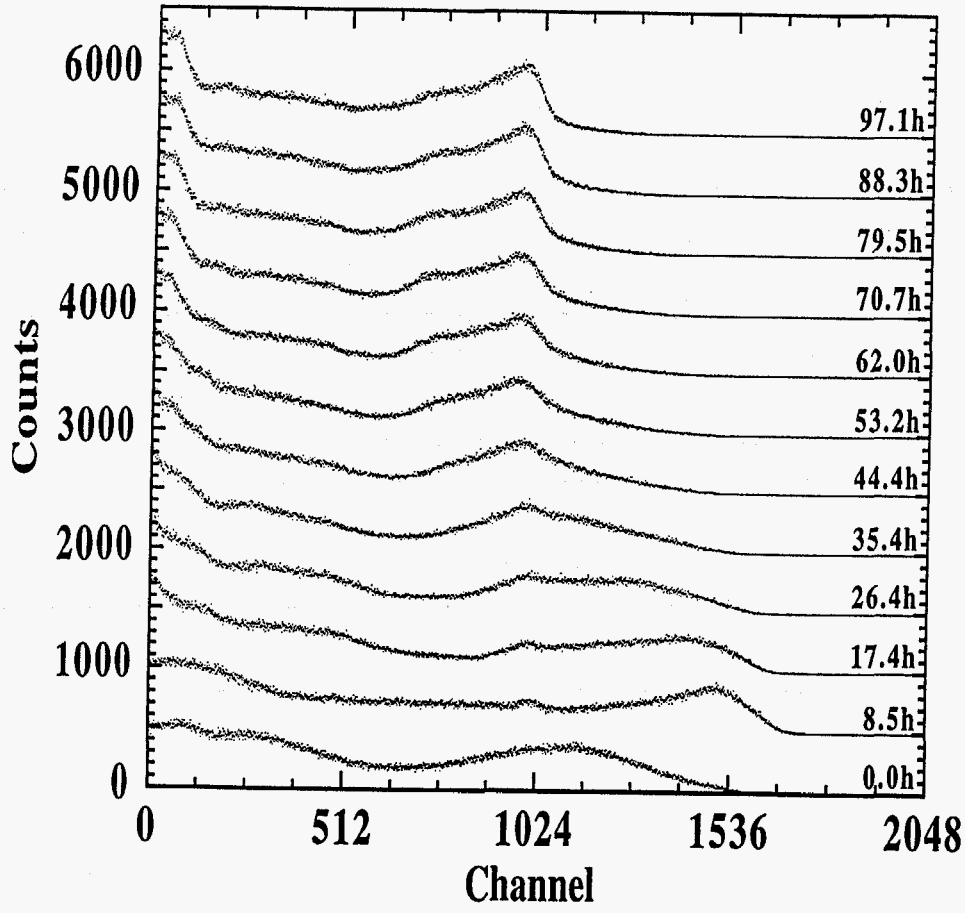
Counts
6000
5000
4000
3000
2000
1000
0
97.1h
88.3h
79.5h
70.7h
62.0h
53.2h
44.4h
35.4h
26.4h
17.4h
8.5h
0.0h
0
512
1024
1536
2048
Channel

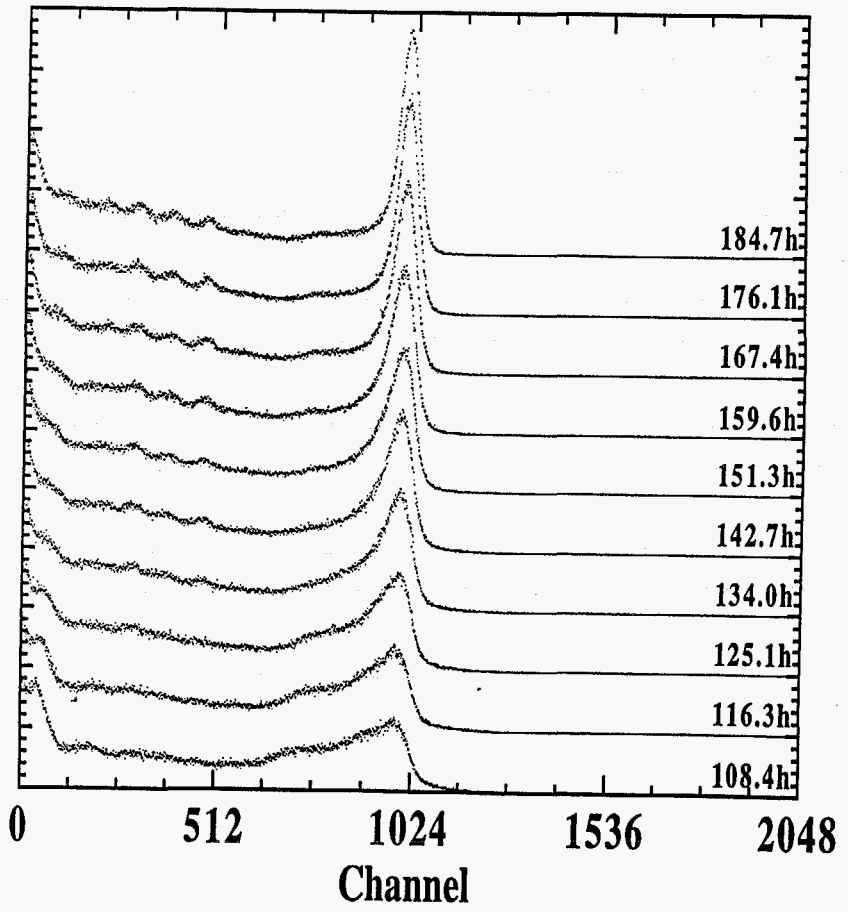
184.7h
176.1h
167.4h
159.6h
151.3h
142.7h
134.0h
125.1h
116.3h
108.4h
0
512
1024
1536
2048
Channel

402

Fig. 2

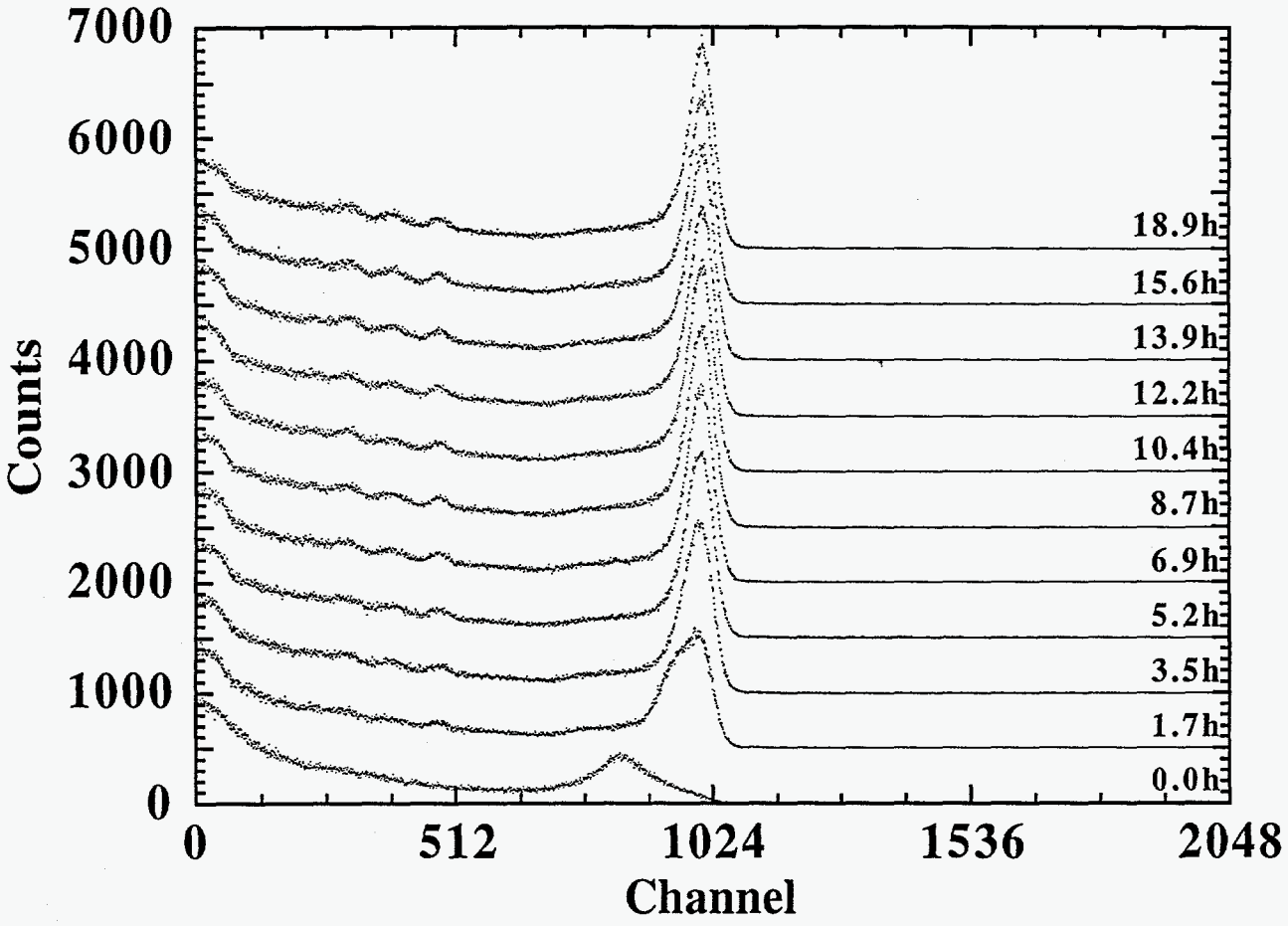
7000
6000
5000
4000
3000
2000
1000
0
Counts
18.9h
15.6h
13.9h
12.2h
10.4h
8.7h
6.9h
5.2h
3.5h
1.7h
0.0h
0
512
1024
1536
2048
Channel

Fig. 3

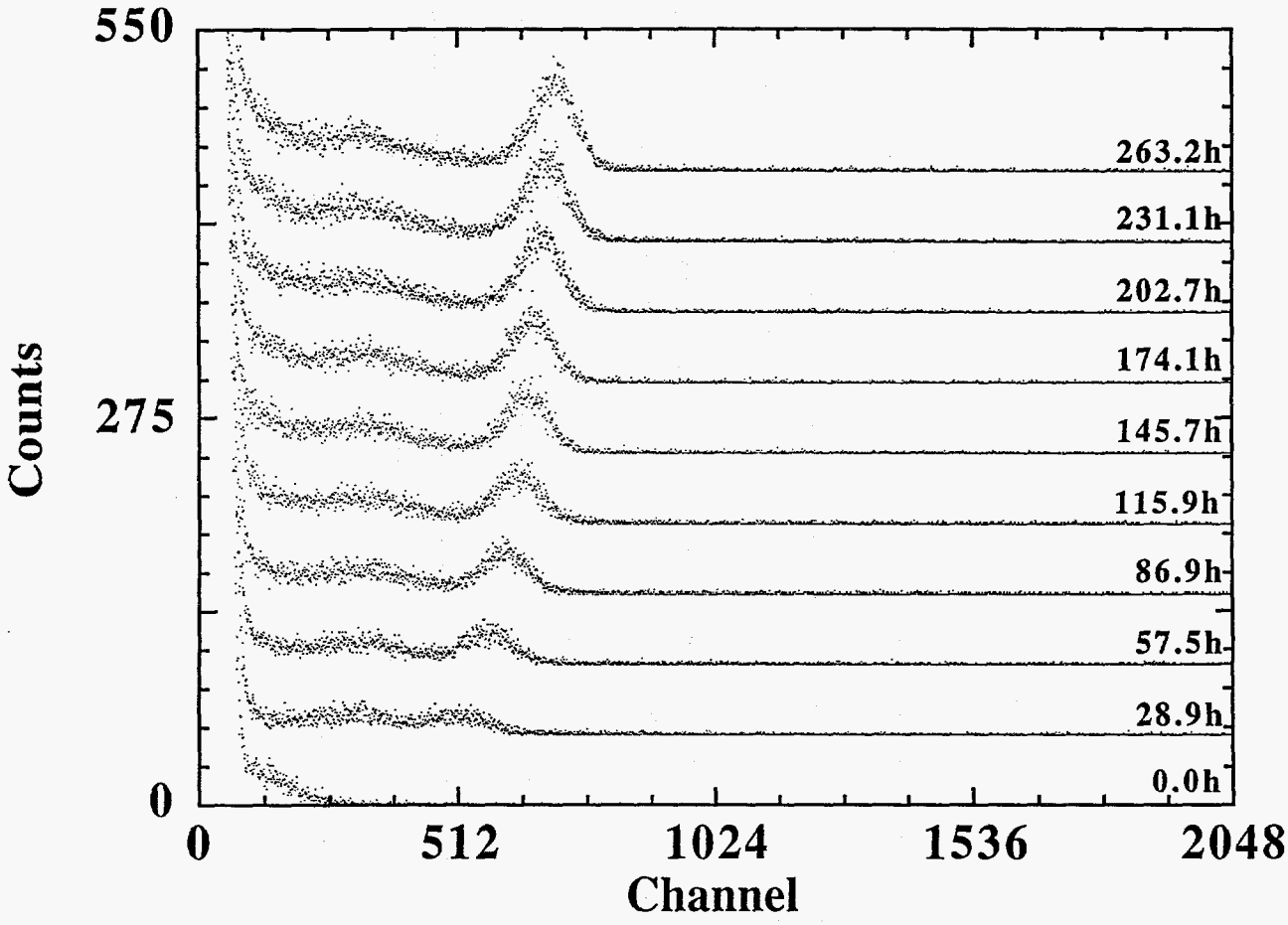
550
275
0
Counts
263.2h
231.1h
202.7h
174.1h
145.7h
115.9h
86.9h
57.5h
28.9h
0.0h
0
512
1024
1536
2048
Channel

Fig. 4

Final version to appear in NIM

Two-Dimensional Photocurrent Mapping of Mercuric Iodide Detector Crystals

B.A. Brunett, D.C. David, T.S.Gilbert, and T.E. Schlesinger
Department of Electrical and Computer Engineering,
Carnegie Mellon University
Pittsburgh, PA 15213

J.M. Van Scyoc, R.B. James
Advanced Materials Research Department,
Sandia National Laboratories
Livermore, CA 94551-0969

We have employed two dimensional photocurrent mapping to determine the material uniformity of a 1 cm^3 cube of mercuric iodide configured as a detector. The sample was mapped over the cross sectional face of the crystal between the two Pd contacts used to bias the sample. We have examined the dependence of photocurrent response on detector bias, and also observed nonuniformities within the detector area. A model predicting the photocurrent as a function of position between the contacts has been related to the experimental results and is also presented.

Introduction

Mercuric iodide has proven to be an excellent material for the fabrication of x-ray and γ-ray spectrometers and these have performed well in a great many applications including medical diagnostic systems, astronomy and astrophysics, portable x-ray fluorescence spectrometers, and so forth [1]. While mercuric iodide spectrometers should have excellent performance characteristics even at γ-ray energies this material is still limited by poor charge collection efficiency for holes and material nonuniformities. This becomes especially apparent when thick (1 cm) detectors are fabricated as is necessary for high stopping power at γ-ray energies. Spectrometer thicknesses can range from less than a millimeter for energies less than 200 keV to 1 centimeter or more for the detection of high energy γ-rays [2]. This requirement for large uniform crystals has led to a considerable research effort in the areas of material growth and processing techniques. In this paper we describe a method for examining the uniformity of the material while it is operating in a geometry nearly identical to that of a spectrometer. This technique produces a two dimensional photocurrent response map of the material across the active region of the device. In this manner the charge collection efficiency across the device area can be studied rather than the average performance of the device. We describe this mapping technique and discuss the experimental results obtained for a 1 cm^3 mercuric iodide crystal.

Two Dimensional Mapping Technique

The 1 cm^3 mercuric iodide crystal was first etched in 10% KI solution to remove any degraded surface layer and facilitate the application of the contacts. One of the C faces was then covered with a plastic shadow mask consisting of a square via hole. The contact area was centered above one of the AB faces and placed against the edge of the C face. Pd was sputter deposited through the shadow mask onto the top C-face to a thickness of a few hundred angstroms as would be typical in a detector fabrication process. To prevent deposition of the Pd onto the AB face of interest, the sample was tilted toward this face effectively shadowing the face from deposition of contact material. Both the time that the sample spent under vacuum and in deposition were minimized to reduce sample damage. The above process was then repeated to produce the second contact on the opposite C-face. Care was taken to center the two contacts above each other. Carbon

DAG was used to attach leads to each contact. The sample and leads were then mounted onto an alumina substrate for robustness and to prevent damage to the sample.

Mechanical translation was used to produce the spatial variation for two dimensional mapping. The translation stage used has a spatial resolution of 1 μm and a motion range of 10 cm^2. In this setup the sample itself is translated while the excitation source remains spatially fixed. The stage was mounted such that the plane of x-y motion was in the vertical direction. The sample was then mounted onto the stage such that the contacts were horizontal and the AB face of interest was both parallel to the plane of motion and perpendicular to the excitation source. This allows for normal incidence with a laser for optical excitation of the cross sectional AB face.

A high voltage supply was used with the positive terminal connected to the top of the sample. Current measurement was achieved using a high precision, low current ammeter with its positive terminal attached to the bottom of the sample. The negative terminals of each component were common. This configuration will produce positive current for positive applied bias voltage. The excitation source consisted of a HeNe laser with a wavelength of 6328 Å which is below the bandgap for HgI_2. The beam was collimated with several microscope objectives such that about 95% of its power was contained within a spot 250 μm in diameter. The power incident onto the sample was 7.1 mW giving a power density of about 3.6 W/cm^2.

To obtain a two dimensional map the sample was first placed under bias and allowed to settle for several hours. Next the excitation source was turned on and the stage incrementally stepped over the area of interest at a resolution of 250 μm. The photocurrent and position of the stage were recorded for each data point in the two dimensional map. This procedure was used to obtain each of the following data sets always using the same scan area and laser excitation.

Experimental Results and Discussion

A series of scans were performed on the sample starting with a bias voltage of negative 500 volts and sequentially decrementing the voltage by 500 volts. In figure 1 we present the two dimensional photocurrent maps obtained for three values of negative bias (the ground connection is at the bottom of each map and the negative electrode is at the top of each map). Each map is plotted with the same scale used in the map obtained at a bias of negative 1500 volts so that we can

compare the results. As can be seen from figure 1 the magnitude of the photocurrent increases with higher bias voltages. This trend is expected realizing that the photocurrent corresponds to collection, complete or partial, of generated carriers. The increase in the bias voltage will increase the average field within the device and thus the average drift velocity of the carriers and therefore we expect this increase in the observed current.

It is also clear that the photocurrent is greatest near the top of the device (i.e. near the negatively biased electrode). This trend is also not unexpected and indicates that electrons are the primary contributors to the photocurrent. Near the negative electrode both electrons and holes are collected with electrons travelling completely across the device. As one moves the excitation source to the positive electrode holes are not collected, since they cannot traverse the entire length of the device, and electrons no longer contribute a full charge to the externally observed current since they travel only a fraction of the distance across the device [3].

General nonuniformities can be also be seen in all of the plots. These can be attributed to localized regions of nonuniform material leading to changes in material properties and a nonuniform electric field. Or, alternatively, these regions can be attributed to defects on the surface of the scan area leading to differences in the amount of absorbed light. To eliminate surface anomalies the sample requires careful preparation. A second series of scans, similar to the ones discussed above, were performed with positive voltages (positively biased electrode at the top of the maps). These are shown in figure 2. The basic trends discussed above also hold true for this series of scans although inverted owing to the fact that the sign of the bias has been switched.

Two major differences in the photocurrent for positive and negative bias voltages are apparent. First, the magnitude of the observed photocurrent varies greatly between the positive and negative bias voltages. One would expect the photocurrent to be nearly symmetric with respect to the polarity of the applied bias. One possible source of this asymmetry may involve the preparation of the sample. During the deposition of the contacts the sample is exposed to vacuum which has been shown to alter the surface properties of the sample [1]. The first Pd contact protects the underlying material during the deposition of the second contact. Hence the material under the second contact is exposed to vacuum for a longer cumulative period of time during these processing steps. Alternatively it is possible that the first contact has an opportunity to react with

the mercuric iodide while under vacuum and possibly experiencing some heating during sputter deposition. Thus, in either case it is possible that the material under the first contact will not be identical to that under the second contact. This will lead to asymmetric contacts and therefore differences in the observed photocurrent. To verify this hypothesis additional experiments using samples purposely prepared asymmetrically must be performed. These experiments could include a sample prepared with one contact left under vacuum significantly longer, heated significantly more, or with a different metal contact material.

A second observation that we make is that there is a band of enhanced charge collection in the central region of the device for the positive applied biases. The magnitude of the photocurrent observed in this band is smaller than that near the cathode but the band is clearly discernible as a region of enhanced photocurrent relative to the immediately neighboring regions. We do not observe this band in the negative scan as there exist large differences between the positive and negative scans as noted above. Nonetheless, it is interesting to note that Knoll and McGregor do predict enhanced charge collection efficiency in the central region between the two contacts in a device depending on the carrier extraction factor [4].

The ability to reproduce the photoresponse for particular set of input conditions is crucial for material analysis. This allows a particular result to be verified or certain phenomenon to be further explored. Mercuric Iodide is extremely sensitive to prior external excitations, namely bias voltage, and polarization effects in this material are well known [5]. Shown in figure 3 are two repeated scans demonstrating this dependence. The first scan in set (A) was taken with an applied bias of negative 1000 volts. Two more scans were then performed with bias voltages of negative 1500 and 2000 volts respectively. The bias voltage was then reduced to negative 1000 volts and a map was again recorded. The time elapsed between the first and second negative 1000 volt scan was approximately 8 hours. As can be seen from the figure the repeatability in this case is poor. In the second set of scans (B) an initial scan was performed with an applied bias of 2000 volts. The sample was then left under bias for approximately 8 hours and the scan was repeated. The second scan agrees well with the first as shown in figure 3. Clearly polarization effects are easily observed in these maps and can greatly affect the observations made with this technique. On the other hand it may be possible to employ this technique to study the details of polarization phenomenon as they

relate to the redistribution of the applied field within a device.

To obtain information about detector efficiency or material uniformity we need to relate the photocurrent to certain physical properties. In particular a model relating photocurrent to the mt product will be explored. We consider a detector configured as shown in figure 4(A). A negative voltage applied to the right side of the detector will cause any carrier generated between the contacts to be swept out of the active region. The charge measured from a detector is given by Knoll and McGregor [4] as

$$Q = qN_o\left(\vartheta_e\left(1-exp\left(-\frac{y_e}{\vartheta_e w}\right)\right)+\vartheta_h\left(1-exp\left(-\frac{y_h}{\vartheta_h w}\right)\right)\right).$$

where N_0 is the total number of carriers produced, w is the detector active region width, y is the distance of the carrier from the respective contact, and ϑ is the charge extraction factor of the respective carrier. The charge extraction factor is given by

$$\vartheta_e = \frac{\mu\tau_e V}{w^2} \qquad \vartheta_h = \frac{\mu\tau_h V}{w^2}$$

where τ is the carrier lifetime and V is the voltage across the active region. Next we relate this charge to the current observed. Consider an excitation source of a particular wavelength and intensity impinging onto the sample. A certain fraction of the light will be reflected back and a certain fraction will be transmitted through the front surface of the sample. A below bandgap excitation was used so there will also be a certain fraction of the light that escapes from the back of the sample. These fractions are the reflection and transmission coefficients [6] and are given by

$$R = R_s\left(1+\frac{(1-R_s)^2 exp(-2\alpha w)}{1-R_s^2 exp(-2\alpha w)}\right) \qquad T = \frac{(1-R_s)^2 exp(-\alpha w)}{1-R_s^2 exp(-2\alpha w)}$$

where R_s is the reflectivity of the HgI_2, air interface and α is the absorption coefficient. Assuming that each photon creates one carrier pair, the number of carriers generated per second is simply the power absorbed divided by the energy of one photon. Combining the above equations gives the

expression for the photocurrent as a function of distance between the contacts below.

$$I(y) = \frac{qP}{h\nu}(1-R-T)\left(\vartheta_e\left(1-exp\left(-\frac{\frac{w}{2}+y}{\vartheta_e}\right)\right)+\vartheta_h\left(1-exp\left(-\frac{\frac{w}{2}-y}{\vartheta_h}\right)\right)\right)$$

A section of the data from the scan at negative 1500 volts was extracted along the y direction for a fixed $x = 0$ and this along with the calculated current is presented in figure 4(B). The values of the parameters used in the above expression are given below.

w=0.95 cm	R_s=20%
V=1500 V	α=2.0x10^{-3} cm^{-1}
P=7.1 mW	$\mu\tau_e$=2.0x10^{-4} cm^2/V
$h\nu$= 3.14x10^{-19} J/sec	$\mu\tau_h$=1.7x10^{-5} cm^2/V

As can be seen in figure 4(B), the calculated photocurrent shows order of magnitude agreement with the experimental results. Several factors have not been accounted for in this model including the voltage drop across the contacts, the nonuniformity of the device as well as the mechanism responsible for carrier generation. These factors should be considered further.

Conclusion

A method has been presented that allows for the measurement of two dimensional maps of the photocurrent generated in mercuric iodide samples in a device geometry. These photocurrent maps were obtained for positive and negative applied bias. We observe general trends that appear to be consistent with the present understanding of the mechanisms of charge transport and collection in these devices including the one dimensional models used to describe these devices. This technique can be used with other materials, with other excitation sources, in pulsed mode, and may be quite useful in understanding the operation of x-ray and γ-ray spectrometers.

References

1. "Semiconductors for Room Temperature Nuclear Detectors", T.E. Schlesinger and R.B. James, editors, Volume **43** in Semiconductors and Semimetals, Academic Press, New York, 1995.
2. H.L. Malm, *IEEE Trans. Nucl. Sci.* **NS-19**, 263(1972).
3. R. Bube, *Phys. Rev.* **106**, 703(1957)
4. G.F. Knoll, D.S. McGregor, *Mat. Res. Symp. Proc.* **302**, 3(1993)
5. M. Schiefer, I. Beinglass, A. Holzer, G. Dishon, *IEEE Trans. Nucl. Sci.* **NS-24**, 148(1977)
6. R.A. Smith, "Semiconductors", 2nd edition, Cambridge University Press, Cambridge, 1978.

Figure Captions

Figure 1: Two dimensional photocurrent maps of 1 cm^2 cross sectional (AB) face of a mercuric iodide crystal with Pd contacts at a sequence of applied bias. The negative electrode is at the top of the maps. Note the enhanced photocurrent near the negative electrode.

Figure 2: Two dimensional photocurrent maps of 1 cm^2 cross sectional (AB) face of a mercuric iodide crystal with Pd contacts at a sequence of applied bias. The positive electrode is at the top of the maps. Note the region of enhanced photocurrent in the central region of the device as well as near the bottom (ground) electrode.

Figure 3: Two dimensional photocurrent maps showing the degree of reproducibility in these measurements. In (A) the bias is 1000 V but not only have eight hours elapsed between scans but the sample had also been subjected to a sequence of other biases (1500 V, 2000 V) between scans while in (B) the sample was held at the same bias, 2000 V, for the entire eight hours.

Figure 4: Geometry (A) used for model calculation of photocurrent and (B) calculated and measured photocurrent for a bias of 1500 V at x=0 as a function of y, the distance between the contacts.

Figure 1
Brunett et. al.

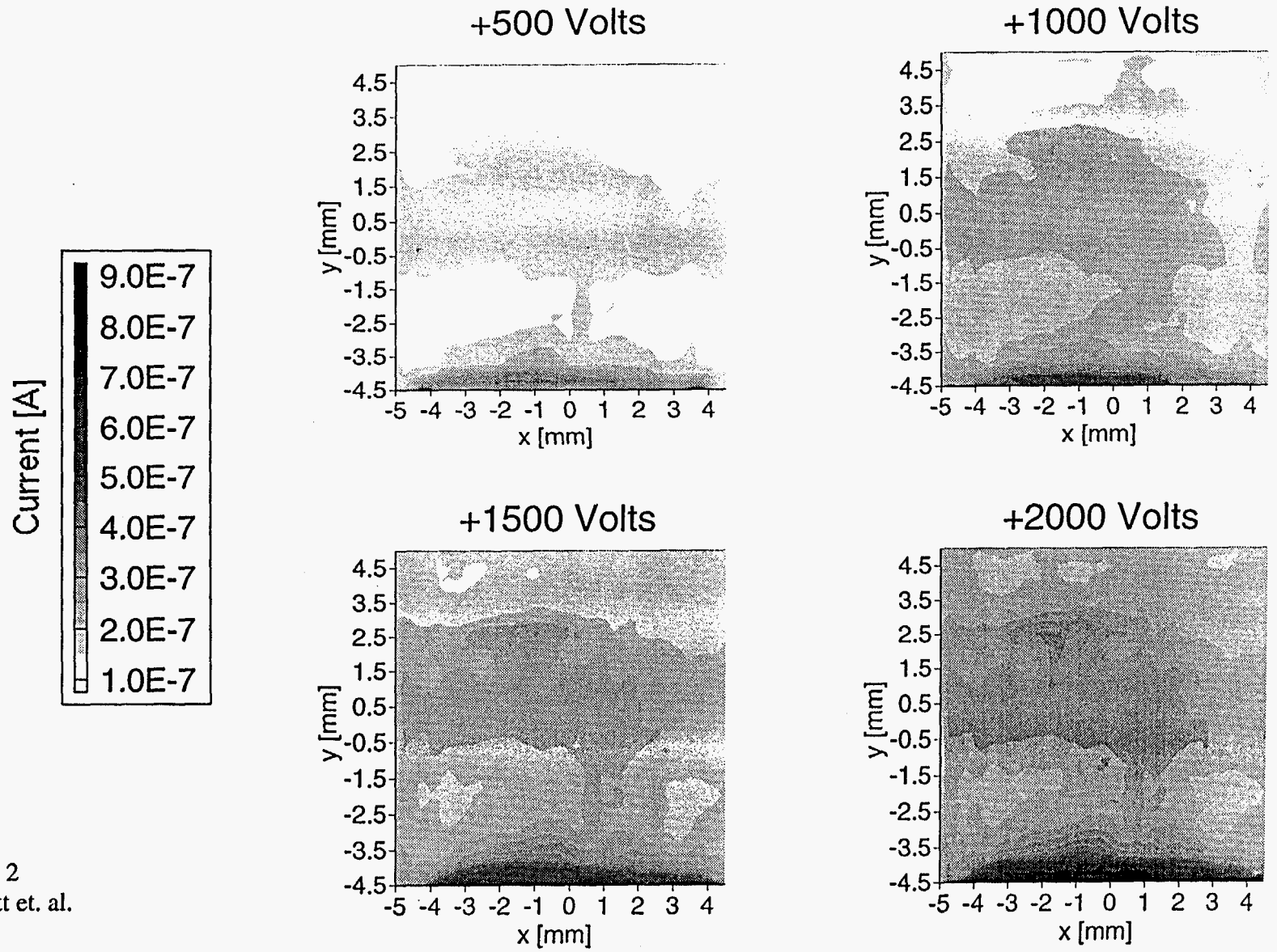

Figure 2
Brunett et. al.

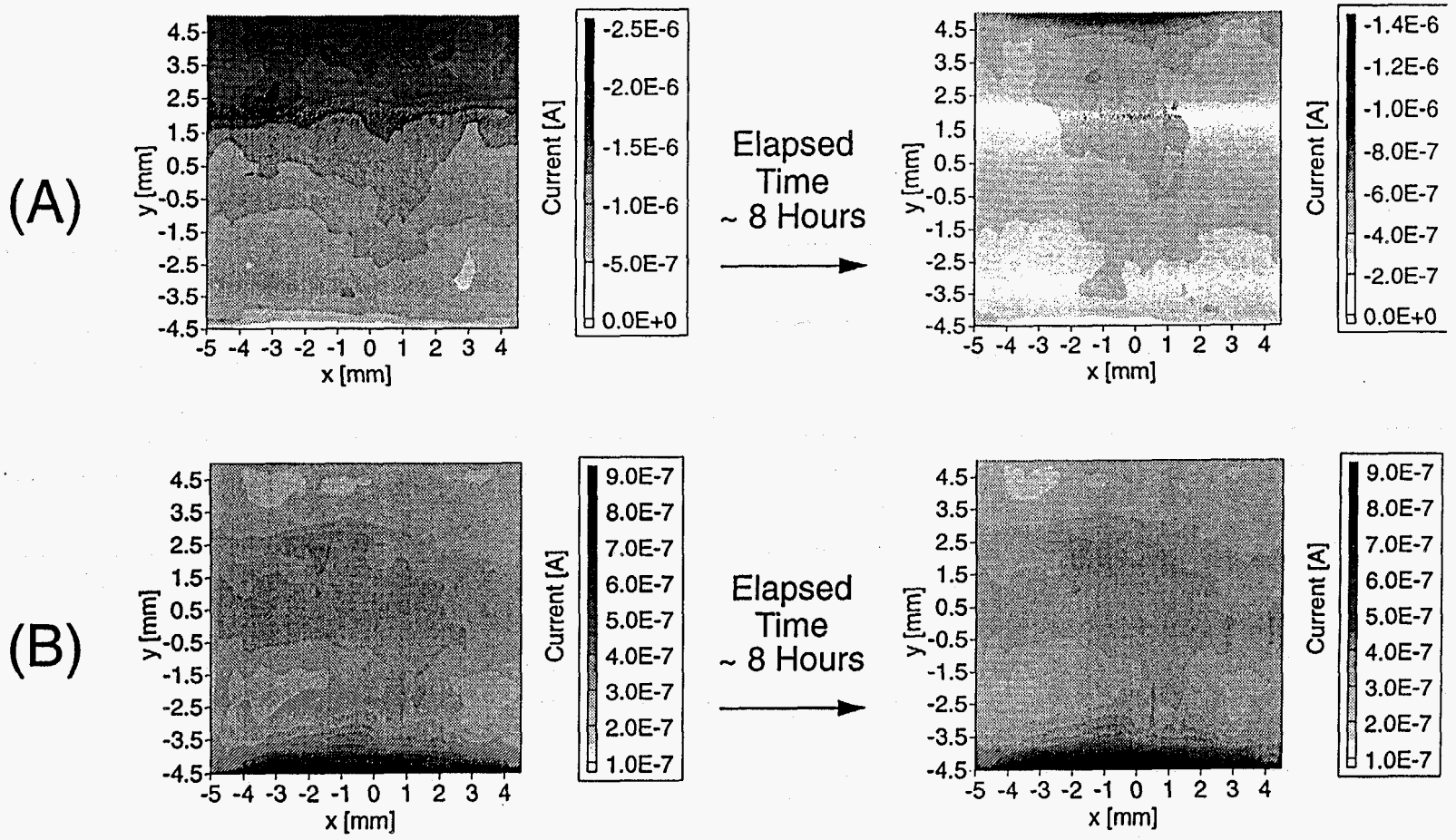

FIgure 3
Brunett et. al.

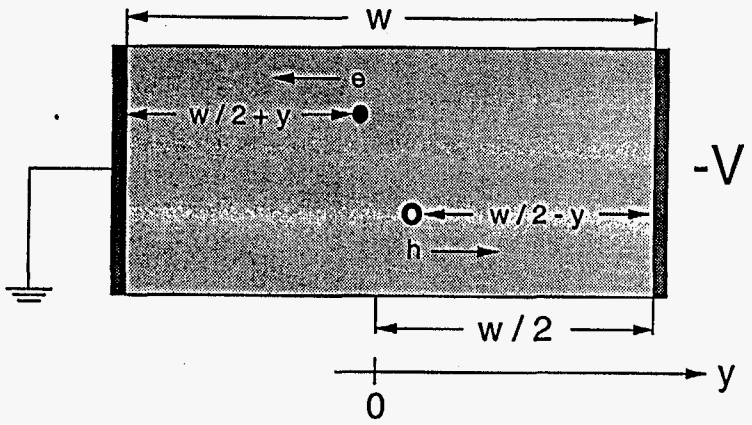

(A)

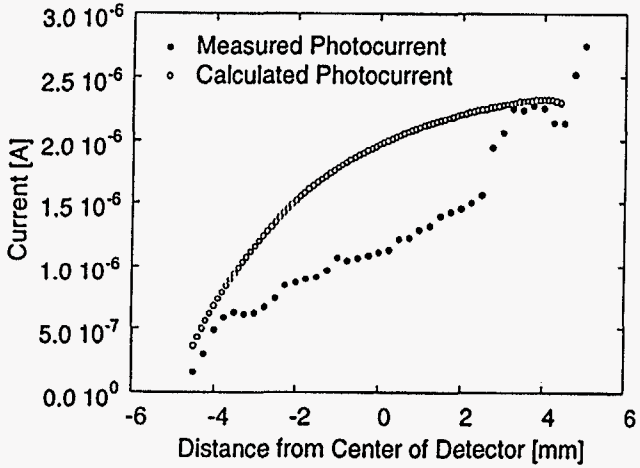

(B)

FIgure 4
Brunett et. al.

Intentionally Left Blank

UNLIMITED RELEASE

INITIAL DISTRIBUTION:

X.J. Bao (2)
TN Technologies, Inc.
Round Rock, TX, 78680

A. Burger (1)
Department of Physics
Fisk University
Nashville, TN, 37208

Y.C. Chang (1)
Department of Physics
University of Illinois
1110 West Green Street
Urbana, Illinois, 61801

J. Cook (1)
TN Technologies, Inc.
Round Rock, TX, 78680

M. Goorsky (1)
Department of Materials Science and Engineering
University of California at Los Angeles
Los Angeles, CA 94550

Hojun Yoon (1)
Department of Materials Science and Engineering
University of California at Los Angeles
Los Angeles, CA 94550

J.S. Iwanczyk (3)
Xsirius, Inc.
Camarillo, CA 93012

Warnick Kernan (1)
Remote Sensing Lab
4600 N. Hollywood Blvd., Bldg. 2211
Las Vegas, NV 89191

Glenn Knoll (1)
Dean, College of Engineering
University of Michigan
2309 EECS Building
Ann Arbor, MI 48109-2116

Richard Malenfant (1)
U.S. Department of Energy
Office of Research and Development, NN-20
1000 Independence Avenue, S.W.
Washington, D.C. 20585

Cal Moss (1)
Los Alamos National Laboratory
NIS-2, MS D436
Los Alamos, NM 87545

M. Natarajan (3)
TN Technologies, Inc.
Round Rock, TX, 78680

B.E. Patt (1)
Xsirius, Inc.
Camarillo, CA 93012

Karl Reinitz (1)
U.S. Department of Energy
Office of Research and Development, NN-20
1000 Independence Avenue, S.W.
Washington, D.C. 20585

M. Roth (1)
Graduate School of Applied Science
Hebrew University of Jerusalem
Jerusalem, Israel, 9190

Bob Scarlett (1)
Los Alamos National Laboratory
MS D460
Los Alamos, NM 87545

T. E. Schlesinger (2)
Department of Electrical and Computer Engineering
Carnegie Mellon University
Pittsburgh, PA 15213

Jack Trombka (1)
Senior Goddard Fellow
Goddard Space Flight Center
MC 691, Bldg. 2, Rm. 235
Greenbelt, Maryland 20771

H. Yao (1)
Department of Electrical Engineering
University of Nebraska
Lincoln, Nebraska, 68588

MS 9161	R.J. Anderson (1)
MS 9402	A. Antolak (1)
MS 9162	Dan Morse (1)
MS 9671	E. Cross (1)
MS 9671	H. Hermon (1)
MS 9409	R.B. James (4)
MS 9409	J.C. Lund (1)
MS 9161	J. Markakis (1)
MS 9402	D. Medlin (1)
MS 9671	D.S. McGregor (1)
MS 9671	R.W. Olsen (1)
MS 9404	C. Perrino (1)
MS 9161	A. Pontau (1)
MS 9161	M. Schieber (2)
MS 9404	E. Soria (1)
MS 9409	R. Stulen (1)
MS 9161	J. VanScyoc (1)
MS 9162	Larry Franks (1)
MS 9403	Jim Wang (1)
MS 9404	George Buffleben (1)
MS9161	Don Cowgill (1)
MS9004	J. Vitko (1)
MS9420	Al West (1)
MS0571	R. L. Ewing (1)
MS0768	R. Moya (1)
MS0351	Robert C. Hughes (1)
MS0469	J. M. Taylor (1)
MS0656	D. L. Mangan (1)
MS9141	Ann Freudendahl (1)
MS0107	Valerie Portillo (1)
MS1380	Rick Calvert (1)
MS1380	David Larson (1)
MS1380	Donna Rix (1)
MS0899	Technical Library, 4414 (4)
MS9021	Technical Communications Department, 8815, for OSTI (10)
MS9021	Technical Communications Department, 8815/Technical Library, MS0899, 4414 (1)
MS9018	Central Technical Files, 8940-2 (3)